DEVELOPMENT OF A PERFORMANCE-BASED SEISMIC DESIGN PHILOSOPHY FOR MID-RISE WOODFRAME CONSTRUCTION

NEESWOOD

NUMERICAL AND EXPERIMENTAL INVESTIGATION OF THE SEISMIC RESPONSE OF LIGHT-FRAME WOOD STRUCTURES

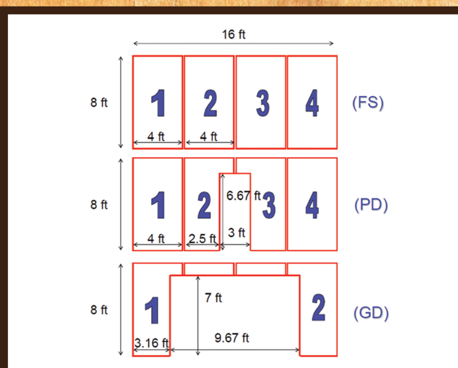

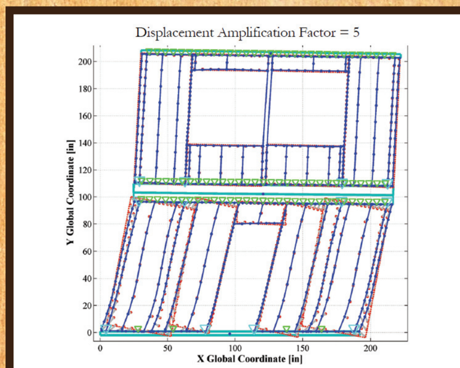

By

Ioannis P. Christovasilis and Andre Filiatrault

Technical Report MCEER-11-0001 ▪ August 8, 2011

This research was conducted at the University at Buffalo, State University of New York and was supported by the National Science Foundation under Grant No. CMMI-0529903 (NEES Research) and CMMI-0402490 (NEES Operations).

Sponsored by the
National Science Foundation
NSF Grant Number CMMI-0529903 and CMMI-0402490

Project Title
Development of a Performance-Based Seismic Design
Philosophy for Mid-Rise Woodframe Construction

Project Team
Colorado State University
University of Delaware
University at Buffalo, State University of New York
Rensselaer Polytechnic Institute
Texas A&M University

Web Site
http://jwv.eng.ua.edu/neeswood_reports.html

DISCLAIMER

NEESWood Report No. 07

Numerical and Experimental Investigation of the Seismic Response of Light-Frame Wood Structures

by

Ioannis P. Christovasilis[1] and Andre Filiatrault[2]

Publication Date: August 8, 2011
Submittal Date: January 15, 2011

Technical Report MCEER-11-0001

NSF Grant Numbers CMMI-0529903 and CMMI-0402490
George E. Brown, Jr. Network for Earthquake Engineering Simulation (NEES)
Program of the National Science Foundation

1 Post-Doctoral Researcher, School of Civil Engineering, Department of Structural Engineering, Institute of Structural Analysis & Aseismic Research, National Technical University of Athens; Former Graduate Student, Department of Civil, Structural and Environmental Engineering, University at Buffalo, State University of New York
2 Professor, Department of Civil, Structural and Environmental Engineering, University at Buffalo, State University of New York

MCEER
University at Buffalo, State University of New York
Red Jacket Quadrangle, Buffalo, NY 14261
Phone: (716) 645-3391; Fax (716) 645-3399
E-mail: *mceer@buffalo.edu*; WWW Site: *http://mceer.buffalo.edu*

Project Overview

NEESWood: Development of a Performance-Based Seismic Design Philosophy for Mid-Rise Woodframe Construction

While woodframe structures have historically performed well with regard to life safety in regions of moderate to high seismicity, these types of low-rise structures have sustained significant structural and nonstructural damage in recent earthquakes. To date, the height of woodframe construction has been limited to approximately four stories, mainly due to a lack of understanding of the dynamic response of taller (mid-rise) woodframe construction, nonstructural limitations such as material fire requirements, and potential damage considerations for nonstructural finishes. Current building code requirements for engineered wood construction around the world are not based on a global seismic design philosophy. Rather, wood elements are designed independently of each other without considering the influence of their stiffness and strength on the other structural components of the structural system. Furthermore, load paths in woodframe construction arising during earthquake shaking are not well understood. These factors, rather than economic considerations, have limited the use of wood to low-rise construction and, thereby, have reduced the economical competitiveness of the wood industry in the U.S. and abroad relative to the steel and concrete industry. This project sought to take on the challenge of developing a direct displacement based seismic design philosophy that provides the necessary mechanisms to safely increase the height of woodframe structures in active seismic zones of the U.S. as well as mitigating damage to low-rise woodframe structures. This was accomplished through the development of a new seismic design philosophy that will make mid-rise woodframe construction a competitive option in regions of moderate to high seismicity. Such a design philosophy falls under the umbrella of the performance-based design paradigm.

In Year 1 of the NEESWood Project, a full-scale seismic benchmark test of a two-story woodframe townhouse unit that required the simultaneous use of the two three-dimensional shake tables at the University of Buffalo's NEES node was performed. As the largest full-scale three-dimensional shake table test ever performed in the U.S., the results of this series of shake table tests on the townhouse serve as a benchmark for both woodframe performance and nonlinear models for seismic analysis of woodframe structures. These efficient analysis tools provide a platform upon which to build the direct displacement based design (DDBD) philosophy. The DDBD methodology relies on the development of key performance requirements such as limiting inter-story deformations. The method incorporates the use of economical seismic protection systems such as supplemental dampers and base isolation systems in order to further increase energy dissipation capacity and/or increase the natural period of the woodframe buildings.

The societal impacts of this new DDBD procedure, aimed at increasing the height of woodframe structures equipped with economical seismic protection systems, is also investigated within the scope of this NEESWood project. Following the development of the DDBD philosophy for mid-rise (and all) woodframe structures, it was applied to the seismic design of a mid-rise (six-story) multi-family residential woodframe condominium/apartment building. This mid-rise woodframe structure was constructed and tested at full-scale in a series of shake table tests on the E-Defense (Miki) shake table in Japan. The use of the E-Defense shake table, the largest 3-D shake table in the world, was necessary to accommodate the height and payload of the mid-rise building.

The research presented in this report focuses on the development of a numerical framework, suitable for nonlinear inelastic, static and dynamic two-dimensional analysis of light-frame wood structures. The framework was validated by simulation examples based on existing experimental results and shake table tests carried out as part of this study as well as other experimental investigations available in the literature. The purpose of the shake table tests was: (1) to benchmark the dynamic characteristics and the seismic performance of a low-rise wood structure with realistic dimensions under various base input intensities, representative of both ordinary and near-field ground motions in southern California, and (2) to investigate the effect of nonstructural components on the seismic response of the test structure. These examples demonstrated the capability of the model to simulate load paths in the structure and predict variations in strength, stiffness and energy dissipation properties of the lateral-load-resisting system. The analysis illustrates that the proposed framework can provide reliable response predictions for structural systems incorporating different geometric configurations, anchorage conditions and gravity loading.

Project Team

John W. van de Lindt, Ph.D., Principal Investigator: Professor and Garry Neil Drummond Endowed Chair, Department of Civil, Construction and Environmental Engineering, The University of Alabama, Box 870205, Tuscaloosa, AL 35487-0205; *jwvandelindt@eng.ua.edu;* formerly of Colorado State University.

Rachel A. Davidson, Ph.D., Co-Principal Investigator: Associate Professor, Department of Civil and Environmental Engineering, University of Delaware, Newark, DE 19716-3120; *rdavidso@udel.edu.*

Andre Filiatrault, Ph.D. Eng., Co-Principal Investigator: Professor, Department of Civil, Structural, and Environmental Engineering, University at Buffalo, State University of New York, Buffalo, NY 14260; *af36@buffalo.edu*.

David V. Rosowsky, Ph.D., Co-Principal Investigator: Professor and Dean of Engineering, Department of Civil and Environmental Engineering, Rensselaer Polytechnic Institute, 110 8th Street, Troy, NY 12180-3590; *rosowd@rpi.edu*; formerly of Texas A&M University.

Michael D. Symans, Ph.D., Co-Principal Investigator: Associate Professor, Department of Civil and Environmental Engineering, Rensselaer Polytechnic Institute, 110 8th Street, Troy, NY 12180-3590; *symans@rpi.edu*.

ABSTRACT

In support of the performance-based seismic design procedures for light-frame wood structures, developed within the NSF-funded NEESWood Project, a dual study with experimental and analytical components was conducted.

In the context of the experimental investigation, a full-scale, two-story, light-frame wood townhouse building was tested on the twin relocatable tri-axial shake tables operating in unison, at the University at Buffalo UB-NEES site. The test structure was designed according to modern US engineered seismic design requirements (ICBO 1988) and constructed according to applicable practices in the 80's in California. Four different test phases were conducted, associated with additional components in the building configuration, as the test structure initially featured only the structural shear walls considered in the design, and progressively interior (gypsum wallboard) and exterior (stucco) wall finishes were installed. The main objectives were to benchmark the dynamic characteristics and the seismic performance of a low-rise townhouse building with realistic dimensions under various base input intensities, representative of both ordinary and near-field ground motions in southern California, and to investigate the effect of non-structural components on the seismic response of the test structure. The test structure performed well under both DE and MCE levels of shaking, satisfying the collapse prevention objective, inherent in code-compliant seismic design. Moreover, the test results demonstrated the beneficial effect of wall-finishes on improving the seismic response of the structure, increasing the stiffness and the strength of the individual shear walls.

The analytical task focused on the development, implementation and validation of a novel numerical framework, suitable for nonlinear inelastic, static and dynamic two-dimensional (2D) analysis of light-frame wood structures. The 2D building model is based on a sub-structuring approach that considers each floor diaphragm as rigid body with three kinematic, and potentially dynamic, degrees-of-freedom (DOF). A sub-structure model is developed for each individual single-story wall assembly that interacts with the adjacent diaphragms and generates the resisting quasi-static internal forces. The 2D shear wall model takes explicit consideration of all sheathing-to-framing connections and offers the option to simulate: (i) deformations in

the framing members, (ii) contact/separation phenomena between framing members and diaphragms, and (iii) any anchoring equipment (i.e. anchor bolts, holdown devices), typically installed in light-frame shear walls to develop a vertical load path that resists overturning moments. Corotational descriptions are used to solve for displacement fields that satisfy the equilibrium equations in the deformed configuration, accounting for geometric nonlinearity (large rotations – small deformations) and P-Δ effects. These attributes result in a nonlinear element capable of capturing the lateral response of shear walls up to their complete failure and, thus, the side-sway collapse of the structure. To validate the proposed numerical framework, a number of simulation examples are presented, based on existing experimental results from pseudo-static tests of single- and two-story full-scale shear wall specimens, as well as shake-table tests of a single-story full-scale structure. These examples demonstrate the capability of the model to accurately simulate load paths in the structure and successfully predict variations in strength, stiffness and energy dissipation properties of the lateral-load-resisting system. The complete set of numerical analyses presented in this study illustrates the versatility of the proposed sub-structure model to provide reliable response predictions for structural systems incorporating different geometric configurations, anchorage conditions and gravity loading.

ACKNOWLEDGEMENTS

The authors gratefully acknowledge the Principal Investigators of the NEESWood project, John van de Lindt, University of Alabama; David Rosowsky, Rensselaer Polytechnic Institute; Micheal Symans, Rensselaer Polytechnic Institute; and Rachel Davidson, University of Delaware. The authors also thank Assawin Wanitkorkul, Connell Wagner (Thailand), for his invaluable contribution in the planning, preparation and execution of the UB Benchmark Tests, and Weichiang Pang, Clemson University, for his contribution to the implementation of the numerical model. Finally, the contribution of the staff of the Structural Engineering Earthquake Simulation Laboratory (SEESL) for their support in the execution of the experimental part of this project is gratefully acknowledged.

Financial support for this project was provided by the National Science Foundation under Grant Nos. CMMI-0529903 (NEES Research) and CMMI-0402490 (NEES Operations). This support is greatly appreciated.

TABLE OF CONTENTS

TABLE OF CONTENTS (CONT'D)

TABLE OF CONTENTS (CONT'D)

TABLE OF CONTENTS (CONT'D)

LIST OF FIGURES

LIST OF FIGURES (CONT'D)

List of Figures (Cont'd)

LIST OF FIGURES (CONT'D)

LIST OF FIGURES (CONT'D)

LIST OF FIGURES (CONT'D)

LIST OF FIGURES (CONT'D)

LIST OF TABLES

LIST OF TABLES (CONT'D)

CHAPTER 1: INTRODUCTION

1.1 Description and Review of the Seismic Behavior of Light-Frame Wood Structures

The research work presented in this report describes the numerical and experimental investigations of the seismic response of light-frame wood structures. These low-rise residential buildings, widely used across North America, typically incorporate sheathed light-frame wood shear walls as a lateral-load-resisting system. Since light-frame wood construction represents about 90% of the residential buildings in the United States and 99% of residences in California (CUREe 1998), a substantial portion of these structures is located in regions of moderate-to-high seismicity and is potentially susceptible to significant earthquake shaking during their life-spans.

Light-frame wood buildings consist of vertical (shear wall) and horizontal (floor) wood diaphragms. Figure 1.1a illustrates a single-story light-frame wood structure. Floor diaphragms distribute gravity and seismically induced loads to the wood shear walls and the seismic behavior of light-frame wood structures is dominated by the racking (shear) deformation of the shear walls along the horizontal directions parallel to the wall planes*.

A wood shear wall, illustrated in Figure 1.1b, typically consists of (i) the framing members inter-connected with framing-to-framing connectors, (ii) the sheathing panels, and (iii) the sheathing-to-framing connectors (nails), typically distributed at a specified spacing along the panel edges. The in-plane lateral resistance is generated at the numerous sheathing-to-framing connections and the developed forces are directly related to the displacement field of the connectors, defined as the difference between the deformations of the panel sheathing and the wood framing (Figure 1.2a,b). It is the resultant connection forces acting on the framing that stabilizes the shear walls under the lateral loads transferred to the sill (bottom) and top plates of the wood frame from the floor diaphragms (Figure 1.2c,d).

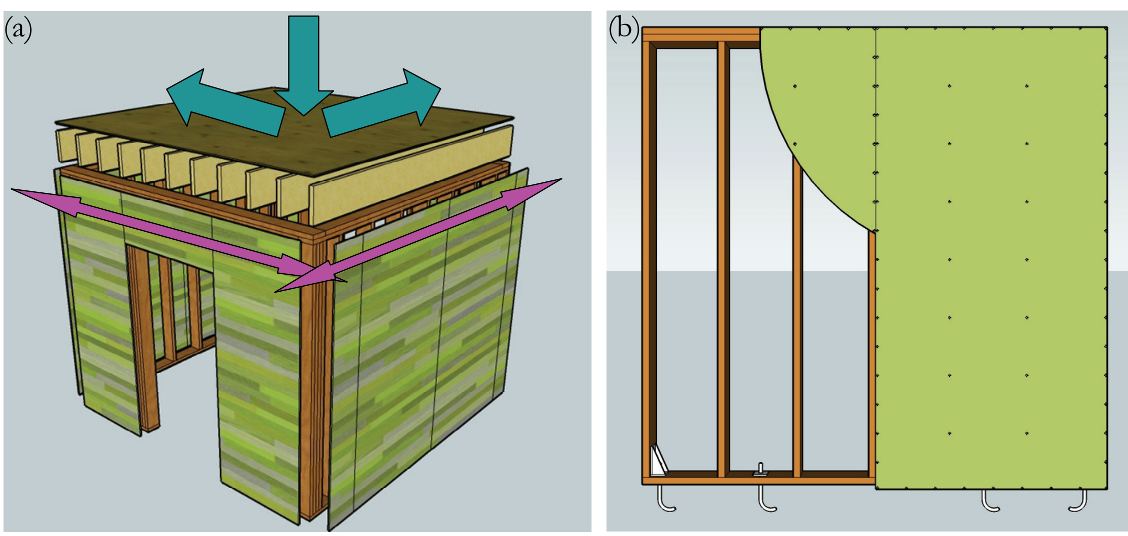

Figure 1.1 Illustration of (a) a Single-Story Light-Frame Wood Structure, and (b) a Wood Shear Wall

* Typically, the lateral resistance of shear walls along the horizontal direction perpendicular to the wall plane is neglected in seismic design of light-frame wood buildings. The basic points provided in this discussion refer to force and displacement fields solely along the wall plane.

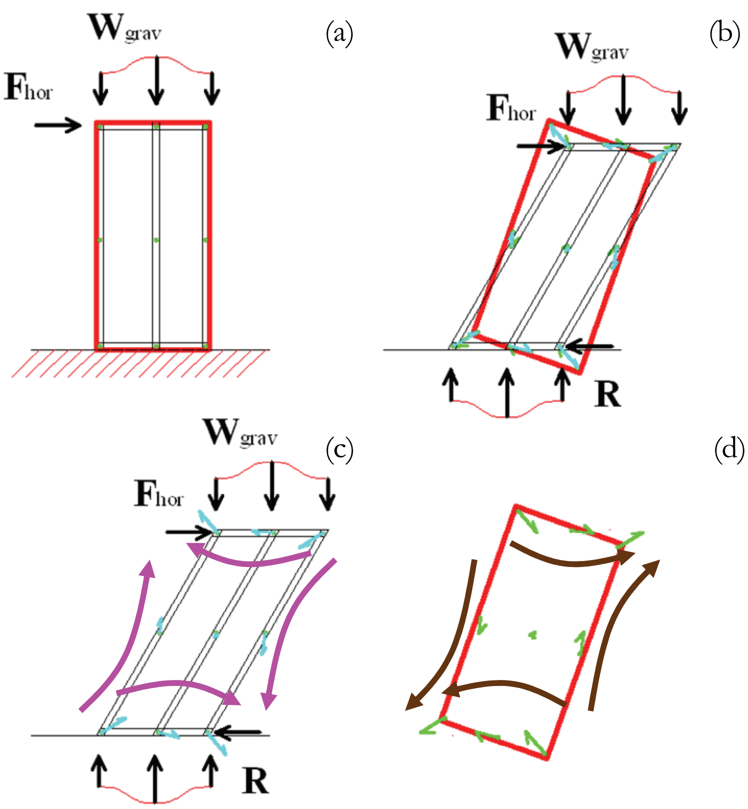

Figure 1.2: Deformation and Free-Body Diagram of a Single-Panel Shear Wall under External Loads

The pure racking deformation of wood shear walls is associated with significant hysteretic damping and dissipated energy by the sheathing-to-framing connections. The force-displacement response of sheathing-to-framing connections, under cyclic loading, exhibits pinching characteristics as well as strength and stiffness degradation (Figure 1.3a), while these characteristics can also be identified in the global cyclic response of light-frame wood shear walls (Figure 1.3b). However, there are other modes of deformation, such as rocking or frictional sliding, that can affect the global lateral stiffness, strength, and energy dissipation characteristics of the inter-story wood walls, and subsequently modify the seismic response of the whole structure. The level of participation of secondary deformation modes other than pure racking kinematic distortion of the frame is related primarily to the load-deformation characteristics of the framing-to-framing connections as well as the shear-transferring and vertical load-anchoring devices between shear walls and floor diaphragms. Loads between light-frame wood members are transferred mainly through bearing and friction, but tensile forces that are developed under equilibrium to lateral forces and that overcome the gravity compressive loads may cause members to detach, exposing (i) the framing-to-framing connectors to tensile deformation fields (separation phenomena) coupled with shear-transferred loads, and (ii) the sheathing-to-framing connectors to modified displacement orbits to accommodate the local discontinuity of the wood framing. These phenomena modify the load paths from the structure to the ground and are associated in most cases with reduced global stiffness and energy dissipation capability.

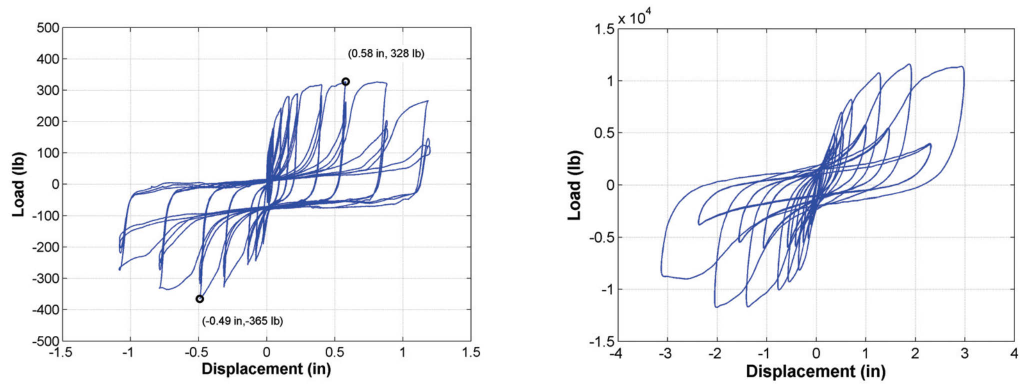

Figure 1.3 Qualitative Demonstration of the Cyclic Response of (a) a Sheathing-to-Framing Connection (from Ekiert and Hong 2006), and (b) a Light-Frame Wood Shear Wall (from Pardoen *et al.* 2003)

Another factor that can affect the seismic behavior and excite secondary modes of deformation is the effect of nonstructural wall finishes. The installation, for example, of interior gypsum wallboard on structural wood shear walls may increase their lateral stiffness and strength, but may also lead to violation of fundamental capacity design principles in cases where the system overstrength produces demands that exceed the actual, as well as the expected, capacity of critical connections.

Therefore, the seismic response of light-frame wood buildings is complex and the seismic performance of new and existing light-frame wood buildings in seismic-prone areas will be affected by various factors, such as:

i. The construction era and, accordingly, the quality of materials and the availability of seismic design and construction standards.

ii. The consideration or not of engineering methods in the design process – since a part of the existing light-frame wood houses are based on non-engineering construction – and the effectiveness of the applicable design codes.

iii. The construction quality and level of detailing in meeting the specified connections or structural details.

iv. The types of interior and exterior wall finish materials and the methods of attachment to the structural members.

v. The variability in mechanical properties of wood due to the inherent inhomogeneity and anisotropy.

As stated wisely in CUREe (1998): *"The seismic response of light-frame wood buildings is largely controlled by the connections of the numerous pieces of material that make up a structure and by the quality and workmanship of these connections."*

1.2 Performance of Light-frame Wood Structures in Past Earthquakes

While light-frame wood buildings have historically performed well with regard to life safety requirements in regions of moderate-to-high seismicity, these types of low-rise structures have sustained significant structural and nonstructural damage in recent earthquakes.

Falk and Soltis (1988), summarizing observations from damage of light-frame wood buildings from past earthquakes, reported the susceptibility to damage of (i) two-story and split-level homes with large garage openings at ground level (1971 San Fernando Earthquake, Figure 1.4a), and (ii) wood houses with short wood stud (cripple) walls in the substructure (1983 Coalinga and 1984 Halls Valley Earthquakes). Other observations from these three seismic events included failures at sill plate connections and homes shifting off foundations. The authors concluded that properly constructed light-frame wood buildings performed well, but indicated prophetically that, in the United States, little work had been performed on the ductility of wood structures.

Damage in light-frame wood buildings was also observed after the 1989 Loma Prieta Earthquake (Figure 1.4b,c), but the 1994 Northridge Earthquake has been recognized as the seismic event that actually highlighted the seismic vulnerability of residential light-frame wood construction. It is indicative that out of the 25 fatalities caused by building damage during the Northridge Earthquake, 24 occurred in light-frame wood buildings (EQE 1995). Most of the fatalities were related to soft/first story collapse of apartment buildings with tuck-under garage (Figure 1.4d), and few to collapse of hillside houses inadequately supported on steep foundations (Hall *et al.* 1995). Extensive damage in structural components and nonstructural wall finishes of light-frame wood buildings was the main contributor to the temporary displacement of 100,000 residents, which persisted as a long-term displacement of 50,000 residents (Perkins *et al.* 1998). The property loss to light-frame wood construction as a result of this single seismic event was estimated at $20 billion (Kircher *et al.* 1997), and exceeded the loss to any other type of construction. Of the $12.3 billion paid out for insurance claims, 78% has been for residential claims, almost all of which was associated with light-frame wood construction (Kircher *et al.* 1997).

Figure 1.4 (a,b,d) Collapse of Two-Story Buildings due to Inadequate Lateral Strength at the Ground Level, and (c) Excessive Lateral Residual Displacements at the First Story of a Mid-Rise Building. All Cases are Related to a Soft-Story Mechanism (Photo Credit: (a,b,c) USGS, (d) Wikipedia)

1.3 Influence of Northridge Earthquake on Current State of Knowledge

The significant damage experienced by light-frame wood construction during the 1994 Northridge Earthquake highlighted the need for a more fundamental understanding of the seismic behavior of structural and nonstructural members and the load paths arising during earthquake shaking. Although studies on the seismic analysis of light-frame wood structures had been conducted for more than twenty years, the state of knowledge was not as advanced as for steel or concrete structures, because of the relative lack of research attention to wood buildings, based on their good historical performance.

"Although 99% of the residences in California are of woodframe construction, there has been surprisingly little research focused on improving their earthquake resistance. The woodframe building's earthquake problems have been overlooked and under-researched. It's a kind of construction that appears to be simple but is actually complex. The seismic folklore in California has led people to believe that wood buildings perform well in earthquakes almost by accident, without the need to test and design them as thoroughly as steel, concrete, or masonry buildings. The Northridge Earthquake proved that assumption false. Even some well-engineered wood buildings suffered surprising amounts of damage."

[Robert Reitherman, CUREe Executive Director (CUREe 1998)]

Furthermore, the huge financial loss and social disruption, as a result of a single seismic event, led the structural engineering community to the realization that the code-provided and minimum-specified level of aseismic protection, associated solely with prevention of substantial loss of life, may not be socially and economically acceptable, for a wide class of structures. Light-frame wood buildings that responded deep in the inelastic range but were not collapse hazards, suffered either from unrepairable level of structural damage, based on engineering or economical considerations, or from levels of structural or/and non-structural damage that questioned the financial profitability of retrofitting them. It was recognized that emphasis should be given, initially, in the production of reliable estimates of loss-hazards for existing and new construction and, secondly, in the development of effective decision-support methods that would lead to economically feasible solutions.

In 1998, the Federal Emergency Management Agency (FEMA) funded the CUREe-Caltech Woodframe Project: "Earthquake Hazard Mitigation of Woodframe Construction". It was a Hazard Mitigation Grant Program award to the California Institute of Technology, with the premise of developing reliable and economical ways of improving woodframe building performance in earthquakes (CUREe 1998). Project participants included many universities, practicing engineers and industry representative, under management of California Universities for Research in Earthquake Engineering (CUREe). As part of the project, extensive experimental programs (from component quasi-static to full-scale shake-table testing) and analytical studies were carried out, focusing on various aspects that affect the local or global seismic behavior of light-frame wood building components. Field investigations were also conducted to examine the earthquake performance of light-frame wood buildings in earthquakes and primarily the Northridge Earthquake. Additionally, other studies were conducted using performance-based concepts to convert physical performance for different seismic demands and associated risks into economic terms and establish a better understanding of the related long-term financial loss under the uncertainty of earthquake shaking. The multi-faceted nature of the project allowed the development of design recommendations and retrofit techniques and the inclusion of important findings in building codes and standards, while education and outreach programs synthesized and presented information in various formats to reach different audiences and to address different topics. The CUREe-Caltech Woodframe Project produced a number of valuable contributions and left a rich heritage of experimental, analytical and economical studies on the earthquake, and the associated life and loss, hazard mitigation of light-frame wood construction.

1.4 Research Motivation

1.4.1 The NEESWood Project

To date, the height of light-frame wood construction has been limited to approximately four stories, mainly due to the lack of understanding of the dynamic response of taller (mid-rise) woodframe construction, nonstructural limitations such as material fire requirements, and potential damage considerations for nonstructural wall finishes. Despite the complexity in the response of light-frame wood structures, this kind of systems has been traditionally designed using simple methods of analysis. Current building code requirements for engineered wood construction around the world are not based on a global seismic design philosophy. Rather, wood elements are designed independently of each other without consideration of the influence that their stiffness and strength have on the other structural components of the structural system. These factors, rather than economic considerations, have limited the use of wood to low-rise construction and, thereby, have reduced the economical competitiveness of the wood industry in the United States and abroad relative to the steel and concrete industry. As a result, the NEESWood Project: "Developing Performance-Based Seismic Design Philosophy for Mid-Rise Light-frame Wood Construction" was developed through the George E. Brown Junior Network for Earthquake Engineering Simulation (NEES) program of the National Science Foundation to address these shortcomings of light-frame wood construction. The NEESWood Project seeks to take on the challenge of developing a seismic design philosophy that will provide the necessary mechanisms to safely increase the height of light-frame wood structures in active seismic zones of the U.S. as well as mitigating damage to low-rise light-frame wood structures. This is being accomplished through the development of a new seismic design philosophy that will make mid-rise light-frame wood construction a reality in regions of moderate-to-high seismicity. Such a design philosophy falls under the umbrella of the performance-based design paradigm.

As part of the NEESWood Project, an experimental program that involved the three-dimensional shake-table testing of a full-scale two-story light-frame wood townhouse building was conducted at the University at Buffalo. The test structure, designed and constructed according to applicable practices in the 80's in California, represented one of the largest building specimens ever tested under three-dimensional earthquake simulation and utilized both twin shake tables at the Structural Engineering and Earthquake Simulation Laboratory (SEESL) at the University at Buffalo for over 9 months. The experimental program, extended in 5 test phases associated with different structural configurations of the building, was selected as such to provide a wide set of recorded data that can enable observation, identification and quantification of fundamental aspects that affect the seismic performance of a light-frame wood building with realistic dimensions, under increased levels – beyond design-basis – of shaking. The qualitative and quantitative observations from the benchmark test results can be directly applicable to performance-based design and analysis procedures, conducted within the NEESWood Project. The testing procedures and the main results of the processed data have been documented by Christovasilis *et al.* (2009a) and are summarized in Chapter 3 of this report.

1.4.2 The ATC-63 Project

While experimental and analytical work on the seismic design and analysis of structures has been advancing, the collapse assessment of structural systems has been of particular research interest, since collapse prevention is the primary performance level implied in code design standards for the maximum considered earthquake level of shaking (MCE event in U.S. code practice). The recently completed FEMA-funded ATC-63 Project: "Quantification of Building System Performance and Response Parameters" (FEMA P695 2009) managed by the Applied Technology Council (ATC) is aimed at quantifying design parameters that have been traditionally used in force-based seismic design practice, such as the force-reduction factor (or R factor). These parameters are directly related to assumptions that simplify the seismic design process of structures that respond in the inelastic range. The methodology described in the ATC-63 Project involves dynamic response-history analyses of nonlinear numerical models under increasing amplitude of earthquake shaking, until collapse is reached. The results of the multi-level sets of analyses are integrated in a codified probabilistic framework to treat epistemic and aleatory uncertainties related to the accuracy of the numerical model and the level of seismic demand. The final outcome of this procedure yields a deterministic quantification of the seismic performance, with respect to a collapse prevention specified level of performance, of a group of archetype buildings with the same lateral-load-resisting system, under an ensemble of MCE events. Thus, the ATC-63 methodology attempts to specify acceptable force-reduction factors for newly developed structural systems, using a performance-based approach that will provide *"equivalent safety against collapse in an earthquake, comparable to the inherent safety against collapse intended by current seismic codes, for buildings with different seismic-force-resisting systems,"* as stated in the general project scope of FEMA P695 (2009).

As part of the ATC-63 Project, an analytical task assigned to the research group at the University at Buffalo consisted of the implementation of the proposed methodology in light-frame wood buildings that incorporated shear walls as a seismic-force-resisting system. Two index buildings were considered for complementary three-dimensional dynamic analyses (Christovasilis *et al.* 2009b), and 16 archetype buildings were considered for the two-dimensional dynamic analyses described in FEMA P695. The numerical models used in these series of nonlinear dynamic analyses – developed under the CUREe-Caltech Woodframe Project by Folz and Filiatrault (2001, 2004a, 2004b) – demonstrated high computational efficiency, because of the simplified numerical formulation that involves lumping the hysteretic behavior of shear walls in equivalent SDOF nonlinear shear springs, but also exposed limitations, due to (i) the inability to predict the reduction in stiffness and strength of shear walls with high aspect ratio, and (ii) the neglection of second order P-Δ effects due to gravity loads. The versatility of the ATC-63 methodology permits to explicitly account for these limitations by assigning a greater modeling uncertainty for archetypes incorporating high aspect ratio walls, as demonstrated in the example application presented in FEMA P695. Regardless of that, the use of more reliable numerical models that account for geometric nonlinearity and simulate additional secondary modes of deformation of light-frame wood shear walls will lead to more accurate estimates of the safety against collapse intended by current seismic codes.

In a paper on challenges and progress in performance-based earthquake engineering, Krawinkler (1999) pointed that the objective of seismic engineering should be to design and build better and more economical structures, and performance-based engineering could serve well under this cause. One important conclusion, based on the discussion provided by Krawinkler (1999), is that performance-based engineering is the starting point for structural engineers to promote a more comprehensive importance of the integrity of structures under any human- or nature-imposed excitation. Yet, in order to implement it, structural engineers must first develop reliable tools for predicting, quantifying and assessing the performance analytically. Analyzing the research objectives that will lead to the development of performance-based engineering, Krawinkler (1999) mentions that, among others, research studies should focus on:

"The development of more reliable analytical procedures that permit a performance evaluation of a wide variety of soil-foundation-structure systems and their components, of nonstructural systems, and of building contents, at all levels of performance, ranging from cosmetic structural or nonstructural damage to structural degradation leading to collapse, and with due consideration given to the uncertainties inherent in the assessment of seismic demands and capacities."

1.5 Scope and Objectives

The scope of the NEESWood Benchmark Tests has been partially discussed in the previous section. The main objectives are:

- To benchmark the dynamic characteristics and the seismic performance of a code-compliant building with realistic dimensions under various base input intensities, representative of both ordinary and near-field ground motions in southern California, and to assess the seismic response under equivalent design and maximum earthquake levels of shaking.

- To investigate the effect of non-structural components on the seismic response of the test structure.

- To identify and document damage in structural and non-structural components by conducting a detailed damage survey after the completion of each seismic test.

The analytical part of the research work described in this report focuses on the development and validation of a novel numerical framework, suitable for nonlinear, inelastic, static and dynamic analysis of 2D models of light-frame wood buildings. The research objectives are:

- The development of an analytical framework to describe the static equilibrium equations of light-frame wood shear walls, considering geometric nonlinearity associated with rotational DOF assuming small deformations, and to solve the static equilibrium equations in the deformed configuration. Primary importance is given to the capability to simulate additional modes of deformation of the wood framing, such as rocking and flexural response, as well as anchoring uplift-restrain devices that are typically installed in such systems. The target is to achieve good predicting capabilities of shear walls with various anchoring conditions (engineered or conventional construction) at a maximized range of global inter-story displacements (small to large, near collapse, story drifts).

- The development of an in-house dedicated computer program to implement the analytical procedures in a numerical framework for multi-step monotonic or cyclic analysis of light-frame wood shear walls under quasi-static forces and prescribed displacements.

- The extension of the developed analytical and numerical procedures to the formulation of 2D numerical models of multi-story light-frame wood buildings and the implementation of solution schemes to calculate the response of wood buildings under static or dynamic loading conditions.

- The development and implementation of preprocessing tools to:

    - Provide a convenient and simple format to import user data related to the numerical model (i.e. geometry and dimensions, material properties, analysis cases, etc.).

    - Provide a mesh generator algorithm that minimizes the amount of input data required to define the geometry of light-frame wood walls and can accommodate various structural configurations.

- The validation of the proposed numerical framework against quasi-static and dynamic tests of full-scale, single- or multi-story, light-frame wood walls or buildings.

1.6 Organization of the Report

This report consists of 7 chapters, 3 appendices, and a list of references. Chapter 0 introduces the fundamentals on the seismic behavior of light-frame wood structures and outlines a summary of the response of such buildings in past earthquakes, while the last sections set the objectives of the research work conducted as part of this report. Chapter 2 presents a literature review of published numerical formulations for the static and dynamic response of light-frame shear walls, extending in part to formulations regarding complete light-frame wood buildings. Chapter 3 summarizes the test procedures and the most important results deduced from the benchmark shake-table tests of a full-scale two-story townhouse structure. Chapter 4 describes the proposed 2D numerical framework for the static and dynamic analysis of light-frame wood buildings, while Chapter 5 presents the validation of the proposed numerical model against quasi-static monotonic and cyclic tests of full-scale single and two-story walls. Chapter 6 provides the validation of the proposed model against the response of a single-story specimen under shake-table testing. Chapter 7 summarizes the work conducted in this report, providing the most important conclusions drawn from this research study and outlining a list of recommendations for future studies. Appendix A and Appendix B present information related to the estimation of the parameters used in the nonlinear connection models described in the validation procedures of Chapter 5 and Chapter 6, respectively. Finally, Appendix C presents a time step convergence study for the numerical model of Chapter 6.

CHAPTER 2: LITERATURE REVIEW ON NUMERICAL MODELING OF LIGHT-FRAME WOOD STRUCTURES

2.1 Introduction

The numerical modeling of light-frame wood structures originated in the second half of the 20th century with the linearized, static, non-iterative analysis of wood sheathed diaphragms and has evolved nowadays to nonlinear static and dynamic response-history analysis of shear walls and complete buildings, using commercial or dedicated user-developed finite element analysis software. The multi-component nature of light-frame wood buildings has favored the use of both simplified-macro and advanced-micro mathematical models, numerically implemented in a finite-element-based computer program, to predict the static or dynamic response of sheathing-to-framing connections, light-frame wood diaphragms and entire light-frame wood buildings – following a sequence based on the physical size of the prototypes mostly studied in analytical and experimental research efforts.

The Finite Element Method (FEM) has been used in a variety of displacement-based, (i) 2D or 3D, (ii) simplified or sophisticated, numerical formulations over the years to describe the cyclic response of buildings or important building components of light-frame wood construction. The reason lies behind the generality and versatility of the FEM, which offers to investigators the capability to analyze structural prototypes of variable physical size at a user-defined (macro to micro) modeling scale, and to integrate the numerical models of all members of a structural assemblage under a unified computational framework. For example, finite element representations of the wood framing, the sheathing panel, and the sheathing-to-framing – and other inter-component – connectors can be integrated in a numerical model of a wood shear wall. On the other hand, the experimental results of shear wall tests can be used to back-track connection spring properties using a minimization procedure of the difference between the actual response and the numerical prediction of the finite element model.

The literature review provided in this chapter attempts to present and discuss some of the relevant published research contributions on the 2D analysis of wood shear walls under horizontal and vertical loads. Additional necessary review on modeling of sheathing-to-framing connections is included, since these connections play, as widely accepted, the most important role in the lateral response of light-frame wood shear walls. Studies on three-dimensional modeling of light-frame wood diaphragms and buildings have also been considered, focusing on the modeling techniques for the in-plane response of wall diaphragms, and the effect of surrounding diaphragms on the in-plane behavior. The response of single-story wood shear walls under in-plane horizontal forces has been studied in a number of analytical, numerical, and experimental research projects. A thorough bibliographic review on the evolution of testing, modeling and reliability analysis of light-frame wood shear walls has been described by van de Lindt (2004).

Shear walls act as the primary lateral-load-resisting system in a light-frame wood structure and are traditionally designed under a force-based procedure that assumes a static horizontal force as a fraction of the tributary weight that is laterally supported by the wall. Construction guidelines or equilibrium-based engineering calculations can provide a capacity-based analysis of vertical load paths developed in the wood framing that can indicate the necessity for installation of (i) holdown devices in the end studs of the shear wall to resist uplifting inner forces, and (ii) anchor bolts in bottom sill plates in a specified spacing to transmit uplifting and lateral inner loads to the foundation. While this design and construction practice leads to a building that can be conceptually – or performance-based – rated to have "superior design and construction quality", the majority of the residential houses in North America has been built with questionable and rather medium-to-poor construction quality (CUREe 1998). With this point in mind, the description of each proposed model attempts to investigate and highlight the application of modeling techniques to describe the effects of vertical load paths and equally acknowledge the assumptions made in boundary conditions or inter-component connections.

Reviewing the available literature on the 2D numerical static analysis of wood shear wall diaphragms reveals that there are two major numerical strategies adopted by researchers to describe the static equilibrium equations of these systems. One strategy utilizes the finite element method to describe the numerous and different material components and compute the response under prescribed boundary and loading conditions. The other strategy attempts to explicitly describe the displacement fields of the wood framing and the sheathing panels, and accordingly the displacement field of each nail connector, through generalized modes of deformation and rigid body modes. The response (generalized force resistance or generalized displacement) under prescribed generalized loading and boundary conditions may then be conveniently calculated by equating external work with the internal strain energy collected cumulatively from the associated deformation modes of the panels and the wood framing, as well as from the slipping of the connectors.

Although the finite element static analysis of a single-panel shear wall can be executed fairly easily on a personal computer based on documented methods, when considering multi-panel shear walls across a single or multiple floors, the numerical solution poses a high computational overhead. Failure to meet these demands leads either to inability of the computer program to conclude the analysis or excessive time to facilitate the solution. The problem becomes more apparent when pursuing a dynamic response-history analysis, since this procedure requires a great number of solution steps for each earthquake record, and the seismic assessment usually involves the execution of multiple dynamic analyses with different ground motions. These reasons have led to the use of both detailed and simplified finite element models, depending on the physical size of the prototype and the type of analysis, favoring simplified modeling techniques, especially for dynamic analysis of 2D or 3D buildings.

The following section presents some of the simplified models proposed in the last two-to-three decades, for the static monotonic analysis of light-frame wood shear walls. Table 2.1 summarizes the most important modeling characteristics of these studies.

2.2 Simplified Numerical Models for Static Monotonic Analysis

Tuomi and McCutcheon (1978) and McCutcheon (1985) described a simple shear wall model with a pure racking distortion of the rigid framing members, assuming that the frame corners move along the diagonals relative to the sheathing panel. The objective of this effort was to obtain a closed-form strength equation, which the authors did, using a two-parameter power curve for the nail uni-dimensional nonlinear elastic response.

Easley *et al.* (1982) also developed shear wall strength formulae, based on experimental observations of the deformation patterns of the nail connectors, when a shear wall is subjected to lateral loads. Using a pre-defined horizontal and vertical force distribution in the nail connectors, based on their geometric location on the sheathing panel, the authors proposed two formulae applicable for response in the linear and in the nonlinear deformation range of the wall, respectively. These equations were developed for standard 4 ft by 8 ft sheathing panels and symmetric location of nail connectors in the plane of the shear wall. Easley *et al.* (1982) validated the suggested equations with monotonic tests of 8 wall specimens and complementary finite element analyses described in the following section.

Gupta and Kuo (1985) in an attempt *"to model wood framed shear walls rationally and as simply as possible"* presented a shear wall model that considered a racking mode for the framing and generalized bending for the studs with rigid sill and top plates. Two modes of shear deformation were considered for the panel assuming a rigid translation of the sheathing with the centre of the wall. The model was used to perform nonlinear static analyses and compare the results with the experimental data as well as with the results from finite element analysis by Easley *et al.* (1982). Gupta and Kuo (1985) concluded, based on a comparison between rigid and flexible studs, that the bending flexibility of the studs plays a secondary role on the global force-deformation characteristics of wood shear walls. Bending in the top and sill plates was not considered at all, partly on the grounds that the finite element analysis results from Easley *et al.* (1982) did not show this bending behavior as clear as for the vertical studs.

Later, Gupta and Kuo (1987a) extended the shear wall model with rigid frame elements to include stud uplift from the sill plate, which was still assumed to be fixed at the foundation. In a companion publication (Gupta and Kuo 1987b), the authors further extended the shear wall model to include uplift of the rigid sill plate from the ground. The final model proposed consisted of seven kinematic defrees-of-freedom (DOF) considering uplift behavior in one end only, under constant static lateral in-plane load, considering (i) two shear DOF for all sheathing panels, (ii) one vertical DOF of the sheathing panels, linearly distributed to all panels from the bearing end (zero uplift) to the tensile end, (iii) one vertical DOF of the sill plate, linearly distributed from the bearing end (zero uplift) to the tensile end, (iv) one vertical DOF of the studs and the top plate, linearly distributed from the bearing end (zero uplift) to the tensile end, and finally (v) one horizontal DOF for the kinematic shear deformation of the studs and top plate. The separation of studs from the top plate was not considered in this study.

Table 2.1 Characteristics of Simplified Numerical Models for Static Monotonic Analysis of Wood Shear Walls

Authors	**Framing**	**Sheathing Panel**	**Sheathing-to-Framing Connectors**	**Framing-to-Framing Connectors**	**Boundary Conditions**	**Comments**
Tuomi and McCutcheon (1978); McCutcheon (1985)	Rigid framing; 1 pure racking DOF	1 shear DOF; panel translates and rotates according to kinematic assumptions	1 DOF; force calculated based on a power curve law	Pin-connections	Fixed base	Provides closed-form solutions of lateral resistance and wall displacement
Easley *et al.* (1982)	Rigid framing; 1 pure racking DOF	1 shear DOF;	2 DOF; Distribution of horizontal and vertical forces based on a pre-defined pattern	Pin-connections	Fixed base	Provides closed-form solutions of lateral resistance and wall displacement
Gupta and Kuo (1985)	1 pure racking DOF; 1 DOF for stud bending	2 shear DOF; panel translates according to kinematic assumptions	1 DOF; force calculated based on a smooth curve	Pin-connections	Fixed base	Stud bending was finally rejected based on the small contribution in the predicted response
Gupta and Kuo (1987a)	1 pure racking DOF; 1 vertical DOF for stud uplifting	2 shear DOF; 1 vertical DOF for uplifting	1 DOF; force calculated based on a smooth curve	Pin-connections at the top plate; uplift allowed uniformly at the bottom of the studs with linear springs	Fixed base	
Gupta and Kuo (1987b)	1 pure racking DOF; 2 vertical DOF for stud and sill plate uplifting; 1 lateral DOF for sill plate slippage	2 shear DOF; 1 vertical DOF for uplifting	1 DOF; force calculated based on a smooth curve	Pin-connections at the top plate; uplift allowed uniformly at the bottom of the studs with linear springs	1 linear horizontal spring for sill plate slippage	7 DOF Wall Element with stud and sill plate uplifting and sill plate slippage for monotonic iterative analysis

Gupta and Kuo (1987b) described a model for the static experimental results of a full-scale single floor rectangular light-frame wood structure with inclined roof in five subsequent construction phases (Tuomi and McCutcheon 1974). They formulated a building three-dimensional model considering diaphragm (plane stress) action of walls, ceiling and sheathed roof, and presented the concept of sub-structuring each diaphragm as a wall element and associating global DOF of the building model with the wall element DOF of the rigid wood framing. The previous model was extended to nine kinematic DOF, where both ends could uplift, and was used to simulate the wall diaphragm perpendicular to the in-plane external force, on the uplifting side of the structure. Although this assumption of rigid framing was acceptable within the context of a simple analysis procedure, it was conceptually accepted that bending did not contribute to the uplifting behavior of the wood shear walls.

These simplified models have been introduced first because they were implemented only for static analysis at various levels of lateral force below the ultimate strength and did not require the use of a dedicated structural analysis computer program. The iteration procedure, if the nonlinear backbone curve of the connectors is defined, involves a rather straightforward numerical implementation of the linear mathematical equations that describe the static response under linear connectors, updating successively the secant stiffness of the connectors, based on the computed deformations of the connectors.

2.3 Finite Element Numerical Models for Static and Dynamic Analysis

This section describes the finite element models suggested and implemented in computer codes or commercial software to predict the static and dynamic response of wood shear walls. The applications of these models for the analysis of light-frame wood buildings in two or three dimensions are also discussed.

Two of the earliest contributions on finite element analysis of wood shear wall diaphragms are those by Polensek (1976) and Foschi (1977). Polensek (1976) described a model to predict the out of plane bending behavior of wood diaphragms, due to normal pressure perpendicular to the sheathing and vertical gravity loads, but did not address the in-plane lateral response, so further information is not provided in this review.

Foschi (1977) presented a finite element model for wood diaphragms using a 2-noded beam element for the wood framing and a 12-noded quadrilateral plane stress element for the sheathing. Sheathing-to-framing connections were described through a 2-noded nonlinear elastic spring aligned in the direction of the differential motion between framing and sheathing under in-plane loads. The framing-to-framing connections were modeled as 3 independent 2-noded nonlinear elastic springs transferring shear, axial and bending moments between the connecting members. Foschi (1977) validated his model using the experimental response of a 60 ft by 20 ft wood horizontal diaphragm, loaded as a simply supported beam with increasing in-plane loads perpendicular to the long diaphragm direction. Good agreement was shown for the deflection predictions in the middle of the 60ft long diaphragm.

In addition to the simplified model and the strength formulae described in the previous section, Easley *et al.* (1982) used an existing structural finite element program to model the response of light-frame wood shear walls with typical dimensions. Wood framing and sheathing panels were modeled with 8-noded plane stress elements, and the sheathing-to-framing connectors were described through two independent orthogonal nonlinear elastic springs. Framing connectors were considered to provide pinned connections between framing members. Easley *et al.* (1982) noted that since separation of the studs from the horizontal top and bottom plates was not considered in the simplified and the finite element model, the formulae provided were applicable to shear walls with framing connections that were effective in transferring tension loads between members.

Itani and Cheung (1984) used 4-noded joint elements with 10 DOF to represent a line of nonlinear connectors in wood shear walls. Standard beam and plane-stress elements were used to mesh the framing and sheathing panels, respectively. Good agreement was observed in predicting the monotonic response of various shear wall tests. Later, Falk and Itani (1989) extended this work and introduced a 20 DOF, 4-noded transfer element to describe the deformations of all the connectors in a single sheathing panel. Using 4 beams and 1 isoparameteric plane-stress element integrated in the proposed formulation provided a less computationally intensive numerical model to be used for the analysis of diaphragms with large dimensions.

Gutkowski and Castillo (1988) developed a finite element program that allowed modeling of exterior and interior sheathing panels in wood shear walls. Standard finite elements were used to simulate deformations in the framing, the panels and the nonlinear nail connectors. Additional framing-to-framing connector springs were employed to model linear response of the two orthogonal translations and one in-plane rotation. Stiffness accounting for the difference in bearing and tension parallel to the contact force was included for these connections, while sheathing bearing was modeled with nonlinear gap elements. Gutkowski and Castillo (1988) verified their model with results of experimental work performed by Patton-Mallory *et al.* (1984) at the U.S. Forest Products Laboratory. The shear wall specimens consisted of (i) gypsum wallboard fastened with drywall screws, (ii) plywood nailed with 8d common nails, (iii) both panel sheathings, one in each side of the wall. Interestingly, while the predictions for single-sheathed walls were very satisfactory, the model over-predicted the strength of double-sheathed walls. One possible reason, discussed by Gutkowski and Castillo (1988), was the reduction of strength in the nail connections due to changes in moisture content and shrinkage, taking place during the month that elapsed from construction to testing of the wall specimens. Gutkowski and Castillo (1988) noted that the actual support conditions existing in the test setup were realistically simulated in the proposed finite element model, raising awareness for the importance of this key point in similar work done by other researchers.

Dolan and Foschi (1991), based on the work by Dolan (1989), extended the finite element program formerly developed by Foschi (1977) to include (i) out of plane bending and buckling of sheathing panels, (ii) bearing between sheathing panels using bilinear connectors, and (iii) sheathing-to-framing connections with three directions of movement and defined ultimate capacity, including discrete and smeared connectors. Framing-to-framing connections are not presented in Dolan and Foschi (1991), which should imply that pinned connections were considered. The predictions of ultimate strength capacity were very well correlated with the experimental results of seven full-scale 8ft-by-8ft shear walls under static lateral loads, conducted by Dolan (1989). In this test setup, the base and top of the wall were rigidly attached to the test frame and the end studs were anchored to the test frame as well (Dolan and Foschi 1991). The authors reported that the response beyond the peak load capacity could not be computed due to numerical difficulties in the solution of the force-controlled solution algorithm.

Later, White and Dolan (1995) developed a 2D shear wall model capable of performing nonlinear static and dynamic analysis. Element formulations were based on Dolan (1989) but out-of-plane deformations were not considered in this study. Two independent orthogonal springs were defined at each sheathing-to-framing connection, with hysteretic rules, described by Dolan (1991), which accounted for pinching and stiffness degradation. Similar static response of the proposed representation to that predicted by the more detailed model by Dolan and Foschi (1991) was observed, and good correlation was achieved with static and dynamic tests described in Dolan (1989).

Filiatrault (1990) developed a simple structural analysis program to predict the behavior of timber shear walls under lateral static loads and earthquake excitations. Considering a pure racking deformation of the wood framing and rigid body motion of the sheathing deformed under constant shear, the author used a total of 5 global DOF to model a single-panel shear wall. Additional panels with 4 DOF each could be considered in the same 2D space. Using the hysteretic connector model by Dolan (1989), Filiatrault (1990) performed dynamic time-history analyses considering 1 horizontal dynamic DOF at the top of the shear wall. The computational efficiency of this simplified model and the relatively good correlation with static and dynamic tests by Dolan (1989) was highlighted by the author, stating that it could be a useful background structural model for reliability-based studies.

Kasal and Leichti (1992) introduced the concept of energetically equivalent simplified finite element modeling as a more computationally effective method to compute the static response of complete light-frame wood buildings. Using a commercial software package, each shear wall was modeled in detail to include in-plane and out-of-plane deformations. The wood framing was defined by shell elements perpendicular to the wall plane while the sheathing panel was defined by shell elements parallel to the wall plane. Three independent nonlinear springs, including nail withdrawal, were utilized for each sheathing-to-framing connector, while pinned conditions were assumed at the stud-to-plate connections. This detailed model was analyzed under static lateral in-plane loads and the horizontal response was computed with respect to the wall drift. This force-displacement relationship was then fitted in an analytical formula and was embodied in a diagonal nonlinear truss element that was subsequently used in the equivalent simplified model. A similar fitting procedure was presented to adjust the bending and torsional linear behavior of the diaphragm wall, based on the results of the detailed model. Later, Kasal *et al.* (1994) extended this procedure to model a one story light-frame wood test structure investigated by Phillips *et al.* (1993), by introducing inter-component connections between vertical and horizontal diaphragms. However, the hysteretic behavior of nailed connections was not properly accounted for, as stated by the authors, and the cyclic tests performed by Phillips *et al.* (1993) could not be directly compared.

Tarabia and Itany (1997a, 1997b) introduced a complete finite element model for dynamic analyses of three-dimensional light-frame wood buildings. For the in-plane lateral behavior of each shear wall, each sheathing panel without openings was assumed to have 2 rigid body translations and 2 constant shear deformations, while sheathing panels incorporating one opening had 4 additional shear deformations. The motion of the frame was expressed through shape functions defined for the 4 corner nodes of the frame surrounding the panel. Sheathing-to-framing connectors were modeled with two independent orthogonal springs that incorporated the hysteretic rules defined by Kivell *et al.* (1981) and accounted for pinching and stiffness degradation through piecewise-linear paths – the backbone curve was nonlinear exponential. Framing connectors with different linear stiffness in compression, tension, and shear were also included. The out-of-plane bending behavior of the wall diaphragms was decoupled from the shear in-plane behavior, neglecting withdrawal of nailed connections. Inter-component connections between diaphragms, similarly in concept to Kasal *et al.* (1994), were assigned in models of complete light-frame wood buildings. Very good agreement was found for predictions of static and dynamic tests of shear walls by Dolan (1989), while predictions of the load redistribution in the house tested by Phillips *et al.* (2003) were satisfactory correlated with the experimental results.

Andreasson (2000) used commercial finite element software to formulate three-dimensional models of wood diaphragms and light-frame wood buildings and to study the static monotonic response under horizontal and vertical loads. Each wall diaphragm consisted of beam and shell elements for the framing and the sheathing panel, respectively, while 3 decoupled springs were used to model sheathing-to-framing as well as framing-to-framing connections. Tension-only springs were used to simulate anchoring connections between studs and horizontal diaphragms and compression-only springs accounted for bearing effects between plates and diaphragms. In-plane connection springs were nonlinear elastic, while out-of-plane framing connections were assumed linear. Andreasson (2000) recognized that the use of 2 independent orthogonal springs for nailed connections yields higher stiffness and strength but a reasonable modification was not possible with the existing element library of the structural analysis code used. For this reason, in the final model the connector (nail) properties were adjusted to fit the finite element predictions with the response obtained from shear wall tests, conducted complementary to this study. The detailed model was used in a number of case-studies, one of which was to calculate the effective gravity load that counteracts uplifting forces in the tension side of a racking shear wall.

Ceccotti *et al.* (2000) simulated each shear wall in a 3D symmetric structure with a rigid pinned 4-noded frame that incorporated additional nonlinear rotational springs at the connections to simulate the shear resistance of the wall assemblage, based on experimental cyclic results. The hysteretic springs incorporated the model proposed by Ceccotti and Vignoli (1989) that accounted for pinching and stiffness degradation through piecewise-linear paths. The flexibility of floor diaphragms was simulated with elastic diagonal braces and a small increase in the response was observed with this configuration, compared to rigid diaphragms.

He *et al.* (2001) presented a computer code capable of modeling 3D light-frame wood structures at the nail level and performing load-controlled or displacement-controlled cyclic static analysis. One of the revolutionary features of this approach was the mechanics-based, micro-modeling of each sheathing-to-framing connection in three dimensions, as described by Foschi (2000), which allows the development of cyclic force-displacement responses of sheathing-to-framing connectors that are load protocol independent. The strains in the plate and beam elements used for panels and framing, respectively, included second-order terms (Green strain) to allow consideration of deflection amplifications due to the effect of axial compressive loads (P-Δ effects). Framing-to-framing connections or anchoring devices were not included in this formulation. The numerical model was verified using monotonic and cyclic shear wall tests conducted by Durham *et al.* (1997) and close correlation was observed throughout the whole deformation ranges. The adoption of a numerical building model including every sheathing-to-framing connector in conjunction with the simulation of these connections with a dedicated micro-model rendered this numerical framework presented by He *et al.* (2001) very computer intensive and highly computationally inefficient. This could be one of the reasons why the model has not been extended to include nonlinear dynamic response-history analysis of light-frame wood structures.

Folz and Filiatrault (2001) proposed a simple 2D finite element model for cyclic analysis of wood shear walls, based partly on the previous work done by Filiatrault (1990), since 1 global DOF was used for the rigid framing and 4 DOF for each sheathing panel. The sheathing-to-framing connections incorporated a hysteretic model that allowed for pinching as well as strength and stiffness degradation, utilizing a nonlinear exponential backbone curve and piecewise-linear paths under cyclic loading. The nail spacing was adjusted internally so that a monotonic analysis with two bi-directional connection springs at the adjusted spacing would yield similar stiffness and force resistance in the initial ascending curve as the monotonic analysis with a single uni-directional connection spring at the original spacing. This eliminated in part the stiffness and strength overestimation, associated with perpendicular decoupled springs. Another convenient feature of this model is the extraction of the optimal SDOF spring parameters for the analyzed shear wall, expressing force and displacement along the horizontal in-plane direction of the wall (Figure 2.1a,b). The model was verified against static and dynamic tests described in Durham *et al.* (1997), and reasonable agreement was found, given the simplicity of the numerical formulation. Later, Folz and Filiatrault (2004a, 2004b) introduced a structural analysis program for the seismic analysis of 3D light-frame wood structures, assuming rigid floor diaphragms and concentrating the nonlinear behavior solely in shear walls connecting floor diaphragms – a similar approach for static analysis was described earlier by Schmidt and Moody (1989). Each shear wall was represented by a SDOF horizontal spring (Figure 2.1c,d), the properties of which could be defined from shear wall tests or from the previously described cyclic analysis program. Folz and Filiatrault (2004a, 2004b) verified the dynamic model with the experimental response of a full-scale two-story light-frame wood structure conducted within the CUREe-Caltech Woodframe Project (Fischer *et al.* 2001). Despite the simplicity, these numerical models have been used in many reliability and seismic analysis studies because of their high computational efficiency. The numerical framework described above is considered to be the current state-of-practice for dynamic response-history analysis of light-frame wood buildings.

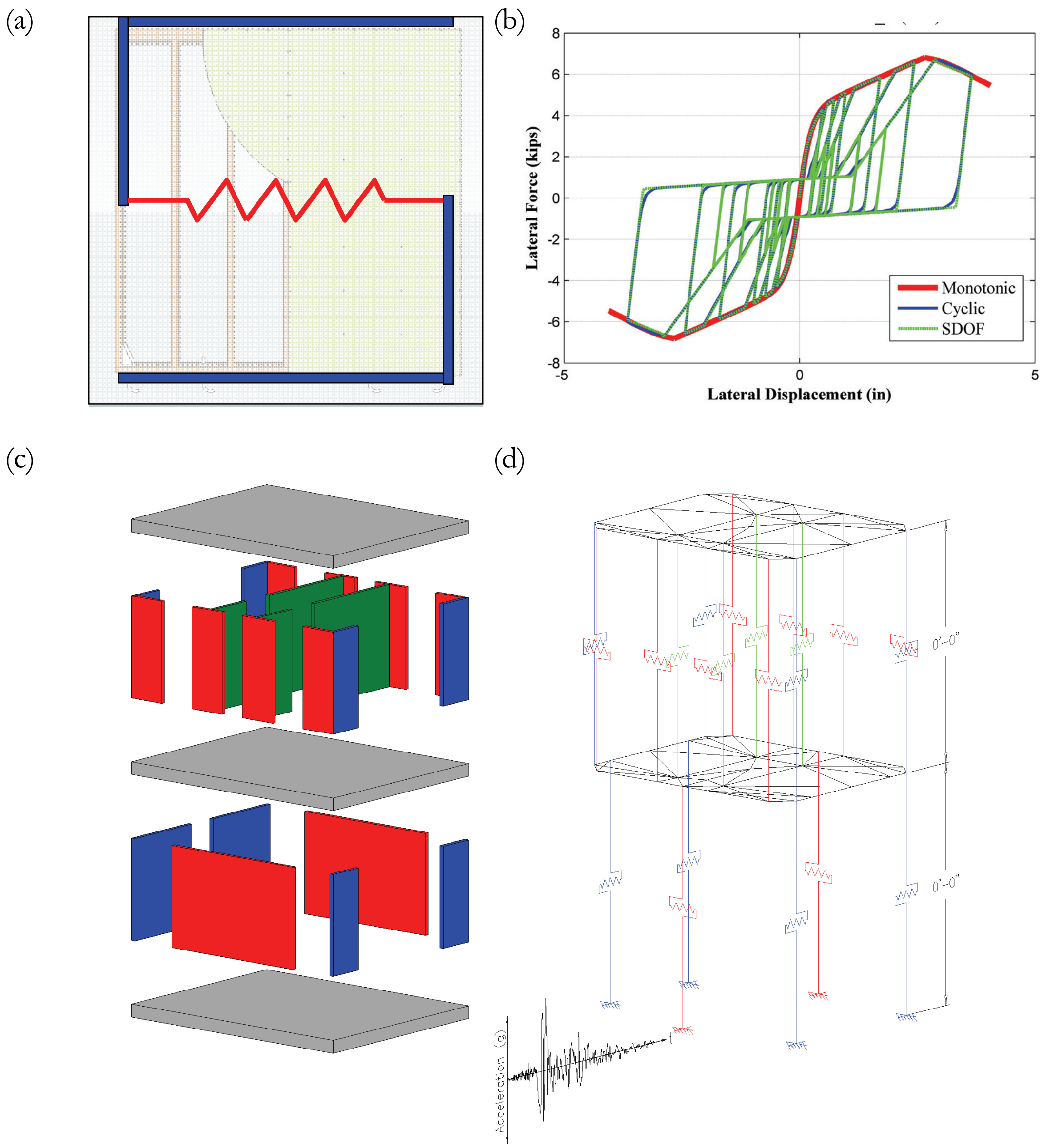

Figure 2.1 Modeling of light-frame wood buildings with CASHEW (Folz and Filiatrault 2001) and SAWS (Folz and Filiatrault 2004a, 2004b), (a) equivalent SDOF spring of a wood shear wall, (b) fitting of SDOF spring parameters to match the cyclic response of the wall assembly, (c) building sketch of a two-story light-frame wood structure, and (d) equivalent "pancake" building model (from Fischer *et al.* 2001)

Dujic and Jarnic (2004) presented a simplified technique to model light-frame wood shear walls in 3D structures. Similarly to other researchers, a detailed 2D FE model was first formulated and the computed shear wall racking response was fitted in a nonlinear equivalent strut model. Standard finite elements were used for the frame and the panels. The sheathing-to-framing connections were modeled with two independent orthogonal springs, while the hysteretic response was defined through piecewise-linear paths and accounted for pinching as well as strength and stiffness degradation. Holdown elements could be also considered at the end studs, while the sill plate was assumed to be fixed in the foundation. The dynamic analysis of the 3D building was carried out in a different finite element program. Floor diaphragms were considered rigid, while shear walls were represented by the pre-defined equivalent struts.

Collins *et al.* (2005a, 2005b) presented a three-dimensional model for light-frame wood structures. The in-plane behavior of the shear walls was simulated as proposed by Kasal and Leichti (1992). The nailing hysteretic model was adopted from Kasal and Xu (1997) and accounted for pinching, strength and stiffness degradation under cyclic loading. Inter-component connections were assigned between diaphragms. The verification of the model was based on the experimental results presented by Paevere *et al.* (2003) on a one story full-scale structure under torsional horizontal cyclic loads.

Judd (2005) used a variety of commercial finite element software to simulate the static and dynamic response of wood shear walls and diaphragms. Standard 2D beam and plane stress elements were used for the framing and sheathing panels, respectively, while framing connections were assumed to be pinned. Judd (2005) utilized various hysteretic models for the sheathing-to-framing connections. One significant contribution and differentiation from previous studies, described by Judd and Fonseca (2005), was the explicit orientation – rotation in the wall plane – of the two orthogonal independent connection springs, according to the initial trajectory of each sheathing-to-framing connection, under lateral loads applied at the top of the wall. This procedure actually requires only one connector spring for the solution of the first step. The global rotation of each uni-directional spring is recorded and enforced throughout the analysis, while the perpendicular springs are added at the initiation of the second step. This modeling technique yielded more accurate predictions of static and dynamic shear wall tests, compared to the case of non-oriented springs used extensively in previous studies. Observing the monotonic backbone curves of shear wall models analyzed with both cases indicated that the peak strength was lower but was achieved at higher wall drifts.

Xu (2006) utilized a commercial finite element program to simulate the response of wood shear walls and performed static and dynamic nonlinear analyses. A detailed model of inter-story shear walls was introduced to ultimately develop a simplified shear wall finite element to be used in 2D or 3D building models. The objective was to include rocking behavior in addition to racking deformations in the equivalent simple model. 2-noded beam and 4-noded shell elements were selected for representing the framing and the panel elements, respectively. The sheathing-to-framing connections consisted of two independent nonlinear springs, oriented as proposed by Judd (2005) and described in the previous paragraph. The hysteresis model was proposed by Foliente (1995), based on previous work by Bouc (1967), Wen (1976, 1980), Baber and Wen (1981), and Baber and Noori (1985). This hysteresis model, which was corrected for two problematic scenarios under cyclic loading, can simulate very well the characteristics of wood connections such as pinching and strength and stiffness degradation. The framing-to-framing connections were assumed linear in shear actions, mentioning the unavailability of such type of connections tests. No tensile resistance was assigned for the end nail withdrawal when vertical studs separated from bottom or sill plates. Xu (2006) analyzed two anchorage conditions (full and intermediate level of uplift resistance) and compared the numerical predictions with shear wall tests performed by Salenikovich (2000). One assumption regarding the boundary conditions in the numerical models of Xu (2006) was that the sill plate was actually fixed at the base. Uplifting was considered only for studs at the bottom that were not anchored with a holdown. No separation between the studs and the top plate is reported in this study. The predictions for walls with full anchorage correlated very well with the test results, while the response of walls with intermediate anchorage (no holdowns, only sill plate anchor bolts) was under-predicted by the numerical model. The final shear wall element consisted of two diagonal hysteretic struts, similarly to previous studies, that could be defined based on analytical or experimental results. Very good agreement was found between the shake-table tests of a two-story light-frame wood house (Fischer *et al.* 2001) and the numerical building model, which consisted of the developed shear wall elements, calibrated from the detailed finite element representations of each single-story wall line of the structure.

Ayoub (2007) introduced a new hysteretic model with energy-based degrading constitutive laws for light-frame wood structures based on previous work by Rahnama and Krawinkler (1993) on general hysteretic degrading modeling. Shear wall models were formulated using commercial finite element software and the sheathing-to-framing connections incorporated the proposed behavior as distributed nonlinear interface elements, acting independently in the two global directions. Beam elements with pinned connections were used for the framing members while shell elements were representing the sheathing panels. The energy-based concepts of deterioration provided good correlation with static shear walls tests, while a SDOF hysteretic spring was also employed to fit experimental or numerical response of shear wall assemblies in an equivalent simple wall model. A 2 DOF building model was formulated that predicted with very good accuracy the shake-table tests of a two-story light-frame wood house (Fischer *et al.* 2001).

Summarizing the description of the proposed numerical modeling techniques for light-frame wood structures, Table 2.2 contains some of the most important characteristics of these previous studies, provided within a simplified concept of reference. For further or more complete details, readers should be directed to the cited publications. Note that only a brief overview of these models was presented above and some modeling details were omitted for sake of brevity.

2.4 Summary

Following the review above of the numerical models proposed for the static and dynamic analysis of light-frame wood buildings, the following observations can be made:

i. The majority of the proposed finite element shear wall models are formulated on the basis of pinned framing-to-framing connections and fixed sill plate to the foundation. There are cases where linear or nonlinear connectors have been assigned between framing members but convenient "strict" boundary conditions are usually considered for the bottom or the top of shear walls or wall assemblies. There has been no numerical model, for cyclic or dynamic analysis, similar to that described by Andreasson (2000) for monotonic static analysis up to the ultimate force capacity, which can incorporate separation of vertical studs from top and sill plates in conjunction with contact phenomena and anchoring devices in the direction normal to the adjacent horizontal diaphragms, which can allow separation and bending of the top and sill plate members. This type of coupled bending-shear-rocking structural response is usually secondary in well anchored light-frame wood shear walls or walls with intermediate anchorage that carry a good portion of the total gravity loads. However, uplifting and rocking behavior has been experimentally observed especially in narrow shear walls with high aspect (height-over-length) ratio (Schmid *et al.* 1994; Dolan and Johnson 1997; Salenikovich 2000) as well as in shake-table tests of full-scale light-frame wood structures (Fischer *et al.* 2001; Christovasilis *et al.* 2009a). Two possible reasons for these omissions can be the numerical difficulty associated with modeling contact/separation conditions and the lack of experimental or analytical studies on the response of these types of connections, other than sheathing-to-framing.

ii. There are no numerical models that can effectively simulate the complex effects of wall finish materials on the response of wood shear walls. It has been experimentally documented and nowadays widely accepted that the interior and exterior nonstructural wall finish materials not only contribute to the lateral stiffness and strength of wood shear walls (Filiatrault *et al.* 2002), but the relatively low force and displacement capacity of these stiff but weak wall components also changes the observed failure mechanisms compared to structural single-sheathed wood shear walls. This is depicted in monotonic backbone curves that compare the response of identical shear walls with or without wall finishes, as well as woodframe walls with the non-structural finishes only (Gatto and Uang 2002; Ceccotti and Karacabeyli 2002; Pardoen *et al.* 2003). The experimental results show, for example, that the lateral resistance of a wood shear wall with exterior structural sheathing and interior gypsum wallboard cannot be accurately predicted by directly super-imposing the lateral contribution of each side of sheathing in a single-sheathed wall. This is more obvious in deformations past the peak lateral strength of the shear wall. Intuitively, if the kinematics of the framing is well defined with no nonlinear behavior, such as the case of pinned framing connections and fixed bottom plate, this coupling effect cannot be really explained[†]. This means that potential nonlinear internal deformations do exist in the framing and the path dependency response of sheathing-to-framing connections change the global hysteretic response after ultimate loads.

iii. The in-plane nonlinear structural response of wood shear walls in complete 2D or 3D buildings has been mostly addressed through the use of one or a pair of "energetically

† Studies by Canadian researchers at Forintek have led to a possible explanation (i.e. the load distribution in the sheathing-to-framing wood connectors is different when nonstructural wall finishes are present, which overload some connectors prematurely and yield failure loads less than the sum of the individual components).

equivalent" – as are mentioned by various researchers – nonlinear hysteretic springs for each inter-story shear wall. In fact, from the building models described in this review, only those proposed by Tarabia and Itany (1997) and He *et al.* (2001) considered a numerical building model at the nail level for nonlinear dynamic and static analysis, respectively. The convenience of the equivalent wall springs is apparent. First for the numerical efficiency that is achieved in processing time when hundreds of DOF have collapsed in a small number of master DOF for each shear wall in a building model. Secondly, numerical fitting of experimental force-displacement curves from shear wall tests can be an alternative to numerical fitting of the predictions of a finite element wall model. This was demonstrated in the international blind prediction study of the seismic response of the full-scale two-story light-frame wood house, tested under uni-axial horizontal shaking as part of the CUREe-Caltech Light-frame wood Project (Fischer *et al.* 2001). Five teams participated in this study and the results have been described by Folz and Filiatrault (2004c). Four of the participating teams considered as of primary importance in the prediction success, the mechanical properties of the prescribed sheathing-to-framing connections in the test structure. Such experimental connection tests data was provided by the organizers in advance. One of the teams, however, used available independent shear wall tests to estimate the response of the walls on the test structure. Nevertheless, the final building models formulated by all teams for dynamic analysis varied from a SDOF to a 3D MDOF system, but shear walls and in some cases floor diaphragms were represented by equivalent springs. The use of equivalency in shear wall modeling entails the belief that the response of each shear wall can be accurately quantified and simplified in a SDOF system. In the case of shear wall models that ignore the framing flexibility and assume a pure racking response under lateral loads, the only global DOF in the framing is indeed the horizontal displacement at the top of the wall. The equivalency can be applied in this case, acknowledging in advance the assumptions and limitations of the simplified model. If framing flexibility is accounted for without any vertical nonlinearity between the framing members (pinned connections and fixed base), the effect of vertical loads will be mostly insignificant and an equivalency can be described for the horizontal global DOF at the top of the wall. Based on the principle of virtual work, any gravity load that causes vertical deformations of the top of a shear wall under lateral horizontal loading, affects the incremental external energy absorbed by the horizontal external force. This means that the horizontal global force of shear walls that respond in a combined shear/bending/rocking behavior will be affected by the magnitude and the distribution of vertical gravity loads and the actual vertical displacements at points of application of the gravity loads. Since the magnitude of gravity loads or the distribution may change during seismic loading, numerical equivalency as used currently in many studies may not be really applicable for shear walls with nonlinear response in the vertical direction.

iv. In all cases where commercial finite element software was employed for cyclic analysis of light-frame wood components, the researchers had to add in the element library additional user-defined hysteretic-spring elements, suitable for the main characteristics of wood connections. This reveals the complexity regarding finite element analysis of light-frame wood structures and explains why a lot of research studies have focused on the development of in-house dedicated numerical models.

Based on this discussion, the numerical framework developed in this report aims at eliminating limitations of existing shear wall models, by relaxing the fixed boundary conditions at the top and bottom of a shear wall and the pinned connections between horizontal and vertical framing members. This enables the simulation of uplifting and rocking modes of deformation, the level of participation of which depends on the specific anchorage conditions, the height-to-width ratio of the shear wall segments and the gravity loads applied. Moreover, contrary to the calibrated macro-modeling approach of each shear wall assembly, the response of each inter-story shear wall is enclosed in a shear wall element that can be used in a 2D building analysis, maintaining the same level of detail in both shear wall and building level nonlinear analyses. Finally, the assumption of small rotations is relaxed by adopting a corotational description of the displacements of the derived finite elements, which leads to solutions that satisfy the equilibrium equations in the deformed configuration. These attributes provide confidence that the numerical framework can be used for the seismic collapse assessment of light-frame wood structures.

Table 2.2 Characteristics of Finite Element Models for Static or Dynamic Analysis of Wood Shear Walls and Light-frame Wood Buildings

Authors	**Framing**	**Panel Sheathing**	**Sheathing-to-Framing Connectors**	**Framing-to-Framing Connectors**	**Boundary Conditions and Comments**	**Software or Computational Platform**	**Dynamic Capability or Use of SDOF Model**
Foschi (1977)	2-noded beam	12-noded Quadrilateral	Uni-directional exponential	3 Independent Springs (2 orthogonal, 1 rotational)	Analysis focused on a horizontal diaphragm under bending deflections. Boundary Conditions for a Shear wall were not of direct interest in this study.	SADT	Not Considered
Easley *et al.* (1982)	8-noded Quadrilateral	8-noded Quadrilateral	2 Independent Orthogonal Springs	Pin-connections	Fixed Base	POLO-FINITE (Dodds and Lopez 1980)	Not Considered
Itani and Cheung (1984)	2-noded beam	4-noded Quadrilateral	4-noded/10-DOF	Pin-connections	Fixed Base	NONSAP	Not Considered
Falk and Itani (1989)	4-noded rectangular frame for each panel	4-noded Quadrilateral for each panel	20 DOF Transfer Element	Not Clearly Stated	Not Clearly Stated	NONSAP	Not Considered
Gutkowski and Castillo (1988)	2-noded beam	4-noded Quadrilateral sheathing bearing	2 Independent Orthogonal Springs	3 Independent Springs (2 orthogonal, 1 rotational)	Fixed Base	WANELS	Not Considered
Dolan (1989); Dolan and Foschi (1991)	2-noded beam	4-noded Quadrilateral; Out of plane bending; sheathing bearing	3 Independent Orthogonal Springs, Discrete and Smeared Connectors	Pin-connections	Fixed Base	SHWALL	Not Considered
Filiatrault (1990)	Rigid framing; 1 pure racking DOF	1 Shear DOF; 3 Rigid body DOF	2 Independent Orthogonal Springs (Dolan 1989)	Pin-connections	Fixed Base	SWAP	SDOF Wall Model for Dynamic Analysis

Table 2.2 Characteristics of Finite Element Models for Static or Dynamic Analysis of Wood Shear Walls and Light-frame Wood Buildings (Continued)

Authors	Framing	Panel Sheathing	Sheathing-to-Framing Connectors	Framing-to-Framing Connectors	Boundary Conditions and Comments	Software or Computational Platform	Dynamic Capability or Use of SDOF Model
Kasal and Leichti (1992); Kasal *et al.* (1994)	2-dimensional shell for Detailed FE Model	2-dimensional shell for Detailed FE Model, sheathing bearing	3 Independent Orthogonal Springs for Initial Detailed FE Model	Pin-connections	Fixed Base	ANSYS	Equivalent Quasisuperelement for dynamic analysis
White and Dolan (1995)	2-noded beam	4-noded Quadrilateral; sheathing bearing	2 Independent Orthogonal Springs (Dolan 1991)	Pin-connections	Fixed Base	WALSEIZ	Full Model Dynamic Analysis
Tarabia and Itany (1997)	4-noded frame around the panel	4 DOF for no opening; 8 DOF for one opening; sheathing bearing	2 Independent Orthogonal Springs (Kivell *et al.* 1981)	Linear Springs with different stiffness for tension, compression, and shear	Inter-component Connections between Diaphragms (Tarabia 1994)	DRAIN-3DX (Prakash and Powell 1993)	Full Model Dynamic Analysis
Andreasson (2000)	2-noded beam	4-noded Quadrilateral; sheathing bearing	3 Independent Orthogonal Springs	3 Independent Orthogonal Springs	Nonlinear modeling of Anchoring devices and boundary connections	ANSYS	Not Considered
Ceccotti *et al.* (2000)	Wall response fitted in rotational springs of rigid framing connections. Hysteretic Spring by Ceccotti and Vignoli (1989)			Pin-connections	Fixed Base. Rigid and Flexible Diaphragms for 2D analysis	DRAIN-3DX (Prakash and Powell 1993)	Equivalent Quasisuperelement for dynamic analysis
He *et al.* (2001)	2-noded beam with 2nd order strain distribution and inelastic material properties	4-noded Quadrilateral with 2nd order strain distribution	Mechanics-based model for 3D interaction. (Foschi 2000)	Pin-connections	Fixed Base	LighFrame3D	Not Considered

Table 2.2 Characteristics of Finite Element Models for Static or Dynamic Analysis of Wood Shear Walls and Light-frame Wood Buildings (Continued)

Authors	**Framing**	**Panel Sheathing**	**Sheathing-to-Framing Connectors**	**Framing-to-Framing Connectors**	**Boundary Conditions and Comments**	**Software or Computational Platform**	**Dynamic Capability or Use of SDOF Model**
Folz and Filiatrault (2001, 2004a, 2004b)	rigid; 1 pure racking DOF;	1 shear DOF; 3 Rigid body DOF	2 Independent Orthogonal Springs.	Pin-connections	Internal modification of nail spacing to account for the use of 2 decoupled springs for nailed connections	CASHEW and SAWS	SDOF Wall Model for Dynamic Analysis
Dujic and Jarnic (2004)	2-noded beam	4-noded Quadrilateral	2 Independent Orthogonal Springs	Pin-connections	Holdowns included	DRAIN-2DX (Prakash and Powell 1993) and CANNY-E (Li 1996)	Equivalent Quasisuperelement for dynamic analysis
Collins *et al.* (2005)	2-dimensional shell for Detailed FE Model	2-dimensional shell for Detailed FE Model, sheathing bearing	3 Independent Orthogonal Springs for Initial Detailed FE Model.(Kasal and Xu 1997)	Pin-connections	Fixed Base	ANSYS (2000)	Equivalent Quasisuperelement for dynamic analysis
Judd and Fonseca (2005)	2-noded beam	8-noded Quadrilateral	2 Independent Orthogonal Springs Oriented at the first trajectory	Pin-connections	Fixed Base	[ABAQUS-ANSYS-CASHEW] - QUICK (Judd 2005)	Equivalent Quasisuperelement for dynamic analysis
Xu (2006)	2-noded beam	4-noded Quadrilateral	2 Independent Orthogonal Springs Oriented at the first trajectory (Foliente 1995)	2 Independent Orthogonal Springs	Fixed Base	ABAQUS	Equivalent Quasisuperelement for dynamic analysis
Ayoub (2007)	2-noded beam	4-noded Quadrilateral	2 Independent Orthogonal Springs	Pin-connections	Fixed Base	DIANA	SDOF Model per Building Story for Dynamic Analysis

CHAPTER 3: EXPERIMENTAL SEISMIC RESPONSE OF A FULL-SCALE LIGHT-FRAME WOOD BUILDING: NEESWOOD BENCHMARK TESTS

3.1 Introduction

As part of the NEESWood Project, an experimental program that involved the three-dimensional shake-table testing of a full-scale two-story light-frame wood townhouse building was conducted at the University at Buffalo (UB). The test structure represented one of the largest building specimens ever tested under three-dimensional earthquake simulation and utilized both twin shake tables at the Structural Engineering and Earthquake Simulation Laboratory (SEESL) at UB for over 9 months. The experimental program, extended in 5 test phases associated with different structural configurations of the building, was selected as such to provide a wide set of recorded data that can enable observation, identification and quantification of fundamental aspects that affect the seismic performance of a light-frame wood building with realistic dimensions, under increased levels – beyond design-basis – of shaking. The qualitative and quantitative observations from the benchmark test results can be directly applicable to performance-based design procedures, conducted within the NEESWood Project, as well as for validation or calibration of numerical models.

This chapter provides a summary of the experimental results generated throughout the 5 different test phases, focusing on the effect of non-structural components on the dynamic characteristics and the seismic performance of the test structure. A detailed presentation of this full-scale experimental project along with a complete description of the experimental data can be found in Christovasilis *et al.* (2009a).

3.2 Description of Test Building

The full-scale test building considered in this study is one of the four California-style index buildings designed within the recently completed CUREE-Caltech Woodframe Project (Reitherman *et al.* 2003). It represents one unit of a two-story townhouse containing three units, having approximately 1800 ft^2 of living space with an attached two-car garage.

Figure 3.1 shows plan views of the first and second floor of the test building, while Figure 3.2 presents exterior wall elevation views. The major structural components of the test building are identified in Figure 3.1 and are described in detail by Christovasilis *et al.* (2009a). The footprint of the test building is 61 ft by 22 ft. The height of the test building from the first floor slab to the roof eaves is 17 ft - 2 in and its total weight is 72 kips.

The design of the test building is based on engineered construction according to the seismic provisions of the 1988 edition of the Uniform Building Code (ICBO 1988) for Seismic Zone 4 and common design practices in California. The design base shear in each orthogonal direction of the building was 13 kips (or 18% of its weight).

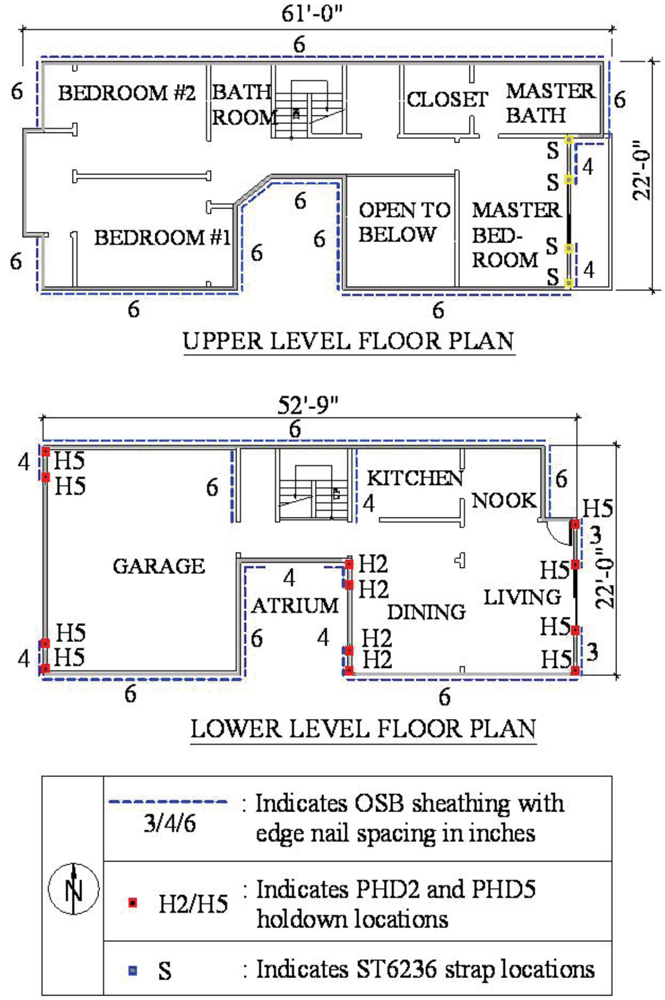

Figure 3.1 Plan Views of Test Building

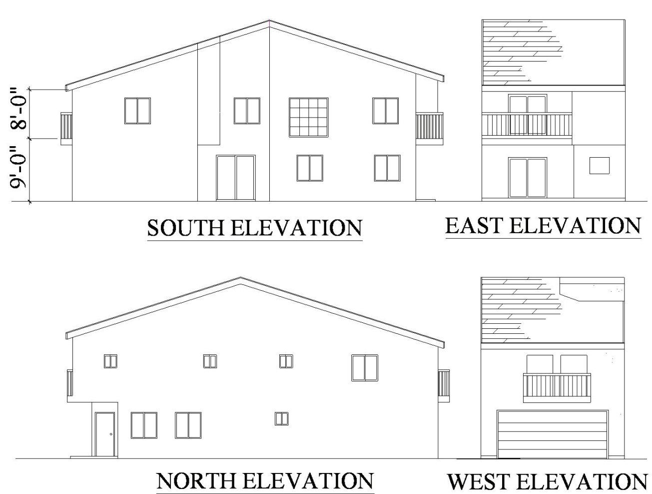

Figure 3.2 Elevation Views of Test Building

All walls of the test building were built with 2x4 Hem-Fir studs except for the North, South and West walls of the garage where 2x6 studs were used. The exterior walls of the test building were covered on the outside with 7/8 in thick stucco over 7/16 in thick OSB sheathed shear walls and 1/2 in thick gypsum wallboard on the inside. Eight penny common nails (0.131 in diameter by 2.5 in long) with spacing of between 3 in to 6 in along panel edges and 12 in along interior studs were used to connect the OSB sheathing to the wood framing. Construction details regarding the two-story townhouse building are given by Reitherman *et al.* (2003) and Christovasilis *et al.* (2009a). Gypsum wallboard panels, 1/2 in thick, were installed on all interior walls and ceiling surfaces and on both sides of interior partitions. All surfaces were taped, mudded and painted. The panels were oriented horizontally on the walls and fastened with #6-1-1/4 in long drywall screws spaced at 16 in on center along the vertical studs only (no fastening along the top and bottom plates). The ceiling panels were fastened with the same screws spaced at 12 in on center. The stucco was attached to the wood framing by a galvanized 16-gage steel wire lath, fastened to the OSB sheathing and vertical studs by 1-1/2 in long staples spaced at 6 in on center. The construction of the test building was conducted by professional contractors to replicate field conditions.

3.3 Shake Table Test Program

3.3.1 Experimental Setup

The twin re-locatable, 50 ton, tri-axial shake tables of the SEESL at UB were utilized for the experiment. The two tables acting in unison were required to accommodate the size and weight of the full-scale test building. The 23 ft by 23 ft extension steel frames available on both shake tables were connected together by a steel link structure to support the entire woodframe structure across the two shake tables with minimal vertical deflection. Threaded A-307 steel rods bolted to the existing extension frames were used as anchor bolts for the sill plates. A 2-1/4 in thick layer of grout was installed on top of the steel base beneath the pressure treated sill plates to simulate the friction of the sill plate against a concrete foundation. Seismic holdowns were installed at the end of various first level narrow wall piers, as shown in Figure 3.1.

3.3.2 Instrumentation

More than 250 sensors were used to monitor the response of the test building during the shake table tests. Displacement transducers were used to measure the absolute horizontal and vertical displacements of the shake tables and of several locations on each floor level of the test building. The displacements of the test building relative to the shake tables could then be obtained by subtracting the shake table displacements from the floor displacements. The uplift and sliding of the sill plate and shear wall studs relative to the floor levels were also monitored at several locations by linear displacement potentiometers. Accelerometers were used to record absolute horizontal and vertical acceleration time-histories at several locations over the shake tables, floor and roof of the test building. All anchor bolts around the perimeter of the test building were instrumented with load cells in order to obtain the distribution of anchor bolt tensile forces at all times during the shake table tests. Additionally, eleven video cameras were used to record each seismic test. A detailed list of instruments used in the shake table tests is given in Christovasilis *et al.* (2009a).

3.3.3 Testing Protocol

Multiple seismic tests were conducted for various configurations of the test building. Table 3.1 presents a summary of the five seismic test phases included in the test program and the corresponding configurations of the test building. Low amplitude white noise tests were also conducted between the seismic tests of each phase to determine the changes in the dynamic characteristics (natural periods, mode shapes and damping) of the test building as it experienced increasing levels of damage during each test phase. The building was repaired after each test phase to return the lateral load-resisting system to its original characteristics before the start of each subsequent test phase. These repairs were extensive and included replacing some of the OSB panels, gypsum wallboards and wood studs. Note that all test phases were performed for a constant mass of the test building by incorporating ballast weights at the floor level for the test phases in which some of the wall finish materials were omitted.

In this chapter, only Phases 1, 3, 4 and 5 are discussed. Information on Test Phase 2, incorporating fluid dampers in selected locations of the test building, is available in Shinde *et al.* (2007). Test Phases 1, 3, 4 and 5 were designed to evaluate the effect of interior and exterior wall finishes on the seismic response of the test building. In Phase 1, the test building incorporated only the wood structural members without any wall finishes. In Phase 3, 1/2 in thick gypsum wallboard was applied to the interior surfaces of the structural perimeter walls and to both sides of the two interior structural shear walls, located at the fist level of the test building in the North-South direction (see Figure 3.1). In Phase 4, gypsum wallboards were also applied to all interior partition walls and ceilings. Finally, in Phase 5, 3-coat, 7/8 in thick, stucco was applied to the exterior walls. Figure 3.3 shows photographs of the Phase 1 and Phase 5 test building ready for testing on the shake tables.

Table 3.1 Test Phases and Building Configurations

Test Phase	**Test Building Configuration**
1	Wood structural elements only
2	Test Phase 1 structure with passive fluid dampers incorporated into selected wood sheathed walls
3	Test Phase 1 structure with 1/2 in thick gypsum wallboard installed with #6-1-1/4 in long screws @ 16 in on center on structural wood sheathed walls
4	Test Phase 3 structure with 1/2 in thick gypsum wallboard installed with #6-1-1/4 in long screws on all walls (16 in on center) and ceilings (12 in on center)
5	Test Phase 4 structure with 7/8 in thick stucco installed with 16 gage steel wire mesh and 1-1/2 in long leg staples @ 6 in on center on all exterior walls

Figure 3.3 Test Building on Shake Tables: (a) without Wall Finishes – Test Phase 1 and
(b) with Wall Finishes – Test Phase 5

3.3.4 Input Ground Motions

Two different types of tri-axial historical ground motions were used for the seismic tests: ordinary ground motions and near-field ground motions. The ordinary ground motions represented a Design Basis Earthquake (DE) having a probability of exceedance of 10% in 50 years (10%/50 years), or equivalently, a return period of 475 years. The 1994 Northridge Earthquake ground motions recorded at Canoga Park, with an amplitude scaling factor of 1.20, were selected as the DE (Krawinkler *et al.* 2000). The near-field ground motions represented a Maximum Considered Earthquake (MCE) having a probability of exceedance of 2% in 50 years (2%/50 years), or a return period of 2475 years. The unscaled 1994 Northridge Earthquake ground motions recorded at Rinaldi were selected as the MCE (Krawinkler *et al.*

2000). Figure 5.4 presents the absolute acceleration response spectra at 5% damping for these two (unscaled) tri-axial seismic records.

In addition to the DE and MCE hazard levels, the Canoga Park ground motions were scaled to simulate hazard levels of 99.9%/50 years, 50%/50 years and 20%/50 years. The resulting Peak Ground Accelerations (PGA) applied in the principal directions of the test building are listed in Table 3.2. Five seismic test levels were considered during each phase of seismic testing. For each seismic test level, two seismic tests were conducted: one tri-axial (3D) test followed by one horizontal bi-axial (2D) test. Note that during Test Phases 1, 3 and 4, only Seismic Test Levels 1 and 2 were conducted in order to limit the damage of the test building to a repairable level. The structure was not repaired between test levels.

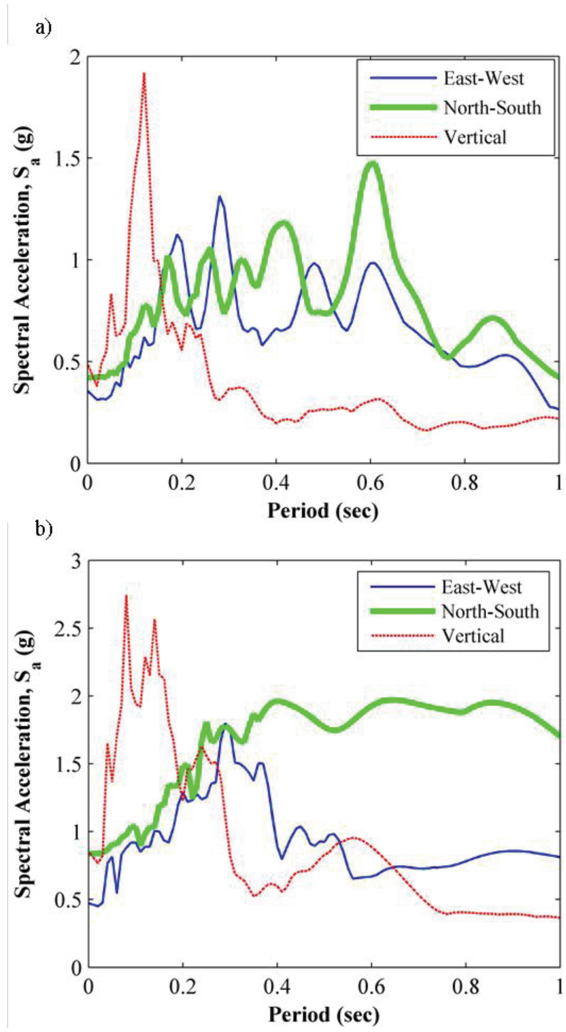

Figure 3.4 Absolute Acceleration Response Spectra for 5% Damping of Earthquake Ground Motions Used in Seismic Tests: (a) Canoga Park Record, (b) Rinaldi Record

Table 3.2 Ground Motions for Seismic Tests

Seismic Test Level	Ground Motions	Hazard Level %/50 years	Scaled PGA (g)		
			East-West	North-South	Vertical
1	1994 Northridge Canoga Park	99.99	0.04	0.05	0.06
2	1994 Northridge Canoga Park	50	0.19	0.22	0.26
3	1994 Northridge Canoga Park	20	0.31	0.36	0.42
4	1994 Northridge Canoga Park	10 (DE)	0.43	0.50	0.59
5	1994 Northridge Rinaldi	2 (MCE)	0.47	0.84	0.85

3.4 Results of Ambient Vibration Tests

Before and after each seismic test, the dynamic properties of the test building were estimated by simulated ambient vibration tests. For this purpose, the test building was excited by a low-level white-noise base acceleration input having a flat (i.e. uniform) spectrum with 0.5–50 Hz frequency band and a Root Mean Square (RMS) amplitude of less than 0.10 g.

The natural periods, mode shapes and associated modal damping ratios were determined through Transfer Functions (TFs) of the story acceleration response of the structure and the base motion. Thirty two horizontal accelerometers, located at the floor and roof levels of the test building, as well as four accelerometers located on the twin shake tables, were used to generate the TFs for each white noise test. The TFs were computed using commercial data analysis software (DADiSP/2002 2006) with dedicated script files developed for this study. The equivalent viscous damping ratios of the test building were determined using the well known half-power bandwidth method (see e.g. Clough and Penzien 1993) applied to the peaks of the TFs.

Figure 3.5 shows the initial fundamental periods and mode shapes, extracted from the ambient vibrations tests in each principal direction of the test building, for Test Phases 1, 3, 4 and 5. Not surprisingly, the fundamental periods of the test building are significantly longer in its transverse (North-South) direction than in its longitudinal (East-West) direction. The first mode shape is mainly associated with transverse deformations of the structure, while the second mode shape demonstrates torsional effects that result in longitudinal and transverse deformations. The introduction of gypsum wallboard finishes on the structural walls in Test Phase 3 causes a reduction in the fundamental period of 9% and 5% along the transverse and longitudinal directions of the test building, respectively. From a single-degree-of-freedom system point of view, these fundamental period reductions correspond to increases in lateral stiffness of 21% and 11% along the transverse and longitudinal directions of the test building, respectively (see (3.1) below). These results indicate that introducing gypsum wallboard finishes on the interior surfaces of the structural walls increased the lateral stiffness of the test building. On the other hand, the introduction of similar gypsum wallboard finishes to all the interior partition walls and ceilings in Test Phase 4 had no effect on the fundamental periods and, thereby, the lateral stiffness of the test building (at least at low levels of shaking). This lack of positive effect can be attributed to the lack of structural connections between the interior partition walls and the floor and roof diaphragms of the test building. Although the bottom plates of the partition walls were nailed to the floor sheathing and joists, the top plates were attached to the underside of the second floor framing and bottom chord of the roof trusses with roof truss clips. These clips contain 1-1/2 in slots to allow vertical truss chord and floor joist movement when gravity loads are applied.

The introduction of stucco on the exterior walls of the test building in Phase 5 causes a reduction in the fundamental period of 3% and 9% along the transverse and longitudinal direction of the test building compared to the Phase 4 configuration. In terms of equivalent lateral stiffness, Phase 5 exhibits an increase in lateral stiffness of 29% and 32% along the transverse and longitudinal directions, respectively, compared to the original Phase 1 building. For both directions, the deformations are concentrated in the first level of the test building, indicating the potential for a weak first story collapse mechanism. The fundamental mode shapes in the longitudinal direction are also affected by torsional response and by the in-plane shear deformations of the floor diaphragm in the stair core area between the two main units of the townhouse, particularly for the Phases 1 and 3. For Phases 4 and 5, the shear deformations of the diaphragm are reduced because of the in-plane stiffness provided by the gypsum ceilings.

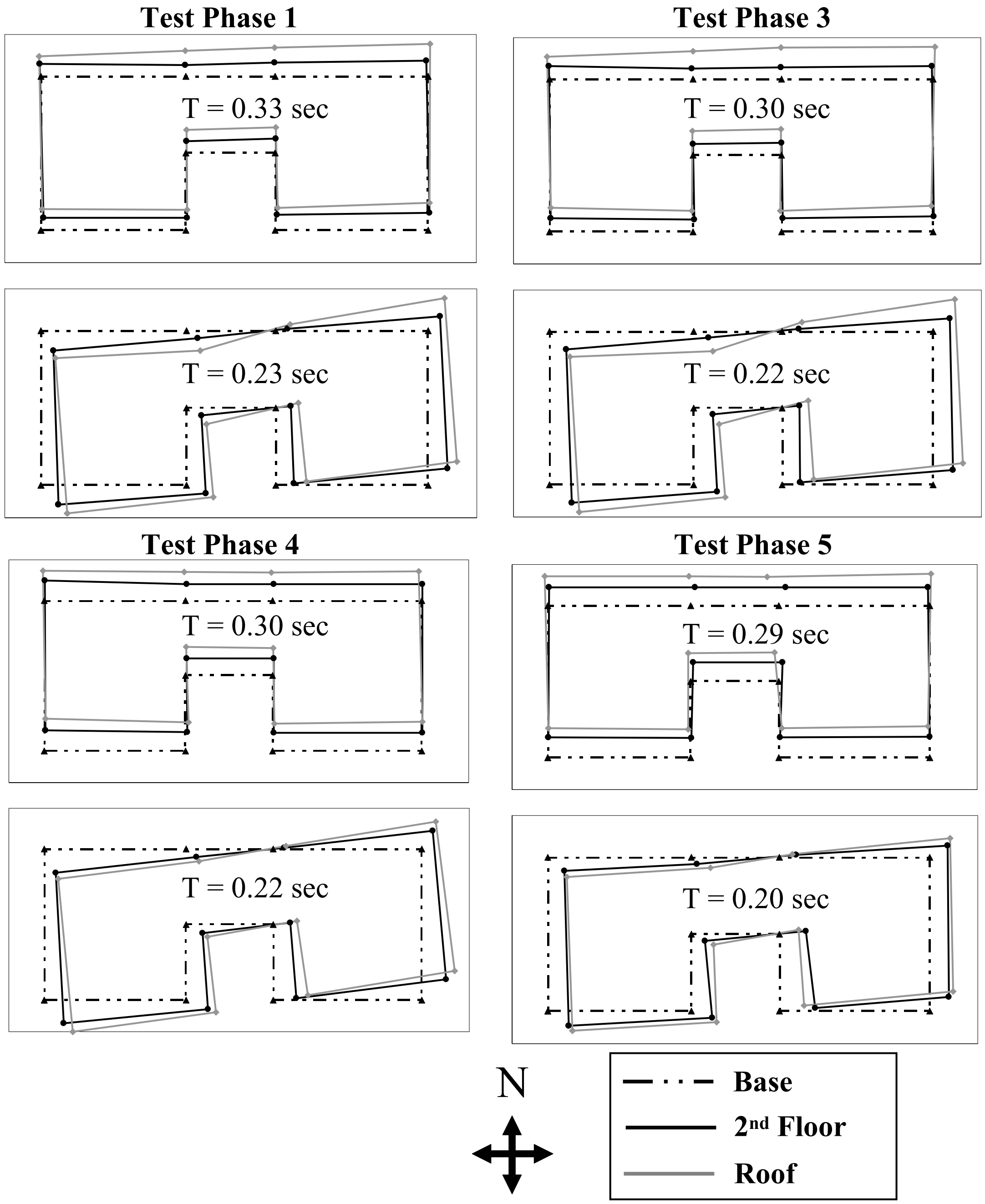

Figure 3.5 Initial Natural Periods and Mode Shapes of Test Building

Figure 3.6 illustrates the deterioration of the equivalent lateral stiffness in the transverse (North-South) direction of the test building through the various seismic tests conducted, assuming a single-degree-of-freedom response of the test building. Since the initial fundamental period T_0 is known, as well as the fundamental period T_i measured after each seismic test, the normalized equivalent lateral stiffness k_i, as a percentage of the initial lateral stiffness k_0 can be calculated after each seismic test as:

$$\frac{k_i}{k_o} = \left(\frac{T_o}{T_i} \right)^2 \tag{3.1}$$

The deterioration of the lateral stiffness is more pronounced for the Test Phase 1 configuration. The stiffness at the end of this phase dropped to less than 60% of the initial stiffness after Test Level 2. The lateral stiffness for the structures of Test Phases 3 and 4 was above 80% of their initial stiffness after Level 2 test; the corresponding value for the Test Phase 5 structure was above 90%. Even after the tri-axial DE Seismic Level 4 test, the lateral stiffness of the Test Phase 5 structure remained above 75% of its initial lateral stiffness. The deterioration was smaller when wall finishes were applied for the same level of simulated ground shaking. Note that the increase of the stiffness that is observed after the final tri-axial test of Seismic Level 5 of Test Phase 5 was due to the repair of damaged anchor bolts in the two walls on the West (garage wall) and East side of the first floor of the benchmark structure, prior to the conduction of the Level 5 tri-axial test, which resulted in a stiffer structure.

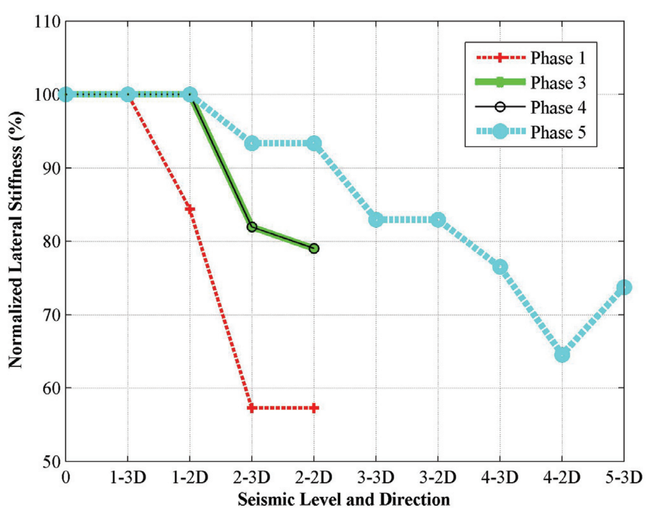

Figure 3.6 Variations of Normalized Lateral Stiffness in North-South Direction of Test Building

Figure 3.7 shows the variations of the first modal equivalent viscous damping ratio measured in the North-South direction of the test building after each seismic test conducted. The first modal damping ratios range from 10 to 20% of critical, with a mean value of around 15% of critical for all test phases.

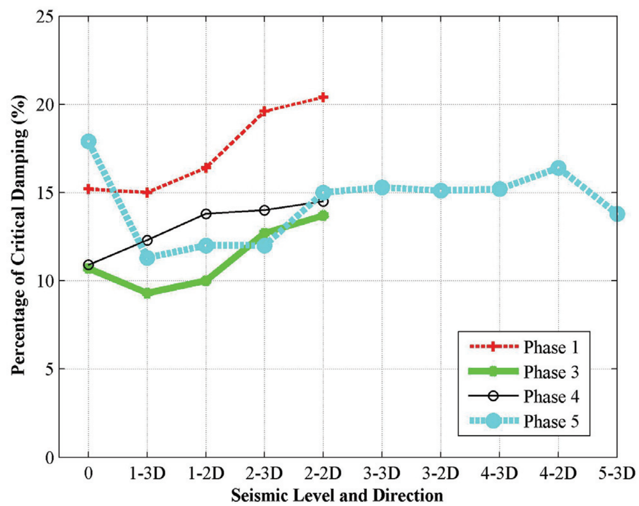

Figure 3.7 Variations of First Modal Damping Ratios in North-South Direction of Test Building

3.5 Results of Seismic Tests

3.5.1 Global Hysteretic Responses

Figure 3.8 shows the global hysteretic responses (base shear force vs relative horizontal displacement at the center of the roof eave level) of the test building during Test Phases 1, 3, 4 and 5, respectively and under Seismic Test Level 2 (see Table 3.2). The base shear was computed by summing the inertia forces at each level of the test building based on horizontal acceleration recordings. The maximum base shear and displacement achieved in each direction are indicated by circles on each graph. As expected, the lateral displacements in the transverse (North-South) direction are significantly larger than those in the longitudinal (East-West) direction.

In Test Phase 1, the wood-only building experienced a peak roof displacement of 2.5 in (1.3% building drift) in its transverse direction under the Seismic Test Level 2 representing excitation intensity of 44% of that expected for the Level 4 Design Earthquake (DE). The introduction of gypsum wallboard finishes on the structural walls in Test Phase 3 resulted in a significant reduction in transverse roof displacements (approximately 44% reduction compared to the wood-only building of Phase 1). The overall hysteretic response of the building in Test Phase 3 is also stiffer than that of Test Phase 1, indicating the important effects that the gypsum wallboard had in stiffening the structural walls. The introduction of gypsum wallboard on the interior partition walls and ceilings in Test Phase 4 resulted in a further reduction of 29% in roof displacements in the transverse direction (1.4 in for Phase 3 vs 1.0 in for Phase 4). Finally, the introduction of stucco on the exterior walls reduced the roof displacements even further to 0.7 in; similar results are observed in the longitudinal direction.

Note in Figure 3.8 that only moderate pinching is observed for the transverse (North-South) direction in the wood-only Test Phase 1 building, while almost linear elastic responses are observed for Test Phases 3, 4 and 5. This result indicates that the wall finishes not only reduce the displacement response of the test building but changed also its overall hysteretic characteristics.

Figure 3.9 shows the effective lateral stiffness in each direction and for each building configuration. The effective stiffness values were obtained by computing the slope linking the positive and negative peak base shear forces and peak roof displacement coordinates from the graphs shown in Figure 3.8. The effective stiffness values increase significantly in both directions with the application of interior wall finishes. The increase of stiffness after the application of the exterior stucco finish in Test Phase 5 is more significant in the longitudinal (East-West) direction than in the transverse (North-South) direction. This can be attributed to the more pronounced shear deformations of the low aspect ratio walls in the longitudinal direction. In the transverse direction, significant foundation uplift and rocking occurred, which reduced the shear stiffness contribution of the wall elements.

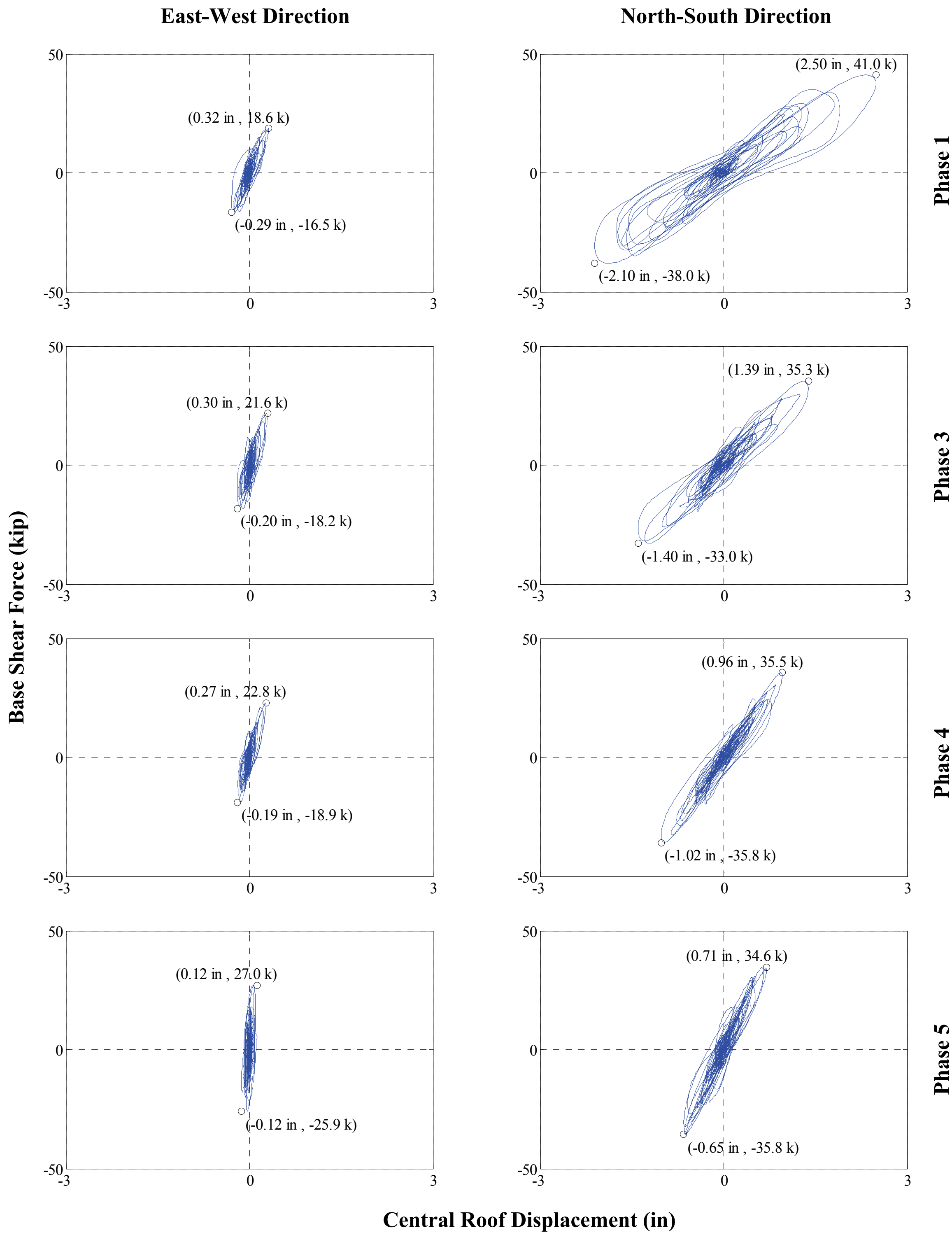

Figure 3.8: Global Hysteretic Responses of Test Building, Test Level 2

Figure 3.10 shows the global hysteretic responses obtained with the complete (Phase 5) building under Test Levels 4 (DE) and 5 (MCE), respectively. In the transverse (North-South) direction, the maximum roof displacement reached 1.6 in (0.8% drift) under the DE level and

4in (2.0 % drift) under the MCE level. Note that the wood-only building of Phase 1 exhibited, under Test Level 2, a peak roof displacement larger than the Phase 5 building under the DE Test Level 4.

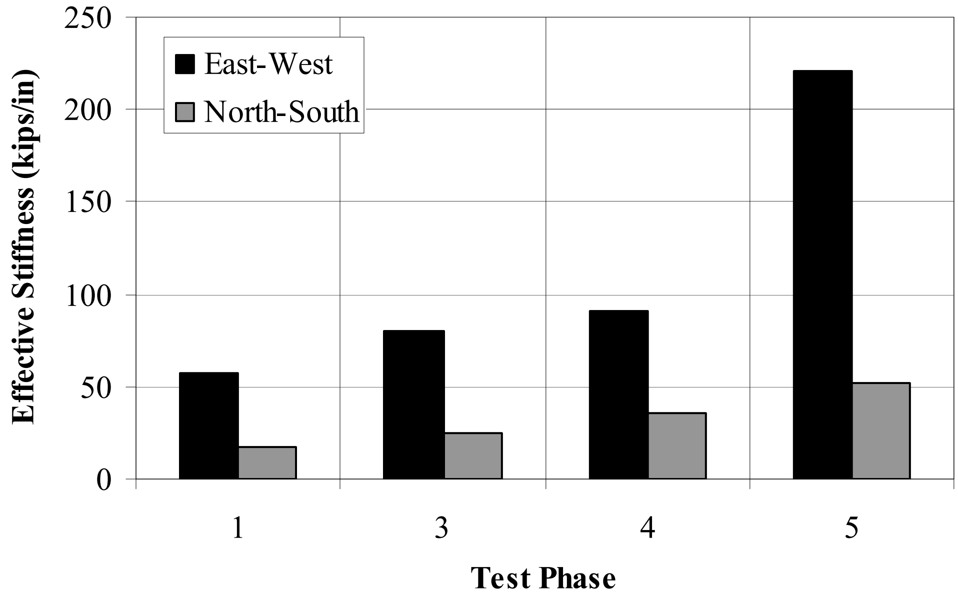

Figure 3.9 Effective Lateral Stiffness of Test Building, Test Level 2

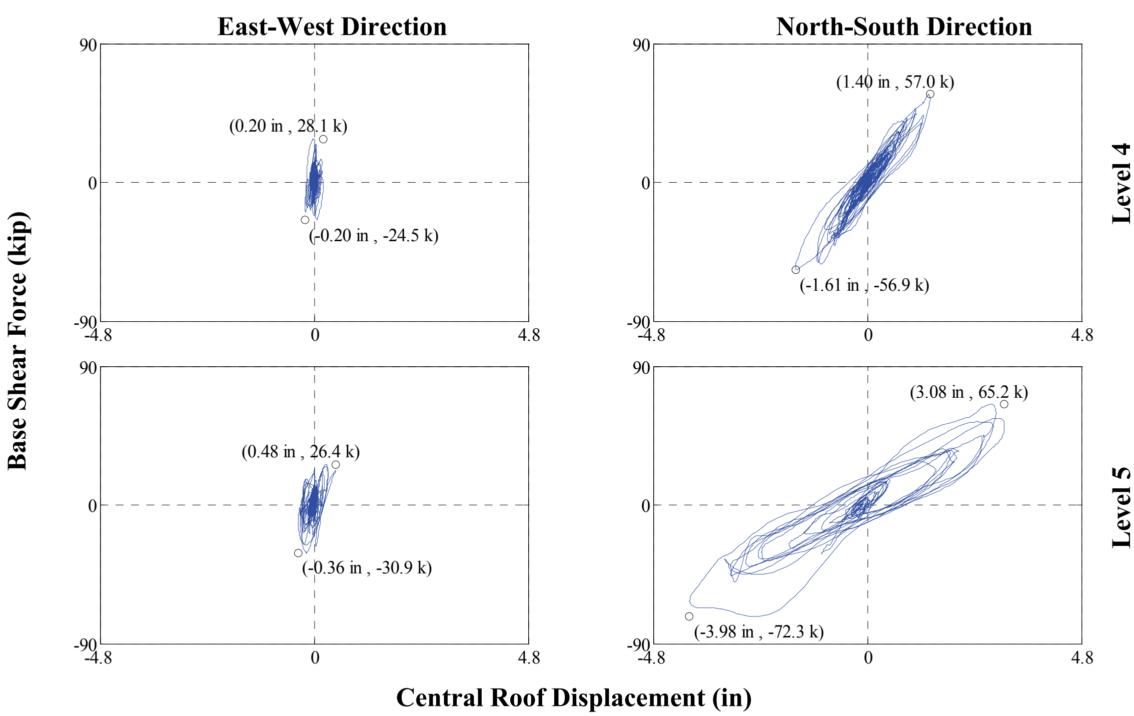

Figure 3.10 Global Hysteretic Responses of Test Building, Test Phase 5

3.5.2 Response of Garage Wall Line

The seismic response of the test building in its transverse (North-South) direction was significantly influenced by the response of the garage wall line at the first level. The narrow wall piers (aspect ratio of 2.5:1) on each side of the garage opening compounded by the significant torsional response of the building under high intensity shaking (Christovasilis *et al.* 2009a), caused this garage wall line to experience the largest inter-story drifts.

Figure 3.11 shows the inter-story drift time-histories measured along the garage wall line during Test Phases 1, 3, 4, and 5, respectively and under Seismic Test Level 2 (see Table 3.2). The garage wall line of the wood-only building of Phase 1 experiences a peak relative displacement of 1.65 in (1.5% inter-story drift) which corresponds to 65% of the total building drift developed in the transverse direction during this test (see Figure 3.8). This result indicates that most of the transverse lateral displacements of the test building in the garage wall line occurred at the first level, which suggests a possible soft-story collapse mechanism under higher amplitude base excitations. Note that this conclusion is valid for the garage wall line only under high level of excitations. For some other wall lines in the building, the second story inter-story drifts could be greater than the first story in some cases under lower amplitude excitation.

Again, the introduction of gypsum wallboard finishes on the structural walls in Test Phase 3 caused a significant reduction in the peak drift experienced by the garage wall line (42% reduction compared to the wood-only building of Phase 1). The response of the Test Phase 4 building, however, is almost identical to that of Phase 3. This can be explained by the fact that very little interior partition wall lines were incorporated in the first level of the test building (see Figure 3.1). The incorporation of exterior stucco finish also caused a significant reduction in the peak drift experienced by the garage wall line (66% reduction compared to the wood-only building of Phase 1 and 42% reduction compared to the Phase 3 building).

Figure 3.12 shows the inter-story drift time-histories measured along the garage wall line of the completed Test Phase 5 building under Seismic Test Levels 4 (DE) and 5 (MCE), respectively.

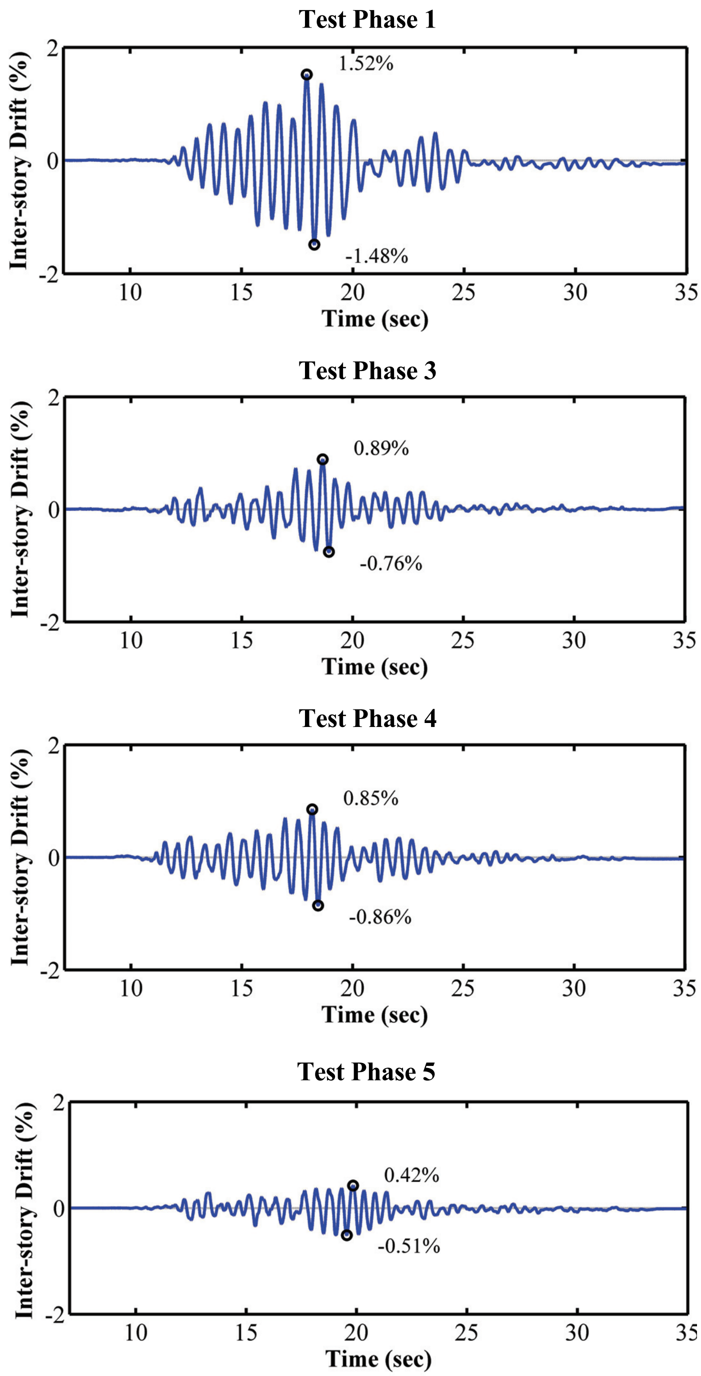

Figure 3.11 Response of Garage Wall Line, Test Level 2

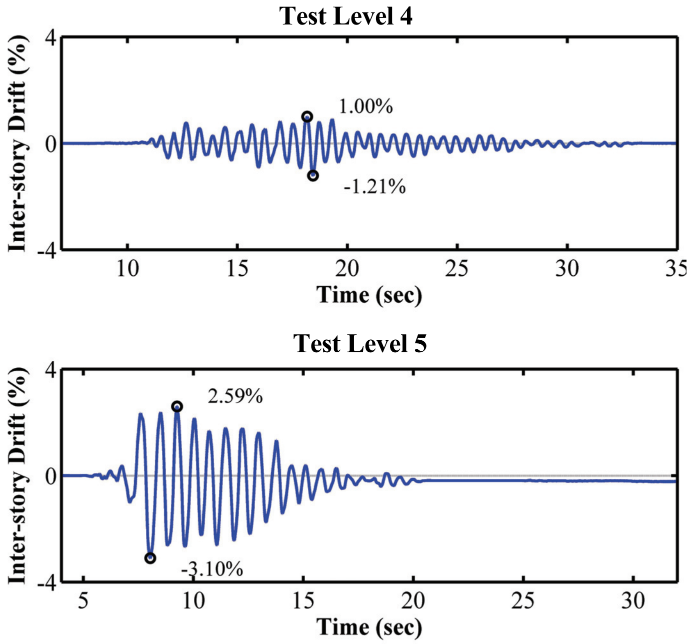

Figure 3.12 Response of Garage Wall Line, Test Phase 5

The Test Phase 5 building experienced peak relative displacements at the garage wall line of 1.3 in (1.2% inter-story drift) and 3.4 in (3.1% inter-story drift) under the DE and MCE levels, respectively. Note again that the wood-only Phase 1 building experienced higher drifts at the garage wall line under Test Level 2 (44% DE) than the complete Test Phase 5 building under Test Level 4 (100% DE). This result again underscores the significant contribution of the wall finishes in improving the seismic response of the test building.

3.5.3 Observed Damage to Test Building

After the completion of each seismic test, a detailed damage survey was conducted on the test building in order to document the evolution of damage with test phases and test levels. In this section, the damage observed on the various structural and non-structural components of the test building is briefly described.

3.5.3.1 Damage to Gypsum Wallboard

Hairline cracking occurred in the gypsum wallboard applied to the interior surfaces of the structural walls of the Phase 3 test building after the Test Level 2 shaking, as shown in Figure 3.13a. This cracking occurred mainly at corners of the openings of the interior shear walls (see Figure 3.1) and propagated with increasing level of shaking.

Ceiling gypsum damage was also observed in the Test Phase 4 building. Cracking of the partition-to-ceiling connections in the transverse direction of the test building started under the Test Level 2 shaking, as shown in Figure 3.13b. Ceiling damage increased in the Test Phase 5 building until a large portion of the ceiling gypsum failed under the Test Level 5 shaking, as shown in Figure 3.13c. This failure occurred in the second level ceiling connecting the two main rectangular units of the test building and can be attributed to the in-plane shear deformation of the ceiling diaphragm at that location (see Figure 3.5).

3.5.3.2 Damage to Stucco

Hairline cracking of stucco in the Phase 5 test building started after the Test Level 2 shaking. This cracking occurred mainly at corners of windows and door openings and propagated with increasing level of shaking. After Test Level 5 (MCE), significant spalling and cracking of stucco occurred around the garage door opening, as shown in Figure 3.14.

3.5.3.3 Damage to Sill Plates

The most significant damage observed in the Test Phase 5 building after Test Level 5 was the splitting of the 2x4 and 2x6 sill plates around the entire perimeter of the building. In particular, the sill plate of the narrow wall piers of the garage separated by more than 1/2 in, as shown in Figure 3.15. It is believed that this damage is the result of combined in-plane and out of plane deformations of the wall panels. In the in-plane direction, sliding of the sill plate relative to the holdown devices can induce longitudinal splitting of the sill plate. In the out-of-plane direction, eccentric vertical loading from the sheathing nails can cause tension splitting perpendicular to grain in the sill plate.

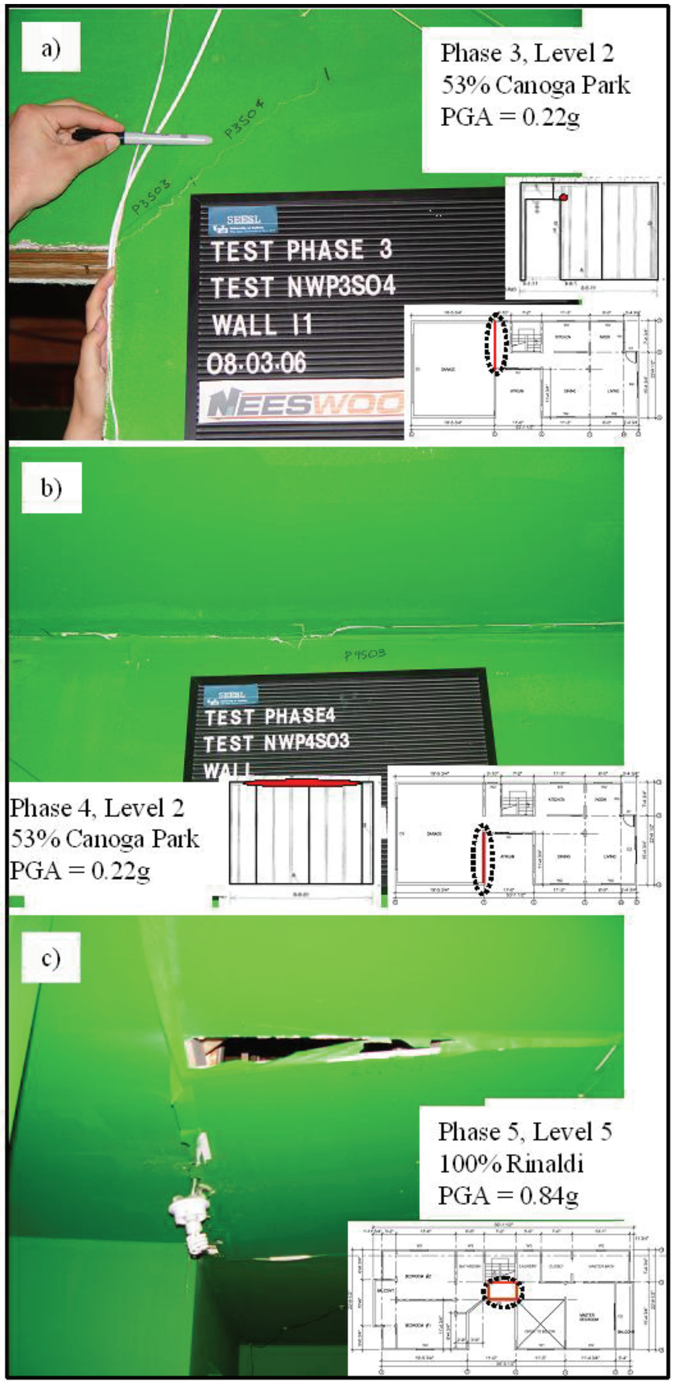

Figure 3.13 Damage to Gypsum Wallboard,
(a) Diagonal Hairline Cracking in Corner of Pedestrian Door Opening, Test Phase 3, Test Level 2,
(b) Cracking of Partition-to-Ceiling Connection, Test Phase 4, Test Level 2, and
(c) Ceiling Failure, Test Phase 5, Test Level 5

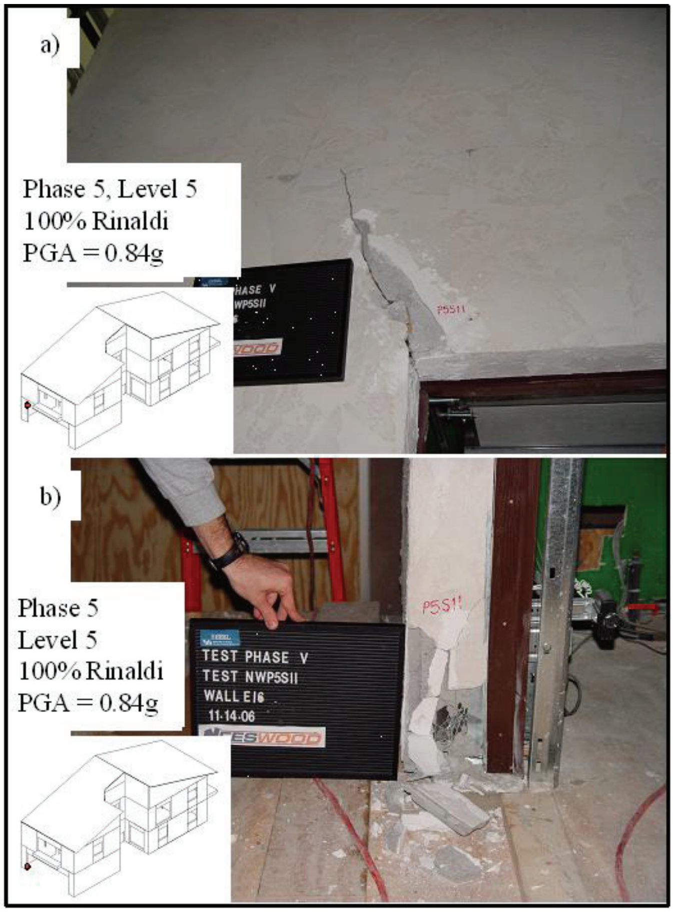

Figure 3.14 Damage to Stucco, Test Phase 5, Test Level 5,
(a) Diagonal Cracking in Corner of Garage Door Opening,
(b) Spalling at Garage Wall Pier

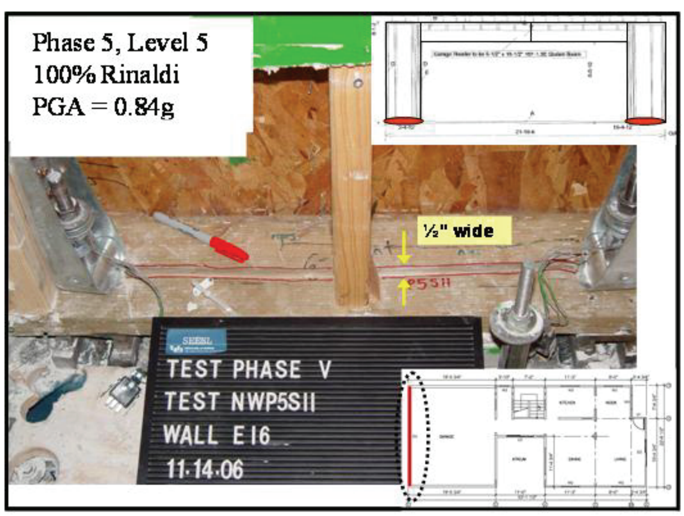

Figure 3.15 Sill Plate Failure, Test Phase 5, Test Level 5

3.5.4 Estimation of Displacement Components

In this section, an attempt to decompose the first floor inter-story displacements of specific walls into different components is presented, by combining in the time domain the recorded data from the wall deformations, the slippage of sill plates and the uplifting response of the end studs. Four exterior walls along the transverse direction were selected (E16, E13, E11 and E8 from Wall Lines 6, 5, 4 and 2, respectively), as shown in Figure 3.16a. Figure 3.16b illustrates the wall configurations, indicating the length of the wall or the wall panel that was instrumented and the locations of the holdowns, in three of the four walls.

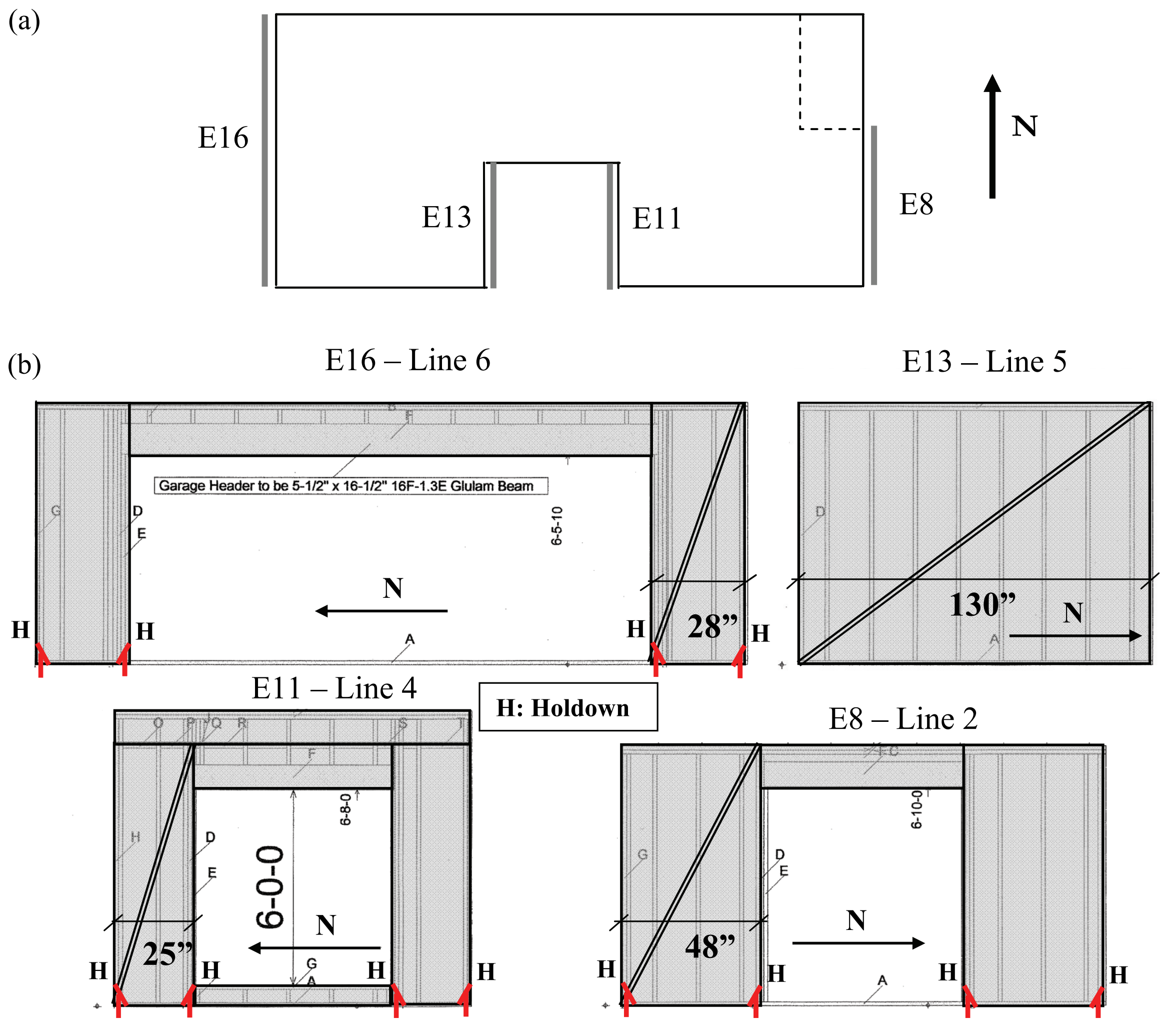

Figure 3.16 (a) Location and (b) Configuration of the Walls used for the Displacement Decomposition

The only displacement component that needed to be evaluated was that caused by the uplifting response of each wall. The displacement time-history at the top of a wall (or a wall panel) can be estimated when the uplift displacement time-histories at the two end studs are known, by defining a wall base angle of rotation and extrapolating the horizontal displacement at the top assuming a rigid body motion.

Figure 3.17 illustrates how the inter-story displacement due to uplifting response was estimated at the garage wall (E16) for the tri-axial Level 2 test of Phase 1 (Test NWP1S17). Figure 3.17a presents the sill-plate uplift displacement time-histories (UP2 and UP4) and Figure 3.17b shows the total uplift displacement time histories (UP1+UP2 and UP3+UP4), at the base corners of the south wall segment of the garage wall. Figure 3.17c plots the horizontal displacement time-histories, $\mathbf{d}_{\mathbf{U,S}}$ and $\mathbf{d}_{\mathbf{U,S+S}}$, due to the sill plate uplift and the sill-plate-plus-stud uplift, respectively, which are given by:

$$\begin{aligned} \mathbf{d}_{\mathbf{U,S}}(t) &= \frac{UP2(t) - UP4(t)}{\mathbf{L}_{\mathbf{Wall}}} \cdot \mathbf{h} \\ \mathbf{d}_{\mathbf{U,S+S}}(t) &= \frac{\left(UP1(t) + UP2(t)\right) - \left(UP3(t) + UP4(t)\right)}{\mathbf{L}_{\mathbf{Wall}}} \cdot \mathbf{h} \end{aligned} \tag{3.2}$$

where $\mathbf{L}_{\mathbf{Wall}}$ is the length of the wall panel, equal to 28 in, and $\mathbf{h}$ is the height of the first floor, equal to 109 in.

Displacements $\mathbf{d}_{\mathbf{U,S}}$ and $\mathbf{d}_{\mathbf{U,S+S}}$ were computed based on the assumption of rigid body rotation of the wall, which holds for narrow wall-piers with high height-to-length ratio, such as these in Walls E16 and E11. Yet, it is not clear if these displacement estimates are reliable in cases of low aspect ratio walls, such as Wall E13, or in cases where two wall panels can interact with each other, such as Walls E11 and E8.

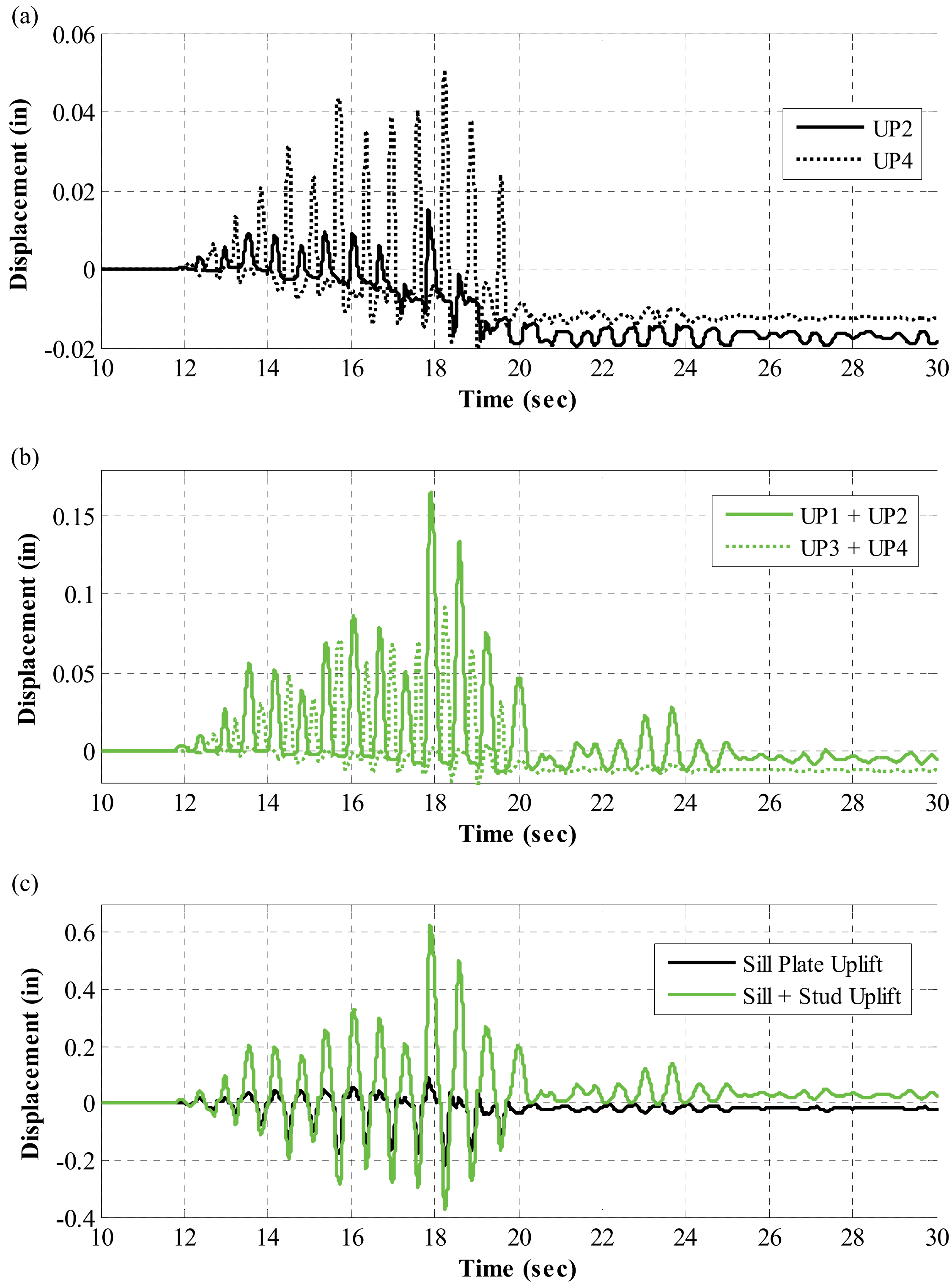

Figure 3.17: (a) Sill Plate Uplift Displacements, (b) Total Uplift Displacements, and (c) Associated Inter-Story Displacement Estimates of the South Segment of the Garage Wall, for Test NWP1S17

Moreover, since the diagonal potentiometers were connected at the sill and top plates of the walls, it is expected that the horizontal displacement due to stud-to-sill-plate uplift should be already included in the wall deformation measurement, provided by the diagonal potentiometer, in cases where the rigid body assumption applies. Figure 3.18a,b present the computed displacement components of Wall E16 for the tri-axial Level 2 tests of Phases 1 and 4, respectively.

In these plots, the inter-story displacement, measured between the floor diaphragms, is compared with the combined displacement at the wall and the sill plate slippage, including the effect only from the sill plate uplift response with respect to the foundation. The explicit effect of the stud uplift is also plotted with the dotted line. It is observed that the combined displacement time-history correlates well with the inter-story displacement time-history and is always smaller (in the absolute sense). The difference between these two lines is an unidentified displacement component, which can include the effect of stud uplift as well as other sources of displacements that are not measured, such as the slippage of the top plate with respect to the diaphragm and the deformation of the floor joists.

Figure 3.19 and Figure 3.20 summarize the normalized displacement components at the time instant of the peak inter-story drift, for all the tri-axial Level 2 tests and the tri-axial tests of Phase 5, respectively. The peak inter-story displacement of each wall line is also indicated, for each test, in white fonts.

Figure 3.19 clearly indicates that the application of wall finish materials reduced the wall deformation ratio of three of the four walls, from high values of around 0.7, observed for Phase 1, to as low as 0.2, observed for Phase 5. Consequently, the sill plate slippage and the sill plate uplift ratios were generally increased after the installation of wall finishes, and a greater portion of the total uplift was due to the sill plate uplift. The garage wall deformation ratio was around 0.5 for all the seismic tests evaluated. It was not affected either by the wall finishes or the level of shaking intensity and the level of deformation (Figure 3.19a and Figure 3.20a). Figure 3.20 shows that the wall deformation ratios remained quite low for all tri-axial tests of Phase 5. The unidentified component ratio varied between 0 and 0.7 and was higher for the Phase 5 displacement decomposition.

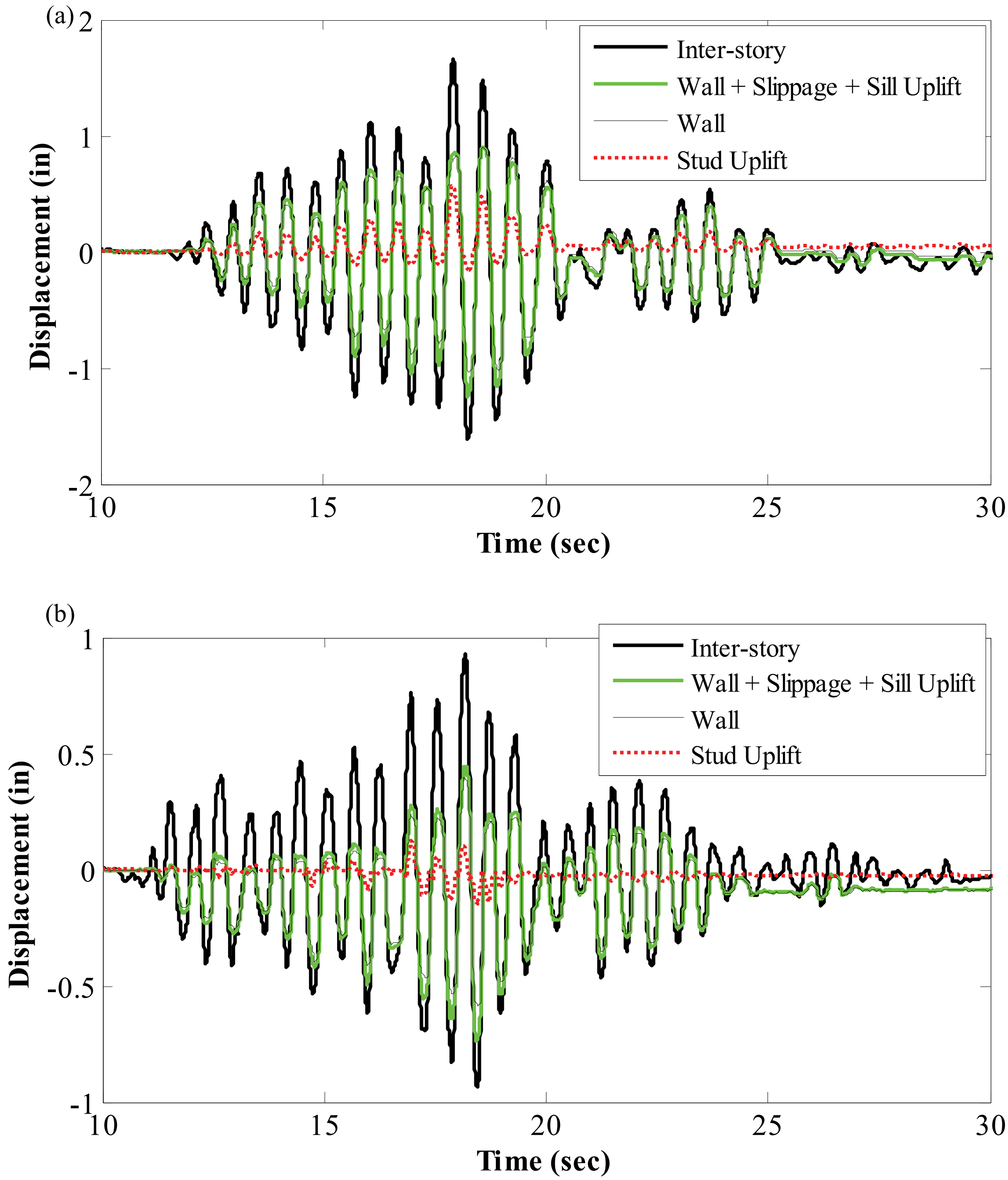

Figure 3.18: Displacement Components of Garage Wall E16 for (a) Test Phase 1, Test Level 2 and (b) Test Phase 4, Test Level 2

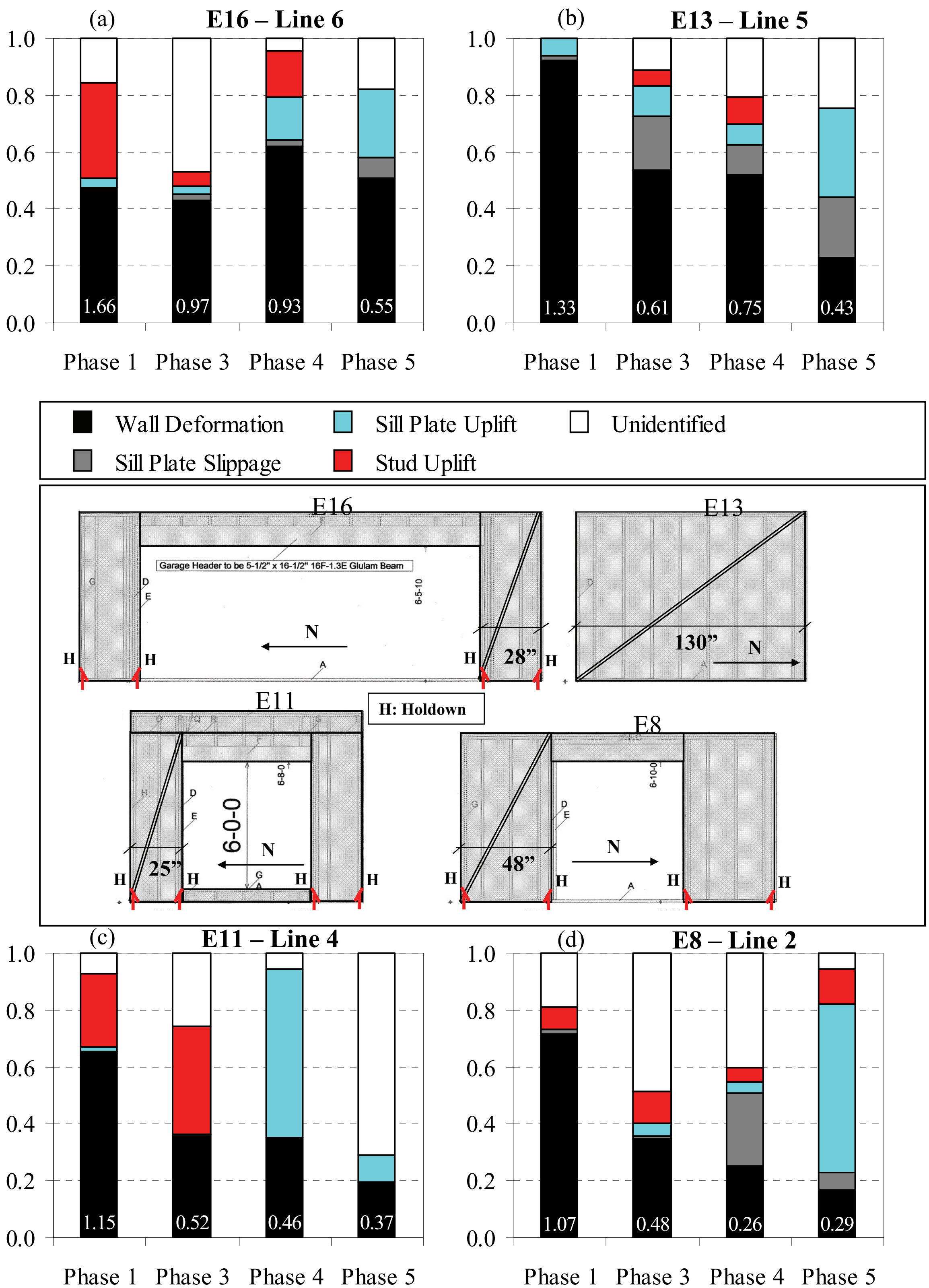

Figure 3.19 Displacement components at the peak inter-story drifts for the Seismic Level 2 tri-axial tests of Phases 1, 3, 4 and 5 and walls (a) E16, (b) E13, (c) E11, and (d) E8. Numerical values in each histogram indicate peak inter-story displacements

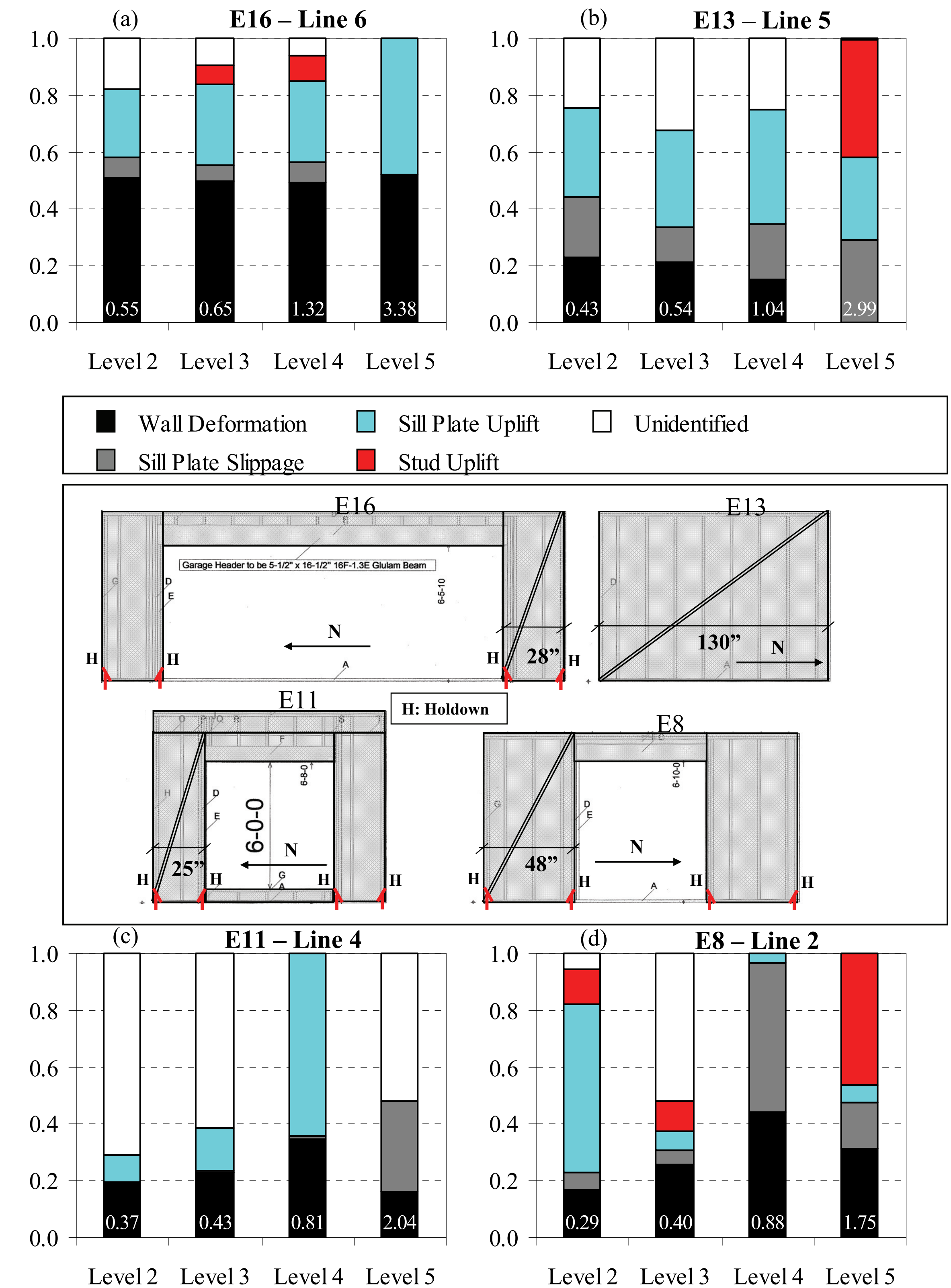

Figure 3.20: Displacement components at the peak inter-story drifts for the tri-axial seismic tests of Phase 5 and walls (a) E16, (b) E13, (c) E11, and (d) E8. Numerical values in each histogram indicate peak inter-story displacements

3.6 Summary

The shake table testing of a full-scale light-frame wood building, conducted as part of the NEESWood Project, has provided an opportunity to study various parameters that influence the dynamic properties and the seismic response of light-frame wood buildings.

The key results obtained in this study are summarized below:

- The test structure of Phase 5, which included all structural and non-structural components, survived under seismic excitations representing the DE and MCE levels of shaking. The seismic response of the test building under three-dimensional base excitations demonstrated torsional behavior resulting from the asymmetric geometry of the structure in the longitudinal (East-West) direction and the reduced effective lateral stiffness of the narrow wall piers first level garage wall in its transverse (North-South) direction. The maximum central roof drift under the DE and MCE events was 0.8% and 2%, respectively, while the maximum inter-story drift at the garage wall was 1.2% and 3.1%, respectively. These responses verified that the collapse prevention requirement, inherent in code-compliant seismic design, was satisfied. No potential loss of life or collapse hazard was identified during or after the execution of the tests.

- The application of gypsum wallboard on the interior surfaces of the structural walls caused a reduction of the initial natural periods of the test building. The same trend was observed after the application of exterior stucco finish. The application of gypsum wallboard on partition walls and ceilings, however, did not affect the initial fundamental period of the test structure.

- The application of gypsum wallboard on the interior surfaces of the structural wood walls reduced significantly the displacement response of both floors of the test structure. The reduction of the maximum transverse inter-story drifts from Phase 1 to Phase 3 was of the order of 40% for Seismic Level 2. The application of gypsum wallboard on the partition walls and the ceilings did not affect much the first level inter-story drifts of the test structure, but further reduced the drifts of the second floor. This is attributed to the fact that the first floor level had only few partition walls compared to the second level of the test structure. Besides the stiffness contribution from the partition walls, the significant reduction of interstory drifts on the second floor was also explained by the increase of diaphragm effect on the roof level. The in-plane stiffness of the roof diaphragm was increased because of the application of the gypsum wallboard to the bottom chords of the roof trusses. On the other hand, the gypsum wallboard ceiling had minimal effect on the floor diaphragm since the structural floor system (plywood panels and the floor joists) alone provided enough in-plane stiffness to "act" as a rigid diaphragm. The application of stucco as exterior finish further reduced the inter-story drifts in both levels of the test structure.

- The equivalent lateral stiffness of the wood-only Phase 1 test structure deteriorated more rapidly through the seismic tests than the other configurations. The transverse equivalent lateral stiffness of the Phase 1 test structure at the end of the Test Level 2 was reduced to less than 60% of its initial transverse stiffness. The transverse lateral stiffness for the structures of Test Phases 3 and 4, incorporating gypsum wallboard, was above 80% of their initial transverse stiffness at the end of the Test Level 2. The corresponding value for the Phase 5 test structure, incorporating stucco as exterior finish, is above 90%.

- The fundamental damping ratios of the test structure in the transverse direction ranged from 10% to 20% of critical, with a mean value of approximately 15% for all the structural configurations.

- For all test phases, the first mode shapes were mainly associated with transverse deformations of the structure. The second mode shapes were also affected by torsional response and by the in-plane shear deformations of the floor diaphragm in the stair core area between the two main units of the townhouse, particularly for the Phases 1 and 3. For Phases 4 and 5, the shear deformations of the diaphragm were reduced because of the in-plane stiffness provided by the gypsum ceilings.

- Hairline cracking occurred in the gypsum wallboard applied to the interior surfaces of the structural walls of the Phase 3 test structure during Test Level 2. This cracking occurred mainly at corners of the openings of the interior shear walls and propagated with increasing level of shaking.

- Ceiling damage was observed in the Phase 4 test structure. Cracking of the partition-to-ceiling connections in the transverse direction of the test building started occurring under Test Level 2. Ceiling damage increased in the Phase 5 test structure until a large portion of the ceiling gypsum failed under Test Level 5 (MCE). This failure occurred in the second level ceiling connecting the two main rectangular units of the test structure and can be attributed to the in-plane shear deformation of the ceiling diaphragm at that location.

- Hairline cracking of stucco in the Phase 5 test building started during Test Level 2. This cracking occurred mainly at corners of windows and door openings and propagated with increasing level of shaking. After Test Level 5 (MCE), significant spalling and cracking of stucco occurred around the garage door opening.

- The most significant damage observed in the Phase 5 test structure after Test Level 5 (MCE) was the splitting of the 2x4 and 2x6 sill plates around the entire perimeter of the building. In particular, the sill plate of the narrow wall piers of the garage separated by more than 1/2 in. This damage would be very costly to repair in a real building.

- The estimation of the inter-story displacement components experienced by various first-story walls demonstrates the participation of secondary modes of deformation beyond the dominant racking shear respose. The Phase 1 structure exhibited the lowest participation of secondary modes, mainly in the form of sill plate and stud uplift. The installation of interior and exterior wall finishes resulted in a limitation of the racking response and an amplification of the secondary modes of deformation.

CHAPTER 4: NUMERICAL FRAMEWORK FOR STATIC AND DYNAMIC ANALYSIS OF TWO-DIMENSIONAL MODELS OF LIGHT-FRAME WOOD STRUCTURES

4.1 Introduction

This chapter presents the analytical derivations and the numerical framework developed within the context of this report so as to compute the static and dynamic response of 2D light-frame wood structure models under lateral loads.

The literature review on numerical modeling of light-frame wood structures, provided in Chapter 2, highlighted the use of simplified shear wall elements to simulate the resistance of individual inter-story wall segments, when analyzing the global response of light-frame wood structures. The structural properties of the simplified shear wall elements were in most cases derived from a detailed single-story shear wall model or from experimental data of shear wall tests with matching geometric and structural configurations.

While this approach of modeling light-frame wood structures offers numerical efficiency reducing the computational overhead needed to execute the analysis, it has been already discussed in Section 2.3 that certain limitations arise in the predicting capabilities of existing formulations. The main reason for these limitations is that the response of a light-frame wood shear wall is not exclusively dependent on the structural characteristics of the shear wall itself (i.e. nailing schedule, anchoring devices, aspect ratio of full-height segments); it is also dependent on the wall boundary conditions, or else the transferred forces and the imposed displacements by the horizontal floor diaphragms at the top and bottom of the shear wall. In turn, the wall boundary conditions are dictated from the characteristics and the global response of the whole structure.

This coupling interaction between the structural components of a light-frame wood structure is not properly accounted for in the existing simplified formulations but may not be pronounced for well anchored shear walls or shear walls with intermediate anchorage that carry a good portion of the gravity load, because in these cases the shear mode of deformation is dominant. However, in cases of shear walls with poor or fair anchorage conditions this coupling interaction becomes significant and requires a more complex formulation that can account for other modes of deformation (i.e. flexural and rocking modes) with due consideration of the interaction effect of the shear walls with the floor diaphragms.

Recognizing that the simulation of a shear wall with a simplified element is not applicable to every case, the model developed in this report considers a detailed element for each shear wall, yet targets to achieve relatively low computational overhead through the development of a convenient and simplified framework to effectively express the interaction between the structural members of a light-frame wood structure. The following section presents the concept of sub-structure modeling applied in the case of 2D light-frame wood structure models.

4.2 Sub-Structure Modeling of Light-Frame Wood Structures

Figure 4.1 illustrates a typical exterior wall of a two-story light-frame wood building that can represent the prototype of a 2D model needed for seismic analysis and design of the structure.

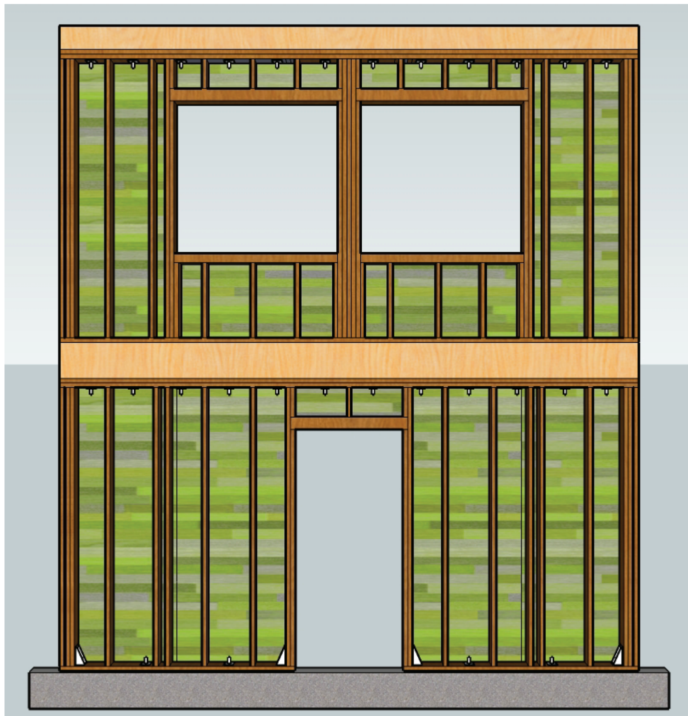

Figure 4.1 Typical Exterior Wall of a Two-Story Light-Frame Wood Building

It was shown in Section 2.1 that a detailed numerical model that explicitly describes framing members, sheathing panels and sheathing-to-framing connections requires the introduction of a great number of kinematic degrees-of-freedom (DOF). When considering the global analysis of a complete building, the use of an excessive number of global DOF can result in high memory demands. Additionally, while this excessive number of DOF is required for the accurate calculation of resisting forces, the DOF needed for the calculation of the inertial forces can be significantly less. It can be, thus, favorable (i) to consider a numerical building model with reduced DOF, called master DOF, which can adequately represent the inertial forces in the global level; and (ii) to use a sub-structuring approach to condense out the numerous DOF of each detailed shear wall model in a set of internal DOF, maintaining only the associated master DOF in the building model.

An efficient selection of master DOF is those associated with the motion and the deformation of the floor diaphragms. If we consider floor diaphragms to be rigid then only 3 DOF in the 2D wall plane – two translations and one rotation – are sufficient to describe the equilibrium equations for each diaphragm. If the shear walls are assumed to deform in a pure shear mode of deformation, the rigid diaphragms shall translate but not rotate, however, if framing axial and bending flexibility is considered, the diaphragms shall translate and rotate within the wall plane. A number of conclusions can be drawn based on this discussion. More specifically:

- The minimum number of DOF needed to describe the boundary conditions of a single-story shear wall is 6, associated with the 3 rigid body motions of the diaphragms above and below the wall, as shown schematically in Figure 4.2.

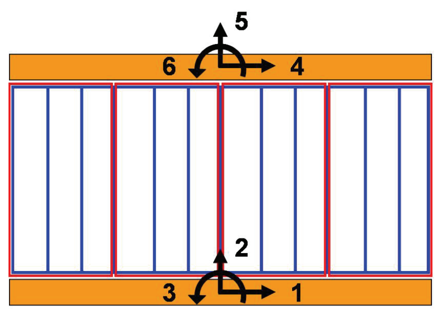

Figure 4.2 Boundary DOF of an Inter-Story Shear Wall Assuming Rigid Diaphragms

- Light-frame wood shear walls act as structural elements with shear, axial and moment interaction, since the motion of the diaphragms affects the framing deformations and, thus, the distribution of sheathing-to-framing resisting forces. This interaction implies that two identical wall segments within the same inter-story shear wall shall not demonstrate identical responses, unless boundary conditions are identical.

- It is not valid to formulate reduced numerical models based on the symmetry of the structure when the shear walls are not restricted to deform in pure shear. The complete length of the building should be considered so that global equilibrium under lateral forces will result in realistic vertical reaction forces based on the actual geometry of the structure.

- Last but not least, an effective simplified shear wall element, to be used as equivalent of a detailed shear wall model in a building model analysis, should address the coupling interaction between the 6 DOF shown in Figure 4.2 and such formulations have not been proposed in the reviewed existing literature.

These observations have led to the development of a numerical framework for the analysis of light-frame wood buildings that considers rigid floor diaphragms as the primary components and addresses the resisting forces generated by the inter-story shear walls through the interaction with the floor diaphragms. This allows the use of a detailed numerical model for each story of the building that is effectively defined as a 2-noded, 6 DOF, displacement-based shear wall element, as shown in Figure 4.3.

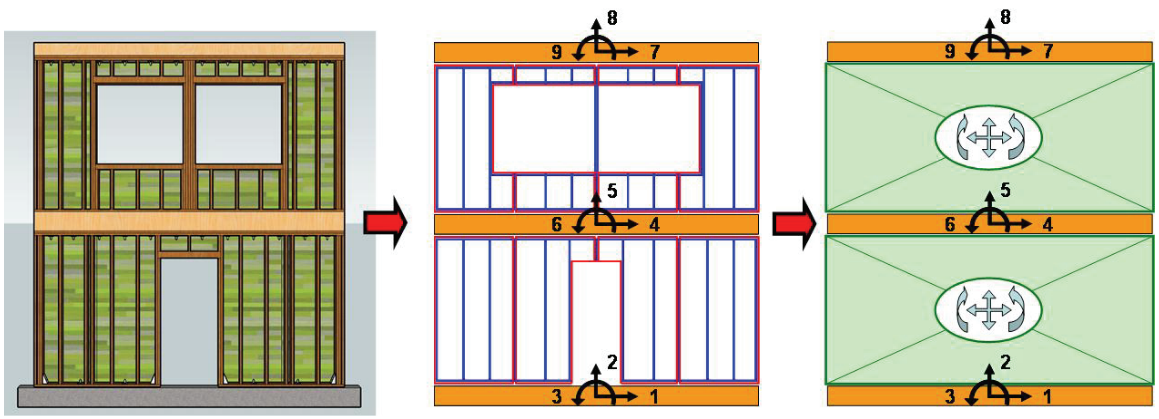

Figure 4.3 Illustration of Master DOF of a Building Model and Shear Wall Elements for the Simulation of Each Story

4.3 Derivation and Solution of Equilibrium Equations of Two-Dimensional Models of Light-Frame Wood Shear Walls under Quasi-static Loading Conditions

4.3.1 Introduction

This section describes the analytical derivations that involve the development of a finite element framework for the expression and solution of the static equilibrium equations of light-frame wood shear walls that assemble a 2D continuous single-story vertical diaphragm of a light-frame wood building.

The fundamental assumption in this study is that floor diaphragms act as rigid bodies. Deformation DOF for floor diaphragms could be included in the developed framework but the simulation of contact and separation phenomena would become more elaborate. It is believed that this assumption is the simplest possible to simulate the boundaries of a shear wall assembly preserving continuity in internal forces and moments throughout the height of the building, associated with the translation and rotation of the diaphragms. Future studies may include the consideration of diaphragm flexibility, always within the same sub-structuring approach since diaphragms are indeed explicit structural components that represent the boundaries of an inter-story wall assembly.

The proposed shear wall element enables the analyst to select between a simplified and a detailed formulation. The former is computationally efficient and predicts reliable results for well-anchored shear walls, while the latter is more computationally intensive but yields more accurate responses and is applicable for both engineered and conventional construction. The main difference between the two options is the approach adopted to describe the wood framing, since the formulations used to describe sheathing panels and sheathing-to-framing connectors are essentially the same. In the **Pure Shear** formulation described in Section 4.3.2, framing is assumed rigid and pin-connected and is considered to be rigidly attached to the floor diaphragms. In the **Model** formulation described in Section 4.3.3, framing members are modeled with linear beam elements, while link-spring elements are utilized to simulate contact/separation phenomena between vertical studs and horizontal plates, contact/separation phenomena between horizontal plates and diaphragms, as well as anchoring connections between framing and diaphragms.

In each case, the proposed numerical framework accounts for geometric nonlinearity associated with large rotations and for P-Δ effects due to gravity loads, assuming small deformations of the structural members that remain linear elastic, such as the individual framing members and the sheathing panels. The solution algorithm implemented to perform nonlinear multi-step analyses is presented in Section 4.3.4.

Additionally, a novel unidirectional phenomenological spring model, described in Section 4.3.5, is developed to capture the nonlinear hysteretic response of sheathing-to-framing connections. The backbone response is described through a smooth curve. The loading and unloading paths, which follow hysteretic rules that demonstrate pinching as well as strength and stiffness degradation, are described through multi-linear force-displacement curves.

4.3.2 Formulation of a Shear Wall Element Suppressing Framing Deformations

The simplified formulation that suppresses framing deformations is introduced first, since it involves the description of fundamental analytical derivations that are utilized in the detailed formulation as well. Let us consider a sample shear wall with a single sheathing panel located within a Global Cartesian System (GCS) *xOy*, as shown in Figure 4.4. The shear wall has length L_W and height H_W, while the lower and upper diaphragms have thicknesses h_1 and h_2, respectively. The sheathing panel has width b, height h and thickness t. The coordinates of the center of the panel are (x_0 , y_0). In this numerical formulation, material nonlinearity is considered solely at the sheathing-to-framing connections, while generalized modes of deformation are considered to describe the sheathing and the framing domain.

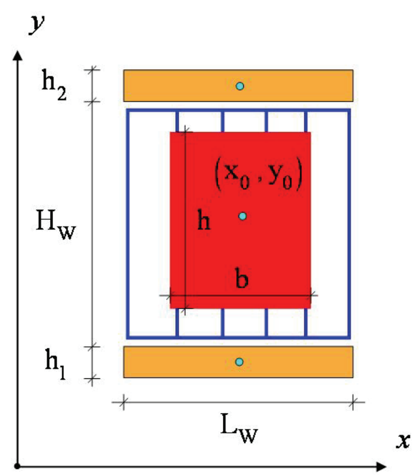

Figure 4.4 Dimensions and Configuration of a Sample Shear Wall

4.3.2.1 Kinematics and Equilibrium Equations of a Sheathing-to-Framing Connector Element

Introduction

A sheathing-to-framing connector can be considered as a linkage between two points, one in the panel and one in the frame. These two points initially exist at the same location in the 2D plane of the wall but they are parts of two independent planar domains. As the two mediums (panel and frame) are displacing in directions specified by the equilibrium equations, the connectors are deformed transferring forces between the mediums. Typically, a pair of orthogonal unidirectional springs that connect the horizontal and vertical translational DOF of the frame and the panel at each connection point, as shown in Figure 4.5b, has been utilized in most of the proposed sheathing-to-framing connection models. It has been recognized, however, that the use of two independent springs tends to over-estimate the strength and energy dissipation characteristics of the connection. Intuitively, the use of a single spring, as shown in Figure 4.5a, is more appropriate for monotonic loading but instability under cyclic loading eliminates this method. Studies presented by Judd (2005) and Judd and Fonseca (2005) have demonstrated that the orientation of each pair of orthogonal springs can be based on the analysis of the shear wall model under infinitesimal lateral deformation, according to the parallel and perpendicular directions of the initial trajectory as shown in Figure 4.5c. This approach produces more reasonable results, eliminating the over-estimation of strength and energy dissipation.

None of the existing formulations have taken, however, into consideration the rotation of the two connecting domains, which is needed in order to express the equilibrium equations in the deformed configuration. Due to material nonlinearity of the orthogonal springs, equilibrating nodal moments have to be computed based on the rotational fixity of each node. Based on the fact that a typical nail connector is embedded by at least 75% of its length to the framing member it is assumed that each pair of orthogonal springs rotates with the associated framing node and is pin-connected to the associated panel. Alternatively, it could be assumed that each pair of springs rotates by the average of the two nodal rotations or by different fractions of the two nodal rotations that sum up to unity, so that an equal rotation of the two nodes will always result in an equal rigid body rotation of the connector element.

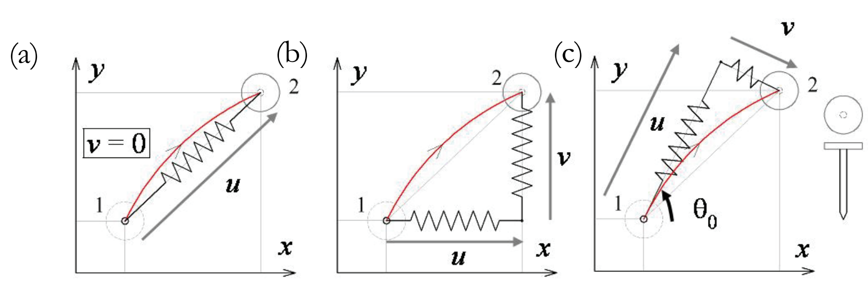

Figure 4.5 Modeling of a Sheathing-to-Framing Connection Using (a) a Single Spring; (b) a Pair of Orthogonal Springs Oriented with the GCS; and (c) a Pair of Orthogonal Springs Oriented with the First Trajectory of the Orbit

Section 4.3.5 presents all the analytical derivations related to the unidirectional constitutive model and the consideration of bidirectional coupling of the two orthogonal connector forces. The remaining part of this section presents the derivations for the general case that a connector is initially oriented with a predefined angle θ_0 with respect to the GCS.

Kinematics of a Sheathing-to-Framing Connector Element

A sheathing-to-framing connector element has 2 orthogonal internal DOF, u_s and v_s, which are defined with respect to an element Local Cartesian System (LCS) $\xi O \eta$. Figure 4.6 illustrates the initial and deformed configuration of a connector element. The element displacement vector $\mathbf{D_S}$ consists of the global translations, u_f and v_f, and the rotation, θ_f, of the framing node, as well as of the global translations, u_p and v_p, of the panel node, and is defined as:

$$\mathbf{D_S} = \left\{ u_f \quad v_f \quad \theta_f \quad u_p \quad v_p \right\}^{\mathrm{T}} \tag{4.1}$$

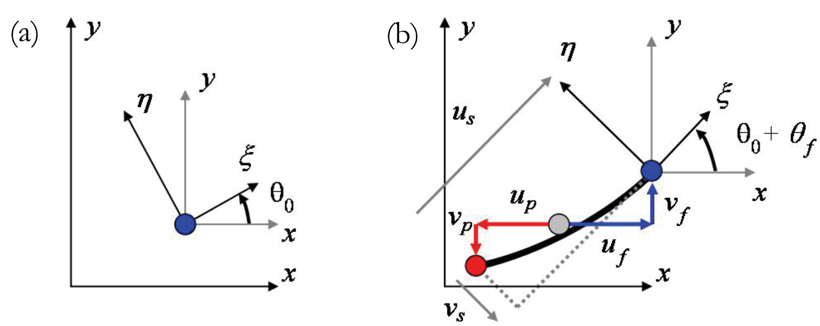

Figure 4.6 (a) Initial and (b) Deformed Configuration of a Sheathing-to-Framing Connector Element

Based on the initial and deformed configuration, the internal displacements are computed as:

$$\begin{Bmatrix} u_s \\ v_s \end{Bmatrix} = \begin{Bmatrix} \cos\left(\theta_0 + \theta_f\right) \cdot \left(u_f - u_p\right) + \sin\left(\theta_0 + \theta_f\right) \cdot \left(v_f - v_p\right) \\ -\sin\left(\theta_0 + \theta_f\right) \cdot \left(u_f - u_p\right) + \cos\left(\theta_0 + \theta_f\right) \cdot \left(v_f - v_p\right) \end{Bmatrix} \Rightarrow$$

$$\begin{Bmatrix} u_s \\ v_s \end{Bmatrix} = \begin{bmatrix} \cos\left(\theta_0 + \theta_f\right) & \sin\left(\theta_0 + \theta_f\right) \\ -\sin\left(\theta_0 + \theta_f\right) & \cos\left(\theta_0 + \theta_f\right) \end{bmatrix} \cdot \begin{bmatrix} 1 & 0 & 0 & -1 & 0 \\ 0 & 1 & 0 & 0 & -1 \end{bmatrix} \cdot \mathbf{D_S} \Rightarrow$$

$$\mathbf{u_S} = \mathbf{\Lambda}\left(\theta_0 + \theta_f\right) \cdot \begin{bmatrix} 1 & 0 & 0 & -1 & 0 \\ 0 & 1 & 0 & 0 & -1 \end{bmatrix} \cdot \mathbf{D_S} \tag{4.2}$$

where $\mathbf{u_S} = \{u_s \;\; v_s\}^{\mathrm{T}}$ and $\mathbf{\Lambda}(\theta)$ has the following properties

$$\begin{Bmatrix} \mathbf{\Lambda}(\theta)^{-1} = \mathbf{\Lambda}(\theta)^{\mathrm{T}} = \mathbf{\Lambda}(-\theta) \\ \\ \mathbf{\Lambda}(\theta_1 + \theta_2) = \mathbf{\Lambda}(\theta_1)\cdot\mathbf{\Lambda}(\theta_2) \end{Bmatrix} \tag{4.3}$$

Using the exact analytical expression of the internal displacements, an internal virtual displacement field $\delta\mathbf{u_S}$ can be computed for a given element virtual displacement $\delta\mathbf{D_S}$.

$$\delta\mathbf{u_S} = \begin{bmatrix} \dfrac{\partial u_s}{\partial u_f} & \dfrac{\partial u_s}{\partial v_f} & \dfrac{\partial u_s}{\partial \theta_f} & \dfrac{\partial u_s}{\partial u_p} & \dfrac{\partial u_s}{\partial v_p} \\ \dfrac{\partial v_s}{\partial u_f} & \dfrac{\partial v_s}{\partial v_f} & \dfrac{\partial v_s}{\partial \theta_f} & \dfrac{\partial v_s}{\partial u_p} & \dfrac{\partial v_s}{\partial v_p} \end{bmatrix} \cdot \delta\mathbf{D_S} \Rightarrow$$

$$\delta\mathbf{u_S} = \begin{bmatrix} \cos(\theta_0+\theta_f) & \sin(\theta_0+\theta_f) & v_s & -\cos(\theta_0+\theta_f) & -\sin(\theta_0+\theta_f) \\ -\sin(\theta_0+\theta_f) & \cos(\theta_0+\theta_f) & -u_s & \sin(\theta_0+\theta_f) & -\cos(\theta_0+\theta_f) \end{bmatrix} \cdot \delta\mathbf{D_S} \Rightarrow$$

$$\delta\mathbf{u_S} = \mathbf{B_S}(\mathbf{D_S})\cdot\delta\mathbf{D_S} \tag{4.4}$$

This derivation leads to an equilibrium matrix $\mathbf{B_S}$, which has elements that are nonlinearly related to the element displacements $\mathbf{D_S}$.

Equilibrium Equations of a Sheathing-to-Framing Connector Element

Figure 4.7 illustrates a free body diagram of a connector element. The element force vector $\mathbf{F_S}$ consists of the global forces, p_f and q_f, and the moment, m_f, of the framing node, as well as of the global forces, p_p and q_p, of the panel node, and is defined as:

$$\mathbf{F_S} = \{p_f \quad q_f \quad m_f \quad p_p \quad q_p\}^{\mathrm{T}} \tag{4.5}$$

The equilibrium equations are computed from the principle of virtual work. Under a virtual displacement field $\delta\mathbf{D_S}$, the internal and external virtual work is equal.

$$\delta\mathrm{W}_{\mathrm{ext}} = \delta\mathrm{W}_{\mathrm{int}} \Rightarrow$$

$$\delta \mathbf{D_S}^{\mathrm{T}} \cdot \mathbf{F_S} = \delta \mathbf{u_S}^{\mathrm{T}} \cdot \begin{Bmatrix} p_s \\ q_s \end{Bmatrix} \Rightarrow$$

$$\delta \mathbf{D_S}^{\mathrm{T}} \cdot \mathbf{F_S} = \delta \mathbf{D_S}^{\mathrm{T}} \cdot \mathbf{B_S}^{\mathrm{T}} \cdot \begin{Bmatrix} p_s \\ q_s \end{Bmatrix} \Rightarrow$$

$$\mathbf{F_S} = \mathbf{B_S}^{\mathrm{T}} \cdot \mathbf{p_S} \tag{4.6}$$

where $\mathbf{p_S} = \{p_s\ q_s\}^{\mathrm{T}}$ are the internal forces in the LCS $\xi O \eta$. Expressing the equilibrium in the deformed configuration leads naturally to the resulting moment at the framing node m_f, as computed from (4.6), which is generally zero if and only if the orthogonal springs are linear elastic with the same stiffness.

$$m_f = v_s \cdot p_s - u_s \cdot q_s \tag{4.7}$$

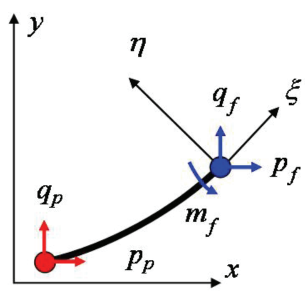

Figure 4.7 Free Body Diagram of a Connector Element

The tangent stiffness matrix of the connector element is computed from the variation of the element force vector with respect to the element displacement vector

$$\mathbf{K_S} = \frac{\partial \mathbf{F_S}}{\partial \mathbf{D_S}} = \frac{\partial \left(\mathbf{B_S}^{\mathrm{T}} \cdot \mathbf{p_S} \right)}{\partial \mathbf{D_S}} = \mathbf{B_S}^{\mathrm{T}} \cdot \frac{\partial \mathbf{p_S}}{\partial \mathbf{u_S}} \cdot \frac{\partial \mathbf{u_S}}{\partial \mathbf{D_S}} + \frac{\partial \left(\mathbf{B_S}^{\mathrm{T}} \right)}{\partial \mathbf{D_S}} \cdot \mathbf{p_S} \Rightarrow$$

$$\mathbf{K_S} = \mathbf{K_{S1}} + \mathbf{K_{S2}} \tag{4.8}$$

The stiffness matrices shown in (4.8) are calculated as:

$$\mathbf{K_{S1}} = \mathbf{B_S}^{\mathrm{T}} \cdot \frac{\partial \mathbf{p_S}}{\partial \mathbf{u_S}} \cdot \frac{\partial \mathbf{u_S}}{\partial \mathbf{D_S}} = \mathbf{B_S}^{\mathrm{T}} \cdot \begin{bmatrix} k_{su} & 0 \\ 0 & k_{sv} \end{bmatrix} \cdot \mathbf{B_S} = \mathbf{B_S}^{\mathrm{T}} \cdot \mathbf{k_S} \cdot \mathbf{B_S} \tag{4.9}$$

$$\mathbf{K_{S2}} = \frac{\partial \left(\mathbf{B_S}^{\mathrm{T}} \right)}{\partial \mathbf{D_S}} \cdot \mathbf{p_S} = \begin{bmatrix} 0 & 0 & -q_f & 0 & 0 \\ & 0 & p_f & 0 & 0 \\ & & -p_f \cdot \left(u_f - u_p \right) - q_f \cdot \left(v_f - v_p \right) & q_f & -p_f \\ & sym & & 0 & 0 \\ & & & & 0 \end{bmatrix} \tag{4.10}$$

where k_{su} and k_{sv} correspond to the tangent stiffness of the orthogonal springs in the LCS. Stiffness matrix $\mathbf{K_{S2}}$ includes higher order effects and is usually neglected, since it does not improve significantly the convergence rate and requires additional calculations.

4.3.2.2 Kinematics and Equilibrium Equations of a Sheathing Panel Element

Introduction

Sheathing panels are assumed to deform in pure shear and remain within the linear elastic range of the material. Each sheathing panel represents an explicit structural component that interacts only with the sheathing-to-framing connectors. Bearing and separation between adjacent sheathing panels is not considered in this formulation.

Kinematics of a Sheathing Panel Element

Panel elements are modeled with 4 DOF, two rigid body translations U and V, one rigid body rotation Θ with respect to the center of the panel, and a uniform pure shear deformation γ, as shown in Figure 4.8.

$$\mathbf{D_P} = \{ U \quad V \quad \Theta \quad \gamma \}^{\mathrm{T}} \tag{4.11}$$

The reasons that led to the selections of these generalized modes of deformation are discussed below:

- The use of nonlinear phenomenological springs to explicitly describe the response of each sheathing-to-framing connection, as shown later in Section 4.3.5, represents a simplified model of the actual response that accounts, among others, for local deformations in the region of the panel surrounding the connector, such as wood crushing and splitting.

- Other than local nonlinear deformations, rectangular sheathing panels typically demonstrate high out-of-plane resistance and elastic deformations within the wall plane. Cracks in sheathing panels are observed in cases where they enclose window and door openings, however, the primary objective is to assess the response of segmented shear walls that consist of full height rectangular panels. Thus, the proposed formulation is limited to rectangular sheathing panels that deform linearly elastic.

- Geometric nonlinearity can be easily included by decomposing the displacement fields in rigid body and internal deformation modes. Adopting a corotational description of the displacement field of a panel element allows the analytical derivation of the nonlinear kinematic equations and leads to solutions that satisfy equilibrium in the deformed configuration.

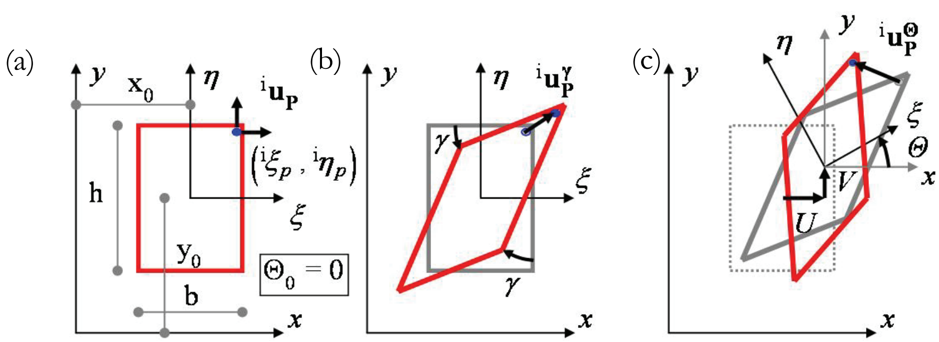

Figure 4.8 (a) Illustration of a Panel Element, (b) Pure Shear Deformation of a Panel Element, and (c) Kinematic DOF of a Panel Element Associated with Rigid Body Motion

Panel Local Cartesian System

If the sample sheathing panel shown in Figure 4.8a is fastened to the wood framing through *n* number of connectors (nails or screws) then there is also *n* number of two-dimensional displacement vectors $\mathbf{u_P} = \{u_p\ v_p\}^T$ that express the motion of the points of the panel along the GCS, which are denoted as ${}^i\mathbf{u_P}$ and i ranges from 1 to *n*.

Let us define a LCS $\xi O\eta$ that originates at the center of the panel and is initially parallel to the GCS as shown in Figure 4.8. The location of each point on the panel is identified through the point local coordinate vector ${}^{i}\boldsymbol{\xi}_{\mathbf{P}}$ where:

$$
{}^{i}\boldsymbol{\xi}_{\mathbf{P}} = \begin{Bmatrix} {}^{i}\xi_p \\ {}^{i}\eta_p \end{Bmatrix}, \quad \begin{Bmatrix} \xi_p \in [\text{-b/2, b/2}] \\ {}^{i}\eta_p \in [\text{-h/2, h/2}] \end{Bmatrix} \tag{4.12}
$$

Panel Shear Deformation

The kinematics of the shear mode of deformation is expressed with respect to the LCS $\xi O\eta$, which rotates with the panel rotation Θ. The point displacement vector ${}^{i}\mathbf{u}_{\mathbf{P}}^{\gamma}$ due to shear deformation is given by:

$$
{}^{i}\mathbf{u}_{\mathbf{P}}^{\gamma} = \begin{Bmatrix} {}^{i}\eta_p \\ {}^{i}\xi_p \end{Bmatrix} \cdot \gamma \tag{4.13}
$$

Panel Rotation

The panel rotation Θ is handled thought the transformation matrix $\boldsymbol{\Lambda}(\Theta)$ defined previously in (4.2) and the point local coordinate vector ${}^{i}\boldsymbol{\xi}_{\mathbf{P}}$. Figure 4.9 shows the initial ${}^{i}\boldsymbol{\xi}_{\mathbf{P}}$ and rotated ${}^{i}\boldsymbol{\xi}_{\mathbf{P}}^{\boldsymbol{\Theta}}$ coordinate vectors of a single point due to rotation Θ given by:

$$
{}^{i}\boldsymbol{\xi}_{\mathbf{P}}^{\boldsymbol{\Theta}} = \begin{bmatrix} \cos\Theta & \text{-}\sin\Theta \\ \sin\Theta & \cos\Theta \end{bmatrix} \cdot {}^{i}\boldsymbol{\xi}_{\mathbf{P}} = \boldsymbol{\Lambda}(\Theta)^{\mathbf{T}} \cdot {}^{i}\boldsymbol{\xi}_{\mathbf{P}} \tag{4.14}
$$

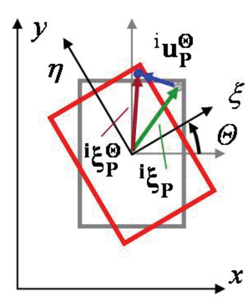

Figure 4.9 Rotation of a Panel

The point displacement vector ${}^{i}\mathbf{u}_{\mathbf{P}}^{\boldsymbol{\Theta}}$ is:

$$ {}^{i}\mathbf{u}_{\mathbf{P}}^{\boldsymbol{\Theta}} = {}^{i}\boldsymbol{\xi}_{\mathbf{P}}^{\boldsymbol{\Theta}} - {}^{i}\boldsymbol{\xi}_{\mathbf{P}} = \boldsymbol{\Lambda}(\Theta)^{\mathbf{T}} \cdot {}^{i}\boldsymbol{\xi}_{\mathbf{P}} - {}^{i}\boldsymbol{\xi}_{\mathbf{P}} \tag{4.15} $$

Panel Rotation and Shear Deformation

If we consider now that in (4.15) the point initial coordinate vector ${}^{i}\boldsymbol{\xi}_{\mathbf{P}}$ includes the point displacement vector from shear deformation ${}^{i}\mathbf{u}_{\mathbf{P}}{}^{\gamma}$, it is:

$$ {}^{i}\boldsymbol{\xi}_{\mathbf{P}}^{\gamma} = {}^{i}\boldsymbol{\xi}_{\mathbf{P}} + {}^{i}\mathbf{u}_{\mathbf{P}}^{\gamma} \tag{4.16} $$

Based on (4.15) and (4.16) it can be written that:

$$ {}^{i}\mathbf{u}_{\mathbf{P}}^{\boldsymbol{\Theta}} = \boldsymbol{\Lambda}(\Theta)^{\mathbf{T}} \cdot {}^{i}\boldsymbol{\xi}_{\mathbf{P}}^{\gamma} - {}^{i}\boldsymbol{\xi}_{\mathbf{P}}^{\gamma} \Rightarrow $$

$$ {}^{i}\mathbf{u}_{\mathbf{P}}^{\boldsymbol{\Theta}} = \boldsymbol{\Lambda}(\Theta)^{\mathbf{T}} \cdot {}^{i}\boldsymbol{\xi}_{\mathbf{P}}^{\gamma} - {}^{i}\boldsymbol{\xi}_{\mathbf{P}} - {}^{i}\mathbf{u}_{\mathbf{P}}^{\gamma} \Rightarrow $$

$$ {}^{i}\mathbf{u}_{\mathbf{P}}^{\boldsymbol{\Theta}} + {}^{i}\mathbf{u}_{\mathbf{P}}^{\gamma} = \boldsymbol{\Lambda}(\Theta)^{\mathbf{T}} \cdot {}^{i}\boldsymbol{\xi}_{\mathbf{P}}^{\gamma} - {}^{i}\boldsymbol{\xi}_{\mathbf{P}} \Rightarrow $$

$$ {}^{i}\mathbf{u}_{\mathbf{P}}^{\boldsymbol{\Theta},\gamma} = \boldsymbol{\Lambda}(\Theta)^{\mathbf{T}} \cdot \left({}^{i}\boldsymbol{\xi}_{\mathbf{P}} + {}^{i}\mathbf{u}_{\mathbf{P}}^{\gamma} \right) - {}^{i}\boldsymbol{\xi}_{\mathbf{P}} \tag{4.17} $$

This means that the displacement of each point ${}^{i}\mathbf{u}_{\mathbf{P}}^{\boldsymbol{\Theta},\gamma}$ due to rotation and shear deformation is a nonlinear function of Θ and γ.

Panel Rigid Translation

We finally define the point displacement vector ${}^{i}\mathbf{u}_{\mathbf{P}}{}^{\mathbf{U,V}}$ from the two rigid body translations U and V as:

$$ {}^{i}\mathbf{u}_{\mathbf{P}}^{\mathbf{U,V}} = \begin{Bmatrix} U \\ V \end{Bmatrix} \tag{4.18} $$

Panel Total Deformation

The point displacement vector ${}^{i}\mathbf{u}_{\mathbf{P}}$ is given by:

$$ {}^{i}\mathbf{u}_{\mathbf{P}} = {}^{i}\mathbf{u}_{\mathbf{P}}^{\mathbf{U,V}} + {}^{i}\mathbf{u}_{\mathbf{P}}^{\boldsymbol{\Theta},\gamma} = {}^{i}\mathbf{u}_{\mathbf{P}}^{\mathbf{U,V}} + \boldsymbol{\Lambda}(\Theta)^{\mathbf{T}} \cdot \left({}^{i}\boldsymbol{\xi}_{\mathbf{P}} + {}^{i}\mathbf{u}_{\mathbf{P}}^{\gamma} \right) - {}^{i}\boldsymbol{\xi}_{\mathbf{P}} \tag{4.19} $$

or

$$ {}^{i}\mathbf{u_P} = f\left(\mathbf{D_P}\right) = \begin{Bmatrix} U \\ V \end{Bmatrix} + \begin{bmatrix} \cos\Theta & -\sin\Theta \\ \sin\Theta & \cos\Theta \end{bmatrix} \cdot \left(\begin{Bmatrix} {}^{i}\xi_p \\ {}^{i}\eta_p \end{Bmatrix} + \begin{Bmatrix} {}^{i}\eta_p \\ {}^{i}\xi_p \end{Bmatrix} \cdot \gamma \right) - \begin{Bmatrix} {}^{i}\xi_p \\ {}^{i}\eta_p \end{Bmatrix} \qquad (4.20) $$

Using the exact analytical expression of the point displacement vector, a virtual displacement field $\delta^{i}\mathbf{u_P}$ can be computed for a given panel virtual displacement $\delta\mathbf{D_P}$.

$$ \delta^{i}\mathbf{u_P} = \begin{bmatrix} \dfrac{\partial^{i}u_P}{\partial U} & \dfrac{\partial^{i}u_P}{\partial V} & \dfrac{\partial^{i}u_P}{\partial \Theta} & \dfrac{\partial^{i}u_P}{\partial \gamma} \\ \dfrac{\partial^{i}v_P}{\partial U} & \dfrac{\partial^{i}v_P}{\partial V} & \dfrac{\partial^{i}v_P}{\partial \Theta} & \dfrac{\partial^{i}v_P}{\partial \gamma} \end{bmatrix} \cdot \delta\mathbf{D_P} \Rightarrow $$

$$ \delta^{i}\mathbf{u_P} = \begin{bmatrix} 1 & 0 & \left(-\sin\Theta\cdot({}^{i}\xi_p + {}^{i}\eta_p\cdot\gamma) - \cos\Theta\cdot({}^{i}\eta_p + {}^{i}\xi_p\cdot\gamma)\right) & \left(\cos\Theta\cdot{}^{i}\eta_p - \sin\Theta\cdot{}^{i}\xi_p\right) \\ 0 & 1 & \left(\cos\Theta\cdot({}^{i}\xi_p + {}^{i}\eta_p\cdot\gamma) - \sin\Theta\cdot({}^{i}\eta_p + {}^{i}\xi_p\cdot\gamma)\right) & \left(\sin\Theta\cdot{}^{i}\eta_p + \cos\Theta\cdot{}^{i}\xi_p\right) \end{bmatrix} \cdot \delta\mathbf{D_P} \Rightarrow $$

$$ \delta^{i}\mathbf{u_P} = \begin{bmatrix} 1 & 0 & -{}^{i}\eta_p^{\mathbf{\Theta},\gamma} & {}^{i}\eta_p^{\mathbf{-\Theta}} \\ 0 & 1 & {}^{i}\xi_p^{\mathbf{\Theta},\gamma} & {}^{i}\xi_p^{\mathbf{-\Theta}} \end{bmatrix} \cdot \delta\mathbf{D_P} = {}^{i}\mathbf{B_P}\left(\mathbf{D_P}\right)\cdot\delta\mathbf{D_P} \qquad (4.21) $$

The nonlinear terms ${}^{i}\boldsymbol{\xi}_\mathbf{P}^{\mathbf{\Theta},\gamma}$ and ${}^{i}\boldsymbol{\xi}_\mathbf{P}^{\mathbf{-\Theta}}$ of matrix ${}^{i}\mathbf{B_P}$ are defined from (4.17) and (4.14), respectively, as:

$$ {}^{i}\boldsymbol{\xi}_\mathbf{P}^{\mathbf{\Theta},\gamma} = \begin{Bmatrix} {}^{i}\xi_p^{\mathbf{\Theta},\gamma} \\ {}^{i}\eta_p^{\mathbf{\Theta},\gamma} \end{Bmatrix} = \begin{bmatrix} \cos\Theta & -\sin\Theta \\ \sin\Theta & \cos\Theta \end{bmatrix} \cdot \left(\begin{Bmatrix} {}^{i}\xi_p \\ {}^{i}\eta_p \end{Bmatrix} + \begin{Bmatrix} {}^{i}\eta_p \\ {}^{i}\xi_p \end{Bmatrix} \cdot \gamma \right) \qquad (4.22) $$

$$ {}^{i}\boldsymbol{\xi}_\mathbf{P}^{\mathbf{-\Theta}} = \begin{Bmatrix} {}^{i}\xi_p^{\mathbf{-\Theta}} \\ {}^{i}\eta_p^{\mathbf{-\Theta}} \end{Bmatrix} = \begin{bmatrix} \cos(-\Theta) & -\sin(-\Theta) \\ \sin(-\Theta) & \cos(-\Theta) \end{bmatrix} \cdot \begin{Bmatrix} {}^{i}\xi_p \\ {}^{i}\eta_p \end{Bmatrix} = \begin{bmatrix} \cos\Theta & \sin\Theta \\ -\sin\Theta & \cos\Theta \end{bmatrix} \cdot \begin{Bmatrix} {}^{i}\xi_p \\ {}^{i}\eta_p \end{Bmatrix} \qquad (4.23) $$

Equilibrium Equations of a Sheathing Panel Element

Figure 4.10 illustrates a free body diagram of a panel element. The element force vector $\mathbf{F_P}$ consists of the generalized forces in the two global directions *P* and *Q*, the generalized moment with respect to the center of the panel *M*, and the generalized shear force *T*, which is energy conjugate to the shear deformation γ.

$$\mathbf{F_P} = \{P \quad Q \quad M \quad T\}^{\mathrm{T}} \tag{4.24}$$

The equilibrium equations are computed from the principle of virtual work. Under a virtual displacement field $\delta\mathbf{D_P}$, the internal and external virtual work is equal.

$$\delta \mathrm{W_{ext}} = \delta \mathrm{W_{int}} \;\Rightarrow$$

$$\delta\mathbf{D_P}^{\mathrm{T}} \cdot \mathbf{F_P} = \sum_{\mathrm{i}=1}^{n} \left(\delta\, {}^{\mathrm{i}}\mathbf{u_P}^{\mathrm{T}} \cdot {}^{\mathrm{i}}\mathbf{p_P} \right) + \int_{\mathrm{V}} \delta\gamma_{\xi\eta} \cdot \mathrm{G} \cdot \gamma_{\xi\eta} \mathrm{dV} \;\Rightarrow$$

$$\delta\mathbf{D_P}^{\mathrm{T}} \cdot \mathbf{F_P} = \sum_{\mathrm{i}=1}^{n} \left(\delta\mathbf{D_P}^{\mathrm{T}} \cdot {}^{\mathrm{i}}\mathbf{B_P}^{\mathrm{T}} \cdot {}^{\mathrm{i}}\mathbf{p_P} \right) + \int_{\mathrm{V}} \delta(\gamma + \gamma) \cdot \mathrm{G} \cdot (\gamma + \gamma)\, \mathrm{dV} \;\Rightarrow$$

$$\delta\mathbf{D_P}^{\mathrm{T}} \cdot \mathbf{F_P} = \delta\mathbf{D_P}^{\mathrm{T}} \cdot \sum_{\mathrm{i}=1}^{n} \left({}^{\mathrm{i}}\mathbf{B_P}^{\mathrm{T}} \cdot {}^{\mathrm{i}}\mathbf{p_P} \right) + \delta\gamma \cdot \left(4 \cdot \mathrm{G} \cdot \mathrm{b} \cdot \mathrm{h} \cdot \mathrm{t} \cdot \gamma \right) \;\Rightarrow$$

$$\delta\mathbf{D_P}^{\mathrm{T}} \cdot \mathbf{F_P} = \delta\mathbf{D_P}^{\mathrm{T}} \cdot \left(\sum_{\mathrm{i}=1}^{n} \left({}^{\mathrm{i}}\mathbf{B_P}^{\mathrm{T}} \cdot {}^{\mathrm{i}}\mathbf{p_P} \right) + \{0 \quad 0 \quad 0 \quad K_G \cdot \gamma\}^{\mathrm{T}} \right) \;\Rightarrow$$

$$\mathbf{F_P} = \sum_{\mathrm{i}=1}^{n} \left({}^{\mathrm{i}}\mathbf{B_P}^{\mathrm{T}} \cdot {}^{\mathrm{i}}\mathbf{p_P} \right) + \{0 \quad 0 \quad 0 \quad K_G \cdot \gamma\}^{\mathrm{T}} \tag{4.25}$$

where ${}^{\mathrm{i}}\mathbf{p_P} = \{{}^{\mathrm{i}}p_p \;\; {}^{\mathrm{i}}q_p\}^{\mathrm{T}}$ is the internal point force vector acting on the panel from the i^{th} connector, G is the shear modulus of the panel and $\gamma_{\xi\eta}$ is the engineering shear strain in the LCS. Since small deformations have been assumed, the generalized shear stiffness of the panel K_G remains constant and independent of the shear deformation γ.

$$K_G = 4 \cdot \mathrm{G} \cdot \mathrm{b} \cdot \mathrm{h} \cdot \mathrm{t} \tag{4.26}$$

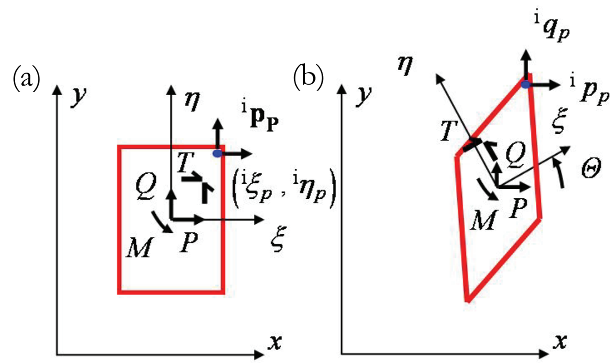

Figure 4.10 Free Body Diagram of a Panel Element in the (a) Undeformed and (b) Deformed Configuration

The tangent stiffness matrix of the panel element is computed from the variation of the element force vector with respect to the element displacement vector

$$\mathbf{K_P} = \frac{\partial \mathbf{F_P}}{\partial \mathbf{D_P}} = \frac{\partial\left(\sum_{i=1}^{n}\left({}^{i}\mathbf{B_P}^{T} \cdot {}^{i}\mathbf{p_P}\right) + \{0 \quad 0 \quad 0 \quad K_G \cdot \gamma\}^{T}\right)}{\partial \mathbf{D_P}} \Rightarrow$$

$$\mathbf{K_P} = \sum_{i=1}^{n}\left({}^{i}\mathbf{B_P}^{T} \cdot \frac{\partial\, {}^{i}\mathbf{p_P}}{\partial\, {}^{i}\mathbf{u_P}} \cdot \frac{\partial\, {}^{i}\mathbf{u_P}}{\partial \mathbf{D_P}}\right) + \sum_{i=1}^{n}\left(\frac{\partial\left({}^{i}\mathbf{B_P}^{T}\right)}{\partial \mathbf{D_P}} \cdot {}^{i}\mathbf{p_P}\right) + \frac{\partial\left(\{0 \quad 0 \quad 0 \quad K_G \cdot \gamma\}^{T}\right)}{\partial \mathbf{D_P}} \Rightarrow$$

$$\mathbf{K_P} = \mathbf{K_{P1}} + \mathbf{K_{P2}} + \mathbf{K_{P3}} \tag{4.27}$$

The stiffness matrices shown in (4.27) are calculated as:

$$\mathbf{K_{P1}} = \sum_{i=1}^{n}\left({}^{i}\mathbf{B_P}^{T} \cdot \frac{\partial\, {}^{i}\mathbf{p_P}}{\partial\, {}^{i}\mathbf{u_P}} \cdot \frac{\partial\, {}^{i}\mathbf{u_P}}{\partial \mathbf{D_P}}\right) = \sum_{i=1}^{n}\left({}^{i}\mathbf{B_P}^{T} \cdot {}^{i}\mathbf{K_S^{PP}} \cdot {}^{i}\mathbf{B_P}\right) \tag{4.28}$$

$$\mathbf{K_{P2}} = \sum_{i=1}^{n}\left(\frac{\partial\left({}^{i}\mathbf{B_P}^{T}\right)}{\partial \mathbf{D_P}} \cdot {}^{i}\mathbf{p_P}\right) \Rightarrow$$

$$
\mathbf{K_{P2}} = \begin{bmatrix} 0 & 0 & 0 & 0 \\ & 0 & 0 & 0 \\ & & -\left({}^{\mathrm{i}}\xi_p^{\mathbf{\Theta},\gamma} \cdot {}^{\mathrm{i}}p_p + {}^{\mathrm{i}}\eta_p^{\mathbf{\Theta},\gamma} \cdot {}^{\mathrm{i}}q_p\right) & \left(-{}^{\mathrm{i}}\xi_p^{-\mathbf{\Theta}} \cdot {}^{\mathrm{i}}p_p + {}^{\mathrm{i}}\eta_p^{-\mathbf{\Theta}} \cdot {}^{\mathrm{i}}q_p\right) \\ sym & & & 0 \end{bmatrix} \tag{4.29}
$$

$$
\mathbf{K_{P3}} = \frac{\partial\left(\left\{0 \quad 0 \quad 0 \quad K_G \cdot \gamma\right\}^{\mathrm{T}}\right)}{\partial \mathbf{D_P}} = \begin{bmatrix} 0 & 0 & 0 & 0 \\ & 0 & 0 & 0 \\ & & 0 & 0 \\ sym & & & K_G \end{bmatrix} \tag{4.30}
$$

where ${}^{\mathrm{i}}\mathbf{K_S^{PP}}$ is the submatrix corresponding to the panel DOF, as computed in (4.8), for the i$^{\mathrm{th}}$ connector. Stiffness matrix $\mathbf{K_{P2}}$ includes higher order effects and is usually neglected, since it does not improve significantly the convergence rate and requires additional calculations.

4.3.2.3 Kinematics and Equilibrium Equations of the Framing Domain

Introduction

The framing members, as discussed earlier, act as rigid beams and the wall assembly, consisting of the framing and the two rigid diaphragms, distorts under a pure kinematic mode of deformation with no internal strain energy. This single mode is essentially associated with the relative horizontal inter-story drift imposed by the diaphragms. However, when considering geometric nonlinearity the vertical inter-story drift is dependent on the horizontal inter-story drift, as shown in Figure 4.11a. In addition, the rigid diaphragms do not rotate relative to each other but the element may be subjected to a rigid body motion, as shown in Figure 4.11b, if the base diaphragm is not restricted against rotation. These reasons dictate that it is desirable to express the displacement field of the framing domain with respect to the 6 DOF of the two diaphragms. After all, these are the boundary DOF of the 2-noded shear wall element that interact with the numerical D_1 building model.

(a)

(b)

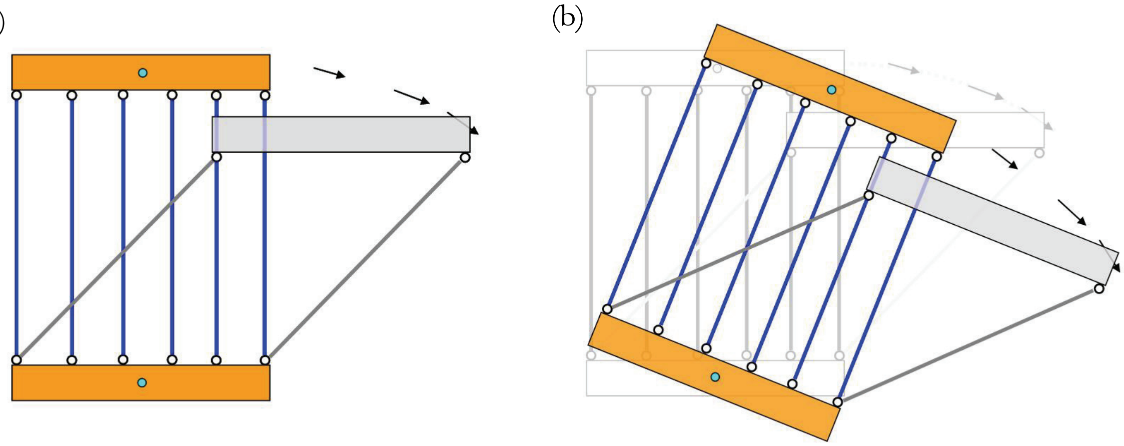

Figure 4.11 (a) Racking Deformation of the Framing Domain, and (b) Rigid Body Rotation of the Framing Domain

This suggests that although the framing members provide no lateral resistance, they do provide vertical resistance to gravity loads, which has to be accounted for in order to include second order P-Δ effects in the numerical response. Conveniently, the two vertical end posts of the shear wall assembly that encloses the full width of the story can be simulated with 2-noded linear truss elements with high axial stiffness that connect the two diaphragms providing no lateral resistance in the initial configuration. Furthermore, the 4 connection points between two diaphragms and the two vertical truss elements enclose the rectangular shear wall domain and existing finite element formulations of a quadrilateral element can be applied to express the kinematics of the framing members. The inherent assumption of straight boundary lines enclosing the quadrilateral domain fits well to the assumption of rigid diaphragms and the use of end-post truss elements.

Kinematics and Equilibrium Equations of a Truss Element

Kinematics of a Truss Element

A truss element has 1 internal DOF u_t which is defined with respect to an element Local Cartesian System (LCS) $\xi O \eta$ that has the ξ axis crossing through the two nodes of the element. Figure 4.12 illustrates the initial and deformed configurations of a truss element. The element displacement vector $\mathbf{D_T}$ consists of the global translations, u_1 and v_1 , and, u_2 and v_2 , of the two nodes and is defined as:

$$\mathbf{D_T} = \{u_1 \quad v_1 \quad u_2 \quad v_2\}^{\mathrm{T}} \tag{4.31}$$

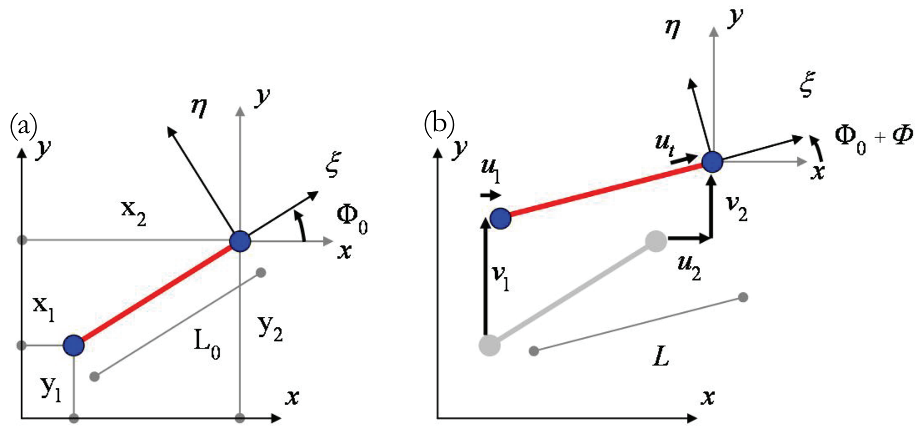

Figure 4.12 (a) Initial and (b) Deformed Configuration of a Truss Element

The initial length L_0 of the truss element is given by:

$$L_0 = \left\| \begin{Bmatrix} x_2 - x_1 \\ y_2 - y_1 \end{Bmatrix} \right\| = \sqrt{(x_2 - x_1)^2 + (y_2 - y_1)^2} \tag{4.32}$$

where x_1, x_2, y_1 and y_2 are the initial global coordinates of the two nodes of the element. The initial angle Φ_0 of the truss element is computed as:

$$\Phi_0 = \begin{cases} (\pi/2)\cdot \mathrm{sgn}(y_2 - y_1) & , \textit{ if } x_2 - x_1 = 0 \\ \arctan\left((y_2 - y_1)/(x_2 - x_1)\right) & , \textit{ if } x_2 - x_1 > 0 \\ \arctan\left((y_2 - y_1)/(x_2 - x_1)\right) + \pi, & \textit{if } x_2 - x_1 < 0 \end{cases} \tag{4.33}$$

where sgn refers to the signum function defined as:

$$\mathrm{sgn}(x) = \begin{cases} 1, & \text{if } x > 0 \\ -1, & \text{if } x < 0 \\ 0, & \text{if } x = 0 \end{cases} \tag{4.34}$$

The actual length L in the deformed configuration is given by:

$$L = \left\| \begin{Bmatrix} x_2 + u_2 - x_1 - u_1 \\ y_2 + v_2 - y_1 - v_1 \end{Bmatrix} \right\| = \sqrt{(x_2 + u_2 - x_1 - u_1)^2 + (y_2 + v_2 - y_1 - v_1)^2} \Rightarrow$$

$$L = \sqrt{L_x^{\ 2} + L_y^{\ 2}} = \sqrt{L_S} \tag{4.35}$$

The element internal deformation u_t can be directly computed as:

$$u_t = L - \mathrm{L}_0 \tag{4.36}$$

Using the exact analytical expression of the internal deformation, a virtual displacement field δu_t can be computed for a given element virtual displacement $\delta\mathbf{D_T}$.

$$\delta u_t = \begin{bmatrix} \dfrac{\partial u_t}{\partial u_1} & \dfrac{\partial u_t}{\partial v_1} & \dfrac{\partial u_t}{\partial u_2} & \dfrac{\partial u_t}{\partial v_2} \end{bmatrix} \cdot \delta\mathbf{D_T} \Rightarrow$$

$$\delta u_t = \frac{\partial L}{\partial L_S} \cdot \begin{bmatrix} \dfrac{\partial L_S}{\partial u_1} & \dfrac{\partial L_S}{\partial v_1} & \dfrac{\partial L_S}{\partial u_2} & \dfrac{\partial L_S}{\partial v_2} \end{bmatrix} \cdot \delta\mathbf{D_T} \Rightarrow$$

$$\delta u_t = \frac{1}{2 \cdot \sqrt{L_S}} \cdot \begin{bmatrix} -2 \cdot L_x & -2 \cdot L_y & 2 \cdot L_x & 2 \cdot L_y \end{bmatrix} \cdot \delta\mathbf{D_T} \Rightarrow$$

$$\delta u_t = \begin{bmatrix} -\cos(\Phi_0 + \mathit{\Phi}) & -\sin(\Phi_0 + \mathit{\Phi}) & \cos(\Phi_0 + \mathit{\Phi}) & \sin(\Phi_0 + \mathit{\Phi}) \end{bmatrix} \cdot \delta\mathbf{D_T} \Rightarrow$$

$$\delta u_t = \mathbf{B_T}(\mathbf{D_T}) \cdot \delta\mathbf{D_T} \tag{4.37}$$

The rotation $\mathit{\Phi}$ of the reference frame in the GCS, as shown in Figure 4.12b, can be computed as:

$$\mathit{\Phi} = \arcsin\left(\frac{(\mathrm{x}_2 - \mathrm{x}_1) \cdot (v_2 - v_1) - (\mathrm{y}_2 - \mathrm{y}_1) \cdot (u_2 - u_1)}{L \cdot \mathrm{L}_0} \right) \tag{4.38}$$

$$\left\{ \begin{array}{l} \sin\mathit{\Phi} = \sin\left((\mathit{\Phi} + \Phi_0) - \Phi_0\right) = \sin(\mathit{\Phi} + \Phi_0) \cdot \cos\Phi_0 - \cos(\mathit{\Phi} + \Phi_0) \cdot \sin\Phi_0 \\ \sin(\mathit{\Phi} + \Phi_0) = \dfrac{\mathrm{y}_2 + v_2 - \mathrm{y}_1 - v_1}{L} \ , \ \cos(\mathit{\Phi} + \Phi_0) = \dfrac{\mathrm{x}_2 + u_2 - \mathrm{x}_1 - u_1}{L} \\ \sin\Phi_0 = \dfrac{\mathrm{y}_2 - \mathrm{y}_1}{\mathrm{L}_0} \qquad\qquad , \ \cos\Phi_0 = \dfrac{\mathrm{x}_2 - \mathrm{x}_1}{\mathrm{L}_0} \end{array} \right\} \tag{4.39}$$

Equilibrium Equations of a Truss Element

Figure 4.13 illustrates a free body diagram of a truss element. The element force vector $\mathbf{F_T}$ consists of the global forces, p_1 and q_1, and, p_2 and q_2, of the two nodes and is defined as:

$$\mathbf{F_T} = \{p_1 \quad q_1 \quad p_2 \quad q_2\}^{\mathrm{T}} \tag{4.40}$$

The equilibrium equations are computed from the principle of virtual work. Under a virtual displacement field $\delta\mathbf{D_T}$, the internal and external virtual work is equal.

$$\delta \mathrm{W_{ext}} = \delta \mathrm{W_{int}} \Rightarrow$$

$$\delta\mathbf{D_T}^{\mathrm{T}} \cdot \mathbf{F_T} = \delta u_t^{\mathrm{T}} \cdot p_t \Rightarrow$$

$$\delta\mathbf{D_T}^{\mathrm{T}} \cdot \mathbf{F_T} = \delta\mathbf{D_T}^{\mathrm{T}} \cdot \mathbf{B_T}^{\mathrm{T}} \cdot p_t \Rightarrow$$

$$\mathbf{F_T} = \mathbf{B_T}^{\mathrm{T}} \cdot p_t \tag{4.41}$$

where p_t is the internal force which is equal to:

$$p_t = k_t \cdot u_t = \frac{EA}{\mathrm{L_0}} \cdot u_t \tag{4.42}$$

where EA is the product of the elastic modulus of the material and the cross-section area of the truss element.

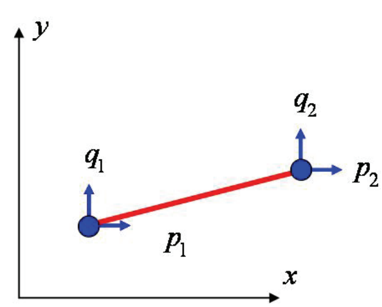

Figure 4.13 Free Body Diagram of a Truss Element

The tangent stiffness matrix of the truss element is computed from the variation of the element force vector with respect to the element displacement vector

$$\mathbf{K_T} = \frac{\partial \mathbf{F_T}}{\partial \mathbf{D_T}} = \frac{\partial\left(\mathbf{B_T}^{\mathrm{T}} \cdot p_t\right)}{\partial \mathbf{D_T}} = \mathbf{B_T}^{\mathrm{T}} \cdot \frac{\partial p_t}{\partial u_t} \cdot \frac{\partial u_t}{\partial \mathbf{D_T}} + \frac{\partial\left(\mathbf{B_T}^{\mathrm{T}}\right)}{\partial \mathbf{D_T}} \cdot p_t \Rightarrow$$

$$\mathbf{K_T} = \mathbf{K_{T1}} + \mathbf{K_{T2}} \tag{4.43}$$

The stiffness matrices shown in (4.8) are calculated as:

$$\mathbf{K_{T1}} = \mathbf{B_T}^{\mathrm{T}} \cdot \frac{\partial p_t}{\partial u_t} \cdot \frac{\partial u_t}{\partial \mathbf{D_T}} = \mathbf{B_T}^{\mathrm{T}} \cdot k_t \cdot \mathbf{B_T} \tag{4.44}$$

$$\mathbf{K_{T2}} = \frac{\partial\left(\mathbf{B_T}^{\mathrm{T}}\right)}{\partial \mathbf{D_T}} \cdot p_t = p_t \cdot \begin{bmatrix} \begin{bmatrix} \dfrac{\partial}{\partial u_1} & \dfrac{\partial}{\partial v_1} & \dfrac{\partial}{\partial u_2} & \dfrac{\partial}{\partial v_2} \end{bmatrix} \cdot \left(-\cos\left(\Phi_0 + \mathit{\Phi}\right)\right) \\ \begin{bmatrix} \dfrac{\partial}{\partial u_1} & \dfrac{\partial}{\partial v_1} & \dfrac{\partial}{\partial u_2} & \dfrac{\partial}{\partial v_2} \end{bmatrix} \cdot \left(-\sin\left(\Phi_0 + \mathit{\Phi}\right)\right) \\ \begin{bmatrix} \dfrac{\partial}{\partial u_1} & \dfrac{\partial}{\partial v_1} & \dfrac{\partial}{\partial u_2} & \dfrac{\partial}{\partial v_2} \end{bmatrix} \cdot \left(\cos\left(\Phi_0 + \mathit{\Phi}\right)\right) \\ \begin{bmatrix} \dfrac{\partial}{\partial u_1} & \dfrac{\partial}{\partial v_1} & \dfrac{\partial}{\partial u_2} & \dfrac{\partial}{\partial v_2} \end{bmatrix} \cdot \left(\sin\left(\Phi_0 + \mathit{\Phi}\right)\right) \end{bmatrix} \Rightarrow$$

$$\mathbf{K_{T2}} = \frac{p_t}{L} \cdot \begin{bmatrix} \sin^2 \mathit{\Phi}_T & -\cos \mathit{\Phi}_T \cdot \sin \mathit{\Phi}_T & -\sin^2 \mathit{\Phi}_T & \cos \mathit{\Phi}_T \cdot \sin \mathit{\Phi}_T \\ & \cos^2 \mathit{\Phi}_T & \cos \mathit{\Phi}_T \cdot \sin \mathit{\Phi}_T & -\cos^2 \mathit{\Phi}_T \\ & & \sin^2 \mathit{\Phi}_T & -\cos \mathit{\Phi}_T \cdot \sin \mathit{\Phi}_T \\ sym & & & \cos^2 \mathit{\Phi}_T \end{bmatrix} \tag{4.45}$$

where $\mathit{\Phi}_T = \Phi_0 + \mathit{\Phi}$. The partial derivatives computed in (4.45) are presented below for three of the elements of the stiffness matrix. Stiffness matrix $\mathbf{K_{T2}}$ includes higher order effects and is usually neglected, since it does not improve significantly the convergence rate and requires additional calculations.

The variation of $\cos \mathit{\Phi}_T$ with respect to u_1 is:

$$\frac{\partial\left(\cos\Phi_T\right)}{\partial u_1}=\frac{\partial\left(\frac{L_x}{L}\right)}{\partial u_1}=\frac{-L-L_x\cdot\left(-\frac{L_x}{L}\right)}{L^2}=\frac{-L^2+L_x{}^2}{L^3}=-\frac{1}{L}\cdot\frac{L_y{}^2}{L^2}\Rightarrow$$

$$\frac{\partial\left(\cos\Phi_T\right)}{\partial u_1}=-\frac{\sin^2\Phi_T}{L} \tag{4.46}$$

The variation of $\cos\Phi_T$ with respect to v_1 is:

$$\frac{\partial\left(\cos\Phi_T\right)}{\partial v_1}=\frac{\partial\left(\frac{L_x}{L}\right)}{\partial v_1}=\frac{0-L_x\cdot\left(-\frac{L_y}{L}\right)}{L^2}=\frac{1}{L}\cdot\frac{L_x}{L}\cdot\frac{L_y}{L}\Rightarrow$$

$$\frac{\partial\left(\cos\Phi_T\right)}{\partial v_1}=\frac{\cos\Phi_T\cdot\sin\Phi_T}{L} \tag{4.47}$$

The variation of $\sin\Phi_T$ with respect to v_1 is:

$$\frac{\partial\left(\sin\Phi_T\right)}{\partial v_1}=\frac{\partial\left(\frac{L_y}{L}\right)}{\partial v_1}=\frac{-L-L_y\cdot\left(-\frac{L_y}{L}\right)}{L^2}=\frac{-L^2+L_y{}^2}{L^3}=-\frac{1}{L}\cdot\frac{L_x{}^2}{L^2}\Rightarrow$$

$$\frac{\partial\left(\sin\Phi_T\right)}{\partial v_1}=-\frac{\cos^2\Phi_T}{L} \tag{4.48}$$

Kinematics and Equilibrium Equations of a Quadrilateral Element

Kinematics of a Quadrilateral Element

A 4-noded quadrilateral element that encloses the framing domain, which is initially orthogonal and aligned to the GCS *xOy*, is utilized to express the kinematics of each point of the framing members that is connected to the sheathing panels through nailing connectors. Assuming for simplicity a single sheathing panel, there are *n* number of internal displacement vectors $\mathbf{u_F}$ that include the two global translations u_f and v_f as well as the rotation θ_f of the framing member, which are denoted as ${}^{\mathrm{i}}\mathbf{u_F}$ and i ranges from 1 to n. The element displacement vector $\mathbf{D_F}$, illustrated in Figure 4.14, consists of the global translations at the four nodes, and is defined as:

$$\mathbf{D_F} = \{u_1 \quad v_1 \quad u_2 \quad v_2 \quad u_3 \quad v_3 \quad u_4 \quad v_4\}^{\mathrm{T}} \tag{4.49}$$

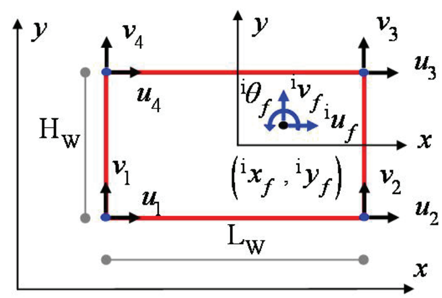

Figure 4.14 Kinematic DOF of the Framing Domain

A Local Cartesian System (LCS) parallel to the GCS that originates from the centre of the quadrilateral element is defined as shown in Figure 4.14, where the location of each point on the framing domain is identified through the point local coordinate vector ${}^{\mathrm{i}}\mathbf{x_F}$. It is reminded that $\mathrm{L_W}$ is the length and $\mathrm{H_W}$ the height of the shear wall assembly.

$$\left\{{}^{\mathrm{i}}\mathbf{x_F}\right\} = \begin{Bmatrix} {}^{\mathrm{i}}x_f \\ {}^{\mathrm{i}}y_f \end{Bmatrix}, \quad \begin{Bmatrix} {}^{\mathrm{i}}x_f \in [\text{-}\mathrm{L_W}/2,\, \mathrm{L_W}/2] \\ {}^{\mathrm{i}}y_f \in [\text{-}\mathrm{H_W}/2,\, \mathrm{H_W}/2] \end{Bmatrix} \tag{4.50}$$

The displacement field can be simply described based on the generalized coordinates ${}^{\mathrm{i}}\xi_f$ and ${}^{\mathrm{i}}\eta_f$ that can be found in the formulation of an isoparametric 4-noded quadrilateral element (Cook et al. 2002).

$$\begin{Bmatrix} {}^{\mathrm{i}}\xi_f = \dfrac{{}^{\mathrm{i}}x_f}{\mathrm{L_W}/2} \\ {}^{\mathrm{i}}\eta_f = \dfrac{{}^{\mathrm{i}}y_f}{\mathrm{H_W}/2} \end{Bmatrix} \tag{4.51}$$

The two global translations ${}^{\mathrm{i}}u_f$ and ${}^{\mathrm{i}}v_f$ can be computed as linear variations of the global displacements at the four nodes:

$$\begin{Bmatrix} {}^{\mathrm{i}}u_f \\ {}^{\mathrm{i}}v_f \end{Bmatrix} = \begin{bmatrix} {}^{\mathrm{i}}N_1 & 0 & {}^{\mathrm{i}}N_2 & 0 & {}^{\mathrm{i}}N_3 & 0 & {}^{\mathrm{i}}N_4 & 0 \\ 0 & {}^{\mathrm{i}}N_1 & 0 & {}^{\mathrm{i}}N_2 & 0 & {}^{\mathrm{i}}N_3 & 0 & {}^{\mathrm{i}}N_4 \end{bmatrix} \cdot \begin{Bmatrix} u_1 \\ v_1 \\ u_2 \\ v_2 \\ u_3 \\ v_3 \\ u_4 \\ v_4 \end{Bmatrix} = {}^{\mathrm{i}}\mathbf{N} \cdot \mathbf{D_F} \qquad (4.52)$$

where ${}^{\mathrm{i}}N_1$ to ${}^{\mathrm{i}}N_4$ are the shape functions given by:

$$\begin{Bmatrix} {}^{\mathrm{i}}N_1 = \frac{1}{4} \cdot \left(1 - {}^{\mathrm{i}}\xi_f\right) \cdot \left(1 - {}^{\mathrm{i}}\eta_f\right) \\ {}^{\mathrm{i}}N_2 = \frac{1}{4} \cdot \left(1 + {}^{\mathrm{i}}\xi_f\right) \cdot \left(1 - {}^{\mathrm{i}}\eta_f\right) \\ {}^{\mathrm{i}}N_3 = \frac{1}{4} \cdot \left(1 + {}^{\mathrm{i}}\xi_f\right) \cdot \left(1 + {}^{\mathrm{i}}\eta_f\right) \\ {}^{\mathrm{i}}N_4 = \frac{1}{4} \cdot \left(1 - {}^{\mathrm{i}}\xi_f\right) \cdot \left(1 + {}^{\mathrm{i}}\eta_f\right) \end{Bmatrix} \qquad (4.53)$$

The rotation of the framing node ${}^{\mathrm{i}}\theta_f$ depends on whether the framing member is initially oriented horizontally or vertically, as shown in Figure 4.15.

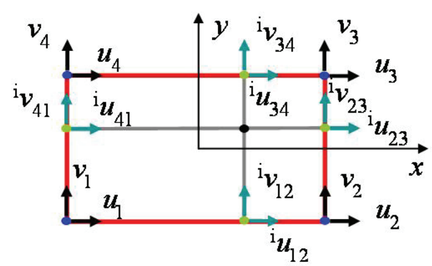

Figure 4.15 Associated Kinematic DOF of a Vertical and a Horizontal Framing Member

Based on (4.38), the rotation of an initially vertical framing member ${}^{\mathrm{i}}\theta_f^v$ is equal to:

$${}^{\mathrm{i}}\theta_f^v = \arcsin\left(- \frac{{}^{\mathrm{i}}u_{34} - {}^{\mathrm{i}}u_{12}}{\sqrt{\left({}^{\mathrm{i}}u_{34} - {}^{\mathrm{i}}u_{12}\right)^2 + \left({}^{\mathrm{i}}v_{34} - {}^{\mathrm{i}}v_{12} + \mathrm{H_W}\right)^2}} \right) = \arcsin\left(- \frac{L_x}{\sqrt{L_x^{\,2} + L_y^{\,2}}} \right) \qquad (4.54)$$

The partial derivative of ${}^{\mathrm{i}}\theta_f^v$ with respect to ${}^{\mathrm{i}}u_{34}$ is equal to:

$$\frac{\partial\, {}^{\mathrm{i}}\theta_f^v}{\partial\, {}^{\mathrm{i}}u_{34}} = \frac{1}{\sqrt{1 - \left(-\frac{L_x}{\sqrt{L_x^{\,2} + L_y^{\,2}}}\right)^2}} \cdot \frac{\partial\left(-\frac{L_x}{\sqrt{L_x^{\,2} + L_y^{\,2}}}\right)}{\partial\, {}^{\mathrm{i}}u_{34}} \Rightarrow$$

$$\frac{\partial\, {}^{\mathrm{i}}\theta_f^v}{\partial\, {}^{\mathrm{i}}u_{34}} = \frac{L}{\sqrt{L_y^{\,2}}} \cdot \left(-\frac{L - L_x \cdot \frac{L_x}{L}}{L^2}\right) = -\frac{1}{L} \cdot \frac{L_y}{L} \Rightarrow$$

$$\frac{\partial\, {}^{\mathrm{i}}\theta_f^v}{\partial\, {}^{\mathrm{i}}u_{34}} = -\frac{1}{L} \cdot \sin\left(\frac{\pi}{2} + {}^{\mathrm{i}}\theta_f^v\right) = -\frac{1}{L} \cdot \cos {}^{\mathrm{i}}\theta_f^v \approx -\frac{1}{\mathrm{H_W}} \cdot \cos {}^{\mathrm{i}}\theta_f^v \tag{4.55}$$

The partial derivative of ${}^{\mathrm{i}}\theta_f^v$ with respect to ${}^{\mathrm{i}}v_{34}$ is equal to:

$$\frac{\partial\, {}^{\mathrm{i}}\theta_f^v}{\partial\, {}^{\mathrm{i}}v_{34}} = \frac{1}{\sqrt{1 - \left(-\frac{L_x}{\sqrt{L_x^{\,2} + L_y^{\,2}}}\right)^2}} \cdot \frac{\partial\left(-\frac{L_x}{\sqrt{L_x^{\,2} + L_y^{\,2}}}\right)}{\partial\, {}^{\mathrm{i}}v_{34}} \Rightarrow$$

$$\frac{\partial\, {}^{\mathrm{i}}\theta_f^v}{\partial\, {}^{\mathrm{i}}v_{34}} = \frac{L}{\sqrt{L_y^{\,2}}} \cdot \left(-\frac{0 - L_x \cdot \frac{L_y}{L}}{L^2}\right) = \frac{1}{L} \cdot \frac{L_x}{L} \Rightarrow$$

$$\frac{\partial\, {}^{\mathrm{i}}\theta_f^v}{\partial\, {}^{\mathrm{i}}v_{34}} = \frac{1}{L} \cdot \cos\left(\frac{\pi}{2} + {}^{\mathrm{i}}\theta_f^v\right) = -\frac{1}{L} \cdot \sin {}^{\mathrm{i}}\theta_f^v \approx -\frac{1}{\mathrm{H_W}} \cdot \sin {}^{\mathrm{i}}\theta_f^v \tag{4.56}$$

Utilizing (4.52), the displacements ${}^{\mathrm{i}}u_{34}$ and ${}^{\mathrm{i}}v_{34}$ are equal to:

$$
\begin{aligned}
u_{34} &= \frac{1}{2}\cdot\left(1 + {}^{\mathrm{i}}\xi_f\right)\cdot u_3 + \frac{1}{2}\cdot\left(1 - {}^{\mathrm{i}}\xi_f\right)\cdot u_4 \\
v_{34} &= \frac{1}{2}\cdot\left(1 + {}^{\mathrm{i}}\xi_f\right)\cdot v_3 + \frac{1}{2}\cdot\left(1 - {}^{\mathrm{i}}\xi_f\right)\cdot v_4
\end{aligned}
\tag{4.57}
$$

Combining (4.55) to (4.57) a virtual rotation $\delta^{\mathrm{i}}\theta_f^v$ can be computed for an element virtual displacement $\delta\mathbf{D_F}$ as:

$$
\delta^{\mathrm{i}}\theta_f^v = \frac{1}{2\cdot \mathrm{H_W}}\cdot
\begin{bmatrix}
\left(1 - {}^{\mathrm{i}}\xi_f\right)\cdot\cos{}^{\mathrm{i}}\theta_f^v \\
\left(1 - {}^{\mathrm{i}}\xi_f\right)\cdot\sin{}^{\mathrm{i}}\theta_f^v \\
\left(1 + {}^{\mathrm{i}}\xi_f\right)\cdot\cos{}^{\mathrm{i}}\theta_f^v \\
\left(1 + {}^{\mathrm{i}}\xi_f\right)\cdot\sin{}^{\mathrm{i}}\theta_f^v \\
-\left(1 + {}^{\mathrm{i}}\xi_f\right)\cdot\cos{}^{\mathrm{i}}\theta_f^v \\
-\left(1 + {}^{\mathrm{i}}\xi_f\right)\cdot\sin{}^{\mathrm{i}}\theta_f^v \\
-\left(1 - {}^{\mathrm{i}}\xi_f\right)\cdot\cos{}^{\mathrm{i}}\theta_f^v \\
-\left(1 - {}^{\mathrm{i}}\xi_f\right)\cdot\sin{}^{\mathrm{i}}\theta_f^v
\end{bmatrix}^{\mathrm{T}}
\cdot\delta\mathbf{D_F} = {}^{\mathrm{i}}\mathbf{N}_{\boldsymbol{\theta}}^{\mathbf{v}}\cdot\delta\mathbf{D_F}
\tag{4.58}
$$

Based on (4.38), the rotation of an initially horizontal framing member ${}^{\mathrm{i}}\theta_f^h$ is equal to:

$$
{}^{\mathrm{i}}\theta_f^h = \arcsin\left(\frac{{}^{\mathrm{i}}v_{23} - {}^{\mathrm{i}}v_{41}}{\sqrt{\left({}^{\mathrm{i}}u_{23} - {}^{\mathrm{i}}u_{41} + \mathrm{L_W}\right)^2 + \left({}^{\mathrm{i}}v_{23} - {}^{\mathrm{i}}v_{41}\right)^2}}\right) = \arcsin\left(\frac{L_y}{\sqrt{L_x^{\,2} + L_y^{\,2}}}\right)
\tag{4.59}
$$

The partial derivative of ${}^{\mathrm{i}}\theta_f^h$ with respect to ${}^{\mathrm{i}}u_{23}$ is equal to:

$$
\frac{\partial\,{}^{\mathrm{i}}\theta_f^h}{\partial\,{}^{\mathrm{i}}u_{23}} = \frac{1}{\sqrt{1 - \left(\dfrac{L_y}{\sqrt{L_x^{\,2} + L_y^{\,2}}}\right)^2}}\cdot\frac{\partial\left(\dfrac{L_y}{\sqrt{L_x^{\,2} + L_y^{\,2}}}\right)}{\partial\,{}^{\mathrm{i}}u_{23}} \Rightarrow
$$

$$\frac{\partial\, {}^{i}\theta_f^h}{\partial\, {}^{i}u_{23}} = \frac{L}{\sqrt{L_x^{\ 2}}} \cdot \frac{0 - L_y \cdot \dfrac{L_x}{L}}{L^2} = -\frac{1}{L} \cdot \frac{L_y}{L} \;\Rightarrow$$

$$\frac{\partial\, {}^{i}\theta_f^h}{\partial\, {}^{i}u_{23}} = -\frac{1}{L} \cdot \sin {}^{i}\theta_f^h \;\approx\; -\frac{1}{\mathrm{L_W}} \cdot \sin {}^{i}\theta_f^h \tag{4.60}$$

The partial derivative of ${}^{i}\theta_f^h$ with respect to ${}^{i}v_{23}$ is equal to:

$$\frac{\partial\, {}^{i}\theta_f^h}{\partial\, {}^{i}v_{23}} = \frac{1}{\sqrt{1 - \left(\dfrac{L_y}{\sqrt{L_x^{\ 2} + L_y^{\ 2}}} \right)^2}} \cdot \frac{\partial \left(\dfrac{L_y}{\sqrt{L_x^{\ 2} + L_y^{\ 2}}} \right)}{\partial\, {}^{i}v_{23}} \;\Rightarrow$$

$$\frac{\partial\, {}^{i}\theta_f^h}{\partial\, {}^{i}v_{23}} = \frac{L}{\sqrt{L_x^{\ 2}}} \cdot \frac{L - L_y \cdot \dfrac{L_y}{L}}{L^2} = \frac{1}{L} \cdot \frac{L_x}{L} \;\Rightarrow$$

$$\frac{\partial\, {}^{i}\theta_f^h}{\partial\, {}^{i}v_{23}} = \frac{1}{L} \cdot \cos {}^{i}\theta_f^h \;\approx\; \frac{1}{\mathrm{L_W}} \cdot \cos {}^{i}\theta_f^h \tag{4.61}$$

Utilizing (4.52), the displacements ${}^{i}u_{23}$ and ${}^{i}v_{23}$ are equal to:

$$\begin{aligned} u_{23} &= \frac{1}{2} \cdot \left(1 - {}^{i}\eta_f\right) \cdot u_2 + \frac{1}{2} \cdot \left(1 + {}^{i}\eta_f\right) \cdot u_3 \\ v_{23} &= \frac{1}{2} \cdot \left(1 - {}^{i}\eta_f\right) \cdot v_2 + \frac{1}{2} \cdot \left(1 + {}^{i}\eta_f\right) \cdot v_3 \end{aligned} \tag{4.62}$$

Combining (4.60) to (4.62) a virtual rotation $\delta^{i}\theta_f^h$ can be computed for an element virtual displacement $\delta\mathbf{D_F}$ as:

$$\delta\,{}^{\mathrm{i}}\theta_f^h = \frac{1}{2\cdot \mathrm{L_W}}\cdot\begin{bmatrix} \left(1 - {}^{\mathrm{i}}\eta_f\right)\cdot\sin{}^{\mathrm{i}}\theta_f^h \\ -\left(1 - {}^{\mathrm{i}}\eta_f\right)\cdot\cos{}^{\mathrm{i}}\theta_f^h \\ -\left(1 - {}^{\mathrm{i}}\eta_f\right)\cdot\sin{}^{\mathrm{i}}\theta_f^h \\ \left(1 - {}^{\mathrm{i}}\eta_f\right)\cdot\cos{}^{\mathrm{i}}\theta_f^h \\ -\left(1 + {}^{\mathrm{i}}\eta_f\right)\cdot\sin{}^{\mathrm{i}}\theta_f^h \\ \left(1 + {}^{\mathrm{i}}\eta_f\right)\cdot\cos{}^{\mathrm{i}}\theta_f^h \\ \left(1 + {}^{\mathrm{i}}\eta_f\right)\cdot\sin{}^{\mathrm{i}}\theta_f^h \\ -\left(1 + {}^{\mathrm{i}}\eta_f\right)\cdot\cos{}^{\mathrm{i}}\theta_f^h \end{bmatrix}^{\mathrm{T}}\cdot\delta\mathbf{D_F} = {}^{\mathrm{i}}\mathbf{N_\theta^h}\cdot\delta\mathbf{D_F} \tag{4.63}$$

Finally, a virtual internal field $\delta\,{}^{\mathrm{i}}\mathbf{u_F}$ is equal to:

$$\delta\,{}^{\mathrm{i}}\mathbf{u_F} = \begin{bmatrix} {}^{\mathrm{i}}\mathbf{N} \\ {}^{\mathrm{i}}\mathbf{N_\theta} \end{bmatrix}\cdot\delta\mathbf{D_F} = {}^{\mathrm{i}}\mathbf{B_F}\left(\mathbf{D_F}\right)\cdot\delta\mathbf{D_F} \tag{4.64}$$

where

$$\begin{aligned} {}^{\mathrm{i}}\mathbf{N_\theta} &= {}^{\mathrm{i}}\mathbf{N_\theta^v},\ \text{if member is vertical} \\ {}^{\mathrm{i}}\mathbf{N_\theta} &= {}^{\mathrm{i}}\mathbf{N_\theta^h},\ \text{if member is horizontal} \end{aligned} \tag{4.65}$$

Contributions to the Quadrilateral Element from the Truss Elements

The global DOF of the two truss elements ${}^{1}\mathbf{D_T}$ and ${}^{2}\mathbf{D_T}$, where the left upper indices 1 and 2 refer to the left and the right vertical trusses, respectively, are related to the quadrilateral DOF $\mathbf{D_F}$ as:

$$\mathbf{D_{FT}} = \begin{Bmatrix} {}^{1}\mathbf{D_T} \\ {}^{2}\mathbf{D_T} \end{Bmatrix} = \begin{bmatrix} 1 & 0 & 0 & 0 & 0 & 0 & 0 & 0 \\ 0 & 1 & 0 & 0 & 0 & 0 & 0 & 0 \\ 0 & 0 & 0 & 0 & 0 & 0 & 1 & 0 \\ 0 & 0 & 0 & 0 & 0 & 0 & 0 & 1 \\ 0 & 0 & 1 & 0 & 0 & 0 & 0 & 0 \\ 0 & 0 & 0 & 1 & 0 & 0 & 0 & 0 \\ 0 & 0 & 0 & 0 & 1 & 0 & 0 & 0 \\ 0 & 0 & 0 & 0 & 0 & 1 & 0 & 0 \end{bmatrix} \cdot \mathbf{D_F} = \mathbf{B_{FT}} \cdot \mathbf{D_F} \tag{4.66}$$

Accordingly, a virtual displacement $\delta\mathbf{D_{FT}}$ is equal to:

$$\delta\mathbf{D_{FT}} = \mathbf{B_{FT}} \cdot \delta\mathbf{D_F} \tag{4.67}$$

Equilibrium Equations of a Quadrilateral Element

Figure 4.16 illustrates a free body diagram of a quadrilateral element. The element force vector $\mathbf{F_F}$ consists of the global forces at the four nodes and is defined as:

$$\mathbf{F_F} = \{p_1 \quad q_1 \quad p_2 \quad q_2 \quad p_3 \quad q_3 \quad p_4 \quad q_4\}^T \tag{4.68}$$

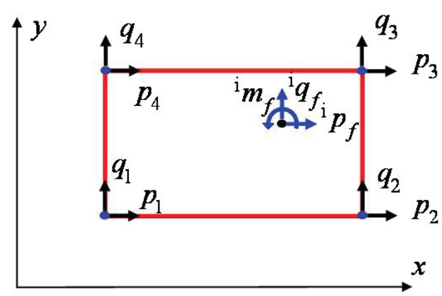

Figure 4.16 Free Body Diagram of a Quadrilateral Element

The internal force vector related to the framing members is ${}^{i}\mathbf{p_F} = \{{}^{i}p_f \; {}^{i}q_f \; {}^{i}m_f\}^T$. The equilibrium equations are computed from the principle of virtual work. Under a virtual displacement field $\delta\mathbf{D_F}$, the internal and external virtual work is equal.

$$\delta W_{ext} = \delta W_{int} \Rightarrow$$

$$\delta \mathbf{D_F}^{\mathrm{T}} \cdot \mathbf{F_F} = \sum_{\mathrm{i}=1}^{n} \left(\delta\, {}^{\mathrm{i}}\mathbf{u_F}^{\mathrm{T}} \cdot {}^{\mathrm{i}}\mathbf{p_F} \right) + \delta \mathbf{D_{FT}}^{\mathrm{T}} \cdot \mathbf{F_{FT}} \Rightarrow$$

$$\delta \mathbf{D_F}^{\mathrm{T}} \cdot \mathbf{F_F} = \sum_{\mathrm{i}=1}^{n} \left(\delta \mathbf{D_F}^{\mathrm{T}} \cdot {}^{\mathrm{i}}\mathbf{B_F}^{\mathrm{T}} \cdot {}^{\mathrm{i}}\mathbf{p_F} \right) + \delta \mathbf{D_F}^{\mathrm{T}} \cdot \mathbf{B_{FT}}^{\mathrm{T}} \cdot \mathbf{F_{FT}} \Rightarrow$$

$$\mathbf{F_F} = \sum_{\mathrm{i}=1}^{n} \left({}^{\mathrm{i}}\mathbf{B_F}^{\mathrm{T}} \cdot {}^{\mathrm{i}}\mathbf{p_F} \right) + \mathbf{B_{FT}}^{\mathrm{T}} \cdot \mathbf{F_{FT}} \tag{4.69}$$

where $\mathbf{F_{FT}}$ contains the global forces of the trusses ${}^{1}\mathbf{F_T}$ and ${}^{2}\mathbf{F_T}$ computed as:

$$\mathbf{F_{FT}} = \begin{Bmatrix} {}^{1}\mathbf{F_T} \\ {}^{2}\mathbf{F_T} \end{Bmatrix} = \begin{Bmatrix} {}^{1}\mathbf{B_T}^{\mathrm{T}} \cdot {}^{1}p_t \\ {}^{2}\mathbf{B_T}^{\mathrm{T}} \cdot {}^{2}p_t \end{Bmatrix} \tag{4.70}$$

The tangent stiffness matrix of the quadrilateral element is computed from the variation of the element force vector with respect to the element displacement vector

$$\mathbf{K_F} = \frac{\partial \mathbf{F_F}}{\partial \mathbf{D_F}} = \frac{\partial \left(\sum_{\mathrm{i}=1}^{n} \left({}^{\mathrm{i}}\mathbf{B_F}^{\mathrm{T}} \cdot {}^{\mathrm{i}}\mathbf{p_F} \right) + \mathbf{B_{FT}}^{\mathrm{T}} \cdot \mathbf{F_{FT}} \right)}{\partial \mathbf{D_F}} \Rightarrow$$

$$\mathbf{K_F} = \sum_{\mathrm{i}=1}^{n} \left({}^{\mathrm{i}}\mathbf{B_F}^{\mathrm{T}} \cdot \frac{\partial\, {}^{\mathrm{i}}\mathbf{p_F}}{\partial\, {}^{\mathrm{i}}\mathbf{u_F}} \cdot \frac{\partial\, {}^{\mathrm{i}}\mathbf{u_F}}{\partial \mathbf{D_F}} \right) + \sum_{\mathrm{i}=1}^{n} \left(\frac{\partial \left({}^{\mathrm{i}}\mathbf{B_F}^{\mathrm{T}} \right)}{\partial \mathbf{D_F}} \cdot {}^{\mathrm{i}}\mathbf{p_F} \right) + \mathbf{B_{FT}}^{\mathrm{T}} \cdot \frac{\partial \mathbf{F_{FT}}}{\partial \mathbf{D_{FT}}} \cdot \frac{\partial \mathbf{D_{FT}}}{\partial \mathbf{D_F}} \Rightarrow$$

$$\mathbf{K_F} = \mathbf{K_{F1}} + \mathbf{K_{F2}} + \mathbf{K_{F3}} \tag{4.71}$$

The stiffness matrices shown in (4.71) are calculated as:

$$\mathbf{K_{F1}} = \sum_{\mathrm{i}=1}^{n} \left({}^{\mathrm{i}}\mathbf{B_F}^{\mathrm{T}} \cdot \frac{\partial\, {}^{\mathrm{i}}\mathbf{p_F}}{\partial\, {}^{\mathrm{i}}\mathbf{u_F}} \cdot \frac{\partial\, {}^{\mathrm{i}}\mathbf{u_F}}{\partial \mathbf{D_F}} \right) = \sum_{\mathrm{i}=1}^{n} \left({}^{\mathrm{i}}\mathbf{B_F}^{\mathrm{T}} \cdot {}^{\mathrm{i}}\mathbf{K_S^{FF}} \cdot {}^{\mathrm{i}}\mathbf{B_F} \right) \tag{4.72}$$

$$\mathbf{K_{F3}} = \mathbf{B_{FT}}^{\mathrm{T}} \cdot \frac{\partial \mathbf{F_{FT}}}{\partial \mathbf{D_{FT}}} \cdot \frac{\partial \mathbf{D_{FT}}}{\partial \mathbf{D_F}} = \mathbf{B_{FT}}^{\mathrm{T}} \cdot \begin{bmatrix} {}^{1}\mathbf{K_T} & \mathbf{0} \\ \mathbf{0} & {}^{2}\mathbf{K_T} \end{bmatrix} \cdot \mathbf{B_{FT}} \tag{4.73}$$

where ${}^{i}\mathbf{K_S}^{\mathbf{FF}}$ is the submatrix corresponding to the framing DOF, as computed in (4.8), for the ith connector. Stiffness matrix $\mathbf{K_{F2}}$, which include higher order effects, is neglected due to the significant computational cost from the existence of two cases (vertical and horizontal members).

Kinematics and Equilibrium Equations of the Rigid Diaphragms

Kinematics of the Rigid Diaphragms

The element displacement vector $\mathbf{D_D}$ consists of the global translations and rotation of the two rigid diaphragms, and is defined as:

$$\mathbf{D_D} = \{U_1 \quad V_1 \quad \Theta_1 \quad U_2 \quad V_2 \quad \Theta_2\}^T \tag{4.74}$$

Figure 4.17 illustrates the kinematic DOF of the diaphragms $\mathbf{D_D}$ and the internal kinematic DOF $\mathbf{D_F}$, as defined in the previous section.

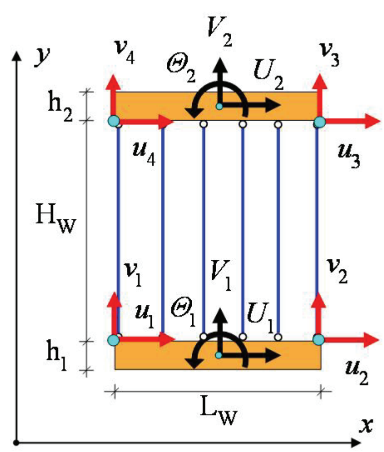

Figure 4.17 Kinematic DOF of the Rigid Diaphragms

The displacement vector of a point on the rigid diaphragm can be expressed by derivations already provided for the panel element formulation. It is reminded that the lower and upper diaphragms have thicknesses h_1 and h_2, respectively. Thus, the internal displacement vector $\mathbf{D_F}$ can be expressed through the global displacement vector $\mathbf{D_D}$ as:

$$
\begin{aligned}
\begin{Bmatrix} u_1 \\ v_1 \end{Bmatrix} &= \begin{Bmatrix} U_1 \\ V_1 \end{Bmatrix} + \begin{bmatrix} \cos\Theta_1 & \text{-}\sin\Theta_1 \\ \sin\Theta_1 & \cos\Theta_1 \end{bmatrix} \cdot \begin{Bmatrix} \text{-L}_W/2 \\ \text{h}_1/2 \end{Bmatrix} - \begin{Bmatrix} \text{-L}_W/2 \\ \text{h}_1/2 \end{Bmatrix} \\
\begin{Bmatrix} u_2 \\ v_2 \end{Bmatrix} &= \begin{Bmatrix} U_1 \\ V_1 \end{Bmatrix} + \begin{bmatrix} \cos\Theta_1 & \text{-}\sin\Theta_1 \\ \sin\Theta_1 & \cos\Theta_1 \end{bmatrix} \cdot \begin{Bmatrix} \text{L}_W/2 \\ \text{h}_1/2 \end{Bmatrix} - \begin{Bmatrix} \text{L}_W/2 \\ \text{h}_1/2 \end{Bmatrix} \\
\begin{Bmatrix} u_3 \\ v_3 \end{Bmatrix} &= \begin{Bmatrix} U_2 \\ V_2 \end{Bmatrix} + \begin{bmatrix} \cos\Theta_2 & \text{-}\sin\Theta_2 \\ \sin\Theta_2 & \cos\Theta_2 \end{bmatrix} \cdot \begin{Bmatrix} \text{L}_W/2 \\ \text{-h}_2/2 \end{Bmatrix} - \begin{Bmatrix} \text{L}_W/2 \\ \text{-h}_2/2 \end{Bmatrix} \\
\begin{Bmatrix} u_4 \\ v_4 \end{Bmatrix} &= \begin{Bmatrix} U_2 \\ V_2 \end{Bmatrix} + \begin{bmatrix} \cos\Theta_2 & \text{-}\sin\Theta_2 \\ \sin\Theta_2 & \cos\Theta_2 \end{bmatrix} \cdot \begin{Bmatrix} \text{-L}_W/2 \\ \text{-h}_2/2 \end{Bmatrix} - \begin{Bmatrix} \text{-L}_W/2 \\ \text{-h}_2/2 \end{Bmatrix}
\end{aligned}
\tag{4.75}
$$

Using the analytical expressions for the internal deformations, a virtual displacement $\delta\mathbf{D_F}$ for a given global virtual displacement $\delta\mathbf{D_D}$ as:

$$
\delta\mathbf{D_F} = \frac{\partial\mathbf{D_F}}{\partial\mathbf{D_D}} \cdot \delta\mathbf{D_D} \;\Rightarrow
$$

$$
\delta\mathbf{D_F} = \begin{bmatrix} \begin{matrix} 1 & 0 & \text{-}Y_1 \\ 0 & 1 & X_1 \\ 1 & 0 & \text{-}Y_2 \\ 0 & 1 & X_2 \end{matrix} & \mathbf{0} \\ \mathbf{0} & \begin{matrix} 1 & 0 & \text{-}Y_3 \\ 0 & 1 & X_3 \\ 1 & 0 & \text{-}Y_4 \\ 0 & 1 & X_4 \end{matrix} \end{bmatrix} \cdot \delta\mathbf{D_D} \;\Rightarrow
$$

$$
\delta\mathbf{D_F} = \mathbf{B_D}\left(\mathbf{D_D}\right) \cdot \delta\mathbf{D_D} \tag{4.76}
$$

where the nonlinear elements of $\mathbf{B_D}$ represent the algebraic distance in the global directions of the respective point from the center of the associated diaphragm, and are computed as:

$$\begin{Bmatrix} X_1 \\ Y_1 \end{Bmatrix} = \begin{bmatrix} \cos\Theta_1 & \text{-}\sin\Theta_1 \\ \sin\Theta_1 & \cos\Theta_1 \end{bmatrix} \cdot \begin{Bmatrix} \text{-L}_W/2 \\ \text{h}_1/2 \end{Bmatrix}$$
$$\begin{Bmatrix} X_2 \\ Y_2 \end{Bmatrix} = \begin{bmatrix} \cos\Theta_1 & \text{-}\sin\Theta_1 \\ \sin\Theta_1 & \cos\Theta_1 \end{bmatrix} \cdot \begin{Bmatrix} \text{L}_W/2 \\ \text{h}_1/2 \end{Bmatrix}$$
$$\begin{Bmatrix} X_3 \\ Y_3 \end{Bmatrix} = \begin{bmatrix} \cos\Theta_2 & \text{-}\sin\Theta_2 \\ \sin\Theta_2 & \cos\Theta_2 \end{bmatrix} \cdot \begin{Bmatrix} \text{L}_W/2 \\ \text{-h}_2/2 \end{Bmatrix} \tag{4.77}$$
$$\begin{Bmatrix} X_4 \\ Y_4 \end{Bmatrix} = \begin{bmatrix} \cos\Theta_2 & \text{-}\sin\Theta_2 \\ \sin\Theta_2 & \cos\Theta_2 \end{bmatrix} \cdot \begin{Bmatrix} \text{-L}_W/2 \\ \text{-h}_2/2 \end{Bmatrix}$$

Equilibrium Equations of the Rigid Diaphragms

Figure 4.18 illustrates a free body diagram of the two rigid diaphragms. The element force vector $\mathbf{F_D}$ consists of the global forces and moments of the two rigid diaphragms, and is defined as:

$$\mathbf{F_D} = \{P_1 \quad Q_1 \quad M_1 \quad P_2 \quad Q_2 \quad M_2\}^{\mathrm{T}} \tag{4.78}$$

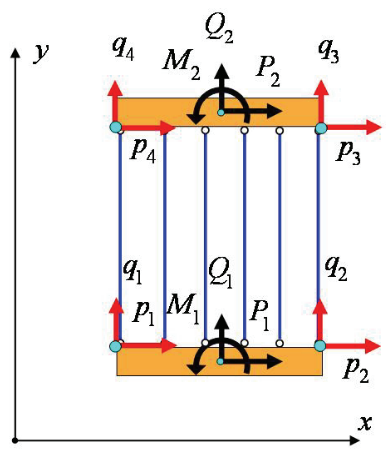

Figure 4.18 Free Body Diagram of the Rigid Diaphragms

The equilibrium equations are computed from the principle of virtual work. Under a virtual displacement field $\delta\mathbf{D_D}$, the internal and external virtual work is equal.

$$\delta \mathrm{W_{ext}} = \delta \mathrm{W_{int}} \;\Rightarrow$$

$$\delta \mathbf{D_D}^{\mathrm{T}} \cdot \mathbf{F_D} = \delta \mathbf{D_F}^{\mathrm{T}} \cdot \mathbf{F_F} \;\Rightarrow$$

$$\delta \mathbf{D_D}^{\mathrm{T}} \cdot \mathbf{F_D} = \delta \mathbf{D_D}^{\mathrm{T}} \cdot \mathbf{B_D}^{\mathrm{T}} \cdot \mathbf{F_F} \;\Rightarrow$$

$$\mathbf{F_D} = \mathbf{B_D}^{\mathrm{T}} \cdot \left(\sum_{\mathrm{i}=1}^{n} \left({}^{\mathrm{i}}\mathbf{B_F}^{\mathrm{T}} \cdot {}^{\mathrm{i}}\mathbf{p_F} \right) + \mathbf{B_{FT}}^{\mathrm{T}} \cdot \mathbf{F_{FT}} \right) \tag{4.79}$$

The tangent stiffness matrix of the two diaphragms is computed from the variation of the element force vector with respect to the element displacement vector

$$\mathbf{K_D} = \frac{\partial \mathbf{F_D}}{\partial \mathbf{D_D}} = \frac{\partial \left(\mathbf{B_D}^{\mathrm{T}} \cdot \mathbf{F_F} \right)}{\partial \mathbf{D_D}} = \mathbf{B_D}^{\mathrm{T}} \cdot \frac{\partial \mathbf{F_F}}{\partial \mathbf{D_F}} \cdot \frac{\partial \mathbf{D_F}}{\partial \mathbf{D_D}} + \frac{\partial \left(\mathbf{B_D}^{\mathrm{T}} \right)}{\partial \mathbf{D_D}} \cdot \mathbf{F_F} \;\Rightarrow$$

$$\mathbf{K_D} = \mathbf{K_{D1}} + \mathbf{K_{D2}} \tag{4.80}$$

The stiffness matrices shown in (4.80) are calculated as:

$$\mathbf{K_{D1}} = \mathbf{B_D}^{\mathrm{T}} \cdot \frac{\partial \mathbf{F_F}}{\partial \mathbf{D_F}} \cdot \frac{\partial \mathbf{D_F}}{\partial \mathbf{D_D}} = \mathbf{B_D}^{\mathrm{T}} \cdot \mathbf{K_F} \cdot \mathbf{B_D} \tag{4.81}$$

$$\mathbf{K_{D2}} = \frac{\partial \left(\mathbf{B_D}^{\mathrm{T}} \right)}{\partial \mathbf{D_D}} \cdot \mathbf{F_F} = \begin{bmatrix} 0 & 0 & 0 & & & \\ & 0 & 0 & & \mathbf{0} & \\ & & {}^{1}k_d & & & \\ & & & 0 & 0 & 0 \\ & sym & & & 0 & 0 \\ & & & & & {}^{2}k_d \end{bmatrix} \tag{4.82}$$

where

$$\left\{ \begin{aligned} {}^{1}k_d &= -\left(X_1 \cdot p_1 + Y_1 \cdot q_1 + X_2 \cdot p_2 + Y_2 \cdot q_2 \right) \\ {}^{2}k_d &= -\left(X_3 \cdot p_3 + Y_3 \cdot q_3 + X_4 \cdot p_4 + Y_4 \cdot q_4 \right) \end{aligned} \right\} \tag{4.83}$$

The stiffness matrix $\mathbf{K_{D2}}$ includes higher order effects and is usually neglected, since it does not improve significantly the convergence rate and requires additional calculations.

4.3.2.4 Global Equilibrium Equations and Global Stiffness Matrix of a Shear Wall Element Suppressing Framing Deformations

The global equilibrium equations and the global tangent stiffness matrix of a shear wall element that suppresses framing deformations can be expressed based on the analytical derivations provided earlier in this section. If N_P is the total number of panels of the shear wall assembly, the total number of global DOF N_{DOF} is equal to:

$$N_{DOF} = 6 + 4 \cdot N_P \tag{4.84}$$

For the sample shear wall, presented in Figure 4.4, $N_P = 1$ and $N_{DOF} = 10$. The equilibrium equations for the panel and the framing domain have been given in (4.25) and (4.79), respectively, and are repeated below:

$$\begin{aligned} \mathbf{F_D} &= \mathbf{B_D}^{\mathrm{T}} \cdot \left(\sum_{\mathrm{i}=1}^{n} \left({}^{\mathrm{i}}\mathbf{B_F}^{\mathrm{T}} \cdot {}^{\mathrm{i}}\mathbf{p_F} \right) + \mathbf{B_{FT}}^{\mathrm{T}} \cdot \mathbf{F_{FT}} \right) \\ \mathbf{F_P} &= \sum_{\mathrm{i}=1}^{n} \left({}^{\mathrm{i}}\mathbf{B_P}^{\mathrm{T}} \cdot {}^{\mathrm{i}}\mathbf{p_P} \right) + \left\{ 0 \quad 0 \quad 0 \quad K_G \cdot \gamma \right\}^{\mathrm{T}} \end{aligned} \tag{4.85}$$

The global tangent stiffness matrix of the shear wall model $\mathbf{K_W}$ is computed as:

$$\mathbf{K_W} = \begin{bmatrix} \dfrac{\partial \mathbf{F_D}}{\partial \mathbf{D_D}} & \dfrac{\partial \mathbf{F_D}}{\partial \mathbf{D_P}} \\ \dfrac{\partial \mathbf{F_P}}{\partial \mathbf{D_D}} & \dfrac{\partial \mathbf{F_P}}{\partial \mathbf{D_P}} \end{bmatrix} = \begin{bmatrix} \mathbf{K_D} & \mathbf{K_{DP}} \\ \mathbf{K_{PD}} & \mathbf{K_P} \end{bmatrix} \tag{4.86}$$

where $\mathbf{K_P}$ and $\mathbf{K_D}$ have been derived in (4.27) and (4.80), respectively. The off diagonal stiffness sub-matrices are computed as:

$$\mathbf{K_{PD}} = \frac{\partial \mathbf{F_P}}{\partial \mathbf{D_D}} = \frac{\partial \left(\sum_{\mathrm{i}=1}^{n} \left({}^{\mathrm{i}}\mathbf{B_P}^{\mathrm{T}} \cdot {}^{\mathrm{i}}\mathbf{p_P} \right) \right)}{\partial \mathbf{D_D}} = \sum_{\mathrm{i}=1}^{n} \left({}^{\mathrm{i}}\mathbf{B_P}^{\mathrm{T}} \cdot \frac{\partial\, {}^{\mathrm{i}}\mathbf{p_P}}{\partial\, {}^{\mathrm{i}}\mathbf{u_F}} \cdot \frac{\partial\, {}^{\mathrm{i}}\mathbf{u_F}}{\partial \mathbf{D_F}} \cdot \frac{\partial \mathbf{D_F}}{\partial \mathbf{D_D}} \right) \Rightarrow$$

$$\mathbf{K_{PD}} = \sum_{\mathrm{i}=1}^{n} \left({}^{\mathrm{i}}\mathbf{B_P}^{\mathrm{T}} \cdot {}^{\mathrm{i}}\mathbf{K_S^{PF}} \cdot {}^{\mathrm{i}}\mathbf{B_F} \cdot \mathbf{B_D} \right) \tag{4.87}$$

where ${}^{i}\mathbf{K}_{\mathbf{S}}^{\mathbf{PF}}$ is the submatrix corresponding to the respective off diagonal terns, as computed in (4.8), for the ith connector. Similarly:

$$\mathbf{K_{DP}} = \left(\mathbf{K_{PD}}\right)^{T} = \sum_{i=1}^{n}\left(\mathbf{B_D}^{T} \cdot {}^{i}\mathbf{B_F}^{T} \cdot {}^{i}\mathbf{K}_{\mathbf{S}}^{\mathbf{FP}} \cdot {}^{i}\mathbf{B_P}\right) \tag{4.88}$$

The incremental equilibrium equations can be written as:

$$\delta\begin{Bmatrix}\mathbf{F_D}\\ \mathbf{F_P}\end{Bmatrix} = \begin{bmatrix}\mathbf{K_D} & \mathbf{K_{DP}}\\ \mathbf{K_{PD}} & \mathbf{K_P}\end{bmatrix}\cdot\delta\begin{Bmatrix}\mathbf{D_D}\\ \mathbf{D_P}\end{Bmatrix} \tag{4.89}$$

Since no external forces are acting on the panel elements ($\delta\mathbf{F_P} = \mathbf{0}$) the equilibrium equations can be condensed to a 6 DOF system that represent the shear wall element in a building model analysis:

$$\delta\mathbf{F_D} = \mathbf{K_D}\cdot\delta\mathbf{D_D} + \mathbf{K_{DP}}\cdot\left(\mathbf{-K_{PP}}^{-1}\cdot\mathbf{K_{PD}}\cdot\delta\mathbf{D_D}\right) \Rightarrow$$

$$\delta\mathbf{F_D} = \mathbf{K}_{\mathbf{W}}^{\mathbf{D}}\cdot\delta\mathbf{D_D} \tag{4.90}$$

where the global stiffness matrix of the shear wall element $\mathbf{K_W}^{\mathbf{D}}$ is:

$$\mathbf{K}_{\mathbf{W}}^{\mathbf{D}} = \mathbf{K_D} - \mathbf{K_{DP}}\cdot\mathbf{K_{PP}}^{-1}\cdot\mathbf{K_{PD}} \tag{4.91}$$

4.3.3 Formulation of a Shear Wall Element Including Framing Deformations

The formulation of a shear wall element that includes framing deformations is introduced in this section. The derivations for the sheathing panel elements and the sheathing-to-framing connector elements remain the same as presented in the previous section for a shear wall element with no framing deformations. The only difference between the two numerical models is the modeling framework adopted for the framing members of the shear wall assembly, while diaphragms are still considered rigid.

Although the assumption of rigid framing members and anchored horizontal plates to the diaphragms led to a simple and computationally efficient formulation to simulate a pure kinematic distortion of the framing domain including geometric nonlinearity, this hypothesis poses limitations on the capability to predict (i) the response of light-frame wood structures with medium-to-poor anchorage conditions and, (ii) the variation of structural performance of fully sheathed wall segments as a result of the height-to-length ratio and the actual anchorage conditions of the segment. In this perspective, the framing members have to be simulated as individual structural components that are inter-connected with framing-to-framing and anchoring connections and interact with the sheathing panels through the associated connectors. It is, thus, selected to represent the framing members with linear elastic beam elements with axial and flexural behavior using center-line modeling of each individual framing component. This approach involves the assignment of a finite element mesh of the vertical and horizontal framing members of the wall assembly and a set of nodes that represent discrete points of the structural components. Each node is described through 3 DOF in the 2D plane and can be assigned at each framing location where sheathing-to-framing connectors exist. Considering a wall segment with no openings the framing configuration will consist of vertical continuous studs connected to the horizontal continuous sill and top plates and a detailed numerical model of the framing domain can be developed as shown in Figure 4.19.

In Figure 4.19, the framing domain of the shear wall assembly is considered as three groups of components: the sill plate members, the top plate members and the internal framing members. These components are meshed with 2-noded beam elements assigning different nodes for each group at the interaction surface, which is actually the location of each plate-to-stud connection at the horizontal boundaries of the wall assembly. This eventually requires the development and use of appropriate interface elements to simulate: (i) the interaction between horizontal and vertical framing members; (ii) the interaction between horizontal boundary plates and diaphragms; and (iii) the structural response of anchoring equipment (i.e. anchor bolts, holdowns).

Clearly, this numerical model offers the versatility to simulate various modes of deformation but also poses challenges on the proper modeling of the adopted modes. Since the formulations are described in static conditions, the interface elements should provide static determinacy to the framing components under a displacement controlled motion of the diaphragms. This prerequisite does not allow the general simulation of coupled friction and contact phenomena, which requires a solution under dynamic conditions with tracking algorithms that identify the modes of deformation in the time domain. Moreover, the solution is sought in the deformed configuration, which means that sliding friction between a vertical stud and a horizontal plate would require tracking of the motion of the stud tip on the horizontal plate. For these reasons, sliding friction is not considered between the framing components and it is assumed that loads parallel to a contact area are transferred independent of the perpendicular normal force and result to minimal horizontal differential displacements. In the perpendicular direction, contact/separation is effectively simulated with a nonlinear elastic spring that ideally transfers only compressive loads.

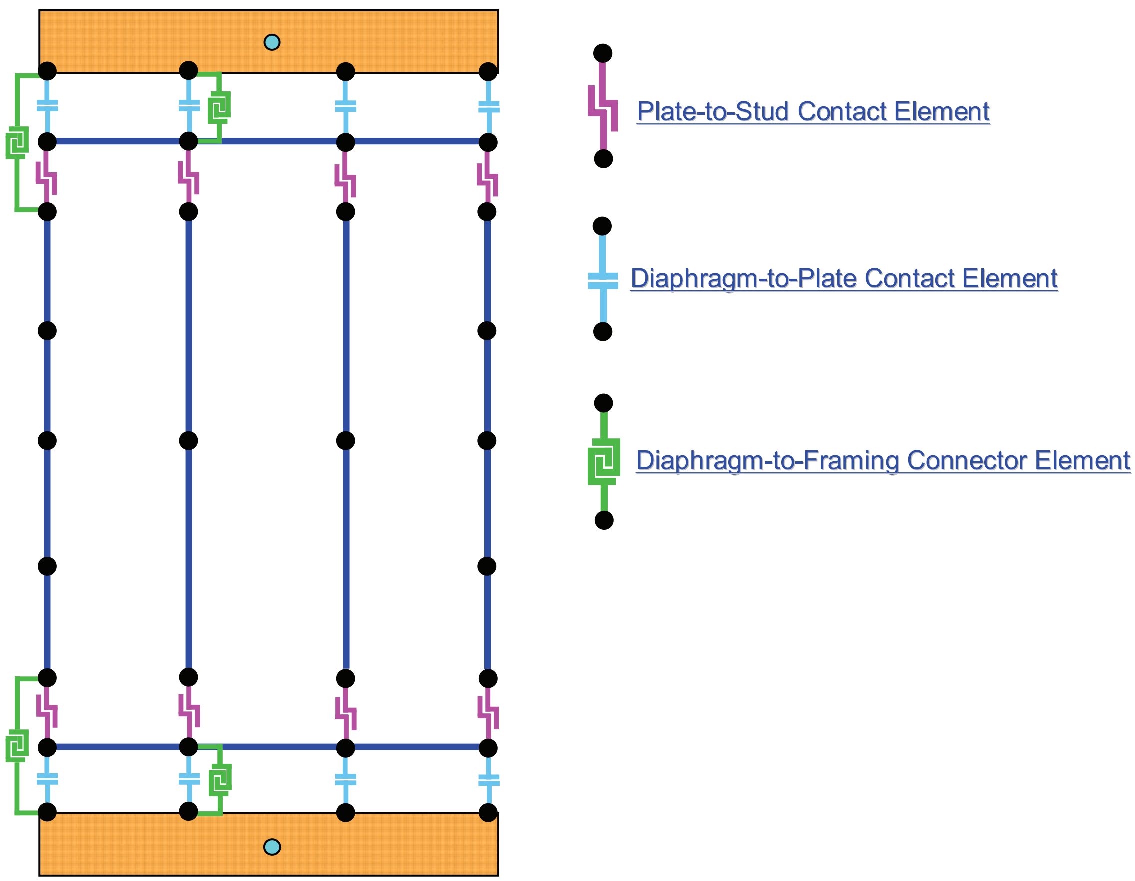

Figure 4.19 Detailed Numerical Model of the Framing Domain

In the initial configuration of a shear wall assembly, the contact area between the plates and studs or diaphragms is horizontal and provides high axial stiffness under bearing condition; that is compressive forces normal to the contact area. Thus, under service loads, a shear wall assembly within a light-frame wood house is subjected to vertical gravitational loads that are transferred to the ground through the framing members of the structure under minimal vertical deformations. In this state of equilibrium, the internal forces in plate-to-stud framing connectors and any anchoring equipment are practically very small, since the vertical load paths are established through the framing domain under contact conditions. Therefore, in a general sense, the assumption of no sliding response is based on the assumption that under gravitational loads the global static friction force along the boundaries of the independent group of components is higher that the lateral strength of the shear wall assembly.

Conveniently, under this assumption the response of the plate-to-stud framing connectors and anchoring equipment need to be defined only along vertical tensile deformations. The tensile strength of the plate-to-stud framing connectors (nail withdrawal) is typically small, so these components can be conservatively neglected. Thus, the location and the response of anchoring equipment in vertical tension will define alone the resistance of the shear wall assembly to overturning, shear-induced loads.

If horizontal blocking is provided, the framing members are meshed with 2-noded beam elements that are pin-connected to the continuous vertical studs. This entails that no separation is accounted between individual members within the internal framing component group. This assumption is valid when analyzing typical segmented shear walls that consist of a number of full height panels positioned horizontally to form a fully-sheathed shear wall segment. Conceptually, separation between any intersecting internal framing members can be considered with the same approach; that is assigning different nodes for each component at the interaction surface and using appropriate 2-noded connector elements to describe the response at the interface. However, it can be claimed that horizontal separation between internal framing members will be minimal in the global wall level since the shear wall is not subjected to extensional horizontal deformations. On the contrary, the shear wall is subjected to bending and lateral loads transferred from the floor diaphragms, which may induce extensional vertical deformations at the global wall level when a rocking motion is involved. In this sense, the consideration of separation of the framing members solely at the stud-to-plate connections is justified, since the major component of the extensional vertical deformations in the framing will be concentrated right at this location in the form of framing separation.

4.3.3.1 Kinematics and Equilibrium Equations of a Beam Element

Kinematics of a Beam Element

A 2-noded beam element has 3 internal DOF $\mathbf{u_B}$; one axial elongation u_b and two node rotations φ_1 and φ_2, which are defined with respect to an element Local Cartesian System (LCS) $\xi O \eta$ that has the ξ axis crossing through the two nodes of the element. Figure 4.20 illustrates the initial and deformed configurations of a beam element. The element displacement vector $\mathbf{D_B}$ consists of the global translations and rotations, u_1, v_1 and θ_1, and u_2, v_2 and θ_2, of the two nodes and is defined as:

$$\mathbf{D_B} = \{u_1 \quad v_1 \quad \theta_1 \quad u_2 \quad v_2 \quad \theta_2\}^T \tag{4.92}$$

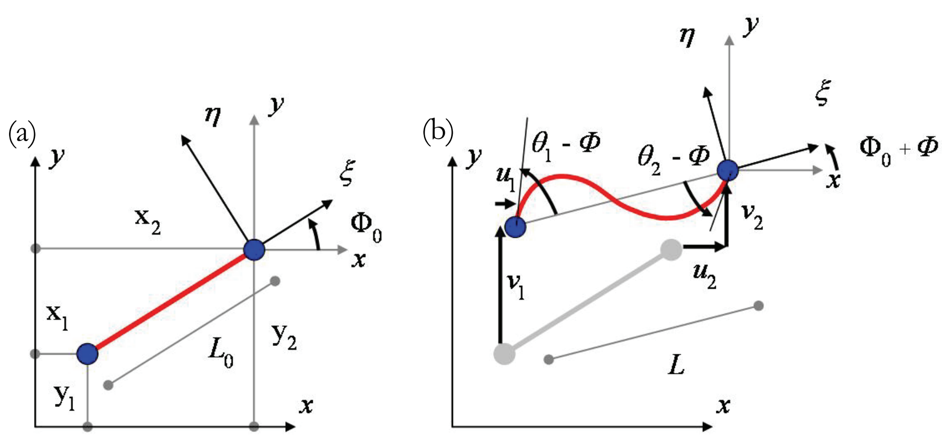

Figure 4.20 (a) Initial and (b) Deformed Configuration of a Beam Element

The initial length L_0 of the beam element is given by:

$$L_0 = \left| \begin{Bmatrix} x_2 - x_1 \\ y_2 - y_1 \end{Bmatrix} \right| = \sqrt{(x_2 - x_1)^2 + (y_2 - y_1)^2} \tag{4.93}$$

where x_1, x_2, y_1 and y_2 are the initial global coordinates of the two nodes of the element. The initial angle Φ_0 of the beam element is computed as:

$$\Phi_0 = \begin{cases} (\pi/2)\cdot \mathrm{sgn}(y_2 - y_1) & , \; if \;\; x_2 - x_1 = 0 \\ \arctan\left((y_2 - y_1)/(x_2 - x_1)\right) & , \; if \;\; x_2 - x_1 > 0 \\ \arctan\left((y_2 - y_1)/(x_2 - x_1)\right) + \pi, & if \;\; x_2 - x_1 < 0 \end{cases} \tag{4.94}$$

where sgn has been defined in (4.34). The actual length L in the deformed configuration is given by:

$$L = \left| \begin{Bmatrix} x_2 + u_2 - x_1 - u_1 \\ y_2 + v_2 - y_1 - v_1 \end{Bmatrix} \right| = \sqrt{\left(x_2 + u_2 - x_1 - u_1\right)^2 + \left(y_2 + v_2 - y_1 - v_1\right)^2} \Rightarrow$$

$$L = \sqrt{L_x^{\,2} + L_y^{\,2}} = \sqrt{L_S} \tag{4.95}$$

The element internal deformations can be computed as:

$$\begin{aligned} u_b &= L - \mathrm{L}_0 \\ \varphi_1 &= \theta_1 - \Phi \\ \varphi_2 &= \theta_2 - \Phi \end{aligned} \tag{4.96}$$

where Φ corresponds to the rotation of the reference frame, as shown in Figure 4.20b, and can be computed as:

$$\Phi = \arcsin\left(\frac{\left(x_2 - x_1\right)\cdot\left(v_2 - v_1\right) - \left(y_2 - y_1\right)\cdot\left(u_2 - u_1\right)}{L \cdot \mathrm{L}_0} \right) \tag{4.97}$$

$$\left\{ \begin{array}{ll} \sin\Phi = \sin\left(\Phi_T - \Phi_0\right) = \sin\Phi_T \cdot \cos\Phi_0 - \cos\Phi_T \cdot \sin\Phi_0 & \\ \sin\Phi_T = \dfrac{y_2 + v_2 - y_1 - v_1}{L} \ , & \cos\Phi_T = \dfrac{x_2 + u_2 - x_1 - u_1}{L} \\ \sin\Phi_0 = \dfrac{y_2 - y_1}{\mathrm{L}_0} \ , & \cos\Phi_0 = \dfrac{x_2 - x_1}{\mathrm{L}_0} \end{array} \right\} \tag{4.98}$$

where $\Phi_T = \Phi_0 + \Phi$. Using the exact analytical expression of the internal deformation, a virtual displacement field $\delta\mathbf{u_B}$ can be computed for a given element virtual displacement $\delta\mathbf{D_B}$.

$$\delta\mathbf{u_B} = \begin{bmatrix} \dfrac{\partial u_b}{\partial u_1} & \dfrac{\partial u_b}{\partial v_1} & \dfrac{\partial u_b}{\partial \theta_1} & \dfrac{\partial u_b}{\partial u_2} & \dfrac{\partial u_b}{\partial v_2} & \dfrac{\partial u_b}{\partial \theta_2} \\ \dfrac{\partial \varphi_1}{\partial u_1} & \dfrac{\partial \varphi_1}{\partial v_1} & \dfrac{\partial \varphi_1}{\partial \theta_1} & \dfrac{\partial \varphi_1}{\partial u_2} & \dfrac{\partial \varphi_1}{\partial v_2} & \dfrac{\partial \varphi_1}{\partial \theta_2} \\ \dfrac{\partial \varphi_2}{\partial u_1} & \dfrac{\partial \varphi_2}{\partial v_1} & \dfrac{\partial \varphi_2}{\partial \theta_1} & \dfrac{\partial \varphi_2}{\partial u_2} & \dfrac{\partial \varphi_2}{\partial v_2} & \dfrac{\partial \varphi_2}{\partial \theta_2} \end{bmatrix} \cdot \delta\mathbf{D_B} \Rightarrow$$

$$\delta\mathbf{u_B} = \begin{bmatrix} -\cos\Phi_T & -\sin\Phi_T & 0 & \cos\Phi_T & \sin\Phi_T & 0 \\ -\sin\Phi_T / L & \cos\Phi_T / L & 1 & \sin\Phi_T / L & -\cos\Phi_T / L & 0 \\ -\sin\Phi_T / L & \cos\Phi_T / L & 0 & \sin\Phi_T / L & -\cos\Phi_T / L & 1 \end{bmatrix} \cdot \delta\mathbf{D_B} \Rightarrow$$

$$\delta\mathbf{u_B} = \mathbf{B_B}\left(\mathbf{D_B}\right) \cdot \delta\mathbf{D_B} \tag{4.99}$$

The first row of $\mathbf{B_B}$ is identical to $\mathbf{B_T}$ computed for the truss element in (4.37). The partial derivatives of the internal rotations φ_1 and φ_2 are computed similarly to the derivations shown in (4.55) and (4.56) for the kinematics of the rigid framing members. $\mathbf{B_B}$ can also be expressed as the product of two matrices, as shown below:

$$\mathbf{B_B} = \begin{bmatrix} -1 & 0 & 0 & 1 & 0 & 0 \\ 0 & 1/L & 1 & 0 & -1/L & 0 \\ 0 & 1/L & 0 & 0 & -1/L & 1 \end{bmatrix} \cdot \begin{bmatrix} \cos\Phi_T & \sin\Phi_T & 0 & & & \\ -\sin\Phi_T & \cos\Phi_T & 0 & & \mathbf{0} & \\ 0 & 0 & 1 & & & \\ & & & \cos\Phi_T & \sin\Phi_T & 0 \\ & \mathbf{0} & & -\sin\Phi_T & \cos\Phi_T & 0 \\ & & & 0 & 0 & 1 \end{bmatrix} \tag{4.100}$$

Equilibrium Equations of a Beam Element

Figure 4.21 illustrates a free body diagram of a beam element. The element force vector $\mathbf{F_B}$ consists of the global forces and moments, p_1, q_1 and m_1, and p_2, q_2 and m_2, of the two nodes and is defined as:

$$\mathbf{F_B} = \left\{ p_1 \quad q_1 \quad m_1 \quad p_2 \quad q_2 \quad m_2 \right\}^{\mathrm{T}} \tag{4.101}$$

The internal force vector is $\mathbf{p_B} = \{p_b\ \tau_1\ \tau_2\}^T$. The equilibrium equations are computed from the principle of virtual work. Under a virtual displacement field $\delta\mathbf{D_B}$, the internal and external virtual work is equal.

$$\delta W_{ext} = \delta W_{int} \Rightarrow$$

$$\delta\mathbf{D_B}^T \cdot \mathbf{F_B} = \delta\mathbf{u_B}^T \cdot \mathbf{p_B} \Rightarrow$$

$$\delta\mathbf{D_B}^T \cdot \mathbf{F_B} = \delta\mathbf{D_B}^T \cdot \mathbf{B_B}^T \cdot \mathbf{p_B} \Rightarrow$$

$$\mathbf{F_B} = \mathbf{B_B}^T \cdot \mathbf{p_B} \tag{4.102}$$

where $\mathbf{p_B}$ is equal to:

$$\begin{Bmatrix} p_b \\ \tau_1 \\ \tau_2 \end{Bmatrix} = \begin{bmatrix} EA/L_0 & 0 & 0 \\ 0 & 4 \cdot EI/L_0 & 2 \cdot EI/L_0 \\ 0 & 2 \cdot EI/L_0 & 4 \cdot EI/L_0 \end{bmatrix} \cdot \begin{Bmatrix} u_b \\ \varphi_1 \\ \varphi_2 \end{Bmatrix} \Rightarrow$$

$$\mathbf{p_B} = \mathbf{k_B} \cdot \mathbf{u_B} \tag{4.103}$$

where *E, A* and *I* are the elastic modulus, cross-section area and moment of inertia of the beam element with respect to in-plane bending. Note that $\mathbf{k_B}$ is constant since it is based on small deformation theory.

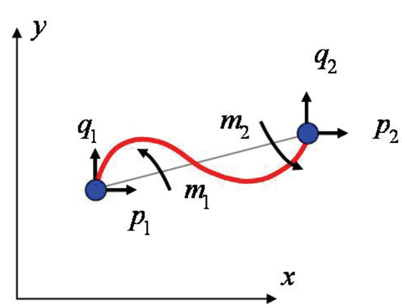

Figure 4.21 Free Body Diagram of a Beam Element

The tangent stiffness matrix of the beam element is computed from the variation of the element force vector with respect to the element displacement vector

$$\mathbf{K_B} = \frac{\partial \mathbf{F_B}}{\partial \mathbf{D_B}} = \frac{\partial\left(\mathbf{B_B}^{\mathrm{T}} \cdot \mathbf{p_B}\right)}{\partial \mathbf{D_B}} = \mathbf{B_B}^{\mathrm{T}} \cdot \frac{\partial \mathbf{p_B}}{\partial \mathbf{u_B}} \cdot \frac{\partial \mathbf{u_B}}{\partial \mathbf{D_B}} + \frac{\partial\left(\mathbf{B_B}^{\mathrm{T}}\right)}{\partial \mathbf{D_B}} \cdot \mathbf{p_B} \Rightarrow$$

$$\mathbf{K_B} = \mathbf{K_{B1}} + \mathbf{K_{B2}} \tag{4.104}$$

The stiffness matrices shown in (4.104) are calculated as:

$$\mathbf{K_{B1}} = \mathbf{B_B}^{\mathrm{T}} \cdot \frac{\partial \mathbf{p_B}}{\partial \mathbf{u_B}} \cdot \frac{\partial \mathbf{u_B}}{\partial \mathbf{D_B}} = \mathbf{B_B}^{\mathrm{T}} \cdot \mathbf{k_B} \cdot \mathbf{B_B} \tag{4.105}$$

$$\mathbf{K_{B2}} = \frac{\partial\left(\mathbf{B_B}^{\mathrm{T}}\right)}{\partial \mathbf{D_B}} \cdot \mathbf{p_B} = \mathbf{K_{B2}^1} + \mathbf{K_{B2}^2} \tag{4.106}$$

$$\mathbf{K_{B2}^1} = \frac{p_b}{L} \cdot \begin{bmatrix} \sin^2 \Phi_T & -\cos\Phi_T \cdot \sin\Phi_T & 0 & -\sin^2 \Phi_T & \cos\Phi_T \cdot \sin\Phi_T & 0 \\ & \cos^2 \Phi_T & 0 & \cos\Phi_T \cdot \sin\Phi_T & -\cos^2 \Phi_T & 0 \\ & & 0 & 0 & 0 & 0 \\ & & & \sin^2 \Phi_T & -\cos\Phi_T \cdot \sin\Phi_T & 0 \\ & sym & & & \cos^2 \Phi_T & 0 \\ & & & & & 0 \end{bmatrix}$$

(4.107)

$$\mathbf{K_{B2}^2} = \frac{\tau_1 + \tau_2}{L^2} \cdot \begin{bmatrix} -\sin(2\cdot\Phi_T) & \cos(2\cdot\Phi_T) & 0 & \sin(2\cdot\Phi_T) & -\cos(2\cdot\Phi_T) & 0 \\ & \sin(2\cdot\Phi_T) & 0 & -\cos(2\cdot\Phi_T) & -\sin(2\cdot\Phi_T) & 0 \\ & & 0 & 0 & 0 & 0 \\ & & & -\sin(2\cdot\Phi_T) & \cos(2\cdot\Phi_T) & 0 \\ & sym & & & \sin(2\cdot\Phi_T) & 0 \\ & & & & & 0 \end{bmatrix}$$

(4.108)

Stiffness matrix $\mathbf{K_{B2}}$ includes higher order effects and is usually neglected, since it does not improve significantly the convergence rate and requires additional calculations.

4.3.3.2 Kinematics and Equilibrium Equations of a Plate-to-Stud Contact Element

Kinematics of a Plate-to-Stud Contact Element

A plate-to-stud contact element is defined as a 2-noded connector that effectively simulates contact and separation of the two nodes in the normal to the contact area direction, while transferring forces parallel to the contact area with no sliding response. The derivations are based on the two-dimensional contact interaction between a point (contact body) and a straight line (target body). Figure 4.22 illustrates the kinematics of a stud-to-plate contact element. The motion of the point is described through the translational DOF of the respective node, u_2 and v_2, defined at the tip of a vertical stud. The motion of the center point of the line is defined through the 3 DOF of the respective node, u_1, v_1 and θ_1, defined at the horizontal plate at the plate-to-stud connection. The kinematic and equilibrium equations are essentially identical to the sheathing-to-framing connector element, described in Section 4.3.2.1. The element displacement vector $\mathbf{D_C}$ is defined as:

$$\mathbf{D_C} = \{u_1 \quad v_1 \quad \theta_1 \quad u_2 \quad v_2\}^{\mathrm{T}} \tag{4.109}$$

A plate-to-stud contact element has 2 orthogonal internal DOF, u_c and v_c, which are defined with respect to an element Local Cartesian System (LCS) $\xi O \eta$ which rotates with the target body. The η axis is always normal to the target surface and positive values represent separation of the two bodies.

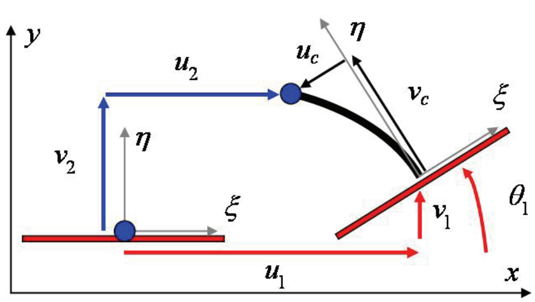

Figure 4.22 Kinematics of a Stud-to-Plate Contact Element

Based on the initial and deformed configuration, the internal displacements are computed as:

$$\begin{Bmatrix} u_c \\ v_c \end{Bmatrix} = \begin{Bmatrix} \cos(\theta_1)\cdot(u_2 - u_1) + \sin(\theta_1)\cdot(v_2 - v_1) \\ \eta_c \cdot\left(-\sin(\theta_1)\cdot(u_2 - u_1) + \cos(\theta_1)\cdot(v_2 - v_1)\right) \end{Bmatrix} \Rightarrow$$

$$\begin{Bmatrix} u_c \\ v_c \end{Bmatrix} = \begin{bmatrix} 1 & 0 \\ 0 & \eta_c \end{bmatrix} \cdot \begin{bmatrix} \cos(\theta_1) & \sin(\theta_1) \\ -\sin(\theta_1) & \cos(\theta_1) \end{bmatrix} \cdot \begin{bmatrix} -1 & 0 & 0 & 1 & 0 \\ 0 & -1 & 0 & 0 & 1 \end{bmatrix} \cdot \mathbf{D_C} \Rightarrow \tag{4.110}$$

where

$$\begin{aligned} \eta_c &= 1, \text{ for a sill-plate-to-stud connector} \\ \eta_c &= -1, \text{ for a top-plate-to-stud connector} \end{aligned} \tag{4.111}$$

Using the exact analytical expression of the internal deformations, a virtual displacement field $\delta\mathbf{u_C}$ can be computed for a given element virtual displacement $\delta\mathbf{D_C}$.

$$\delta\mathbf{u_C} = \begin{bmatrix} \dfrac{\partial u_c}{\partial u_1} & \dfrac{\partial u_c}{\partial v_1} & \dfrac{\partial u_c}{\partial \theta_1} & \dfrac{\partial u_c}{\partial u_2} & \dfrac{\partial u_c}{\partial v_2} \\ \dfrac{\partial v_c}{\partial u_1} & \dfrac{\partial v_c}{\partial v_1} & \dfrac{\partial v_c}{\partial \theta_1} & \dfrac{\partial v_c}{\partial u_2} & \dfrac{\partial v_c}{\partial v_2} \end{bmatrix} \cdot \delta\mathbf{D_C} \Rightarrow$$

$$\delta\mathbf{u_C} = \begin{bmatrix} -\cos(\theta_1) & -\sin(\theta_1) & v_c/\eta_c & \cos(\theta_1) & \sin(\theta_1) \\ \eta_c\cdot\sin(\theta_1) & -\eta_c\cdot\cos(\theta_1) & -u_c\cdot\eta_c & -\eta_c\cdot\sin(\theta_1) & \eta_c\cdot\cos(\theta_1) \end{bmatrix} \cdot \delta\mathbf{D_C} \Rightarrow$$

$$\delta\mathbf{u_C} = \mathbf{B_C}\left(\mathbf{D_C}\right)\cdot\delta\mathbf{D_C} \tag{4.112}$$

Constitutive Model of a Plate-to-Stud Contact Element

The constitutive model developed for the plate-to-stud contact element yields the contact forces $\mathbf{p_C} = \{p_c\ q_c\}^T$, as a function of the internal displacements $\mathbf{u_C}$. The forces are uncoupled since, as mentioned earlier, sliding response is not considered.

The response in the normal direction has been historically described with a linear spring that exhibits different stiffness in the positive and negative direction. Along the positive direction the stiffness is very low and simulates the separation of the bodies, while along the negative direction the stiffness is very high and simulates the bearing/contact of the bodies. The use of this constitutive model requires the selection of appropriate stiffness values to establish a satisfying level of accuracy in the numerical analysis. The accuracy can be directly related to the error in the penetration displacement for a given compressive force, as well as the error in the tensile force for a given tensile displacement. Since the use of constant stiffness offers no upper bounds on both the maximum penetration displacement and the maximum tensile force, appropriate – in terms of accuracy – stiffness values often leads to a great differential change of stiffness, which is concentrated at a single displacement point, the origin. This large difference in the stiffness is likely to cause numerical difficulties in the solution procedure leading to low convergence rates and increased probability of no convergence for a constant convergence criterion.

Building on the discussion provided above, the constitutive model proposed herein effectively simulates absolute contact conditions related to minimal penetration under compressive forces and minimal resistance under extensional displacements. Figure 4.23 illustrates the force-displacement response of the contact spring along the normal direction, while (4.113) shows the nonlinear mathematical formulation. The parameters d_{tol} and f_{tol} in (4.113) are positive real values that are selected as such to be small enough to be considered close to zero, as shown in (4.114).

$$q_c = \begin{cases} f_{tol} \cdot \left(1 - \dfrac{d_{tol}}{v_c + d_{tol}} \right) & , v_c \ \geq \ -0.99 \cdot d_{tol} \\ -99 \cdot f_{tol} + 10e04 \cdot \dfrac{f_{tol}}{d_{tol}} \cdot \left(v_c - 0.99 \cdot d_{tol} \right) & , v_c \ < \ -0.99 \cdot d_{tol} \end{cases} \tag{4.113}$$

$$\left(\left(d_{tol}, f_{tol} \right) > 0 \right) \cup \left(\left(d_{tol}, f_{tol} \right) \ \approx \ 0 \right) \tag{4.114}$$

The characteristics of the response shown in Figure 4.23 are favorably suited for the numerical simulation of contact/separation phenomena under quasi-static conditions. The tensile force is bounded by f_{tol} while the penetration is not exactly but nearly bounded by d_{tol}. The change of stiffness is nonlinearly distributed along the displacement range resulting in a smooth force-displacement response. As a result, the solution can be achieved with very good convergence rates, which are not very sensitive to the user parameters d_{tol} and f_{tol}.

The tangent stiffness in the normal direction k_{cv} is equal to:

$$k_{cv} = \begin{cases} \dfrac{f_{tol} \cdot d_{tol}}{\left(v_c + d_{tol}\right)^2} &, v_c \geq \text{-0.99} \cdot d_{tol} \\ 10\text{e}04 \cdot \dfrac{f_{tol}}{d_{tol}} &, v_c < \text{-0.99} \cdot d_{tol} \end{cases} \tag{4.115}$$

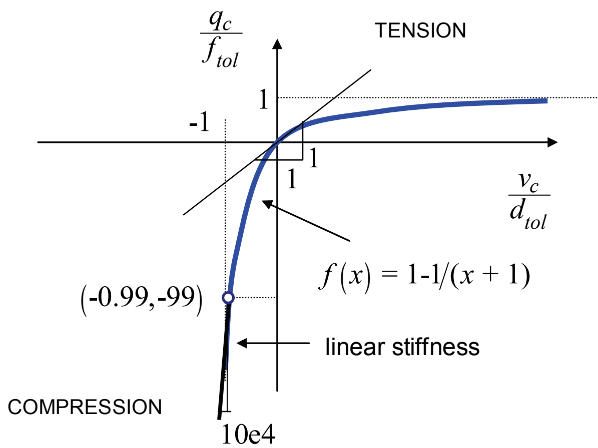

Figure 4.23 Force-Displacement Response of a Stud-to-Plate Contact Element along the Normal Direction

The response in the direction parallel to the contact area can be described with a linear spring with high axial stiffness, since no sliding is permitted. Again, the use of very high stiffness causes numerical difficulties in the solution procedure and in such cases it is typically more convenient to use constraint equations – through the use of Lagrange multipliers – that yield no differential displacement by directly imposing the displacement constraint. However, this approach is not applicable in this case because the orientation of the contact area is not known a priori, rather depends on the rotation of the target body. To overcome any numerical difficulties associated with the use of stiff linear springs to represent rigid behavior – this approach is known as penalty method – the model presented previously for the response along the normal direction is slightly modified to yield favorable response characteristics for numerical analysis of rigid connections.

Figure 4.24 illustrates the force-displacement response of the contact spring along the parallel direction, while (4.116) shows the nonlinear mathematical formulation. The parameters d_{tol} and f_{tol} are defined as previously and could potentially be the same. As shown in Figure 4.24, the initial stiffness, defined as the ratio between f_{tol} and d_{tol}, need not be significantly high while differential displacements are bounded within acceptable margins, because of the hardening of the response.

$$p_c = \begin{Bmatrix} -\operatorname{sgn}(u_c)\cdot f_{tol}\cdot\left(1+\dfrac{d_{tol}}{|u_c| - d_{tol}}\right) & , |u_c| \le 0.99\cdot d_{tol} \\ \operatorname{sgn}(u_c)\cdot\left(99\cdot f_{tol} + 10e04\cdot\dfrac{f_{tol}}{d_{tol}}\cdot\left(|u_c| - 0.99\cdot d_{tol}\right)\right) & , |u_c| > 0.99\cdot d_{tol} \end{Bmatrix} \tag{4.116}$$

where sgn has been defined in (4.34).

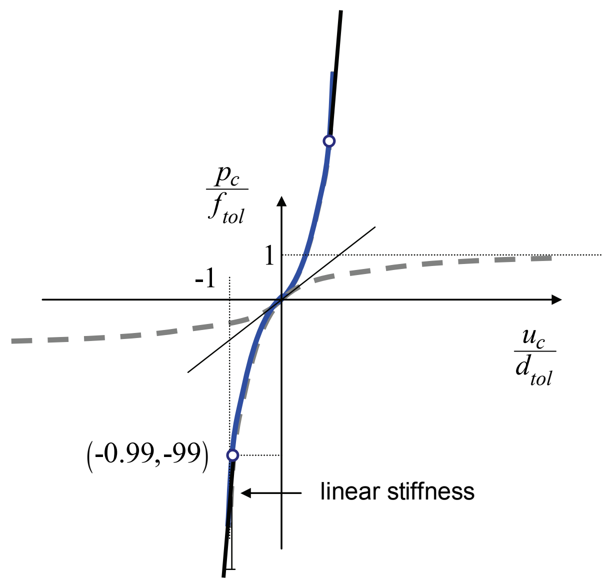

Figure 4.24 Force-Displacement Response of a Stud-to-Plate Contact Element along the Parallel Direction

The tangent stiffness in the parallel direction k_{cu} is equal to:

$$k_{cu} = \begin{Bmatrix} \dfrac{f_{tol}\cdot d_{tol}}{\left(|u_c| - d_{tol}\right)^2} & , |u_c| \le 0.99\cdot d_{tol} \\ 10e04\cdot\dfrac{f_{tol}}{d_{tol}} & , |u_c| > 0.99\cdot d_{tol} \end{Bmatrix} \tag{4.117}$$

Equilibrium Equations of a Plate-to-Stud Contact Element

Figure 4.25 illustrates a free body diagram of a plate-to-stud contact element. The element force vector $\mathbf{F_C}$ consists of the global forces at the two nodes and the moment at the framing node and is defined as:

$$\mathbf{F_C} = \{p_1 \quad q_1 \quad m_1 \quad p_2 \quad q_2\}^{\mathrm{T}} \tag{4.118}$$

The equilibrium equations are computed from the principle of virtual work. Under a virtual displacement field $\delta\mathbf{D_C}$, the internal and external virtual work is equal.

$$\delta \mathrm{W}_{\mathrm{ext}} = \delta \mathrm{W}_{\mathrm{int}} \Rightarrow$$

$$\delta\mathbf{D_C}^{\mathrm{T}} \cdot \mathbf{F_C} = \delta\mathbf{u_C}^{\mathrm{T}} \cdot \begin{Bmatrix} p_c \\ q_c \end{Bmatrix} \Rightarrow$$

$$\delta\mathbf{D_C}^{\mathrm{T}} \cdot \mathbf{F_C} = \delta\mathbf{D_C}^{\mathrm{T}} \cdot \mathbf{B_C}^{\mathrm{T}} \cdot \begin{Bmatrix} p_c \\ q_c \end{Bmatrix} \Rightarrow$$

$$\mathbf{F_C} = \mathbf{B_C}^{\mathrm{T}} \cdot \mathbf{p_C} \tag{4.119}$$

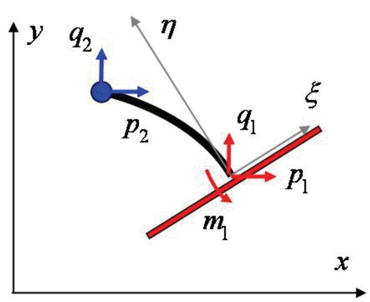

Figure 4.25 Free Body Diagram of a Stud-to-Plate Contact Element

The tangent stiffness matrix of the connector element is computed from the variation of the element force vector with respect to the element displacement vector

$$\mathbf{K_C} = \frac{\partial \mathbf{F_C}}{\partial \mathbf{D_C}} = \frac{\partial\left(\mathbf{B_C}^{\mathrm{T}} \cdot \mathbf{p_C}\right)}{\partial \mathbf{D_C}} = \mathbf{B_C}^{\mathrm{T}} \cdot \frac{\partial \mathbf{p_C}}{\partial \mathbf{u_C}} \cdot \frac{\partial \mathbf{u_C}}{\partial \mathbf{D_C}} + \frac{\partial\left(\mathbf{B_C}^{\mathrm{T}}\right)}{\partial \mathbf{D_C}} \cdot \mathbf{p_C} \Rightarrow$$

$$\mathbf{K_C} = \mathbf{K_{C1}} + \mathbf{K_{C2}} \tag{4.120}$$

The stiffness matrices shown in (4.120) are calculated as:

$$\mathbf{K_{C1}} = \mathbf{B_C}^{\mathrm{T}} \cdot \frac{\partial \mathbf{p_C}}{\partial \mathbf{u_C}} \cdot \frac{\partial \mathbf{u_C}}{\partial \mathbf{D_C}} = \mathbf{B_C}^{\mathrm{T}} \cdot \begin{bmatrix} k_{cu} & 0 \\ 0 & k_{cv} \end{bmatrix} \cdot \mathbf{B_C} = \mathbf{B_C}^{\mathrm{T}} \cdot \mathbf{k_C} \cdot \mathbf{B_C} \tag{4.121}$$

$$\mathbf{K_{C2}} = \frac{\partial\left(\mathbf{B_C}^{\mathrm{T}}\right)}{\partial \mathbf{D_C}} \cdot \mathbf{p_C} = \begin{bmatrix} 0 & 0 & q_2 & 0 & 0 \\ & 0 & -p_2 & 0 & 0 \\ & & -p_2 \cdot (u_2 - u_1) - q_2 \cdot (v_2 - v_1) & -q_2 & p_2 \\ & sym & & 0 & 0 \\ & & & & 0 \end{bmatrix} \tag{4.122}$$

Stiffness matrix $\mathbf{K_{C2}}$ includes higher order effects and is usually neglected, since it does not improve significantly the convergence rate and requires additional calculations.

4.3.3.3 Kinematics and Equilibrium Equations of a Diaphragm-to-Plate Contact Element

Introduction

Diaphragm-to-plate contact elements are developed to simulate a beam on a rigid foundation. Analogous to the previous descriptions, in this case each node of the horizontal sill or top plate represents a contact body, while each diaphragm represents a target body. This ensures that penetration criteria will be satisfied at the nodes but not necessarily along the internal length of each beam element. However, the framing members are typically meshed with a fine grid due to the location of evenly spaced nodes at the sheathing-to-framing connectors. Nodes also exist at any intersection with the vertical studs. So, the beam is subjected to concentrated forces and moments at the nodes and satisfying the penetration criteria at all the nodes with a fine mesh results in very small penetration error along the internal length of the beam elements. Sliding motion is not permitted parallel to the diaphragm but the beam can detach in the direction normal to the diaphragm. So, unlike plate-to-stud contact elements, diaphragm-to-plate contact elements assigned for example at the sill plate boundary of the shear wall assembly will feature different and distinct contact bodies but a single common target body, the rigid diaphragm.

Kinematics of a Diaphragm-to-Plate Contact Element

Figure 4.26 illustrates the kinematics of a diaphragm-to-plate contact element. The element displacement vector $\mathbf{D_{DC}}$ is defined as:

$$\mathbf{D_{DC}} = \{U_1 \quad V_1 \quad \Theta_1 \quad u_2 \quad v_2\}^{\mathrm{T}} \tag{4.123}$$

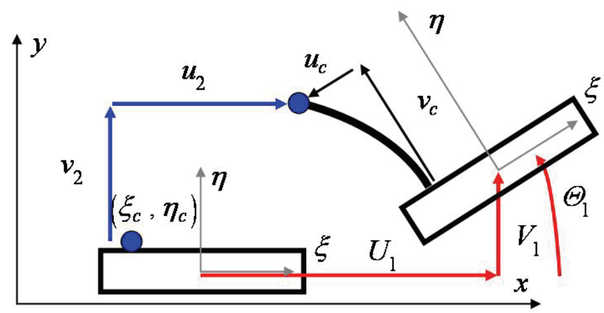

Figure 4.26 Kinematics of a Diaphragm-to-Plate Contact Element

The internal deformations $\mathbf{u_C} = \{u_c \; v_c\}^{\mathrm{T}}$ can be computed as shown for a plate-to-stud contact element in (4.110) by expressing the point DOF $\{u_1 \; v_1 \; \theta_1\}^{\mathrm{T}}$ with respect to the diaphragm displacements DOF $\{U_1 \; V_1 \; \Theta_1\}^{\mathrm{T}}$:

$$\begin{Bmatrix} u_1 \\ v_1 \\ \theta_1 \end{Bmatrix} = \begin{Bmatrix} \begin{Bmatrix} U_1 \\ V_1 \end{Bmatrix} + \left(\mathbf{\Lambda}(\Theta_1)^{\mathbf{T}} - \begin{bmatrix} 1 & 0 \\ 0 & 1 \end{bmatrix} \right) \cdot \begin{Bmatrix} \xi_c \\ \eta_c \end{Bmatrix} \\ \Theta_1 \end{Bmatrix} \tag{4.124}$$

where ξ_c and η_c are the initial point coordinates with respect to the center of the diaphragm. A virtual displacement field $\delta\mathbf{u_C}$ can be computed for a given element virtual field $\delta\mathbf{D_{DC}}$ as:

$$\delta\mathbf{u_C} = \frac{\partial \mathbf{u_C}}{\partial \mathbf{D_{DC}}} \cdot \delta\mathbf{D_{DC}} = \frac{\partial \mathbf{u_C}}{\partial \mathbf{D_C}} \cdot \frac{\partial \mathbf{D_C}}{\partial \mathbf{D_{DC}}} \cdot \delta\mathbf{D_{DC}} \Rightarrow$$

$$\delta\mathbf{u_C} = \mathbf{B_C} \cdot \begin{bmatrix} 1 & 0 & -\eta_c^{\Theta} & 0 & 0 \\ 0 & 1 & \xi_c^{\Theta} & 0 & 0 \\ 0 & 0 & 1 & 0 & 0 \\ 0 & 0 & 0 & 1 & 0 \\ 0 & 0 & 0 & 0 & 1 \end{bmatrix} \cdot \delta\mathbf{D_{DC}} = \mathbf{B_C} \cdot \mathbf{B_D} \cdot \delta\mathbf{D_{DC}} \Rightarrow$$

$$\delta \mathbf{u_C} = \mathbf{B_{DC}}\left(\mathbf{D_{DC}}\right) \cdot \delta \mathbf{D_{DC}} \tag{4.125}$$

where $\mathbf{B_C}$ is computed in (4.112) after substituting the variables as shown in (4.124). Furthermore, ξ_c^{Θ} and η_c^{Θ} are the coordinates of the point on the diaphragm at the actual deformed configuration, computed as:

$$\begin{Bmatrix} \xi_c^{\Theta} \\ \eta_c^{\Theta} \end{Bmatrix} = \mathbf{\Lambda}\left(\Theta_1\right)^{\mathbf{T}} \cdot \begin{Bmatrix} \xi_c \\ \eta_c \end{Bmatrix} \tag{4.126}$$

Constitutive Model of a Diaphragm-to-Plate Contact Element

The constitutive model in the direction normal to the contact area is the same as shown in (4.113) for the plate-to-stud contact element. The force-displacement response in the direction parallel to the contact area can be either linear or as shown earlier in (4.116).

Equilibrium Equations of a Diaphragm-to-Plate Contact Element

Figure 4.27 illustrates a free body diagram of a diaphragm-to-plate contact element. The element force vector $\mathbf{F_{DC}}$ consists of the global forces at the two nodes and the moment at the framing node and is defined as:

$$\mathbf{F_{DC}} = \left\{P_1 \quad Q_1 \quad M_1 \quad p_2 \quad q_2\right\}^{\mathrm{T}} \tag{4.127}$$

The equilibrium equations are computed from the principle of virtual work. Under a virtual displacement field $\delta\mathbf{D_{DC}}$, the internal and external virtual work is equal.

$$\delta \mathrm{W_{ext}} = \delta \mathrm{W_{int}} \Rightarrow$$

$$\delta \mathbf{D_{DC}}^{\mathrm{T}} \cdot \mathbf{F_{DC}} = \delta \mathbf{u_C}^{\mathrm{T}} \cdot \mathbf{p_C} \Rightarrow$$

$$\delta \mathbf{D_{DC}}^{\mathrm{T}} \cdot \mathbf{F_{DC}} = \delta \mathbf{D_{DC}}^{\mathrm{T}} \cdot \mathbf{B_{DC}}^{\mathrm{T}} \cdot \mathbf{p_C} \Rightarrow$$

$$\mathbf{F_{DC}} = \mathbf{B_{DC}}^{\mathrm{T}} \cdot \mathbf{p_C} = \mathbf{B_D}^{\mathrm{T}} \cdot \mathbf{B_C}^{\mathrm{T}} \cdot \mathbf{p_C} = \mathbf{B_D}^{\mathrm{T}} \cdot \mathbf{F_C} \tag{4.128}$$

where $\mathbf{p_C} = \{p_c\ q_c\}^{\mathrm{T}}$ is the internal force vector.

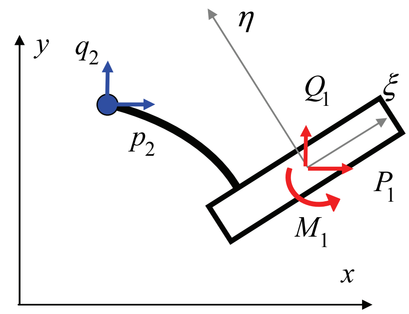

Figure 4.27 Free Body Diagram of a Diaphragm-to-Plate Contact Element

The tangent stiffness matrix of the element is computed from the variation of the element force vector with respect to the element displacement vector

$$\mathbf{K_{DC}} = \frac{\partial \mathbf{F_{DC}}}{\partial \mathbf{D_{DC}}} = \frac{\partial\left(\mathbf{B_D}^{\mathrm{T}} \cdot \mathbf{F_C}\right)}{\partial \mathbf{D_{DC}}} = \mathbf{B_D}^{\mathrm{T}} \cdot \frac{\partial \mathbf{F_C}}{\partial \mathbf{D_C}} \cdot \frac{\partial \mathbf{D_C}}{\partial \mathbf{D_{DC}}} + \frac{\partial\left(\mathbf{B_D}^{\mathrm{T}}\right)}{\partial \mathbf{D_{DC}}} \cdot \mathbf{F_C} \Rightarrow$$

$$\mathbf{K_{DC}} = \mathbf{K_{DC1}} + \mathbf{K_{DC2}} \tag{4.129}$$

The stiffness matrices shown in (4.129) are calculated as:

$$\mathbf{K_{DC1}} = \mathbf{B_D}^{\mathrm{T}} \cdot \frac{\partial \mathbf{F_C}}{\partial \mathbf{D_C}} \cdot \frac{\partial \mathbf{D_C}}{\partial \mathbf{D_{DC}}} = \mathbf{B_D}^{\mathrm{T}} \cdot \mathbf{K_C} \cdot \mathbf{B_D} \tag{4.130}$$

$$\mathbf{K_{DC2}} = \frac{\partial\left(\mathbf{B_D}^{\mathrm{T}}\right)}{\partial \mathbf{D_{DC}}} \cdot \mathbf{F_C} = \begin{bmatrix} 0 & 0 & 0 & 0 & 0 \\ & 0 & 0 & 0 & 0 \\ & & -p_2 \cdot \xi_c^{\Theta} - q_2 \cdot \eta_c^{\Theta} & 0 & 0 \\ & sym & & 0 & 0 \\ & & & & 0 \end{bmatrix} \tag{4.131}$$

Stiffness matrix $\mathbf{K_{DC2}}$ includes higher order effects and is usually neglected, since it does not improve significantly the convergence rate and requires additional calculations.

4.3.3.4 Kinematics and Equilibrium Equations of a Diaphragm-to-Framing Connector Element

The diaphragm-to-framing connector elements are developed to simulate anchoring equipment such as anchor bolts and holdowns. Such equipment is typically used at the base of the first-story of light-frame wood structures to provide a good level of lateral and overturning support. Since these elements connect diaphragms and nodes that belong either to the horizontal plates (anchor bolts) or to the tip of vertical studs (holdowns) the derivations involved are essentially identical to those described in Section 4.3.3.3 for diaphragm-to-plate contact elements. The force-displacement response in the direction parallel to the diaphragm can be either linear or as shown earlier in (4.116). The response normal to the diaphragm can be either elastic or nonlinear inelastic, using the phenomenological connector model developed for sheathing-to-framing connectors. Appendices A and B contain information on identified parameters used for a nonlinear response of anchoring equipment.

4.3.3.5 Global Equilibrium Equations and Global Stiffness Matrix of a Shear Wall Element Including Framing Deformations

The global equilibrium equations and the global tangent stiffness matrix of a shear wall element that includes framing deformations can be expressed based on the analytical derivations provided earlier in this section. If N_P is the total number of panels of the shear wall assembly and N_F is the total number of nodes defining the framing domain, the total number of global DOF N_{DOF} is equal to:

$$N_{DOF} = 6 + 3 \cdot N_F + 4 \cdot N_P \tag{4.132}$$

The incremental equilibrium equations can be written in matrix format as:

$$\delta \begin{Bmatrix} \mathbf{F_D} \\ \mathbf{F_F} \\ \mathbf{F_P} \end{Bmatrix} = \begin{bmatrix} \mathbf{K_{DD}} & \mathbf{K_{DF}} & \mathbf{K_{DP}} \\ \mathbf{K_{FD}} & \mathbf{K_{FF}} & \mathbf{K_{FP}} \\ \mathbf{K_{PD}} & \mathbf{K_{PF}} & \mathbf{K_{PP}} \end{bmatrix} \cdot \delta \begin{Bmatrix} \mathbf{D_D} \\ \mathbf{D_F} \\ \mathbf{D_P} \end{Bmatrix} \tag{4.133}$$

where the subscript "**D**" denotes the 6 DOF associated with the two diaphragms, the subscript "**F**" denotes the DOF associated with the framing domain, and the subscript "**P**" denotes the DOF associated with the panel elements. The global stiffness matrix $\mathbf{K_W}$ can be further decomposed in 4 components as:

$$\mathbf{K_W} = \mathbf{K_W^1} + \mathbf{K_W^2} + \mathbf{K_W^3} + \mathbf{K_W^4} \tag{4.134}$$

where each stiffness matrix represents cotributions from the different structural compoenents, as described in the following sections.

Stiffness Contributions from Sheathing-to-Framing Connector and Panel Elements

The stiffness contributions from the sheathing-to-framing connector and the panel elements are described as:

$$\mathbf{K}^{\mathbf{1}}_{\mathbf{W}} = \begin{bmatrix} \mathbf{0} & \mathbf{0} & \mathbf{0} \\ \mathbf{0} & \mathbf{K}^{\mathbf{1}}_{\mathbf{FF}} & \mathbf{K}^{\mathbf{1}}_{\mathbf{FP}} \\ \mathbf{0} & \mathbf{K}^{\mathbf{1}}_{\mathbf{PF}} & \mathbf{K}^{\mathbf{1}}_{\mathbf{PP}} \end{bmatrix} \tag{4.135}$$

where the individual stiffness matrices are shown for a single panel with *n* number of connectors. The panel element equilibrium matrices ${}^{i}\mathbf{B}_{\mathbf{P}}$ have been previously defined in (4.21):

$$\mathbf{K}^{\mathbf{1}}_{\mathbf{FP}} = \begin{bmatrix} {}^{1}\mathbf{K}^{\mathbf{FF}}_{\mathbf{S}} & \dots & \mathbf{0} & \dots & \mathbf{0} \\ \dots & \dots & \dots & \dots & \dots \\ \mathbf{0} & \dots & {}^{i}\mathbf{K}^{\mathbf{FF}}_{\mathbf{S}} & \dots & \mathbf{0} \\ \dots & \dots & \dots & \dots & \dots \\ \mathbf{0} & \dots & \mathbf{0} & \dots & {}^{n}\mathbf{K}^{\mathbf{FF}}_{\mathbf{S}} \end{bmatrix} \qquad \mathbf{K}^{\mathbf{1}}_{\mathbf{FP}} = \begin{bmatrix} {}^{1}\mathbf{K}^{\mathbf{FP}}_{\mathbf{S}} \cdot {}^{1}\mathbf{B}_{\mathbf{P}} \\ \dots\dots\dots\dots \\ {}^{i}\mathbf{K}^{\mathbf{FP}}_{\mathbf{S}} \cdot {}^{i}\mathbf{B}_{\mathbf{P}} \\ \dots\dots\dots\dots \\ {}^{n}\mathbf{K}^{\mathbf{FP}}_{\mathbf{S}} \cdot {}^{n}\mathbf{B}_{\mathbf{P}} \end{bmatrix}$$

$$\mathbf{K}^{\mathbf{1}}_{\mathbf{PF}} = \left(\mathbf{K}^{\mathbf{1}}_{\mathbf{FP}}\right)^{\mathbf{T}} \qquad \mathbf{K}^{\mathbf{1}}_{\mathbf{PP}} = \mathbf{K}_{\mathbf{P}} \tag{4.136}$$

where ${}^{i}\mathbf{K}_{\mathbf{S}}$ and $\mathbf{K}_{\mathbf{P}}$ have been given in (4.8) and (4.27), respectively.

Stiffness Contributions from Beam Elements

The stiffness contributions from the beam elements are described as:

$$\mathbf{K}^{\mathbf{2}}_{\mathbf{W}} = \begin{bmatrix} \mathbf{0} & \mathbf{0} & \mathbf{0} \\ \mathbf{0} & \mathbf{K}^{\mathbf{2}}_{\mathbf{FF}} & \mathbf{0} \\ \mathbf{0} & \mathbf{0} & \mathbf{0} \end{bmatrix} \tag{4.137}$$

where $\mathbf{K}^{\mathbf{2}}_{\mathbf{FF}}$ is the stiffness matrix that results from all the individual 6-by-6 beam element stiffness matrices and is built according to the connectivity of each beam element.

Stiffness Contributions from Plate-to-Stud Contact Elements

The stiffness contributions from the plate-to-stud contact elements are described as:

$$\mathbf{K}_{\mathbf{W}}^{3} = \begin{bmatrix} \mathbf{0} & \mathbf{0} & \mathbf{0} \\ \mathbf{0} & \mathbf{K}_{\mathbf{FF}}^{3} & \mathbf{0} \\ \mathbf{0} & \mathbf{0} & \mathbf{0} \end{bmatrix} \tag{4.138}$$

where $\mathbf{K}^{3}_{\mathbf{FF}}$ is the stiffness matrix that results from all the individual plate-to-stud contact elements which are connected to nodes of the framing domain.

Stiffness Contributions from Diaphragm-to-Stud Contact Elements and Diaphragm-to-Framing Connector Elements

The stiffness contributions from the diaphragm-to-plate contact elements and the diaphragm-to-framing connector elements are described as:

$$\mathbf{K}_{\mathbf{W}}^{4} = \begin{bmatrix} \mathbf{K}_{\mathbf{DD}}^{4} & \mathbf{K}_{\mathbf{DF}}^{4} & \mathbf{0} \\ \mathbf{K}_{\mathbf{FD}}^{4} & \mathbf{K}_{\mathbf{FF}}^{4} & \mathbf{0} \\ \mathbf{0} & \mathbf{0} & \mathbf{0} \end{bmatrix} \tag{4.139}$$

where $\mathbf{K}^{4}_{\mathbf{W}}$ is the stiffness matrix that results from all the individual contact and connector elements that connect the diaphragm with the framing nodes of the horizontal plates.

Global Stiffness Matrix of Shear Wall Element

The global stiffness matrix $\mathbf{K}_{\mathbf{W}}$ can now be written as:

$$\mathbf{K}_{\mathbf{W}} = \begin{bmatrix} \mathbf{K}_{\mathbf{DD}}^{4} & \mathbf{K}_{\mathbf{DF}}^{4} & \mathbf{0} \\ \mathbf{K}_{\mathbf{FD}}^{4} & \sum\limits_{\mathbf{i}=\mathbf{1}}^{\mathbf{4}} \mathbf{K}_{\mathbf{FF}}^{\mathbf{i}} & \mathbf{K}_{\mathbf{FP}}^{1} \\ \mathbf{0} & \mathbf{K}_{\mathbf{PF}}^{1} & \mathbf{K}_{\mathbf{PP}}^{1} \end{bmatrix} \tag{4.140}$$

The final 6-by-6 global stiffness matrix of the shear wall element is computed by static condensation of the DOF associated with the framing domain and the panels. Since no external forces are acting on the sheathing panels or the framing nodes the equilibrium equations can be condensed to a 6 DOF system that represent the shear wall element in a building model analysis. The stiffness matrix $\mathbf{K^D}_\mathbf{W}$ is

$$\mathbf{K_W^D} = \mathbf{K_{DD}^4} - \left(\begin{bmatrix} \mathbf{K_{DF}^4} & \mathbf{0} \end{bmatrix} \cdot \begin{bmatrix} \sum_{i=1}^{4} \mathbf{K_{FF}^i} & \mathbf{K_{FP}^1} \\ \mathbf{K_{PF}^1} & \mathbf{K_{PP}^1} \end{bmatrix}^{-1} \cdot \begin{bmatrix} \mathbf{K_{FD}^4} \\ \mathbf{0} \end{bmatrix} \right) \tag{4.141}$$

4.3.4 Solution Algorithm of a Shear Wall Element under Quasi-Static Loading Conditions

4.3.4.1 Introduction

This section summarizes the solution algorithm utilized to solve the quasi-static equilibrium equations of a shear wall element under prescribed load and displacement controlled boundary conditions. Due to geometric and material nonlinearity the solution procedure is facilitated in the time domain and static equilibrium is sought at discrete time instants that can be conveniently considered to have a constant time increment Δt. The use of this artificial time increment is convenient when multiple displacement constraints with nonzero values are applied, or when additionally external loads are also considered at certain DOF. The motion of the system is expressed by the global displacement vector $\mathbf{D}$ with dimensions N_{DOF}-by-1, where N_{DOF} is the total number of global DOF. Initially, at $t = 0$, $\{\mathbf{D}\}^0 = \{\mathbf{0}\}$. Equilibrium at each time instant $t = \tau$ is satisfied when external and internal forces are equal. These forces are expressed through the vectors $\mathbf{P}_{ext}$ and $\mathbf{P}_{int}$, respectively, and have the same dimensions with $\mathbf{D}$. Initially, $\{\mathbf{P}_{ext}\}^0 = \{\mathbf{P}_{int}\}^0 = \{\mathbf{0}\}$ and equilibrium is expressed as:

$$\left\{\mathbf{P_{ext}}\right\}^\tau = \left\{\mathbf{P_{int}}\right\}^\tau \tag{4.142}$$

$\mathbf{P}_{int}$ results from the addition of the internal forces of all the finite elements that build up the numerical model. Since equilibrium is expressed in the deformed configuration the internal element forces are not linearly related to the element displacements even if the elements are assumed to follow a linear elastic material law. However, the internal forces and the tangent stiffness matrices of the elements that follow either a linear elastic or nonlinear elastic material law can be expressed with respect to the element displacements at that time instant as:

$$\left\{\begin{array}{l} \{\mathbf{P_{int}}\}^{\tau} \rightarrow f\left(\{\mathbf{D}\}^{\tau}\right) \\ [\mathbf{K}]^{\tau} = \left.\dfrac{\partial \mathbf{P_{int}}}{\partial \mathbf{D}}\right|_{t=\tau} \rightarrow f\left(\{\mathbf{D}\}^{\tau}\right) \end{array}\right\} \tag{4.143}$$

where $[\mathbf{K}]^{\tau}$ is the tangent global stiffness matrix of the numerical model at time τ.

On the contrary, the internal forces and the tangent stiffness matrices of the elements that follow a nonlinear inelastic material law depend on the history of the displacement field as well as on the element displacements at that time instant. The nonlinear inelastic response is typically defined with respect to the variation of the displacements from a known equilibrium state and can be conveniently considered to depend on a set of parameters $\mathbf{Z}$ which are known at the initial equilibrium state, define the nonlinear inelastic material laws embedded in the respective elements, and change for each new equilibrium state. If $\{\mathbf{P_{int}}\}^{\tau}$, $\{\mathbf{D}\}^{\tau}$ and $\mathbf{Z}^{\tau}$ are known and the variation of the displacements $\Delta\mathbf{D}$ is given over a time increment Δt such as $\{\mathbf{D}\}^{\tau+\Delta t} = \{\mathbf{D}\}^{\tau} + \Delta\mathbf{D}$, the internal forces and the tangent stiffness matrices at time $t = \tau + \Delta t$ can be expressed as:

$$\left\{\begin{array}{l} \{\mathbf{P_{int}}\}^{\tau+\Delta t} \rightarrow f\left(\{\mathbf{D}\}^{\tau+\Delta t}, Z^{\tau}\right) \\ [\mathbf{K}]^{\tau+\Delta t} = \left.\dfrac{\partial \mathbf{P_{int}}}{\partial \mathbf{D}}\right|_{t=\tau+\Delta t} \rightarrow f\left(\{\mathbf{D}\}^{\tau+\Delta t}, Z^{\tau}\right) \\ Z^{\tau+\Delta t} \rightarrow f\left(\{\mathbf{D}\}^{\tau+\Delta t}, \{\mathbf{P_{int}}\}^{\tau+\Delta t}, Z^{\tau}\right) \end{array}\right\} \tag{4.144}$$

For convenience (4.144) will be used as a general representation of the internal forces of the numerical model based on both geometric and material nonlinearity.

4.3.4.2 Application of Constraints

This section describes how to apply the displacement constraints imposed on the numerical model. A single-point constraint sets a single DOF to a known value, which often is zero, while a multi-point constraint imposes a relationship among two or more DOF. In the case of a shear wall element, only single-point constraints are potentially imposed on the global DOF of the diaphragms. In any case, the total number of constraints C_{DOF} is always less than the total number of DOF N_{DOF}. A number of constraint equations that relate global displacement DOF can be written in the form:

$$\mathbf{Q} = \mathbf{C} \cdot \mathbf{D} \tag{4.145}$$

where $\mathbf{Q}$ is a C_{DOF} x 1 vector and $\mathbf{C}$ is a C_{DOF} x N_{DOF} matrix that both contain constants. For discussion, $\mathbf{D}$ can be rearranged and partitioned such as (4.145) becomes:

$$\mathbf{Q} = \begin{bmatrix} \mathbf{C_f} & \mathbf{C_c} \end{bmatrix} \cdot \begin{Bmatrix} \mathbf{D_f} \\ \mathbf{D_c} \end{Bmatrix} \tag{4.146}$$

where $\mathbf{D_f}$ are the unconstrained DOF and $\mathbf{D_c}$ are the constrained DOF. Because there are as many constrained DOF as many constraint equations, matrix $\mathbf{C_c}$ is square and nonsingular. Given the constraint equations, the solution matrix can be written as:

$$\begin{Bmatrix} \mathbf{F_f} \\ \mathbf{F_c} \\ \mathbf{Q} \end{Bmatrix} = \begin{bmatrix} \mathbf{K_{ff}} & \mathbf{K_{fc}} & \mathbf{C_f}^{\mathbf{T}} \\ \mathbf{K_{cf}} & \mathbf{K_{cc}} & \mathbf{C_c}^{\mathbf{T}} \\ \mathbf{C_f} & \mathbf{C_c} & \mathbf{0} \end{bmatrix} \cdot \begin{Bmatrix} \mathbf{D_f} \\ \mathbf{D_c} \\ \boldsymbol{\lambda} \end{Bmatrix} \tag{4.147}$$

where $\boldsymbol{\lambda}$ are forces of constraint. The solution is then equal to:

$$\begin{Bmatrix} \mathbf{D_f} \\ \mathbf{D_c} \\ \boldsymbol{\lambda} \end{Bmatrix} = \begin{bmatrix} \mathbf{K_{ff}} & \mathbf{K_{fc}} & \mathbf{C_f}^{\mathbf{T}} \\ \mathbf{K_{cf}} & \mathbf{K_{cc}} & \mathbf{C_c}^{\mathbf{T}} \\ \mathbf{C_f} & \mathbf{C_c} & \mathbf{0} \end{bmatrix}^{-1} \cdot \begin{Bmatrix} \mathbf{F_f} \\ \mathbf{F_c} \\ \mathbf{Q} \end{Bmatrix} \tag{4.148}$$

For single-point constraints (4.147) can be further simplified because $\mathbf{C_f}$ is a zero matrix. Each row of $\mathbf{Q}$ is equal to the value imposed on the respective constrained DOF. It is:

$$\begin{Bmatrix} \mathbf{F_f} \\ \mathbf{F_c} \\ \mathbf{Q} \end{Bmatrix} = \begin{bmatrix} \mathbf{K_{ff}} & \mathbf{K_{fc}} & \mathbf{0} \\ \mathbf{K_{cf}} & \mathbf{K_{cc}} & \mathbf{C_c}^{\mathbf{T}} \\ \mathbf{0} & \mathbf{C_c} & \mathbf{0} \end{bmatrix} \cdot \begin{Bmatrix} \mathbf{D_f} \\ \mathbf{D_c} \\ \boldsymbol{\lambda} \end{Bmatrix} \Rightarrow$$

$$\begin{Bmatrix} \mathbf{F_f} \\ \mathbf{Q} \end{Bmatrix} = \begin{bmatrix} \mathbf{K_{ff}} & \mathbf{K_{fc}} \\ \mathbf{0} & \mathbf{C_c} \end{bmatrix} \cdot \begin{Bmatrix} \mathbf{D_f} \\ \mathbf{D_c} \end{Bmatrix} \Rightarrow$$

$$\begin{Bmatrix} \mathbf{D_f} \\ \mathbf{D_c} \end{Bmatrix} = \begin{bmatrix} \mathbf{K_{ff}} & \mathbf{K_{fc}} \\ \mathbf{0} & \mathbf{C_c} \end{bmatrix}^{-1} \cdot \begin{Bmatrix} \mathbf{F_f} \\ \mathbf{Q} \end{Bmatrix} \tag{4.149}$$

The solution presented in (4.149) is well suited for numerical analysis of large systems with a few single-point constrained DOF, because no rearranging of the global stiffness matrix is required. Although the derivations provided above are for illustration with the DOF rearranged so that constrained and unconstrained DOF are separated, in a real numerical application the facilitation of (4.149) would simply require substituting the equilibrium equation of the constrained DOF with the associated constrain equation. Any forces acting on the constrained DOF $\mathbf{F_c}$ will not affect the solution, which is dependent on the forces applied on unconstrained DOF $\mathbf{F_f}$ and the differential motion of constrained DOF if elements of $\mathbf{Q}$ are nonzero.

4.3.4.3 Execution of a Multi-Step Analysis

A multi-step analysis procedure can be generally described in the time domain as discussed in the introductory part of this section. For any time instant τ the single-point constrained DOF $\mathbf{D_c}$ follow predefined paths so that:

$$\{\mathbf{Q}\}^{\tau} = \begin{bmatrix} \mathbf{0} & \mathbf{C_c} \end{bmatrix} \cdot \begin{Bmatrix} \mathbf{D_f} \\ \mathbf{D_c} \end{Bmatrix}^{\tau} \tag{4.150}$$

Any external forces acting on the unconstrained DOF $\mathbf{D_f}$ are also defined along the time domain. The external forces corresponding to the constrained DOF represent the reaction forces, which can be found after the convergence of each solution step. The external force vector $\mathbf{P_{ext}}$ can be written as:

$$\mathbf{P_{ext}} = \begin{Bmatrix} \mathbf{F_f} \\ \mathbf{F_c} \end{Bmatrix} = \begin{Bmatrix} \mathbf{F_{ext}} \\ \mathbf{R_{ext}} \end{Bmatrix} \tag{4.151}$$

where $\mathbf{F_{ext}}$ is a (N_{DOF} - C_{DOF})-by-1 vector that represents the applied external forces and $\mathbf{R_{ext}}$ is a C_{DOF}-by-1 vector that represents the reaction forces. Thus, $\{\mathbf{F_{ext}}\}^{\tau}$ is known a priori. Similarly, the internal force vector $\mathbf{P_{int}}$ can be written as:

$$\mathbf{P_{int}} = \begin{Bmatrix} \mathbf{F_{int}} \\ \mathbf{R_{int}} \end{Bmatrix} \tag{4.152}$$

Let us now describe the strategy for the execution of an incremental solution step from an equilibrium state at t = τ to the equilibrium state at t = τ + Δt. Since equilibrium is satisfied at t = τ, it can be written that:

$$\{\mathbf{P_{ext}}\}^{\tau} = \{\mathbf{P_{int}}\}^{\tau} \tag{4.153}$$

Also, $\{\mathbf{D}\}^{\tau}$, $[\mathbf{K}]^{\tau}$ and $\mathbf{Z}^{\tau}$ are known quantities. At time t = τ + Δt the external force vector $\{\mathbf{F_{ext}}\}^{\tau+\Delta t}$ and the displacements of constrained DOF $\{\mathbf{D_c}\}^{\tau+\Delta t}$ are known. The motion of the structure will depend on the variation of the external loads and the constrained displacements expressed as:

$$\{\Delta\mathbf{F_{ext}}\}^{\tau+\Delta t} = \{\mathbf{F_{ext}}\}^{\tau+\Delta t} - \{\mathbf{F_{ext}}\}^{\tau} \tag{4.154}$$

and

$$\begin{aligned} &\{\Delta\mathbf{D_c}\}^{\tau+\Delta t} = \{\mathbf{D_c}\}^{\tau+\Delta t} - \{\mathbf{D_c}\}^{\tau} \Rightarrow \\ &\{\mathbf{Q}\}^{\tau+\Delta t} - \{\mathbf{Q}\}^{\tau} = [\mathbf{0} \quad \mathbf{C_c}]\cdot\begin{Bmatrix} \Delta\mathbf{D_f} \\ \Delta\mathbf{D_c} \end{Bmatrix}^{\tau+\Delta t} \Rightarrow \\ &\{\Delta\mathbf{Q}\}^{\tau+\Delta t} = [\mathbf{0} \quad \mathbf{C_c}]\cdot\{\Delta\mathbf{D}\}^{\tau+\Delta t} \end{aligned} \tag{4.155}$$

If the response of the system was assumed to be linear, the equilibrium would be found directly by deriving that:

$$\{\mathbf{P_{ext}}\}^{\tau} + \{\Delta\mathbf{P_{ext}}\}^{\tau+\Delta t} = \{\mathbf{P_{int}}\}^{\tau} + \{\Delta\mathbf{P_{int}}\}^{\tau+\Delta t} \Rightarrow$$

$$\{\mathbf{P_{ext}}\}^{\tau+\Delta t} - \{\mathbf{P_{int}}\}^{\tau} = \{\Delta\mathbf{P_{int}}\}^{\tau+\Delta t} = [\mathbf{K}]^{\tau}\{\Delta\mathbf{D}\}^{\tau+\Delta t} \Rightarrow$$

$$\begin{Bmatrix} \{\mathbf{F_{ext}}\}^{\tau+\Delta t} - \{\mathbf{F_{int}}\}^{\tau} \\ \{\mathbf{R_{ext}}\}^{\tau+\Delta t} - \{\mathbf{R_{int}}\}^{\tau} \end{Bmatrix} = \begin{bmatrix} \mathbf{K_{ff}} & \mathbf{K_{fc}} \\ \mathbf{K_{cf}} & \mathbf{K_{cc}} \end{bmatrix}^{\tau} \{\Delta\mathbf{D}\}^{\tau+\Delta t} \tag{4.156}$$

Combining (4.155) and (4.156) as shown in (4.149) yields the following variation of the displacement field:

$$\{\Delta\mathbf{D}\}^{\tau+\Delta t} = \begin{bmatrix} [\mathbf{K_{ff}}]^{\tau} & [\mathbf{K_{fc}}]^{\tau} \\ \mathbf{0} & \mathbf{C_c} \end{bmatrix}^{-1} \cdot \begin{Bmatrix} \{\mathbf{F_{ext}}\}^{\tau+\Delta t} - \{\mathbf{F_{int}}\}^{\tau} \\ \{\Delta\mathbf{Q}\}^{\tau+\Delta t} \end{Bmatrix} \tag{4.157}$$

Since the response of the system is nonlinear, a Newton-Raphson iterative procedure, which drives the load imbalance between external and internal forces to zero, is utilized to define the equilibrium state. A general description of the adopted procedure can be found in Cook et al. (2002). Each iteration is denoted with an index j where j = {1,2,3,…} and any quantities found at that iteration carry the subscript j. Quantities specifying the initial conditions of the iterations carry the subscript j-1.

Initiation of Solution Step

Before the beginning of the iterations the following assignments are made.

$$\begin{Bmatrix} \mathbf{F_{ext}} = \{\mathbf{F_{ext}}\}^{\tau+\Delta t} \\ \{\mathbf{F_{int}}\}_0 = \{\mathbf{F_{int}}\}^{\tau} \\ [\mathbf{K}]_0 = [\mathbf{K}]^{\tau} \\ \{\mathbf{D}\}_0 = \{\mathbf{D}\}^{\tau} \\ \{\Delta\mathbf{Q}\}_1 = \{\Delta\mathbf{Q}\}^{\tau+\Delta t} \\ \mathbf{Z} = \mathbf{Z}^{\tau} \end{Bmatrix} \tag{4.158}$$

Initiation of First Iteration

Invoking (4.157) the displacement increment $\{\Delta\mathbf{D}\}_j$ is found which is added to the current displacement vector $\{\mathbf{D}\}_{j-1}$

$$\{\Delta\mathbf{D}\}_j = \begin{bmatrix} [\mathbf{K_{ff}}]_{j-1} & [\mathbf{K_{fc}}]_{j-1} \\ \mathbf{0} & \mathbf{C_c} \end{bmatrix}^{-1} \cdot \begin{Bmatrix} \mathbf{F_{ext}} - \{\mathbf{F_{int}}\}_{j-1} \\ \{\Delta\mathbf{Q}\}_j \end{Bmatrix} \tag{4.159}$$

$$\{\mathbf{D}\}_j = \{\mathbf{D}\}_{j-1} + \{\Delta\mathbf{D}\}_j \tag{4.160}$$

Based on the new displacement vector and the parameters $\mathbf{Z}$ that correspond to the equilibrium state at $t = \tau$, the new internal force vector and the new tangent stiffness matrix are computed, as shown in (4.144).

$$\begin{Bmatrix} \{\mathbf{P_{int}}\}_j \rightarrow f\left(\{\mathbf{D}\}_j ,\, Z\right) \\ [\mathbf{K}]_j \rightarrow f\left(\{\mathbf{D}\}_j ,\, Z\right) \\ Z_j \rightarrow f\left(\{\mathbf{D}\}_j ,\, \{\mathbf{P_{int}}\}_j ,\, Z\right) \end{Bmatrix} \tag{4.161}$$

The load imbalance $\{\mathbf{LI}\}_j$ between external and internal forces that correspond to the unconstrained DOF can now be computed as:

$$\{\mathbf{LI}\}_j = \mathbf{F_{ext}} - \{\mathbf{F_{int}}\}_j \tag{4.162}$$

Convergence is satisfied when the load imbalance $\{\mathbf{LI}\}_j$ is sufficiently small according to a selected norm of $\{\mathbf{LI}\}_j$ and a specified tolerance ε. The Euclidean norm is selected to compute the length of the imbalance force between all the global active DOF and apply the convergence criterion. Convergence is satisfied when:

$$\left\|\{\mathbf{LI}\}_j\right\| = \left(\{\mathbf{LI}\}_j^{\mathrm{T}} \cdot \{\mathbf{LI}\}_j\right)^{1/2} \leq |\varepsilon| \tag{4.163}$$

Initiation of Successive Iterations

If the convergence criterion is not satisfied, iterations are performed carrying out (4.159) to (4.162) until (4.163) is valid. $\{\mathbf{LI}\}_j$ is the driving force of the successive iteration when $j \rightarrow j+1$. (4.159) can now be written as:

$$\{\Delta\mathbf{D}\}_j = \begin{bmatrix} [\mathbf{K_{ff}}]_{j-1} & [\mathbf{K_{fc}}]_{j-1} \\ \mathbf{0} & \mathbf{C_c} \end{bmatrix}^{-1} \cdot \begin{Bmatrix} \{\mathbf{LI}\}_{j-1} \\ \{\Delta\mathbf{Q}\}_j \end{Bmatrix} \tag{4.164}$$

where

$$\{\Delta\mathbf{Q}\}_j = \begin{cases} \{\Delta\mathbf{Q}\}_1 \text{, if j = 1} \\ \mathbf{0} \quad \text{, if j > 1} \end{cases} \tag{4.165}$$

As shown in (4.165), the displacements of the constrained DOF after the first iteration are set by default to zero values. Since iterative displacements are added to the total displacements, the differential motion of the constrained DOF from τ to $\tau+\Delta t$ has already been applied during the first iteration.

End of the Solution Step

When convergence is satisfied, the equilibrium state has been defined at t = $\tau+\Delta t$ such as:

$$\begin{Bmatrix} \{\mathbf{D}\}^{\tau+\Delta t} = \{\mathbf{D}\}_j \\ [\mathbf{K}]^{\tau+\Delta t} = [\mathbf{K}]_j \\ \{\mathbf{P_{int}}\}^{\tau+\Delta t} = \{\mathbf{P_{int}}\}_j \\ \{\mathbf{R_{ext}}\}^{\tau+\Delta t} = \{\mathbf{R_{int}}\}_j \\ \mathbf{Z}^{\tau+\Delta t} = \mathbf{Z}_j \end{Bmatrix} \tag{4.166}$$

The solution of the next time step can be executed based on the new equilibrium state found at the current solution step.

4.3.5 Constitutive Model of a Sheathing-to-Framing Connector Element

4.3.5.1 Introduction

This section describes the analytical derivations developed to simulate the response of a sheathing-to-framing connection assembly under unidirectional and bidirectional loading. As discussed earlier, the lateral resistance of a shear wall assembly results from the interaction of two planar domains – the framing and the sheathing – that takes place at the numerous nailing connections that fasten each sheathing panel on the framing members. Nails are dowel-type fasteners with typical diameter less than 0.25 in and typical length between 2 and 3 in. The response under general bidirectional loading is complex due to material nonlinearity observed in the form of wood crushing at the boundaries with the steel connector as well as in the form of axial, shear, and flexural deformations of the steel connector itself. The response of this type of connections can be experimentally identified by quasi-static connection tests of sheathing-to-framing assemblies. The test setup of such type of experimentation is designed to apply monotonic or cyclic displacement histories along one direction of the 2D plane. The direction of loading in the wall plane is defined with respect to the direction of the wood grains in the framing lumber, which run parallel to the length of the member. Thus, two different test configurations are typically used. In the first configuration, the specimens are loaded in such a way to produce nail deformation parallel to the grain of the framing lumber, while in the second configuration, the nail deformations are imposed along a direction perpendicular to the grain of the framing lumber, as shown in Figure 4.28a,b. The test setup used by Ekiert and Hong (2006) for loading parallel and perpendicular to grain is shown in Figure 4.28c,d.

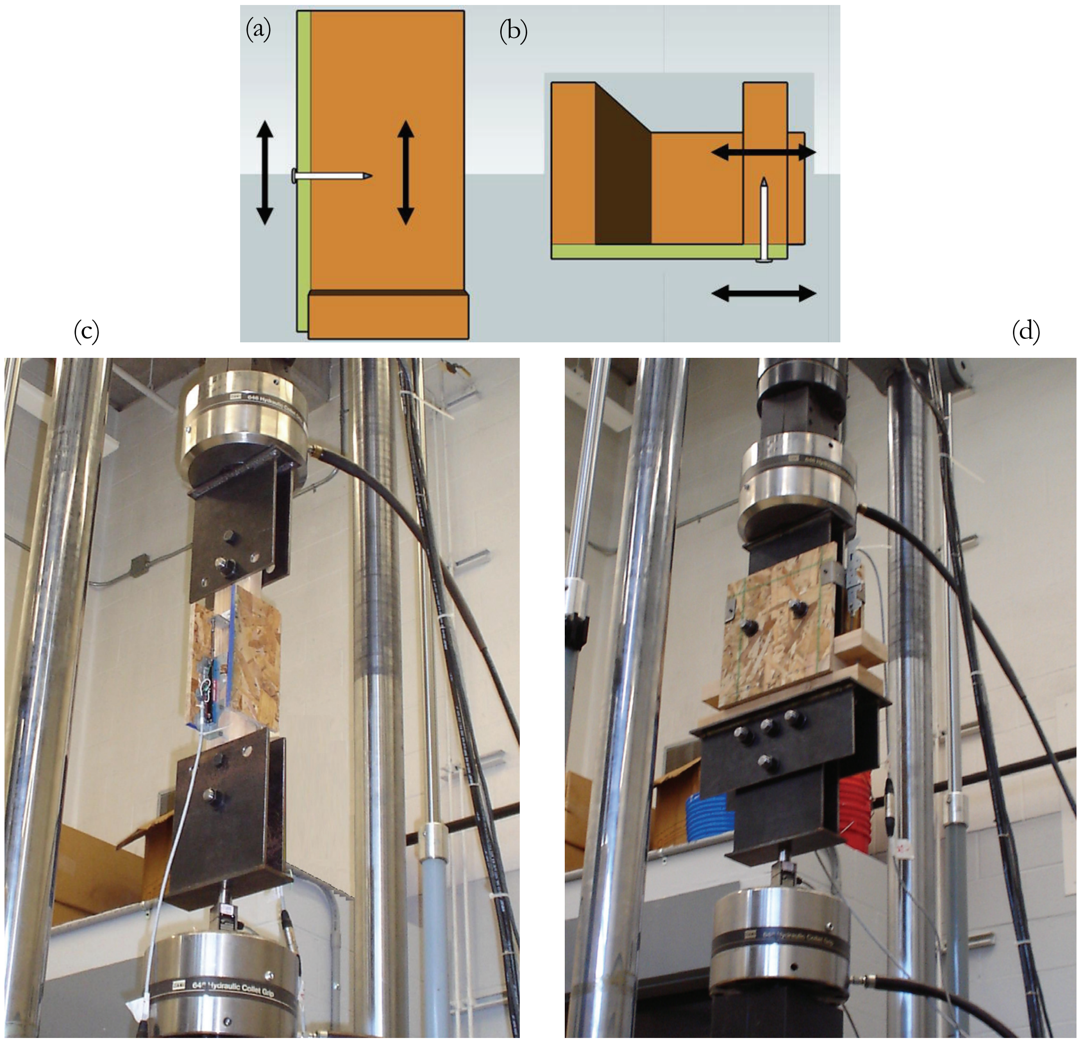

Figure 4.28 (a) Direction of Nailing Deformation Parallel to Grain, (b) Direction of Nailing Deformation Perpendicular to Grain, (c) Parallel to Grain Connection Test Setup with 2x4 Framing, and (d) Perpendicular to Grain Connection Test Setup with 2x4 Framing (from Ekiert and Hong 2006)

Figure 4.29a illustrates the monotonic and the cyclic response of a sheathing-to-framing connector under loading parallel to grain, while Figure 4.29b shows the displacement protocol imposed for the cyclic test. The displacement corresponds to the differential displacement of the two wood mediums and the force corresponds to the shear resistance developed by the sheathing-to-framing connector. These results have been generated by Ekiert and Hong (2006) as part of the NEESWood Project and have been documented in the NEESWood benchmark test report (Christovasilis *et al.* 2009a).

The monotonic force-displacement response can be characterized as a curve with no apparent yield point and yield plateau. The initial stiffness decreases almost along the entire displacement range and a discrete capping point that defines the strength of the connection can be defined.

The cyclic response exhibits two main characteristics. First, the response is nonlinear inelastic but the force-displacement curves lie mainly in the 1^{st} and the 4^{th} quadrant in the sense that the system cannot develop significant resisting forces on unloading paths; that is paths that bring a displaced connector to the initial position. Secondly, the loading paths, which displace the connector from the initial configuration, corresponding to each direction, depend highly on the maximum displacement previously experienced at this particular direction. Loading paths along virgin displacement ranges follow closely the backbone curve but under cyclic loading along the same displacement ranges the resisting forces are lower than the previous cycle. The main force degradation is observed at the second cycle and leads to a pinching response followed by a hardening behavior when the displacements approach and exceed the maximum experienced displacement. These characteristics result principally from the bearing effect of the resisting forces developed between the wood mediums and the steel connector and secondarily from the friction between the three components during deformation.

4.3.5.2 Unidirectional Response

The unidirectional force-displacement response under cyclic loading has been considered in most research studies on the analysis of light-frame wood systems as a unidirectional spring with phenomenological, user-defined, hysteretic laws that adequately reproduce the experimental response observed from testing of sheathing-to-framing assemblies (see Chapter 2). Few studies have simulated each sheathing-to-framing connector similarly to an elasto-plastic pile embedded in a nonlinear foundation (Foschi 2000 and Chui *et al.* 1998). These more advanced formulations are necessary to understand and identify in a greater detail the nonlinear response of this type of connections but the required computational overhead to simulate a wood shear wall assembly, which contains numerous connectors, under this approach is too high. Eventually, when these detailed formulations are well established, they should lead to simplified accurate hysteretic rules that can be used within a nonlinear spring. The phenomenological model developed in this study is mainly based on previous work from Sivaselvan and Reinhorn (1999) but utilizes findings from other studies related to the specific response of wood connections (Foschi 1977; Girhammar *et al.* 2004) and the modeling of strength and stiffness degradation phenomena (Ibarra *et al.* 2005, Ayoub 2007).

(a)

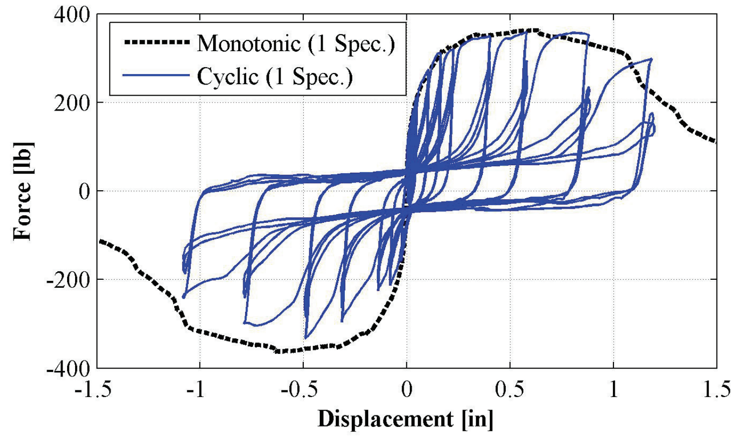

(b)

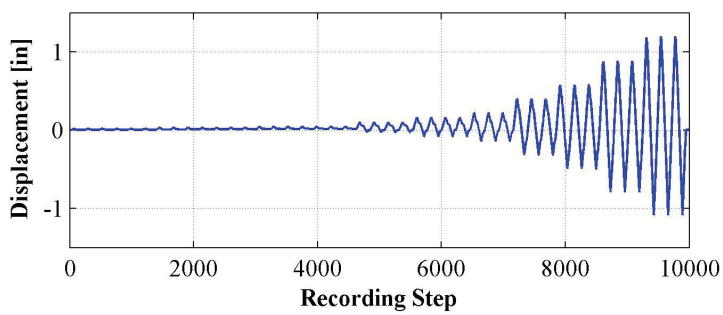

Figure 4.29 (a) Monotonic and Cyclic Response Parallel to Grain; 8d Common Nails; 7/16 in Thick OSB Panel; 2x4 Hem-Fir Lumber; (b) Cyclic Displacement Protocol

The implementation is based on a set of 14 branches that define all the possible hysteretic paths and a set of rules in the form of a logic tree that govern the transition between branches. The model requires 10 input parameters, which are presented in Table 4.1. The first 5 parameters are related to the basic hysteretic model with pinching response. These are the initial elastic stiffness K_o; the initial yield force F_{yo}; the initial post-yield stiffness ratio α_o as a fraction of the initial elastic stiffness; the pinching force ratio σ as a fraction of the initial yield force; and the pinching displacement ratio σ_u as a secondary parameter related to the displacement at the pinching force σF_{yo}. The remaining 5 parameters are related to the specific modes of strength and stiffness degradation that can be potentially integrated in the hysteretic response. These are the displacements at the initiation and at the ultimate displacement-based strength degradation, u_{ini} and u_{ult} respectively; the energy-based strength degradation parameter β; the energy-based reloading stiffness degradation parameter γ; and the displacement-based unloading stiffness degradation parameter κ.

Table 4.1 Nomenclature and Description of the 10 Input Model Parameters

Parameters	Units (US customary)	Range	Description
K_o	lbs/in	$(0, +\infty)$	Initial elastic stiffness
F_{yo}	lbs	$(0, +\infty)$	Initial yield force
α_o	-	$[0, 1]$	Initial post-yield stiffness ratio (fraction of the initial elastic stiffness)
σ	-	$[0, 1]$	Pinching force ratio (fraction of the initial yield force)
σ_u	-	$[0, 1]$	Pinching displacement ratio (secondary parameter related to the displacement at the pinching force σF_{yo})
u_{ini}	in	$(0, u_{ult})$	Displacement at initiation of displacement-based strength degradation
u_{ult}	in	$(u_{ini}, +\infty)$	Displacement at ultimate displacement-based strength degradation
β	-	$[0, 1]$	Parameter related to the energy-based strength degradation
γ	lbs^{-1}	$[0, +\infty)$	Parameter related to energy-based reloading stiffness degradation
κ	-	$(0, +\infty)$	Parameter related to displacement-based unloading stiffness degradation

Basic Hysteretic Model with Pinching Response

Figure 4.30a illustrates the displacement histories and Figure 4.30b the force-displacement responses of the basic hysteretic model with pinching response that does not incorporate any degradation modes. The main displacement history (shown in black) follows steps 0 to 7 and a secondary history (shown in grey) diverges following steps 6' to 9'. The two-digit circled numbers identify the path index I_{path} of each branch. The first digit identifies the type of the hysteretic path (1 to 6) and the second digit identifies the direction of motion (1 or 2).

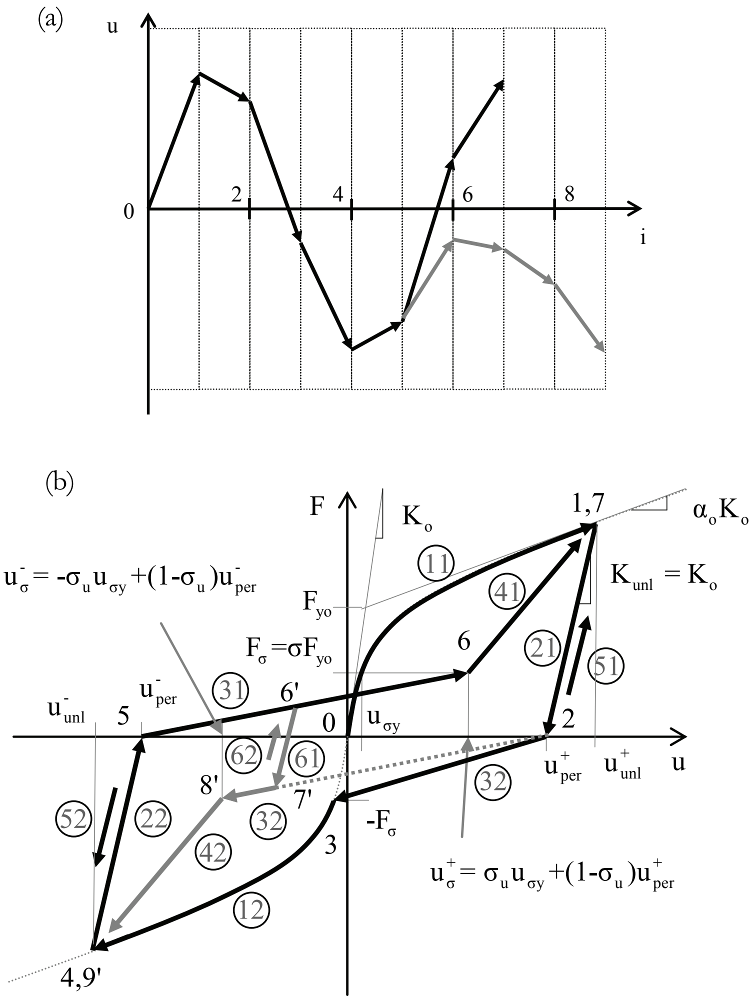

Figure 4.30 Basic Hysteretic Model with Pinching Response: (a) Displacement History; and (b) Force-Displacement History

Backbone Curves – Branches 11 and 12

The backbone force F_{BB} is expressed as a function of the displacement – or slip – u experienced by the nailing connection as:

$$F_{BB}(u) = \text{sgn}(u) \cdot \left(F_{yo} \cdot (1\text{-}\alpha_o) + \alpha_o \cdot K_o \cdot |u|\right) \cdot \left(1 - e^{-\frac{K_o \cdot |u|}{F_{yo} \cdot (1-\alpha_o)}}\right) \tag{4.167}$$

where sgn is the signum function.

The nonlinear function shown in (4.167) was first proposed by Foschi (1977) by defining the term $F_{yo}(1\text{-}\alpha_o) = F_o$ as the input parameter, which corresponds to the force intercept of the post-elastic linear curve at u = 0. This function has been widely used in many studies related to wood structures because it exhibits no pure initial elastic range and a smooth transition from the elastic to the plastic range.

The stiffness of the backbone curve K_{BB} is equal to:

$$K_{BB}(u) = \frac{\partial F_{BB}(u)}{\partial u} \Rightarrow$$

$$K_{BB}(u) = \alpha_o \cdot K_o \cdot \left(1 - e^{-\frac{K_o \cdot |u|}{F_{yo} \cdot (1-\alpha_o)}} \right) + \left(F_{yo} \cdot (1-\alpha_o) + \alpha_o \cdot K_o \cdot |u| \right) \cdot e^{-\frac{K_o \cdot |u|}{F_{yo} \cdot (1-\alpha_o)}} \cdot \frac{K_o}{F_{yo} \cdot (1-\alpha_o)} \quad (4.168)$$

Basic Unloading Curves – Branches 21 and 22

The basic unloading curves are linear branches with stiffness K_{unl} equal to the initial stiffness K_o and initiate upon displacement reversal from a backbone curve. The hysteretic paths originate from the unloading displacement $u_{unl}^{+/-}$ and terminate when a permanent displacement $u_{per}^{+/-}$ is established at zero force, as shown in Figure 4.30b.

Primary Reloading Curves – Branches 31 and 32

The primary reloading curves are linear branches that follow after the basic unloading curves and establish the pinching response of the nonlinear model. Originating from the permanent displacement $u_{per}^{+/-}$ the pinching point denoted as $(u_\sigma^{+/-}, F_\sigma^{+/-})$ is defined as:

$$\left\{ \begin{array}{c} u_\sigma^{+/-} = (+/-) \cdot \sigma_u \cdot u_{\sigma y} + \left(1 - \sigma_u\right) \cdot u_{per}^{+/-} \\ \\ F_\sigma^{+/-} = (+/-) \cdot \sigma \cdot F_{yo} \end{array} \right\} \quad (4.169)$$

where $u_{\sigma y}$ corresponds to the displacement at which the backbone force is equal to σF_{yo}. The pinching displacement $u_\sigma^{+/-}$ is computed each time a permanent displacement $u_{per}^{+/-}$, greater than the existing one, is established in the same direction.

Secondary Reloading Curves – Branches 41 and 42

The secondary reloading curves are linear branches that follow after the primary reloading curves and connect the pinching point ($u_\sigma^{+/-}$, $F_\sigma^{+/-}$), defined previously, with the backbone point that corresponds to the unloading displacement $u_{unl}^{+/-}$ established in the given direction. These branches represent the hardening behavior observed in pinching systems when the transient displacement approaches the previously established maximum unloading displacement.

Basic Reloading Curves – Branches 51 and 52

The basic reloading curves are linear branches with stiffness equal to the initial stiffness K_o and initiate upon displacement reversal from the basic unloading curves 21 and 22. The hysteretic paths originate from the displacement reversal point and terminate at the unloading displacement $u_{unl}^{+/-}$, as shown in Figure 4.30b.

Internal Loading Curves – Branches 61 and 62

The internal loading curves are linear branches with stiffness equal to the initial stiffness K_o and initiate upon displacement reversal from the primary and secondary reloading curves 31, 32, 41 and 42. Similarly, the internal curves terminate at one of the primary or secondary reloading curves.

Model with Hysteretic Degradation Modes

Unloading Stiffness Degradation

The stiffness of the basic unloading curves (21 and 22), the basic reloading curves (51 and 52) and the internal loading curves (61 and 62) is computed based on the pivot rule, proposed by Park *et al.* (1987). According to this rule, the load-reversal branches are assumed to target a pivot point on the initial elastic branch at a force of κF_{yo} on the opposite side, where κ is the stiffness degradation parameter. The unloading stiffness K_{unl} is computed with respect to the current displacement u_{cur} and force F_{cur} as:

$$K_{unl}\left(u_{cur}, F_{cur}\right) = \frac{\operatorname{sgn}\left(u_{cur} - F_{cur}/K_o\right)\cdot F_{cur} + \kappa\cdot F_{yo}}{\operatorname{sgn}\left(u_{cur} - F_{cur}/K_o\right)\cdot K_o\cdot u_{cur} + \kappa\cdot F_{yo}}\cdot K_o \qquad (4.170)$$

Strength Degradation

Strength and post-elastic stiffness degradation is implemented with the consideration of two damage indices u_{max} and H; u_{max} is the maximum absolute displacement experienced by the system and H is the non-recoverable hysteretic strain energy dissipated, which excludes the elastic energy retrieved if the system unloads to zero force. These damage indices are associated to damage functions, S_U and S_H, which lead to complete failure of the resisting mechanism of the system under excessive displacements (displacement-based) or excessive hysteretic strain-energy dissipation (energy-based). The degraded backbone force $F_{D,BB}$ is expressed as:

$$F_{D,BB}(u, u_{max}, H) = \mathrm{sgn}(u) \cdot \left(F_y \cdot (1-\alpha) + \alpha \cdot K_o \cdot |u|\right) \cdot \left(1 - e^{-\frac{K_o \cdot |u|}{F_y \cdot (1-\alpha)}}\right) \tag{4.171}$$

where F_y and *a* are the degraded yield force and post-elastic stiffness ratio defined as:

$$\begin{Bmatrix} F_y(u_{max}, H) = F_{yo} \cdot S_U(u_{max}) \cdot S_H(H) \\ \alpha(u_{max}, H) = \alpha_o \cdot S_U(u_{max}) \cdot S_H(H) \end{Bmatrix} \tag{4.172}$$

The displacement-based damage function S_U is defined as:

$$S_U(u_{max}) = \exp\left(-\frac{{u_{max}}^{c_1}}{c_2}\right) \tag{4.173}$$

where c_1 and c_2 are positive parameters. A generic plot of the shape of this damage function is illustrated in Figure 4.31. Due to the fact that c_1 and c_2 have no physical interpretation, they are computed based on the input parameters u_{ini} and u_{ult} that represent the displacements at which the degradation initiates ($S_U(u_{ini}) = 0.999$) and terminates ($S_U(u_{ult}) = 0.001$), respectively. If these two parameters are defined, then c_1 and c_2 are equal to:

$$\begin{Bmatrix} c_1 = \left(-\ln\left(-\ln(0.001)\right) + \ln\left(-\ln(0.999)\right)\right) / \left(\ln(u_{int}) - \ln(u_{ult})\right) \\ c_2 = -\left({u_{ult}}^{c_1}\right) / \ln(0.001) \end{Bmatrix} \tag{4.174}$$

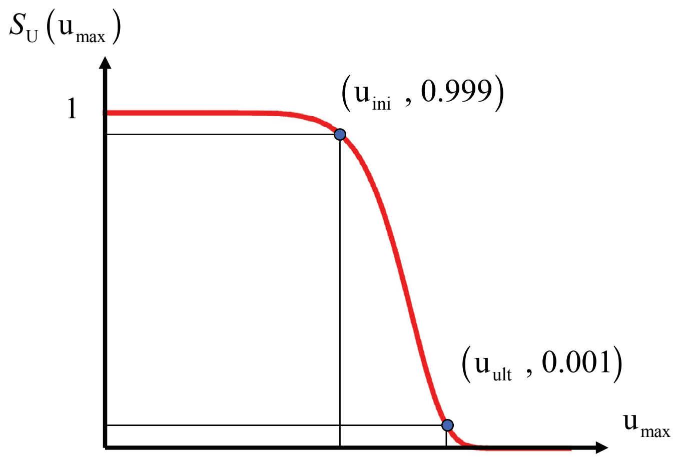

Figure 4.31 Plot of Damage Function S_U

The displacement-based damage function was proposed by Girhammar *et al.* (2004) and was implemented as an additional multiplier to the backbone force function introduced by Foschi (1977) and shown in (4.167). In this study, it is used as a damage-function to reduce the yield force and the post-elastic stiffness.

The energy-based damage function S_H is defined similarly to Sivaselvan and Reinhorn (1999) as:

$$S_H(H) = 1 - \frac{\beta}{1-\beta} \cdot \frac{H}{H_{ult}} \geq 0 \tag{4.175}$$

where β is input parameter and H_{ult} is the hysteretic energy dissipated by the degraded backbone curve, for monotonic loading up to the ultimate displacement u_{ult}, considering only the displacement-based degradation, i.e. assigning $u_{max} = u$ and $H = 0$:

$$H_{ult} = \int_0^{u_{ult}} \left(F_y(u,0)\cdot(1-\alpha(u,0)) + \alpha(u,0)\cdot K_o \cdot u\right)\cdot\left(1 - e^{-\frac{K_o \cdot u}{F_y(u,0)\cdot(1-\alpha(u,0))}}\right)du \tag{4.176}$$

The non-recoverable hysteretic energy H is computed based on u_{cur} and F_{cur} as:

$$H = H_{str} - \frac{(F_{cur})^2}{2\cdot K_{unl}(u_{cur}, F_{cur})} \tag{4.177}$$

where H_{str} is the total strain energy of the system at the current point. The degraded yield force F_y and post-elastic stiffness ratio a is dependent on the non-recoverable strain energy H, which in turn depends on the degraded current force as shown in (4.177). Thus, equations (4.171) and (4.172) are implicit and the solution is computed with an iterative procedure, using the non-recoverable strain energy from the previous step as a first estimate.

Accelerated Reloading Stiffness Degradation

The accelerated reloading stiffness degradation has been used by Ibarra *et al.* (2005) to capture a specific behavior of degrading hysteretic systems. It has been observed in cyclic force-displacement loops that the secondary reloading curves (41 and 42) do not target the backbone curve at the point that corresponds to the unloading displacement $u_{unl}^{+/-}$ established in the given direction, but at a displacement $u_{tar}^{+/-}$ that is greater in absolute values from $u_{unl}^{+/-}$, depending on the number of hysteretic cycles occurred and the amount of dissipated energy. Many of the existing formulations incorporate the increase of $u_{tar}^{+/-}$ by a constant input parameter that relates the ratio of the target over the unloading displacement. In this study, the target displacement is computed based on the amount of non-recoverable energy dissipated from the instant the unloading displacement is established. Thus, $u_{tar}^{+/-}$ is computed as:

$$u_{tar}^{+/-} = (+/-) \cdot \gamma \cdot \left(H - H_{unl}^{+/-}\right) + u_{unl}^{+/-} \tag{4.178}$$

where γ is input parameter and $H_{unl}^{+/-}$ is the non-recoverable hysteretic energy dissipated until the instant the unloading displacement is established. Equation (4.178) is implicit and the solution is computed with an iterative procedure, using the non-recoverable strain energy from the previous step as a first estimate.

Hysteretic Responses Illustrating Adopted Degradation Modes

The effects of the degradation modes on the hysteretic response of the system are illustrated in Figure 4.33 to Figure 4.38, for two displacement histories shown in Figure 4.32. The first displacement history (Figure 4.32a) consists of 4 symmetric cycles with increasing amplitude, while the second one (Figure 4.32b) contains the same individual cycles in the opposite order, resulting in cycles of decreasing amplitude. The hysteretic responses are normalized to the initial yield force F_{yo} and the initial yield displacement u_{yo}, which is equal to F_{yo}/K_o. The other 3 parameters that affect the basic hysteretic model are kept constant ($\alpha_o = 0.1$ and $\sigma = \sigma_u = 0.3$). The parameters that control the degradation modes are assigned to initial values that mitigate the degradation effects ($u_{ini} / u_{yo} = 20 > 10$, $u_{ult} / u_{yo} = 25 > u_{ini} / u_{yo}$, $\beta = \gamma = 0$ and $\kappa = 200$).

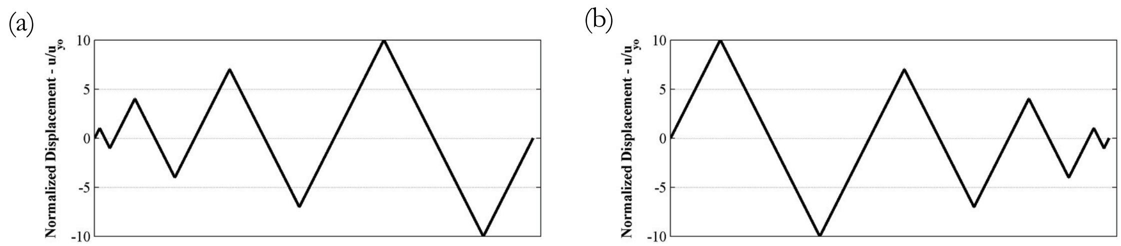

Figure 4.32 Displacement Histories with Cycles of (a) Increasing Amplitude, and (b) Decreasing Amplitude

Figure 4.33 shows the cyclic response of the basic hysteretic model without any degradation modes. The response under virgin displacements follows the backbone curve and the pinching stiffness is decreasing under cycles of increasing amplitude, but is constant under cycles of decreasing amplitude. The hysteretic shape of the pinching response can be modified by varying the parameters σ_u and σ that control the displacement and the force of the pinching point, respectively, as shown earlier in (4.169).

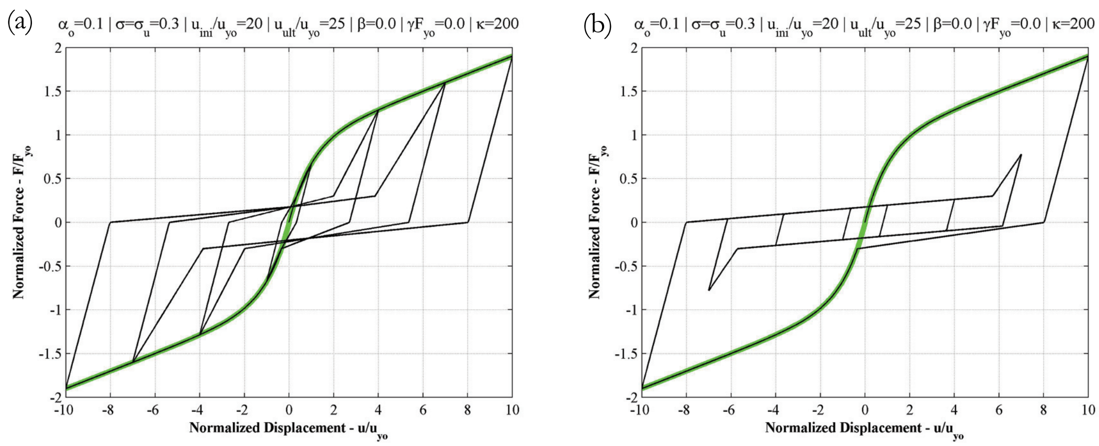

Figure 4.33 Hysteretic Responses of Basic Model without Degradation Modes under Displacement Histories with Cycles of (a) Increasing Amplitude, and (b) Decreasing Amplitude

Figure 4.34 shows the cyclic response of the basic hysteretic model that incorporates unloading stiffness degradation for $\kappa = 5$. This means that the load-reversal branches target a pivot point on the initial elastic branch at a force of $5F_{yo}$ on the opposite side.

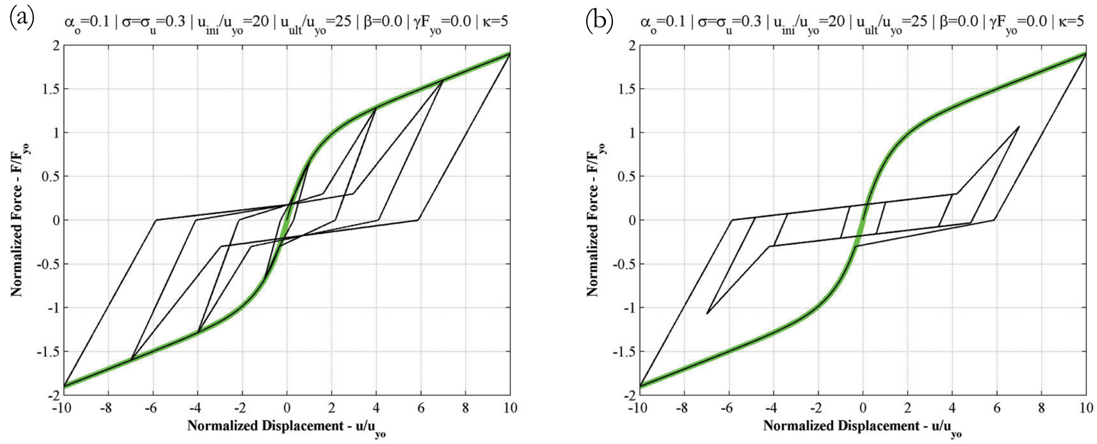

Figure 4.34 Hysteretic Responses of Basic Model with Unloading Stiffness Degradation under Displacement Histories with Cycles of (a) Increasing Amplitude, and (b) Decreasing Amplitude

Figure 4.35 demonstrates the cyclic response of the basic hysteretic model that incorporates displacement-based strength degradation. This response is obtained for $u_{ini} = 2u_{yo}$ and $u_{ult} = 15u_{yo}$. This mode of degradation results in a nonlinear smooth backbone response that can accommodate softening and ductile failure of the system. Moreover, the backbone force-displacement responses in the positive and negative directions are coupled with a single damage index (u_{max}), which results in modified envelope curves between the two displacement histories.

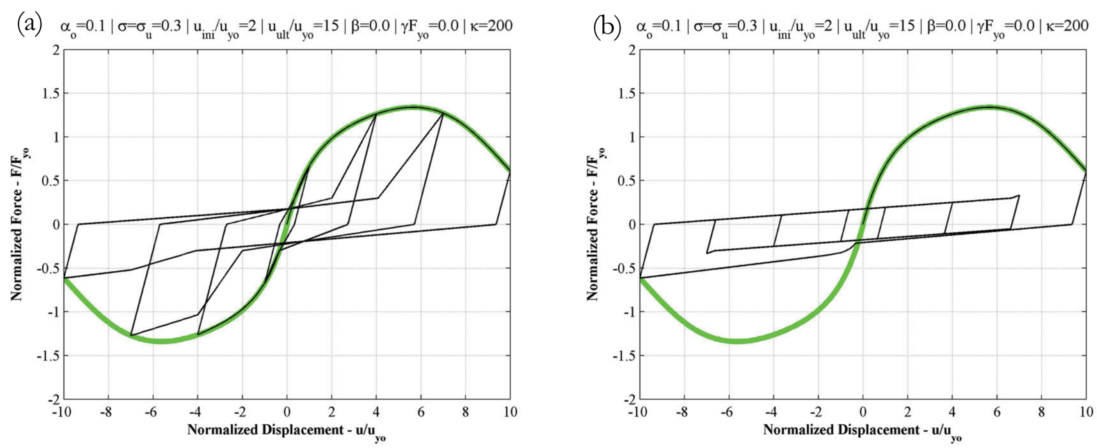

Figure 4.35 Hysteretic Responses of Basic Model with Displacement-Based Strength Degradation under Displacement Histories with Cycles of (a) Increasing Amplitude, and (b) Decreasing Amplitude

Figure 4.36 demonstrates the cyclic response of the basic hysteretic model that incorporates energy-based strength degradation. This response is obtained for β = 0.2. This mode of degradation reduces the envelope forces as a result of the non-recoverable hysteretic energy dissipated. Furthermore, it does not modify the pinching forces for the displacement history with cycles of decreasing amplitude (Figure 4.36b).

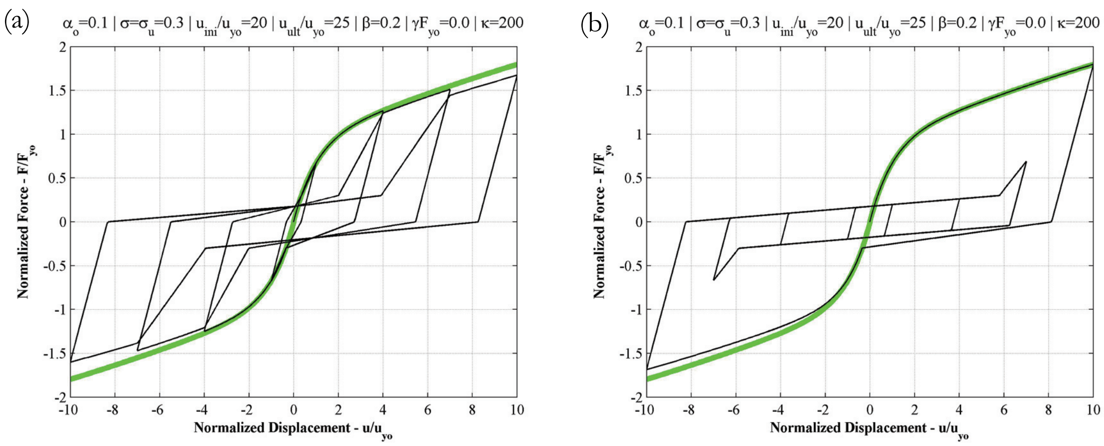

Figure 4.36 Hysteretic Responses of Basic Model with Energy-Based Strength Degradation under Displacement Histories with Cycles of (a) Increasing Amplitude, and (b) Decreasing Amplitude

Figure 4.37 demonstrates the cyclic response of the basic hysteretic model that incorporates accelerated stiffness degradation. This response is obtained for $\gamma = 0.2/F_{yo}$. This mode of degradation increases in magnitude the target displacement of the reloading curves as a function of the non-recoverable hysteretic energy dissipated from the instant of unloading.

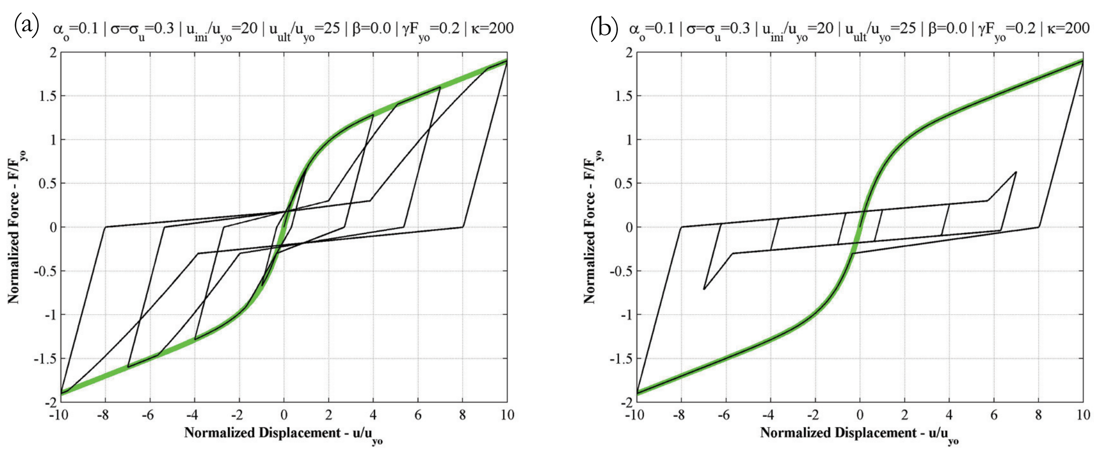

Figure 4.37 Hysteretic Responses of Basic Model with Accelerated Reloading Stiffness Degradation under Displacement Histories with Cycles of (a) Increasing Amplitude, and (b) Decreasing Amplitude

Figure 4.38 demonstrates the cyclic response of the basic hysteretic model that combines all the degradation modes. The 10 user input parameters can be calibrated so as to reproduce the hysteretic response of sheathing-to-framing connections or other components (i.r. holdown equipment). Appendix A and B contain calibrated parameters for different components that were considered in the validation studies conducted as part of this report.

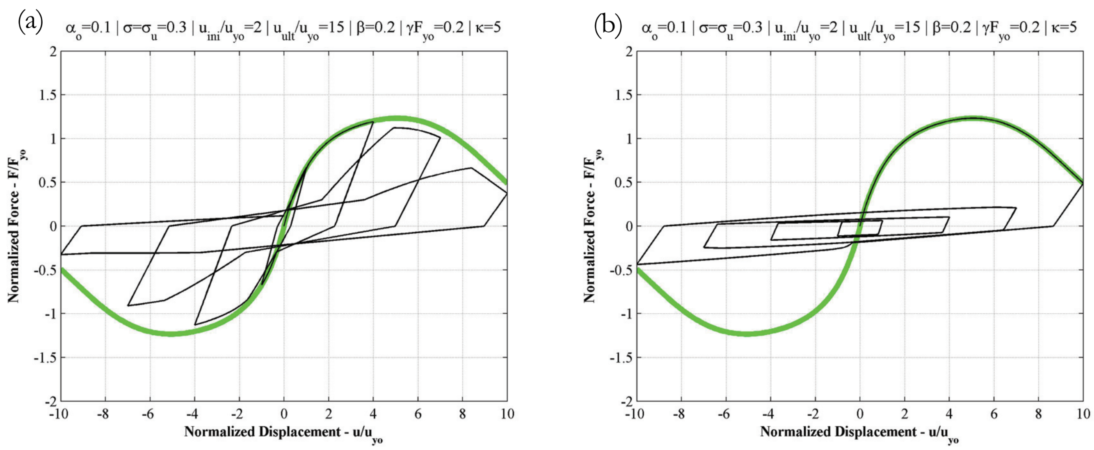

Figure 4.38 Hysteretic Responses of Basic Model with Combined Degradation Modes under Displacement Histories with Cycles of (a) Increasing Amplitude, and (b) Decreasing Amplitude

4.3.5.3 Bidirectional Response

The bidirectional response of each sheathing-to-framing connector element in the proposed shear wall model can be simulated with 4 different approaches related to the consideration or not of (i) a coupling interaction, and (ii) an initial orientation of each pair of orthogonal unidirectional independent springs. The numerical models, used in the validation studies presented in Chapter 5 and Chapter 6, are analyzed with the consideration of both the interaction and the orientation of each pair of springs.

Interaction of Orthogonal Springs in the Local Coordinate System

As discussed in Section 4.3.2.1, a sheathing-to-framing connector element has 2 orthogonal internal DOF in the wall plane u and v, which are defined with respect to an element Local Cartesian System (LCS) $\xi O\eta$ (see Figure 4.6). The orthogonal forces are typically computed using a pair of independent unidirectional nonlinear springs with the same properties. The independent forces p and q in this case are defined as:

$$\begin{Bmatrix} p = F_{\text{UNI}}(u) \\ q = F_{\text{UNI}}(v) \end{Bmatrix} \tag{4.179}$$

where F_{UNI} is the functional that computes the resisting forces under unidirectional displacement loading. This approach is simplified but acceptable within the general perspective of macro-modeling of this type of connections with zero-length elements[‡]. However, the lack of interaction leads to unrealistic response when one of the springs has failed exceeding the ultimate displacement but the orthogonal spring can still provide a resisting force. In order to alleviate this undesirable effect, a damage function S_{R} is defined to introduce an interaction between the two components. The orthogonal forces p_{int} and q_{int} including the implemented interaction are computed as:

$$\begin{Bmatrix} p_{int} = S_{\mathrm{R}}\left(\mathrm{r}_{\max}, \mathrm{u}_{\max}\right) \cdot p = \dfrac{S_{\mathrm{U}}\left(\mathrm{r}_{\max}\right)}{S_{\mathrm{U}}\left(\mathrm{u}_{\max}\right)} \cdot F_{\mathrm{UNI}}\left(u\right) \\ q_{int} = S_{\mathrm{R}}\left(\mathrm{r}_{\max}, \mathrm{v}_{\max}\right) \cdot q = \dfrac{S_{\mathrm{U}}\left(\mathrm{r}_{\max}\right)}{S_{\mathrm{U}}\left(\mathrm{v}_{\max}\right)} \cdot F_{\mathrm{UNI}}\left(v\right) \end{Bmatrix} \tag{4.180}$$

where S_{U} is the displacement-based damage function defined in (4.173), $\mathrm{u}_{\max}$ and $\mathrm{v}_{\max}$ are the maximum absolute displacements in the horizontal and vertical (local) directions, and $\mathrm{r}_{\max}$ is the maximum radius computed as the square-root-of-sum-of-squares of each pair of input displacements.

The unidirectional cyclic displacement history, shown in Figure 4.39a, is used as the basic input for a number of analyses utilizing the input nail parameters computed in Appendix B. The effect of the direction of the displacement history in the 2D plane is investigated for 3 different angles (θ = 15°, 30° and 45°) with respect to the horizontal axis, as shown in Figure 4.39b. For each angle, the hysteretic responses in the two orthogonal directions are computed for 3 different cases, as illustrated in Figure 4.40. The first case corresponds to a pair of independent orthogonal springs aligned to the horizontal and vertical directions. The second case corresponds to a single spring oriented to the input direction. The third case corresponds to the response of the independent orthogonal springs of the first case, modified for coupling interaction as shown in (4.180).

‡ The actual response under general bidirectional loading is coupled and complex, since a mechanics-based approach (Foschi 2000, Chui *et al.* 1998) requires the consideration of additional internal DOF.

(a)

(b)

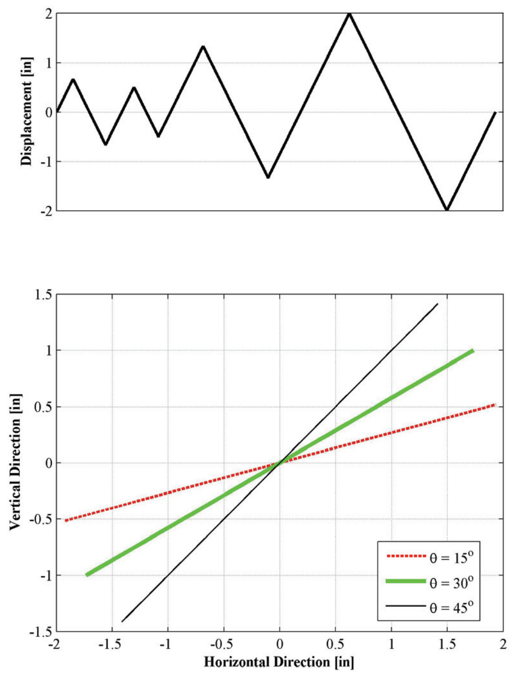

Figure 4.39 (a) Unidirectional Input Displacement History and (b) Plan View of Bidirectional Displacement Input

The results shown in Figure 4.40 demonstrate that the use of a pair of independent springs can produce significantly overestimated resisting forces with respect to a single spring oriented in the direction of loading. The implemented interaction reduces the independent spring forces, providing better correlation with the oriented spring components, and drives both springs to failure when the radius (r_{max}) approaches the ultimate displacement. However, the overestimation of strength and post-elastic stiffness of the ascending part of the backbone curve is not completely eliminated. The effects of the spring interaction on the lateral response of a shear wall model are demonstrated in the example presented in the third part of this section.

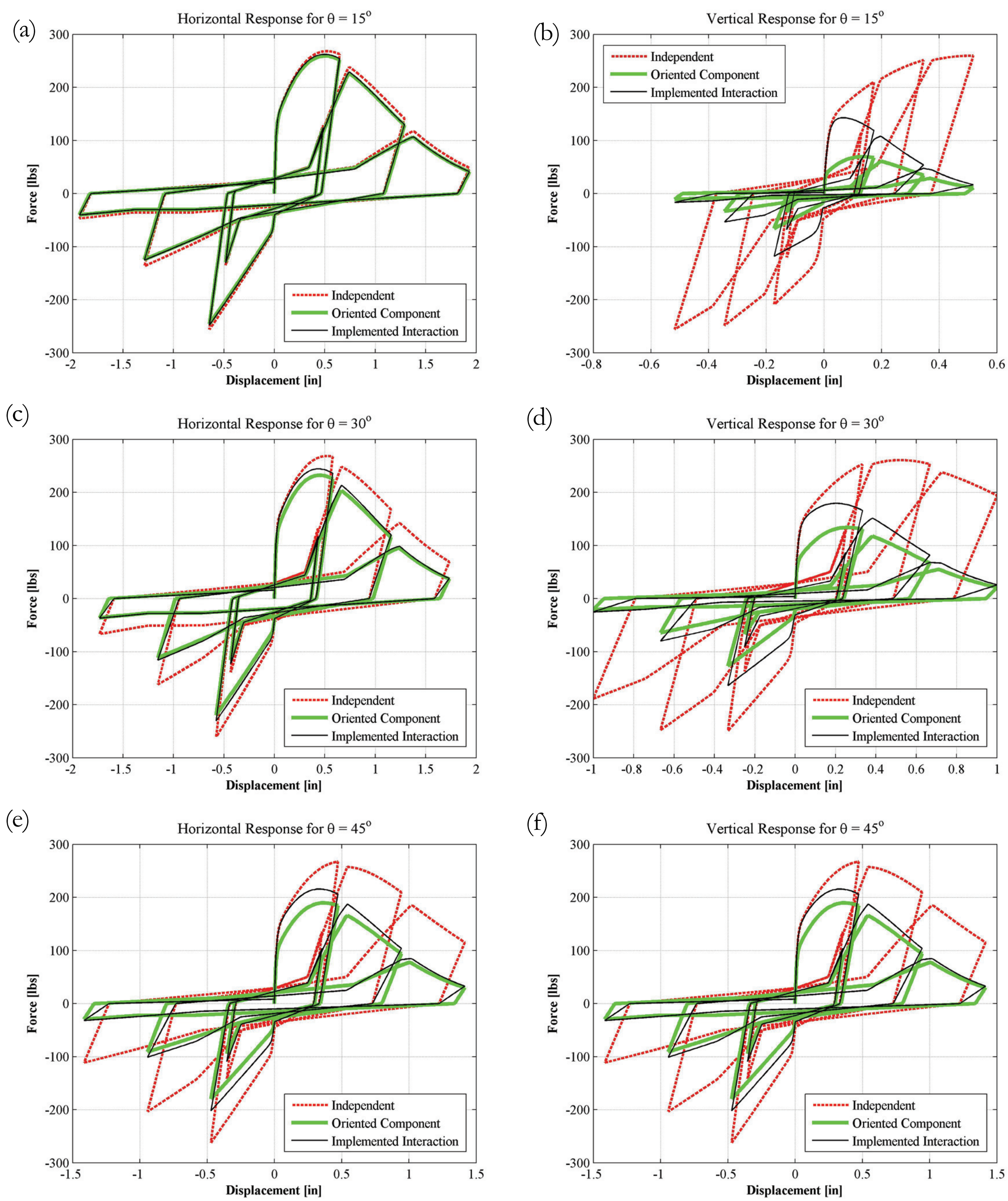

Figure 4.40 Vertical and Horizontal Hysteretic Responses of Connections for (a, b) θ = 15°, (c, d) θ = 30°, and (e, f) θ = 45°

Orientation of Orthogonal Springs

As discussed in Section 4.3.2.1, each pair of unidirectional orthogonal springs rotates with the associated framing node rotation θ_f, but the initial orientation angle θ_0 is an input variable. The typical option is to select $\theta_0 = 0$ for each connector element, aligning the springs to the global directions. Judd and Fonseca (2005) proposed an alternative approach to define the orientation angle of each connector element in a shear wall finite element analysis by orienting each pair of springs according to the initial trajectory of the given connector, computed under lateral loading. This approach is proposed on the basis that under lateral wall deformation each sheathing-to-framing connection deforms mainly along a single direction with a given angle with respect to the global directions. This was verified in a number of numerical analyses presented by Judd (2005), which demonstrated that the orientation of the springs resulted in a reduction of the post-elastic stiffness and the capping force of the backbone shear wall responses, compared to the non-oriented cases.

It is important to note that Judd and Fonseca (2005) assumed pinned connections between framing members and fixed sill plate to the ground in the numerical shear wall models. In this case, the axial and moment interaction in the shear response of the shear wall model is neglected and the only internal DOF is the differential lateral displacement between the top and bottom boundaries. This results in a single resisting mechanism that is independent of the gravity loads and the direction of loading[§]. If sheathing-to-framing connector elements are assumed to be linear elastic, the lateral response of the wall is also linear elastic for a small lateral differential displacement, so the computed initial angles are also unbiased by the amplitude of the imposed differential displacement. This fundamental behavior of a shear wall assembly is captured in the proposed numerical framework by the simplified **Pure Shear** formulation that considers pinned connections between rigid framing members and fixed boundaries to the base and floor diaphragms. Under this approach, a single-step analysis to determine the initial orientation of each connector can be executed by subjecting each shear wall element to an inter-story lateral displacement, constraining the 3 DOF of the bottom diaphragm, as well as the rotational DOF of the top diaphragm. The latter is selected to translate horizontally by 0.5% and vertically by -0.0012% of the wall height[**]. The sheathing-to-framing connector elements are simulated by a pair of linear elastic springs, which means that the response is equal to a single spring oriented to the trajectory of the connector. The initial angle θ_0 of each connector element is equal to the substraction of the rotation of the framing node θ_f from the actual orientation angle computed in the deformed configuration.

§ This means that for each connector element the absolute difference between the initial orientation angles computed for a positive and a negative lateral loading will be around 180 degrees.

** The vertical displacement is computed as (cos(arcsin(0.5/100)) – 1)*100% of the wall height

An analogous approach has not been implemented for a shear wall element described with the detailed **Model** formulation, which can simulate contact/separation effects between framing members and diaphragms, and capture axial, moment and shear deformations of the framing domain. In this case, the floor diaphragms of the building model translate in both directions and rotate in the wall plane when subjected to lateral loads, thus, the initial response of each shear wall element depends on the initial response of the whole building under a lateral force or displacement profile. Moreover, the fundamentally nonlinear elastic behavior of contact/separation phenomena leads to a system that can potentially demonstrate a nonlinear initial response, even if the sheathing-to-framing connections are linear elastic. For these reasons, the single-step analysis to determine the initial orientation of each connector in a shear wall element is executed using the simplified **Pure Shear** formulation independently of the formulation selected for the actual analysis (**Pure Shear** or **Model**). The effects of the spring orientation on the lateral response of a shear wall model are demonstrated in the following example.

4.3.5.4 Shear Wall Application Example for Investigation of Different Bidirectional Models

In order to demonstrate the effects of spring interaction and orientation on the lateral response of a shear wall, the numerical model of the single-story structure presented in the validation studies of Chapter 6 is used to perform a number of monotonic and cyclic pushover analyses. The prototype structure consists of an 8 ft long by 8 ft high shear wall that incorporates a single OSB panel, 4 ft by 8 ft, at the center. Edge and field nailing is specified at 6 in and 12 in oc. The structural configuration and the material properties used in the numerical analyses are presented in Section 6.2 and Section 6.3, respectively.

Pure Shear Formulation and No Gravity Loads

First, the **Pure Shear** formulation is employed to compute the monotonic as well as the cyclic response under the displacement protocol shown in Figure 4.41. Figure 4.42 illustrates the numerical model and indicates 4 connector elements that are monitored, in order to visualize their deformations in the wall plane. For this case, no gravity loads are applied to the floor diaphragm. All 4 different combinations, based on the consideration or not of the interaction and the orientation of each sheathing-to-framing connector, are analyzed and the results are illustrated in Figure 4.43.

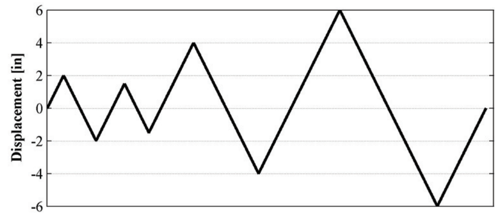

Figure 4.41 Cyclic Displacement Protocol Used in the Application Example

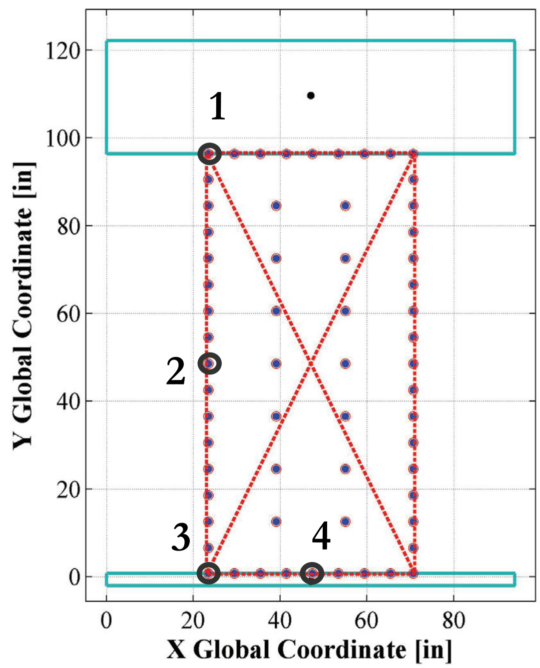

Figure 4.42 Numerical Model of the Application Example for **Pure Shear** Formulation and Indication of Monitored Connector Elements

The monotonic analysis results (Figure 4.43a) demonstrate that the spring orientation leads to a system that is more flexible in the post-elastic ascending regime, compared to the non-oriented case, and the capping force is lower, yet achieved at a greater displacement. These observations are consistent with the results presented by Judd and Fonseca (2005). The coupling interaction, when considered for the oriented case, results in a small reduction of the resisting forces in the descending regime of the backbone response past the capping point. This means that the connector elements deform primarily in the oriented directions until the system develops its maximum strength. The coupling interaction combined with the non-oriented case results in a small reduction of the capping force and the descending response converges to the response of the oriented case with interaction. The cyclic analysis results (Figure 4.43b) show that the pinching response is similar among the 4 cases and the differences are concentrated in the backbone loading curves, where the response is affected similarly to the monotonic analyses. Figure 4.43c and Figure 4.43d illustrate the initial deformed shape for a small positive and negative inter-story drift of 0.05%, respectively, for the case of no orientation or interaction. It can be observed that under both loading directions each connector deforms in the wall plane by the same amplitude but in opposite directions.

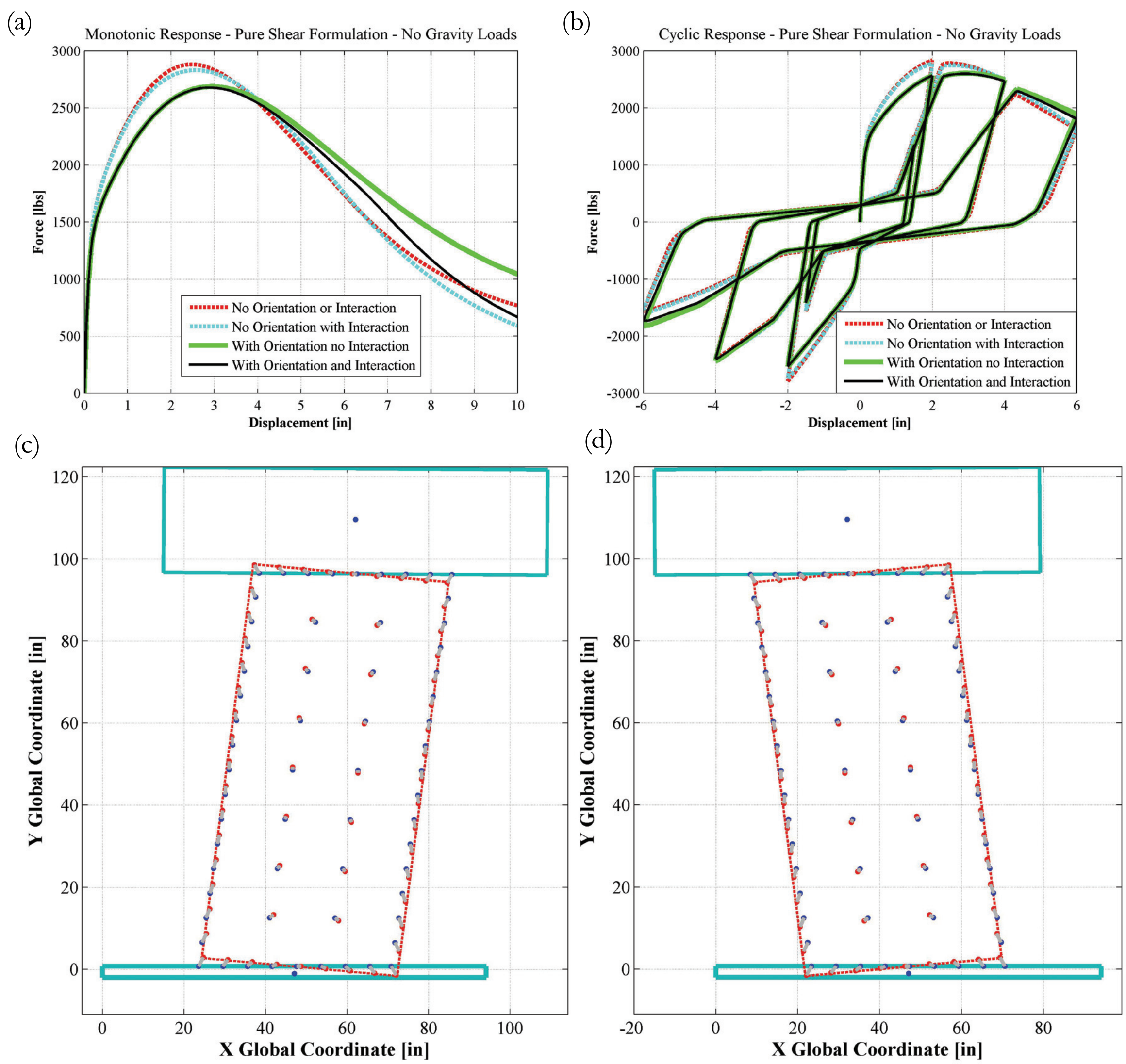

Figure 4.43 (a, b) Monotonic and Cyclic Pushover Results for **Pure Shear** Formulation and No Gravity Loads, and (c, d) Initial Deformed Shape of the Numerical Model for 0.05% Positive and Negative Inter-Story Drift

The global bidirectional displacement orbits of 4 connector elements (see Figure 4.42), extracted from the cyclic analyses, are illustrated in Figure 4.44, where each panel shows the orbits of a single connector computed under the 4 different analysis cases. The displacements are computed by substracting the global displacements of the sheathing node from the global displacements of the framing node.

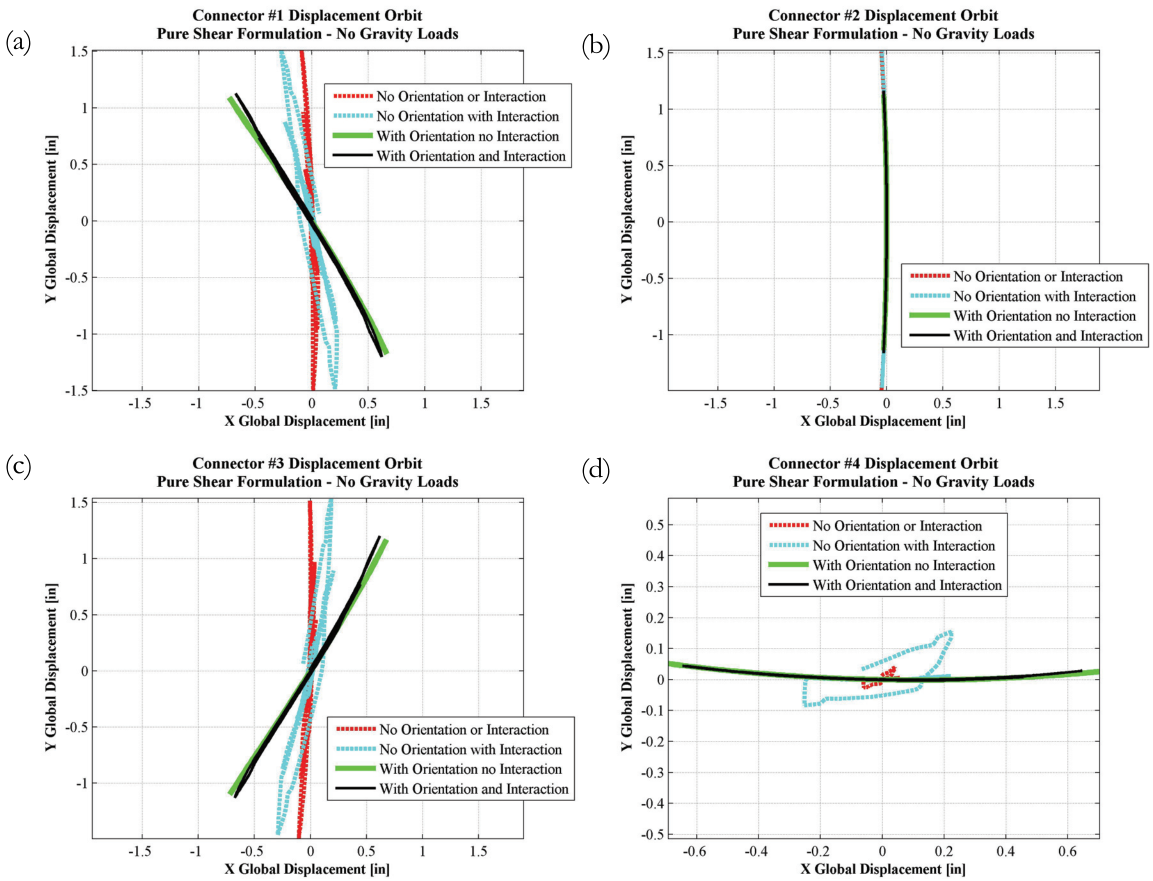

Figure 4.44 Displacement Orbits from Cyclic Analysis for **Pure Shear** Formulation and No Gravity Loads for (a) Connector #1, (b) Connector #2, (c) Connector #3, and (d) Connector #4

The results verify that the principal deformations of the oriented connectors are unidirectional. The non-oriented connectors follow modified orbits, compared to the oriented ones, with respect to the direction or the magnitude of the deformations. The interaction of non-oriented connectors results in modified directions that are closer to the oriented ones. Note that the initial trajectories for each connector are similar among the 4 cases but the actual trajectories of the non-oriented connectors are modified because of the alignment of all the connectors to zero initial angles. Since the global response of each connector depends on the initial orientation, a random selection should equally consider initial orientation angles between 0 and 45 degrees, which is the invariant radial span of a pair of orthogonal nonlinear springs.

Figure 4.45 shows the local bidirectional displacement orbits of the 4 connector elements, computed under the 4 different analysis cases. The local displacements are computed as a function of the orientation angle θ_0 and the framing rotation θ_f of each connector element, as shown in (4.2).

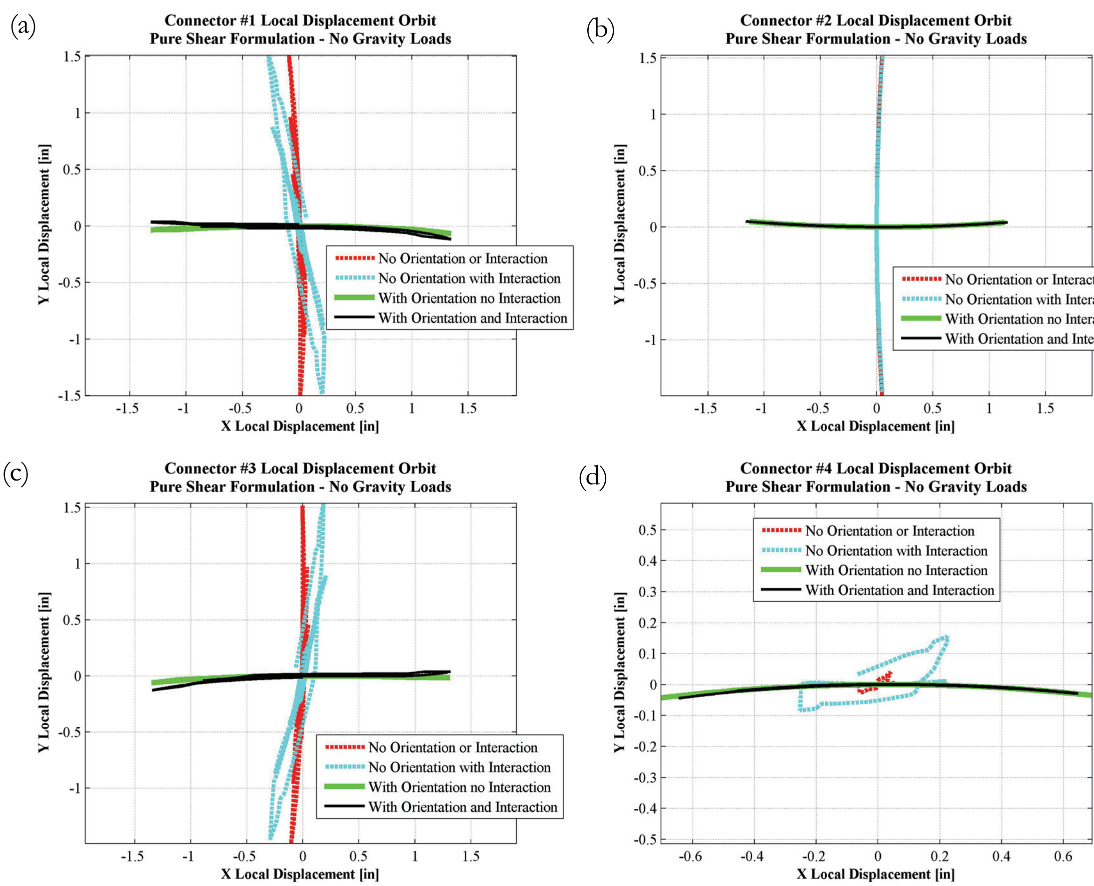

Figure 4.45 Local Displacement Orbits from Cyclic Analysis for **Pure Shear** Formulation and No Gravity Loads for (a) Connector #1, (b) Connector #2, (c) Connector #3, and (d) Connector #4

The local deformations of the oriented connectors lie principally along the local horizontal direction, which means that the initial orientation angles were correctly estimated a priori from the single-step orientation analysis.

Model Formulation and No Gravity Loads

For a second application, the detailed **Model** formulation is employed to compute the monotonic and cyclic responses for the same 4 analysis cases. This approach considers contact/separation effects between framing members and diaphragms, and captures axial, moment and shear deformations of the framing domain. Thus, the numerical model, shown in Figure 4.46, incorporates the specific anchorage conditions of the prototype structure, as described in Section 6.2. For this case, no gravity loads are applied to the floor diaphragm. The results are illustrated in Figure 4.47.

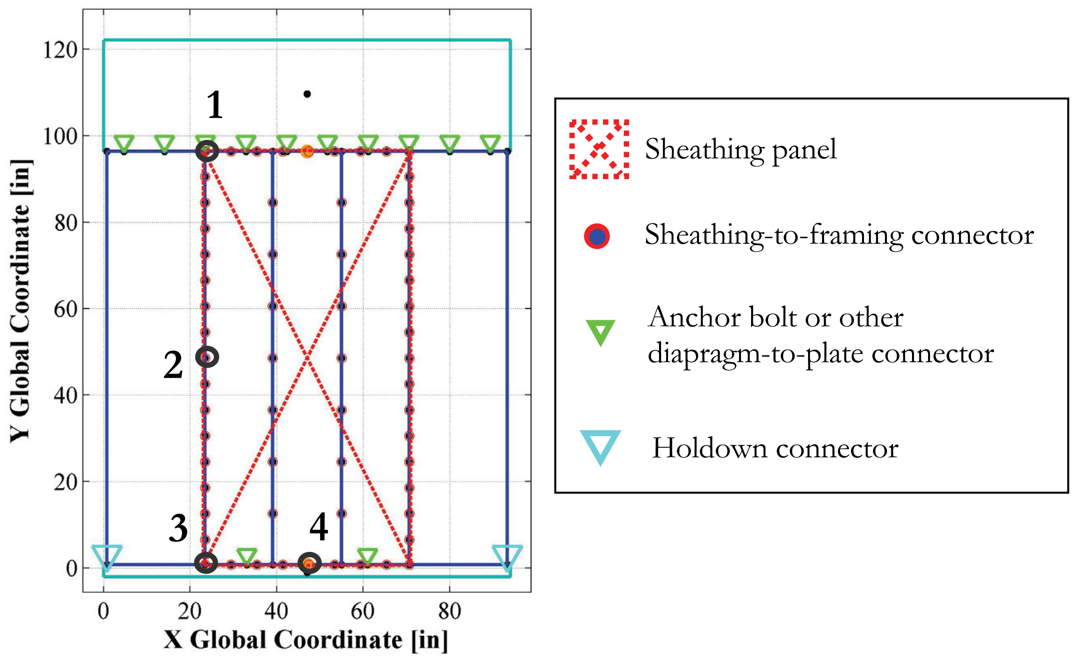

Figure 4.46 Numerical Model of the Application Example for **Model** Formulation and Indication of Monitored Connector Elements

The monotonic (Figure 4.47a) and cyclic (Figure 4.47b) analysis results show a different trend compared to the **Pure Shear** formulation, because both non-oriented models demonstrate lower resisting forces, compared to the oriented ones. The coupling interaction modifies the response of the oriented model, reducing the resisting forces and providing a better correlation with the non-oriented responses.

It is also observed that the capping forces among the 4 cases range below 1000 lbs, while with the **Pure Shear** formulation the capping forces were above 2500 lbs. This significant reduction in the shear, or lateral, resistance of the shear wall element is attributed to the inability of the axial and moment resisting mechanisms to provide the required boundary conditions for a racking deformation of the wall. Indeed, the initial deformed shapes, shown in Figure 4.47c and Figure 4.47d, illustrate that the floor diaphragm rotates and translates vertically as a result of a lateral load, thus, the existence of a gravity load would increase the resistance. Furthermore, the end wall stud under tension separates from the top plate because the tensile strength of plate-to-stud connections in the vertical direction is small and conservatively ignored in the numerical model. Since the holdowns are not located at the end studs of the sheathing panel, the panel and the associated vertical studs demonstrate a rocking response within the wall plane, while the sheathing-to-framing deformations are concentrated mainly along the sill and top plates.

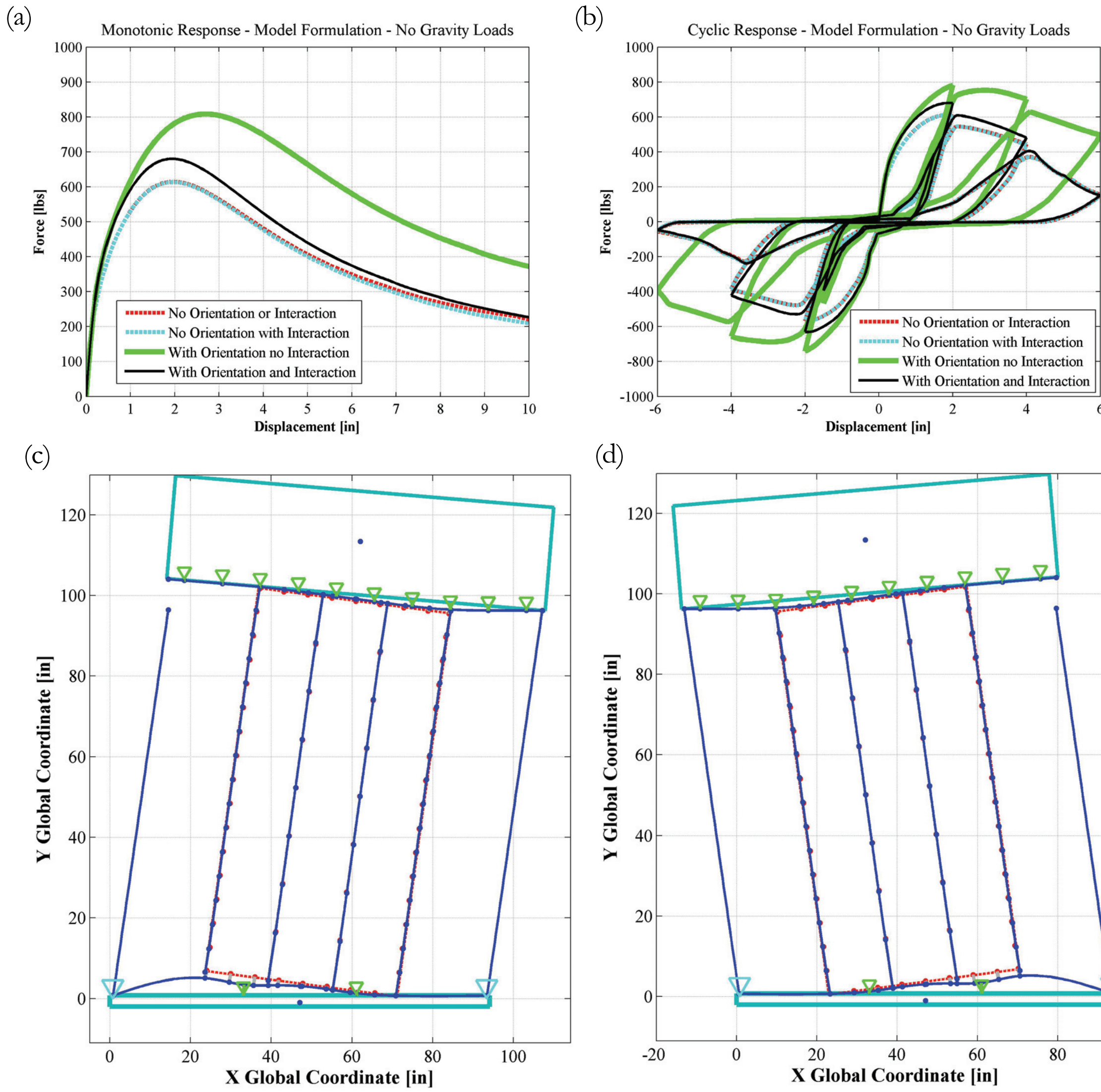

Figure 4.47 (a, b) Monotonic and Cyclic Pushover Results for **Model** Formulation and No Gravity Loads, and (c, d) Initial Deformed Shape of the Numerical Model for 0.05% Positive and Negative Inter-Story Drift

The global bidirectional displacement orbits of the 4 connector elements (see Figure 4.46), extracted from the cyclic analyses, are illustrated in Figure 4.48, where each panel shows the orbits of a single connector computed under the 4 different analysis cases.

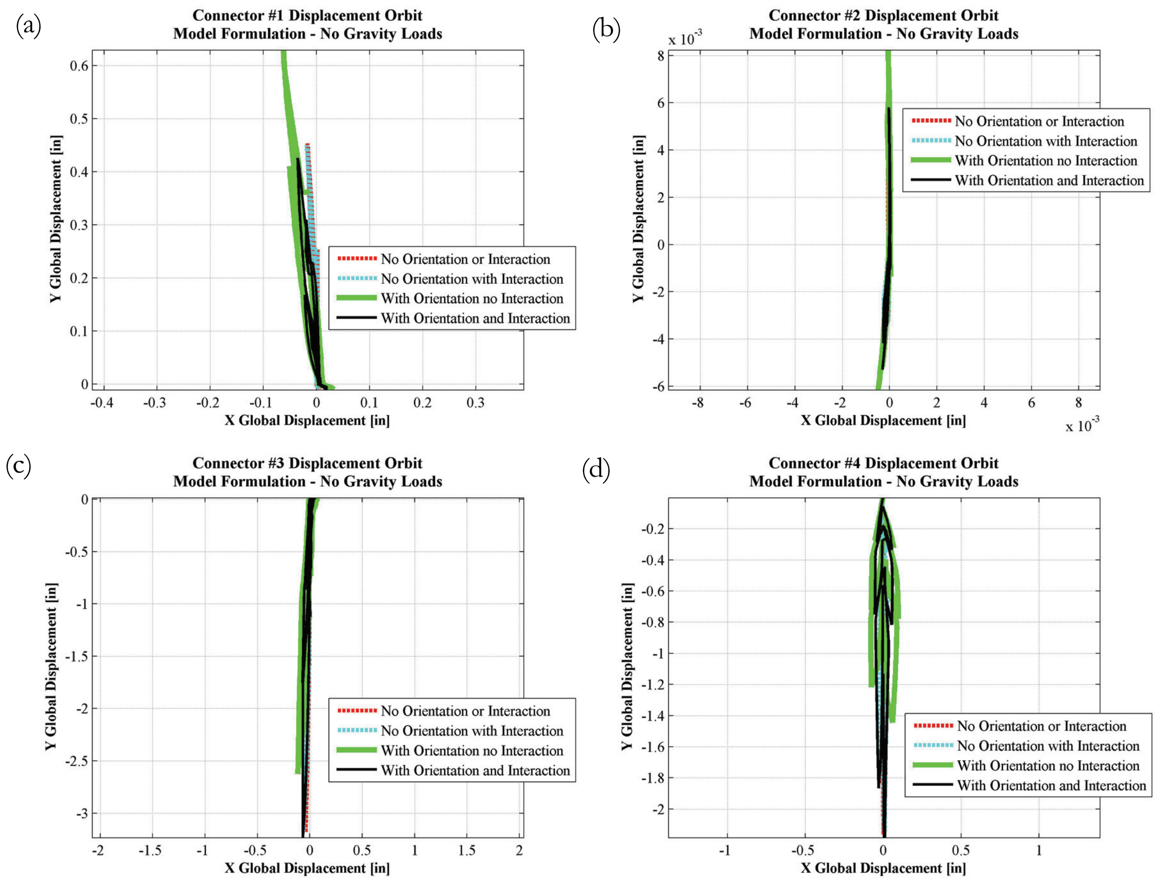

Figure 4.48 Displacement Orbits from Cyclic Analysis for **Model** Formulation and No Gravity Loads for (a) Connector #1, (b) Connector #2, (c) Connector #3, and (d) Connector #4

These plots clearly show that the principal deformations of all the connector elements are in the vertical direction. However, the deformations are not distributed along both positive and negative directions. The only exception applies to Connector #2, which is subjected to very small deformations because the vertical stud rotates with the sheathing panel. Connector #1 is mainly deformed under a negative lateral load, while Connector #3 is deformed under a positive lateral load. Connector #4 is deformed under both cases because of the rocking motion of the sheathing panel. These deformation characteristics pose challenges on the definition of a consistent approach to determine the initial orientation angles of connector elements with the **Model** formulation.

The local displacements orbits, illustrated in Figure 4.49, verify that the orientation angles computed from the **Pure Shear** formulation are not accurate, but the consideration of coupling interaction provides similar amplitudes of the deformations with the non-oriented models. So, the orientation and interaction of the connector elements did not modify their principal deformations compared to the non-oriented ones, but yielded higher resisting forces because the coupling interaction implemented does not completely eliminate the overestimation of the response compared to a single oriented spring, as shown earlier in Figure 4.40.

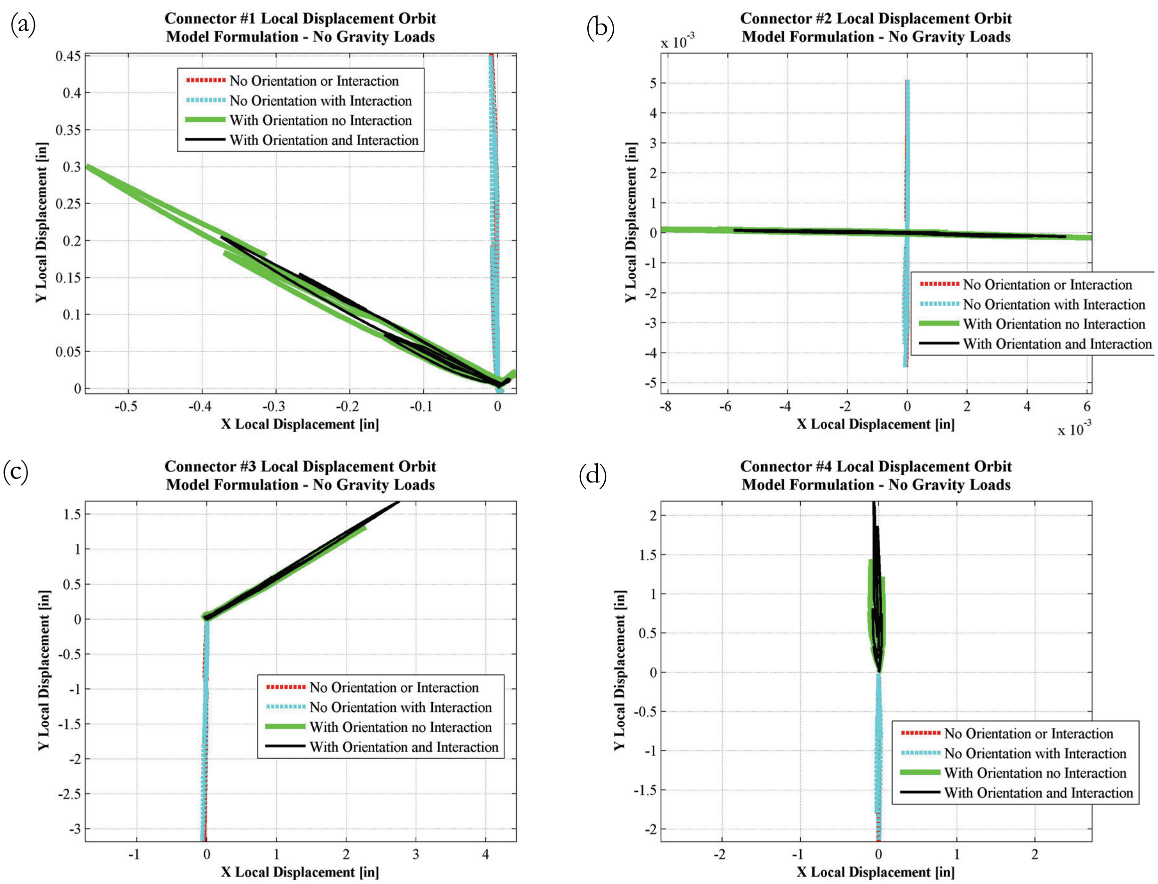

Figure 4.49 Local Displacement Orbits from Cyclic Analysis for **Model** Formulation and No Gravity Loads for (a) Connector #1, (b) Connector #2, (c) Connector #3, and (d) Connector #4

Model Formulation and Gravity Load of 6700 lbs

The third analysis case considers the **Model** formulation with the actual gravity load of the test specimen of 6700 lbs. This gravity load is applied initially in a separate nonlinear analysis case, which yields the initial conditions for the subsequent lateral displacement-controlled analysis. The same 4 different models are considered and the results are illustrated in Figure 4.50.

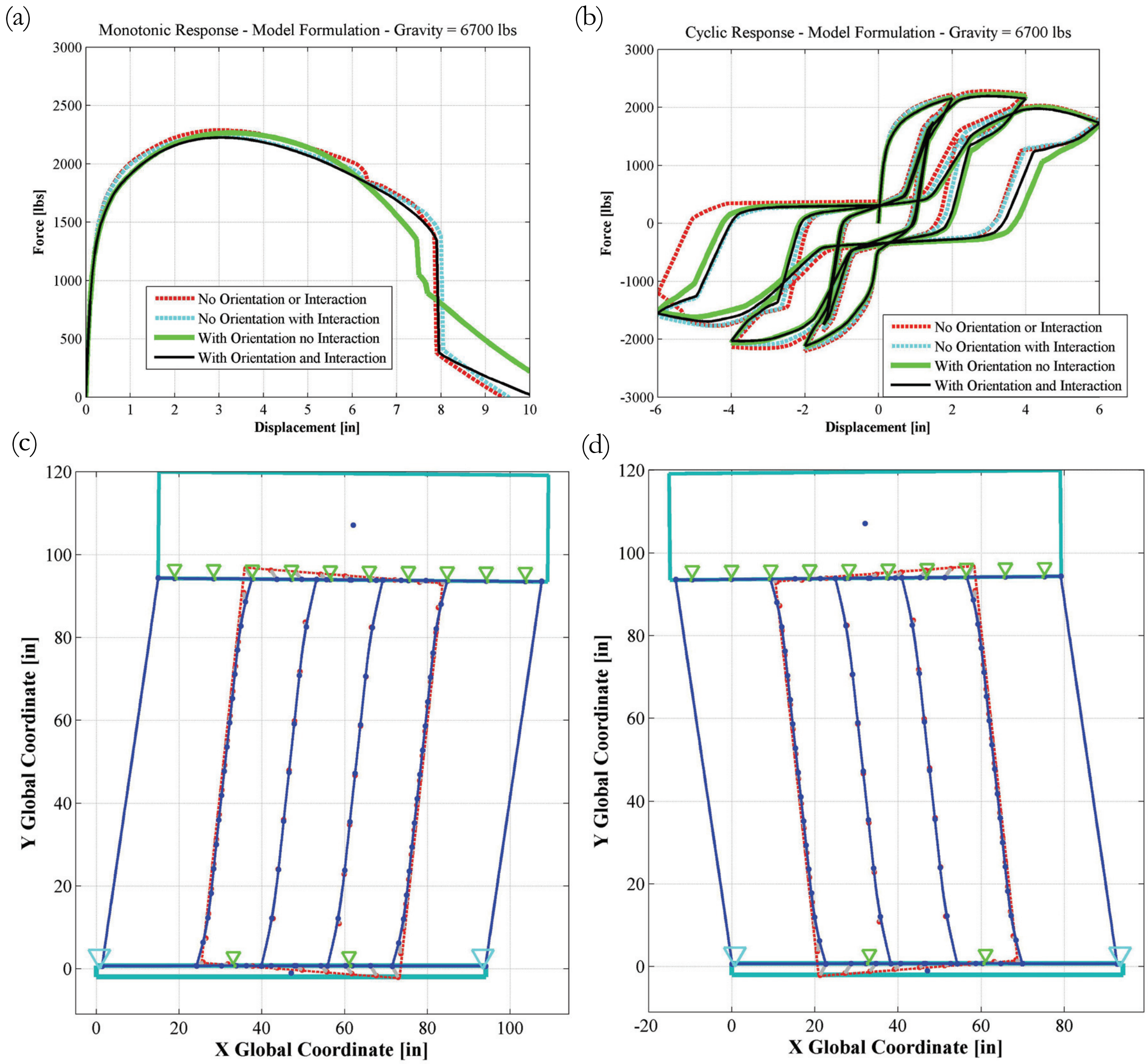

Figure 4.50 (a, b) Monotonic and Cyclic Pushover Results for **Model** Formulation and Gravity = 6700 lbs, and (c, d) Initial Deformed Shape of the Numerical Model for 0.05% Positive and Negative Inter-Story Drift

The responses from the monotonic (Figure 4.50a) and cyclic (Figure 4.50b) analyses are very similar among the 4 different models and the response for the connectors with orientation and interaction is the most conservative. The gravity load has contributed significantly to the improvement of the lateral response and the capping forces range above 2000 lbs. The initial deformed shapes, illustrated in Figure 4.50c and Figure 4.50d, demonstrate similar deformations to the **Pure Shear** formulation, with the addition of the bending deformations of the vertical framing members.

Figure 4.51 illustrates the global bidirectional displacement orbits of the monitored connector elements extracted from the cyclic analyses. The principal deformations of the oriented connectors are unidirectional, while the non-oriented connectors follow modified orbits, compared to the oriented ones. The interaction of non-oriented connectors results in modified directions that are closer to the oriented ones.

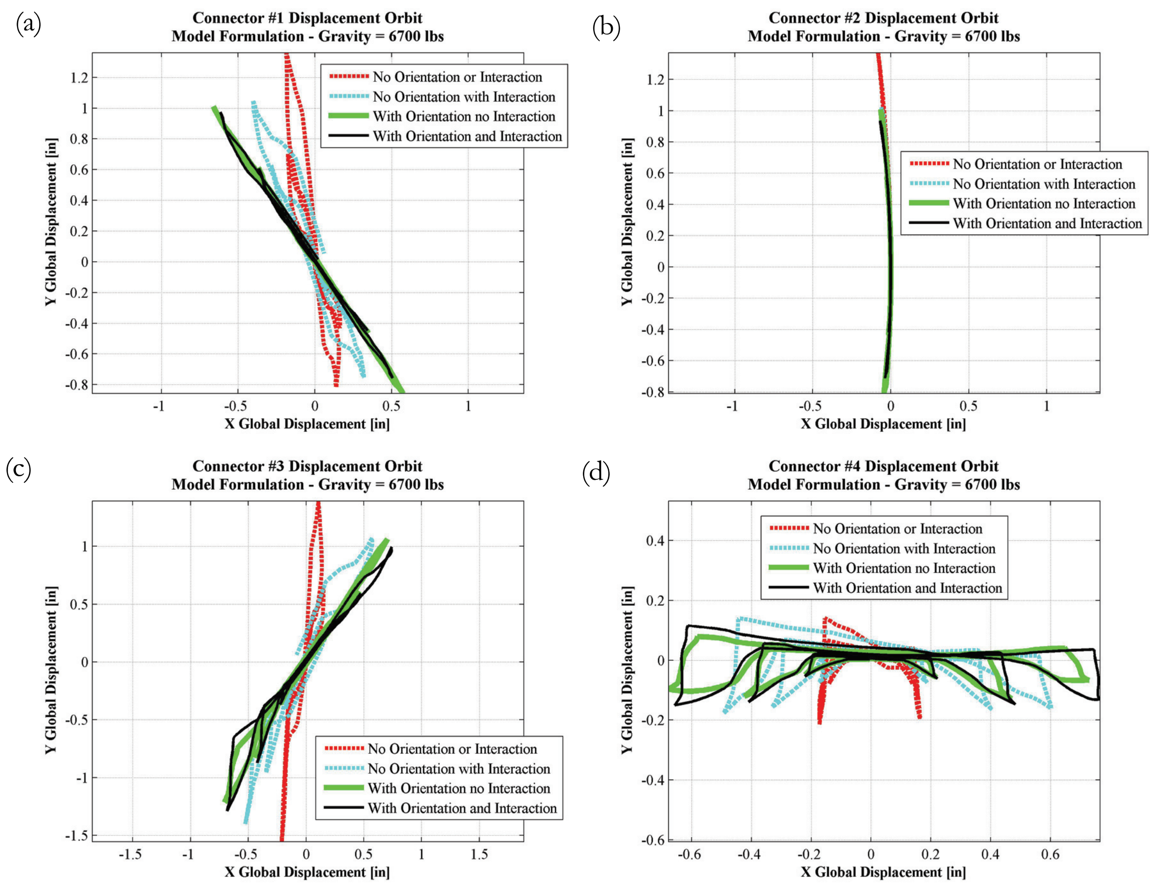

Figure 4.51 Displacement Orbits from Cyclic Analysis for **Model** Formulation and Gravity = 6700 lbs for (a) Connector #1, (b) Connector #2, (c) Connector #3, and (d) Connector #4

Figure 4.52 shows the local bidirectional displacement orbits of the 4 connector elements, computed under the 4 different analysis cases. The local deformations of the oriented connectors lie principally along the local horizontal direction, which means that the initial orientation angles were correctly estimated a priori from the single-step orientation analysis based on the **Pure Shear** formulation.

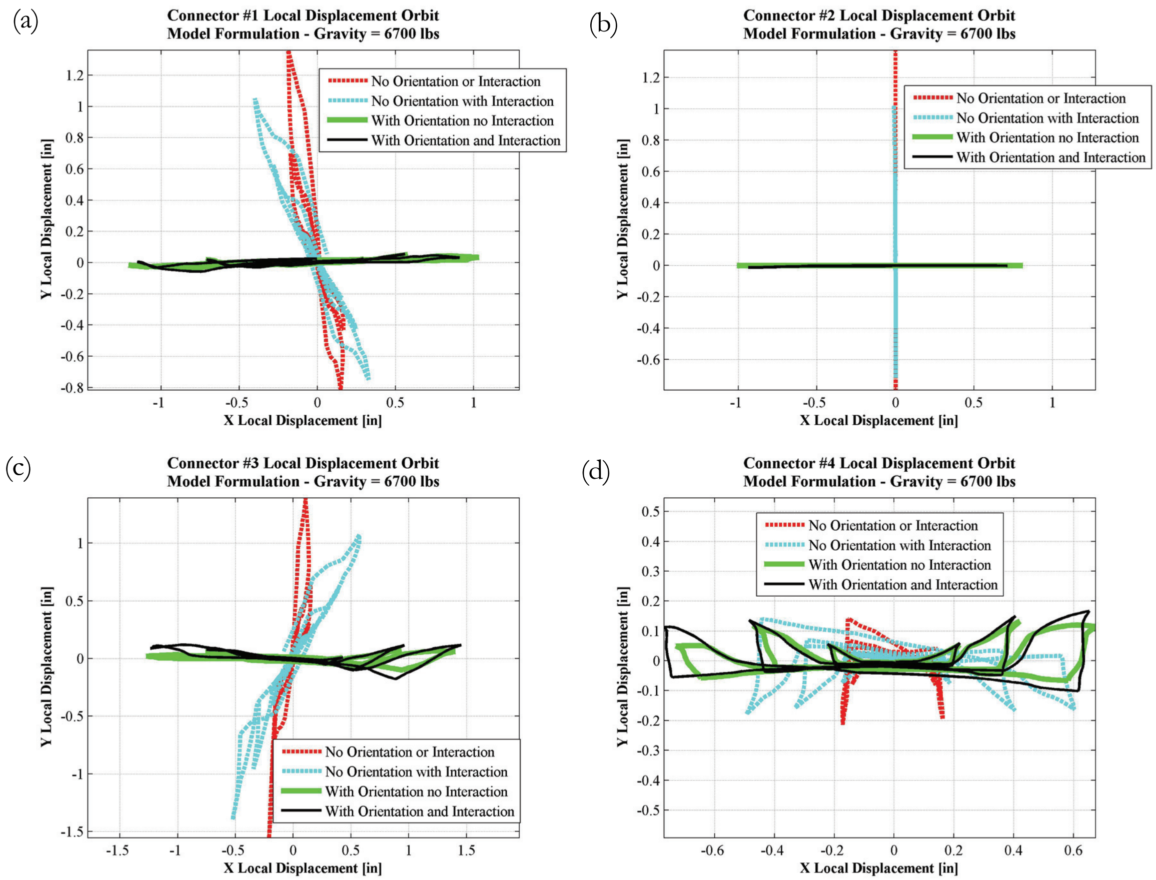

Figure 4.52 Local Displacement Orbits from Cyclic Analysis for **Model** Formulation and Gravity = 6700 lbs for (a) Connector #1, (b) Connector #2, (c) Connector #3, and (d) Connector #4

Summary

The consideration of the proposed coupling interaction between the pair of orthogonal nonlinear springs of each connector element results in more conservative lateral responses of the shear wall systems, compared to the independent pairs of springs with the same orientation angles. However, the coupling interaction does not completely eliminate the overestimation of the response, as shown for the **Model** formulation with no gravity loads. This is consistent with the results shown earlier in Figure 4.40. It is interesting to note that the non-oriented and oriented responses with coupling interaction have smaller differences in both the deformations of the connectors and the resisting forces with respect to the models without interaction. This indicates that the development of a coupling interaction approach that can favorably eliminate any overestimation of the response shown in Figure 4.40 for different orientation angles, will lead to the same shear wall responses independently of the initial orientation angles of the connector elements.

The orientation of the connector elements, according to the initial trajectories from an analysis that is based on the **Pure Shear** formulation, is consistently conservative when the **Pure Shear** formulation is used for the nonlinear analysis. In the case of the **Model** formulation, the effect depends on the overall structural characteristics of the shear wall system and the gravity loads.

4.4 Derivation and Solution of Equilibrium Equations of Two-Dimensional Models of Light-Frame Wood Structures under Dynamic/Seismic Loading Conditions

4.4.1 Formulation of a Building Model

This section describes the analytical derivations that involve the development of a finite element framework for the expression and solution of the dynamic equilibrium equations of a 2D model of a light-frame wood building. Having introduced in Section 4.3 the sub-structure model of each inter-story wood shear wall that leads to a 2-noded shear wall element, the procedure described herein is based on the existing knowledge of the formulation of numerical models for response-history nonlinear inelastic analysis in the time domain.

As shown in Figure 4.53, each rigid diaphragm is represented with one node with 3 DOF while a *k*-story building is represented by *k* number of sub-structure shear wall elements that are connected in series. The global stiffness matrix of the building model $\mathbf{K_{BM}}$ resources from the contributions of each shear wall element through the 6-by-6 stiffness matrix ${}^{i}\mathbf{K^{D}}_{\mathbf{W}}$, where the subscript i ranges from 1 to *k*. Assuming that the base diaphragm is fixed to the ground, the number of DOF $\mathbf{N_{DOF}}$ is:

$$\mathrm{N}_{\mathrm{DOF}} = 3 \cdot k \tag{4.181}$$

and the fist-story element contributes to the global stiffness matrix the lower right 3-by-3 submatrix of ${}^{1}\mathbf{K^{D}}_{\mathbf{W}}$. The stiffness matrix of each shear wall element is computed as shown in (4.91) or (4.141), depending on the two analysis options.

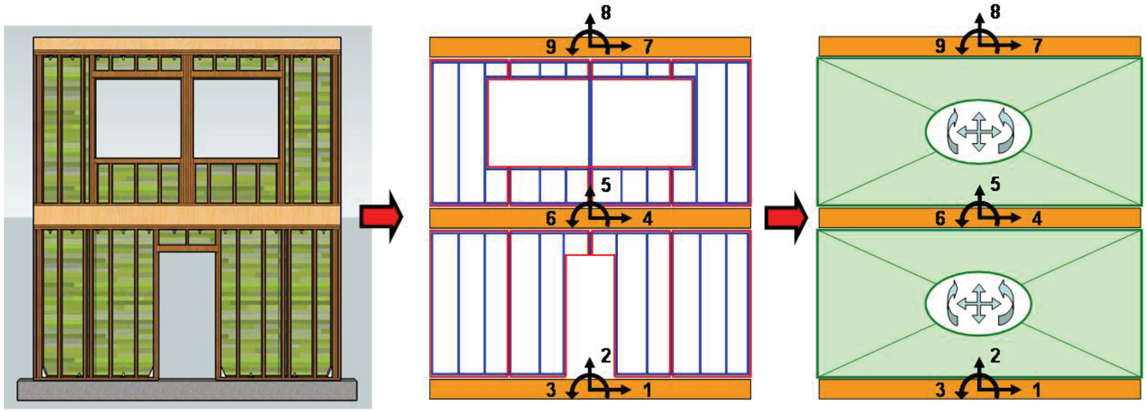

Figure 4.53 Illustration of Master DOF of a Building Model and Shear Wall Elements for the Simulation of Each Story

The global mass matrix $\mathbf{M_{BM}}$ is calculated from the floor masses that are explicitly assigned for each diaphragm. If m_i is the translational mass assigned to the ith floor, the 3-by-3 mass matrix ${}^{i}\mathbf{M}$ is equal to:

$$ {}^{i}\mathbf{M} = \begin{bmatrix} m_i & 0 & 0 \\ 0 & m_i & 0 \\ 0 & 0 & m_{rot,i} \end{bmatrix} \tag{4.182} $$

where

$$ m_{rot,i} = \frac{m_i}{12} \cdot \left(\left(L_W \right)^2 + \left(h_i \right)^2 \right) \tag{4.183} $$

and L_W is the length of the building model, while h_i is the thickness of the ith floor diaphragm.

The global damping matrix is formulated utilizing a Rayleigh damping scheme that considers the global damping matrix $\mathbf{C_{BM}}$ to be proportional to the mass and the initial stiffness global matrices of the numerical model:

$$ \mathbf{C_{BM}} = c_m \cdot \mathbf{M_{BM}} + c_k \cdot \mathbf{K_{BM}} \tag{4.184} $$

where c_m and c_k are scalar multipliers with units sec^{-1} and sec, respectively, that are computed based on the eigen-value analysis of the undamped structure. Using a classical damping matrix that retains the orthogonality properties with the eigen-vectors – or mode shapes – of the system provides a simple way to (i) assign the desired modal damping ratios ζ_1 and ζ_2 at two of the natural periods of the system T_1 and T_2, and (ii) estimate the damping ratios provided for every period of interest, based on the initial stiffness and mass matrices of the model.

It should be noted that the principal energy dissipation mechanism is provided by the hysteretic damping produced by the nonlinear inelastic response of sheathing-to-framing and diaphragm-to-framing connections. Therefore, the viscous damping properties are conceptually estimated based only on supplemental energy dissipating mechanisms in the structure, such as slippage and sliding friction between structural components. The modal damping ratios are considered in the majority of the research studies to range around 1-2% of critical, for the first and second natural modes of vibration.

The modal damping ratio ζ_i at each natural period T_i is given by:

$$\zeta_i = \frac{\mathbf{\Phi}_i^{T} \cdot \mathbf{C_{BM}} \cdot \mathbf{\Phi}_i}{2 \cdot \mathbf{\Phi}_i^{T} \cdot \mathbf{M_{BM}} \cdot \mathbf{\Phi}_i \cdot \left(2 \cdot \pi / T_i \right)} \Rightarrow$$

$$\zeta_i = \frac{c_m \cdot \mathbf{M}_i + c_k \cdot \mathbf{K}_i}{4 \cdot \pi \cdot \mathbf{M}_i} \cdot T_i \Rightarrow$$

$$\zeta_i = \frac{c_m}{4 \cdot \pi} \cdot T_i + \pi \cdot c_k \cdot \frac{1}{T_i} \tag{4.185}$$

where $\mathbf{\Phi}_i$ is the mode shape of the i^{th} mode and $\mathbf{M}_i$ and $\mathbf{K}_i$ the generalized mass and generalized stiffness, respectively. Provided that T_1 and T_2 are not equal, the multipliers needed to provide the desired ζ_1 and ζ_2 are given by:

$$\left.\begin{aligned} \zeta_1 &= \frac{c_m}{4 \cdot \pi} \cdot T_1 + \pi \cdot c_k \cdot \frac{1}{T_1} \\ \zeta_2 &= \frac{c_m}{4 \cdot \pi} \cdot T_2 + \pi \cdot c_k \cdot \frac{1}{T_2} \end{aligned}\right\} \Rightarrow$$

$$\begin{Bmatrix} c_m \\ c_k \end{Bmatrix} = \begin{bmatrix} \frac{T_1}{4\cdot\pi} & \frac{\pi}{T_1} \\ \frac{T_2}{4\cdot\pi} & \frac{\pi}{T_2} \end{bmatrix}^{-1} \cdot \begin{Bmatrix} \zeta_1 \\ \zeta_2 \end{Bmatrix} \Rightarrow$$

$$\left\{ \begin{aligned} c_m &= 4\pi \cdot \frac{T_2 \cdot \zeta_2 - T_1 \cdot \zeta_1}{(T_2)^2 - (T_1)^2} \\ c_k &= \frac{T_1 \cdot T_2 \cdot (T_2 \cdot \zeta_1 - T_1 \cdot \zeta_2)}{\pi \cdot \left((T_2)^2 - (T_1)^2\right)} \end{aligned} \right\} \tag{4.186}$$

4.4.2 Solution Algorithm of a Building Model under Dynamic Loading Conditions

This section summarizes the solution algorithm utilized to solve the dynamic equilibrium equations of a numerical building model under a prescribed base acceleration time history. The solution procedure is developed in the time domain and dynamic equilibrium is sought at discrete time instants with a constant time increment Δt. Equilibrium at each time instant $t = \tau$ is satisfied when external forces are equilibrated under the summation of inertial, viscous and internal forces:

$$\{\mathbf{F_{ext}}\}^{\tau} = \{\mathbf{F_{int}}\}^{\tau} + \mathbf{M_{BM}} \cdot \{\mathbf{A_{ABS}}\}^{\tau} + \mathbf{C_{BM}} \cdot \{\mathbf{V}\}^{\tau} \tag{4.187}$$

where $\{\mathbf{A_{ABS}}\}^{\tau}$ and $\{\mathbf{V}\}^{\tau}$ are the N_{DOF}-by-1 absolute acceleration and relative velocity vectors, respectively, of the numerical model. The absolute acceleration can be written as:

$$\{\mathbf{A_{ABS}}\}^{\tau} = \{\mathbf{A}\}^{\tau} + \{\mathbf{A_{GR}}\}^{\tau} = \{\mathbf{A}\}^{\tau} + \mathbf{r} \cdot \begin{Bmatrix} a_x \\ a_y \end{Bmatrix}^{\tau} \tag{4.188}$$

where $\{\mathbf{A}\}^{\tau}$ is the relative acceleration vector; a_x and a_y are the input ground accelerations in the respective global directions; $\mathbf{r}$ is a N_{DOF} -by-2 matrix that contains unit values at the first column along the rows of horizontal DOF and at the second column along the rows of vertical DOF. Combining (4.187) and (4.188) the equilibrium is written as:

$$\left\{\mathbf{F_{ext}}\right\}^{\tau} - \mathbf{M_{BM}} \cdot \mathbf{r} \cdot \begin{Bmatrix} a_x \\ a_y \end{Bmatrix}^{\tau} = \left\{\mathbf{F_{int}}\right\}^{\tau} + \mathbf{M_{BM}} \cdot \left\{\mathbf{A}\right\}^{\tau} + \mathbf{C_{BM}} \cdot \left\{\mathbf{V}\right\}^{\tau} \tag{4.189}$$

The equilibrium is sought at time t = τ + Δt and is expressed by:

$$\left\{\mathbf{F_{ext}}\right\}^{\tau+\Delta t} - \mathbf{M_{BM}} \cdot \mathbf{r} \cdot \begin{Bmatrix} a_x \\ a_y \end{Bmatrix}^{\tau+\Delta t} = \left\{\mathbf{F_{int}}\right\}^{\tau+\Delta t} + \mathbf{M_{BM}} \cdot \left\{\mathbf{A}\right\}^{\tau+\Delta t} + \mathbf{C_{BM}} \cdot \left\{\mathbf{V}\right\}^{\tau+\Delta t} \tag{4.190}$$

The internal forces and the tangent stiffness matrix of the building model follow a nonlinear inelastic material law and depend on the history of the displacement field – set of known parameters $\mathbf{Z}^{\tau}$ at the last equilibrium state - as well as on the element displacements at that time instant $\{\mathbf{D}\}^{\tau+\Delta t}$., as shown below:

$$\begin{Bmatrix} \left\{\mathbf{F_{int}}\right\}^{\tau+\Delta t} \rightarrow f\left(\left\{\mathbf{D}\right\}^{\tau+\Delta t}, Z^{\tau}\right) \\ \left[\mathbf{K_{BM}}\right]^{\tau+\Delta t} = \left.\dfrac{\partial \mathbf{F_{int}}}{\partial \mathbf{D}}\right|_{t=\tau+\Delta t} \rightarrow f\left(\left\{\mathbf{D}\right\}^{\tau+\Delta t}, Z^{\tau}\right) \\ Z^{\tau+\Delta t} \rightarrow f\left(\left\{\mathbf{D}\right\}^{\boldsymbol{\tau+\Delta t}}, \left\{\mathbf{F_{int}}\right\}^{\tau+\Delta t}, Z^{\tau}\right) \end{Bmatrix} \tag{4.191}$$

Utilizing the Newmark method (Newmark 1959) with numerical factors γ and β the relative velocities and displacements at t + Δt are given by:

$$\begin{aligned} \left\{\mathbf{V}\right\}^{\tau+\Delta t} &= \left\{\mathbf{V}\right\}^{\tau} + \Delta t \cdot \left(\left(1 - \gamma\right) \cdot \left\{\mathbf{A}\right\}^{\tau} + \gamma \cdot \left\{\mathbf{A}\right\}^{\tau+\Delta t}\right) \\ \left\{\mathbf{D}\right\}^{\tau+\Delta t} &= \left\{\mathbf{D}\right\}^{\tau} + \Delta t \cdot \left\{\mathbf{V}\right\}^{\tau} + \frac{1}{2} \cdot \Delta t^2 \cdot \left(\left(1 - 2\beta\right) \cdot \left\{\mathbf{A}\right\}^{\tau} + 2\beta \cdot \left\{\mathbf{A}\right\}^{\tau+\Delta t}\right) \end{aligned} \tag{4.192}$$

The relative acceleration vector $\{\mathbf{A}\}^{\tau+\Delta t}$ is computed from (4.192) based on $\{\mathbf{D}\}^{\tau+\Delta t}$ and the known equilibrium state at τ as:

$$\left\{\mathbf{D}\right\}^{\tau+\Delta t} - \left\{\mathbf{D}\right\}^{\tau} - \Delta t \cdot \left\{\mathbf{V}\right\}^{\tau} - \frac{1}{2} \cdot \Delta t^2 \cdot \left(1 - 2\beta\right) \cdot \left\{\mathbf{A}\right\}^{\tau} = \beta \cdot \Delta t^2 \cdot \left\{\mathbf{A}\right\}^{\tau+\Delta t} \Rightarrow$$

$$\left\{\mathbf{A}\right\}^{\tau+\Delta t} = \frac{1}{\beta \cdot \Delta t^2} \cdot \left(\left\{\mathbf{D}\right\}^{\tau+\Delta t} - \left\{\mathbf{D}\right\}^{\tau}\right) - \frac{1}{\beta \cdot \Delta t} \cdot \left\{\mathbf{V}\right\}^{\tau} - \left(\frac{1}{2\beta} - 1\right) \cdot \left\{\mathbf{A}\right\}^{\tau} \tag{4.193}$$

Similarly the relative velocity vector $\{\mathbf{V}\}^{\tau+\Delta t}$ is equal to:

$$\{\mathbf{V}\}^{\tau+\Delta t} = \frac{\gamma}{\beta\cdot\Delta t}\cdot\left(\{\mathbf{D}\}^{\tau+\Delta t} - \{\mathbf{D}\}^{\tau}\right) - \left(\frac{\gamma}{\beta} - 1\right)\cdot\{\mathbf{V}\}^{\tau} - \Delta t\cdot\left(\frac{\gamma}{2\beta} - 1\right)\cdot\{\mathbf{A}\}^{\tau} \quad (4.194)$$

The internal force vector $\{\mathbf{F_{int}}\}^{\tau+\Delta t}$ is approximated from a first order Taylor expansion as:

$$\{\mathbf{F_{int}}\}^{\tau+\Delta t} = \{\mathbf{F_{int}}\}^{\tau} + [\mathbf{K_{BM}}]^{\tau}\cdot\left(\{\mathbf{D}\}^{\tau+\Delta t} - \{\mathbf{D}\}^{\tau}\right) \quad (4.195)$$

Substituting (4.193), (4.194) and (4.195) into the equilibrium equation of (4.190) leads to a single-step prediction of the displacement increment $\Delta\mathbf{D}$:

$$\begin{aligned}
&\{\mathbf{F_{ext}}\}^{\tau+\Delta t} - \mathbf{M_{BM}}\cdot\mathbf{r}\cdot\begin{Bmatrix}\mathbf{a_x}\\ \mathbf{a_y}\end{Bmatrix}^{\tau+\Delta t} = \{\mathbf{F_{int}}\}^{\tau} + [\mathbf{K_{BM}}]^{\tau}\cdot\left(\{\mathbf{D}\}^{\tau+\Delta t} - \{\mathbf{D}\}^{\tau}\right) + \ldots \\
&\mathbf{M_{BM}}\cdot\left(\frac{1}{\beta\cdot\Delta t^2}\cdot\left(\{\mathbf{D}\}^{\tau+\Delta t} - \{\mathbf{D}\}^{\tau}\right) - \frac{1}{\beta\cdot\Delta t}\cdot\{\mathbf{V}\}^{\tau} - \left(\frac{1}{2\beta} - 1\right)\cdot\{\mathbf{A}\}^{\tau}\right) + \ldots \quad \Rightarrow \\
&\mathbf{C_{BM}}\cdot\left(\frac{\gamma}{\beta\cdot\Delta t}\cdot\left(\{\mathbf{D}\}^{\tau+\Delta t} - \{\mathbf{D}\}^{\tau}\right) - \left(\frac{\gamma}{\beta} - 1\right)\cdot\{\mathbf{V}\}^{\tau} - \Delta t\cdot\left(\frac{\gamma}{2\beta} - 1\right)\cdot\{\mathbf{A}\}^{\tau}\right)
\end{aligned}$$

$$\begin{aligned}
&\left([\mathbf{K_{BM}}]^{\tau} + \frac{1}{\beta\cdot\Delta t^2}\cdot\mathbf{M_{BM}} + \frac{\gamma}{\beta\cdot\Delta t}\cdot\mathbf{C_{BM}}\right)\cdot\{\Delta\mathbf{D}\} = \ldots \\
&\{\mathbf{F_{ext}}\}^{\tau+\Delta t} - \mathbf{M_{BM}}\cdot\mathbf{r}\cdot\begin{Bmatrix}a_x\\ a_y\end{Bmatrix}^{\tau+\Delta t} - \Big\{\ \{\mathbf{F_{int}}\}^{\tau} + \ldots \\
&\mathbf{M_{BM}}\cdot\left(-\frac{1}{\beta\cdot\Delta t}\cdot\{\mathbf{V}\}^{\tau} - \left(\frac{1}{2\beta} - 1\right)\cdot\{\mathbf{A}\}^{\tau}\right) + \ldots \\
&\mathbf{C_{BM}}\cdot\left(-\left(\frac{\gamma}{\beta} - 1\right)\cdot\{\mathbf{V}\}^{\tau} - \Delta t\cdot\left(\frac{\gamma}{2\beta} - 1\right)\cdot\{\mathbf{A}\}^{\tau}\right)\ \Big\}
\end{aligned} \quad (4.196)$$

Since the response of the system is nonlinear, a Newton-Raphson iterative procedure, which drives the load imbalance to zero, is utilized to define the equilibrium state. Each iteration is denoted with an index j where j = {1,2,3,…} and any quantities found at that iteration carry the subscript j. Quantities specifying initial conditions of the iterations carry the subscript j-1.

Initiation of Solution Step

Before the beginning of the iterations the following assignments are made.

$$\left\{\begin{array}{l} \mathbf{F_{ext}} = \{\mathbf{F_{ext}}\}^{\tau+\Delta t} - \mathbf{M_{BM}} \cdot \mathbf{r} \cdot \begin{Bmatrix} a_x \\ a_y \end{Bmatrix}^{\tau+\Delta t} \\ \{\mathbf{F_{int}}\}_0 = \{\mathbf{F_{int}}\}^{\tau} \\ [\mathbf{K_{BM}}]_0 = [\mathbf{K_{BM}}]^{\tau} \\ \{\mathbf{D}\}_0 = \{\mathbf{D}\}^{\tau} \\ \{\mathbf{V}\}_0 = \{\mathbf{V}\}^{\tau} \\ \{\mathbf{A}\}_0 = \{\mathbf{A}\}^{\tau} \\ \mathbf{Z} = \mathbf{Z}^{\tau} \end{array}\right\} \tag{4.197}$$

Iterative Solution

Invoking (4.196) in an incremental form the displacement increment $\{\Delta\mathbf{D}\}_j$ is found and added to the current displacement vector $\{\mathbf{D}\}_{j\text{-}1}$. The dynamic tangent stiffness matrix $[\mathbf{K_D}]_{\mathbf{j\text{-}1}}$ is equal to:

$$[\mathbf{K_D}]_{j\text{-}1} = [\mathbf{K_{BM}}]_{j\text{-}1} + \frac{1}{\beta \cdot \Delta t^2} \cdot \mathbf{M_{BM}} + \frac{\gamma}{\beta \cdot \Delta t} \cdot \mathbf{C_{BM}} \tag{4.198}$$

The load imbalance $\{\mathbf{LI}\}_{j\text{-}1}$ at the initiation of the iteration is:

$$\{\mathbf{LI}\}_{j\text{-}1} = \mathbf{F_{ext}} - \{\mathbf{F_{int}}\}_{j\text{-}1} - \mathbf{M_{BM}} \cdot \{\mathbf{A}\}_{j\text{-}1} - \mathbf{C_{BM}} \cdot \{\mathbf{V}\}_{j\text{-}1} \tag{4.199}$$

The displacement iterative increment is:

$$\{\Delta\mathbf{D}\}_j = \left([\mathbf{K_D}]_{j\text{-}1}\right)^{-1} \cdot \{\mathbf{LI}\}_{j\text{-}1} \tag{4.200}$$

$$\{\mathbf{D}\}_j = \{\mathbf{D}\}_{j\text{-}1} + \{\Delta\mathbf{D}\}_j \tag{4.201}$$

Based on the new displacement vector and the parameters **Z** that correspond to the equilibrium state at t = τ, the new internal force vector and the new tangent stiffness matrix are computed, as shown in (4.191).

$$\begin{aligned} &\{\mathbf{F_{int}}\}_j \;\rightarrow f\left(\{\mathbf{D}\}_j,\, Z\right) \\ &[\mathbf{K_{BM}}]_j \;\rightarrow f\left(\{\mathbf{D}\}_j,\, Z\right) \\ &Z_j \;\rightarrow f\left(\{\mathbf{D}\}_j,\, \{\mathbf{F_{int}}\}_j,\, Z\right) \end{aligned} \tag{4.202}$$

Additionally, the relative velocity and acceleration vectors are computed based on (4.193) and (4.194):

$$\begin{aligned} \{\mathbf{V}\}_j &= \frac{\gamma}{\beta\cdot\Delta t}\cdot\left(\{\mathbf{D}\}_j - \{\mathbf{D}\}^{\tau}\right) - \left(\frac{\gamma}{\beta} - 1\right)\cdot\{\mathbf{V}\}^{\tau} - \Delta t\cdot\left(\frac{\gamma}{2\beta} - 1\right)\cdot\{\mathbf{A}\}^{\tau} \\ \{\mathbf{A}\}_j &= \frac{1}{\beta\cdot\Delta t^2}\cdot\left(\{\mathbf{D}\}_j - \{\mathbf{D}\}^{\tau}\right) - \frac{1}{\beta\cdot\Delta t}\cdot\{\mathbf{V}\}^{\tau} - \left(\frac{1}{2\beta} - 1\right)\cdot\{\mathbf{A}\}^{\tau} \end{aligned} \tag{4.203}$$

The load imbalance $\{\mathbf{LI}\}_j$ can now be computed as:

$$\{\mathbf{LI}\}_j = \mathbf{F_{ext}} - \{\mathbf{F_{int}}\}_j - \mathbf{M_{BM}}\cdot\{\mathbf{A}\}_j - \mathbf{C_{BM}}\cdot\{\mathbf{V}\}_j \tag{4.204}$$

Convergence is satisfied when the load imbalance $\{\mathbf{LI}\}_j$ is sufficiently small according to a selected norm of $\{\mathbf{LI}\}_j$ and a specified tolerance ε. The Euclidean norm is selected to compute the length of the imbalance force between all the global active DOF and apply the convergence criterion. Convergence is satisfied when:

$$\left\|\{\mathbf{LI}\}_j\right\| = \left(\{\mathbf{LI}\}_j^{T}\cdot\{\mathbf{LI}\}_j\right)^{1/2} \;\leq\; |\varepsilon| \tag{4.205}$$

Initiation of Successive Iterations

If the convergence criterion is not satisfied, iterations are performed carrying out (4.198) to (4.204) until (4.205) is valid. $\{\mathbf{LI}\}_j$ is the driving force of the successive iteration when j → j+1. (4.196) can now be written as:

$$\left(\left[\mathbf{K_D}\right]_{j\text{-}1}\right)\cdot\left\{\Delta\mathbf{D}\right\}_j = \mathbf{F_{ext}} - \left\{\mathbf{F_{int}}\right\}_{j\text{-}1} - \mathbf{M_{BM}}\cdot\left\{\mathbf{A}\right\}_{j\text{-}1} - \mathbf{C_{BM}}\cdot\left\{\mathbf{V}\right\}_{j\text{-}1}$$

End of the Solution Step

When convergence is satisfied, the equilibrium state has been defined at t = $\tau+\Delta t$ such as:

$$\left\{\begin{array}{l}\left\{\mathbf{D}\right\}^{\tau+\Delta t} = \left\{\mathbf{D}\right\}_j \\ \left\{\mathbf{A}\right\}^{\tau+\Delta t} = \left\{\mathbf{A}\right\}_j \\ \left\{\mathbf{V}\right\}^{\tau+\Delta t} = \left\{\mathbf{V}\right\}_j \\ \left[\mathbf{K_{BM}}\right]^{\tau+\Delta t} = \left[\mathbf{K_{BM}}\right]_j \\ \left\{\mathbf{F_{int}}\right\}^{\tau+\Delta t} = \left\{\mathbf{F_{int}}\right\}_j \\ \mathbf{Z}^{\tau+\Delta t} = \mathbf{Z}_j \end{array}\right\} \tag{4.206}$$

The solution of the next time step can be executed based on the new equilibrium state found at the current solution step.

4.5 Summary of the Proposed Numerical Framework

This chapter introduces a numerical framework for the nonlinear inelastic, static and dynamic analysis of light-frame wood buildings. The numerical formulation addresses the two-dimensional (2D) in-plane response of inter-story light-frame wood shear walls that incorporate single-sided sheathing panels, which are the structural elements considered in the seismic design. Considering each inter-story shear wall assembly as a single sub-structure element with internal nonlinear DOF, a 2D building model is formulated that represents a vertical continuous wall diaphragm of a prototype building. This is the first fundamental step towards the three-dimensional analysis of complete light-frame wood buildings with additional non-structural components.

The 2D building model is based on a sub-structuring approach that considers each floor diaphragm as rigid body with 3 kinematic and potentially dynamic degrees-of-freedom (DOF) in the vertical plane. A sub-structure element is developed for each individual single-story wall assembly that interacts with the adjacent diaphragms, above and below, and generates the resisting quasi-static internal forces. Utilizing floor diaphragms as boundary elements of the sub-structures developed for each story allows simulation of other modes of deformation (i.e. flexural and rocking modes), with due consideration of the interaction effects between shear walls and floor diaphragms.

The 2D shear wall model consists of a number of finite elements developed to simulate the structural components, such as sheathing panels, framing members and inter-component connections. Sheathing panels are described with 4 generalized DOF and linear elastic behavior while sheathing-to-framing connections are described with two orthogonal coupled phenomenological springs that exhibit pinching, strength deterioration and stiffness degradation. Each orthogonal pair of springs representing a single sheathing-to-framing connection is rotated according to the initial trajectory computed under infinitesimal lateral wall deformation. The proposed shear wall element enables the analyst to select between a simplified and a detailed formulation to describe the wood framing components. In the former case, referred as **Pure Shear** formulation, framing is assumed rigid and pin-connected and is considered to be rigidly attached to the floor diaphragms. In the latter case, referred as **Model** formulation, framing members are represented with linear elastic beam elements with axial and flexural behavior using centre-line modelling of each individual framing component. This approach offers the option to simulate contact/separation phenomena between vertical studs and horizontal plates, contact/separation phenomena between horizontal plates and diaphragms, as well as anchoring connections between framing and diaphragms (i.e. anchor bolts, holdowns), typically installed in light-frame shear walls to develop a vertical load path that resists overturning moments. The use of corotational descriptions of the displacement fields of the finite elements implemented in the proposed numerical framework accounts for geometric nonlinearity associated with large rotations and for P-Δ effects due to gravity loads, assuming small deformations of the structural members that remain linear elastic, such as the individual framing members and the sheathing panels. These attributes result in a nonlinear element that satisfies equilibrium in the deformed configuration and is capable of capturing the lateral response of shear walls up to their complete failure and, thus, the side-sway collapse of the structure.

Validation of the numerical framework with experimental testing data from full-scale specimen is presented in the next two chapters.

CHAPTER 5: MODEL VALIDATION FOR STATIC, MONOTONIC AND CYCLIC ANALYSIS

5.1 Introduction

This chapter presents two validation examples that attempt to demonstrate the potential of the proposed numerical framework to better predict the response of light-frame shear walls or wall assemblies under lateral quasi-static monotonic or cyclic loading. Test data from various shear wall tests, conducted by Pardoen *et al.* (2003), have been used to compare numerical predictions and experimental responses at a global level (i.e. inter-story response) as well as at a local level (i.e. end-post uplift and holdown response) when possible. Two numerical predictions are illustrated throughout the various figures. One is labeled **Pure Shear** and represents the simplified numerical model described in Section 4.3.2 that considers nonlinear inelastic action solely at the sheathing-to-framing connections, assuming a pure kinematic distortion of rigid framing members and fixed plate-to-diaphragm boundary conditions. The second prediction is labeled **Model** and represents the numerical model described in Section 4.3.3 that accounts for framing flexibility and nonlinear phenomena between framing members and diaphragms.

5.2 Example 1: Single-Story Shear Walls

The selected experimental data for this first example have been generated by Pardoen *et al.* (2003) within the CUREe-Caltech Woodframe Project. As part of this experimental task, 26 groups of single-story light-frame shear walls, with the same dimensions but various structural and material configurations, were tested under monotonic and cyclic displacement-controlled protocols.

5.2.1 Test Specimens

The wall dimensions of all specimens were equal to 16 ft long by 8 ft high, while 3 different configurations were considered, as shown in Figure 5.1. The first configuration consisted of four panels forming a Fully Sheathed (FS) wall, while the second configuration incorporated a door opening in the center of the wall and is denoted as a Pedestrian Door (PD) wall. The last configuration incorporated a Garage Door (GD) with one wall segment at each end with a relatively high Aspect Ratio (AR), defined as the height-to-length ratio, of 2.5. Each of the 3 groups consisted of 3 identical specimens. One specimen was tested under monotonic loading and the remaining two specimens were tested under cyclic loading using the CUREe loading protocol (Krawinkler *et al.* 2003). The framing consisted of nominal 2x4 studs spaced at 16 in on center (oc). The lumber used for framing was Douglas-Fir Number 1 or better. The top plate and the vertical studs with holdown devices consisted of two framing members. The sheathing provided was Oriented Strand Board (OSB), 3/8 in thick. Sheathing panels were fastened to the framing with 8d box gun nails, 2.5 in long with 0.113 in diameter. Edge nailing was specified at 6 in oc for the FS and PD configurations and at 3 in oc for the GD wall. Field nailing was specified at 12 in oc for all specimens.

Table 5.1 tabulates design parameters, such as the lateral ASD capacity and the uplifting design force, for the investigated shear walls. The AR adjustment factor, adopted in recent design codes (IBC 2006) to reduce the design strength of wall segments with AR higher than 2, is equal to 0.8 for GD wall, indicating a reduction in design strength of 20%.

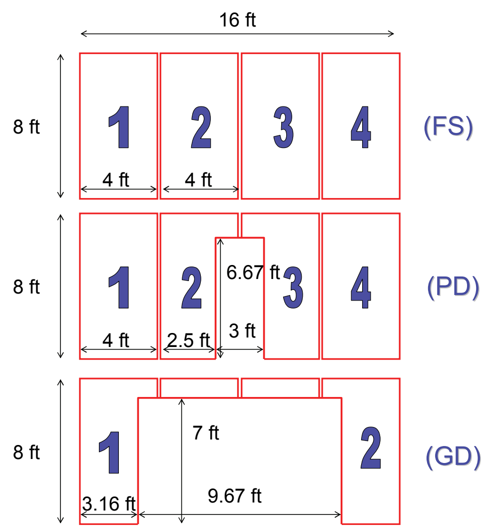

Figure 5.1 Geometric and Panel Configurations of the Shear Walls Simulated in Example 1

5.2.2 Test Setup

The testing configuration was designed to provide *(i)* in-plane loading and support conditions only at the framing members, *(ii)* capability to develop in-plane vertical deformations, and *(iii)* overall stability along the out-of-plane horizontal direction. An elevation view of the test setup is presented in Figure 5.2. Two steel channel beams were used at the base and the top of the wall specimens to simulate the diaphragm boundary conditions. The base steel beam was attached to the laboratory strong floor through bolted and welded connections to provide a rigid reaction boundary, while the framing was connected with anchor bolts and holdown devices, welding the bolts on the steel beam. The top steel beam, a MC10x28.5 channel, was attached to the double top plate of the wall with 3/8 in diameter lag screws spaced at 6 in. The racking shear forces were applied to the steel beam with a 50 kips capacity hydraulic actuator (see Figure 5.2).

Table 5.1 Design Parameters for Investigated Shear Walls in Example 1

Wall Configuration	**FS**	**PD**	**GD**
Aspect Ratio	8/16 = 0.5	8/6.5 = 1.23	8/3.16 = 2.53
No. of Segments	1	2	2
Nailing Schedule	Edge Nailing @ 6 in oc Field Nailing @ 12 in oc		Edge Nailing @ 3 in oc Field Nailing @ 12 in oc
ASD Capacity (force per length)	260 plf		490 plf
Aspect Ratio Adjustment Factor	1	1	2·3.16/8 = 0.8
ASD Capacity (force - including aspect ratio adjustment factor and number of segments)	260·16·1·1 = 4160 lbs	260·6.5·1·2 = 3380 lbs	490·3.16·0.8·2 = 2462 lbs
Uplifting Design Force	260·8 = 2080 lbs		490·8 = 3920 lbs

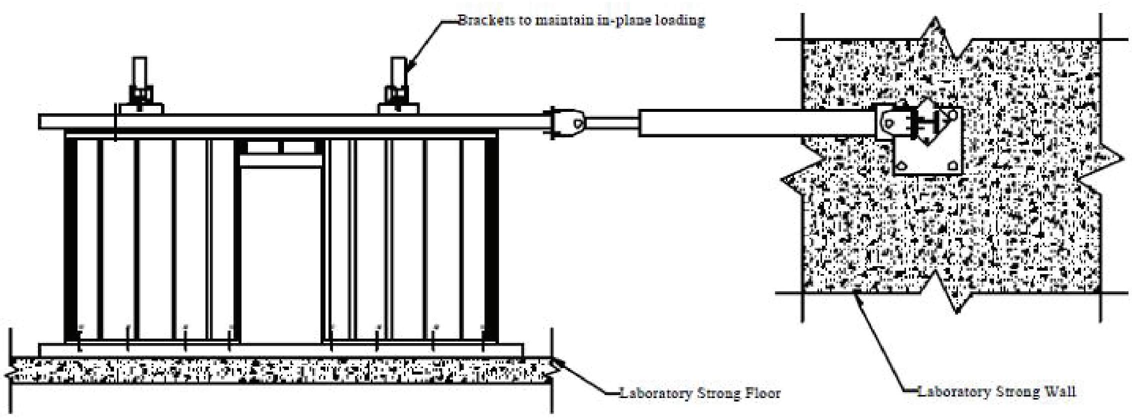

Figure 5.2 Elevation View of Test Setup (from Pardoen *et al.* 2003)

5.2.3 Cyclic Test Protocol

The CUREe loading protocol, developed by Krawinkler *et al.* (2003), consists of 40 cycles, as shown in Figure 5.3a, where each cycle represents a symmetric oscilation with a predefined amplitude in the positive and negative directions. The loading protocol is normalized to a reference displacement D_{ref} that is associated with the monotonic response of an identical test specimen. The normalized protocol consists of 6 initiation cycles of amplitude 0.05 and 8 primary cycles of increasing amplitude of 0.075, 0.1, 0.2, 0.3, 0.4, 0.7, 1.0 and 1.5. Each primary cycle is followed by 6, 3 or 2 training cycles with an amplitude 75% that of the corresponding primary cycle. The reference displacement D_{ref} is computed by Pardoen *et al.* (2003) as 60% of the monotonic displacement capacity D_m , which is the displacement in the softening regime of the monotonic response at which the force is 80% of the ultimate force F_{ult} , as shown in Figure 5.3b.

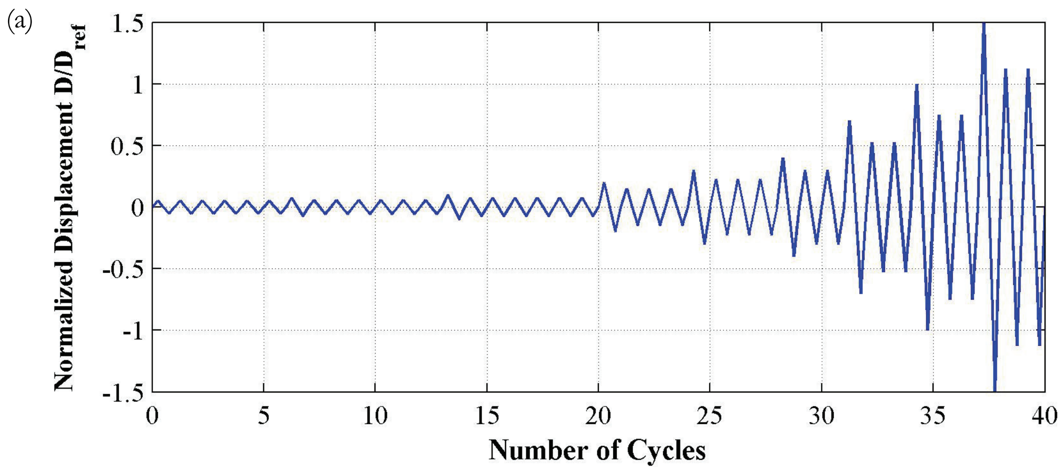

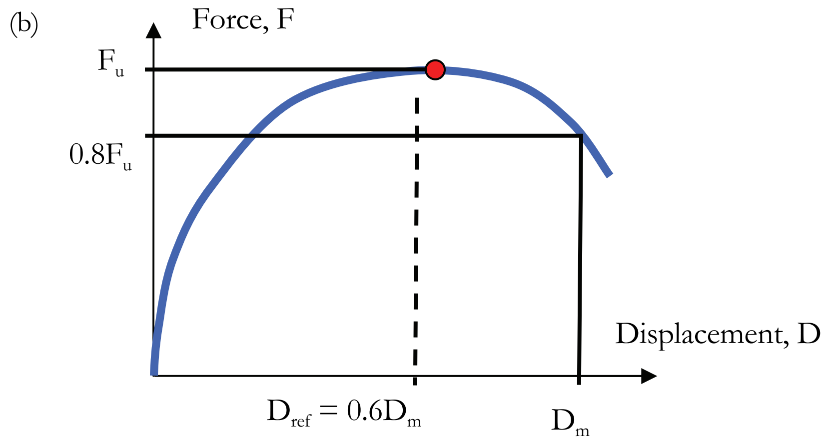

Figure 5.3 (a) Normalized CUREe Loading Protocol, and (b) Definition of Monotonic Displacement Capacity D_m for a Sample Monotonic Response

5.2.4 Framing Configuration and Boundary Connections

Figure 5.4 to Figure 5.6 illustrate the structural configuration and boundary connections of each shear wall specimen (top) along with the equivalent numerical model (bottom). The FS wall, designed as a single assembly, has one holdown at each wall's end post. On the contrary the PD and GD walls are designed as two assemblies, featuring holdowns at the end posts of the interior openings as well. Simpson Strong-Tie™ HTT22 holdowns with a 5/8 in diameter bolt and anchor bolts with a 1/2 in diameter bolt were used for all test specimens.

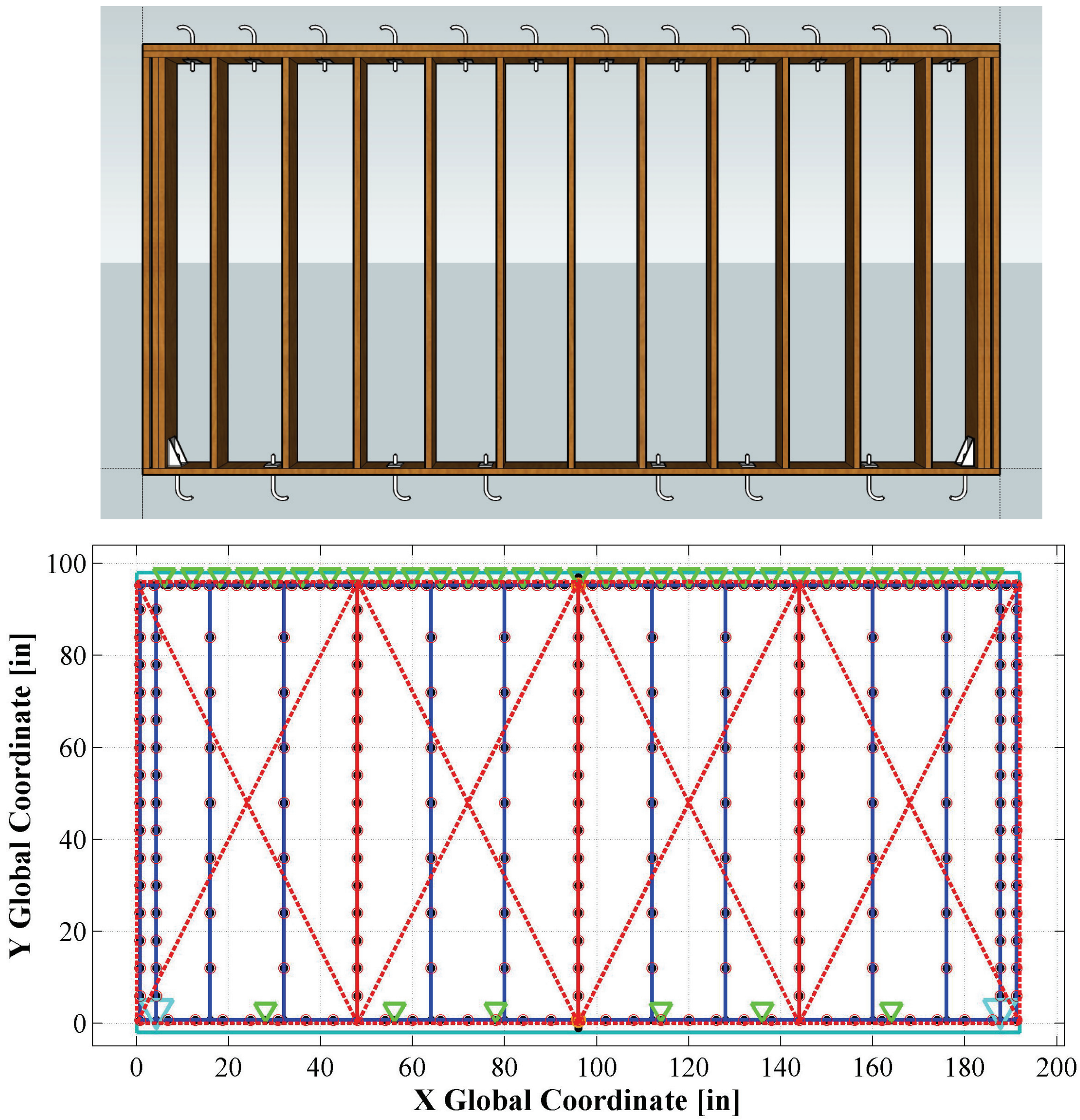

Figure 5.4 Structural Configuration (top) and Numerical Model (bottom) of FS Wall

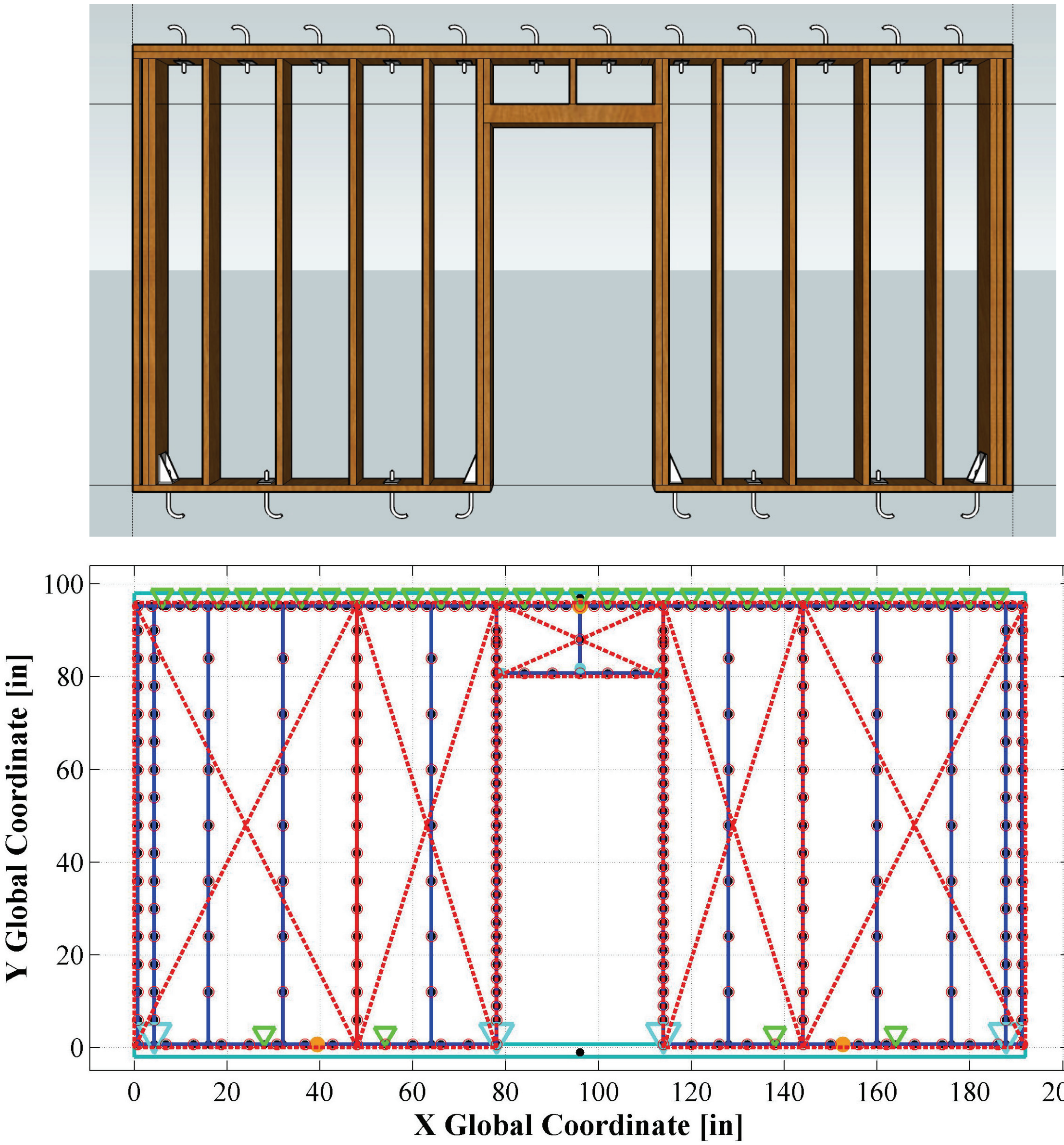

Figure 5.5 Structural Configuration (top) and Numerical Model (bottom) of PD Wall

As specified in the report by Pardoen *et al.* (2003), the end post of each wall assembly consisted of three vertical framing members. The outer member was independent from the remaining two and had a distance of 0.5 in from the adjacent stud. The remaining two members were connected at the bottom with the nails used to attach the holdown to the inner third stud. Nailing was provided at the specified distance across the length of the outer and the inner stud. Thus, the numerical models feature two independent vertical studs, assigning double axial and bending stiffness in the inner framing member. Similarly, internal posts of the PD and GD walls with holdowns at the base, as well as horizontal top plates, consisted of two framing members, but nailing was provided across the length of both members. In this case, the numerical models feature a single member with half of the specified nailing distance and double axial and bending stiffness. It should be noted that only rectangular panels can be assigned in the numerical model, thus, the cut-out sections of the sheathing panels above the PD and GD wall openings where simulated with independent panels, as shown in Figure 5.5 and Figure 5.6.

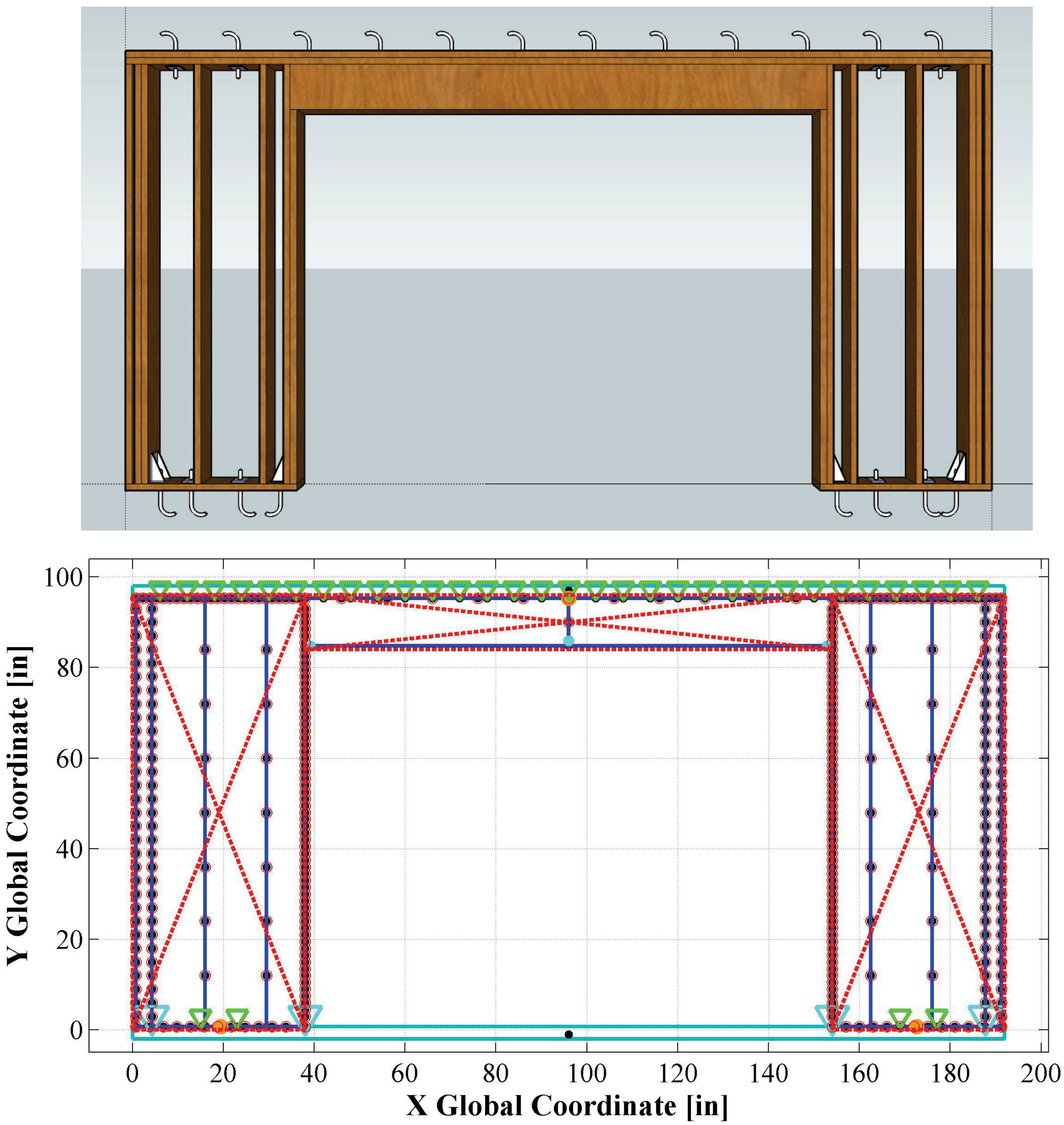

Figure 5.6 Structural Configuration (top) and Numerical Model (bottom) of GD Wall

The gravitational force applied on the upper diaphragm was estimated around 1000 lbs accounting for the weight of the top steel beam and cover plates (780 lbs) as well as half of the weight of the shear wall specimen (1/2·440 lbs for FS wall).

5.2.5 Material and Spring Connector Properties

Table 5.2 presents basic dimensions and associated typical material properties for the linear elastic beam and panel elements utilized in the numerical analyses. The modulus of elasticity of the beam elements was specified from Table 4A in NDS (2005) for Douglas-Fir Number 1 grade. The elastic modulus of OSB was estimated based on typical properties given by manufacturers.

Table 5.2 Dimensions and Material Properties of Linear Elastic Beam and Panel Elements

Sheathing Panels Oriented Strand Board	**Shear modulus** [psi]	**Thickness** [in]
	220000	3/8
Wood framing 2x4 Douglas-Fir	**Modulus of elasticity** [psi]	**Cross section dimensions** [in]
	1700000	1.5x3.5

Table 5.3 presents the properties of the linear and nonlinear elastic elements utilized to simulate the interaction between framing members and diaphragms. The force in the normal – initially vertical – direction relative to the contact area is computed from the nonlinear elastic response given in (4.113), using the input parameters d_{tol} and f_{tol} shown in Table 5.3. The response in the direction parallel to the contact area is computed according to the nonlinear elastic relationship given in (4.116) for stud-to-plate contact elements, which effectively minimizes the flexibility in this direction. On the contrary, the diaphragm-to-plate contact elements are considered to act linearly elastic with a very low stiffness of 100 lbs/in. This low value is used in order to reduce unrealistic catenary action along the horizontal plate when uplifting from the diaphragm. Note that the resistance in this direction is provided by the diaphragm-to-framing connection elements.

Table 5.4 presents the properties of the diaphragm-to-framing connection elements. The stiffness parallel to the contact area is 50000 lbs/in for holdowns and anchor bolts at the bottom of the wall, and 10000 lbs/in for the lag screws at the top of the wall. The response of the holdowns in the normal direction is the only nonlinear inelastic behavior considered in the diaphragm-to-framing connection elements. The spring parameters for nonlinear holdown connectors were estimated as described in Appendix A. The stiffness normal to the contact area is 10000 lbs/in and 5000 lbs/in for the anchor bolts and the lag screws, respectively.

Table 5.3 Properties of Linear and Nonlinear Elastic Contact Elements

Elements	**Direction relative to contact**	**Behavior**	**Input parameters**		
			d_{tol} [in]	f_{tol} [lbs]	**Elastic stiffness** [lbs/in]
Stud-to-plate contact elements	Parallel	Nonlinear elastic (4.116)	0.0001	0.1	N/A
	Normal	Nonlinear elastic (4.113)	0.0001	0.1	N/A
Diaphragm-to-plate contact elements	Parallel	Linear elastic	N/A	N_A	100
	Normal	Nonlinear elastic (4.113)	0.0001	0.1	N/A

Table 5.4 Properties of Diaphragm-to-Framing Connection Elements

Elements	**Direction relative to contact**	**Behavior**	**Elastic stiffness** [lbs/in]
Holdowns at the bottom of the wall	Parallel	Linear	50000
	Normal	Nonlinear inelastic	150000
Holdowns at the top of the wall	Parallel	N/A	N/A
	Normal	N/A	N/A
Anchor bolts at the bottom of the wall	Parallel	Linear	50000
	Normal	Linear	10000
Anchor bolts at the top of the wall	Parallel	Linear	10000
	Normal	Linear	5000

The parameters of the sheathing-to-framing nonlinear springs were based on experimental connection data generated by Fisher *et al.* (2001). The identification process and the spring parameters are presented in Appendix A. Table 5.5 summarizes the basic characteristics of the backbone curve of the nonlinear springs utilized for modeling sheathing-to-framing and holdown connections. Figure 5.7 illustrates the monotonic and cyclic response of each unidirectional nail spring. The bidirectional response is implemented with an orientation and a coupling interaction of each pair of springs, as described in Section 4.3.5.3.

Table 5.5 Characteristics of Backbone Curve of Nonlinear Inelastic Springs

	Initial Stiffness [lbs/in]	**Yield Force** [lbs]	**Capping Force** [lbs]	**Displacement at Capping Force** [in]	**Displacement at Failure** [in]
3/8 in OSB / 8d Box Gun Nails / 2x4 Douglas-Fir	12650	141.9	266.8	0.54	3.30
HTT22 Holdown Spring	150000	8000	10415.4	0.53	1.80

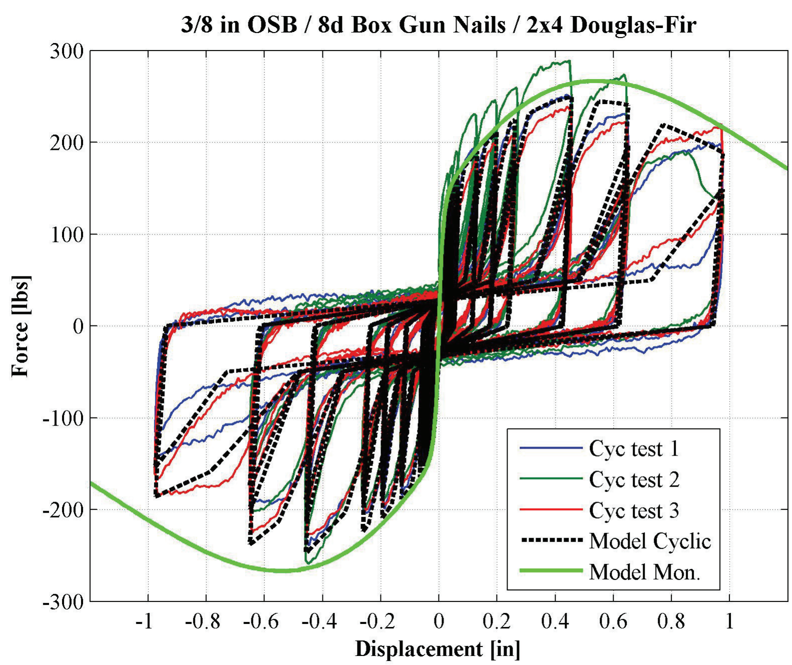

Figure 5.7 Monotonic and Cyclic Response of a Unidirectional Nail Spring for [3/8 in OSB / 8d Box Gun Nails / 2x4 Douglas-Fir]

5.2.6 Comparison of Global Experimental Responses and Numerical Predictions

This section presents the comparison of global responses between experimental and numerical data, generated for each wall configuration. Figure 5.8 illustrates the monotonic pushover test results from one specimen along with the numerical predictions for the three wall configurations. The ASD capacity per IBC (2006) is shown with a dashed line.

Concentrating first on the ascending branch of the backbone curves up to the capping point (point of maximum strength); it is observed that the **Model** responses achieve a good correlation with the **Test** responses in terms of force and stiffness variations along the examined deformation range. As expected, the **Pure Shear** model generally predicts higher global stiffness and strength characteristics compared to the **Model** predictions. For all cases, the reduction in stiffness and strength observed in the **Model** responses lead to more accurate predictions of the experimental behavior. This statement does not hold only for the strength predictions of the PD wall. For this case, the strength prediction is more accurate for **Pure Shear** response, yet the initial ascending branch of the backbone curve is more accurately represented by the **Model** response. It should be noted that the maximum experimental strength of the PD wall is higher than that of the FS wall although its allowable design force is lower by about 20% that of FS wall, as shown earlier in Table 5.1.. On the contrary the numerical strength predictions are consistent with the allowable forces (i.e. lower strength for PD wall compared to FS wall), which implies that there is an additional resisting mechanism in the test specimen that is not reflected in the numerical models. The differences observed between the two numerical predictions indicate the level of participation of modes of deformation other than pure kinematic frame distortion. For the FS and PD wall configurations that consist of walls segments with low aspect ratios (see Table 5.1), the increase of capping force for **Pure Shear** response is about 5-10%, compared to the **Model** response. On the contrary, the increase of capping force is beyond 30% for the GD wall when framing deformations are not considered. This difference suggests participation of uplifting and overturning modes, justified by the high aspect ratio of the GD wall segments. This difference also justifies the use of the aspect ratio adjustment factor in IBC (2006) for walls with aspect ratio greater than 2. Interestingly, the reduction of 20% in design allowable strength compares well with the relative reduction of 20-25% in maximum strength, considering the effect of the aspect ratio in the **Model** responses. For all three cases, the predicted **Model** displacements at the forces corresponding to the ASD Capacity per IBC (2006) are closer to the **Test** displacements than the **Pure Shear** predictions.

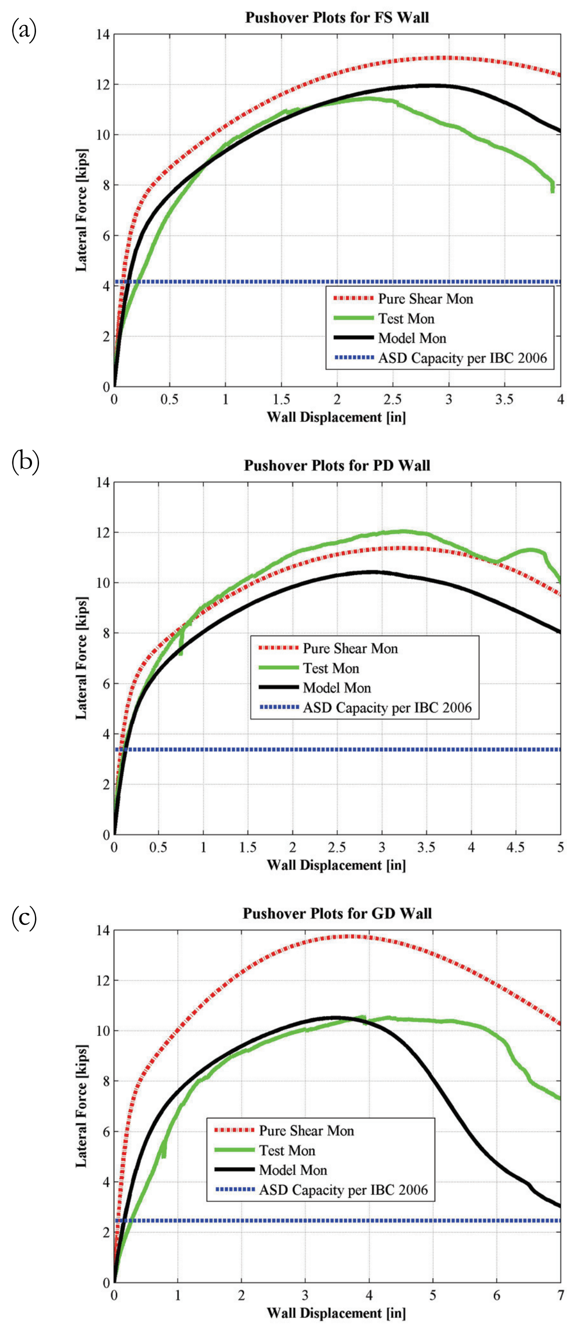

Figure 5.8 Comparison of Monotonic Response for (a) FS Wall, (b) PD Wall, and (c) GD Wall

Based on the experimental results, the monotonic displacement capacity D_m was equal to 3.55, 5.10 and 6.55 in for FS, PD and GD walls, respectively. Thus, the reference displacement D_{ref} used in the corresponding cyclic protocol for each structural configuration was accordingly equal to 2.15, 3.05 and 3.90 in for FS, PD and GD walls, respectively.

Figure 5.9 illustrates the cyclic pushover test results for two different test specimens (labels **Test A** and **Test B**) along with the numerical **Model** predictions, for the three wall configurations. In general, the predicted cyclic behavior is well correlated with the experimental response exhibiting in-cycle and cyclic strength degradation and pinching characteristics, consistent with the test observations.

For FS and PD walls, the numerical envelope forces in the post-elastic regime range between 0~15% percent lower than the experimental forces, except for the response of PD wall – **Test A** – in the positive direction (Figure 5.9c). In this case, the maximum experimental strength is similar in magnitude to the strength observed in the monotonic test and higher than the strength observed in the negative direction or any direction of the second identical test (Test B). These differences in the response could be related to (i) the contribution of the cut-out sections above the door opening, which are actually parts of full-height sheathing panels, and (ii) the higher tie-down preload in the holdown devices of **Test A**, compared to **Test B**, as shown later and discussed in Section 5.2.7. For GD wall, the numerical envelope forces are in very good agreement with the experimental envelope forces.

Summarizing the experimental and numerical global responses, Figure 5.10 illustrates the monotonic and cyclic pushover curves on the left column (Figure 5.10a,c,e) and the associated cumulative strain energy dissipation from the cyclic responses on the right column (Figure 5.10b,d,f). These figures show that the **Pure Shear** responses tend to predict not only higher stiffness and strengths, but also fatter hysteresis loops during pinching response. This difference is more pronounced for the GD wall leading to significant overestimation of the energy dissipation capability. The energy dissipation capability predicted by the **Model** responses is consistently lower than the energy dissipated by the **Test** responses but the overall rate of dissipation is reasonably predicted throughout the deformation ranges.

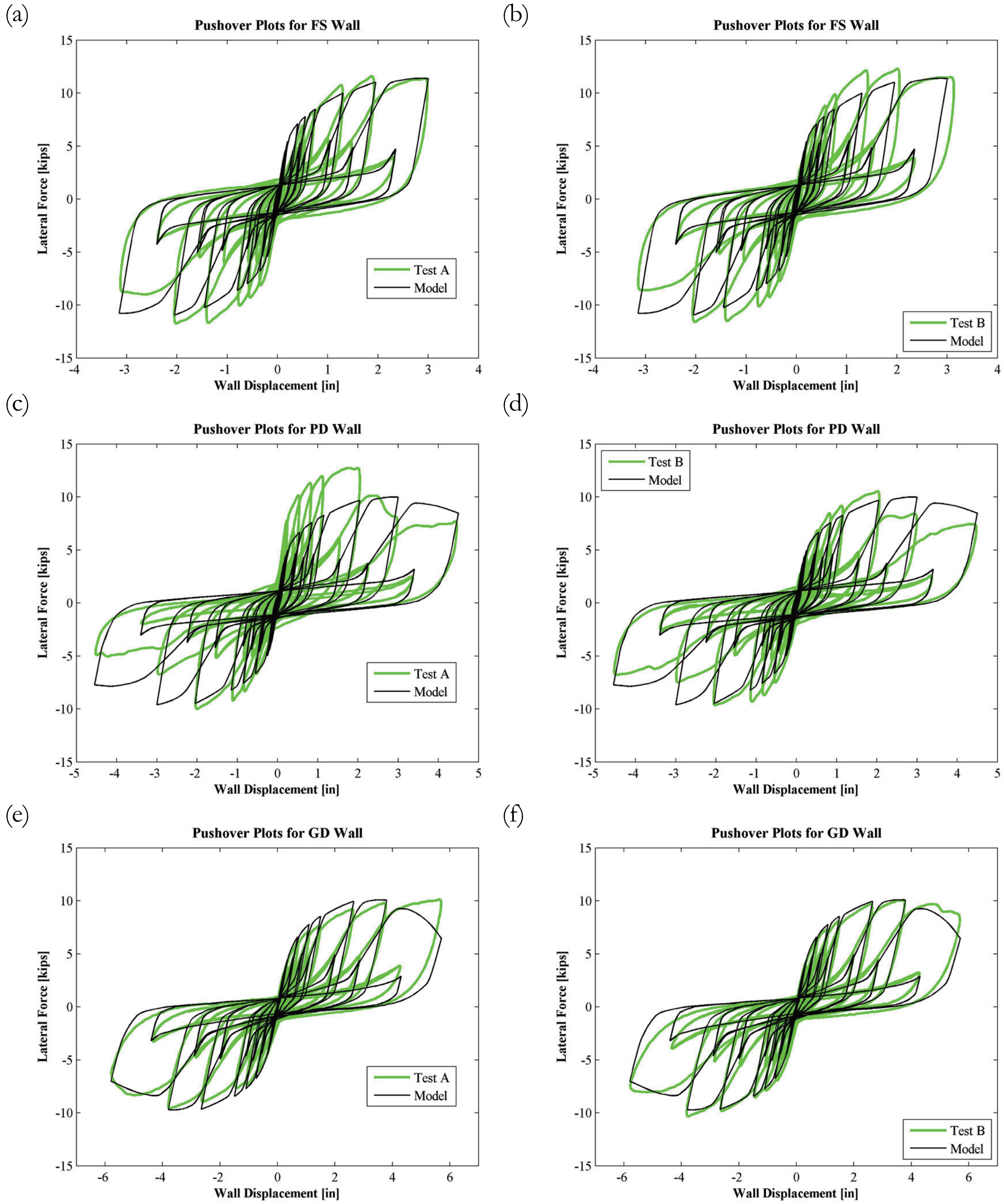

Figure 5.9 Comparison of Cyclic Response from Two Specimens for (a,b) FS Wall, (c,d) PD Wall, and (e,f) GD Wall

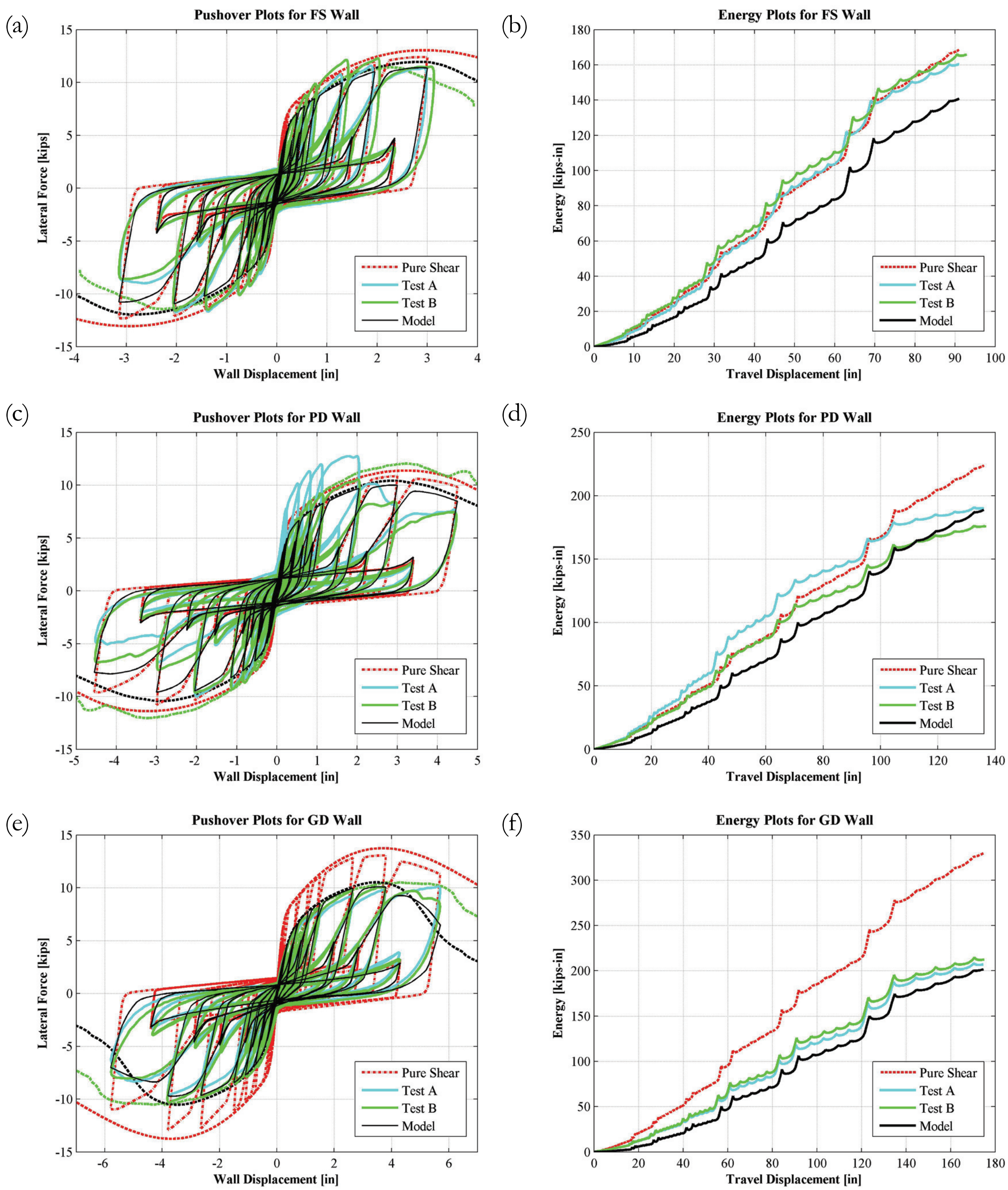

Figure 5.10 Comparison of Cyclic Response and Dissipated Energy for (a,b) FS Wall, (c,d) PD Wall, and (e,f) GD Wall

5.2.7 Comparison of Local Experimental Responses and Numerical Predictions

This section presents the comparison of local responses between experimental and numerical data, generated for each wall configuration. Note that experimental data of local responses were available only for the cyclic tests and numerical predictions are provided only by the **Model** formulation.

Figure 5.11 illustrates the vertical displacements at the bottom of the end posts (studs) as a function of the global lateral wall displacement. First and foremost, the uplifting behavior predicted by the numerical analyses is qualitatively validated by the associated experimental data. This can be expected based on the low gravity load of 1000 lbs that cannot contribute sufficiently to the overturning resistance, as well as on the fact that the end vertical studs are not anchored to the base (see Figure 5.4 to Figure 5.6). Quantitatively, the predicted uplifting (positive) displacements are in good agreement with the the experimental displacements for all wall configurations. Thus, maximum values are similar for FS and PD walls and almost double for GD walls. This is observed in both analytical and experimental responses and is justified by the reduced nailing schedule from 6 in to 3 in considered for the GD wall. This eventually results to greater uplifting design forces by a factor of 2, as shown earlier at Table 5.1. The negative displacement values observed in the experimental results represent compressive deformation (crushing) of the sill plate along the member's thickness and perpendicular to grain. These phenomena are not considered in the numerical model assuming absolute contact conditions and no cross-grain deformations in the framing.

Figure 5.12 to Figure 5.14 illustrate the force-uplift response of the holdowns installed in the FS, PD and GD walls, respectively. The predictions presented refer to both forces and displacements, since these are related to internal actions and deformations of the shear wall components. It is observed that the response of holdowns installed at the wall ends is underestimated by the numerical model, while the response of holdowns installed at the inner posts (adjacent to the interior opening for PD and GD walls) is reasonably predicted. This may be attributed to the different approach selected to model the external and internal end posts, as described earlier in Section 5.2.4 and based on the report by Pardoen *et al.* (2003). The internal posts are considered as a single member with half of the specified nailing distance, while the external posts are simulated with two independent members with the specified nailing distance.

If these two members are not independent then the uplifting force in the external holdown studs will be increased.

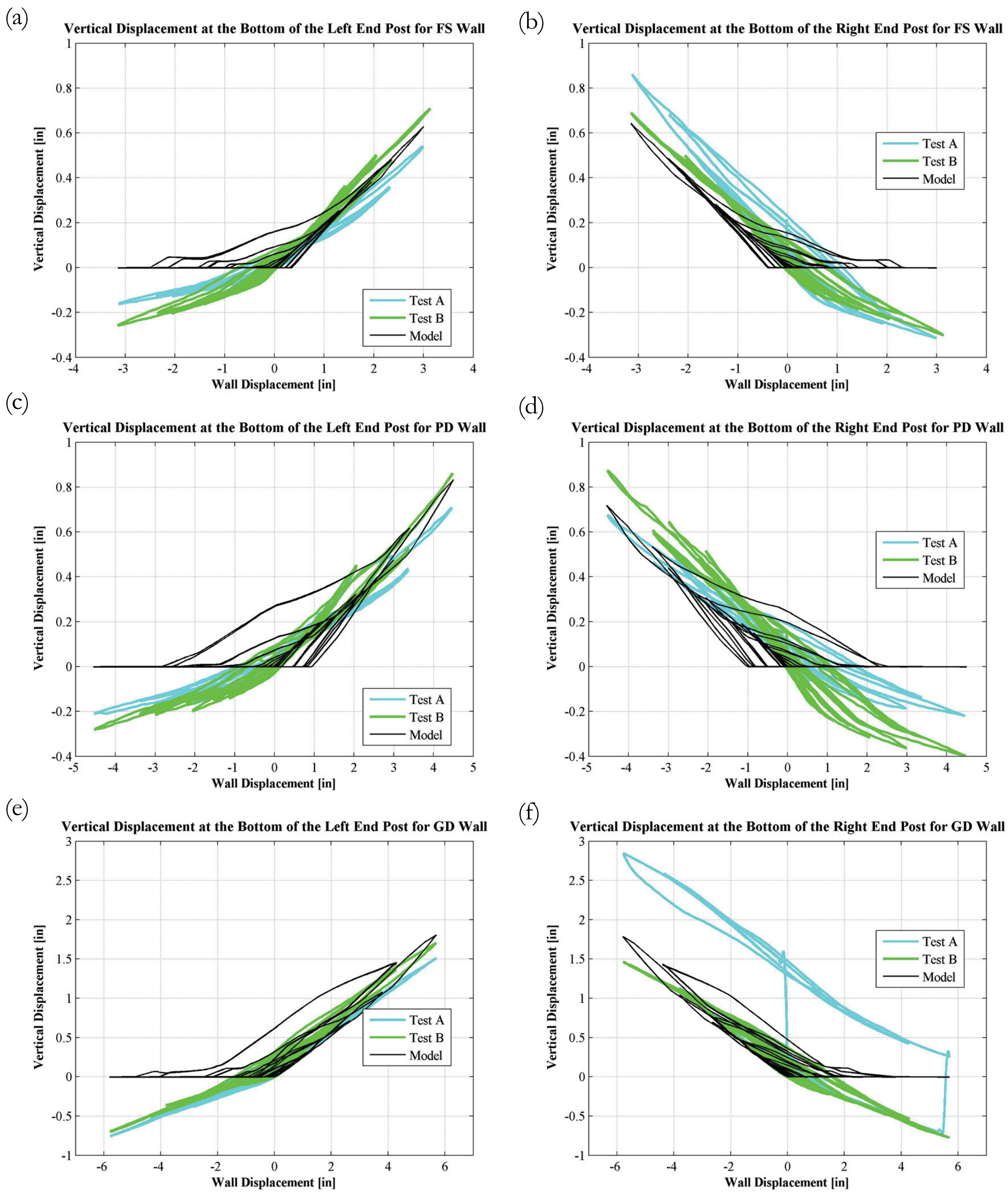

Figure 5.11 Comparison of End Post Bottom Uplift for (a,b) FS Wall, (c,d) PD Wall, and (e,f) GD Wall

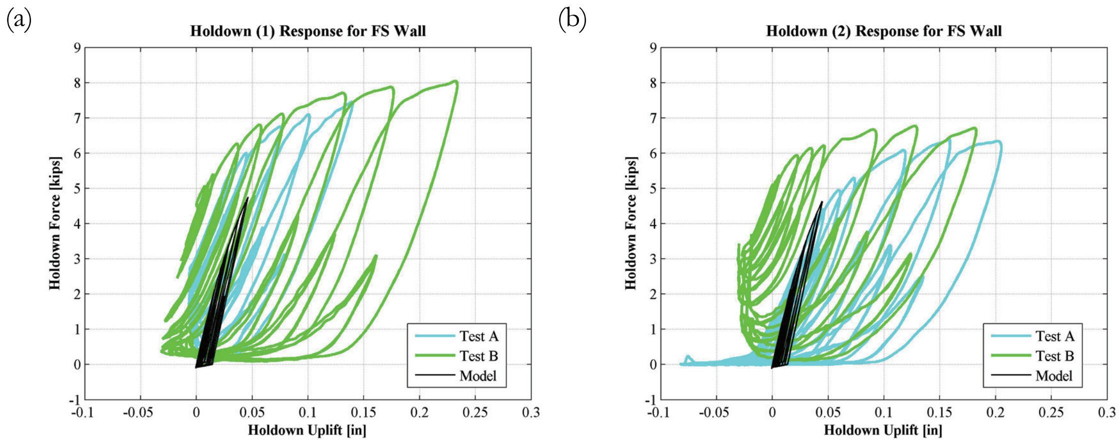

Figure 5.12 Comparison of Holdown Response for FS Wall

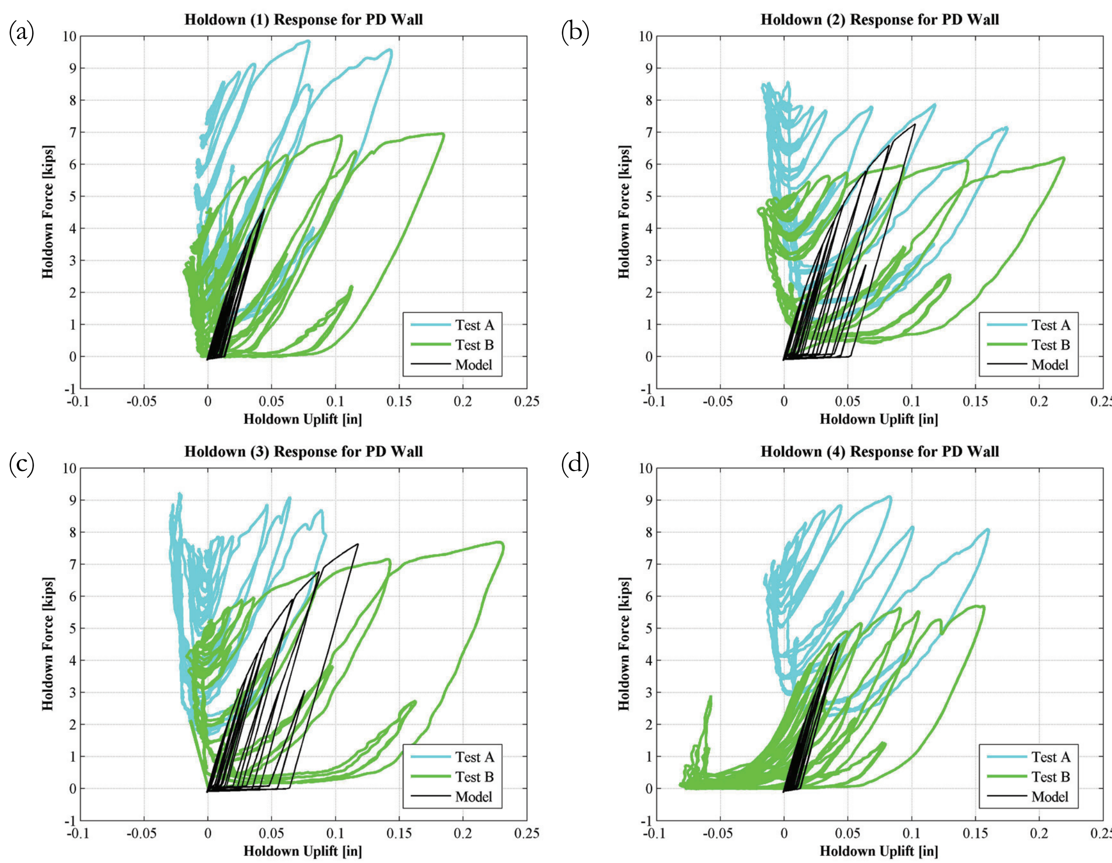

Figure 5.13 Comparison of Holdown Response for PD Wall

Note the higher tie-down preload in the holdown devices of **Test A**, compared to **Test B**, for PD wall in Figure 5.13, which are also greater for the holdowns resisting uplift under loading in the positive direction (Figure 5.13a,c). This could explain the difference in the horizontal response of the two identical specimens. The nonlinear axial model used in the numerical model for the uplift response of the holdown connectors does not account for the effects of preload or the eccentricity of the vertical resistance of about 2 in, from the center of the holdown bolt to the center of the adjacent vertical stud. A mechanics-based model that can consider such effects in conjuction with the shear response of the wood-to-plate connectors would provide more accurate predictions, given that the preload is known for each test.

Although it is accepted that there is room for improvement in the numerical predictions of the holdown responses, it is argued that given the modeling assumptions and material property uncertainties, the differences observed are acceptable. Furthermore, the “blind” predictions presented herein do not involve any trial-and-error fitting of material or spring properties to provide a more accurate prediction of the experimental response.

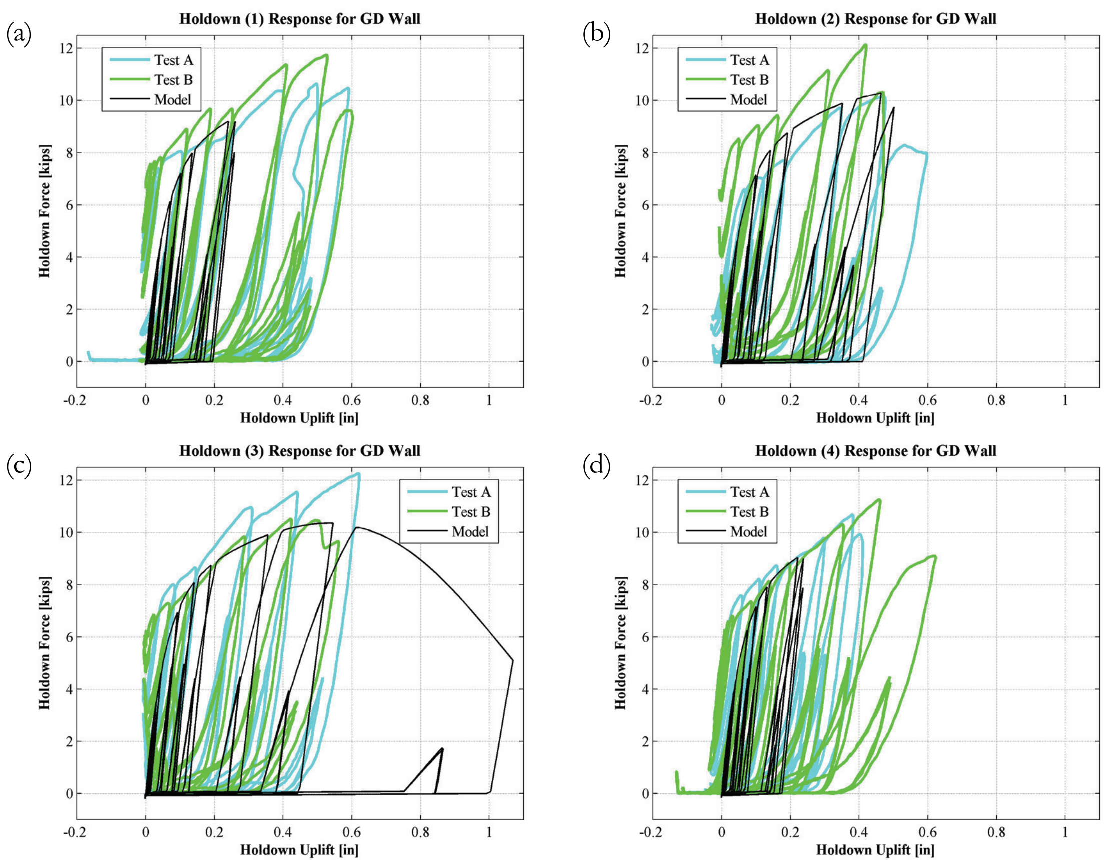

Figure 5.14 Comparison of Holdown Response for GD Wall

5.2.8 Predicted Deformed Shapes of Wall Configurations

Figure 5.15 summarizes the backbone curves predicted by the **Model** monotonic pushover analyses for the three wall specimens. Two points are identified in each curve, as listed in Table 5.6, and are used to plot the predicted deformed shapes of the numerical models. The first point corresponds to the maximum (capping) force and the second point corresponds to a degraded state with 25% of the maximum force. Figure 5.16 to Figure 5.21 illustrate the deformed shapes captured for the FS, PD and GD wall configurations at these selected points on the backbone curve. A common observation for all wall configurations is that the left end post separates from the sill plate while the adjacent holdown stud separates from the top plate. This indicates a clock-wise rotation of the top diaphragm that causes the field studs to separate from the sill or top plate according to the local load path developed. The internal framing deformations are more pronounced for the GD wall and this justifies the significant difference between the numerical predictions and test data when these deformations are not considered.

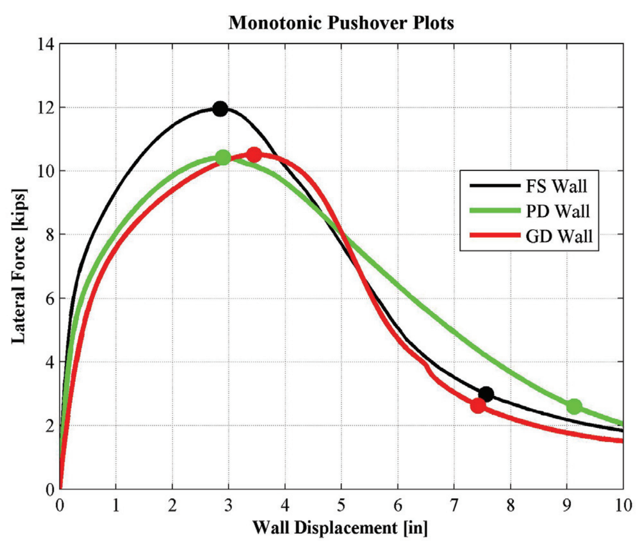

Figure 5.15 Monotonic Pushover Predictions and Indication of the Point of the Analysis Plotted in Figure 5.16 to 5.21

Table 5.6 Characteristics of the Backbone Curve of the Model Predictions

	FS Wall	PD Wall	GD Wall
Capping force [kips]	11.95	10.42	10.51
Displacement @ cap. force [in]	2.85	2.90	3.45
Displacement @ 25% of cap. force [in]	7.55	9.10	7.45

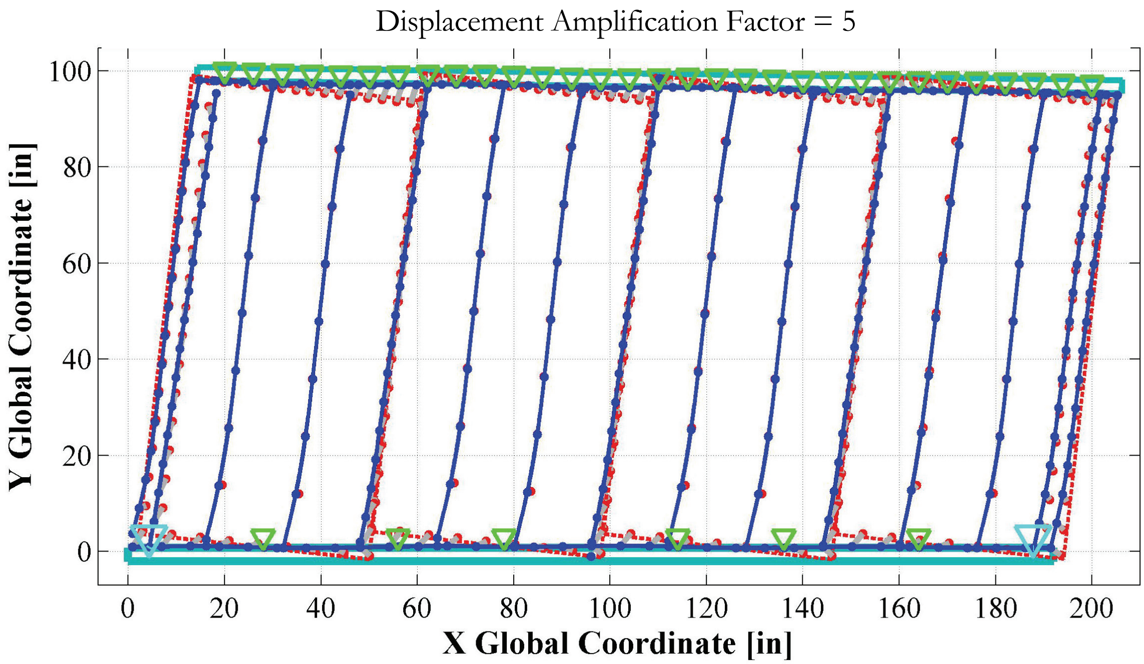

Figure 5.16 Deformed Shape of FS Wall from Monotonic Analysis at Global Lateral Displacement of +2.85 in

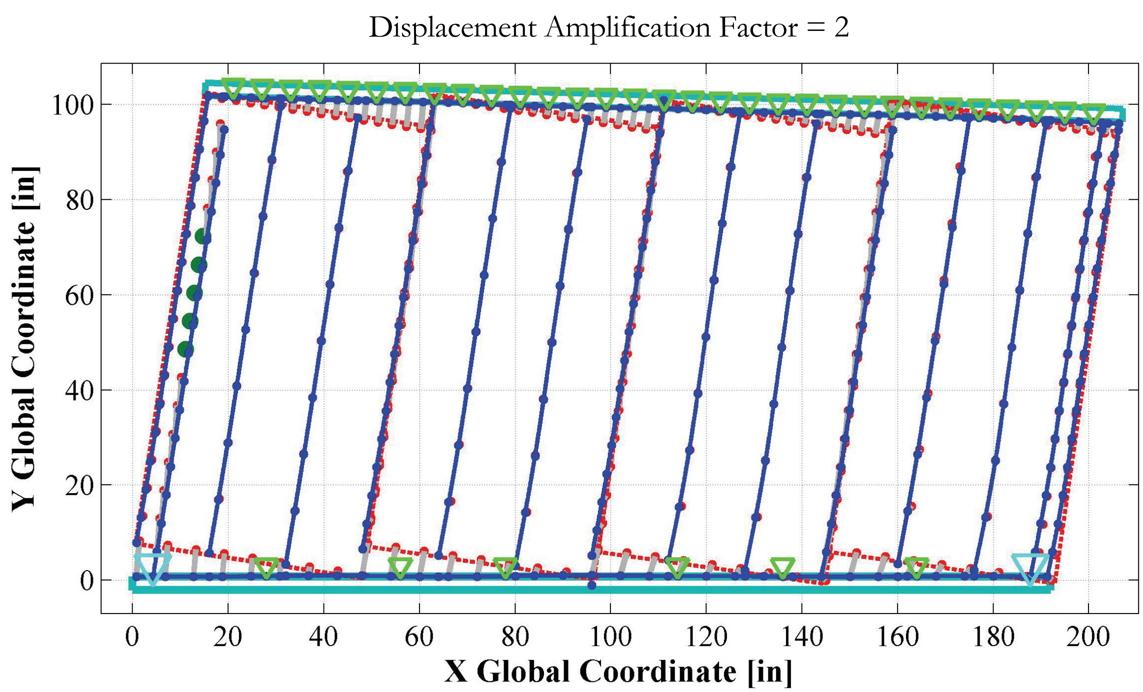

Figure 5.17 Deformed Shape of FS Wall from Monotonic Analysis at Global Lateral Displacement of +7.55 in

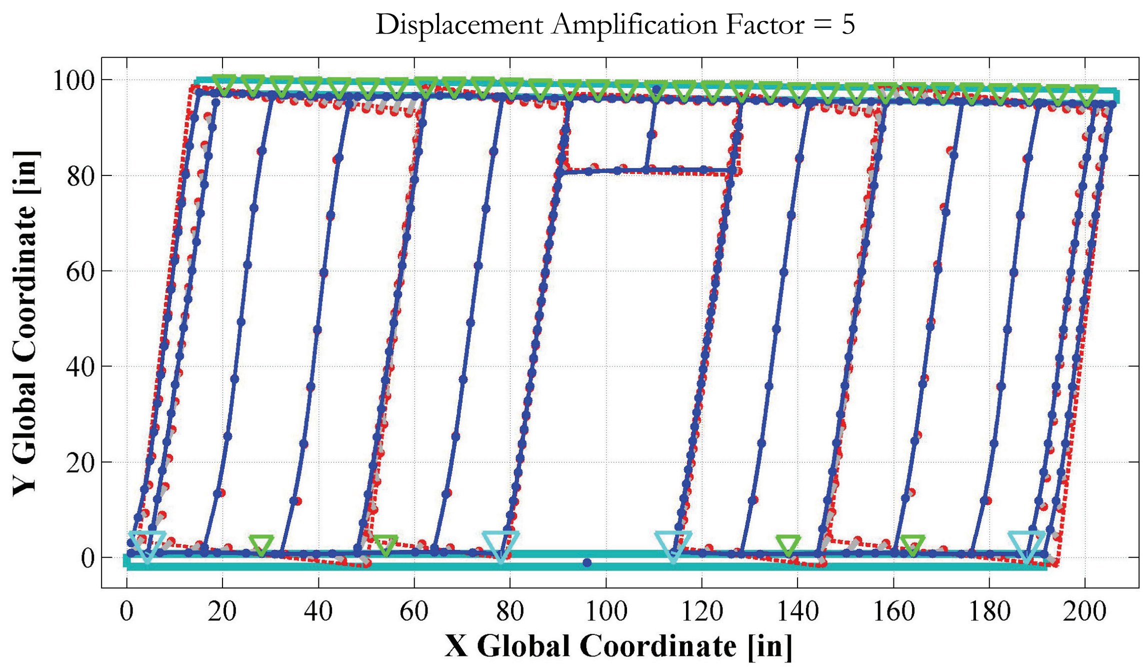

Figure 5.18 Deformed Shape of PD Wall from Monotonic Analysis at Global Lateral Displacement of +2.90 in

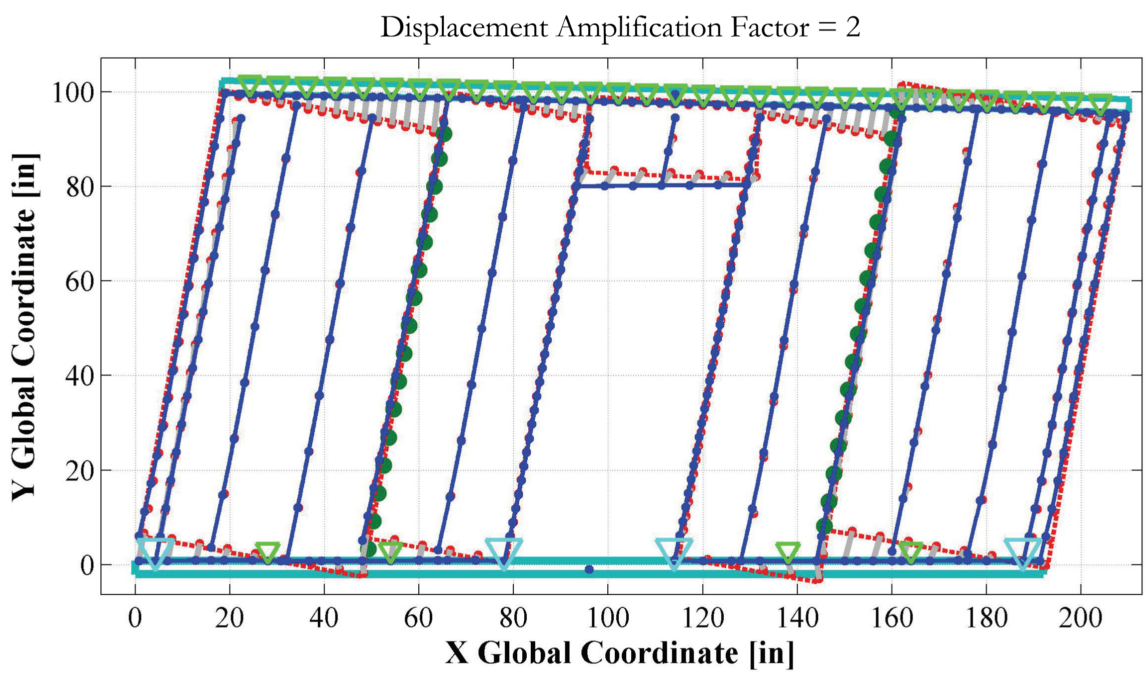

Figure 5.19 Deformed Shape of PD Wall from Monotonic Analysis at Global Lateral Displacement of +9.10 in

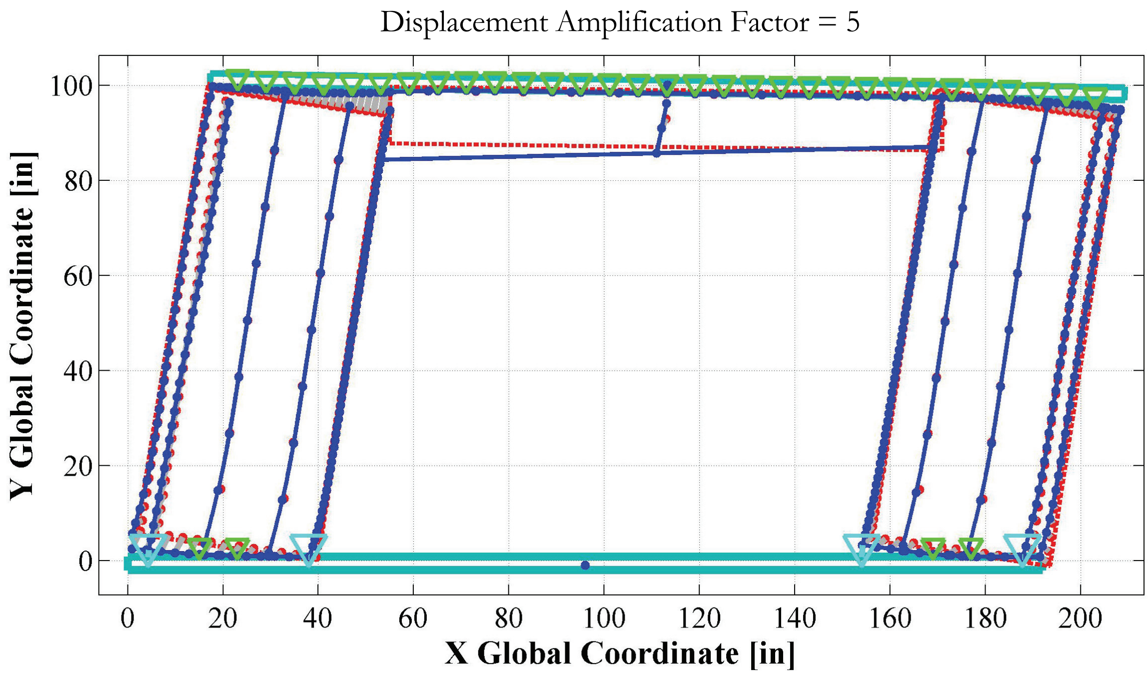

Figure 5.20 Deformed Shape of GD Wall from Monotonic Analysis at Global Lateral Displacement of +3.45 in

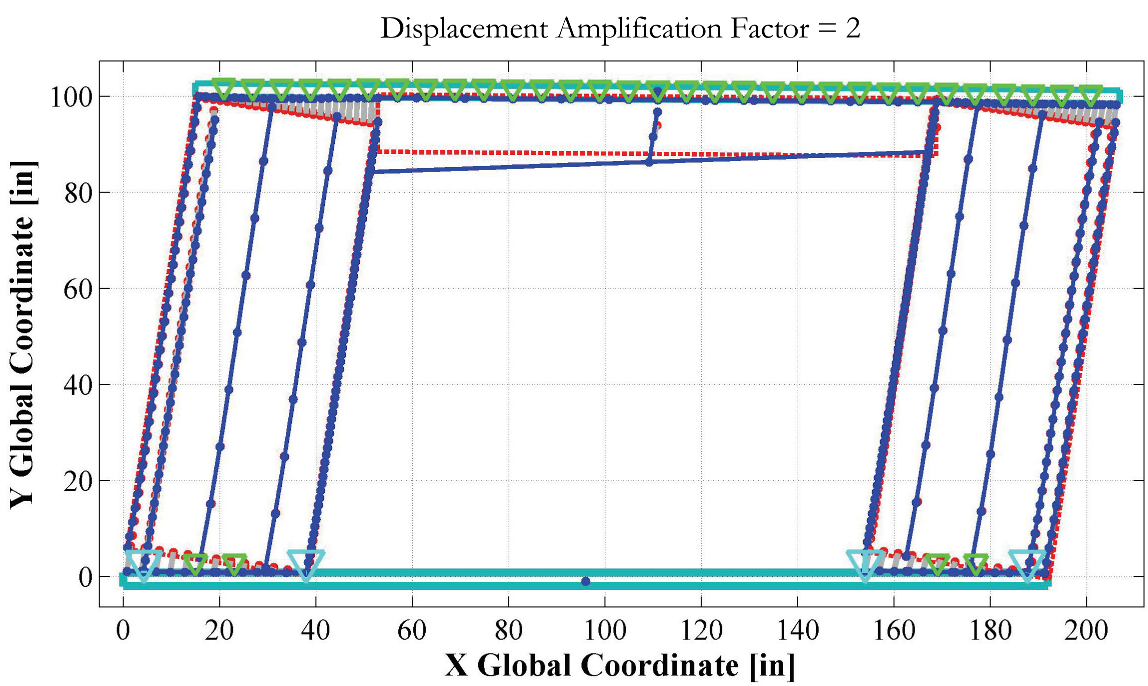

Figure 5.21 Deformed Shape of GD Wall from Monotonic Analysis at Global Lateral Displacement of +7.45 in

5.3 Example 2: Two-Story Shear Walls

The experimental data utilized in this second example have been generated by Pardoen *et al.* (2003) within the CUREe-Caltech Woodframe Project. Further to the single-story shear wall test results, which have been used in the first validation example presented in Section 5.2, Pardoen *et al.* (2003) performed pseudo-static testing of two-story light-frame wood shear walls. Two different groups were considered, each group consisting of only one specimen, which was tested under cyclic loading using the CUREe loading protocol (Krawinkler *et al.* 2001).

5.3.1 Test Specimens

The dimensions of the two-story specimens were equal to 16 ft long by 17 ft high, as shown in Figure 5.22. Each story had a clear height of 8 ft, while the diaphragm between the two stories was 1 ft high. The first specimen featured fully-sheathed walls in both stories and is denoted as FS2S wall. The first story of the second specimen incorporated a pedestrian door opening, similarly to the single-story specimens presented in Section 5.2, while the second story incorporated two large window openings in the mid span of the wall. This specimen, denoted as PD2S wall, was identical to the east side of the two-story full-scale light-frame wood house tested in the University of California, San Diego, within an experimental shake-table task of the CUREe-Caltech Woodframe Project (Fischer *et al.* 2001, Filiatrault *et al.* 2002).

The framing consisted of nominal 2x4 studs spaced at 16 in oc, using Douglas–Fir lumber graded No. 1 or better. The top plate and the vertical studs with holdown devices consisted of two framing members. The sheathing provided was Oriented Strand Board (OSB) 3/8 in thick. Sheathing panels were fastened to the framing with 8d box gun nails, 2.5 in long with 0.113 in diameter. Edge and filed nailing was specified at 6 in and 12 in oc, respectively.

5.3.2 Test Setup

The testing configuration was similar to that described in Section 5.2.2 for the single-story specimens. To enable the application of lateral forces at both levels, an additional steel beam was fastened to the double top plate of the second-story wall with 3/8 in diameter lag screws spaced at 6 in oc. The racking shear forces were applied to the steel beams of the first and second story through a vertical spreader beam, which was in turn attached to the actuator, as shown in Figure 5.23. The total weight acting at the top of the walls was estimated at 1300 lbs and 1000 lbs for the first and second story, respectively.

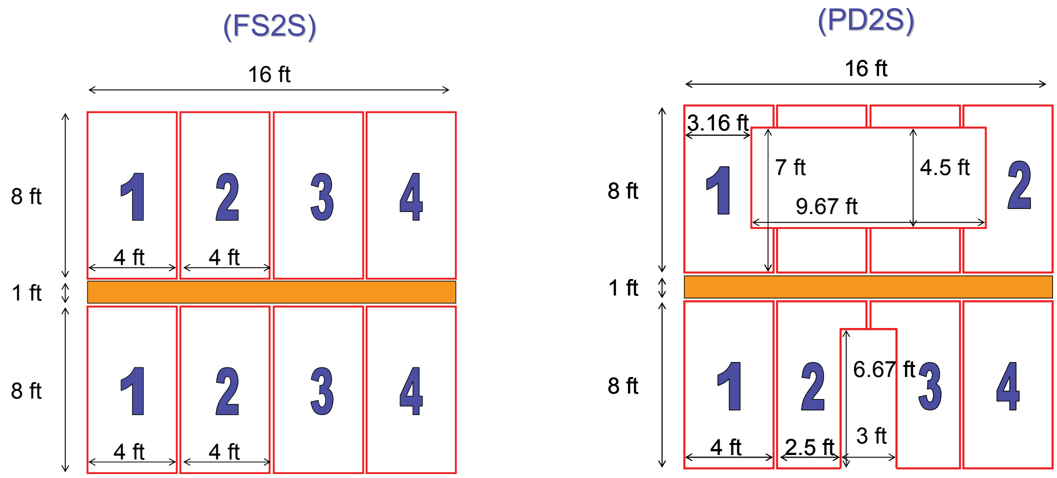

Figure 5.22 Geometry and Panel Configurations of the 2-Story Shear Walls Tested by Pardoen et al (2003)

Figure 5.23 Photo of PD2S Wall during Testing (from Pardoen *et al.* 2003)

5.3.3 Framing Configuration and Boundary Connections

Figure 5.24 and Figure 5.25 illustrate the framing configuration and boundary connections of each two-story specimen (left) along with the equivalent numerical model (right). Similarly to the single-story walls, each story featured double top plates and inner vertical posts and triple wall end posts. The same nailing pattern was applied, providing edge nailing at 6 in oc to both framing members for top plates and vertical posts, except for the top plates of the second-story walls, which were nailed along one framing member only. The top steel beam, a MC10x28.5 channel, was attached to the double top plate of the wall with 3/8 in diameter lag screws spaced at 6 in oc. Simpson HTT22 tension ties with a 5/8 in diameter bolt and anchor bolts with a 1/2 in diameter bolt were used to anchor the base of the first-story walls. Additionally, CS16 tension coiled straps were connected to the studs of the first- and second-story walls to provide overturning resistance to the upper story. As a result, two additional vertical studs with an edge nailing schedule were installed at the first-story of the PD2S wall. The sill plates of the second story-walls are assumed to be nailed to the diaphragm below according to construction practices, although no information is provided in the experimental report by Pardoen *et al.* (2003). These connections are considered at 6 in oc, similarly to the top-plate anchor bolts but with different material properties. Similarly to the single-story specimens with wall openings, the cut-out sections of the sheathing above and below openings of PD2S wall were considered as independent panels, as shown in Figure 5.25.

5.3.4 Material and Spring Connector Properties

Material properties presented in Section 5.2.4 for single-story walls are applicable to the numerical models of the two-story specimens as well. Table 5.2 presented basic dimensions and associated typical material properties for the linear elastic beam and panel elements, while Table 5.3 presented the properties of the nonlinear elastic contact springs. Table 5.7 and Table 5.8 present the properties of the diaphragm-to-framing connection elements for the first and second story of the models, respectively. Regarding uplift restraining devices, the properties of the vertical connection springs representing the CS16 straps were estimated from the spring properties already specified for HTT22 holdowns, as described in Appendix A. Note that each strap was modeled with two independent nonlinear springs that connected the corresponding studs of the first- and second-story walls to the floor diaphragm acting perpendicular to the floor diaphragm. This limitation arises from the adopted modeling framework for multi-story buildings, presented in Section 4.4, which allows interaction between shear walls and diaphragms but does not allow interaction between shear walls of different stories. Table 5.9 summarizes the basic characteristics of the backbone curve of the nonlinear springs utilized for anchoring connections

Table 5.7 Properties of Diaphragm-to-Framing Connection Elements Utilized for the First Story Numerical Model

Elements	**Direction relative to contact**	**Behavior**	**Elastic stiffness** [lbs/in]
Holdowns at the bottom of the wall	Parallel	Linear	50000
	Normal	Nonlinear inelastic	150000
Holdowns at the top of the wall	Parallel	Linear	20000
	Normal	Nonlinear inelastic	60000
Anchor bolts at the bottom of the wall	Parallel	Linear	50000
	Normal	Linear	10000
Anchor bolts at the top of the wall	Parallel	Linear	10000
	Normal	Linear	5000

Table 5.8 Properties of Diaphragm-to-Framing Connection Elements Utilized for the Second Story Numerical Model

Elements	**Direction relative to contact**	**Behavior**	**Elastic stiffness** [lbs/in]
Holdowns at the bottom of the wall	Parallel	Linear	20000
	Normal	Nonlinear inelastic	60000
Holdowns at the top of the wall	Parallel	N/A	N/A
	Normal	N/A	N/A
Anchor bolts at the bottom of the wall	Parallel	Linear	1000
	Normal	Linear	500
Anchor bolts at the top of the wall	Parallel	Linear	10000
	Normal	Linear	5000

Table 5.9 Characteristics of Backbone Curve of Nonlinear Inelastic Springs

	Initial Stiffness [lbs/in]	**Yield Force** [lbs]	**Capping Force** [lbs]	**Displacement at Capping Force** [in]	**Displacement at Failure** [in]
HTT22 Holdown Spring (bottom of 1st story walls)	150000	8000	10415.4	0.53	1.80
CS16 Strap Spring (top of 1st story walls and bottom of 2nd story walls)	60000	3200	4166.2	0.53	1.80

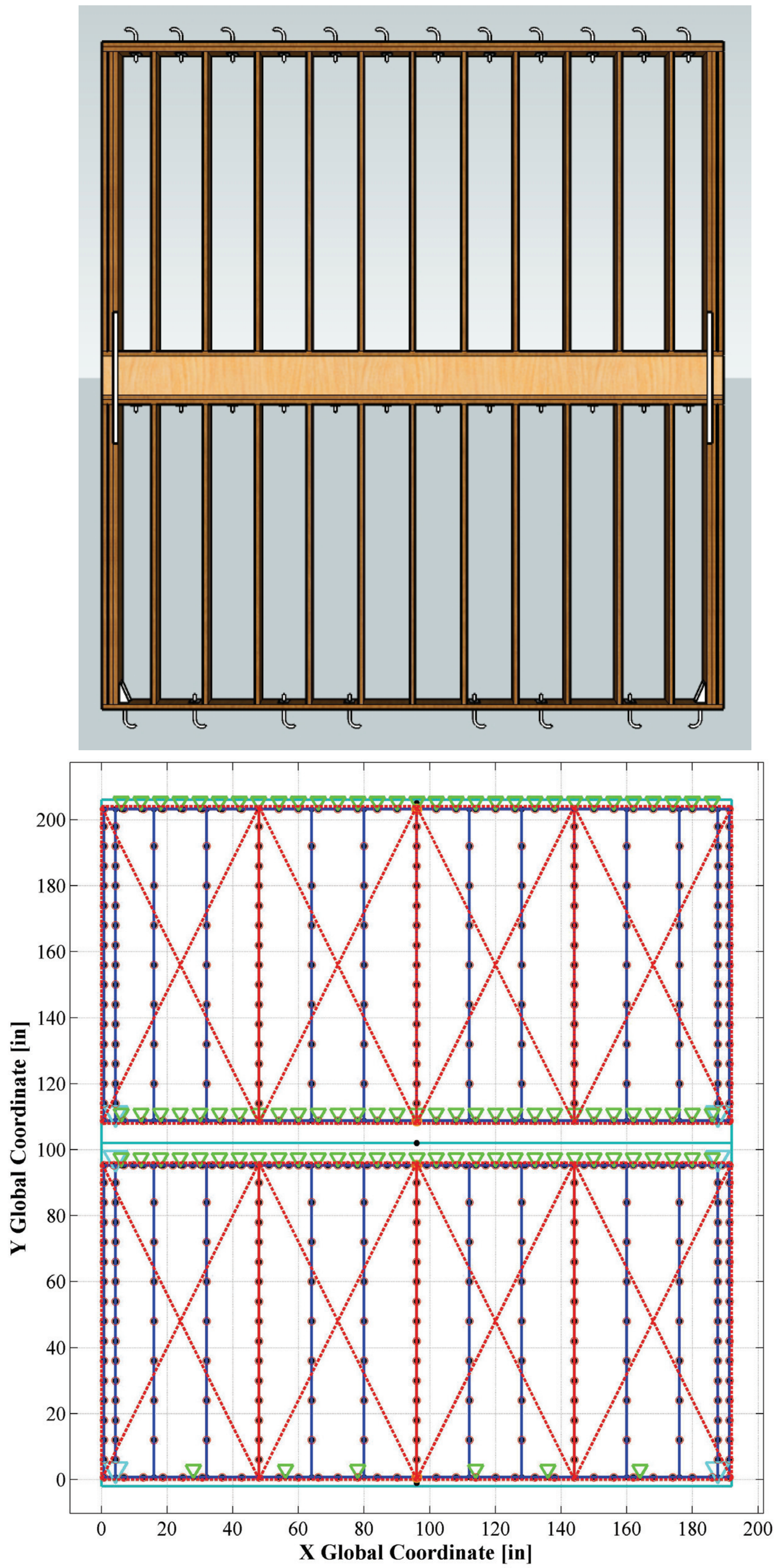

Figure 5.24 Structural Configuration (top) and Numerical Model (bottom) of FS2S Wall

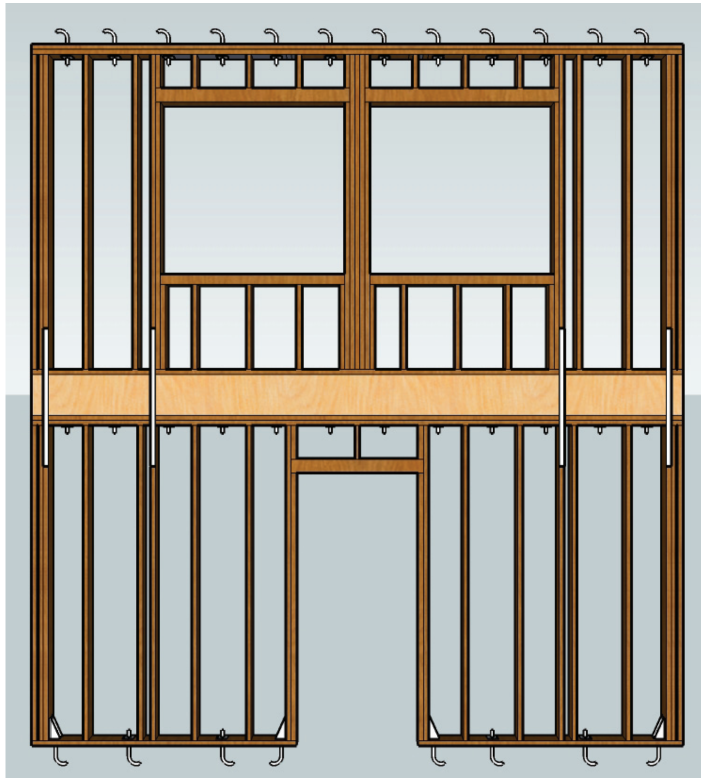

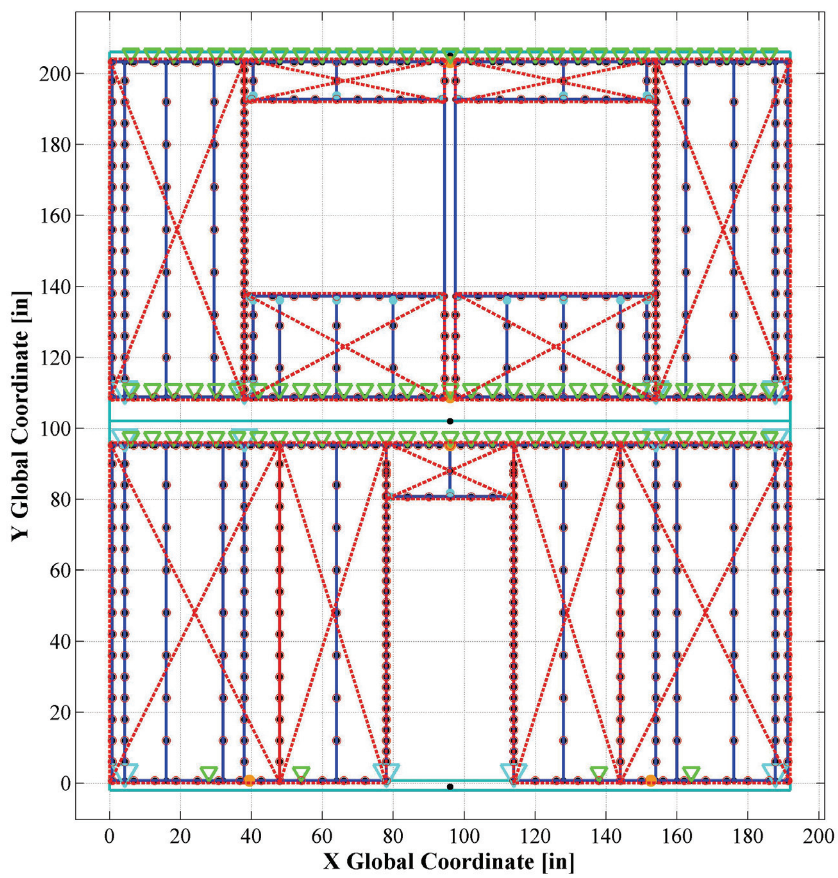

Figure 5.25 Structural Configuration (top) and Numerical Model (bottom) of PD2S Wall

5.3.5 Comparison of Global Experimental Responses and Numerical Predictions

Figure 5.26 illustrates experimental and predicted hysteretic force-displacement responses for each story of the two wall specimens.

The first-story walls **Model** predictions of envelope forces in the post-elastic regime range between 10~20% percent lower than the experimental forces for inter-story displacements that are less than 2 in for the FS2S wall and less than 3 in for the PD2S wall. Past these displacement ranges, the **Test** responses demonstrate strength and stiffness degradation that the **Model** responses do not capture. Deterioration in strength is more evident for the PD2S wall and for positive displacements of the FS2S wall. Interestingly, there is no obvious strength degradation for negative displacements of the FS2S wall. Observations of local responses, such as the force-displacement characteristics of holdown ties at the base of the first-story walls, can provide additional information to explain the experimental and numerical responses. This discussion is provided in Section 5.3.6 referring to Figure 5.30.

The **Model** predictions of the responses of the second-story walls are in relatively good agreement with the experimental results for the entire displacement range. For the FS2S wall, the predicted envelope curve demonstrates about 10% higher forces than the experimental envelope curve, at the same inter-story horizontal drifts. For the PD2S wall, predicted and experimental forces of the envelope curve are very well correlated. However, both numerical models under-estimate the energy dissipation capability and predict unloading curves that recover a greater part of the accumulated strain energy than what was observed experimentally. This may be attributed to inelastic action in uplift-restrain connections that is not considered in the numerical models.

Figure 5.27 illustrates global experimental and numerical responses that include both **Model** and **Pure Shear** predictions, as well as the strain energy absorbed in each story of each specimen.

Concentrating first on the first-story walls, the **Pure Shear** responses predict about 5-10% higher forces than the **Test** responses. Similarly to what was observed for single-story walls with wall segments of low aspect ratio, the **Pure Shear** predictions dissipate more energy than the **Model** predictions but the overall hysteretic response is not significantly different between both numerical models.

On the contrary, the **Pure Shear** predictions for the second-story walls demonstrate significant overestimation of the developed forces compared to the **Model** and **Test** responses. Maximum forces from the **Pure Shear** predictions are more than 20% higher than the experimental forces for both FS2S and PD2S walls.

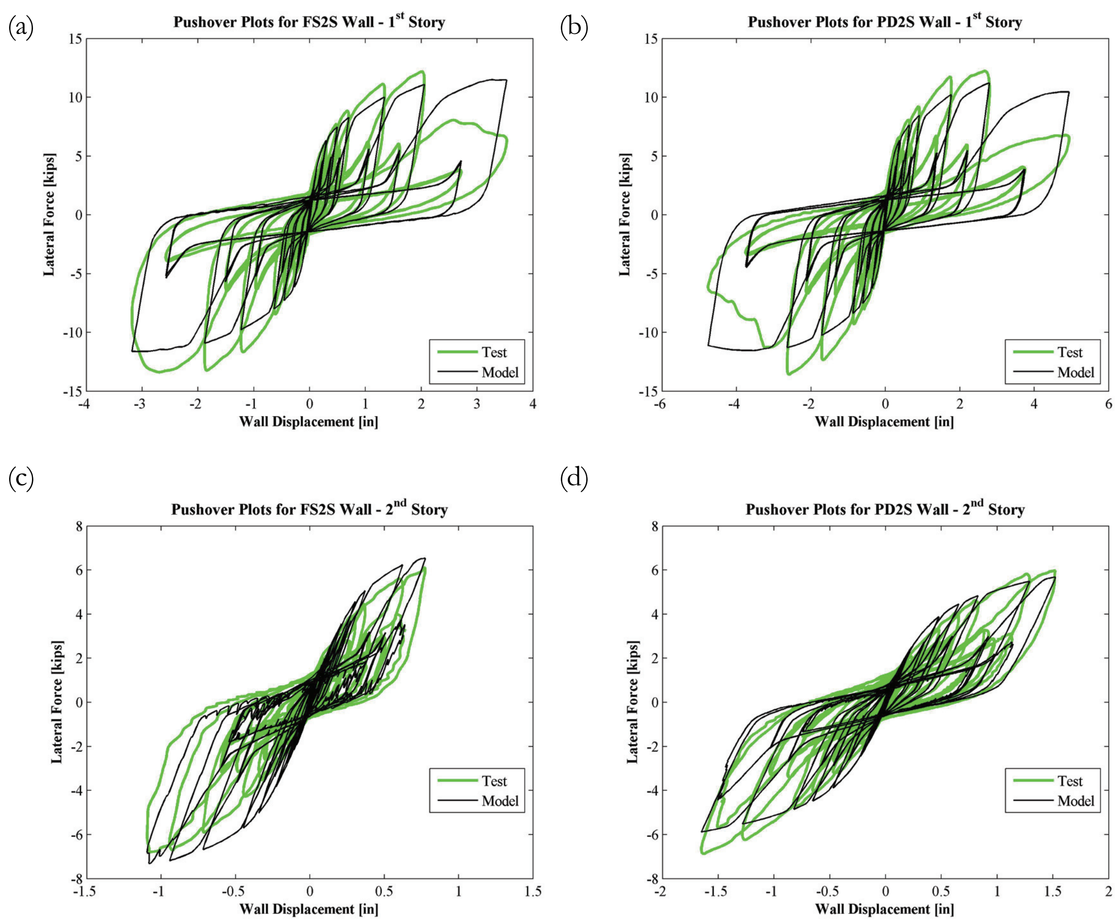

Figure 5.26 Comparison of Cyclic Response for (a,c) FS2S Wall, and (b,d) PD2S Wall

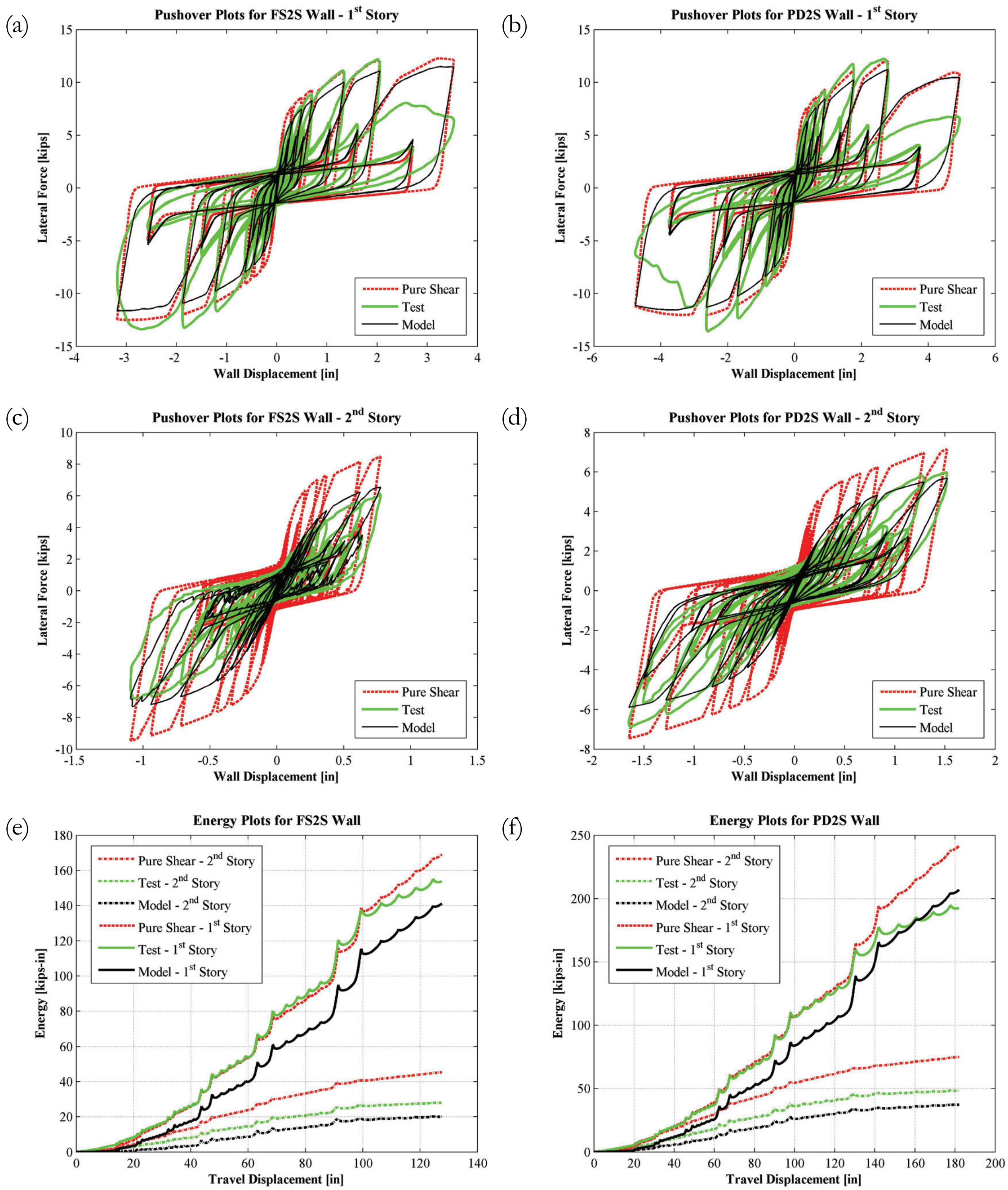

Figure 5.27 Comparison of Cyclic Response and Dissipated Energy for (a,c,e) FS2S Wall, and (b,d,f) PD2S Wall

The difference in predicted forces of the second story may also be attributed in part to the fact that the floor diaphragms are restrained from rotating in the **Pure Shear** formulation. Thus, any imposed horizontal inter-story drift translates to the same exact internal wall deformation. On the contrary, rotation of the first-floor diaphragm introduces an inter-story horizontal component that modifies the actual wall internal deformations. Deformed shapes of the numerical models shown in Figure 5.31 and Figure 5.32 demonstrate that the rotation of the floor diaphragm in this case actually reduces the effective second-floor inter-story displacement, which effectively leads to lower resisting forces. More discussion on this subject is provided in Section 5.3.7.

5.3.6 Comparison of Local Experimental Responses and Numerical Predictions

This section presents the comparison of local responses between experimental and numerical data, generated for each 2-story specimen. Figure 5.28 illustrates the vertical displacements at the bottom of the end posts of the first story, as a function of the global lateral inter-story wall displacement. The maximum uplift displacements of the **Test** responses ranged around 0.8-0.9 in, while the **Model** responses predicted maximum uplift displacements of 0.5-0.6 in. Experimental results also demonstrate a negative compressive deformation due to crushing of the sill plate perpendicular to grain, as shown later in Figure 5.41a of Section 5.5. This compressive flexibility is not considered in the numerical model.

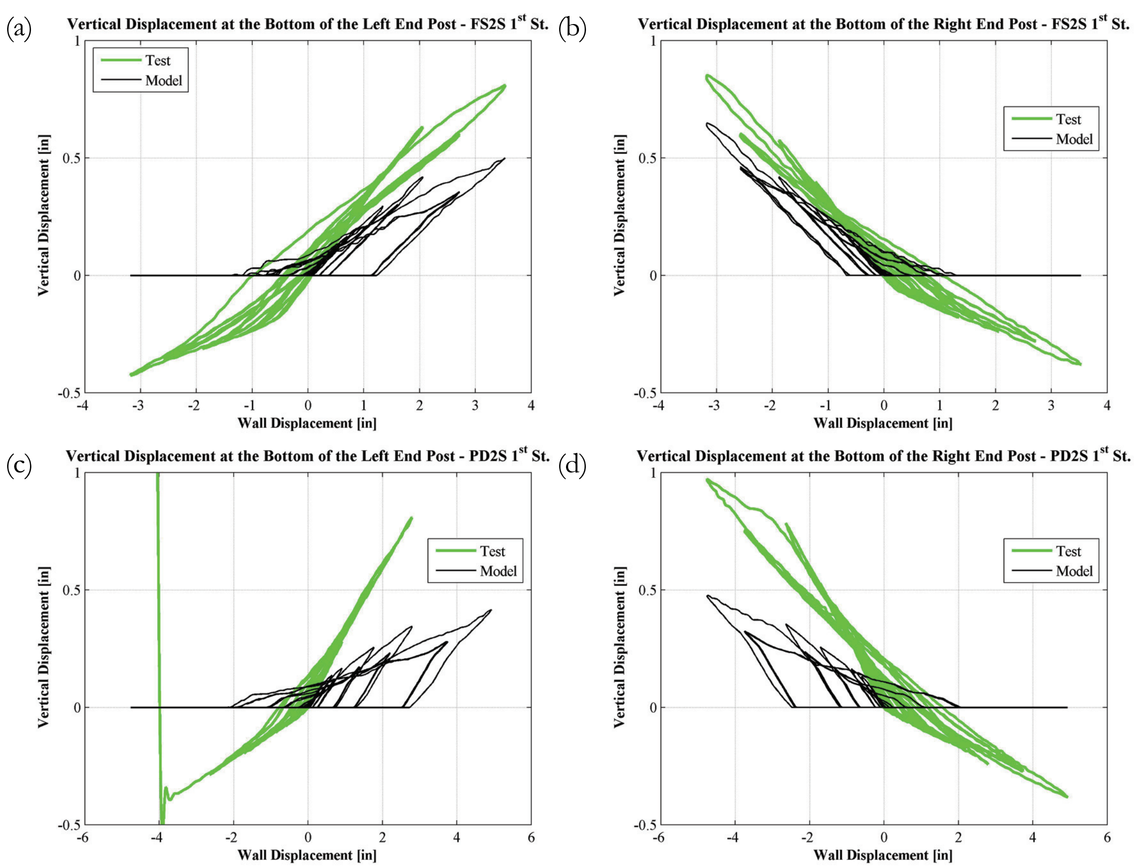

Figure 5.28 Comparison of End Post Bottom Uplift of 1st-Story for (a,b) FS2S Wall, and (c,d) PD2S Wall

Figure 5.29 illustrates the vertical displacements at the bottom of the end posts of the second story relative to the diaphragm below, as a function of the global lateral inter-story wall displacement. For the FS2S wall, experimental and numerical responses are in good agreement and demonstrate reduced end post uplift displacements, compared to the first story, with maximum values less than 0.2 in. For the PD2S wall, the numerical model over-predicts the maximum uplift displacements by about 0.2 in.

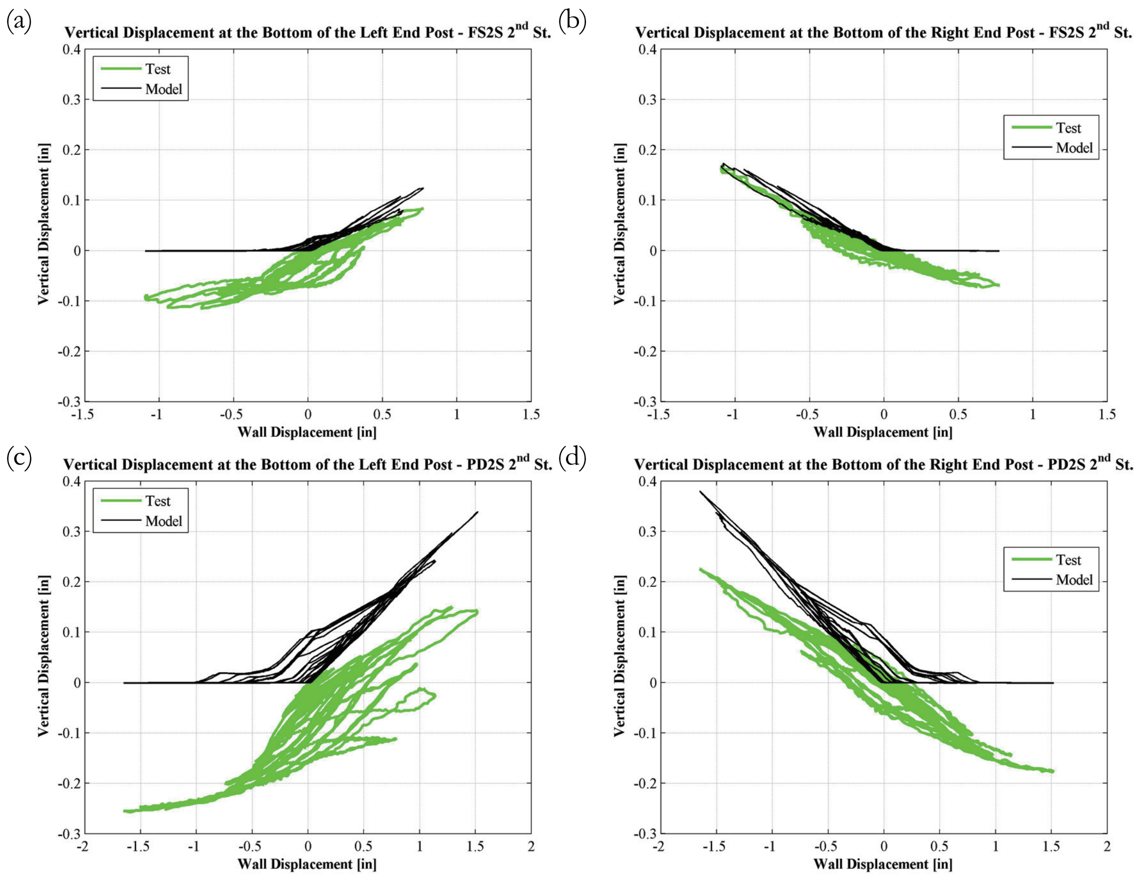

Figure 5.29 Comparison of End Post Bottom Uplift of 2nd-Story for (a,b) FS2S Wall, and (c,d) PD2S Wall

Figure 5.30 presents a comparison of the force-displacement response of holdown devices. Figure 5.30a,b illustrate the response of the holdowns installed in the first story of the FS2S wall; while Figure 5.30c,d,e,f illustrate the response of the holdowns installed in the first story of the PD2S wall. It is observed that the holdown forces are predicted well by the numerical model, but the corresponding deformations are under-predicted by about 60%. However, the good agreement in developed forces gives confidence that the load paths to resist external actions predicted by the model are realistic.

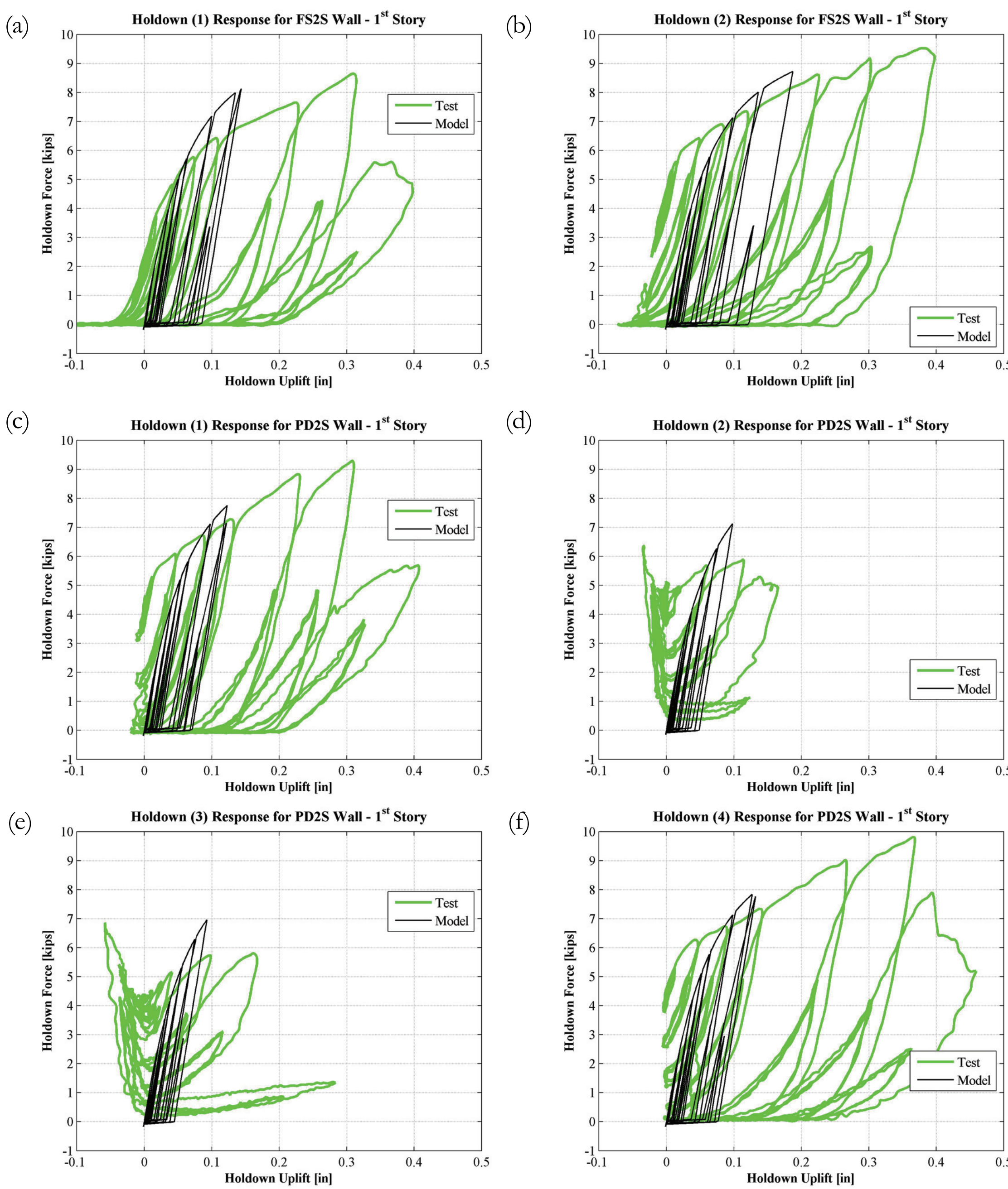

Figure 5.30 Comparison of Holdown Response of 1st-Story for (a,b) FS2S Wall, and (c,d,e,f) PD2S Wall

Similarly to the first-story hysteretic responses shown in Figure 5.26, the experimental uplifting forces are degraded during the last virgin cycles; the cycles that reach the maximum inter-story displacements. The only exception applies to the holdown installed at the right end post of the FS2S wall, as shown in Figure 5.26c, for which no strength deterioration is observed. This is consistent with the absence of strength deterioration in the developed horizontal inter-story forces when horizontal displacements are negative – directed towards the left – resulting in uplifting of the right end of the wall (Figure 5.26a). First, this observation verifies the importance of well-designed anchoring devices that will effectively suppress uplifting phenomena, allowing the development of the maximum potential in strength and energy dissipation capability of the shear wall system. Second, it justifies the proposed modeling framework that is focused on the simulation of interaction nonlinear phenomena between framing members.

5.3.7 Predicted Deformed Shapes of Wall Configurations

Figure 5.31 and Figure 5.32 illustrate the deformed shapes of the numerical models for the FS2S and PD2S walls, respectively, at the instant of the maximum positive horizontal global displacement of the first story.

For the FS2S wall, the first story exhibits sill plate and stud uplift at the left wall end, as a result of the tensile vertical equilibrium forces. Separation of field studs from the top or bottom plate is observed in the left part of the wall while the right part is deformed primarily in shear. The second story wall is subjected to a much lower inter-story drift and exhibits very small deformations. Additionally, the floor diaphragms rotate clock-wise in the direction of the external overturning actions, which results in lower internal wall deformations.

For the PD2S wall, both wall segments of the first story exhibit sill plate and stud uplift at the left end post, but the uplifting deformations are more pronounced for the right segment. The second story wall also exhibits uplifting of the sill plate at the left wall end, as well as separation of the top plate from the roof diaphragm at the right wall end. Rotation of the floor diaphragms, similarly to the FS2S wall, tends to reduce the internal wall deformations.

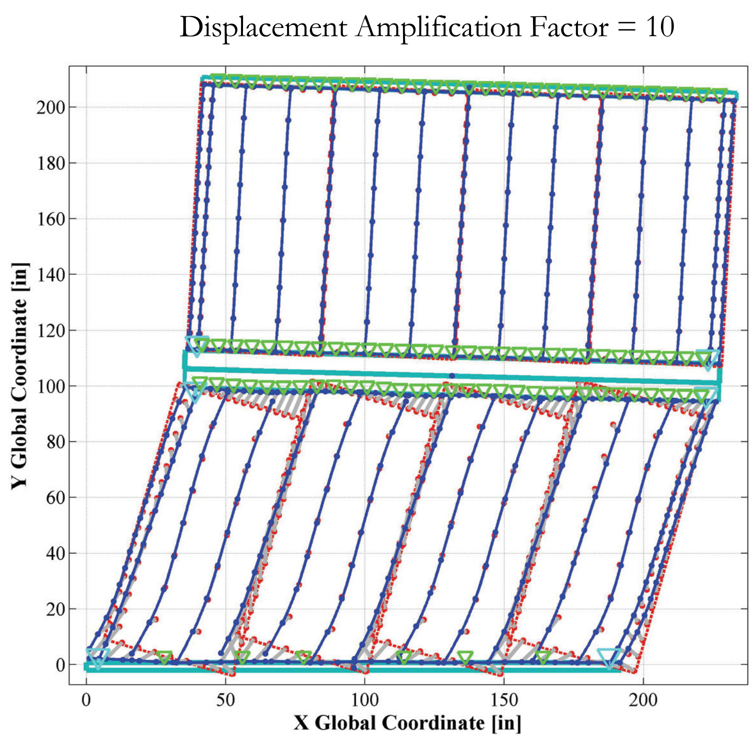

Figure 5.31 Deformed Shape of FS2S Wall at Global Lateral Displacements of +3.53 in (1st Story) and +4.15 in (2nd Story)

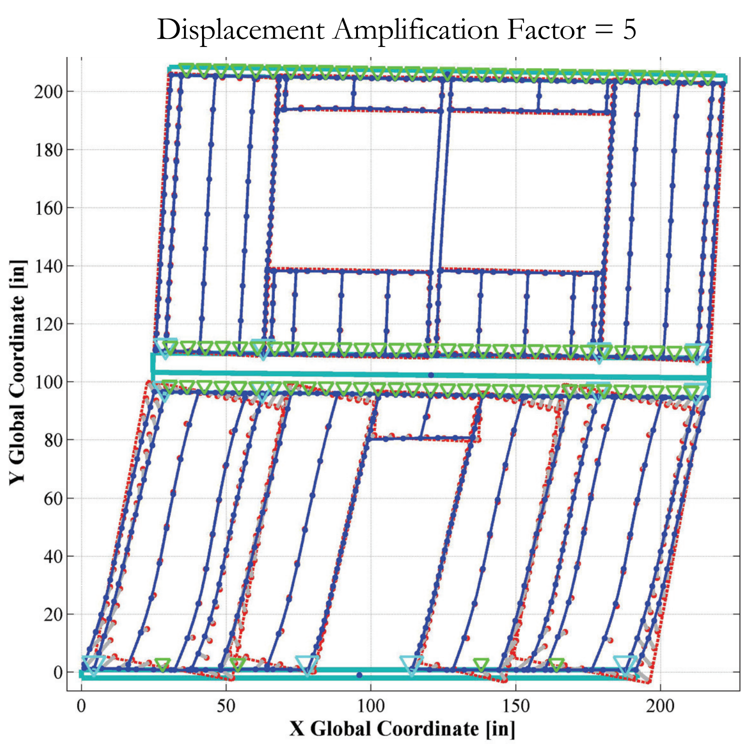

Figure 5.32 Deformed Shape of PD2S Wall at Global Lateral Displacements of +4.93 in (1st Story) and +6.06 in (2nd Story)

5.4 Numerical Example of Single-Story Shear Walls without Holdown Equipment

To further investigate the capabilities of the numerical framework, the numerical models developed for the singe-story walls of Example 1 (Section 5.2) are modified to represent shear wall segments without any holdown equipment by removing the diaphragm-to-framing connectors attached to end studs. These modified models are then subjected to the same loading protocols corresponding to each of the three cases and their predicted cyclic responses are illustrated in Figure 5.33. Figure 5.34 summarizes the backbone curves from the monotonic pushover analyses. Two points are identified in each curve, as listed in Table 5.10, and are used to plot the predicted deformed shapes of the numerical models. The first point corresponds to the maximum (capping) force and the second point corresponds to a degraded state with 25% of the maximum force. Figure 5.35 to Figure 5.40 illustrate the deformed shapes captured for the FS, PD and GD wall configurations.

The analysis results clearly demonstrate that the removal of holdowns results in substantially lower stiffness, strength and energy dissipation capability of the shear wall system. The capping force developed under monotonic loading is reduced by about 30%, 40% and 60% for FS, PD and GD walls, respectively, compared to the models with holdown devices. The displacement at the capping force is also reduced by 40% for FS and PD walls, but only 3% for GD wall. This is attributed to the fact that the removal of holdowns results in different failure modes of FS and PD walls, as illustrated in Figure 5.36 and Figure 5.38. The absence of overturning resistance induces a rocking mode of deformation, characterized by the separation of the sill plate from the vertical studs and the progressive failure of the attached sheathing-to-framing connectors at the base of the wall. It should be noted that the **Pure Shear** formulation cannot predict these differences in the response between anchored and unchored walls, which in turn is the key feature of the **Model** formulation and the proposed detailed numerical framework.

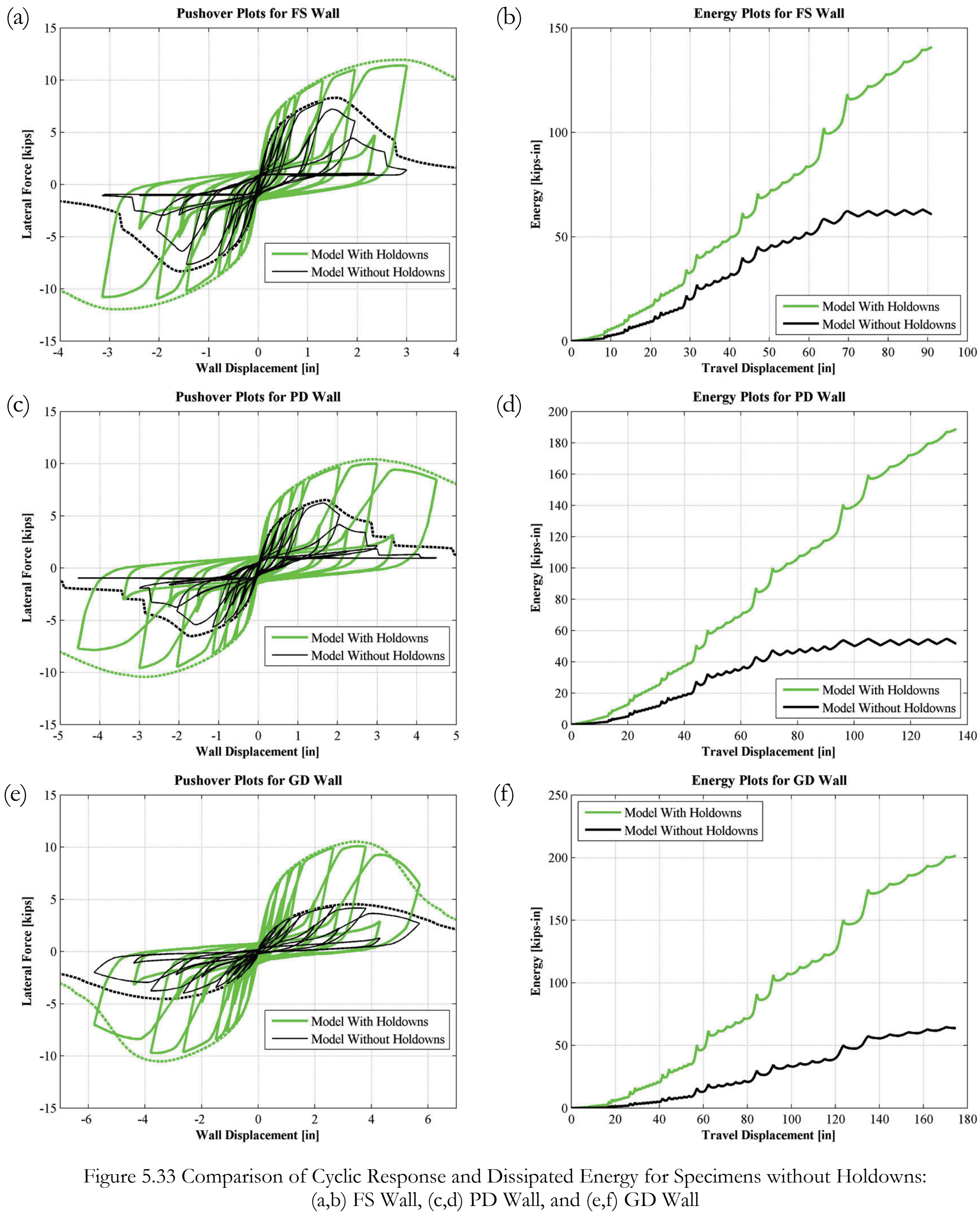

Figure 5.33 Comparison of Cyclic Response and Dissipated Energy for Specimens without Holdowns: (a,b) FS Wall, (c,d) PD Wall, and (e,f) GD Wall

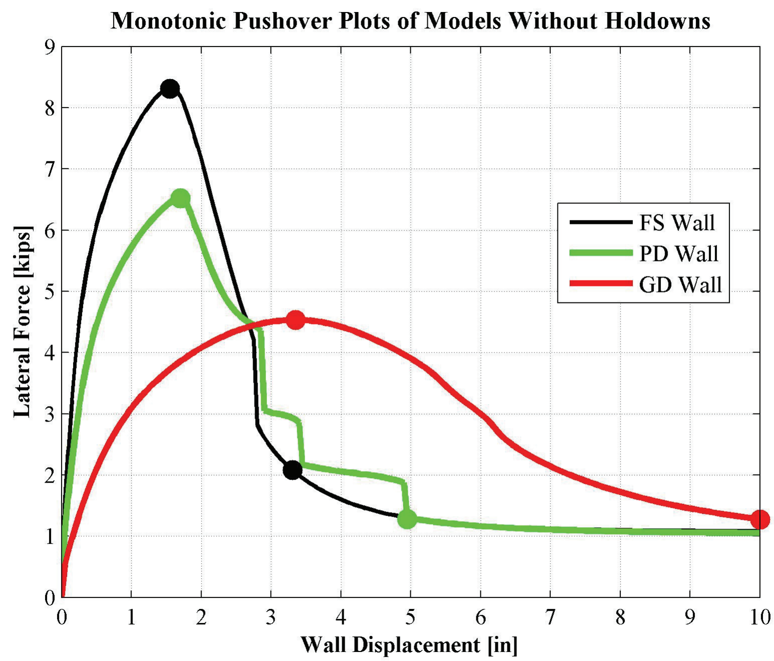

Figure 5.34 Monotonic Pushover Predictions and Indication of the Point of the Analysis Plotted in Figure 5.35 to 5.40

Table 5.10 Characteristics of the Backbone Curve of the Model without Holdown Predictions

	FS Wall	PD Wall	GD Wall
Capping force [kips]	8.31	6.52	4.53
Displacement @ cap. force [in]	1.55	1.70	3.35
Displacement @ 25% of cap. force [in]	3.30	4.95	10.00

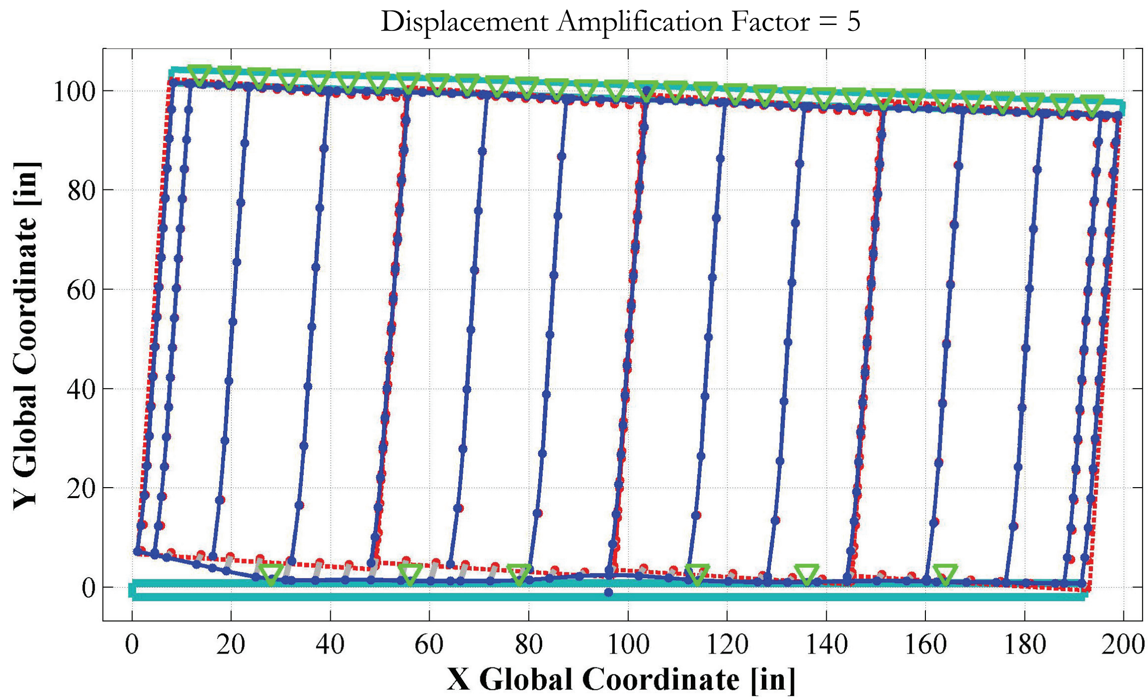

Figure 5.35 Deformed Shape of FS Wall without Holdowns from Monotonic Analysis at Lateral Displacement of +1.55 in

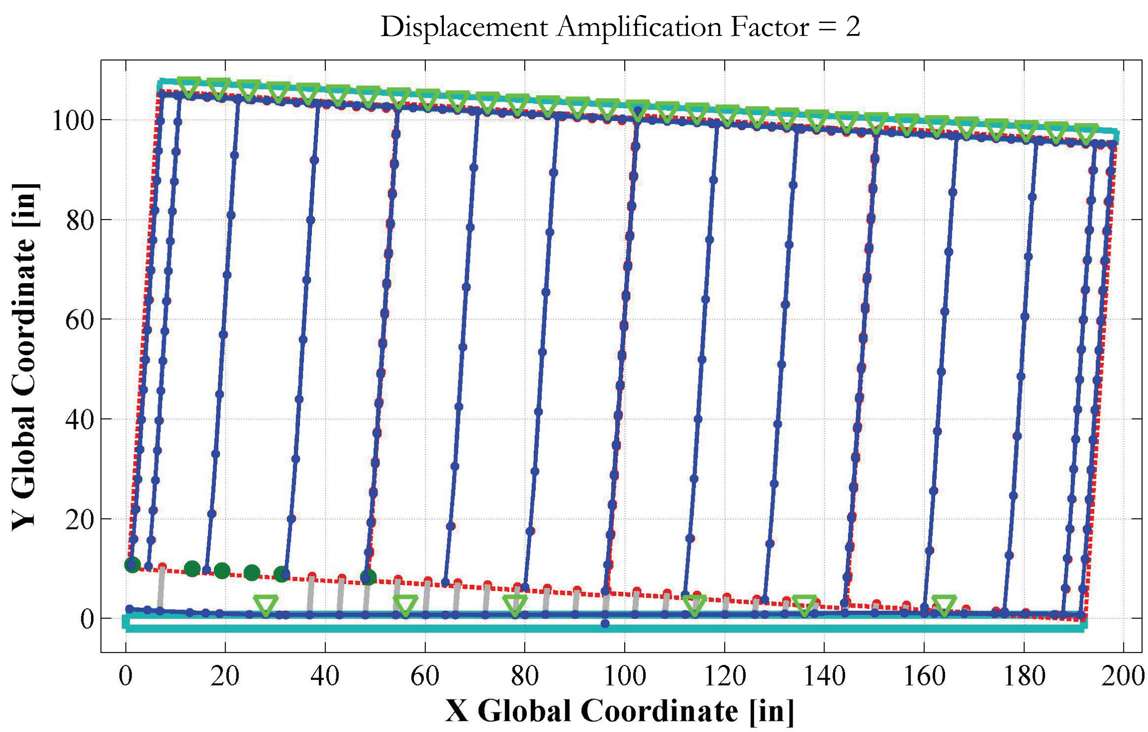

Figure 5.36 Deformed Shape of FS Wall without Holdowns from Monotonic Analysis at Lateral Displacement of +3.30 in

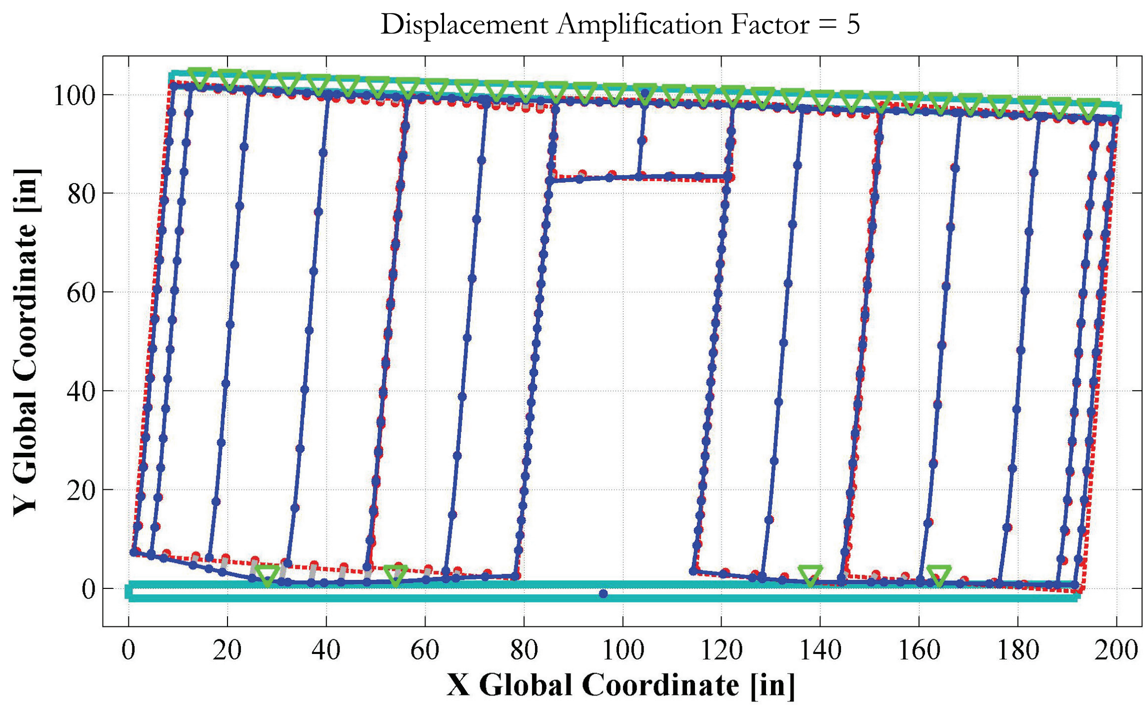

Figure 5.37 Deformed Shape of PD Wall without Holdowns from Monotonic Analysis at Lateral Displacement of +1.70 in

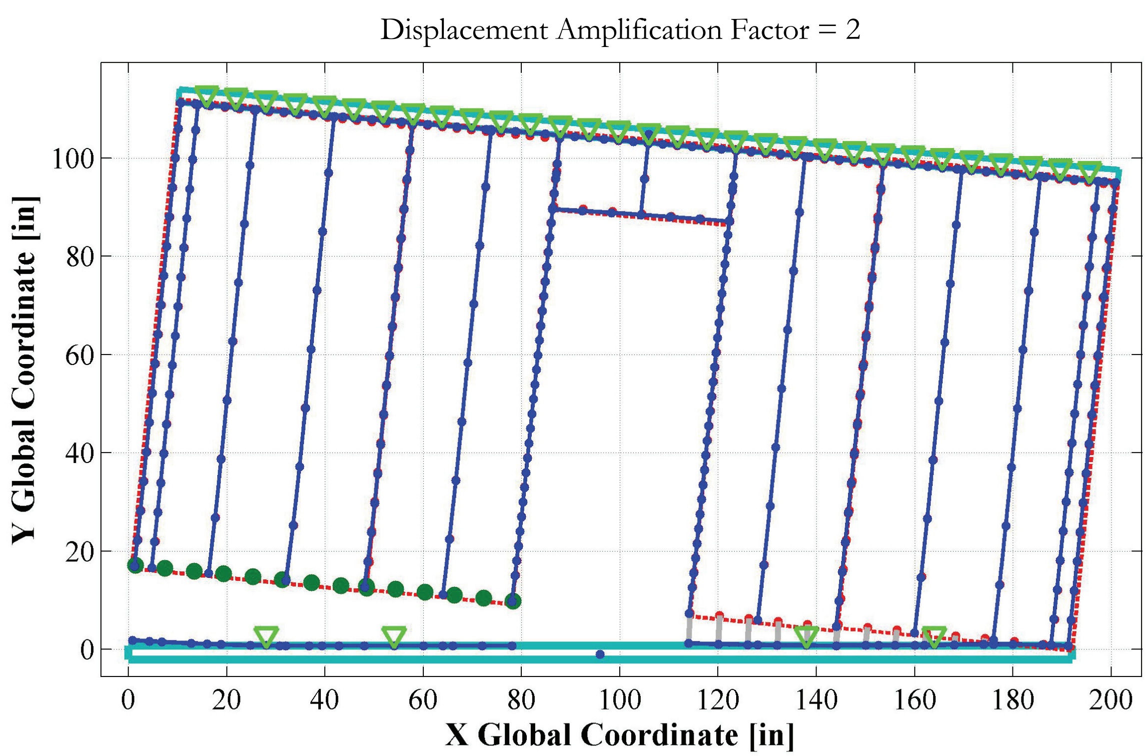

Figure 5.38 Deformed Shape of PD Wall without Holdowns from Monotonic Analysis at Lateral Displacement of +4.95 in

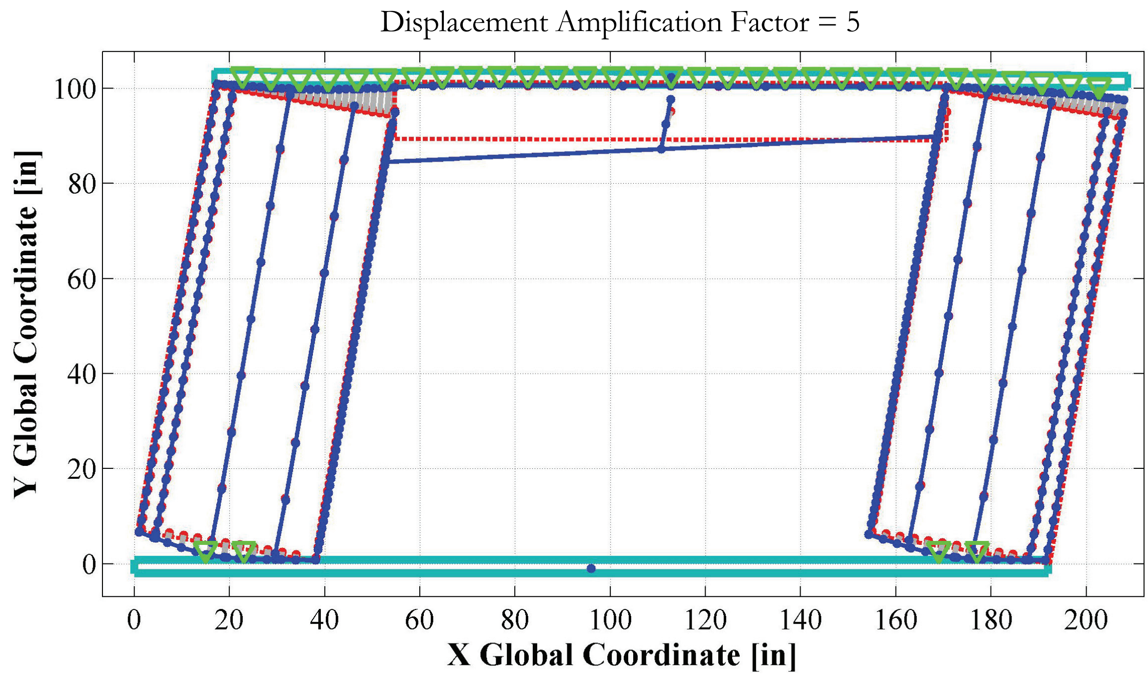

Figure 5.39 Deformed Shape of GD Wall without Holdowns from Monotonic Analysis at Lateral Displacement of +3.35 in

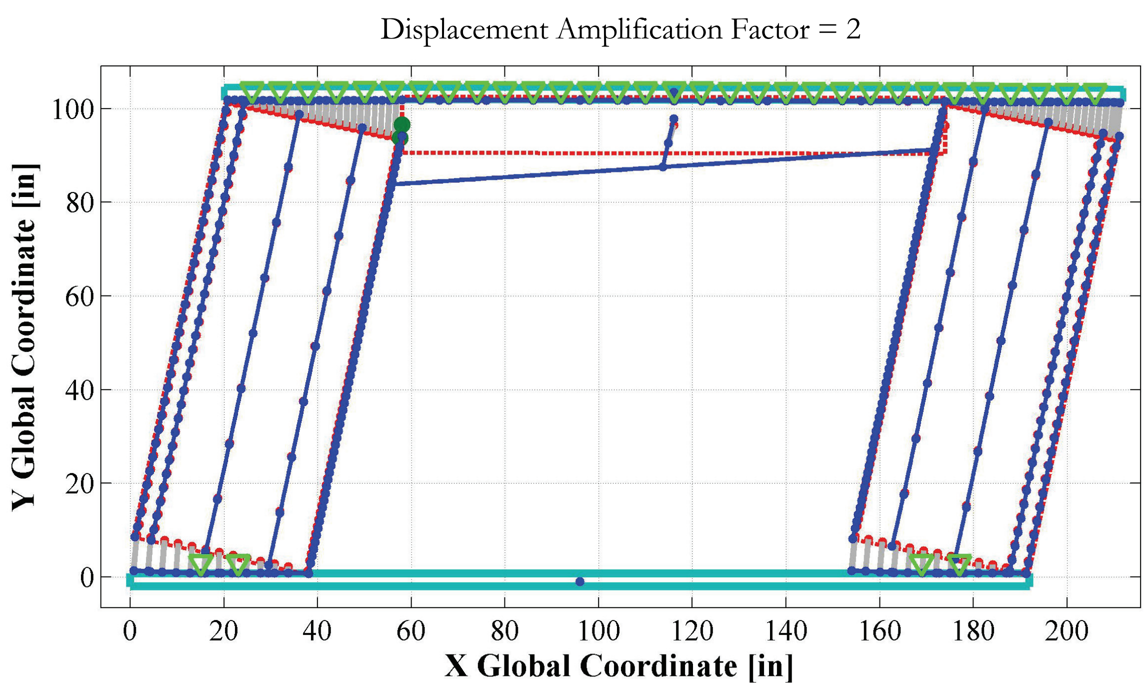

Figure 5.40 Deformed Shape of GD Wall without Holdowns from Monotonic Analysis at Lateral Displacement of +10.0 in

5.5 Summary of Predicting Capabilities of the Proposed Numerical Model

This section summarizes the main conclusions regarding the capability of the proposed **Model** to blind predict the experimental response of single- and two-story light-frame wood shear walls under lateral quasi-static monotonic or cyclic loading. The test specimens featured uplift restraining components (holdowns, anchor bolts and straps for two-story walls) and the conclusions apply to well-anchored light-frame shear wall systems under low gravity loads.

It has to be noted that the material properties utilized in the numerical models represent average values, based on experimental results or engineering handbooks. The inherent variability of fundamental properties of wood components has not been considered in this study, since a deterministic model has been adopted for the representation of the physical behavior. This fact justifies in part differences between experimental results and numerical predictions of light-frame wood shear walls.

In general, the global inter-story hysteretic response is predicted very well by the **Model** formulation, independently of the structural and geometric characteristics of the shear wall. This is better understood when considering that numerical predictions of the **Pure Shear** formulation achieve a good correlation for first-story walls with low Aspect Ratio (AR) wall segments – below a value of 2 – but significantly over-estimate stiffness, strength and energy dissipation characteristics of wall segments with high AR or generally second-story walls. The consideration of framing flexibility and contact/separation between framing members and diaphragms leads to better estimates of the actual response by modifying the force and displacement characteristics that result in more flexible responses, compared to the **Pure Shear** responses, with lower energy dissipation capability. The effectiveness of the detailed model is more pronounced for (i) the GD wall, which consisted of two high AR wall piers, and (ii) the second-story of the FS2S and PD2S walls, in the sense that for these cases the difference between the two numerical predictions is significant. The comparison of local responses, such as the end post uplift displacement and the holdown hysteretic response, demonstrated that predictions are less accurate when comparing local displacements but provide good accuracy when comparing local forces. This difference can also be attributed to secondary modes of deformation in the holdown devices, such as plate bending and frame-to-plate connector slip, which are not accounted for by the axial spring element of the numerical model. It is also important to note that the numerical results predict similar variations of local responses for different wall configurations to the variations observed in the experimental results.

To close the discussion, Figure 5.41 illustrates close-up view images of the GD wall specimen at three locations after testing along with the deformed shape of the numerical model shown earlier in Figure 5.21. Figure 5.41a focuses on the connection of the header with the inner studs. It is shown that the header has actually separated from the jack studs, while the full height stud has also detached from the top plate. This is similar to what is predicted by the model in Figure 5.41d and justifies the modeling technique of the GD wall regarding the header, given that separation between framing members is not considered within the wall but only between sill/top plates and studs. The horizontal beam representing the header has a high axial and bending stiffness but the sheathing panel covering the header is not nailed along the bottom edge. This allows the vertical studs of the full height pier to separate from the top plate, without imposing additional tensile strength from the header. Figure 5.41b shows the cross-grain crushing of the sill plate under compressive load carried from the stud above. As mentioned, this mode of deformation is not considered in the proposed model, but could be integrated in the response of the contact spring that connects the sill plate and the stud. Figure 5.41c focuses on the bottom of the wall end that is under tensile vertical forces. Again, the observed deformed shape matches the predicted deformed shape shown in Figure 5.41d. The outer and the field stud has uplifted from the sill plate, while the studs anchored with the holdown remain connected to the sill plate. These correlations demonstrate that the proposed numerical framework predicts realistic load paths within the shear wall.

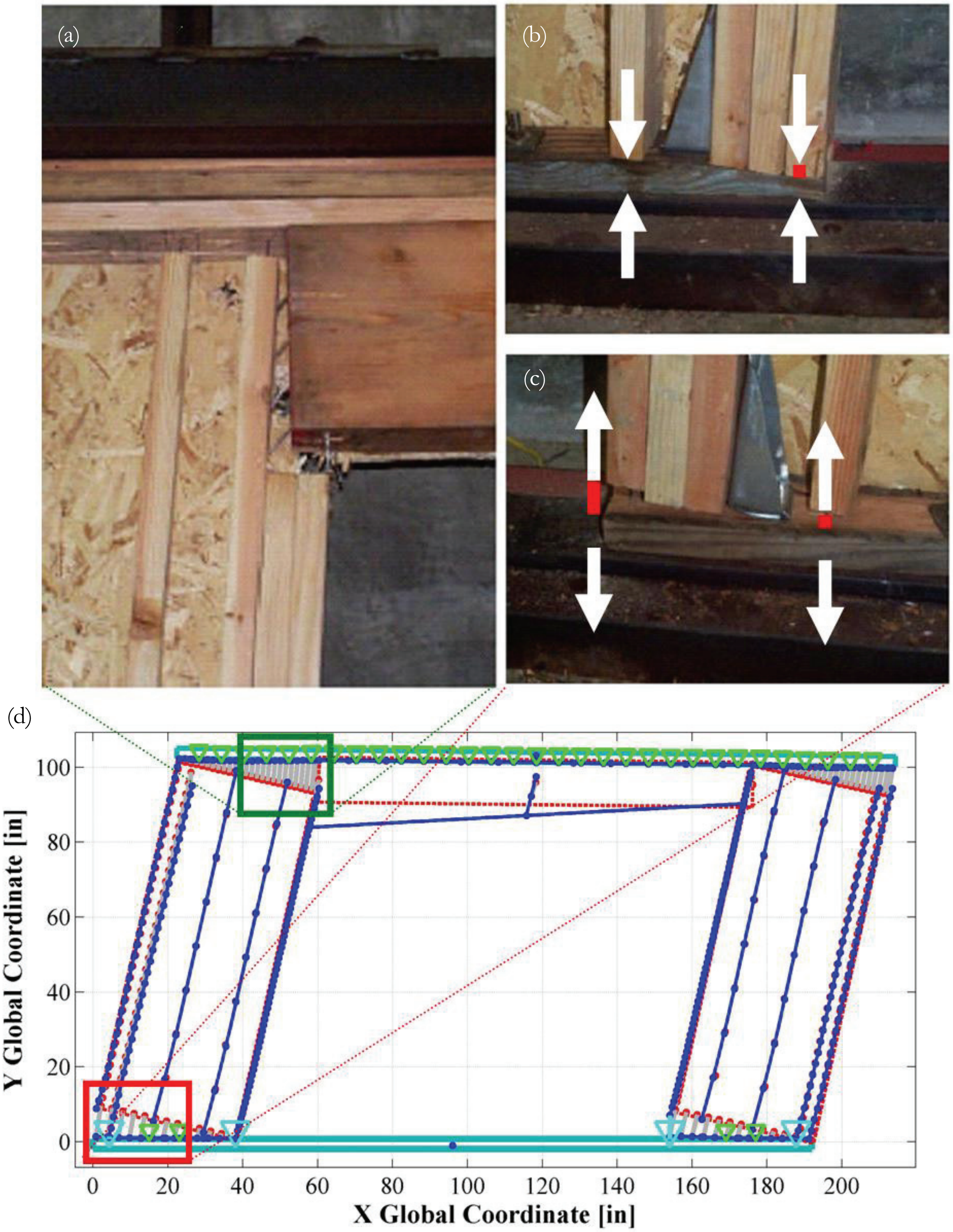

Figure 5.41 Correlation of Deformation Patterns between (a,b,c) Experimental, and (d) Numerical Deformed Shapes

CHAPTER 6: MODEL VALIDATION FOR DYNAMIC ANALYSIS

6.1 Introduction

This chapter investigates the capabilities of the proposed numerical framework for dynamic time-history analysis of a 2D model of a light-frame wood structure. The experimental shake-table tests utilized in this example have been conducted and documented by Shinde and Symans (2010), as part of the NEESWood Project. Similarly to the validation examples of Chapter 5, two numerical predictions are illustrated throughout the various figures. One is labeled **Pure Shear** and represents the simplified numerical model described in Section 4.3.2, while the second prediction is labeled **Model** and represents the detailed numerical model described in Section 4.3.3.

6.2 Test Specimen

The test specimen consisted of two identical shear walls aligned parallel to the direction of shaking. The top of the walls was connected to a horizontal floor diaphragm, consisting of wooden truss joists, 9 and 1/2 in deep, with blocking. On top of the diaphragm and along the direction of shaking, a 9 ft long steel beam (W14x120) was connected to the truss joists and provided part of the seismic mass. Additional lead bricks were uniformly distributed over the steel beam and the diaphragm for a total weight of 13200 lbs (or 825 lb/ft per wall) acting on both walls (Shinde and Symans 2010). Figure 6.1 shows a photo of the test specimen on the shaking table at the Rensselaer Polytechnic Institute (RPI).

Each shear wall was about 8 ft long by 8 ft high and incorporated a single OSB panel 4 ft by 8 ft because it served as a benchmark structure for comparison with a retrofitted damper-wall with similar dimensions (Shinde and Symans 2010). The framing consisted of nominal 2x6 studs spaced at 16 in oc. The lumber used for framing was Spruce-Pine-Fir. The top plate and the end studs consisted of two framing members. The sheathing provided was OSB, 7/16 in thick. Sheathing panels were fastened to the framing with 8d common nails, 2.5 in long with 0.131 in diameter. Edge and field nailing was specified at 6 in and 12 in oc, respectively. Simpson Strong-Tie™ HD6A holdowns with 7/8 in diameter A325 steel bolts were used to connect the double end studs to the shake-table through the sill plate. Additionally, two 7/8 in diameter anchor bolts with 3 in square washers were used to connect the central portion of the sill plate to the shake-table.

Figure 6.1 Photo of the Test Specimen (from Shinde and Symans 2010)

The double top plate was connected to the floor joists with A34 framing clips at 9 in oc, while additional A35 framing clips were used to connect the top plate to the rim joist. More information on connection details can be found in Shinde and Symans (2010).

Since the two shear walls were identical and their recorded experimental responses were very similar – no significant torsion was identified in the vertical direction – the equivalent numerical model simulated a single shear wall with half of the total weight supported (6700 lbs including half of the wall's self weight).

Figure 6.2 illustrates the structural configuration of the shear wall specimen (left) and the equivalent numerical model (right). The master DOF of the building model are identified as the two global translations, U and V, and the in-plane rotation Θ of the center of the rigid diaphragm. The 3-by-3 mass matrix **M** assuming uniform mass distribution is equal to:

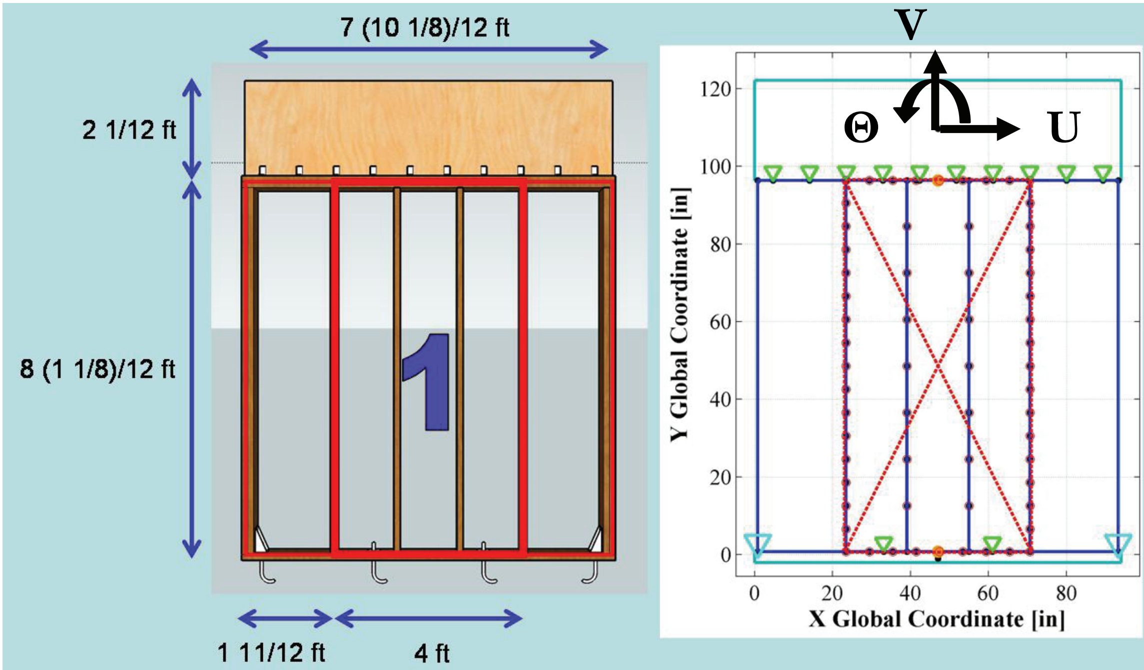

Figure 6.2 Structural Configuration (left) and Numerical Model (right) of the RPI Wall

$$\mathbf{M} = \frac{1}{386.4} \cdot \begin{bmatrix} 6700 & 0 & 0 \\ & 6700 & 0 \\ \text{sym} & & 6700 \cdot \dfrac{94^2 + 25^2}{12} \end{bmatrix} [\text{lbs} \cdot \text{sec}^2/\text{in}] \tag{6.1}$$

6.3 Material and Spring Connector Properties

Table 6.1 presents basic dimensions and associated typical material properties for the linear elastic beam and panel elements utilized in the numerical analyses. The modulus of elasticity of the beam elements was specified from Table 4A in NDS (2005) for Spruce-Pine-Fir Stud grade. The elastic modulus of OSB was estimated based on typical properties given by manufacturers.

Table 6.2 presents the properties of the linear and nonlinear elastic elements utilized to simulate the interaction between framing members and diaphragms. The force in the normal – initially vertical – direction relative to the contact area is computed from the nonlinear elastic response given in (4.113), using the input parameters d_{tol} and f_{tol} shown in Table 6.2. The response in the direction parallel to the contact area is computed according to the nonlinear elastic relationship given in (4.116) for stud-to-plate contact elements, which effectively minimizes the flexibility in this direction. On the contrary, the diaphragm-to-plate contact elements are considered to act linearly elastic with a very low stiffness of 100 lbs/in. This low value is used in order to reduce unrealistic catenary action along the horizontal plate when uplifting from the diaphragm. Note that the resistance in this direction is provided by the diaphragm-to-framing connection elements.

Table 6.3 presents the properties of the diaphragm-to-framing connection elements. The stiffness parallel to the contact area is 50000 lbs/in for holdowns and anchor bolts at the bottom of the wall, and 20000 lbs/in for the connections at the top of the wall. The response of the holdowns in the normal direction is the only nonlinear inelastic behavior considered in the diaphragm-to-framing connection elements. The spring parameters for nonlinear holdown connectors were estimated as described in Appendix B. The stiffness normal to the contact area is 20000 lbs/in for the anchor bolts at the bottom of the wall and 2000 lbs/in for the framing clips at the top of the wall.

Table 6.1 Dimensions and Material Properties of Linear Elastic Beam and Panel Elements

Sheathing Panels Oriented Strand Board	**Shear modulus** [psi]	**Thickness** [in]
	220000	7/16
Wood framing 2x6 Spruce-Pine-Fir	**Modulus of elasticity** [psi]	**Cross section dimensions** [in]
	1200000	1.5x5.5

Table 6.2 Properties of Linear and Nonlinear Elastic Contact Elements

Elements	**Direction relative to contact**	**Behavior**	**Input parameters**		
			d_{tol} [in]	f_{tol} [lbs]	**Elastic stiffness** [lbs/in]
Stud-to-plate contact elements	Parallel	Nonlinear elastic (4.116)	0.0001	0.1	N/A
	Normal	Nonlinear elastic (4.113)	0.0001	0.1	N/A
Diaphragm-to-plate contact elements	Parallel	Linear elastic	N/A	N_A	100
	Normal	Nonlinear elastic (4.113)	0.0001	0.1	N/A

Table 6.3 Properties of Diaphragm-to-Framing Connection Elements

Elements	Direction relative to contact	Behavior	Elastic stiffness [lbs/in]
Holdowns at the bottom of the wall	Parallel	Linear	50000
	Normal	Nonlinear inelastic	120000
Holdowns at the top of the wall	Parallel	N/A	N/A
	Normal	N/A	N/A
Anchor bolts at the bottom of the wall	Parallel	Linear	50000
	Normal	Linear	20000
Anchor bolts at the top of the wall	Parallel	Linear	20000
	Normal	Linear	2000

The parameters of the sheathing-to-framing nonlinear springs were based on experimental connection data generated by Ekiert and Hong (2006). The identification process and the spring parameters are presented in Appendix B. Table 6.4 summarizes the basic characteristics of the backbone curve of the nonlinear springs utilized for modeling sheathing-to-framing and holdown connections. Figure 6.3 illustrates the monotonic and cyclic response of each unidirectional nail spring. The bidirectional response is implemented with an orientation and an interaction of each pair of springs, as described in Section 4.3.5.3.

Table 6.4 Characteristics of Backbone Curve of Nonlinear Inelastic Springs

	Initial Stiffness [lbs/in]	**Yield Force** [lbs]	**Capping Force** [lbs]	**Displacement at Capping Force** [in]	**Displacement at Failure** [in]
7/16 in OSB / 8d Common Nails / 2x6 Spruce-Pine-Fir	11800	137.4	268.3	0.52	3.42
HD6A Holdown Spring	120000	6400.0	8332.1	0.53	1.80

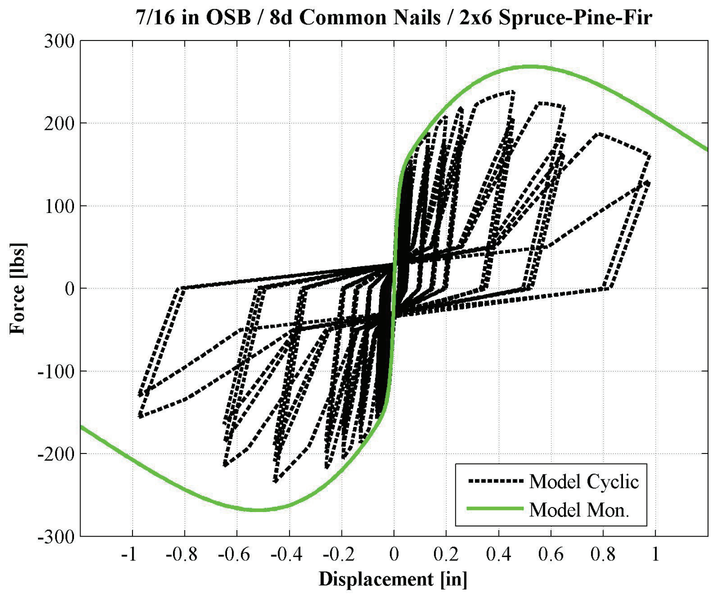

Figure 6.3 Monotonic and Cyclic Response of a Unidirectional Nail Spring for [7/16 in OSB / 8d Common Nails / 2x6 Spruce-Pine-Fir]

6.4 Input Ground Motions

Three shake-table tests with increasing amplitude were conducted using the same test structure. The ground motions were selected from the 1994 Northridge Earthquake. The first two shake-table tests were conducted using the Canoga Park record with an amplitude scale factor of 0.12 and 0.40, respectively. The third shake-table test was conducted using the Rinaldi record, with an amplitude scale factor of 0.40. The acceleration response spectra corresponding to the achieved ground motions recorded from the shake table during testing are illustrated in Figure 6.4. The response spectra of the original recorded motions have been presented in Section 3.3.4

6.5 Comparison of Natural Periods and Illustration of Numerical Mode Shapes

The natural period of the test structure was identified through white noise input of 0.02 in amplitude and 0-30 Hz bandwidth (Shinde and Symans 2010). Table 6.5 presents the fundamental natural period identified before any seismic test was conducted as well as the three numerically predicted natural periods of the two models. The numerical natural periods correspond to the global stiffness matrix that is obtained after application of the gravity load of 6700 lbs.

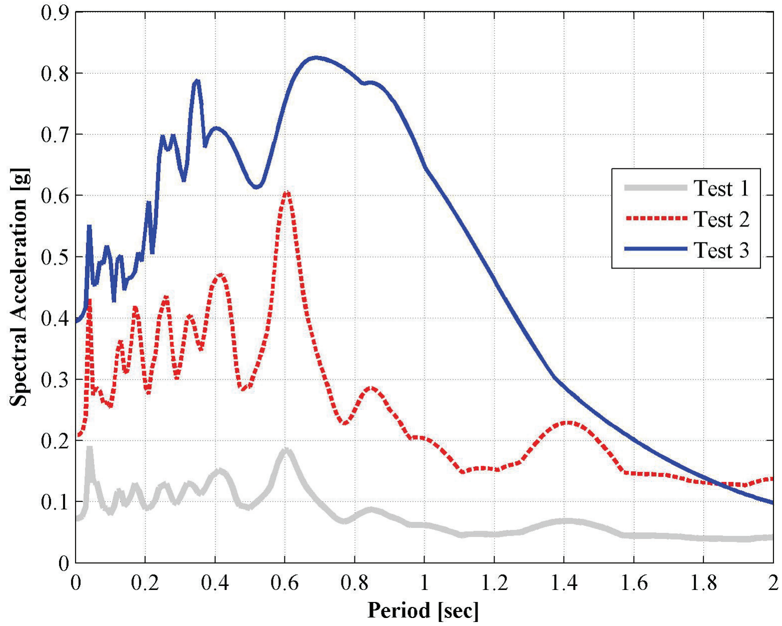

Figure 6.4 Acceleration Response Spectra of the Achieved Input Ground Motions

Table 6.5 Experimental and Numerical Natural Periods in seconds

Mode	Experimental	Numerical (**Model**)	Numerical (**Pure Shear**)
1	0.258	0.271	0.218
2	N/A	0.029	0.011
3	N/A	0.023	0.007

The fundamental period of the test specimen is 0.26 sec, which agrees well with the **Model** prediction of 0.27 sec. The **Pure Shear** formulation predicts a stiffer system that corresponds to a natural period of 0.22 sec. This difference corresponds to an increase of the initial stiffness of the detailed model by 50%. The periods of the higher modes predicted by the numerical models are also presented for sake of completeness. Note the separation between the first and the higher natural periods in the numerical models. This results from the high axial and bending stiffness of the framing members. Figure 6.5 illustrates the 3 **Model** mode shapes, while Table 6.6 and Table 6.7 list the displacements of the corresponding mode shapes for the **Model** and the **Pure Shear** formulations, respectively. The 1st mode shape is associated with the horizontal racking deformation of the shear wall, the 2nd mode shape is related to the axial deformation of the vertical framing members and the 3rd mode shape is associated with the rotation of the rigid diaphragm.

(a)

(b)

(c)

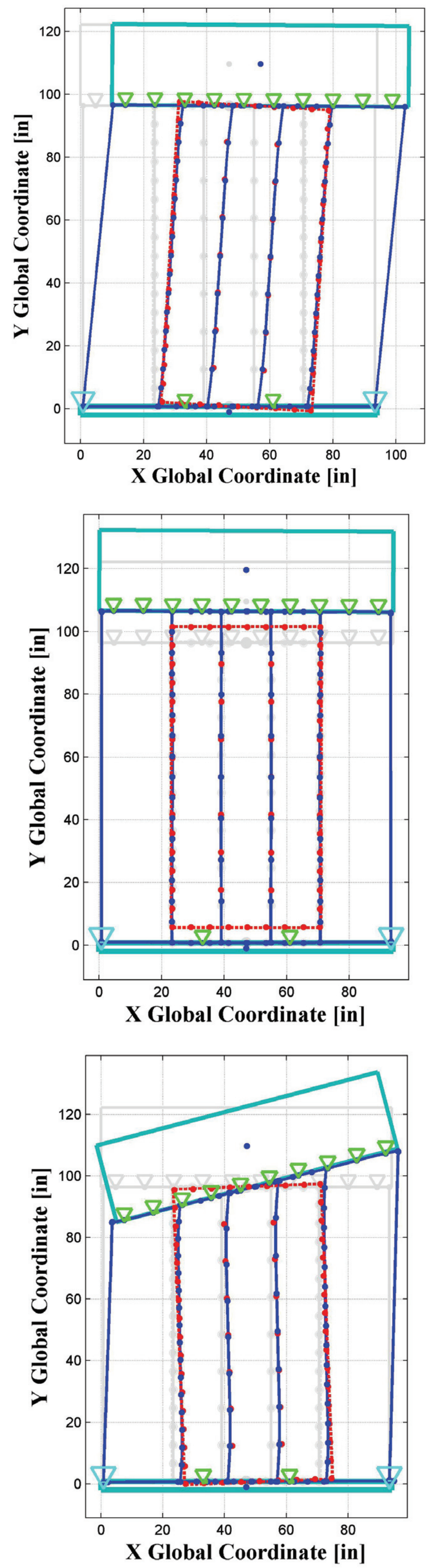

Figure 6.5 Plots of Numerical **Model** Mode Shapes: (a) Mode 1; (b) Mode 2; and (c) Mode 3

Table 6.6 Numerical **Model** Mode Shapes

Master DOF (see Fig. 6.2)	Mode		
	1	2	3
U [in]	1.000E+00	-2.821E-05	4.279E-01
V [in]	9.764E-06	1.000E+00	2.782E-02
Θ [rad]	-5.993E-04	-3.894E-05	9.034E-01

Table 6.7 Numerical **Pure Shear** Mode Shapes

Master DOF (see Fig. 6.2)	Mode		
	1	2	3
U [in]	1.000E+00	-4.547E-07	6.065E-02
V [in]	3.362E-07	1.000E+00	1.538E-03
Θ [rad]	-7.688E-05	-1.950E-06	9.982E-01

6.6 Input Data for Dynamic Nonlinear Analysis

Stiffness and mass proportional Rayleigh damping, as described in Section 4.4.1, was selected such as to provide a damping ratio of 1% of critical for the 1st (horizontal) and the 2nd (vertical) mode of vibration, which is applicable when nonlinear hysteretic response is considered for the sheathing-to-framing connections, as discussed previously in Section 4.4.1. Figure 6.6 illustrates the modal damping ratios specified for each numerical formulation, computed as shown in (4.185). These are not identical since the stiffness matrices are not identical.

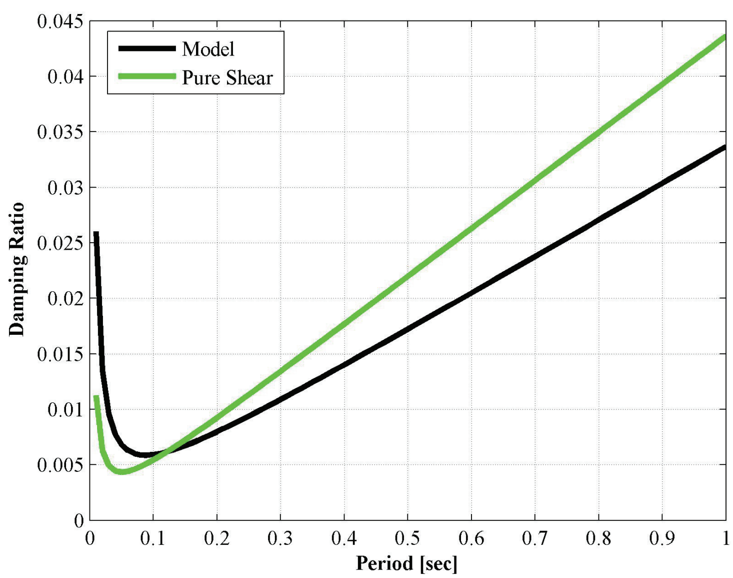

Mode	Viscous Damping Ratio ζ_i	
	Model	**Pure Shear**
1	0.010	0.010
2	0.010	0.010
3	0.012	0.016

Figure 6.6 Rayleigh Damping Specified For Each Numerical Formulation

The Newmark constant acceleration method with $\beta = 1/4$ and $\gamma = 1/2$ with Newton-Raphson iterations, as described in Section 4.4.2, was selected as the time integration scheme. The time step used in the nonlinear dynamic analysis was equal to 0.005 sec and every solution step was recorded in the output file. The experimental data were recorded at the same time step of 0.005 sec (200 Hz sampling frequency) and were filtered with a 5^{th} order low-pass filter with a cut-off frequency of 25 Hz. An additional analysis case was executed to investigate if a smaller time step of 0.001 sec provided significant differences in the numerical responses. The results from this case, presented in Appendix C, indicated that a time step of 0.005 sec was adequate in providing almost identical responses with the case of a smaller time step of 0.001 sec. Thus, due to the computational efficiency, the first option was selected.

6.7 Comparison of Global Experimental Responses and Numerical Predictions

The experimentally recorded horizontal responses of the two identical shear walls, acting in the direction of shaking, were averaged in order to obtain a single set that can be compared with the numerical response of a single shear wall model. This process yielded the averaged absolute displacement, velocity and acceleration responses of the sill and the top plate, or else the bottom and the top of the shear wall framing. Additionally, the absolute acceleration and displacement responses of the shake table were recorded along the centerline of the two shear walls. The inter-story wall displacement is defined as the differential displacement between the top plate and the shake table. The horizontal resisting force is computed from the absolute acceleration at the top plate[††]. Thus, the integration of the experimental force-displacement response provides the hysteretic strain and damping energy response. The inter-story wall velocity is defined as the differential velocity between the top and the sill plate. Since the numerical models do not account for horizontal slippage between top plate and diaphragm, the numerical horizontal displacement, velocity and acceleration response of the top plate is directly computed from the response of the floor diaphragm.

The three shake-table motions recorded were merged into a single motion with 10 sec interval of zero intensity between each record. This motion was then used for a single nonlinear dynamic analysis of the building model. The experimental and numerical responses for each of

[††] Computed as minus the mass times the acceleration.

the three shake-table tests conducted are presented in the following figures. Figure 6.7 to Figure 6.9 present data relevant to **Test 1** to **Test 3**, respectively. Figure 6.10 presents data relevant to all three tests. Each of these figures presents the force-displacement response; the strain and damping energy response; the time histories of the inter-story displacement and velocity; and the time history of the top of wall absolute acceleration. Accordingly, Table 6.8 to Table 6.10 list the maximum and minimum response values for **Test 1** to **Test 3**, respectively, and provide the percentage differences between experimental and numerical maximum and minimum values.

Commenting first on the numerical predictions for **Test 1**, it is observed that the test specimen exhibits a hysteretic response even for quite small inter-story displacements of about 0.1 in. This response is not predicted by the numerical models and it is believed that it originates from the horizontal response between framing-to-framing and framing-to-diaphragm connections. These connections in the numerical model are considered to be rigid due to the difficulty in assessing the actual behavior – depends on the friction between these components that is related to the actual vertical force – and the weak contribution of this behavior in the global response under medium-to-high ground excitation. As a result, the hysteretic strain energy dissipated by the numerical models is about 40%~45% of the actual energy dissipated during the test. Maximum displacements are under-estimated but the **Model** predictions provide a better correlation compared to the **Pure Shear** predictions.

Commenting on the predictions for **Test 2**, the numerical force-displacement hysteretic responses are fairly well correlated to the experimental ones. It is observed, however, that the experimental loops do not exhibit the distinct pinching response that is usually observed during pseudo-static cyclic tests. Thus, the numerical predictions fail to closely follow the experimental response. Maximum inter-story displacements are under-estimated by about 35% (**Model**) and 50% (**Pure Shear**) and maximum forces are over-estimated by about 10% for both formulations. The hysteretic strain energy dissipated by the numerical models is about 75% of the actual energy dissipated during the test. **Model** predictions correlate better with the experimental results than **Pure Shear** predictions.

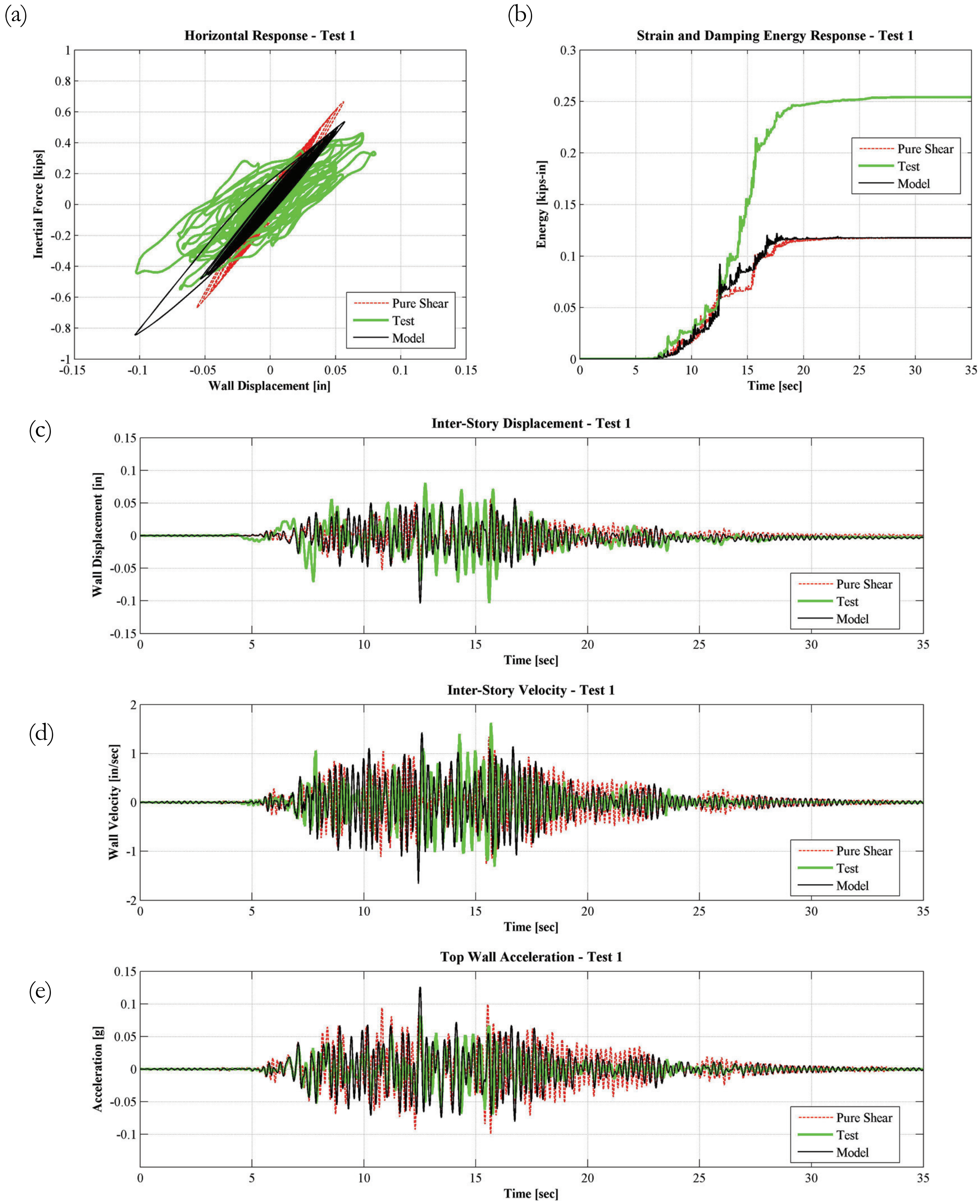

Figure 6.7 Comparison of Experimental and Analytical Data for **Test 1**: (a) Hysteretic Response; (b) Hysteretic Strain Energy; (c) Inter-Story Displacement Time History; Inter-Story Velocity Time History; and (e) Top of Wall Absolute Acceleration Time History

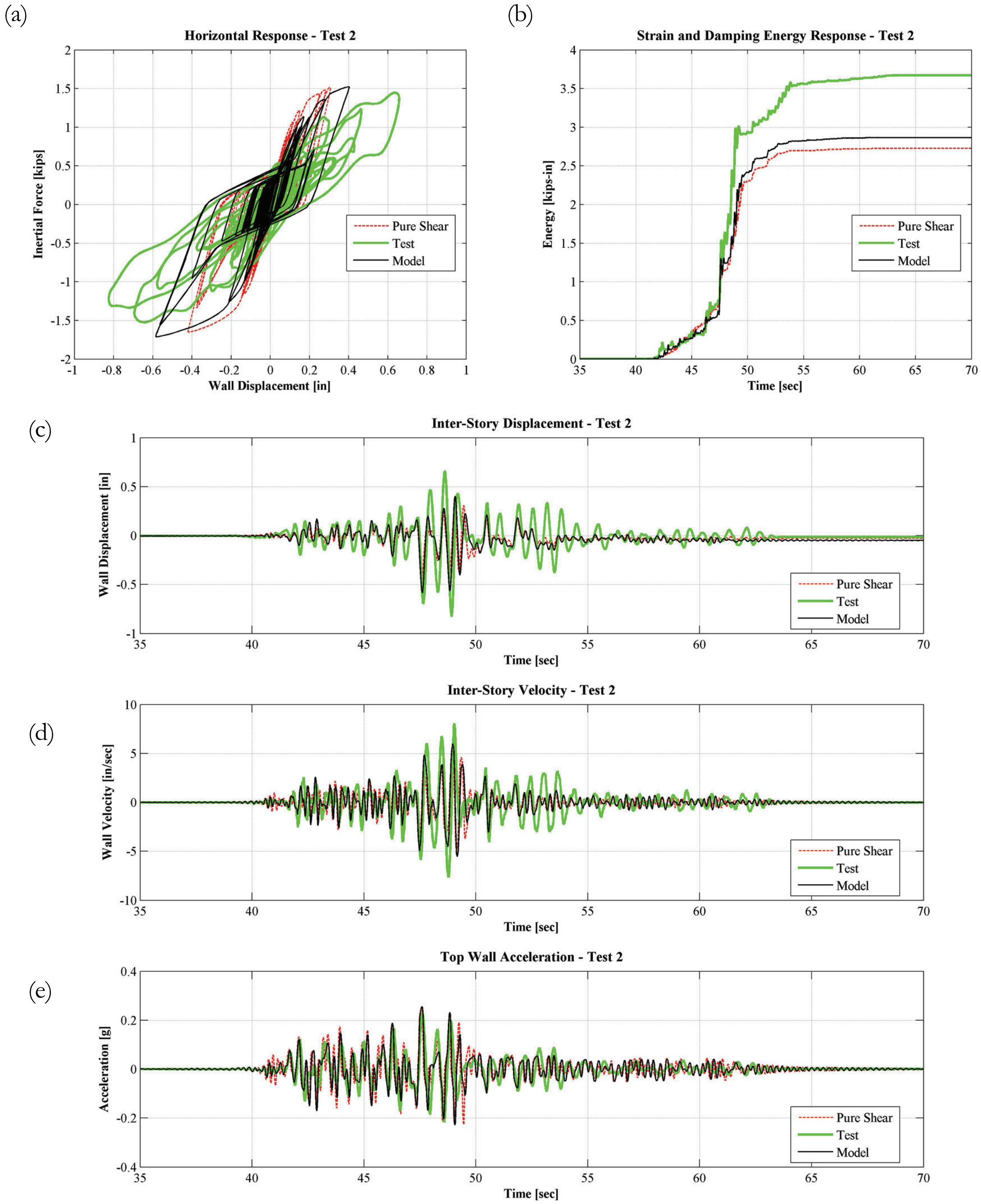

Figure 6.8 Comparison of Experimental and Analytical Data for **Test 2**: (a) Hysteretic Response; (b) Hysteretic Strain Energy; (c) Inter-Story Displacement Time History; Inter-Story Velocity Time History; and (e) Top of Wall Absolute Acceleration Time History

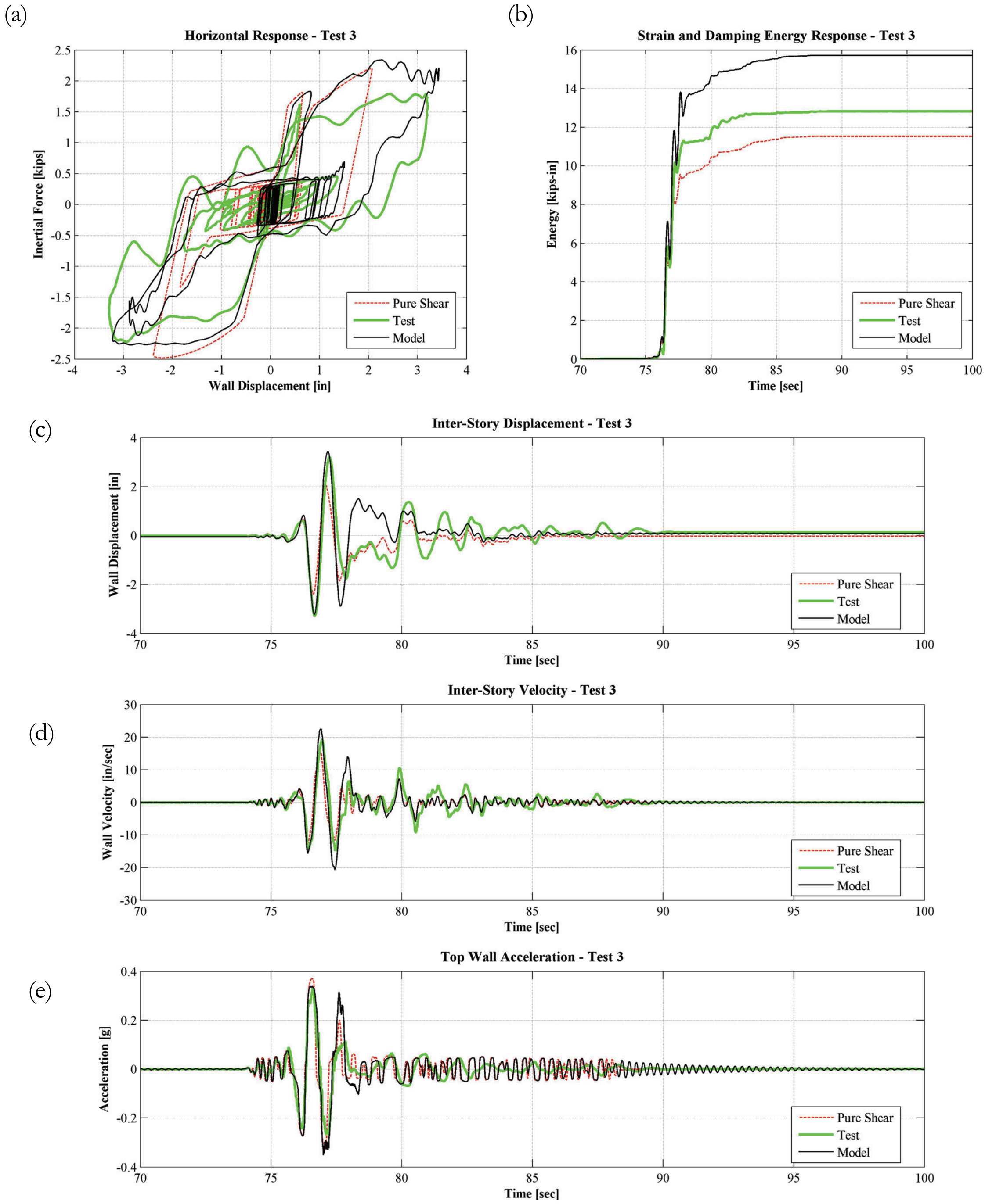

Figure 6.9 Comparison of Experimental and Analytical Data for **Test 3**: (a) Hysteretic Response; (b) Hysteretic Strain Energy; (c) Inter-Story Displacement Time History; Inter-Story Velocity Time History; and (e) Top of Wall Absolute Acceleration Time History

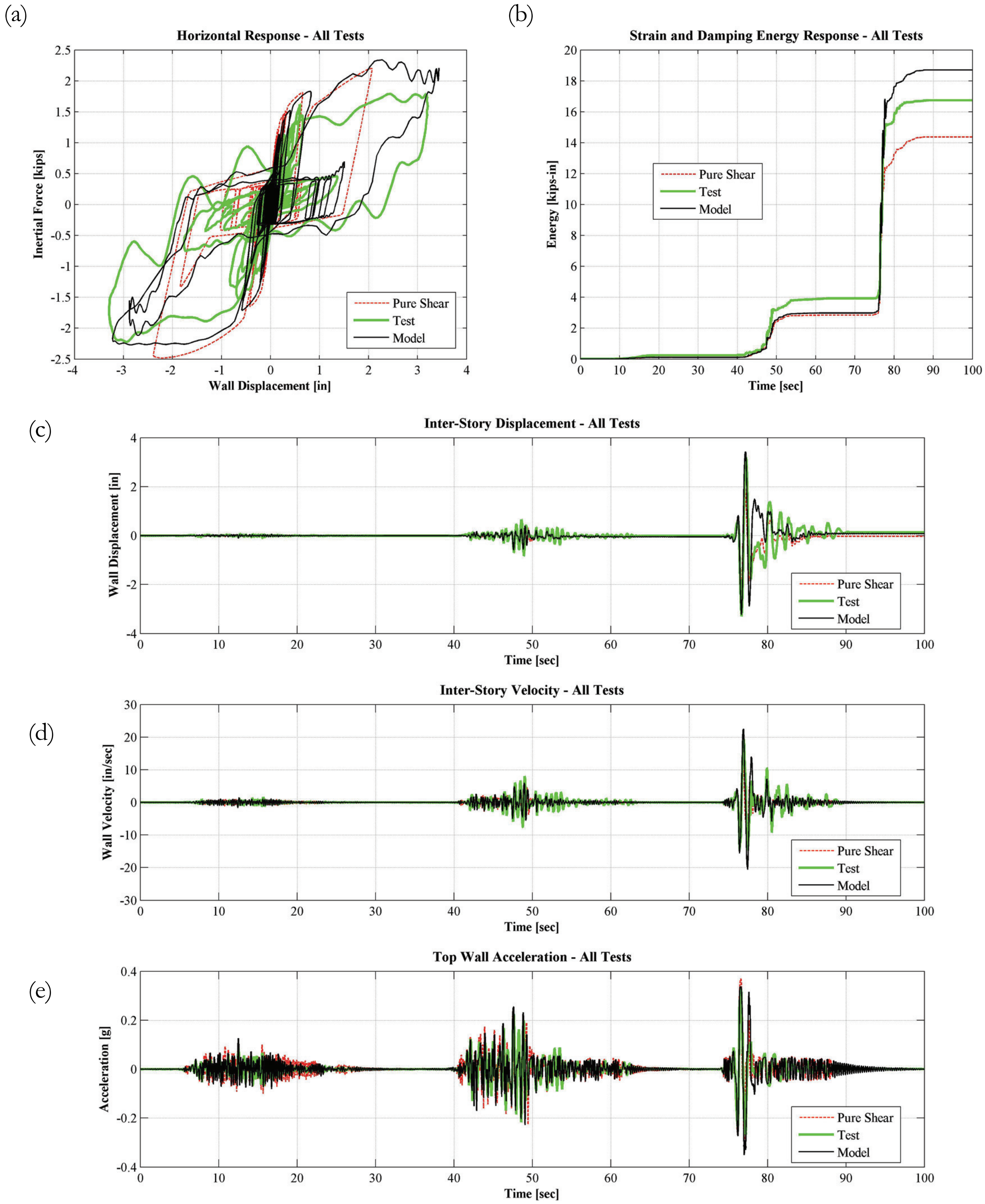

Figure 6.10 Comparison of Experimental and Analytical Data for All Tests: (a) Hysteretic Response; (b) Hysteretic Strain Energy; (c) Inter-Story Displacement Time History; Inter-Story Velocity Time History; and (e) Top of Wall Absolute Acceleration Time History

Table 6.8 Comparison of Maximum and Minimum Values between Experimental and Numerical Responses for **Test 1**

	Test		Model		Pure Shear	
	Positive	Negative	Positive	Negative	Positive	Negative
Inter-Story Displacement [in]	0.08	-0.10	0.06	-0.10	0.06	-0.06
Force [kip]	0.46	-0.55	0.54	-0.84	0.67	-0.67
Inter-Story Velocity [in]	1.62	-1.31	1.42	-1.66	1.34	-1.26
Top of Wall Abs. Acceleration [g]	0.08	-0.07	0.13	-0.08	0.10	-0.10
Percentage Difference (%)						
Inter-Story Displacement	N/A	N/A	-29.3	0.6	-30.3	-45.3
Force	N/A	N/A	15.9	53.3	43.7	21.1
Inter-Story Velocity	N/A	N/A	-12.2	26.7	-17.7	-3.6
Top of Wall Abs. Acceleration	N/A	N/A	53.3	15.9	21.2	43.8

Table 6.9 Comparison of Maximum and Minimum Values between Experimental and Numerical Responses for **Test 2**

	Test		Model		Pure Shear	
	Positive	Negative	Positive	Negative	Positive	Negative
Inter-Story Displacement [in]	0.66	-0.82	0.40	-0.58	0.31	-0.42
Force [kip]	1.45	-1.52	1.52	-1.71	1.51	-1.65
Inter-Story Velocity [in]	8.04	-7.63	5.98	-5.53	4.57	-4.86
Top of Wall Abs. Acceleration [g]	0.23	-0.22	0.26	-0.23	0.25	-0.23
Percentage Difference (%)						
Inter-Story Displacement	N/A	N/A	-38.7	-29.1	-53.3	-49.0
Force	N/A	N/A	5.2	12.4	4.5	8.3
Inter-Story Velocity	N/A	N/A	-25.6	-27.6	-43.1	-36.3
Top of Wall Abs. Acceleration	N/A	N/A	12.4	5.2	8.3	4.5

Table 6.10 Comparison of Maximum and Minimum Values between Experimental and Numerical Responses for **Test 3**

	Test		Model		Pure Shear	
	Positive	Negative	Positive	Negative	Positive	Negative
Inter-Story Displacement [in]	3.21	-3.29	3.43	-3.22	2.07	-2.39
Force [kip]	1.79	-2.22	2.34	-2.27	2.20	-2.48
Inter-Story Velocity [in]	19.36	-14.75	22.58	-20.54	15.37	-12.92
Top of Wall Abs. Acceleration [g]	0.33	-0.27	0.34	-0.35	0.37	-0.33
Percentage Difference (%)						
Inter-Story Displacement	N/A	N/A	7.0	-2.2	-35.4	-27.4
Force	N/A	N/A	31.0	2.1	23.0	11.6
Inter-Story Velocity	N/A	N/A	16.6	39.3	-20.6	-12.4
Top of Wall Abs. Acceleration	N/A	N/A	2.1	31.0	11.6	23.0

Regarding the predictions for **Test 3**, the **Model** formulation provides the best correlation among the 3 tests. Maximum inter-story displacements are within 7% difference while forces are over-estimated by about 15%, as an average of the two directions. The strain energy dissipated is similar to the experimental strain energy. Similarly to the previous cases, the **Pure Shear** formulation provides a stiffer numerical model. It is also observed that the **Model** response exhibits a high-frequency oscillation especially at maximum and minimum displacement ranges. This is attributed to the vibration in the vertical direction of the shear wall and can be eliminated by increasing the modal damping specified for the 2nd mode of vibration, from 1% to 5% for example. It has been observed, however, that due to consideration of geometric nonlinearity the damping mechanism in the vertical direction provides resistance in the horizontal direction, as well, for inter-story drifts higher than 3%~4%. This is not desirable when assessing the collapse margin of the numerical model, thus, a low damping ratio in the vertical direction has been considered more appropriate.

6.8 Summary

A single-story shear wall specimen that was subjected to three shake-table tests with ground motions of increasing amplitude was used to assess the capabilities of the proposed numerical building model for dynamic nonlinear time-history analysis. The numerical models were based on estimated properties of the structural elements – derived from available component test data, engineering properties, and engineering judgment – providing a blind prediction of the experimental response. The numerical results are in reasonably good agreement with the experimental results, there is, however, room for improvement in the estimation of the structural component properties or modification of constitutive models that can provide more accurate predictions.

CHAPTER 7: SUMMARY, CONCLUSIONS AND RECOMMENDATIONS

7.1 Summary and Conclusions

In support of the performance-based seismic design procedures for light-frame wood structures, developed within the NSF-funded NEESWood Project, a dual study with experimental and analytical components has been presented in this report. This chapter provides a summary and the main conclusions from each research work.

7.1.1 Experimental Study

In the context of the experimental investigation, a full-scale, two-story, light-frame wood townhouse building was tested on the twin relocatable tri-axial shake tables operating in unison, at the University at Buffalo UB-NEES site. The test structure was designed according to modern US engineered seismic design requirements (ICBO 1988) and constructed according to applicable practices in the 80's in California. Four different test phases were conducted, associated with additional components in the building configuration, as the test structure initially featured only the structural shear walls considered in the design, and progressively interior (gypsum wallboard) and exterior (stucco) wall finishes were installed.

The main objectives were to benchmark the dynamic characteristics and the seismic performance of a code-compliant building with realistic dimensions under various base input intensities, representative of both ordinary and near-field ground motions in southern California, and to investigate the effect of non-structural components on the seismic response of the test structure. Additional objectives included the documentation of damage in structural and non-structural components by conducting a detailed damage survey after the completion of each seismic test.

The main conclusions from this experimental study are listed below:

- The test structure incorporating all structural and non-structural components (Phase 5), performed well under seismic excitations representing the DE and MCE levels of shaking. The seismic response of the test building under three-dimensional base excitations demonstrated torsional behavior resulting from the asymmetric geometry of the structure in the longitudinal (East-West) direction and the reduced effective stiffness of the narrow wall piers at the first level garage wall in its transverse (North-South) direction. The maximum central roof drift under the DE and MCE events was 0.8% and 2%, respectively, while the maximum inter-story drift at the garage wall was 1.2% and 3.1%, respectively. These responses verified that the collapse prevention requirement, inherent in code-compliant seismic design, was satisfied. No potential loss of life or collapse hazard was identified during or after the execution of the tests.

- The application of gypsum wallboard on the interior surfaces of the structural wood walls reduced significantly the displacement response of both floors of the test structure. The reduction of the maximum transverse inter-story drifts from Phase 1 to Phase 3 was of the order of 40% for Seismic Level 2 (44% of DE). The application of gypsum wallboard on the partition walls and the ceilings did not affect much the first level inter-story drifts of the test structure, but further reduced the drifts of the second floor. This is attributed to the fact that the first floor level had only few partition walls compared to the second level of the test structure. Besides the stiffness contribution from the partition walls, the significant reduction of interstory drifts on the second floor was also explained by the increase of diaphragm effect on the roof level. The application of stucco as exterior finish further reduced the inter-story drifts in both levels of the test structure.

- The good performance of the test structure was associated with inelastic deformations that resulted in limited damage in structural and non-structural components. The most common type of damage, for shear walls subjected to inter-story drifts greater than 1%, included:

    - Sheathing pull-out at wall corners and permanent differential movement of adjacent panels.

    - Cracking and splitting of sill and top plates and cracking of studs attached to holdowns.

    - Crushing of gypsum wallboard at wall corners and buckling of gypsum wallboard at door openings.

    - Cracking of stucco on door and window openings and cracking and spalling of stucco at the corners of the structure.

Besides these observations, the experimental data from the NEESWood benchmark tests represents a unique dataset for the validation of three-dimensional numerical models of low-rise light-frame wood structures that can simulate both structural and non-structural components.

7.1.2 Analytical Study

The analytical task focused on the development, implementation and validation of a novel numerical framework, suitable for the nonlinear inelastic, static and dynamic analysis of light-frame wood buildings. The numerical formulation addresses the two-dimensional (2D) in-plane response of inter-story light-frame wood shear walls that incorporate single-sided sheathing panels, which are the structural elements considered in the seismic design. Considering each inter-story shear wall assembly as a single sub-structure element with internal nonlinear DOF, a 2D building model is formulated that represents a vertical continuous wall diaphragm of a prototype building. This is the first fundamental step towards the three-dimensional analysis of complete light-frame wood buildings with additional non-structural components.

The 2D building model is based on a sub-structuring approach that considers each floor diaphragm as rigid body with 3 kinematic and potentially dynamic degrees-of-freedom (DOF) in the vertical plane. A sub-structure element is developed for each individual single-story wall assembly that interacts with the adjacent diaphragms, above and below, and generates the resisting quasi-static internal forces. Utilizing floor diaphragms as boundary elements of the sub-structures developed for each story allows simulation of other modes of deformation (i.e. flexural and rocking modes) of the framing domain, with due consideration of the interaction effects between shear walls and floor diaphragms.

The 2D shear wall model consists of a number of finite elements developed to simulate the structural components, such as sheathing panels, framing members and inter-component connections. Sheathing panels are orthogonal, by default, and are described with 4 generalized DOF and linear elastic behavior. No bearing phenomena are included between sheathing panels. The sheathing-to-framing connections are described with two orthogonal coupled phenomenological springs that exhibit pinching, strength deterioration and stiffness degradation. Each orthogonal pair of springs representing a single sheathing-to-framing connection is rotated according to the initial trajectory of the connector force computed under infinitesimal lateral wall deformation. The proposed shear wall element enables the analyst to select between a simplified and a detailed formulation to describe the wood framing components. In the former case, referred as **Pure Shear** formulation, framing is assumed rigid and pin-connected and is considered to be rigidly attached to the floor diaphragms. In the latter case, referred as **Model** formulation, framing members are represented with linear elastic beam elements with axial and flexural behavior using centre-line modelling of each individual framing component. This approach enables the consideration of contact/separation phenomena between vertical studs and horizontal plates, contact/separation phenomena between horizontal plates and diaphragms, as well as anchoring equipment between framing and diaphragms (i.e. anchor bolts, holdowns), typically installed in light-frame shear walls to develop a vertical load path that resists overturning moments. The use of corotational descriptions of the displacement fields of the finite elements implemented in the proposed numerical framework accounts for geometric nonlinearity associated with large rotations and for P-Δ effects due to gravity loads, assuming small deformations of the structural members that remain linear elastic, such as the individual framing members and the sheathing panels.

To validate the proposed numerical framework, a number of simulation examples were presented, based on existing experimental results from pseudo-static tests of single- and two-story full-scale shear wall specimens, as well as shake-table tests of a single-story full-scale structure.

The results from the validation studies of single- and two-story specimens under quasi-static displacement-controlled loading conditions (Pardoen *et al.* 2003) led to the following conclusions:

- The numerical models based on the detailed **Model** formulation provide reliable estimates of the lateral hysteretic responses of engineered single- and two-story specimens carrying minimal gravity loads, independently of the aspect ratio of the shear wall segments or the location of the shear wall assemblies (first or second story). The numerical models successfully reproduce the behavioral characteristics of the test specimens under monotonic and cyclic displacement protocols that drive the system deep into the inelastic range, providing a consistent response under yielding, hardening, softening and pinching behavior. The predicted backbone forces, extracted from the cyclic responses, tend to be on average within 5%-10% lower than the experimental forces along the post-elastic ascending and descending regime. As a result, the hysteretic strain energy dissipation capability is consistently underestimated in the numerical predictions.

- The numerical models based on the **Pure Shear** formulation provide good estimates of the lateral hysteretic responses of engineered shear wall assemblies with low aspect ratio segments, which are located at the first story. For these cases, the predicted backbone forces, extracted from the cyclic responses, tend to be on average within 5%-10% higher than the experimental forces and correlate well with the strain energy dissipation capability. However, the responses of the high aspect ratio Garage Door (GD) wall and both second story wall assemblies clearly demonstrate that the **Pure Shear** formulation significantly overestimates the strength, stiffness and energy dissipation capability, compared to the experimental responses.

- The effectiveness of the detailed model is more pronounced for (i) the GD wall, which consists of two high AR wall piers, and (ii) the second-story walls of the two-story specimens, since for these cases the differences between detailed and simplified numerical predictions are significant. Although these differences were expected for the GD wall and are consistent to the use of the aspect ratio adjustment factor in IBC (2006), the differences in the cyclic response of the second story walls provide evidence that the response of engineered shear wall segments located at higher floors of a light-frame wood structure may deviate from the expected racking response, even for low aspect ratio wall segments.

- The comparison of local responses from the **Model** formulation results, such as the end post uplift displacement and the holdown hysteretic response, demonstrated that predictions are less accurate when comparing local displacements but provide good accuracy when comparing local forces. It is also important to note that the numerical results predict similar variations of local responses, for different wall configurations, to the variations observed in the experimental results.

- The deformed shapes of the GD wall model are well correlated to the deformations of the actual test specimen, demonstrating that the load paths developed within the shear wall domain were realistic.

Complementary numerical analyses were performed to assess the effect of holdown equipment on the lateral performance of the three single-story shear wall specimens, by removing the diaphragm-to-stud connector elements from the detailed numerical models. The analysis results clearly demonstrate that the removal of holdowns results in substantially lower stiffness, strength and energy dissipation capability of the shear wall system, when the gravity loads applied are minimal. The computation of the numerical responses of such poorly-anchored shear wall assemblies represents a key feature of the proposed numerical framework and provides the means to obtain reliable performance estimates of both engineered and conventional shear wall construction.

The validation studies based on the unidirectional shake table test results of a single-story symmetric structure (Shinde and Symans 2010) verify the applicability of the sub-structure modeling approach to perform nonlinear dynamic response-history analysis with shear wall models that include all the primary sources of nonlinear inelastic behavior. Despite the high gravity load applied at the floor diaphragm that results in small backbone force differences between simplified and detailed models, the dynamic nature of the excitation leads to higher inter-story drifts of the detailed model compared to the simplified one. The numerical results are in reasonable agreement with the experimental results, but there is still room for improvement in the estimation of the structural component properties or modification of constitutive models that can provide more accurate predictions.

7.2 Recommendations

The main recommendations derived from this research work are summarized below:

- The interior and exterior wall finish nonstructural components contribute to an increase of the lateral stiffness of shear wall assemblies and modify the dynamic characteristics of a light-frame wood building, reducing the building drifts under low level earthquake shaking. For the experimental structure and based on the ambient vibration tests, the increase in the lateral stiffness from the installation of gypsum wallboard and stucco was 15% and 30%, respectively, on average for each principal direction. Although these components are not considered in the seismic design, the contribution to the lateral resistance can be considered for capacity design of anchorage equipment and boundary connections.

- The design objectives of a light-frame wood building within a performance-based approach should consider the repair costs associated with damage in structural and nonstructural components.

- Low aspect ratio shear walls with good anchorage conditions are the most reliable configurations because they demonstrate a robust lateral hysteretic response that depends less than other configurations on the gravity loads applied and the specific boundary conditions. Well-anchored high aspect ratio wall segments are more susceptible to a rocking response that involves separation of the end studs from the top plate. This mode of deformation is amplified when interior gypsum wallboard is fastened to the vertical studs of the shear wall framing.

7.3 Future Work

The following future research work is recommended based on the experimental and analytical studies described in this report:

- Use of the detailed shear wall model to apply the methodology described in FEMA P695 (2009) and to quantify design parameters that have been traditionally used in force-based seismic design practice, such as the force-reduction factor (or R factor). The use of reliable numerical models that account for large displacements and simulate additional secondary modes of deformation of light-frame wood shear walls will lead to more accurate estimates of the safety against collapse intended by current seismic codes, compared to existing simplified state-of-practice numerical models.

- Use of the detailed shear wall model to benchmark the monotonic response of typical single-story assemblies with respect to the structural configuration, the nailing schedule, the anchorage conditions and the gravity loads. Use of the generated results within the displacement-based design procedures developed within the NEESWood Project.

- Development of a three dimensional (3D) building model based on the existing sub-structuring approach that will allow to customize the level of detailing in the numerical simulation of each sub-structure shear wall and diaphragm element according to the problem specifics, such as: the actual size and structural configuration of the prototype structure, the type of analysis to be executed, the level of accuracy desired, and the available computational power.

- Modification of the existing numerical framework to include two-sided shear wall models that will allow the simulation of internal gypsum wallboard.

- Validation of the 3D model with the experimental benchmark tests.

CHAPTER 8: REFERENCES

Andreasson, S., 2000. "Three-Dimensional Interaction in Stabilization of Multi-Storey Timber Frame Building Systems," Ph.D. Thesis, Division of Structural Engineering, Lund University, Lund, Sweden.

Applied Technology Council, Redwood City, California 94065, <www.ATCouncil.org>.

Ayoub, A., 2007. "Seismic Analysis of Wood Building Structures," *Engineering Structures,* **29**:213-223.

Baber, T. T. and Noori, M. N., 1985. "Random Vibration of Degrading, Pining Systems," *Journal of Engineering Mechanics,* ASCE, **111**(8):1010-1026.

Baber, T. T. and Wen, Y. K., 1981. "Random Vibration of Hysteretic Degrading Systems," *Journal of Engineering Mechanics Division,* ASCE, **107**(6):1069-1087.

Bouc, R., 1967. "Force Vibration of Mechanical Systems with Hysteresis", *Proceedings of 4th Conference on Nonlinear Oscillation,* Prague, Czechoslovakia.

Ceccotti, A. and Karacabeyli, E., 2002. "Validation of Seismic Design Parameters for Wood-Frame Shearwall Systems", *Canadian Journal of Civil Engineering,* **29**(3):484-498.

Ceccotti, A. and Vignoli, A., 1989. “A Pinching Hysteretic Model for Semirigid Joints,” *European Earthquake Engineering Journal,* Vol. 3, pp. 3-9.

Ceccotti, A., Follesa, M. and Karacabeyli, E., 2000. “3D Seismic Analysis of Multi-Storey Wood Frame Construction”, *Proceedings of World Conference on Timber Engineering,* British Columbia, Canada.

Christovasilis, I. P., Filiatrault, A. and Wanitkorkul, A., 2009a. “Seismic Testing of a Full-Scale Two-Story Light-Frame Wood Building: NEESWood Benchmark Test,” MCEER Technical Report 09-0005, Multidisciplinary Center for Earthquake Engineering, Buffalo, New York, 14260.

Christovasilis, I. P., Filiatrault, A., Constantinou, M. C. and Wanitkorkul, A., 2009b. “Incremental Dynamic Analysis of Woodframe Buildings,” *Journal of Earthquake Engineering and Structural Dynamics,* **38**(4):477-496.

Chui, Y. H., Ni, C. and Jiang, L., 1998. “Finite-Element Model for Nailed Wood Joints under Reversed Cyclic Load,” *Journal of Structural Engineering,* ASCE, **124**(1): 96-103.

Clough, R. W., and Penzien, J. (1993). *Dynamic of Structures*, 2nd Ed., McGraw-Hill, New York.

Collins, M., Kasal, B., Paevere, P. and Foliente, G. C., 2005a. “Three-Dimensional Model of Light Frame Wood Buildings. I: Model Description,” *Journal of Structural Engineering,* ASCE, **131**(4):676-683.

Collins, M., Kasal, B., Paevere, P. J. and Foliente, G. C., 2005b. “Three-Dimensional Model of Light Frame Wood Buildings. I: Experimental Investigation and Validation of Analytical Model,” *Journal of Structural Engineering,* ASCE, **131**(4):684-692.

CUREe, 1998. CUREe-Caltech Woodframe Project Newsletter, Issue No. 1, available online at http://www.curee.org/projects/woodframe/.

DADiSP/2002 (2006). “DADiSP The Ultimate Engineering Spreadsheet,” DSP Development Corporation, Boston, MA.

Dodds, R. H. and Lopez, L. A., 1980. “A Generalized Software System for Nonlinear Analysis,” *Advances in Earthquake Engineering Software,* **2**(4).

Dolan, J. D. and Foschi, R. O., 1991. “Structural Analysis Model for Static Loads on Timber Shear Walls,” *Journal of Structural Engineering,* ASCE, **117**(3):851-861.

Dolan, J. D. and Johnson, A. C., 1997. “Monotonic Tests of Long Shear Walls with Openings,” Department of Wood Science and Forests Products, Report No. TE-1996-001, Virginia Polytechnic Institute and State University, Blacksburg, Virginia.

Dolan, J. D., 1989. “The Dynamic Response of Timber Shear Walls,” Ph.D. Thesis, The University of British Columbia, at Vancouver, British Columbia, Canada.

Dolan, J. D., 1991. "A Numerical Model to Predict the Dynamic Response of Timber Shear Walls," *Proceedings of International Timber Engineering Conference,* London, UK.

Dujic, B. and Zarnic, R., 2004. "Method for Modelling Dynamic Response of Timber Frame Building," *Proceedings of the 8th World Conference on Timber Engineering*, Lahti, Finland.

Durham, J., Prion, H. G. L., Lam, F. and He, M., 1997. "Earthquake Resistance of Shear Walls with Oversized Sheathing Panels." *Proceedings, Recent Advances in Understanding Full-Scale Behavior in Wood Buildings,* Forest Products Society, Madison, Wisconsin, pp. 57-64.

Easley, J. T., Foomani, M. and Dodds, R. H., 1982. "Formulas for Wood Shear Walls," *Journal of the Structural Division,* ASCE, **108**(11):2460-2478.

Ekiert, C. and Hong, J. 2006. "Framing-to-Sheathing Connection Tests in Support of NEESWood Project," Network of Earthquake Engineering Simulation Host Institution: State University of New York at University at Buffalo, Buffalo, NY. 20 p.

EQE International and the Governor's Office of Emergency Services, 1995. *The Northridge Earthquake of January 17, 1994*: *Report of Data Collection and Analysis*, Part A, p. 5-18 (Sacramento, CA: Office of Emergency Services).

Falk, R. H. and Itani, R. Y., 1989. "Finite Element Modeling of Wood Diaphragms," *Journal of Structural Engineering,* ASCE, **115**(3):543-559.

Falk, R. H. and Soltis, L. A., 1988. "Seismic Behavior of Low-rise Wood Framed Buildings," *The Shock and Vibration Digest*, **20**(12):3-7.

FEMA P695, 2009. "Quantification of Building Seismic Performance Factors," prepared by Applied Technology Council, Redwood City, California 94065, <www.ATCouncil.org>.

Filiatrault, A., Fischer, D., Folz, B. and Uang, C. M., 2002. "Seismic Testing of Two-Story Woodframe House: Influence of Wall Finish Materials," *Journal of Structural Engineering,* ASCE, **128**(10): 1337-1345.

Filitrault, A., 1990. "Static and Dynamic Analysis of Timber Shear Walls," *Canadian Journal of Civil Engineering,* **17**(4):643-651.

Fischer, D., Filiatrault, A., Folz, B., Uang, C. M. and Seible, F., 2001. "Shake Table Tests of a Two-Story Woodframe House," CUREe Publication No. W-06, CUREE-Caltech Woodframe Project.

Foliente, G. C., 1995. "Hysteresis Modeling of Wood Joints and Structural Systems," *Journal of Structural Engineering,* ASCE, **121**(6): 1013-1022.

Folz, B. and Filiatrault, A., 2001. "Cyclic Analysis of Wood Shear Walls," *Journal of Structural Engineering,* ASCE, **127**(4):433-441.

Folz, B. and Filiatrault, A., 2004a. "Seismic Analysis of Woodframe Structures. I: Model Formulation," *Journal of Structural Engineering,* ASCE, **130**(9):1353-1360.

Folz, B. and Filiatrault, A., 2004b. "Seismic Analysis of Woodframe Structures. II: Model Implementation and Verification," *Journal of Structural Engineering,* ASCE, **130**(9):1361-1370.

Folz, B. and Filiatrault, A., 2004c. "Blind Predictions of the Seismic Response of a Woodframe House: An International Benchmark Study," *Earthquake Spectra,* 20(3):825-851.

Foschi, R. O., 1977. "Analysis of Wood Diaphragms and Trusses. Part I: Diaphragms," *Canadian Journal of Civil Engineering,* **4**(3):345-352.

Foschi, R. O., 2000. "Modeling the Hysteretic Response of Mechanical Connections for Wood Structures," *Proceedings of World Conference on Timber Engineering,* British Columbia, Canada.

Gatto, K. and Uang, C. M., 2002. "Cyclic Response of Woodframe Shear Walls: Loading Protocol and Rate of Loading Effects," CUREe Publication No. W-16, CUREE-Caltech Woodframe Project.

Girhammar, U. A., Bovim, N. I. and Kallsner, B., 2004. "Characteristic of Sheathing-to-Timber Joints in Wood Shear Walls," *Proceedings of the 8th World Conference on Timber Engineering,* Lahti, Finland.

Gupta, A. K. and Kuo, G. P., 1985. "Behavior of Wood-Framed Shear Walls," *Journal of Structural Engineering,* ASCE, **111**(8):1722-1733.

Gupta, A. K. and Kuo, G. P., 1987a. "Wood-Framed Shear Walls With Uplifting," *Journal of Structural Engineering,* ASCE, **113**(2):241-259.

Gupta, A. K. and Kuo, G. P., 1987b. "Modeling of a Wood-Framed House," *Journal of Structural Engineering,* ASCE, **113**(2):260-278.

Gutkowski, R. M. and Castillo, A. L., 1988. "Single- and Double-Sheathed Wood Shear Wall Study," *Journal of Structural Engineering,* ASCE, **114**(6):1268-1284.

Hall, J. F. (Primary Contributor), Schmid, B., Comerio, M. and Russell, J., 1996. "Northridge Earthquake of January 17 1994 Reconnaissance Report Volume 2: Wood Buildings," *Earthquake Spectra*, **12**(S1), p. 125-176.

He, M., Lam, F. and Foschi, R. O., 2001. "Modeling Three-Dimensional Timber Light-Frame Buildings," *Journal of Structural Engineering,* ASCE, **127**(8):901-913.

Ibarra, L. F., Medina, R. A. and Krawinkler, H., 2005. "Hysteretic Models that Incorporate Strength and Stiffness Deterioration," *Earthquake Engineering and Structural Dynamics*, **34**:1489-1511.

IBC, 2006. "International Building Code," International Code Council, Falls Church, Virginia.

ICBO, 1988. "Uniform Building Code, 1988 edition," International Conference of Building Officials, Whittier, California.

Itani, R. Y. and Cheung, C. K., 1984. "Nonlinear Analysis of Sheathed Wood Diaphragms," *Journal of Structural Engineering,* ASCE, **110**(9):2137-2147.

Judd, J. P. and Fonseca, F. S., 2005. "Analytical Model for Sheathing-to-Framing Connections in Wood Shear Walls and Diaphragms," *Journal of Structural Engineering,* ASCE, **131**(2):345-352.

Judd, J. P., 2005. "Analytical Modeling of Wood-Frame Shear Walls and Diaphragms," M.Sc. Thesis, Department of Civil and Environmental Engineering, Brigham Young University, Provo, Utah.

Kasal, B. and Leichti, R. J., 1992. "Nonlinear Finite-Element Model for Light-Frame Stud Walls," *Journal of Structural Engineering,* ASCE, **118**(11):3122-3135.

Kasal, B., Leichti, R. J. and Itani, R. Y., 1994. "Nonlinear Finite-Element Model of Complete Light-Frame Wood Structures," *Journal of Structural Engineering,* ASCE, **120**(1):100-119.

Kircher, C. A., Reitherman, R. K., Whitman, R. V. and Arnold, C., 1997. "Estimation of Earthquake Losses to Buildings," *Earthquake Spectra*, **13**(4).

Kivell, T., Moss, P. J. and Carr, A. J., 1981. "Hysteretic Modeling of Moment-Resting Nailed Timber Joints," *Bulletin of New Zealand National Society for Earthquake Engineering,* **14**(4):233-243.

Krawinkler, H., 1999. "Challenges and Progress in Performance-Based Earthquake Engineering," *International Seminar on Seismic Engineering for Tomorrow – In Honor of Professor Hiroshi Akiyama,* Tokyo, Japan.

Krawinkler, H., Parisi, F., Ibarra, L., Ayoub, A. and Medina, R., 2003. "Development of a Testing Protocol for Woodframe Structures", CUREe Publication No. W-02, CUREE-Caltech Woodframe Project.

Li, K. N., 1996. "Three-Dimensional Nonlinear Dynamic Structural Analysis Computer Program Package CANNY-E," *CANNY Consultant Pte Ltd*, Singapore.

Mathworks, 2009. "Matlab documentation," Mathworks, 3 Apple Hill Drive, Natick, MA.

McCutcheon, W. J., 1985. "Racking Deformations in Wood Shear Walls," *Journal of the Structural Division,* ASCE, **111**(2):257-269.

Mosalam, K.M., Machado, C., Gliniorz, K-U., Naito, C., Kunkel, U. and Mahin, S. (2002) "Seismic Evaluation of an Asymmetric Three-Story Woodframe Building" CUREE-Caltech Woodframe Project Report No. W-19, Consortium of Universities for Research in Earthquake Engineering, Richmond, CA.

National Design Specification for Wood Construction, 2005. American Forest and Paper Association, Washington, D.C.

Newmark, N. M., 1959. "A Method of Computation for Structural Dynamics," *Journal of the Engineering Mechanics Division,* ASCE, **5**(3):67-94.

Paevere, P. J., Foliente, G. C. and Kasal, B., 2003. "Load-Sharing and Redistribution in a One-Story Woodframe Building," *Journal of Structural Engineering,* ASCE, **129**(9):1275-1284.

Pardoen, G. C., Walman, A., Kazanjy, R. P., Freund, E. and Hamilton, C. H., 2003. "Testing and Analysis of One-Story and Two-Story Shear Walls Under Cyclic Loading," CUREe Publication No. W-25, CUREE-Caltech Woodframe Project.

Park, Y. J., Reinhorn, A. M. and Kunnath, S. K., 1987. "IDARC: Inelastic damage analysis of reinforced concrete frame–shear-wall structures," NCEER Report 87-0008, State University of New York at Buffalo, Buffalo, N.Y.

Patton-Mallory, M., Gutkowski, R. M. and Soltis, L. A., 1984. "Racking Performance of Light-Frame Walls Sheathed on Two Sides," M.Sc. Thesis, Colorado State University, Fort Collins, Colorado.

Perkins, J. B., Boatwright, J. and Chaqui, B., 1998. Housing Damage and Resulting Shelter Needs: Model Testing and Refinement Using Northridge Data, *Proceedings of the NEHRP Conference and Workshop on Research on the Northridge, California Earthquake of January 17, 1994*, Vol. IV, p. IV-135 (Richmond, CA: California Universities for Research in Earthquake Engineering).

Phillips, T. L., Itani, R. Y. and McLean, D. I., 1993. "Lateral Load Sharing by Diaphragms in Wood-Framed Buildings," *Journal of Structural Engineering,* ASCE, **119**(5):1556-1571.

Polensek, A., 1976. "Finite-Element Analysis of Wood-Stud Walls," *Journal of the Structural Division,* ASCE, **102**(7):1317-1335.

Prakash, V. and Powell, G. H., 1993. DRAIN-2DX, DRAIN-3DX and DRAIN BUILDING: Base program design documentation, *Report No. UCB/SEMM-93/17*, University of California, Berkeley, California.

Rahnama, M. and Krawinkler, H., 1993. "Effects of Soft Soils and Hysteresis Model on Seismic Demands," John A. Blume Earthquake Engineering Center, Report No. 108, Department of Civil Engineering, Stanford University, Stanford, California.

Reitherman, R., Cobeen, K. and Serban, K., 2003. "Design documentation of woodframe project index buildings," CUREE-Caltech Woodframe Project Report No. W-29, Consortium of Universities for Research in Earthquake Engineering, Richmond, CA, 2003, 258 p.

Salenikovich, A. J., 2000. "The Racking Performance of Light-Frame Shear Walls," Ph.D. Thesis, Department of Wood Science and Forest Products, Virginia Polytechnic Institute and State University, Blacksburg, Virginia.

Schmid, B. L., Nielse, R. J. and Linderman, R. R., 1994. "Narrow Plywood Shear Panels," *Earthquake Spectra,* **10**(3):569-588.

Schmidt, R. J. and Moody, R. C., 1989. "Modeling Laterally Loaded Light-Frame Buildings," *Journal of Structural Engineering,* ASCE, **115**(1):201-217.

Shinde, J.K., Symans, M.D., Filiatrault, A. and Van de Lindt, J.W., 2007. "Application of seismic protection systems to woodframed buildings: full-scale testing and field implementation," Proc. 5th NEES Annual Meeting, Snowbird, UT.

Sivaselvan, M. V. and Reinhorn, A. M., 1999. "Hysteretic Models for Cyclic Behavior of Deteriorating Inelastic Structures," MCEER Report 99-0018, Multidisciplinary Center for Earthquake Engineering, Buffalo, New York, 14260.

Tarabia, A. M. and Itani, R. Y., 1997a. "Seismic Response of Light-Frame Wood Buildings," *Journal of Structural Engineering,* ASCE, **123**(11):1470-1477.

Tarabia, A. M. and Itani, R. Y., 1997b. "Static and Dynamic Modeling of Light-Frame Wood Buildings," *Computers and Structures,* **63**(2):319-334.

Tuomi, R. L. and McCutcheon, W. J., 1974. "Testing of a Full-Scale House under Simulated Snowloads and Windloads," *Research Paper FPL 234,* U.S. Department of Agriculture, Forest Products Laboratory, Madison, Wisconsin.

Tuomi, R. L. and McCutcheon, W. J., 1978. "Racking Strength of Light-Frame Nailed Walls," *Journal of the Structural Division,* ASCE, 104(**7**):1131-1140.

USGS, 2009. U.S. Geological Survey website, <http://www.usgs.gov/>.

van de Lindt, J. W., 2004. "Evolution of Wood Shear Wall Testing, Modeling, and Reliability Analysis: Bibliography," *Practice Periodical on Structural Design and Construction,* ASCE, **9**(1):44-53.

Wen, Y. K., 1976. "Method for Random Vibration of Hysteretic Systems," *Journal of the Structural Division,* ASCE, 102(**2**):249-263.

Wen, Y. K., 1980. "Equivalent Linearization for Hysteretic Systems under Random Excitation," *Journal of Applied Mechanics*, ASME. 47:150-154.

White, M. W. and Dolan, J. D., 1995. "Nonlinear Shear-Wall Analysis," *Journal of Structural Engineering,* ASCE, **121**(11):1629-1635.

White, T.W. and Ventura, C., 2007. "Seismic behavior of residential wood-frame construction in British-Columbia: Part I – modeling and validation," Proceedings of the Ninth Canadian Conference on Earthquake Engineering, Ottawa, Canada, 10 p.

Xu, J., 2006. "Development of a General Dynamic Hysteretic Light-Frame Structure Model and Study on the Torsional Behavior of Open-Front Light-Frame Structures," Ph.D. Thesis, Department of Civil and Environmental Engineering, Washington State University, Pullman, Washington.

APPENDIX A: PARAMETER ESTIMATION OF THE NONLINEAR INELASTIC SPRINGS UTILIZED IN THE NUMERICAL MODELS OF CHAPTER 5

A.1 Estimated Parameters

The parameters needed to describe the unidirectional response of nonlinear inelastic springs, utilized in the numerical models presented in Chapter 5, are listed in Table A.1.

Table A.1 Parameters of Nonlinear Inelastic Springs Utilized in Chapter 5

	K_o [lbs/in]	F_{yo} [lbs]	α_o [-]	σ [-]	σ_u [-]	u_{ini} [in]	u_{ult} [in]	β [-]	γ [lbs^{-1}]	κ [-]
3/8 in OSB / 8d Box Gun Nails / 2x4 Douglas-Fir	12649.9	141.9	0.040	0.350	0.221	0.011	3.30	0.05	3.87E-04	50.0
HTT22 Holdown Spring	150000	8000	0.050	0.010	0.250	0.150	1.80	0.05	5.00E-05	20.0
CS16 Strap Spring	60000	3200	0.050	0.010	0.250	0.150	1.80	0.05	1.25E-04	20.0

A.2 Parameter Estimation for Sheathing-to-Framing Spring

The parameters for the sheathing-to-framing nonlinear springs were defined based on unidirectional cyclic tests of 3 sheathing-to-framing connection specimens (Fischer *et al.* 2001). The specimens consisted of the same material and geometric properties (3/8 in OSB / 8d box nails / 2x4 Douglas-Fir) as the shear wall specimens and were tested parallel to the grain of the framing lumber.

The parameter estimation was executed using a MATLAB (Mathworks 2009) integrated subroutine that employs a minimization procedure to yield the optimum model parameters. Assigning an initial set of parameters **p**, where **p** is a 10-by-1 vector, and utilizing the recorded displacement history of each connection test **d**, the nonlinear force history **f**(**p**,**d**) predicted by the numerical model is used to define the objective function H(**p**) to be minimized as:

$$H(\mathbf{p}) = \left(\left\|\mathbf{c} - \mathbf{f}(\mathbf{p},\mathbf{d})\right\|_2\right)^2 = \left(\left\|\begin{bmatrix} c_1 \\ c_2 \\ \ldots \\ c_n \end{bmatrix} - \begin{bmatrix} f_1(\mathbf{p},\mathbf{d}) \\ f_2(\mathbf{p},\mathbf{d}) \\ \ldots \\ f_n(\mathbf{p},\mathbf{d}) \end{bmatrix}\right\|_2\right)^2 = \sum_{i=1}^{n}\left[\left(c_i - f_i(\mathbf{p},\mathbf{d})\right)^2\right] \qquad \text{(A.1)}$$

where **c** is a n-by-1 vector that contains the experimentally recorded force history and n corresponds to the number of recorded steps.

Instead of computing the optimum parameters for each cyclic test and then calculating the final parameters as the average of the 3 sets, a single optimization procedure was executed using the data from the tests as a single set. Since the number of recorded steps was the same for all tests, no weighting factor was considered in the objective function. The parameters estimated from the identification procedure are listed in Table A.1. The hysteretic response and the associated strain energy for the cyclic tests and the numerical prediction are shown in Figure A.1.

A.3 Parameter Estimation for HTT22 Holdown Spring

The parameters for the HTT22 holdown spring were estimated from the force-displacement history deducted from the cyclic **Test A** of the Garage Door wall, shown in Figure 5.14b. A single experimental response was used because at this stage the intention was to acquire acceptable parameters for the nonlinear numerical response and not to define the optimum parameters for a specific holdown device. The latter should be performed in conjunction with analytical and numerical studies at the component level, which would provide the capability to estimate the parameters for similar devices as well.

The parameters estimated from the identification procedure are listed in Table A.1. The hysteretic response and the associated strain energy for the cyclic test and the numerical prediction are shown in Figure A.2.

Note that the tension allowable load provided by the specifications was 4165 lbs at a deflection of 0.152 in, thus, for a linear response the stiffness would be 27400 lbs/in.

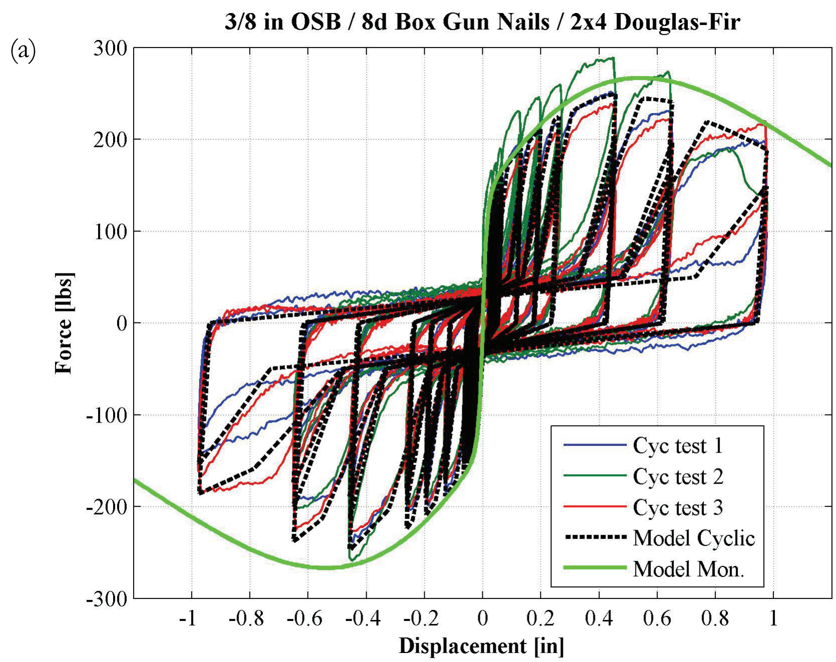

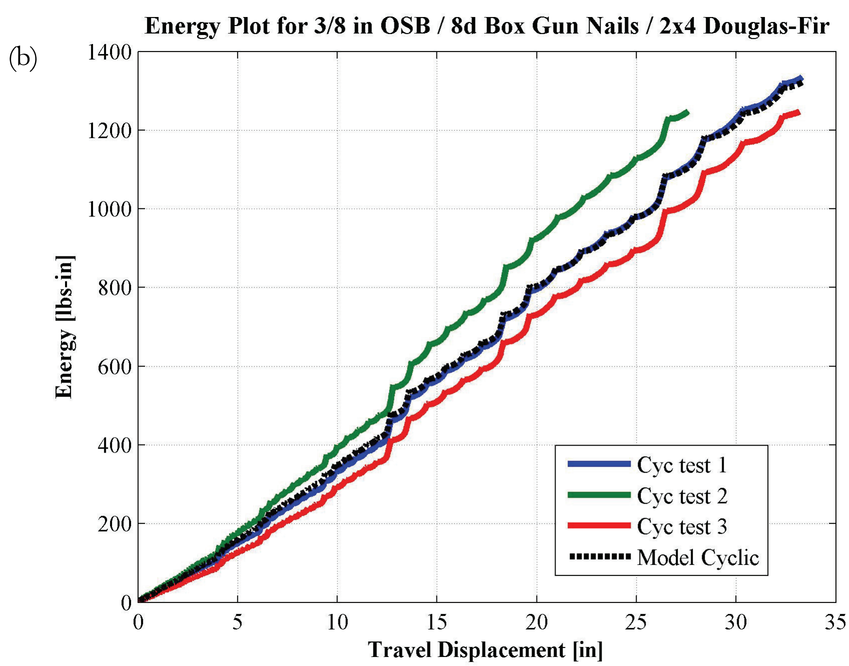

Figure A.1 (a) Monotonic and Cyclic Response, and (b) Strain Energy Response of a Unidirectional Nail Spring for: [3/8 in OSB / 8d Box Gun Nails / 2x4 Douglas-Fir]

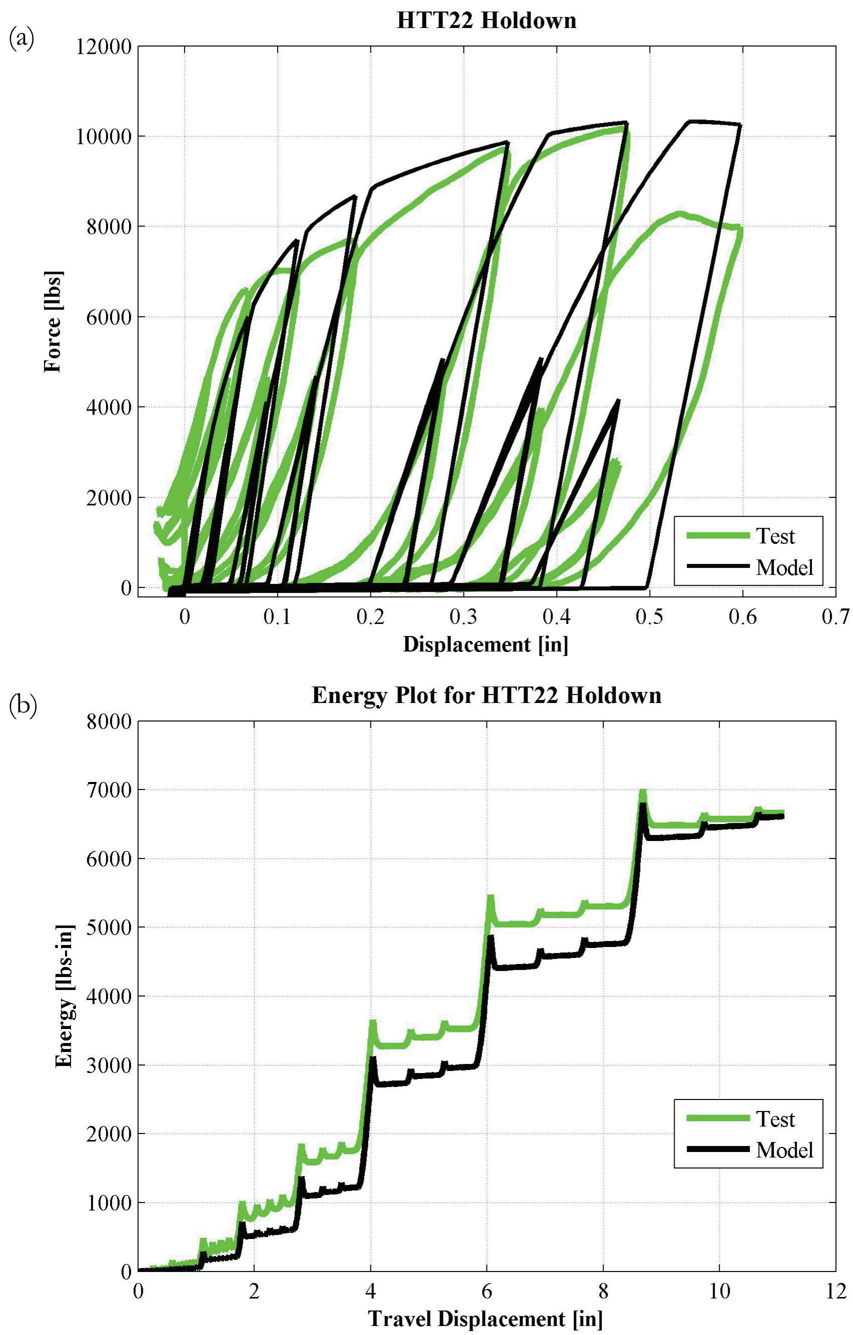

Figure A.2 (a) Monotonic and Cyclic Response, and (b) Strain Energy Response of a HTT22 Holdown Spring

A.4 Parameter Estimation for CS16 Strap Spring

The parameters for the CS16 strap spring were estimated directly from the parameters already defined for the HTT22 holdown spring, due to lack of experimental data for this type of component. The tension allowable load for the CS16 strap was 1705 lbs which is 40% that of the HTT22 holdown (4165 lbs). Thus, the initial stiffness K_o and yield force F_{yo} were selected as 40% of the values assigned for the HTT22 holdown spring. The remaining parameters were not modified except for the parameter γ which was multiplied by the inverse of 40% which is equal to 2.5.

The parameters for the CS16 strap spring are listed in Table A.1. The assumed hysteretic response for the two devices is shown in Figure A.3.

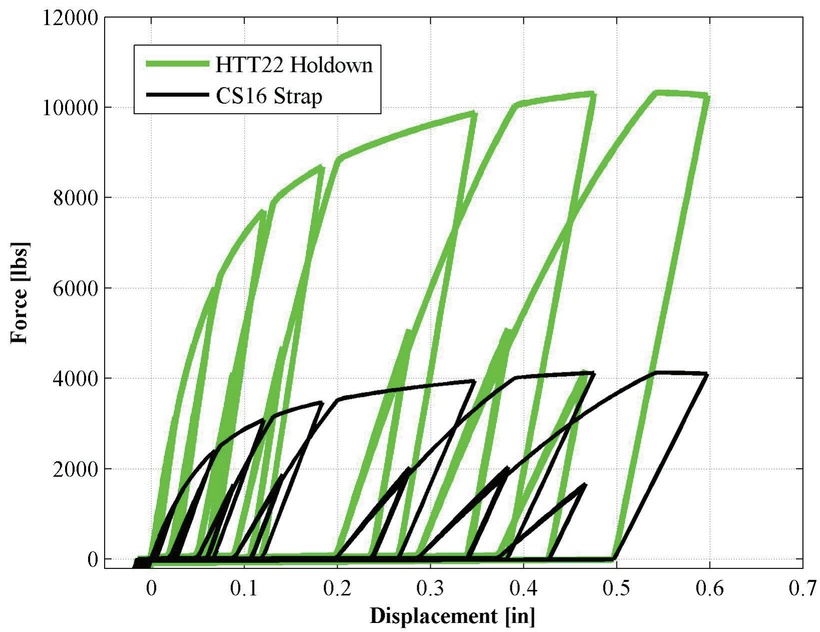

Figure A.3 Cyclic Responses of a CS16 Strap and HTT22 Holdown Spring

APPENDIX B: PARAMETER ESTIMATION OF THE NONLINEAR INELASTIC SPRINGS UTILIZED IN THE NUMERICAL MODELS OF CHAPTER 6

B.1 Estimated Parameters

The parameters needed to describe the unidirectional response of nonlinear inelastic springs, utilized in the numerical models presented in Chapter 6, are listed in Table B.1.

Table B.1 Parameters of Nonlinear Inelastic Springs Utilized in Chapter 6

	K_o [lbs/in]	F_{yo} [lbs]	α_o [-]	σ [-]	σ_u [-]	u_{ini} [in]	u_{ult} [in]	β [-]	γ [lbs^{-1}]	κ [-]
7/16 in OSB / 8d Common Nails / 2x6 Spruce-Pine-Fir	11800.2	137.4	0.050	0.365	0.265	0.007	3.42	0.10	4.55E-04	5.7
HD6A Holdown Spring	120000	6400	0.050	0.010	0.250	0.150	1.80	0.05	6.25E-05	20.0

B.2 Parameter Estimation for Sheathing-to-Framing Spring

The parameters for the sheathing-to-framing nonlinear springs were defined based on unidirectional monotonic and cyclic tests of sheathing-to-framing connection specimens (Ekiert and Hong 2006). The specimens consisted of 7/16 in OSB, 8d common nails and 2x6 Hem-Fir framing lumber. Since the test specimen was constructed with Spruce-Pine-Fir lumber, a modification in the final spring parameters was executed based on the specific gravity of the two framing materials, as described later in this section.

The existence of both cyclic and monotonic pushover tests, conducted both perpendicular and parallel to grain, gave the opportunity to synthesize these test data in order to find the parameters for the sheathing-to-framing connectors that better represent the most probable response, independent of grain orientation.

B.2.1 Processing of Monotonic Test Data

The objective was to construct a representative backbone curve independent of grain orientation.

First, the monotonic pushover curves were interpolated at equal displacement intervals of 0.001 in. This interpolation was possible because the recording frequency was quite small with displacements intervals of the order of 10E-04 in and the displacement history was a 1-1 ascending function with respect to the number of recording steps. This procedure also reduced the number of recording steps to about 2000, which is more manageable than the 67000 steps of the original signals.

Subsequently, the median force at each displacement was computed for each group of curves representing loading perpendicular and parallel to grain, as shown in Figure B.1. The median response was preferred from the mean or average response because it yielded a smoother backbone curve. Furthermore, the capping forces were almost equal for both directions of loading (280 lbs and 278 lbs for perpendicular and parallel to grain, respectively) but the corresponding displacements were quite different (0.344 in and 0.917 in for loading perpendicular and parallel to grain, respectively).

In order to synthesize the two median backbone curves shown in Figure B.1, each signal was first modified to remove local force fluctuations, so as to yield a force-displacement function that is 1-1 ascending up to the point of capping force and 1-1 descending, from the point of capping force to the point of failure. The original and modified signals are shown in Figure B.2.

Subsequently, the backbone curves were normalized with respect to the capping force so that the maximum force value was equal to 1. Then, the modified signals were interpolated at equal force increments of 0.001. This allowed calculating the median displacement between the two loading cases for the same fraction of the resisting force. The final median backbone curve shown in Figure B.2 was the product of the median normalized curve and the median capping force of the two original curves that was equal to 279 lbs.

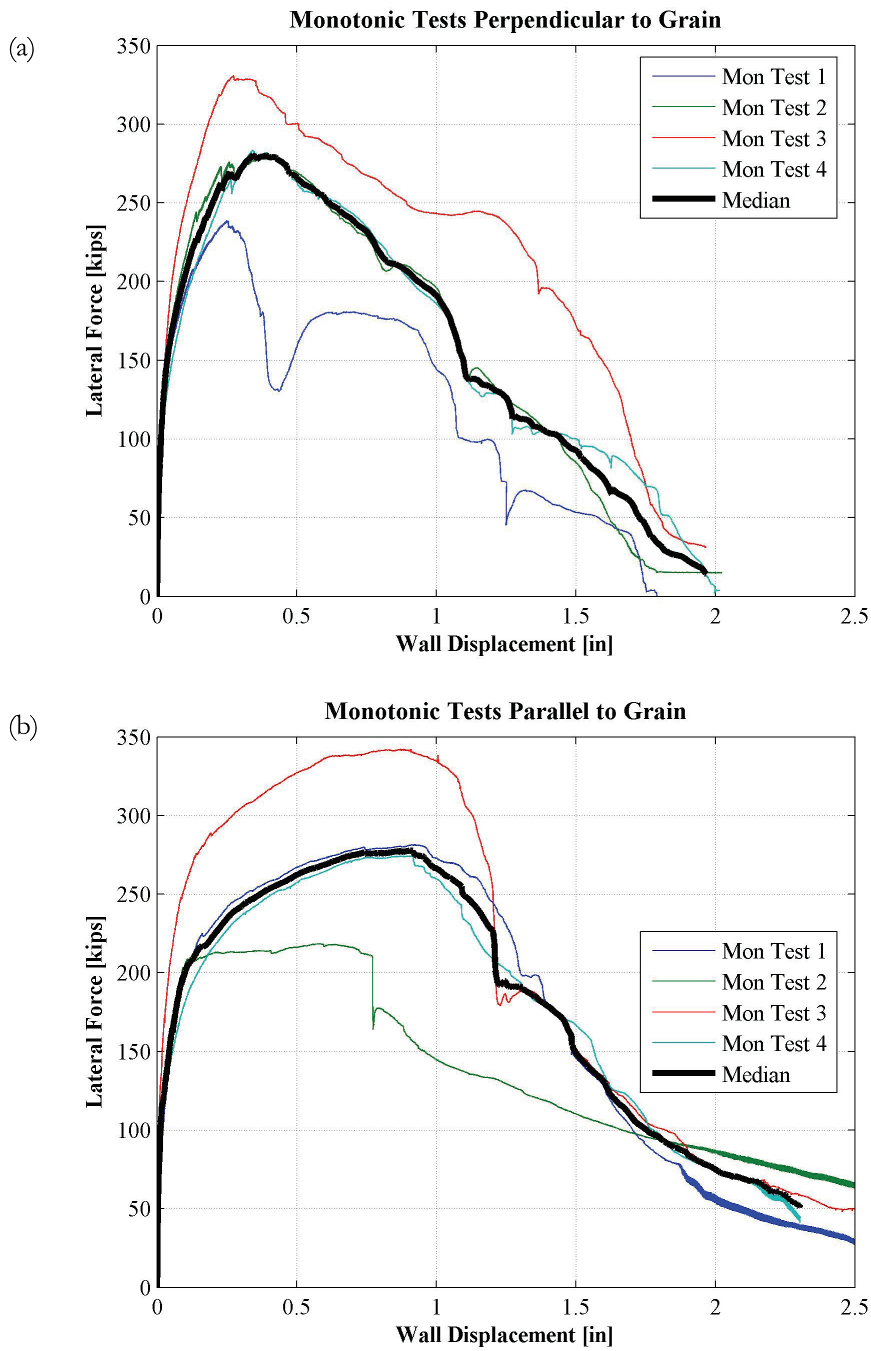

Figure B.1 Experimental and Median Backbone Curves for Loading (a) Perpendicular to Grain, and (b) Parallel to Grain for [7/16 in OSB / 8d Common Nails / 2x6 Hem-Fir]

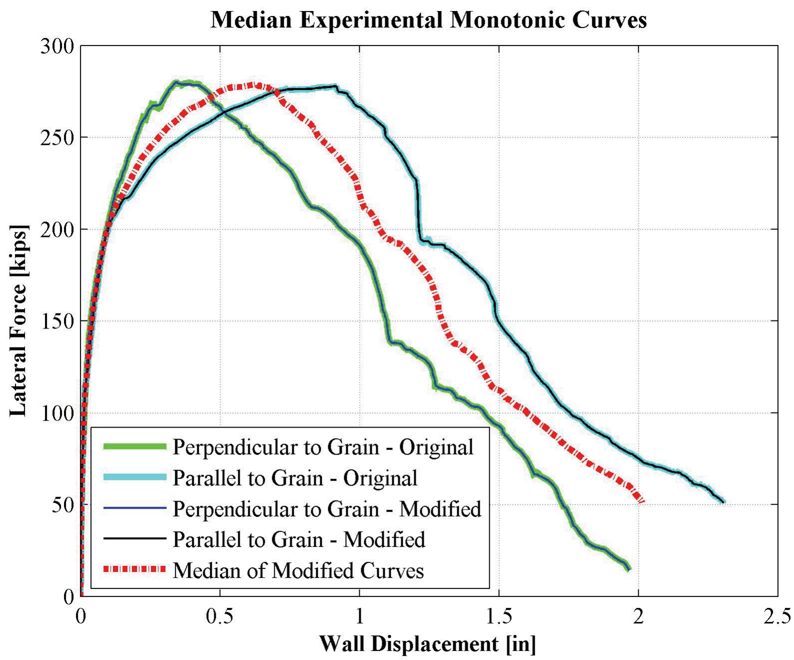

Figure B.2 Median Backbone Curves for
[7/16 in OSB / 8d Common Nails / 2x6 Hem-Fir]

B.2.2 Minimization Procedure and Final Parameters

The minimization procedure that has been described in Appendix A was used again with some minor modifications. Thus, a single optimization procedure was executed using the data from the tests as a single set. Moreover, it was decided to assign 50% of the weight in the calibration against the median backbone curve and 50% of the weight in the calibration against the cyclic tests available. A total of 16 cyclic tests were available (8 for loading perpendicular to grain and 8 for loading parallel to grain), each containing 5000 recording steps. Using a weight factor of unity for each cyclic data point, the total weight was equal to 16*5000, which is equal to 80000. The single monotonic curve consisted of 2013 points. Since the weight between cyclic and monotonic test data was the same, each monotonic data point was assigned a weight factor equal to 80000/2013, which is equal to 39.74. The parameters estimated from the identification procedure are listed in Table B.2. The hysteretic response and the associated strain energy for the monotonic cyclic tests and the numerical prediction are shown in Figure B.3.

(a)

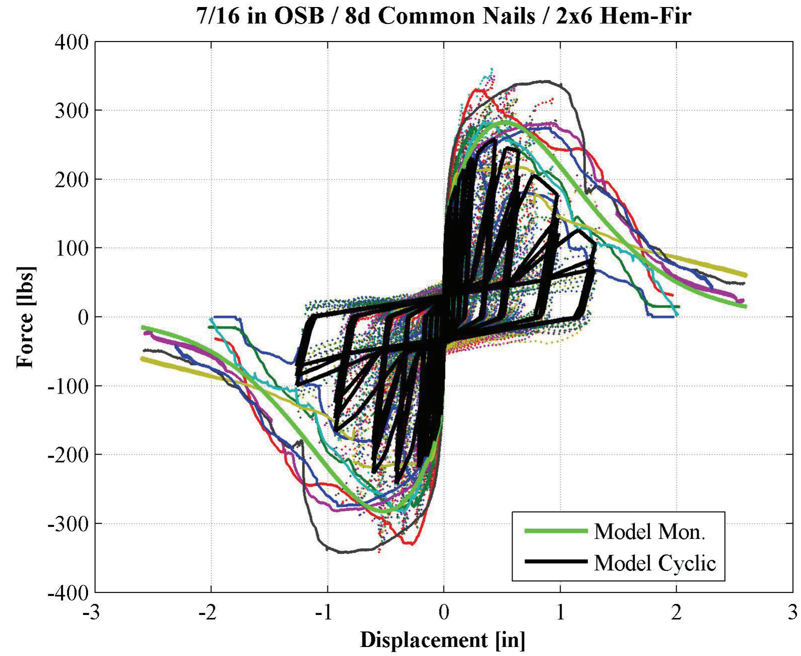

(b)

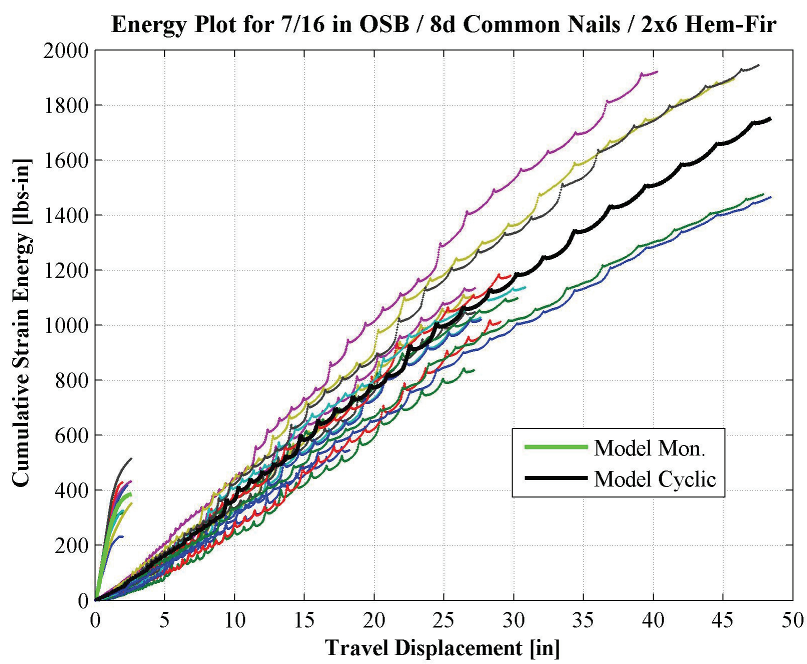

Figure B.3 (a) Monotonic and Cyclic Response, and (b) Strain Energy Response of a Unidirectional Nail Spring for: [7/16 in OSB / 8d Common Nails / 2x6 Hem-Fir]

As mentioned in the introductory section of this appendix, the test specimen was constructed with Spruce-Pine-Fir lumber, while the nail connection specimens were constructed with Hem-Fir lumber. The former material has a specific gravity of 0.42 and a dowel bearing strength of 3350 psi, while the latter has a specific gravity of 0.43 and a dowel bearing strength of 3500 psi, based on Table 11.3.2 and Table 11.3.2A of NDS (2005). It was assumed, for simplicity, that the strength of the two connections was correlated similarly to the dowel bearing strength. Thus, the strength of the Spruce-Pine-Fir connections was about 95% (3350/3500*100) that of the Hem-Fir connections. Therefore, the initial stiffness K_o and yield force F_{yo} were selected as 95% of the values assigned for the Hem-Fir connections. The remaining parameters were not modified except for the parameter γ which was multiplied by the inverse of 95%.

Table B.2 Parameters of Nonlinear Inelastic Sheathing-to-Framing Springs

	K_o [lbs/in]	F_{yo} [lbs]	α_o [-]	σ [-]	σ_u [-]	u_{ini} [in]	u_{ult} [in]	β [-]	γ [lbs^{-1}]	κ [-]
7/16 in OSB / 8d Common Nails / 2x6 Hem-Fir	12412.2	144.6	0.050	0.365	0.265	0.007	3.42	0.10	4.33E-04	5.7
7/16 in OSB / 8d Common Nails / 2x6 Spruce-Pine-Fir	11800.2	137.4	0.050	0.365	0.265	0.007	3.42	0.10	4.55E-04	5.7

B.3 Parameter Estimation for HD6A Holdown Spring

The parameters for the HD6A holdown spring were estimated directly from the parameters already defined for the HTT22 holdown spring, due to lack of experimental data for this type of component. The tension allowable load for the HD6A holdown was 3305 lbs which is 80% that of the HTT22 holdown (4165 lbs). Thus, the initial stiffness K_o and yield force F_{yo} were selected as 80% of the values assigned for the HTT22 holdown spring. The remaining parameters were not modified except for the parameter γ which was multiplied by the inverse of 80% which is equal to 1.25.

The parameters for the HD6A holdown spring are listed in Table B.1. The assumed hysteretic response for the two devices is shown in Figure B.4.

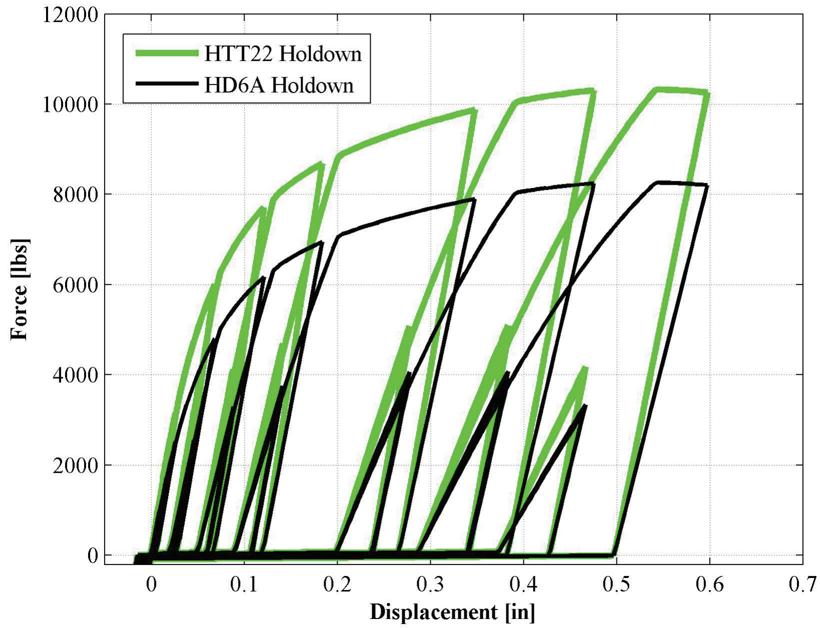

Figure B.4 Cyclic Responses of a HD6A and a HTT22 Holdown Spring

APPENDIX C: CONVERGENCE STUDY ON THE TIME STEP FOR NONLINEAR DYNAMIC ANALYSIS OF CHAPTER 6

A convergence study was executed in order to investigate the optimum time step (Δt), to be used in the nonlinear dynamic analysis, in terms of numerical accuracy and numerical efficiency. Only the **Model** formulation was used in these analyses. The test data were recorded at a sampling frequency of 200 Hz, thus, a time step of 0.005 sec was the first and most logical selection for the analysis time step. Furthermore, the fundamental period of the numerical model (0.27 sec) was more than 50 times larger than 0.005 sec. An additional analysis was executed with a time step of 0.001 sec. The output frequency was reduced to 1 every 5 analysis steps, thus, both numerical predictions provided the output data at the same time step of 0.005 sec. Subsequently, maximum and minimum response values were computed and are presented in Table C.1 to Table C.3 for **Test 1** to **Test 3**, respectively. Note that the values shown for a time step of 0.005 sec are the same as those listed in Chapter 6.

The results indicate that the differences between the two analysis cases are quite small. For **Test 1** and **Test 2**, maximum and minimum values are different by less than 0.5%. For **Test 3**, differences exceed 0.5% only for the maximum lateral force and the minimum absolute acceleration at the top of the wall. Given that the analysis with a time step of 0.005 sec is executed almost 5 times quicker than the same analysis with a time step of 0.001 sec and the numerical results are almost identical, the former time step was selected as optimum for the given dynamic nonlinear analyses.

Table C.1 Comparison of Maximum and Minimum Values for **Test 1**

	Δt = 0.001 sec		**Δt = 0.005 sec**	
	Positive	Negative	Positive	Negative
Inter-Story Displacement [in]	0.06	-0.10	0.06	-0.10
Force [kip]	0.54	-0.84	0.54	-0.84
Inter-Story Velocity [in]	1.42	-1.66	1.42	-1.66
Top of Wall Abs. Acceleration [g]	0.13	-0.08	0.13	-0.08
	Percentage Difference (%)			
Inter-Story Displacement	N/A	N/A	0.2	-0.2
Force	N/A	N/A	0.1	-0.1
Inter-Story Velocity	N/A	N/A	0.3	-0.4
Top of Wall Abs. Acceleration	N/A	N/A	-0.1	0.1

Table C.2 Comparison of Maximum and Minimum Values for **Test 2**

	Δt = 0.001 sec		**Δt = 0.005 sec**	
	Positive	Negative	Positive	Negative
Inter-Story Displacement [in]	0.40	-0.58	0.40	-0.58
Force [kip]	1.52	-1.71	1.52	-1.71
Inter-Story Velocity [in]	5.97	-5.51	5.98	-5.53
Top of Wall Abs. Acceleration [g]	0.26	-0.23	0.26	-0.23
	Percentage Difference (%)			
Inter-Story Displacement	N/A	N/A	0.0	0.2
Force	N/A	N/A	0.0	0.0
Inter-Story Velocity	N/A	N/A	0.1	0.2
Top of Wall Abs. Acceleration	N/A	N/A	0.0	0.0

Table C.3 Comparison of Maximum and Minimum Values for **Test 3**

	Δt = 0.001 sec		**Δt = 0.005 sec**	
	Positive	Negative	Positive	Negative
Inter-Story Displacement [in]	3.44	-3.21	3.43	-3.22
Force [kip]	2.30	-2.27	2.34	-2.27
Inter-Story Velocity [in]	22.47	-20.62	22.58	-20.54
Top of Wall Abs. Acceleration [g]	0.34	-0.34	0.34	-0.35
	Percentage Difference (%)			
Inter-Story Displacement	N/A	N/A	-0.2	0.3
Force	N/A	N/A	1.7	-0.2
Inter-Story Velocity	N/A	N/A	0.5	-0.4
Top of Wall Abs. Acceleration	N/A	N/A	-0.2	1.7

MCEER Technical Reports

MCEER publishes technical reports on a variety of subjects written by authors funded through MCEER. These reports are available from both MCEER Publications and the National Technical Information Service (NTIS). Requests for reports should be directed to MCEER Publications, MCEER, University at Buffalo, State University of New York, 133A Ketter Hall, Buffalo, New York 14260. Reports can also be requested through NTIS, P.O. Box 1425, Springfield, Virginia 22151. NTIS accession numbers are shown in parenthesis, if available.

NCEER-87-0001 "First-Year Program in Research, Education and Technology Transfer," 3/5/87, (PB88-134275, A04, MF-A01).

NCEER-87-0002 "Experimental Evaluation of Instantaneous Optimal Algorithms for Structural Control," by R.C. Lin, T.T. Soong and A.M. Reinhorn, 4/20/87, (PB88-134341, A04, MF-A01).

NCEER-87-0003 "Experimentation Using the Earthquake Simulation Facilities at University at Buffalo," by A.M. Reinhorn and R.L. Ketter, to be published.

NCEER-87-0004 "The System Characteristics and Performance of a Shaking Table," by J.S. Hwang, K.C. Chang and G.C. Lee, 6/1/87, (PB88-134259, A03, MF-A01). This report is available only through NTIS (see address given above).

NCEER-87-0005 "A Finite Element Formulation for Nonlinear Viscoplastic Material Using a Q Model," by O. Gyebi and G. Dasgupta, 11/2/87, (PB88-213764, A08, MF-A01).

NCEER-87-0006 "Symbolic Manipulation Program (SMP) - Algebraic Codes for Two and Three Dimensional Finite Element Formulations," by X. Lee and G. Dasgupta, 11/9/87, (PB88-218522, A05, MF-A01).

NCEER-87-0007 "Instantaneous Optimal Control Laws for Tall Buildings Under Seismic Excitations," by J.N. Yang, A. Akbarpour and P. Ghaemmaghami, 6/10/87, (PB88-134333, A06, MF-A01). This report is only available through NTIS (see address given above).

NCEER-87-0008 "IDARC: Inelastic Damage Analysis of Reinforced Concrete Frame - Shear-Wall Structures," by Y.J. Park, A.M. Reinhorn and S.K. Kunnath, 7/20/87, (PB88-134325, A09, MF-A01). This report is only available through NTIS (see address given above).

NCEER-87-0009 "Liquefaction Potential for New York State: A Preliminary Report on Sites in Manhattan and Buffalo," by M. Budhu, V. Vijayakumar, R.F. Giese and L. Baumgras, 8/31/87, (PB88-163704, A03, MF-A01). This report is available only through NTIS (see address given above).

NCEER-87-0010 "Vertical and Torsional Vibration of Foundations in Inhomogeneous Media," by A.S. Veletsos and K.W. Dotson, 6/1/87, (PB88-134291, A03, MF-A01). This report is only available through NTIS (see address given above).

NCEER-87-0011 "Seismic Probabilistic Risk Assessment and Seismic Margins Studies for Nuclear Power Plants," by Howard H.M. Hwang, 6/15/87, (PB88-134267, A03, MF-A01). This report is only available through NTIS (see address given above).

NCEER-87-0012 "Parametric Studies of Frequency Response of Secondary Systems Under Ground-Acceleration Excitations," by Y. Yong and Y.K. Lin, 6/10/87, (PB88-134309, A03, MF-A01). This report is only available through NTIS (see address given above).

NCEER-87-0013 "Frequency Response of Secondary Systems Under Seismic Excitation," by J.A. HoLung, J. Cai and Y.K. Lin, 7/31/87, (PB88-134317, A05, MF-A01). This report is only available through NTIS (see address given above).

NCEER-87-0014 "Modelling Earthquake Ground Motions in Seismically Active Regions Using Parametric Time Series Methods," by G.W. Ellis and A.S. Cakmak, 8/25/87, (PB88-134283, A08, MF-A01). This report is only available through NTIS (see address given above).

NCEER-87-0015 "Detection and Assessment of Seismic Structural Damage," by E. DiPasquale and A.S. Cakmak, 8/25/87, (PB88-163712, A05, MF-A01). This report is only available through NTIS (see address given above).

NCEER-87-0016 "Pipeline Experiment at Parkfield, California," by J. Isenberg and E. Richardson, 9/15/87, (PB88-163720, A03, MF-A01). This report is available only through NTIS (see address given above).

NCEER-87-0017 "Digital Simulation of Seismic Ground Motion," by M. Shinozuka, G. Deodatis and T. Harada, 8/31/87, (PB88-155197, A04, MF-A01). This report is available only through NTIS (see address given above).

NCEER-87-0018 "Practical Considerations for Structural Control: System Uncertainty, System Time Delay and Truncation of Small Control Forces," J.N. Yang and A. Akbarpour, 8/10/87, (PB88-163738, A08, MF-A01). This report is only available through NTIS (see address given above).

NCEER-87-0019 "Modal Analysis of Nonclassically Damped Structural Systems Using Canonical Transformation," by J.N. Yang, S. Sarkani and F.X. Long, 9/27/87, (PB88-187851, A04, MF-A01).

NCEER-87-0020 "A Nonstationary Solution in Random Vibration Theory," by J.R. Red-Horse and P.D. Spanos, 11/3/87, (PB88-163746, A03, MF-A01).

NCEER-87-0021 "Horizontal Impedances for Radially Inhomogeneous Viscoelastic Soil Layers," by A.S. Veletsos and K.W. Dotson, 10/15/87, (PB88-150859, A04, MF-A01).

NCEER-87-0022 "Seismic Damage Assessment of Reinforced Concrete Members," by Y.S. Chung, C. Meyer and M. Shinozuka, 10/9/87, (PB88-150867, A05, MF-A01). This report is available only through NTIS (see address given above).

NCEER-87-0023 "Active Structural Control in Civil Engineering," by T.T. Soong, 11/11/87, (PB88-187778, A03, MF-A01).

NCEER-87-0024 "Vertical and Torsional Impedances for Radially Inhomogeneous Viscoelastic Soil Layers," by K.W. Dotson and A.S. Veletsos, 12/87, (PB88-187786, A03, MF-A01).

NCEER-87-0025 "Proceedings from the Symposium on Seismic Hazards, Ground Motions, Soil-Liquefaction and Engineering Practice in Eastern North America," October 20-22, 1987, edited by K.H. Jacob, 12/87, (PB88-188115, A23, MF-A01). This report is available only through NTIS (see address given above).

NCEER-87-0026 "Report on the Whittier-Narrows, California, Earthquake of October 1, 1987," by J. Pantelic and A. Reinhorn, 11/87, (PB88-187752, A03, MF-A01). This report is available only through NTIS (see address given above).

NCEER-87-0027 "Design of a Modular Program for Transient Nonlinear Analysis of Large 3-D Building Structures," by S. Srivastav and J.F. Abel, 12/30/87, (PB88-187950, A05, MF-A01). This report is only available through NTIS (see address given above).

NCEER-87-0028 "Second-Year Program in Research, Education and Technology Transfer," 3/8/88, (PB88-219480, A04, MF-A01).

NCEER-88-0001 "Workshop on Seismic Computer Analysis and Design of Buildings With Interactive Graphics," by W. McGuire, J.F. Abel and C.H. Conley, 1/18/88, (PB88-187760, A03, MF-A01). This report is only available through NTIS (see address given above).

NCEER-88-0002 "Optimal Control of Nonlinear Flexible Structures," by J.N. Yang, F.X. Long and D. Wong, 1/22/88, (PB88-213772, A06, MF-A01).

NCEER-88-0003 "Substructuring Techniques in the Time Domain for Primary-Secondary Structural Systems," by G.D. Manolis and G. Juhn, 2/10/88, (PB88-213780, A04, MF-A01).

NCEER-88-0004 "Iterative Seismic Analysis of Primary-Secondary Systems," by A. Singhal, L.D. Lutes and P.D. Spanos, 2/23/88, (PB88-213798, A04, MF-A01).

NCEER-88-0005 "Stochastic Finite Element Expansion for Random Media," by P.D. Spanos and R. Ghanem, 3/14/88, (PB88-213806, A03, MF-A01).

NCEER-88-0006 "Combining Structural Optimization and Structural Control," by F.Y. Cheng and C.P. Pantelides, 1/10/88, (PB88-213814, A05, MF-A01).

NCEER-88-0007 "Seismic Performance Assessment of Code-Designed Structures," by H.H-M. Hwang, J-W. Jaw and H-J. Shau, 3/20/88, (PB88-219423, A04, MF-A01). This report is only available through NTIS (see address given above).

NCEER-88-0008 "Reliability Analysis of Code-Designed Structures Under Natural Hazards," by H.H-M. Hwang, H. Ushiba and M. Shinozuka, 2/29/88, (PB88-229471, A07, MF-A01). This report is only available through NTIS (see address given above).

NCEER-88-0009 "Seismic Fragility Analysis of Shear Wall Structures," by J-W Jaw and H.H-M. Hwang, 4/30/88, (PB89-102867, A04, MF-A01).

NCEER-88-0010 "Base Isolation of a Multi-Story Building Under a Harmonic Ground Motion - A Comparison of Performances of Various Systems," by F-G Fan, G. Ahmadi and I.G. Tadjbakhsh, 5/18/88, (PB89-122238, A06, MF-A01). This report is only available through NTIS (see address given above).

NCEER-88-0011 "Seismic Floor Response Spectra for a Combined System by Green's Functions," by F.M. Lavelle, L.A. Bergman and P.D. Spanos, 5/1/88, (PB89-102875, A03, MF-A01).

NCEER-88-0012 "A New Solution Technique for Randomly Excited Hysteretic Structures," by G.Q. Cai and Y.K. Lin, 5/16/88, (PB89-102883, A03, MF-A01).

NCEER-88-0013 "A Study of Radiation Damping and Soil-Structure Interaction Effects in the Centrifuge," by K. Weissman, supervised by J.H. Prevost, 5/24/88, (PB89-144703, A06, MF-A01).

NCEER-88-0014 "Parameter Identification and Implementation of a Kinematic Plasticity Model for Frictional Soils," by J.H. Prevost and D.V. Griffiths, to be published.

NCEER-88-0015 "Two- and Three- Dimensional Dynamic Finite Element Analyses of the Long Valley Dam," by D.V. Griffiths and J.H. Prevost, 6/17/88, (PB89-144711, A04, MF-A01).

NCEER-88-0016 "Damage Assessment of Reinforced Concrete Structures in Eastern United States," by A.M. Reinhorn, M.J. Seidel, S.K. Kunnath and Y.J. Park, 6/15/88, (PB89-122220, A04, MF-A01). This report is only available through NTIS (see address given above).

NCEER-88-0017 "Dynamic Compliance of Vertically Loaded Strip Foundations in Multilayered Viscoelastic Soils," by S. Ahmad and A.S.M. Israil, 6/17/88, (PB89-102891, A04, MF-A01).

NCEER-88-0018 "An Experimental Study of Seismic Structural Response With Added Viscoelastic Dampers," by R.C. Lin, Z. Liang, T.T. Soong and R.H. Zhang, 6/30/88, (PB89-122212, A05, MF-A01). This report is available only through NTIS (see address given above).

NCEER-88-0019 "Experimental Investigation of Primary - Secondary System Interaction," by G.D. Manolis, G. Juhn and A.M. Reinhorn, 5/27/88, (PB89-122204, A04, MF-A01).

NCEER-88-0020 "A Response Spectrum Approach For Analysis of Nonclassically Damped Structures," by J.N. Yang, S. Sarkani and F.X. Long, 4/22/88, (PB89-102909, A04, MF-A01).

NCEER-88-0021 "Seismic Interaction of Structures and Soils: Stochastic Approach," by A.S. Veletsos and A.M. Prasad, 7/21/88, (PB89-122196, A04, MF-A01). This report is only available through NTIS (see address given above).

NCEER-88-0022 "Identification of the Serviceability Limit State and Detection of Seismic Structural Damage," by E. DiPasquale and A.S. Cakmak, 6/15/88, (PB89-122188, A05, MF-A01). This report is available only through NTIS (see address given above).

NCEER-88-0023 "Multi-Hazard Risk Analysis: Case of a Simple Offshore Structure," by B.K. Bhartia and E.H. Vanmarcke, 7/21/88, (PB89-145213, A05, MF-A01).

NCEER-88-0024 "Automated Seismic Design of Reinforced Concrete Buildings," by Y.S. Chung, C. Meyer and M. Shinozuka, 7/5/88, (PB89-122170, A06, MF-A01). This report is available only through NTIS (see address given above).

NCEER-88-0025 "Experimental Study of Active Control of MDOF Structures Under Seismic Excitations," by L.L. Chung, R.C. Lin, T.T. Soong and A.M. Reinhorn, 7/10/88, (PB89-122600, A04, MF-A01).

NCEER-88-0026 "Earthquake Simulation Tests of a Low-Rise Metal Structure," by J.S. Hwang, K.C. Chang, G.C. Lee and R.L. Ketter, 8/1/88, (PB89-102917, A04, MF-A01).

NCEER-88-0027 "Systems Study of Urban Response and Reconstruction Due to Catastrophic Earthquakes," by F. Kozin and H.K. Zhou, 9/22/88, (PB90-162348, A04, MF-A01).

NCEER-88-0028 "Seismic Fragility Analysis of Plane Frame Structures," by H.H-M. Hwang and Y.K. Low, 7/31/88, (PB89-131445, A06, MF-A01).

NCEER-88-0029 "Response Analysis of Stochastic Structures," by A. Kardara, C. Bucher and M. Shinozuka, 9/22/88, (PB89-174429, A04, MF-A01).

NCEER-88-0030 "Nonnormal Accelerations Due to Yielding in a Primary Structure," by D.C.K. Chen and L.D. Lutes, 9/19/88, (PB89-131437, A04, MF-A01).

NCEER-88-0031 "Design Approaches for Soil-Structure Interaction," by A.S. Veletsos, A.M. Prasad and Y. Tang, 12/30/88, (PB89-174437, A03, MF-A01). This report is available only through NTIS (see address given above).

NCEER-88-0032 "A Re-evaluation of Design Spectra for Seismic Damage Control," by C.J. Turkstra and A.G. Tallin, 11/7/88, (PB89-145221, A05, MF-A01).

NCEER-88-0033 "The Behavior and Design of Noncontact Lap Splices Subjected to Repeated Inelastic Tensile Loading," by V.E. Sagan, P. Gergely and R.N. White, 12/8/88, (PB89-163737, A08, MF-A01).

NCEER-88-0034 "Seismic Response of Pile Foundations," by S.M. Mamoon, P.K. Banerjee and S. Ahmad, 11/1/88, (PB89-145239, A04, MF-A01).

NCEER-88-0035 "Modeling of R/C Building Structures With Flexible Floor Diaphragms (IDARC2)," by A.M. Reinhorn, S.K. Kunnath and N. Panahshahi, 9/7/88, (PB89-207153, A07, MF-A01).

NCEER-88-0036 "Solution of the Dam-Reservoir Interaction Problem Using a Combination of FEM, BEM with Particular Integrals, Modal Analysis, and Substructuring," by C-S. Tsai, G.C. Lee and R.L. Ketter, 12/31/88, (PB89-207146, A04, MF-A01).

NCEER-88-0037 "Optimal Placement of Actuators for Structural Control," by F.Y. Cheng and C.P. Pantelides, 8/15/88, (PB89-162846, A05, MF-A01).

NCEER-88-0038 "Teflon Bearings in Aseismic Base Isolation: Experimental Studies and Mathematical Modeling," by A. Mokha, M.C. Constantinou and A.M. Reinhorn, 12/5/88, (PB89-218457, A10, MF-A01). This report is available only through NTIS (see address given above).

NCEER-88-0039 "Seismic Behavior of Flat Slab High-Rise Buildings in the New York City Area," by P. Weidlinger and M. Ettouney, 10/15/88, (PB90-145681, A04, MF-A01).

NCEER-88-0040 "Evaluation of the Earthquake Resistance of Existing Buildings in New York City," by P. Weidlinger and M. Ettouney, 10/15/88, to be published.

NCEER-88-0041 "Small-Scale Modeling Techniques for Reinforced Concrete Structures Subjected to Seismic Loads," by W. Kim, A. El-Attar and R.N. White, 11/22/88, (PB89-189625, A05, MF-A01).

NCEER-88-0042 "Modeling Strong Ground Motion from Multiple Event Earthquakes," by G.W. Ellis and A.S. Cakmak, 10/15/88, (PB89-174445, A03, MF-A01).

NCEER-88-0043 "Nonstationary Models of Seismic Ground Acceleration," by M. Grigoriu, S.E. Ruiz and E. Rosenblueth, 7/15/88, (PB89-189617, A04, MF-A01).

NCEER-88-0044 "SARCF User's Guide: Seismic Analysis of Reinforced Concrete Frames," by Y.S. Chung, C. Meyer and M. Shinozuka, 11/9/88, (PB89-174452, A08, MF-A01).

NCEER-88-0045 "First Expert Panel Meeting on Disaster Research and Planning," edited by J. Pantelic and J. Stoyle, 9/15/88, (PB89-174460, A05, MF-A01).

NCEER-88-0046 "Preliminary Studies of the Effect of Degrading Infill Walls on the Nonlinear Seismic Response of Steel Frames," by C.Z. Chrysostomou, P. Gergely and J.F. Abel, 12/19/88, (PB89-208383, A05, MF-A01).

NCEER-88-0047 "Reinforced Concrete Frame Component Testing Facility - Design, Construction, Instrumentation and Operation," by S.P. Pessiki, C. Conley, T. Bond, P. Gergely and R.N. White, 12/16/88, (PB89-174478, A04, MF-A01).

NCEER-89-0001 "Effects of Protective Cushion and Soil Compliancy on the Response of Equipment Within a Seismically Excited Building," by J.A. HoLung, 2/16/89, (PB89-207179, A04, MF-A01).

NCEER-89-0002 "Statistical Evaluation of Response Modification Factors for Reinforced Concrete Structures," by H.H-M. Hwang and J-W. Jaw, 2/17/89, (PB89-207187, A05, MF-A01).

NCEER-89-0003 "Hysteretic Columns Under Random Excitation," by G-Q. Cai and Y.K. Lin, 1/9/89, (PB89-196513, A03, MF-A01).

NCEER-89-0004 "Experimental Study of `Elephant Foot Bulge' Instability of Thin-Walled Metal Tanks," by Z-H. Jia and R.L. Ketter, 2/22/89, (PB89-207195, A03, MF-A01).

NCEER-89-0005 "Experiment on Performance of Buried Pipelines Across San Andreas Fault," by J. Isenberg, E. Richardson and T.D. O'Rourke, 3/10/89, (PB89-218440, A04, MF-A01). This report is available only through NTIS (see address given above).

NCEER-89-0006 "A Knowledge-Based Approach to Structural Design of Earthquake-Resistant Buildings," by M. Subramani, P. Gergely, C.H. Conley, J.F. Abel and A.H. Zaghw, 1/15/89, (PB89-218465, A06, MF-A01).

NCEER-89-0007 "Liquefaction Hazards and Their Effects on Buried Pipelines," by T.D. O'Rourke and P.A. Lane, 2/1/89, (PB89-218481, A09, MF-A01).

NCEER-89-0008 "Fundamentals of System Identification in Structural Dynamics," by H. Imai, C-B. Yun, O. Maruyama and M. Shinozuka, 1/26/89, (PB89-207211, A04, MF-A01).

NCEER-89-0009 "Effects of the 1985 Michoacan Earthquake on Water Systems and Other Buried Lifelines in Mexico," by A.G. Ayala and M.J. O'Rourke, 3/8/89, (PB89-207229, A06, MF-A01).

NCEER-89-R010 "NCEER Bibliography of Earthquake Education Materials," by K.E.K. Ross, Second Revision, 9/1/89, (PB90-125352, A05, MF-A01). This report is replaced by NCEER-92-0018.

NCEER-89-0011 "Inelastic Three-Dimensional Response Analysis of Reinforced Concrete Building Structures (IDARC-3D), Part I - Modeling," by S.K. Kunnath and A.M. Reinhorn, 4/17/89, (PB90-114612, A07, MF-A01). This report is available only through NTIS (see address given above).

NCEER-89-0012 "Recommended Modifications to ATC-14," by C.D. Poland and J.O. Malley, 4/12/89, (PB90-108648, A15, MF-A01).

NCEER-89-0013 "Repair and Strengthening of Beam-to-Column Connections Subjected to Earthquake Loading," by M. Corazao and A.J. Durrani, 2/28/89, (PB90-109885, A06, MF-A01).

NCEER-89-0014 "Program EXKAL2 for Identification of Structural Dynamic Systems," by O. Maruyama, C-B. Yun, M. Hoshiya and M. Shinozuka, 5/19/89, (PB90-109877, A09, MF-A01).

NCEER-89-0015 "Response of Frames With Bolted Semi-Rigid Connections, Part I - Experimental Study and Analytical Predictions," by P.J. DiCorso, A.M. Reinhorn, J.R. Dickerson, J.B. Radziminski and W.L. Harper, 6/1/89, to be published.

NCEER-89-0016 "ARMA Monte Carlo Simulation in Probabilistic Structural Analysis," by P.D. Spanos and M.P. Mignolet, 7/10/89, (PB90-109893, A03, MF-A01).

NCEER-89-P017 "Preliminary Proceedings from the Conference on Disaster Preparedness - The Place of Earthquake Education in Our Schools," Edited by K.E.K. Ross, 6/23/89, (PB90-108606, A03, MF-A01).

NCEER-89-0017 "Proceedings from the Conference on Disaster Preparedness - The Place of Earthquake Education in Our Schools," Edited by K.E.K. Ross, 12/31/89, (PB90-207895, A012, MF-A02). This report is available only through NTIS (see address given above).

NCEER-89-0018 "Multidimensional Models of Hysteretic Material Behavior for Vibration Analysis of Shape Memory Energy Absorbing Devices, by E.J. Graesser and F.A. Cozzarelli, 6/7/89, (PB90-164146, A04, MF-A01).

NCEER-89-0019 "Nonlinear Dynamic Analysis of Three-Dimensional Base Isolated Structures (3D-BASIS)," by S. Nagarajaiah, A.M. Reinhorn and M.C. Constantinou, 8/3/89, (PB90-161936, A06, MF-A01). This report has been replaced by NCEER-93-0011.

NCEER-89-0020 "Structural Control Considering Time-Rate of Control Forces and Control Rate Constraints," by F.Y. Cheng and C.P. Pantelides, 8/3/89, (PB90-120445, A04, MF-A01).

NCEER-89-0021 "Subsurface Conditions of Memphis and Shelby County," by K.W. Ng, T-S. Chang and H-H.M. Hwang, 7/26/89, (PB90-120437, A03, MF-A01).

NCEER-89-0022 "Seismic Wave Propagation Effects on Straight Jointed Buried Pipelines," by K. Elhmadi and M.J. O'Rourke, 8/24/89, (PB90-162322, A10, MF-A02).

NCEER-89-0023 "Workshop on Serviceability Analysis of Water Delivery Systems," edited by M. Grigoriu, 3/6/89, (PB90-127424, A03, MF-A01).

NCEER-89-0024 "Shaking Table Study of a 1/5 Scale Steel Frame Composed of Tapered Members," by K.C. Chang, J.S. Hwang and G.C. Lee, 9/18/89, (PB90-160169, A04, MF-A01).

NCEER-89-0025 "DYNA1D: A Computer Program for Nonlinear Seismic Site Response Analysis - Technical Documentation," by Jean H. Prevost, 9/14/89, (PB90-161944, A07, MF-A01). This report is available only through NTIS (see address given above).

NCEER-89-0026 "1:4 Scale Model Studies of Active Tendon Systems and Active Mass Dampers for Aseismic Protection," by A.M. Reinhorn, T.T. Soong, R.C. Lin, Y.P. Yang, Y. Fukao, H. Abe and M. Nakai, 9/15/89, (PB90-173246, A10, MF-A02). This report is available only through NTIS (see address given above).

NCEER-89-0027 "Scattering of Waves by Inclusions in a Nonhomogeneous Elastic Half Space Solved by Boundary Element Methods," by P.K. Hadley, A. Askar and A.S. Cakmak, 6/15/89, (PB90-145699, A07, MF-A01).

NCEER-89-0028 "Statistical Evaluation of Deflection Amplification Factors for Reinforced Concrete Structures," by H.H.M. Hwang, J-W. Jaw and A.L. Ch'ng, 8/31/89, (PB90-164633, A05, MF-A01).

NCEER-89-0029 "Bedrock Accelerations in Memphis Area Due to Large New Madrid Earthquakes," by H.H.M. Hwang, C.H.S. Chen and G. Yu, 11/7/89, (PB90-162330, A04, MF-A01).

NCEER-89-0030 "Seismic Behavior and Response Sensitivity of Secondary Structural Systems," by Y.Q. Chen and T.T. Soong, 10/23/89, (PB90-164658, A08, MF-A01).

NCEER-89-0031 "Random Vibration and Reliability Analysis of Primary-Secondary Structural Systems," by Y. Ibrahim, M. Grigoriu and T.T. Soong, 11/10/89, (PB90-161951, A04, MF-A01).

NCEER-89-0032 "Proceedings from the Second U.S. - Japan Workshop on Liquefaction, Large Ground Deformation and Their Effects on Lifelines, September 26-29, 1989," Edited by T.D. O'Rourke and M. Hamada, 12/1/89, (PB90-209388, A22, MF-A03).

NCEER-89-0033 "Deterministic Model for Seismic Damage Evaluation of Reinforced Concrete Structures," by J.M. Bracci, A.M. Reinhorn, J.B. Mander and S.K. Kunnath, 9/27/89, (PB91-108803, A06, MF-A01).

NCEER-89-0034 "On the Relation Between Local and Global Damage Indices," by E. DiPasquale and A.S. Cakmak, 8/15/89, (PB90-173865, A05, MF-A01).

NCEER-89-0035 "Cyclic Undrained Behavior of Nonplastic and Low Plasticity Silts," by A.J. Walker and H.E. Stewart, 7/26/89, (PB90-183518, A10, MF-A01).

NCEER-89-0036 "Liquefaction Potential of Surficial Deposits in the City of Buffalo, New York," by M. Budhu, R. Giese and L. Baumgrass, 1/17/89, (PB90-208455, A04, MF-A01).

NCEER-89-0037 "A Deterministic Assessment of Effects of Ground Motion Incoherence," by A.S. Veletsos and Y. Tang, 7/15/89, (PB90-164294, A03, MF-A01).

NCEER-89-0038 "Workshop on Ground Motion Parameters for Seismic Hazard Mapping," July 17-18, 1989, edited by R.V. Whitman, 12/1/89, (PB90-173923, A04, MF-A01).

NCEER-89-0039 "Seismic Effects on Elevated Transit Lines of the New York City Transit Authority," by C.J. Costantino, C.A. Miller and E. Heymsfield, 12/26/89, (PB90-207887, A06, MF-A01).

NCEER-89-0040 "Centrifugal Modeling of Dynamic Soil-Structure Interaction," by K. Weissman, Supervised by J.H. Prevost, 5/10/89, (PB90-207879, A07, MF-A01).

NCEER-89-0041 "Linearized Identification of Buildings With Cores for Seismic Vulnerability Assessment," by I-K. Ho and A.E. Aktan, 11/1/89, (PB90-251943, A07, MF-A01).

NCEER-90-0001 "Geotechnical and Lifeline Aspects of the October 17, 1989 Loma Prieta Earthquake in San Francisco," by T.D. O'Rourke, H.E. Stewart, F.T. Blackburn and T.S. Dickerman, 1/90, (PB90-208596, A05, MF-A01).

NCEER-90-0002 "Nonnormal Secondary Response Due to Yielding in a Primary Structure," by D.C.K. Chen and L.D. Lutes, 2/28/90, (PB90-251976, A07, MF-A01).

NCEER-90-0003 "Earthquake Education Materials for Grades K-12," by K.E.K. Ross, 4/16/90, (PB91-251984, A05, MF-A05). This report has been replaced by NCEER-92-0018.

NCEER-90-0004 "Catalog of Strong Motion Stations in Eastern North America," by R.W. Busby, 4/3/90, (PB90-251984, A05, MF-A01).

NCEER-90-0005 "NCEER Strong-Motion Data Base: A User Manual for the GeoBase Release (Version 1.0 for the Sun3)," by P. Friberg and K. Jacob, 3/31/90 (PB90-258062, A04, MF-A01).

NCEER-90-0006 "Seismic Hazard Along a Crude Oil Pipeline in the Event of an 1811-1812 Type New Madrid Earthquake," by H.H.M. Hwang and C-H.S. Chen, 4/16/90, (PB90-258054, A04, MF-A01).

NCEER-90-0007 "Site-Specific Response Spectra for Memphis Sheahan Pumping Station," by H.H.M. Hwang and C.S. Lee, 5/15/90, (PB91-108811, A05, MF-A01).

NCEER-90-0008 "Pilot Study on Seismic Vulnerability of Crude Oil Transmission Systems," by T. Ariman, R. Dobry, M. Grigoriu, F. Kozin, M. O'Rourke, T. O'Rourke and M. Shinozuka, 5/25/90, (PB91-108837, A06, MF-A01).

NCEER-90-0009 "A Program to Generate Site Dependent Time Histories: EQGEN," by G.W. Ellis, M. Srinivasan and A.S. Cakmak, 1/30/90, (PB91-108829, A04, MF-A01).

NCEER-90-0010 "Active Isolation for Seismic Protection of Operating Rooms," by M.E. Talbott, Supervised by M. Shinozuka, 6/8/9, (PB91-110205, A05, MF-A01).

NCEER-90-0011 "Program LINEARID for Identification of Linear Structural Dynamic Systems," by C-B. Yun and M. Shinozuka, 6/25/90, (PB91-110312, A08, MF-A01).

NCEER-90-0012 "Two-Dimensional Two-Phase Elasto-Plastic Seismic Response of Earth Dams," by A.N. Yiagos, Supervised by J.H. Prevost, 6/20/90, (PB91-110197, A13, MF-A02).

NCEER-90-0013 "Secondary Systems in Base-Isolated Structures: Experimental Investigation, Stochastic Response and Stochastic Sensitivity," by G.D. Manolis, G. Juhn, M.C. Constantinou and A.M. Reinhorn, 7/1/90, (PB91-110320, A08, MF-A01).

NCEER-90-0014 "Seismic Behavior of Lightly-Reinforced Concrete Column and Beam-Column Joint Details," by S.P. Pessiki, C.H. Conley, P. Gergely and R.N. White, 8/22/90, (PB91-108795, A11, MF-A02).

NCEER-90-0015 "Two Hybrid Control Systems for Building Structures Under Strong Earthquakes," by J.N. Yang and A. Danielians, 6/29/90, (PB91-125393, A04, MF-A01).

NCEER-90-0016 "Instantaneous Optimal Control with Acceleration and Velocity Feedback," by J.N. Yang and Z. Li, 6/29/90, (PB91-125401, A03, MF-A01).

NCEER-90-0017 "Reconnaissance Report on the Northern Iran Earthquake of June 21, 1990," by M. Mehrain, 10/4/90, (PB91-125377, A03, MF-A01).

NCEER-90-0018 "Evaluation of Liquefaction Potential in Memphis and Shelby County," by T.S. Chang, P.S. Tang, C.S. Lee and H. Hwang, 8/10/90, (PB91-125427, A09, MF-A01).

NCEER-90-0019 "Experimental and Analytical Study of a Combined Sliding Disc Bearing and Helical Steel Spring Isolation System," by M.C. Constantinou, A.S. Mokha and A.M. Reinhorn, 10/4/90, (PB91-125385, A06, MF-A01). This report is available only through NTIS (see address given above).

NCEER-90-0020 "Experimental Study and Analytical Prediction of Earthquake Response of a Sliding Isolation System with a Spherical Surface," by A.S. Mokha, M.C. Constantinou and A.M. Reinhorn, 10/11/90, (PB91-125419, A05, MF-A01).

NCEER-90-0021 "Dynamic Interaction Factors for Floating Pile Groups," by G. Gazetas, K. Fan, A. Kaynia and E. Kausel, 9/10/90, (PB91-170381, A05, MF-A01).

NCEER-90-0022 "Evaluation of Seismic Damage Indices for Reinforced Concrete Structures," by S. Rodriguez-Gomez and A.S. Cakmak, 9/30/90, PB91-171322, A06, MF-A01).

NCEER-90-0023 "Study of Site Response at a Selected Memphis Site," by H. Desai, S. Ahmad, E.S. Gazetas and M.R. Oh, 10/11/90, (PB91-196857, A03, MF-A01).

NCEER-90-0024 "A User's Guide to Strongmo: Version 1.0 of NCEER's Strong-Motion Data Access Tool for PCs and Terminals," by P.A. Friberg and C.A.T. Susch, 11/15/90, (PB91-171272, A03, MF-A01).

NCEER-90-0025 "A Three-Dimensional Analytical Study of Spatial Variability of Seismic Ground Motions," by L-L. Hong and A.H.-S. Ang, 10/30/90, (PB91-170399, A09, MF-A01).

NCEER-90-0026 "MUMOID User's Guide - A Program for the Identification of Modal Parameters," by S. Rodriguez-Gomez and E. DiPasquale, 9/30/90, (PB91-171298, A04, MF-A01).

NCEER-90-0027 "SARCF-II User's Guide - Seismic Analysis of Reinforced Concrete Frames," by S. Rodriguez-Gomez, Y.S. Chung and C. Meyer, 9/30/90, (PB91-171280, A05, MF-A01).

NCEER-90-0028 "Viscous Dampers: Testing, Modeling and Application in Vibration and Seismic Isolation," by N. Makris and M.C. Constantinou, 12/20/90 (PB91-190561, A06, MF-A01).

NCEER-90-0029 "Soil Effects on Earthquake Ground Motions in the Memphis Area," by H. Hwang, C.S. Lee, K.W. Ng and T.S. Chang, 8/2/90, (PB91-190751, A05, MF-A01).

NCEER-91-0001 "Proceedings from the Third Japan-U.S. Workshop on Earthquake Resistant Design of Lifeline Facilities and Countermeasures for Soil Liquefaction, December 17-19, 1990," edited by T.D. O'Rourke and M. Hamada, 2/1/91, (PB91-179259, A99, MF-A04).

NCEER-91-0002 "Physical Space Solutions of Non-Proportionally Damped Systems," by M. Tong, Z. Liang and G.C. Lee, 1/15/91, (PB91-179242, A04, MF-A01).

NCEER-91-0003 "Seismic Response of Single Piles and Pile Groups," by K. Fan and G. Gazetas, 1/10/91, (PB92-174994, A04, MF-A01).

NCEER-91-0004 "Damping of Structures: Part 1 - Theory of Complex Damping," by Z. Liang and G. Lee, 10/10/91, (PB92-197235, A12, MF-A03).

NCEER-91-0005 "3D-BASIS - Nonlinear Dynamic Analysis of Three Dimensional Base Isolated Structures: Part II," by S. Nagarajaiah, A.M. Reinhorn and M.C. Constantinou, 2/28/91, (PB91-190553, A07, MF-A01). This report has been replaced by NCEER-93-0011.

NCEER-91-0006 "A Multidimensional Hysteretic Model for Plasticity Deforming Metals in Energy Absorbing Devices," by E.J. Graesser and F.A. Cozzarelli, 4/9/91, (PB92-108364, A04, MF-A01).

NCEER-91-0007 "A Framework for Customizable Knowledge-Based Expert Systems with an Application to a KBES for Evaluating the Seismic Resistance of Existing Buildings," by E.G. Ibarra-Anaya and S.J. Fenves, 4/9/91, (PB91-210930, A08, MF-A01).

NCEER-91-0008 "Nonlinear Analysis of Steel Frames with Semi-Rigid Connections Using the Capacity Spectrum Method," by G.G. Deierlein, S-H. Hsieh, Y-J. Shen and J.F. Abel, 7/2/91, (PB92-113828, A05, MF-A01).

NCEER-91-0009 "Earthquake Education Materials for Grades K-12," by K.E.K. Ross, 4/30/91, (PB91-212142, A06, MF-A01). This report has been replaced by NCEER-92-0018.

NCEER-91-0010 "Phase Wave Velocities and Displacement Phase Differences in a Harmonically Oscillating Pile," by N. Makris and G. Gazetas, 7/8/91, (PB92-108356, A04, MF-A01).

NCEER-91-0011 "Dynamic Characteristics of a Full-Size Five-Story Steel Structure and a 2/5 Scale Model," by K.C. Chang, G.C. Yao, G.C. Lee, D.S. Hao and Y.C. Yeh," 7/2/91, (PB93-116648, A06, MF-A02).

NCEER-91-0012 "Seismic Response of a 2/5 Scale Steel Structure with Added Viscoelastic Dampers," by K.C. Chang, T.T. Soong, S-T. Oh and M.L. Lai, 5/17/91, (PB92-110816, A05, MF-A01).

NCEER-91-0013 "Earthquake Response of Retaining Walls; Full-Scale Testing and Computational Modeling," by S. Alampalli and A-W.M. Elgamal, 6/20/91, to be published.

NCEER-91-0014 "3D-BASIS-M: Nonlinear Dynamic Analysis of Multiple Building Base Isolated Structures," by P.C. Tsopelas, S. Nagarajaiah, M.C. Constantinou and A.M. Reinhorn, 5/28/91, (PB92-113885, A09, MF-A02).

NCEER-91-0015 "Evaluation of SEAOC Design Requirements for Sliding Isolated Structures," by D. Theodossiou and M.C. Constantinou, 6/10/91, (PB92-114602, A11, MF-A03).

NCEER-91-0016 "Closed-Loop Modal Testing of a 27-Story Reinforced Concrete Flat Plate-Core Building," by H.R. Somaprasad, T. Toksoy, H. Yoshiyuki and A.E. Aktan, 7/15/91, (PB92-129980, A07, MF-A02).

NCEER-91-0017 "Shake Table Test of a 1/6 Scale Two-Story Lightly Reinforced Concrete Building," by A.G. El-Attar, R.N. White and P. Gergely, 2/28/91, (PB92-222447, A06, MF-A02).

NCEER-91-0018 "Shake Table Test of a 1/8 Scale Three-Story Lightly Reinforced Concrete Building," by A.G. El-Attar, R.N. White and P. Gergely, 2/28/91, (PB93-116630, A08, MF-A02).

NCEER-91-0019 "Transfer Functions for Rigid Rectangular Foundations," by A.S. Veletsos, A.M. Prasad and W.H. Wu, 7/31/91, to be published.

NCEER-91-0020 "Hybrid Control of Seismic-Excited Nonlinear and Inelastic Structural Systems," by J.N. Yang, Z. Li and A. Danielians, 8/1/91, (PB92-143171, A06, MF-A02).

NCEER-91-0021 "The NCEER-91 Earthquake Catalog: Improved Intensity-Based Magnitudes and Recurrence Relations for U.S. Earthquakes East of New Madrid," by L. Seeber and J.G. Armbruster, 8/28/91, (PB92-176742, A06, MF-A02).

NCEER-91-0022 "Proceedings from the Implementation of Earthquake Planning and Education in Schools: The Need for Change - The Roles of the Changemakers," by K.E.K. Ross and F. Winslow, 7/23/91, (PB92-129998, A12, MF-A03).

NCEER-91-0023 "A Study of Reliability-Based Criteria for Seismic Design of Reinforced Concrete Frame Buildings," by H.H.M. Hwang and H-M. Hsu, 8/10/91, (PB92-140235, A09, MF-A02).

NCEER-91-0024 "Experimental Verification of a Number of Structural System Identification Algorithms," by R.G. Ghanem, H. Gavin and M. Shinozuka, 9/18/91, (PB92-176577, A18, MF-A04).

NCEER-91-0025 "Probabilistic Evaluation of Liquefaction Potential," by H.H.M. Hwang and C.S. Lee," 11/25/91, (PB92-143429, A05, MF-A01).

NCEER-91-0026 "Instantaneous Optimal Control for Linear, Nonlinear and Hysteretic Structures - Stable Controllers," by J.N. Yang and Z. Li, 11/15/91, (PB92-163807, A04, MF-A01).

NCEER-91-0027 "Experimental and Theoretical Study of a Sliding Isolation System for Bridges," by M.C. Constantinou, A. Kartoum, A.M. Reinhorn and P. Bradford, 11/15/91, (PB92-176973, A10, MF-A03).

NCEER-92-0001 "Case Studies of Liquefaction and Lifeline Performance During Past Earthquakes, Volume 1: Japanese Case Studies," Edited by M. Hamada and T. O'Rourke, 2/17/92, (PB92-197243, A18, MF-A04).

NCEER-92-0002 "Case Studies of Liquefaction and Lifeline Performance During Past Earthquakes, Volume 2: United States Case Studies," Edited by T. O'Rourke and M. Hamada, 2/17/92, (PB92-197250, A20, MF-A04).

NCEER-92-0003 "Issues in Earthquake Education," Edited by K. Ross, 2/3/92, (PB92-222389, A07, MF-A02).

NCEER-92-0004 "Proceedings from the First U.S. - Japan Workshop on Earthquake Protective Systems for Bridges," Edited by I.G. Buckle, 2/4/92, (PB94-142239, A99, MF-A06).

NCEER-92-0005 "Seismic Ground Motion from a Haskell-Type Source in a Multiple-Layered Half-Space," A.P. Theoharis, G. Deodatis and M. Shinozuka, 1/2/92, to be published.

NCEER-92-0006 "Proceedings from the Site Effects Workshop," Edited by R. Whitman, 2/29/92, (PB92-197201, A04, MF-A01).

NCEER-92-0007 "Engineering Evaluation of Permanent Ground Deformations Due to Seismically-Induced Liquefaction," by M.H. Baziar, R. Dobry and A-W.M. Elgamal, 3/24/92, (PB92-222421, A13, MF-A03).

NCEER-92-0008 "A Procedure for the Seismic Evaluation of Buildings in the Central and Eastern United States," by C.D. Poland and J.O. Malley, 4/2/92, (PB92-222439, A20, MF-A04).

NCEER-92-0009 "Experimental and Analytical Study of a Hybrid Isolation System Using Friction Controllable Sliding Bearings," by M.Q. Feng, S. Fujii and M. Shinozuka, 5/15/92, (PB93-150282, A06, MF-A02).

NCEER-92-0010 "Seismic Resistance of Slab-Column Connections in Existing Non-Ductile Flat-Plate Buildings," by A.J. Durrani and Y. Du, 5/18/92, (PB93-116812, A06, MF-A02).

NCEER-92-0011 "The Hysteretic and Dynamic Behavior of Brick Masonry Walls Upgraded by Ferrocement Coatings Under Cyclic Loading and Strong Simulated Ground Motion," by H. Lee and S.P. Prawel, 5/11/92, to be published.

NCEER-92-0012 "Study of Wire Rope Systems for Seismic Protection of Equipment in Buildings," by G.F. Demetriades, M.C. Constantinou and A.M. Reinhorn, 5/20/92, (PB93-116655, A08, MF-A02).

NCEER-92-0013 "Shape Memory Structural Dampers: Material Properties, Design and Seismic Testing," by P.R. Witting and F.A. Cozzarelli, 5/26/92, (PB93-116663, A05, MF-A01).

NCEER-92-0014 "Longitudinal Permanent Ground Deformation Effects on Buried Continuous Pipelines," by M.J. O'Rourke, and C. Nordberg, 6/15/92, (PB93-116671, A08, MF-A02).

NCEER-92-0015 "A Simulation Method for Stationary Gaussian Random Functions Based on the Sampling Theorem," by M. Grigoriu and S. Balopoulou, 6/11/92, (PB93-127496, A05, MF-A01).

NCEER-92-0016 "Gravity-Load-Designed Reinforced Concrete Buildings: Seismic Evaluation of Existing Construction and Detailing Strategies for Improved Seismic Resistance," by G.W. Hoffmann, S.K. Kunnath, A.M. Reinhorn and J.B. Mander, 7/15/92, (PB94-142007, A08, MF-A02).

NCEER-92-0017 "Observations on Water System and Pipeline Performance in the Limón Area of Costa Rica Due to the April 22, 1991 Earthquake," by M. O'Rourke and D. Ballantyne, 6/30/92, (PB93-126811, A06, MF-A02).

NCEER-92-0018 "Fourth Edition of Earthquake Education Materials for Grades K-12," Edited by K.E.K. Ross, 8/10/92, (PB93-114023, A07, MF-A02).

NCEER-92-0019 "Proceedings from the Fourth Japan-U.S. Workshop on Earthquake Resistant Design of Lifeline Facilities and Countermeasures for Soil Liquefaction," Edited by M. Hamada and T.D. O'Rourke, 8/12/92, (PB93-163939, A99, MF-E11).

NCEER-92-0020 "Active Bracing System: A Full Scale Implementation of Active Control," by A.M. Reinhorn, T.T. Soong, R.C. Lin, M.A. Riley, Y.P. Wang, S. Aizawa and M. Higashino, 8/14/92, (PB93-127512, A06, MF-A02).

NCEER-92-0021 "Empirical Analysis of Horizontal Ground Displacement Generated by Liquefaction-Induced Lateral Spreads," by S.F. Bartlett and T.L. Youd, 8/17/92, (PB93-188241, A06, MF-A02).

NCEER-92-0022 "IDARC Version 3.0: Inelastic Damage Analysis of Reinforced Concrete Structures," by S.K. Kunnath, A.M. Reinhorn and R.F. Lobo, 8/31/92, (PB93-227502, A07, MF-A02).

NCEER-92-0023 "A Semi-Empirical Analysis of Strong-Motion Peaks in Terms of Seismic Source, Propagation Path and Local Site Conditions, by M. Kamiyama, M.J. O'Rourke and R. Flores-Berrones, 9/9/92, (PB93-150266, A08, MF-A02).

NCEER-92-0024 "Seismic Behavior of Reinforced Concrete Frame Structures with Nonductile Details, Part I: Summary of Experimental Findings of Full Scale Beam-Column Joint Tests," by A. Beres, R.N. White and P. Gergely, 9/30/92, (PB93-227783, A05, MF-A01).

NCEER-92-0025 "Experimental Results of Repaired and Retrofitted Beam-Column Joint Tests in Lightly Reinforced Concrete Frame Buildings," by A. Beres, S. El-Borgi, R.N. White and P. Gergely, 10/29/92, (PB93-227791, A05, MF-A01).

NCEER-92-0026 "A Generalization of Optimal Control Theory: Linear and Nonlinear Structures," by J.N. Yang, Z. Li and S. Vongchavalitkul, 11/2/92, (PB93-188621, A05, MF-A01).

NCEER-92-0027 "Seismic Resistance of Reinforced Concrete Frame Structures Designed Only for Gravity Loads: Part I - Design and Properties of a One-Third Scale Model Structure," by J.M. Bracci, A.M. Reinhorn and J.B. Mander, 12/1/92, (PB94-104502, A08, MF-A02).

NCEER-92-0028 "Seismic Resistance of Reinforced Concrete Frame Structures Designed Only for Gravity Loads: Part II - Experimental Performance of Subassemblages," by L.E. Aycardi, J.B. Mander and A.M. Reinhorn, 12/1/92, (PB94-104510, A08, MF-A02).

NCEER-92-0029 "Seismic Resistance of Reinforced Concrete Frame Structures Designed Only for Gravity Loads: Part III - Experimental Performance and Analytical Study of a Structural Model," by J.M. Bracci, A.M. Reinhorn and J.B. Mander, 12/1/92, (PB93-227528, A09, MF-A01).

NCEER-92-0030 "Evaluation of Seismic Retrofit of Reinforced Concrete Frame Structures: Part I - Experimental Performance of Retrofitted Subassemblages," by D. Choudhuri, J.B. Mander and A.M. Reinhorn, 12/8/92, (PB93-198307, A07, MF-A02).

NCEER-92-0031 "Evaluation of Seismic Retrofit of Reinforced Concrete Frame Structures: Part II - Experimental Performance and Analytical Study of a Retrofitted Structural Model," by J.M. Bracci, A.M. Reinhorn and J.B. Mander, 12/8/92, (PB93-198315, A09, MF-A03).

NCEER-92-0032 "Experimental and Analytical Investigation of Seismic Response of Structures with Supplemental Fluid Viscous Dampers," by M.C. Constantinou and M.D. Symans, 12/21/92, (PB93-191435, A10, MF-A03). This report is available only through NTIS (see address given above).

NCEER-92-0033 "Reconnaissance Report on the Cairo, Egypt Earthquake of October 12, 1992," by M. Khater, 12/23/92, (PB93-188621, A03, MF-A01).

NCEER-92-0034 "Low-Level Dynamic Characteristics of Four Tall Flat-Plate Buildings in New York City," by H. Gavin, S. Yuan, J. Grossman, E. Pekelis and K. Jacob, 12/28/92, (PB93-188217, A07, MF-A02).

NCEER-93-0001 "An Experimental Study on the Seismic Performance of Brick-Infilled Steel Frames With and Without Retrofit," by J.B. Mander, B. Nair, K. Wojtkowski and J. Ma, 1/29/93, (PB93-227510, A07, MF-A02).

NCEER-93-0002 "Social Accounting for Disaster Preparedness and Recovery Planning," by S. Cole, E. Pantoja and V. Razak, 2/22/93, (PB94-142114, A12, MF-A03).

NCEER-93-0003 "Assessment of 1991 NEHRP Provisions for Nonstructural Components and Recommended Revisions," by T.T. Soong, G. Chen, Z. Wu, R-H. Zhang and M. Grigoriu, 3/1/93, (PB93-188639, A06, MF-A02).

NCEER-93-0004 "Evaluation of Static and Response Spectrum Analysis Procedures of SEAOC/UBC for Seismic Isolated Structures," by C.W. Winters and M.C. Constantinou, 3/23/93, (PB93-198299, A10, MF-A03).

NCEER-93-0005 "Earthquakes in the Northeast - Are We Ignoring the Hazard? A Workshop on Earthquake Science and Safety for Educators," edited by K.E.K. Ross, 4/2/93, (PB94-103066, A09, MF-A02).

NCEER-93-0006 "Inelastic Response of Reinforced Concrete Structures with Viscoelastic Braces," by R.F. Lobo, J.M. Bracci, K.L. Shen, A.M. Reinhorn and T.T. Soong, 4/5/93, (PB93-227486, A05, MF-A02).

NCEER-93-0007 "Seismic Testing of Installation Methods for Computers and Data Processing Equipment," by K. Kosar, T.T. Soong, K.L. Shen, J.A. HoLung and Y.K. Lin, 4/12/93, (PB93-198299, A07, MF-A02).

NCEER-93-0008 "Retrofit of Reinforced Concrete Frames Using Added Dampers," by A. Reinhorn, M. Constantinou and C. Li, to be published.

NCEER-93-0009 "Seismic Behavior and Design Guidelines for Steel Frame Structures with Added Viscoelastic Dampers," by K.C. Chang, M.L. Lai, T.T. Soong, D.S. Hao and Y.C. Yeh, 5/1/93, (PB94-141959, A07, MF-A02).

NCEER-93-0010 "Seismic Performance of Shear-Critical Reinforced Concrete Bridge Piers," by J.B. Mander, S.M. Waheed, M.T.A. Chaudhary and S.S. Chen, 5/12/93, (PB93-227494, A08, MF-A02).

NCEER-93-0011 "3D-BASIS-TABS: Computer Program for Nonlinear Dynamic Analysis of Three Dimensional Base Isolated Structures," by S. Nagarajaiah, C. Li, A.M. Reinhorn and M.C. Constantinou, 8/2/93, (PB94-141819, A09, MF-A02).

NCEER-93-0012 "Effects of Hydrocarbon Spills from an Oil Pipeline Break on Ground Water," by O.J. Helweg and H.H.M. Hwang, 8/3/93, (PB94-141942, A06, MF-A02).

NCEER-93-0013 "Simplified Procedures for Seismic Design of Nonstructural Components and Assessment of Current Code Provisions," by M.P. Singh, L.E. Suarez, E.E. Matheu and G.O. Maldonado, 8/4/93, (PB94-141827, A09, MF-A02).

NCEER-93-0014 "An Energy Approach to Seismic Analysis and Design of Secondary Systems," by G. Chen and T.T. Soong, 8/6/93, (PB94-142767, A11, MF-A03).

NCEER-93-0015 "Proceedings from School Sites: Becoming Prepared for Earthquakes - Commemorating the Third Anniversary of the Loma Prieta Earthquake," Edited by F.E. Winslow and K.E.K. Ross, 8/16/93, (PB94-154275, A16, MF-A02).

NCEER-93-0016 "Reconnaissance Report of Damage to Historic Monuments in Cairo, Egypt Following the October 12, 1992 Dahshur Earthquake," by D. Sykora, D. Look, G. Croci, E. Karaesmen and E. Karaesmen, 8/19/93, (PB94-142221, A08, MF-A02).

NCEER-93-0017 "The Island of Guam Earthquake of August 8, 1993," by S.W. Swan and S.K. Harris, 9/30/93, (PB94-141843, A04, MF-A01).

NCEER-93-0018 "Engineering Aspects of the October 12, 1992 Egyptian Earthquake," by A.W. Elgamal, M. Amer, K. Adalier and A. Abul-Fadl, 10/7/93, (PB94-141983, A05, MF-A01).

NCEER-93-0019 "Development of an Earthquake Motion Simulator and its Application in Dynamic Centrifuge Testing," by I. Krstelj, Supervised by J.H. Prevost, 10/23/93, (PB94-181773, A-10, MF-A03).

NCEER-93-0020 "NCEER-Taisei Corporation Research Program on Sliding Seismic Isolation Systems for Bridges: Experimental and Analytical Study of a Friction Pendulum System (FPS)," by M.C. Constantinou, P. Tsopelas, Y-S. Kim and S. Okamoto, 11/1/93, (PB94-142775, A08, MF-A02).

NCEER-93-0021 "Finite Element Modeling of Elastomeric Seismic Isolation Bearings," by L.J. Billings, Supervised by R. Shepherd, 11/8/93, to be published.

NCEER-93-0022 "Seismic Vulnerability of Equipment in Critical Facilities: Life-Safety and Operational Consequences," by K. Porter, G.S. Johnson, M.M. Zadeh, C. Scawthorn and S. Eder, 11/24/93, (PB94-181765, A16, MF-A03).

NCEER-93-0023 "Hokkaido Nansei-oki, Japan Earthquake of July 12, 1993, by P.I. Yanev and C.R. Scawthorn, 12/23/93, (PB94-181500, A07, MF-A01).

NCEER-94-0001 "An Evaluation of Seismic Serviceability of Water Supply Networks with Application to the San Francisco Auxiliary Water Supply System," by I. Markov, Supervised by M. Grigoriu and T. O'Rourke, 1/21/94, (PB94-204013, A07, MF-A02).

NCEER-94-0002 "NCEER-Taisei Corporation Research Program on Sliding Seismic Isolation Systems for Bridges: Experimental and Analytical Study of Systems Consisting of Sliding Bearings, Rubber Restoring Force Devices and Fluid Dampers," Volumes I and II, by P. Tsopelas, S. Okamoto, M.C. Constantinou, D. Ozaki and S. Fujii, 2/4/94, (PB94-181740, A09, MF-A02 and PB94-181757, A12, MF-A03).

NCEER-94-0003 "A Markov Model for Local and Global Damage Indices in Seismic Analysis," by S. Rahman and M. Grigoriu, 2/18/94, (PB94-206000, A12, MF-A03).

NCEER-94-0004 "Proceedings from the NCEER Workshop on Seismic Response of Masonry Infills," edited by D.P. Abrams, 3/1/94, (PB94-180783, A07, MF-A02).

NCEER-94-0005 "The Northridge, California Earthquake of January 17, 1994: General Reconnaissance Report," edited by J.D. Goltz, 3/11/94, (PB94-193943, A10, MF-A03).

NCEER-94-0006 "Seismic Energy Based Fatigue Damage Analysis of Bridge Columns: Part I - Evaluation of Seismic Capacity," by G.A. Chang and J.B. Mander, 3/14/94, (PB94-219185, A11, MF-A03).

NCEER-94-0007 "Seismic Isolation of Multi-Story Frame Structures Using Spherical Sliding Isolation Systems," by T.M. Al-Hussaini, V.A. Zayas and M.C. Constantinou, 3/17/94, (PB94-193745, A09, MF-A02).

NCEER-94-0008 "The Northridge, California Earthquake of January 17, 1994: Performance of Highway Bridges," edited by I.G. Buckle, 3/24/94, (PB94-193851, A06, MF-A02).

NCEER-94-0009 "Proceedings of the Third U.S.-Japan Workshop on Earthquake Protective Systems for Bridges," edited by I.G. Buckle and I. Friedland, 3/31/94, (PB94-195815, A99, MF-A06).

NCEER-94-0010 "3D-BASIS-ME: Computer Program for Nonlinear Dynamic Analysis of Seismically Isolated Single and Multiple Structures and Liquid Storage Tanks," by P.C. Tsopelas, M.C. Constantinou and A.M. Reinhorn, 4/12/94, (PB94-204922, A09, MF-A02).

NCEER-94-0011 "The Northridge, California Earthquake of January 17, 1994: Performance of Gas Transmission Pipelines," by T.D. O'Rourke and M.C. Palmer, 5/16/94, (PB94-204989, A05, MF-A01).

NCEER-94-0012 "Feasibility Study of Replacement Procedures and Earthquake Performance Related to Gas Transmission Pipelines," by T.D. O'Rourke and M.C. Palmer, 5/25/94, (PB94-206638, A09, MF-A02).

NCEER-94-0013 "Seismic Energy Based Fatigue Damage Analysis of Bridge Columns: Part II - Evaluation of Seismic Demand," by G.A. Chang and J.B. Mander, 6/1/94, (PB95-18106, A08, MF-A02).

NCEER-94-0014 "NCEER-Taisei Corporation Research Program on Sliding Seismic Isolation Systems for Bridges: Experimental and Analytical Study of a System Consisting of Sliding Bearings and Fluid Restoring Force/Damping Devices," by P. Tsopelas and M.C. Constantinou, 6/13/94, (PB94-219144, A10, MF-A03).

NCEER-94-0015 "Generation of Hazard-Consistent Fragility Curves for Seismic Loss Estimation Studies," by H. Hwang and J-R. Huo, 6/14/94, (PB95-181996, A09, MF-A02).

NCEER-94-0016 "Seismic Study of Building Frames with Added Energy-Absorbing Devices," by W.S. Pong, C.S. Tsai and G.C. Lee, 6/20/94, (PB94-219136, A10, A03).

NCEER-94-0017 "Sliding Mode Control for Seismic-Excited Linear and Nonlinear Civil Engineering Structures," by J. Yang, J. Wu, A. Agrawal and Z. Li, 6/21/94, (PB95-138483, A06, MF-A02).

NCEER-94-0018 "3D-BASIS-TABS Version 2.0: Computer Program for Nonlinear Dynamic Analysis of Three Dimensional Base Isolated Structures," by A.M. Reinhorn, S. Nagarajaiah, M.C. Constantinou, P. Tsopelas and R. Li, 6/22/94, (PB95-182176, A08, MF-A02).

NCEER-94-0019 "Proceedings of the International Workshop on Civil Infrastructure Systems: Application of Intelligent Systems and Advanced Materials on Bridge Systems," Edited by G.C. Lee and K.C. Chang, 7/18/94, (PB95-252474, A20, MF-A04).

NCEER-94-0020 "Study of Seismic Isolation Systems for Computer Floors," by V. Lambrou and M.C. Constantinou, 7/19/94, (PB95-138533, A10, MF-A03).

NCEER-94-0021 "Proceedings of the U.S.-Italian Workshop on Guidelines for Seismic Evaluation and Rehabilitation of Unreinforced Masonry Buildings," Edited by D.P. Abrams and G.M. Calvi, 7/20/94, (PB95-138749, A13, MF-A03).

NCEER-94-0022 "NCEER-Taisei Corporation Research Program on Sliding Seismic Isolation Systems for Bridges: Experimental and Analytical Study of a System Consisting of Lubricated PTFE Sliding Bearings and Mild Steel Dampers," by P. Tsopelas and M.C. Constantinou, 7/22/94, (PB95-182184, A08, MF-A02).

NCEER-94-0023 "Development of Reliability-Based Design Criteria for Buildings Under Seismic Load," by Y.K. Wen, H. Hwang and M. Shinozuka, 8/1/94, (PB95-211934, A08, MF-A02).

NCEER-94-0024 "Experimental Verification of Acceleration Feedback Control Strategies for an Active Tendon System," by S.J. Dyke, B.F. Spencer, Jr., P. Quast, M.K. Sain, D.C. Kaspari, Jr. and T.T. Soong, 8/29/94, (PB95-212320, A05, MF-A01).

NCEER-94-0025 "Seismic Retrofitting Manual for Highway Bridges," Edited by I.G. Buckle and I.F. Friedland, published by the Federal Highway Administration (PB95-212676, A15, MF-A03).

NCEER-94-0026 "Proceedings from the Fifth U.S.-Japan Workshop on Earthquake Resistant Design of Lifeline Facilities and Countermeasures Against Soil Liquefaction," Edited by T.D. O'Rourke and M. Hamada, 11/7/94, (PB95-220802, A99, MF-E08).

NCEER-95-0001 "Experimental and Analytical Investigation of Seismic Retrofit of Structures with Supplemental Damping: Part 1 - Fluid Viscous Damping Devices," by A.M. Reinhorn, C. Li and M.C. Constantinou, 1/3/95, (PB95-266599, A09, MF-A02).

NCEER-95-0002 "Experimental and Analytical Study of Low-Cycle Fatigue Behavior of Semi-Rigid Top-And-Seat Angle Connections," by G. Pekcan, J.B. Mander and S.S. Chen, 1/5/95, (PB95-220042, A07, MF-A02).

NCEER-95-0003 "NCEER-ATC Joint Study on Fragility of Buildings," by T. Anagnos, C. Rojahn and A.S. Kiremidjian, 1/20/95, (PB95-220026, A06, MF-A02).

NCEER-95-0004 "Nonlinear Control Algorithms for Peak Response Reduction," by Z. Wu, T.T. Soong, V. Gattulli and R.C. Lin, 2/16/95, (PB95-220349, A05, MF-A01).

NCEER-95-0005 "Pipeline Replacement Feasibility Study: A Methodology for Minimizing Seismic and Corrosion Risks to Underground Natural Gas Pipelines," by R.T. Eguchi, H.A. Seligson and D.G. Honegger, 3/2/95, (PB95-252326, A06, MF-A02).

NCEER-95-0006 "Evaluation of Seismic Performance of an 11-Story Frame Building During the 1994 Northridge Earthquake," by F. Naeim, R. DiSulio, K. Benuska, A. Reinhorn and C. Li, to be published.

NCEER-95-0007 "Prioritization of Bridges for Seismic Retrofitting," by N. Basöz and A.S. Kiremidjian, 4/24/95, (PB95-252300, A08, MF-A02).

NCEER-95-0008 "Method for Developing Motion Damage Relationships for Reinforced Concrete Frames," by A. Singhal and A.S. Kiremidjian, 5/11/95, (PB95-266607, A06, MF-A02).

NCEER-95-0009 "Experimental and Analytical Investigation of Seismic Retrofit of Structures with Supplemental Damping: Part II - Friction Devices," by C. Li and A.M. Reinhorn, 7/6/95, (PB96-128087, A11, MF-A03).

NCEER-95-0010 "Experimental Performance and Analytical Study of a Non-Ductile Reinforced Concrete Frame Structure Retrofitted with Elastomeric Spring Dampers," by G. Pekcan, J.B. Mander and S.S. Chen, 7/14/95, (PB96-137161, A08, MF-A02).

NCEER-95-0011 "Development and Experimental Study of Semi-Active Fluid Damping Devices for Seismic Protection of Structures," by M.D. Symans and M.C. Constantinou, 8/3/95, (PB96-136940, A23, MF-A04).

NCEER-95-0012 "Real-Time Structural Parameter Modification (RSPM): Development of Innervated Structures," by Z. Liang, M. Tong and G.C. Lee, 4/11/95, (PB96-137153, A06, MF-A01).

NCEER-95-0013 "Experimental and Analytical Investigation of Seismic Retrofit of Structures with Supplemental Damping: Part III - Viscous Damping Walls," by A.M. Reinhorn and C. Li, 10/1/95, (PB96-176409, A11, MF-A03).

NCEER-95-0014 "Seismic Fragility Analysis of Equipment and Structures in a Memphis Electric Substation," by J-R. Huo and H.H.M. Hwang, 8/10/95, (PB96-128087, A09, MF-A02).

NCEER-95-0015 "The Hanshin-Awaji Earthquake of January 17, 1995: Performance of Lifelines," Edited by M. Shinozuka, 11/3/95, (PB96-176383, A15, MF-A03).

NCEER-95-0016 "Highway Culvert Performance During Earthquakes," by T.L. Youd and C.J. Beckman, available as NCEER-96-0015.

NCEER-95-0017 "The Hanshin-Awaji Earthquake of January 17, 1995: Performance of Highway Bridges," Edited by I.G. Buckle, 12/1/95, to be published.

NCEER-95-0018 "Modeling of Masonry Infill Panels for Structural Analysis," by A.M. Reinhorn, A. Madan, R.E. Valles, Y. Reichmann and J.B. Mander, 12/8/95, (PB97-110886, MF-A01, A06).

NCEER-95-0019 "Optimal Polynomial Control for Linear and Nonlinear Structures," by A.K. Agrawal and J.N. Yang, 12/11/95, (PB96-168737, A07, MF-A02).

NCEER-95-0020 "Retrofit of Non-Ductile Reinforced Concrete Frames Using Friction Dampers," by R.S. Rao, P. Gergely and R.N. White, 12/22/95, (PB97-133508, A10, MF-A02).

NCEER-95-0021 "Parametric Results for Seismic Response of Pile-Supported Bridge Bents," by G. Mylonakis, A. Nikolaou and G. Gazetas, 12/22/95, (PB97-100242, A12, MF-A03).

NCEER-95-0022 "Kinematic Bending Moments in Seismically Stressed Piles," by A. Nikolaou, G. Mylonakis and G. Gazetas, 12/23/95, (PB97-113914, MF-A03, A13).

NCEER-96-0001 "Dynamic Response of Unreinforced Masonry Buildings with Flexible Diaphragms," by A.C. Costley and D.P. Abrams," 10/10/96, (PB97-133573, MF-A03, A15).

NCEER-96-0002 "State of the Art Review: Foundations and Retaining Structures," by I. Po Lam, to be published.

NCEER-96-0003 "Ductility of Rectangular Reinforced Concrete Bridge Columns with Moderate Confinement," by N. Wehbe, M. Saiidi, D. Sanders and B. Douglas, 11/7/96, (PB97-133557, A06, MF-A02).

NCEER-96-0004 "Proceedings of the Long-Span Bridge Seismic Research Workshop," edited by I.G. Buckle and I.M. Friedland, to be published.

NCEER-96-0005 "Establish Representative Pier Types for Comprehensive Study: Eastern United States," by J. Kulicki and Z. Prucz, 5/28/96, (PB98-119217, A07, MF-A02).

NCEER-96-0006 "Establish Representative Pier Types for Comprehensive Study: Western United States," by R. Imbsen, R.A. Schamber and T.A. Osterkamp, 5/28/96, (PB98-118607, A07, MF-A02).

NCEER-96-0007 "Nonlinear Control Techniques for Dynamical Systems with Uncertain Parameters," by R.G. Ghanem and M.I. Bujakov, 5/27/96, (PB97-100259, A17, MF-A03).

NCEER-96-0008 "Seismic Evaluation of a 30-Year Old Non-Ductile Highway Bridge Pier and Its Retrofit," by J.B. Mander, B. Mahmoodzadegan, S. Bhadra and S.S. Chen, 5/31/96, (PB97-110902, MF-A03, A10).

NCEER-96-0009 "Seismic Performance of a Model Reinforced Concrete Bridge Pier Before and After Retrofit," by J.B. Mander, J.H. Kim and C.A. Ligozio, 5/31/96, (PB97-110910, MF-A02, A10).

NCEER-96-0010 "IDARC2D Version 4.0: A Computer Program for the Inelastic Damage Analysis of Buildings," by R.E. Valles, A.M. Reinhorn, S.K. Kunnath, C. Li and A. Madan, 6/3/96, (PB97-100234, A17, MF-A03).

NCEER-96-0011 "Estimation of the Economic Impact of Multiple Lifeline Disruption: Memphis Light, Gas and Water Division Case Study," by S.E. Chang, H.A. Seligson and R.T. Eguchi, 8/16/96, (PB97-133490, A11, MF-A03).

NCEER-96-0012 "Proceedings from the Sixth Japan-U.S. Workshop on Earthquake Resistant Design of Lifeline Facilities and Countermeasures Against Soil Liquefaction, Edited by M. Hamada and T. O'Rourke, 9/11/96, (PB97-133581, A99, MF-A06).

NCEER-96-0013 "Chemical Hazards, Mitigation and Preparedness in Areas of High Seismic Risk: A Methodology for Estimating the Risk of Post-Earthquake Hazardous Materials Release," by H.A. Seligson, R.T. Eguchi, K.J. Tierney and K. Richmond, 11/7/96, (PB97-133565, MF-A02, A08).

NCEER-96-0014 "Response of Steel Bridge Bearings to Reversed Cyclic Loading," by J.B. Mander, D-K. Kim, S.S. Chen and G.J. Premus, 11/13/96, (PB97-140735, A12, MF-A03).

NCEER-96-0015 "Highway Culvert Performance During Past Earthquakes," by T.L. Youd and C.J. Beckman, 11/25/96, (PB97-133532, A06, MF-A01).

NCEER-97-0001 "Evaluation, Prevention and Mitigation of Pounding Effects in Building Structures," by R.E. Valles and A.M. Reinhorn, 2/20/97, (PB97-159552, A14, MF-A03).

NCEER-97-0002 "Seismic Design Criteria for Bridges and Other Highway Structures," by C. Rojahn, R. Mayes, D.G. Anderson, J. Clark, J.H. Hom, R.V. Nutt and M.J. O'Rourke, 4/30/97, (PB97-194658, A06, MF-A03).

NCEER-97-0003 “Proceedings of the U.S.-Italian Workshop on Seismic Evaluation and Retrofit,” Edited by D.P. Abrams and G.M. Calvi, 3/19/97, (PB97-194666, A13, MF-A03).

NCEER-97-0004 "Investigation of Seismic Response of Buildings with Linear and Nonlinear Fluid Viscous Dampers," by A.A. Seleemah and M.C. Constantinou, 5/21/97, (PB98-109002, A15, MF-A03).

NCEER-97-0005 "Proceedings of the Workshop on Earthquake Engineering Frontiers in Transportation Facilities," edited by G.C. Lee and I.M. Friedland, 8/29/97, (PB98-128911, A25, MR-A04).

NCEER-97-0006 "Cumulative Seismic Damage of Reinforced Concrete Bridge Piers," by S.K. Kunnath, A. El-Bahy, A. Taylor and W. Stone, 9/2/97, (PB98-108814, A11, MF-A03).

NCEER-97-0007 "Structural Details to Accommodate Seismic Movements of Highway Bridges and Retaining Walls," by R.A. Imbsen, R.A. Schamber, E. Thorkildsen, A. Kartoum, B.T. Martin, T.N. Rosser and J.M. Kulicki, 9/3/97, (PB98-108996, A09, MF-A02).

NCEER-97-0008 "A Method for Earthquake Motion-Damage Relationships with Application to Reinforced Concrete Frames," by A. Singhal and A.S. Kiremidjian, 9/10/97, (PB98-108988, A13, MF-A03).

NCEER-97-0009 "Seismic Analysis and Design of Bridge Abutments Considering Sliding and Rotation," by K. Fishman and R. Richards, Jr., 9/15/97, (PB98-108897, A06, MF-A02).

NCEER-97-0010 "Proceedings of the FHWA/NCEER Workshop on the National Representation of Seismic Ground Motion for New and Existing Highway Facilities," edited by I.M. Friedland, M.S. Power and R.L. Mayes, 9/22/97, (PB98-128903, A21, MF-A04).

NCEER-97-0011 "Seismic Analysis for Design or Retrofit of Gravity Bridge Abutments," by K.L. Fishman, R. Richards, Jr. and R.C. Divito, 10/2/97, (PB98-128937, A08, MF-A02).

NCEER-97-0012 "Evaluation of Simplified Methods of Analysis for Yielding Structures," by P. Tsopelas, M.C. Constantinou, C.A. Kircher and A.S. Whittaker, 10/31/97, (PB98-128929, A10, MF-A03).

NCEER-97-0013 "Seismic Design of Bridge Columns Based on Control and Repairability of Damage," by C-T. Cheng and J.B. Mander, 12/8/97, (PB98-144249, A11, MF-A03).

NCEER-97-0014 "Seismic Resistance of Bridge Piers Based on Damage Avoidance Design," by J.B. Mander and C-T. Cheng, 12/10/97, (PB98-144223, A09, MF-A02).

NCEER-97-0015 “Seismic Response of Nominally Symmetric Systems with Strength Uncertainty,” by S. Balopoulou and M. Grigoriu, 12/23/97, (PB98-153422, A11, MF-A03).

NCEER-97-0016 “Evaluation of Seismic Retrofit Methods for Reinforced Concrete Bridge Columns,” by T.J. Wipf, F.W. Klaiber and F.M. Russo, 12/28/97, (PB98-144215, A12, MF-A03).

NCEER-97-0017 “Seismic Fragility of Existing Conventional Reinforced Concrete Highway Bridges,” by C.L. Mullen and A.S. Cakmak, 12/30/97, (PB98-153406, A08, MF-A02).

NCEER-97-0018 “Loss Asssessment of Memphis Buildings,” edited by D.P. Abrams and M. Shinozuka, 12/31/97, (PB98-144231, A13, MF-A03).

NCEER-97-0019 “Seismic Evaluation of Frames with Infill Walls Using Quasi-static Experiments,” by K.M. Mosalam, R.N. White and P. Gergely, 12/31/97, (PB98-153455, A07, MF-A02).

NCEER-97-0020 “Seismic Evaluation of Frames with Infill Walls Using Pseudo-dynamic Experiments,” by K.M. Mosalam, R.N. White and P. Gergely, 12/31/97, (PB98-153430, A07, MF-A02).

NCEER-97-0021 “Computational Strategies for Frames with Infill Walls: Discrete and Smeared Crack Analyses and Seismic Fragility,” by K.M. Mosalam, R.N. White and P. Gergely, 12/31/97, (PB98-153414, A10, MF-A02).

NCEER-97-0022 "Proceedings of the NCEER Workshop on Evaluation of Liquefaction Resistance of Soils," edited by T.L. Youd and I.M. Idriss, 12/31/97, (PB98-155617, A15, MF-A03).

MCEER-98-0001 "Extraction of Nonlinear Hysteretic Properties of Seismically Isolated Bridges from Quick-Release Field Tests," by Q. Chen, B.M. Douglas, E.M. Maragakis and I.G. Buckle, 5/26/98, (PB99-118838, A06, MF-A01).

MCEER-98-0002 "Methodologies for Evaluating the Importance of Highway Bridges," by A. Thomas, S. Eshenaur and J. Kulicki, 5/29/98, (PB99-118846, A10, MF-A02).

MCEER-98-0003 "Capacity Design of Bridge Piers and the Analysis of Overstrength," by J.B. Mander, A. Dutta and P. Goel, 6/1/98, (PB99-118853, A09, MF-A02).

MCEER-98-0004 "Evaluation of Bridge Damage Data from the Loma Prieta and Northridge, California Earthquakes," by N. Basoz and A. Kiremidjian, 6/2/98, (PB99-118861, A15, MF-A03).

MCEER-98-0005 "Screening Guide for Rapid Assessment of Liquefaction Hazard at Highway Bridge Sites," by T. L. Youd, 6/16/98, (PB99-118879, A06, not available on microfiche).

MCEER-98-0006 "Structural Steel and Steel/Concrete Interface Details for Bridges," by P. Ritchie, N. Kauhl and J. Kulicki, 7/13/98, (PB99-118945, A06, MF-A01).

MCEER-98-0007 "Capacity Design and Fatigue Analysis of Confined Concrete Columns," by A. Dutta and J.B. Mander, 7/14/98, (PB99-118960, A14, MF-A03).

MCEER-98-0008 "Proceedings of the Workshop on Performance Criteria for Telecommunication Services Under Earthquake Conditions," edited by A.J. Schiff, 7/15/98, (PB99-118952, A08, MF-A02).

MCEER-98-0009 "Fatigue Analysis of Unconfined Concrete Columns," by J.B. Mander, A. Dutta and J.H. Kim, 9/12/98, (PB99-123655, A10, MF-A02).

MCEER-98-0010 "Centrifuge Modeling of Cyclic Lateral Response of Pile-Cap Systems and Seat-Type Abutments in Dry Sands," by A.D. Gadre and R. Dobry, 10/2/98, (PB99-123606, A13, MF-A03).

MCEER-98-0011 "IDARC-BRIDGE: A Computational Platform for Seismic Damage Assessment of Bridge Structures," by A.M. Reinhorn, V. Simeonov, G. Mylonakis and Y. Reichman, 10/2/98, (PB99-162919, A15, MF-A03).

MCEER-98-0012 "Experimental Investigation of the Dynamic Response of Two Bridges Before and After Retrofitting with Elastomeric Bearings," by D.A. Wendichansky, S.S. Chen and J.B. Mander, 10/2/98, (PB99-162927, A15, MF-A03).

MCEER-98-0013 "Design Procedures for Hinge Restrainers and Hinge Sear Width for Multiple-Frame Bridges," by R. Des Roches and G.L. Fenves, 11/3/98, (PB99-140477, A13, MF-A03).

MCEER-98-0014 "Response Modification Factors for Seismically Isolated Bridges," by M.C. Constantinou and J.K. Quarshie, 11/3/98, (PB99-140485, A14, MF-A03).

MCEER-98-0015 "Proceedings of the U.S.-Italy Workshop on Seismic Protective Systems for Bridges," edited by I.M. Friedland and M.C. Constantinou, 11/3/98, (PB2000-101711, A22, MF-A04).

MCEER-98-0016 "Appropriate Seismic Reliability for Critical Equipment Systems: Recommendations Based on Regional Analysis of Financial and Life Loss," by K. Porter, C. Scawthorn, C. Taylor and N. Blais, 11/10/98, (PB99-157265, A08, MF-A02).

MCEER-98-0017 "Proceedings of the U.S. Japan Joint Seminar on Civil Infrastructure Systems Research," edited by M. Shinozuka and A. Rose, 11/12/98, (PB99-156713, A16, MF-A03).

MCEER-98-0018 "Modeling of Pile Footings and Drilled Shafts for Seismic Design," by I. PoLam, M. Kapuskar and D. Chaudhuri, 12/21/98, (PB99-157257, A09, MF-A02).

MCEER-99-0001 "Seismic Evaluation of a Masonry Infilled Reinforced Concrete Frame by Pseudodynamic Testing," by S.G. Buonopane and R.N. White, 2/16/99, (PB99-162851, A09, MF-A02).

MCEER-99-0002 "Response History Analysis of Structures with Seismic Isolation and Energy Dissipation Systems: Verification Examples for Program SAP2000," by J. Scheller and M.C. Constantinou, 2/22/99, (PB99-162869, A08, MF-A02).

MCEER-99-0003 "Experimental Study on the Seismic Design and Retrofit of Bridge Columns Including Axial Load Effects," by A. Dutta, T. Kokorina and J.B. Mander, 2/22/99, (PB99-162877, A09, MF-A02).

MCEER-99-0004 "Experimental Study of Bridge Elastomeric and Other Isolation and Energy Dissipation Systems with Emphasis on Uplift Prevention and High Velocity Near-source Seismic Excitation," by A. Kasalanati and M. C. Constantinou, 2/26/99, (PB99-162885, A12, MF-A03).

MCEER-99-0005 "Truss Modeling of Reinforced Concrete Shear-flexure Behavior," by J.H. Kim and J.B. Mander, 3/8/99, (PB99-163693, A12, MF-A03).

MCEER-99-0006 "Experimental Investigation and Computational Modeling of Seismic Response of a 1:4 Scale Model Steel Structure with a Load Balancing Supplemental Damping System," by G. Pekcan, J.B. Mander and S.S. Chen, 4/2/99, (PB99-162893, A11, MF-A03).

MCEER-99-0007 "Effect of Vertical Ground Motions on the Structural Response of Highway Bridges," by M.R. Button, C.J. Cronin and R.L. Mayes, 4/10/99, (PB2000-101411, A10, MF-A03).

MCEER-99-0008 "Seismic Reliability Assessment of Critical Facilities: A Handbook, Supporting Documentation, and Model Code Provisions," by G.S. Johnson, R.E. Sheppard, M.D. Quilici, S.J. Eder and C.R. Scawthorn, 4/12/99, (PB2000-101701, A18, MF-A04).

MCEER-99-0009 "Impact Assessment of Selected MCEER Highway Project Research on the Seismic Design of Highway Structures," by C. Rojahn, R. Mayes, D.G. Anderson, J.H. Clark, D'Appolonia Engineering, S. Gloyd and R.V. Nutt, 4/14/99, (PB99-162901, A10, MF-A02).

MCEER-99-0010 "Site Factors and Site Categories in Seismic Codes," by R. Dobry, R. Ramos and M.S. Power, 7/19/99, (PB2000-101705, A08, MF-A02).

MCEER-99-0011 "Restrainer Design Procedures for Multi-Span Simply-Supported Bridges," by M.J. Randall, M. Saiidi, E. Maragakis and T. Isakovic, 7/20/99, (PB2000-101702, A10, MF-A02).

MCEER-99-0012 "Property Modification Factors for Seismic Isolation Bearings," by M.C. Constantinou, P. Tsopelas, A. Kasalanati and E. Wolff, 7/20/99, (PB2000-103387, A11, MF-A03).

MCEER-99-0013 "Critical Seismic Issues for Existing Steel Bridges," by P. Ritchie, N. Kauhl and J. Kulicki, 7/20/99, (PB2000-101697, A09, MF-A02).

MCEER-99-0014 "Nonstructural Damage Database," by A. Kao, T.T. Soong and A. Vender, 7/24/99, (PB2000-101407, A06, MF-A01).

MCEER-99-0015 "Guide to Remedial Measures for Liquefaction Mitigation at Existing Highway Bridge Sites," by H.G. Cooke and J. K. Mitchell, 7/26/99, (PB2000-101703, A11, MF-A03).

MCEER-99-0016 "Proceedings of the MCEER Workshop on Ground Motion Methodologies for the Eastern United States," edited by N. Abrahamson and A. Becker, 8/11/99, (PB2000-103385, A07, MF-A02).

MCEER-99-0017 "Quindío, Colombia Earthquake of January 25, 1999: Reconnaissance Report," by A.P. Asfura and P.J. Flores, 10/4/99, (PB2000-106893, A06, MF-A01).

MCEER-99-0018 "Hysteretic Models for Cyclic Behavior of Deteriorating Inelastic Structures," by M.V. Sivaselvan and A.M. Reinhorn, 11/5/99, (PB2000-103386, A08, MF-A02).

MCEER-99-0019 "Proceedings of the 7th U.S.- Japan Workshop on Earthquake Resistant Design of Lifeline Facilities and Countermeasures Against Soil Liquefaction," edited by T.D. O'Rourke, J.P. Bardet and M. Hamada, 11/19/99, (PB2000-103354, A99, MF-A06).

MCEER-99-0020 "Development of Measurement Capability for Micro-Vibration Evaluations with Application to Chip Fabrication Facilities," by G.C. Lee, Z. Liang, J.W. Song, J.D. Shen and W.C. Liu, 12/1/99, (PB2000-105993, A08, MF-A02).

MCEER-99-0021 "Design and Retrofit Methodology for Building Structures with Supplemental Energy Dissipating Systems," by G. Pekcan, J.B. Mander and S.S. Chen, 12/31/99, (PB2000-105994, A11, MF-A03).

MCEER-00-0001 "The Marmara, Turkey Earthquake of August 17, 1999: Reconnaissance Report," edited by C. Scawthorn; with major contributions by M. Bruneau, R. Eguchi, T. Holzer, G. Johnson, J. Mander, J. Mitchell, W. Mitchell, A. Papageorgiou, C. Scaethorn, and G. Webb, 3/23/00, (PB2000-106200, A11, MF-A03).

MCEER-00-0002 "Proceedings of the MCEER Workshop for Seismic Hazard Mitigation of Health Care Facilities," edited by G.C. Lee, M. Ettouney, M. Grigoriu, J. Hauer and J. Nigg, 3/29/00, (PB2000-106892, A08, MF-A02).

MCEER-00-0003 "The Chi-Chi, Taiwan Earthquake of September 21, 1999: Reconnaissance Report," edited by G.C. Lee and C.H. Loh, with major contributions by G.C. Lee, M. Bruneau, I.G. Buckle, S.E. Chang, P.J. Flores, T.D. O'Rourke, M. Shinozuka, T.T. Soong, C-H. Loh, K-C. Chang, Z-J. Chen, J-S. Hwang, M-L. Lin, G-Y. Liu, K-C. Tsai, G.C. Yao and C-L. Yen, 4/30/00, (PB2001-100980, A10, MF-A02).

MCEER-00-0004 "Seismic Retrofit of End-Sway Frames of Steel Deck-Truss Bridges with a Supplemental Tendon System: Experimental and Analytical Investigation," by G. Pekcan, J.B. Mander and S.S. Chen, 7/1/00, (PB2001-100982, A10, MF-A02).

MCEER-00-0005 "Sliding Fragility of Unrestrained Equipment in Critical Facilities," by W.H. Chong and T.T. Soong, 7/5/00, (PB2001-100983, A08, MF-A02).

MCEER-00-0006 "Seismic Response of Reinforced Concrete Bridge Pier Walls in the Weak Direction," by N. Abo-Shadi, M. Saiidi and D. Sanders, 7/17/00, (PB2001-100981, A17, MF-A03).

MCEER-00-0007 "Low-Cycle Fatigue Behavior of Longitudinal Reinforcement in Reinforced Concrete Bridge Columns," by J. Brown and S.K. Kunnath, 7/23/00, (PB2001-104392, A08, MF-A02).

MCEER-00-0008 "Soil Structure Interaction of Bridges for Seismic Analysis," I. PoLam and H. Law, 9/25/00, (PB2001-105397, A08, MF-A02).

MCEER-00-0009 "Proceedings of the First MCEER Workshop on Mitigation of Earthquake Disaster by Advanced Technologies (MEDAT-1), edited by M. Shinozuka, D.J. Inman and T.D. O'Rourke, 11/10/00, (PB2001-105399, A14, MF-A03).

MCEER-00-0010 "Development and Evaluation of Simplified Procedures for Analysis and Design of Buildings with Passive Energy Dissipation Systems, Revision 01," by O.M. Ramirez, M.C. Constantinou, C.A. Kircher, A.S. Whittaker, M.W. Johnson, J.D. Gomez and C. Chrysostomou, 11/16/01, (PB2001-105523, A23, MF-A04).

MCEER-00-0011 "Dynamic Soil-Foundation-Structure Interaction Analyses of Large Caissons," by C-Y. Chang, C-M. Mok, Z-L. Wang, R. Settgast, F. Waggoner, M.A. Ketchum, H.M. Gonnermann and C-C. Chin, 12/30/00, (PB2001-104373, A07, MF-A02).

MCEER-00-0012 "Experimental Evaluation of Seismic Performance of Bridge Restrainers," by A.G. Vlassis, E.M. Maragakis and M. Saiid Saiidi, 12/30/00, (PB2001-104354, A09, MF-A02).

MCEER-00-0013 "Effect of Spatial Variation of Ground Motion on Highway Structures," by M. Shinozuka, V. Saxena and G. Deodatis, 12/31/00, (PB2001-108755, A13, MF-A03).

MCEER-00-0014 "A Risk-Based Methodology for Assessing the Seismic Performance of Highway Systems," by S.D. Werner, C.E. Taylor, J.E. Moore, II, J.S. Walton and S. Cho, 12/31/00, (PB2001-108756, A14, MF-A03).

MCEER-01-0001 "Experimental Investigation of P-Delta Effects to Collapse During Earthquakes," by D. Vian and M. Bruneau, 6/25/01, (PB2002-100534, A17, MF-A03).

MCEER-01-0002 "Proceedings of the Second MCEER Workshop on Mitigation of Earthquake Disaster by Advanced Technologies (MEDAT-2)," edited by M. Bruneau and D.J. Inman, 7/23/01, (PB2002-100434, A16, MF-A03).

MCEER-01-0003 "Sensitivity Analysis of Dynamic Systems Subjected to Seismic Loads," by C. Roth and M. Grigoriu, 9/18/01, (PB2003-100884, A12, MF-A03).

MCEER-01-0004 "Overcoming Obstacles to Implementing Earthquake Hazard Mitigation Policies: Stage 1 Report," by D.J. Alesch and W.J. Petak, 12/17/01, (PB2002-107949, A07, MF-A02).

MCEER-01-0005 "Updating Real-Time Earthquake Loss Estimates: Methods, Problems and Insights," by C.E. Taylor, S.E. Chang and R.T. Eguchi, 12/17/01, (PB2002-107948, A05, MF-A01).

MCEER-01-0006 "Experimental Investigation and Retrofit of Steel Pile Foundations and Pile Bents Under Cyclic Lateral Loadings," by A. Shama, J. Mander, B. Blabac and S. Chen, 12/31/01, (PB2002-107950, A13, MF-A03).

MCEER-02-0001 "Assessment of Performance of Bolu Viaduct in the 1999 Duzce Earthquake in Turkey" by P.C. Roussis, M.C. Constantinou, M. Erdik, E. Durukal and M. Dicleli, 5/8/02, (PB2003-100883, A08, MF-A02).

MCEER-02-0002 "Seismic Behavior of Rail Counterweight Systems of Elevators in Buildings," by M.P. Singh, Rildova and L.E. Suarez, 5/27/02. (PB2003-100882, A11, MF-A03).

MCEER-02-0003 "Development of Analysis and Design Procedures for Spread Footings," by G. Mylonakis, G. Gazetas, S. Nikolaou and A. Chauncey, 10/02/02, (PB2004-101636, A13, MF-A03, CD-A13).

MCEER-02-0004 "Bare-Earth Algorithms for Use with SAR and LIDAR Digital Elevation Models," by C.K. Huyck, R.T. Eguchi and B. Houshmand, 10/16/02, (PB2004-101637, A07, CD-A07).

MCEER-02-0005 "Review of Energy Dissipation of Compression Members in Concentrically Braced Frames," by K.Lee and M. Bruneau, 10/18/02, (PB2004-101638, A10, CD-A10).

MCEER-03-0001 "Experimental Investigation of Light-Gauge Steel Plate Shear Walls for the Seismic Retrofit of Buildings" by J. Berman and M. Bruneau, 5/2/03, (PB2004-101622, A10, MF-A03, CD-A10).

MCEER-03-0002 "Statistical Analysis of Fragility Curves," by M. Shinozuka, M.Q. Feng, H. Kim, T. Uzawa and T. Ueda, 6/16/03, (PB2004-101849, A09, CD-A09).

MCEER-03-0003 "Proceedings of the Eighth U.S.-Japan Workshop on Earthquake Resistant Design f Lifeline Facilities and Countermeasures Against Liquefaction," edited by M. Hamada, J.P. Bardet and T.D. O'Rourke, 6/30/03, (PB2004-104386, A99, CD-A99).

MCEER-03-0004 "Proceedings of the PRC-US Workshop on Seismic Analysis and Design of Special Bridges," edited by L.C. Fan and G.C. Lee, 7/15/03, (PB2004-104387, A14, CD-A14).

MCEER-03-0005 "Urban Disaster Recovery: A Framework and Simulation Model," by S.B. Miles and S.E. Chang, 7/25/03, (PB2004-104388, A07, CD-A07).

MCEER-03-0006 "Behavior of Underground Piping Joints Due to Static and Dynamic Loading," by R.D. Meis, M. Maragakis and R. Siddharthan, 11/17/03, (PB2005-102194, A13, MF-A03, CD-A00).

MCEER-04-0001 "Experimental Study of Seismic Isolation Systems with Emphasis on Secondary System Response and Verification of Accuracy of Dynamic Response History Analysis Methods," by E. Wolff and M. Constantinou, 1/16/04 (PB2005-102195, A99, MF-E08, CD-A00).

MCEER-04-0002 "Tension, Compression and Cyclic Testing of Engineered Cementitious Composite Materials," by K. Kesner and S.L. Billington, 3/1/04, (PB2005-102196, A08, CD-A08).

MCEER-04-0003 "Cyclic Testing of Braces Laterally Restrained by Steel Studs to Enhance Performance During Earthquakes," by O.C. Celik, J.W. Berman and M. Bruneau, 3/16/04, (PB2005-102197, A13, MF-A03, CD-A00).

MCEER-04-0004 "Methodologies for Post Earthquake Building Damage Detection Using SAR and Optical Remote Sensing: Application to the August 17, 1999 Marmara, Turkey Earthquake," by C.K. Huyck, B.J. Adams, S. Cho, R.T. Eguchi, B. Mansouri and B. Houshmand, 6/15/04, (PB2005-104888, A10, CD-A00).

MCEER-04-0005 "Nonlinear Structural Analysis Towards Collapse Simulation: A Dynamical Systems Approach," by M.V. Sivaselvan and A.M. Reinhorn, 6/16/04, (PB2005-104889, A11, MF-A03, CD-A00).

MCEER-04-0006 "Proceedings of the Second PRC-US Workshop on Seismic Analysis and Design of Special Bridges," edited by G.C. Lee and L.C. Fan, 6/25/04, (PB2005-104890, A16, CD-A00).

MCEER-04-0007 "Seismic Vulnerability Evaluation of Axially Loaded Steel Built-up Laced Members," by K. Lee and M. Bruneau, 6/30/04, (PB2005-104891, A16, CD-A00).

MCEER-04-0008 "Evaluation of Accuracy of Simplified Methods of Analysis and Design of Buildings with Damping Systems for Near-Fault and for Soft-Soil Seismic Motions," by E.A. Pavlou and M.C. Constantinou, 8/16/04, (PB2005-104892, A08, MF-A02, CD-A00).

MCEER-04-0009 "Assessment of Geotechnical Issues in Acute Care Facilities in California," by M. Lew, T.D. O'Rourke, R. Dobry and M. Koch, 9/15/04, (PB2005-104893, A08, CD-A00).

MCEER-04-0010 "Scissor-Jack-Damper Energy Dissipation System," by A.N. Sigaher-Boyle and M.C. Constantinou, 12/1/04 (PB2005-108221).

MCEER-04-0011 "Seismic Retrofit of Bridge Steel Truss Piers Using a Controlled Rocking Approach," by M. Pollino and M. Bruneau, 12/20/04 (PB2006-105795).

MCEER-05-0001 "Experimental and Analytical Studies of Structures Seismically Isolated with an Uplift-Restraint Isolation System," by P.C. Roussis and M.C. Constantinou, 1/10/05 (PB2005-108222).

MCEER-05-0002 "A Versatile Experimentation Model for Study of Structures Near Collapse Applied to Seismic Evaluation of Irregular Structures," by D. Kusumastuti, A.M. Reinhorn and A. Rutenberg, 3/31/05 (PB2006-101523).

MCEER-05-0003 "Proceedings of the Third PRC-US Workshop on Seismic Analysis and Design of Special Bridges," edited by L.C. Fan and G.C. Lee, 4/20/05, (PB2006-105796).

MCEER-05-0004 "Approaches for the Seismic Retrofit of Braced Steel Bridge Piers and Proof-of-Concept Testing of an Eccentrically Braced Frame with Tubular Link," by J.W. Berman and M. Bruneau, 4/21/05 (PB2006-101524).

MCEER-05-0005 "Simulation of Strong Ground Motions for Seismic Fragility Evaluation of Nonstructural Components in Hospitals," by A. Wanitkorkul and A. Filiatrault, 5/26/05 (PB2006-500027).

MCEER-05-0006 "Seismic Safety in California Hospitals: Assessing an Attempt to Accelerate the Replacement or Seismic Retrofit of Older Hospital Facilities," by D.J. Alesch, L.A. Arendt and W.J. Petak, 6/6/05 (PB2006-105794).

MCEER-05-0007 "Development of Seismic Strengthening and Retrofit Strategies for Critical Facilities Using Engineered Cementitious Composite Materials," by K. Kesner and S.L. Billington, 8/29/05 (PB2006-111701).

MCEER-05-0008 "Experimental and Analytical Studies of Base Isolation Systems for Seismic Protection of Power Transformers," by N. Murota, M.Q. Feng and G-Y. Liu, 9/30/05 (PB2006-111702).

MCEER-05-0009 "3D-BASIS-ME-MB: Computer Program for Nonlinear Dynamic Analysis of Seismically Isolated Structures," by P.C. Tsopelas, P.C. Roussis, M.C. Constantinou, R. Buchanan and A.M. Reinhorn, 10/3/05 (PB2006-111703).

MCEER-05-0010 "Steel Plate Shear Walls for Seismic Design and Retrofit of Building Structures," by D. Vian and M. Bruneau, 12/15/05 (PB2006-111704).

MCEER-05-0011 "The Performance-Based Design Paradigm," by M.J. Astrella and A. Whittaker, 12/15/05 (PB2006-111705).

MCEER-06-0001 "Seismic Fragility of Suspended Ceiling Systems," H. Badillo-Almaraz, A.S. Whittaker, A.M. Reinhorn and G.P. Cimellaro, 2/4/06 (PB2006-111706).

MCEER-06-0002 "Multi-Dimensional Fragility of Structures," by G.P. Cimellaro, A.M. Reinhorn and M. Bruneau, 3/1/06 (PB2007-106974, A09, MF-A02, CD A00).

MCEER-06-0003 "Built-Up Shear Links as Energy Dissipators for Seismic Protection of Bridges," by P. Dusicka, A.M. Itani and I.G. Buckle, 3/15/06 (PB2006-111708).

MCEER-06-0004 "Analytical Investigation of the Structural Fuse Concept," by R.E. Vargas and M. Bruneau, 3/16/06 (PB2006-111709).

MCEER-06-0005 "Experimental Investigation of the Structural Fuse Concept," by R.E. Vargas and M. Bruneau, 3/17/06 (PB2006-111710).

MCEER-06-0006 "Further Development of Tubular Eccentrically Braced Frame Links for the Seismic Retrofit of Braced Steel Truss Bridge Piers," by J.W. Berman and M. Bruneau, 3/27/06 (PB2007-105147).

MCEER-06-0007 "REDARS Validation Report," by S. Cho, C.K. Huyck, S. Ghosh and R.T. Eguchi, 8/8/06 (PB2007-106983).

MCEER-06-0008 "Review of Current NDE Technologies for Post-Earthquake Assessment of Retrofitted Bridge Columns," by J.W. Song, Z. Liang and G.C. Lee, 8/21/06 (PB2007-106984).

MCEER-06-0009 "Liquefaction Remediation in Silty Soils Using Dynamic Compaction and Stone Columns," by S. Thevanayagam, G.R. Martin, R. Nashed, T. Shenthan, T. Kanagalingam and N. Ecemis, 8/28/06 (PB2007-106985).

MCEER-06-0010 "Conceptual Design and Experimental Investigation of Polymer Matrix Composite Infill Panels for Seismic Retrofitting," by W. Jung, M. Chiewanichakorn and A.J. Aref, 9/21/06 (PB2007-106986).

MCEER-06-0011 "A Study of the Coupled Horizontal-Vertical Behavior of Elastomeric and Lead-Rubber Seismic Isolation Bearings," by G.P. Warn and A.S. Whittaker, 9/22/06 (PB2007-108679).

MCEER-06-0012 "Proceedings of the Fourth PRC-US Workshop on Seismic Analysis and Design of Special Bridges: Advancing Bridge Technologies in Research, Design, Construction and Preservation," Edited by L.C. Fan, G.C. Lee and L. Ziang, 10/12/06 (PB2007-109042).

MCEER-06-0013 "Cyclic Response and Low Cycle Fatigue Characteristics of Plate Steels," by P. Dusicka, A.M. Itani and I.G. Buckle, 11/1/06 06 (PB2007-106987).

MCEER-06-0014 "Proceedings of the Second US-Taiwan Bridge Engineering Workshop," edited by W.P. Yen, J. Shen, J-Y. Chen and M. Wang, 11/15/06 (PB2008-500041).

MCEER-06-0015 "User Manual and Technical Documentation for the REDARS™ Import Wizard," by S. Cho, S. Ghosh, C.K. Huyck and S.D. Werner, 11/30/06 (PB2007-114766).

MCEER-06-0016 "Hazard Mitigation Strategy and Monitoring Technologies for Urban and Infrastructure Public Buildings: Proceedings of the China-US Workshops," edited by X.Y. Zhou, A.L. Zhang, G.C. Lee and M. Tong, 12/12/06 (PB2008-500018).

MCEER-07-0001 "Static and Kinetic Coefficients of Friction for Rigid Blocks," by C. Kafali, S. Fathali, M. Grigoriu and A.S. Whittaker, 3/20/07 (PB2007-114767).

MCEER-07-0002 "Hazard Mitigation Investment Decision Making: Organizational Response to Legislative Mandate," by L.A. Arendt, D.J. Alesch and W.J. Petak, 4/9/07 (PB2007-114768).

MCEER-07-0003 "Seismic Behavior of Bidirectional-Resistant Ductile End Diaphragms with Unbonded Braces in Straight or Skewed Steel Bridges," by O. Celik and M. Bruneau, 4/11/07 (PB2008-105141).

MCEER-07-0004 “Modeling Pile Behavior in Large Pile Groups Under Lateral Loading,” by A.M. Dodds and G.R. Martin, 4/16/07(PB2008-105142).

MCEER-07-0005 “Experimental Investigation of Blast Performance of Seismically Resistant Concrete-Filled Steel Tube Bridge Piers,” by S. Fujikura, M. Bruneau and D. Lopez-Garcia, 4/20/07 (PB2008-105143).

MCEER-07-0006 “Seismic Analysis of Conventional and Isolated Liquefied Natural Gas Tanks Using Mechanical Analogs,” by I.P. Christovasilis and A.S. Whittaker, 5/1/07.

MCEER-07-0007 “Experimental Seismic Performance Evaluation of Isolation/Restraint Systems for Mechanical Equipment – Part 1: Heavy Equipment Study,” by S. Fathali and A. Filiatrault, 6/6/07 (PB2008-105144).

MCEER-07-0008 “Seismic Vulnerability of Timber Bridges and Timber Substructures,” by A.A. Sharma, J.B. Mander, I.M. Friedland and D.R. Allicock, 6/7/07 (PB2008-105145).

MCEER-07-0009 “Experimental and Analytical Study of the XY-Friction Pendulum (XY-FP) Bearing for Bridge Applications,” by C.C. Marin-Artieda, A.S. Whittaker and M.C. Constantinou, 6/7/07 (PB2008-105191).

MCEER-07-0010 “Proceedings of the PRC-US Earthquake Engineering Forum for Young Researchers,” Edited by G.C. Lee and X.Z. Qi, 6/8/07 (PB2008-500058).

MCEER-07-0011 “Design Recommendations for Perforated Steel Plate Shear Walls,” by R. Purba and M. Bruneau, 6/18/07, (PB2008-105192).

MCEER-07-0012 “Performance of Seismic Isolation Hardware Under Service and Seismic Loading,” by M.C. Constantinou, A.S. Whittaker, Y. Kalpakidis, D.M. Fenz and G.P. Warn, 8/27/07, (PB2008-105193).

MCEER-07-0013 “Experimental Evaluation of the Seismic Performance of Hospital Piping Subassemblies,” by E.R. Goodwin, E. Maragakis and A.M. Itani, 9/4/07, (PB2008-105194).

MCEER-07-0014 “A Simulation Model of Urban Disaster Recovery and Resilience: Implementation for the 1994 Northridge Earthquake,” by S. Miles and S.E. Chang, 9/7/07, (PB2008-106426).

MCEER-07-0015 “Statistical and Mechanistic Fragility Analysis of Concrete Bridges,” by M. Shinozuka, S. Banerjee and S-H. Kim, 9/10/07, (PB2008-106427).

MCEER-07-0016 “Three-Dimensional Modeling of Inelastic Buckling in Frame Structures,” by M. Schachter and AM. Reinhorn, 9/13/07, (PB2008-108125).

MCEER-07-0017 “Modeling of Seismic Wave Scattering on Pile Groups and Caissons,” by I. Po Lam, H. Law and C.T. Yang, 9/17/07 (PB2008-108150).

MCEER-07-0018 “Bridge Foundations: Modeling Large Pile Groups and Caissons for Seismic Design,” by I. Po Lam, H. Law and G.R. Martin (Coordinating Author), 12/1/07 (PB2008-111190).

MCEER-07-0019 “Principles and Performance of Roller Seismic Isolation Bearings for Highway Bridges,” by G.C. Lee, Y.C. Ou, Z. Liang, T.C. Niu and J. Song, 12/10/07 (PB2009-110466).

MCEER-07-0020 “Centrifuge Modeling of Permeability and Pinning Reinforcement Effects on Pile Response to Lateral Spreading,” by L.L Gonzalez-Lagos, T. Abdoun and R. Dobry, 12/10/07 (PB2008-111191).

MCEER-07-0021 “Damage to the Highway System from the Pisco, Perú Earthquake of August 15, 2007,” by J.S. O’Connor, L. Mesa and M. Nykamp, 12/10/07, (PB2008-108126).

MCEER-07-0022 “Experimental Seismic Performance Evaluation of Isolation/Restraint Systems for Mechanical Equipment – Part 2: Light Equipment Study,” by S. Fathali and A. Filiatrault, 12/13/07 (PB2008-111192).

MCEER-07-0023 “Fragility Considerations in Highway Bridge Design,” by M. Shinozuka, S. Banerjee and S.H. Kim, 12/14/07 (PB2008-111193).

MCEER-07-0024 "Performance Estimates for Seismically Isolated Bridges," by G.P. Warn and A.S. Whittaker, 12/30/07 (PB2008-112230).

MCEER-08-0001 "Seismic Performance of Steel Girder Bridge Superstructures with Conventional Cross Frames," by L.P. Carden, A.M. Itani and I.G. Buckle, 1/7/08, (PB2008-112231).

MCEER-08-0002 "Seismic Performance of Steel Girder Bridge Superstructures with Ductile End Cross Frames with Seismic Isolators," by L.P. Carden, A.M. Itani and I.G. Buckle, 1/7/08 (PB2008-112232).

MCEER-08-0003 "Analytical and Experimental Investigation of a Controlled Rocking Approach for Seismic Protection of Bridge Steel Truss Piers," by M. Pollino and M. Bruneau, 1/21/08 (PB2008-112233).

MCEER-08-0004 "Linking Lifeline Infrastructure Performance and Community Disaster Resilience: Models and Multi-Stakeholder Processes," by S.E. Chang, C. Pasion, K. Tatebe and R. Ahmad, 3/3/08 (PB2008-112234).

MCEER-08-0005 "Modal Analysis of Generally Damped Linear Structures Subjected to Seismic Excitations," by J. Song, Y-L. Chu, Z. Liang and G.C. Lee, 3/4/08 (PB2009-102311).

MCEER-08-0006 "System Performance Under Multi-Hazard Environments," by C. Kafali and M. Grigoriu, 3/4/08 (PB2008-112235).

MCEER-08-0007 "Mechanical Behavior of Multi-Spherical Sliding Bearings," by D.M. Fenz and M.C. Constantinou, 3/6/08 (PB2008-112236).

MCEER-08-0008 "Post-Earthquake Restoration of the Los Angeles Water Supply System," by T.H.P. Tabucchi and R.A. Davidson, 3/7/08 (PB2008-112237).

MCEER-08-0009 "Fragility Analysis of Water Supply Systems," by A. Jacobson and M. Grigoriu, 3/10/08 (PB2009-105545).

MCEER-08-0010 "Experimental Investigation of Full-Scale Two-Story Steel Plate Shear Walls with Reduced Beam Section Connections," by B. Qu, M. Bruneau, C-H. Lin and K-C. Tsai, 3/17/08 (PB2009-106368).

MCEER-08-0011 "Seismic Evaluation and Rehabilitation of Critical Components of Electrical Power Systems," S. Ersoy, B. Feizi, A. Ashrafi and M. Ala Saadeghvaziri, 3/17/08 (PB2009-105546).

MCEER-08-0012 "Seismic Behavior and Design of Boundary Frame Members of Steel Plate Shear Walls," by B. Qu and M. Bruneau, 4/26/08 . (PB2009-106744).

MCEER-08-0013 "Development and Appraisal of a Numerical Cyclic Loading Protocol for Quantifying Building System Performance," by A. Filiatrault, A. Wanitkorkul and M. Constantinou, 4/27/08 (PB2009-107906).

MCEER-08-0014 "Structural and Nonstructural Earthquake Design: The Challenge of Integrating Specialty Areas in Designing Complex, Critical Facilities," by W.J. Petak and D.J. Alesch, 4/30/08 (PB2009-107907).

MCEER-08-0015 "Seismic Performance Evaluation of Water Systems," by Y. Wang and T.D. O'Rourke, 5/5/08 (PB2009-107908).

MCEER-08-0016 "Seismic Response Modeling of Water Supply Systems," by P. Shi and T.D. O'Rourke, 5/5/08 (PB2009-107910).

MCEER-08-0017 "Numerical and Experimental Studies of Self-Centering Post-Tensioned Steel Frames," by D. Wang and A. Filiatrault, 5/12/08 (PB2009-110479).

MCEER-08-0018 "Development, Implementation and Verification of Dynamic Analysis Models for Multi-Spherical Sliding Bearings," by D.M. Fenz and M.C. Constantinou, 8/15/08 (PB2009-107911).

MCEER-08-0019 "Performance Assessment of Conventional and Base Isolated Nuclear Power Plants for Earthquake Blast Loadings," by Y.N. Huang, A.S. Whittaker and N. Luco, 10/28/08 (PB2009-107912).

MCEER-08-0020 "Remote Sensing for Resilient Multi-Hazard Disaster Response – Volume I: Introduction to Damage Assessment Methodologies," by B.J. Adams and R.T. Eguchi, 11/17/08 (PB2010-102695).

MCEER-08-0021 "Remote Sensing for Resilient Multi-Hazard Disaster Response – Volume II: Counting the Number of Collapsed Buildings Using an Object-Oriented Analysis: Case Study of the 2003 Bam Earthquake," by L. Gusella, C.K. Huyck and B.J. Adams, 11/17/08 (PB2010-100925).

MCEER-08-0022 "Remote Sensing for Resilient Multi-Hazard Disaster Response – Volume III: Multi-Sensor Image Fusion Techniques for Robust Neighborhood-Scale Urban Damage Assessment," by B.J. Adams and A. McMillan, 11/17/08 (PB2010-100926).

MCEER-08-0023 "Remote Sensing for Resilient Multi-Hazard Disaster Response – Volume IV: A Study of Multi-Temporal and Multi-Resolution SAR Imagery for Post-Katrina Flood Monitoring in New Orleans," by A. McMillan, J.G. Morley, B.J. Adams and S. Chesworth, 11/17/08 (PB2010-100927).

MCEER-08-0024 "Remote Sensing for Resilient Multi-Hazard Disaster Response – Volume V: Integration of Remote Sensing Imagery and VIEWS^{TM} Field Data for Post-Hurricane Charley Building Damage Assessment," by J.A. Womble, K. Mehta and B.J. Adams, 11/17/08 (PB2009-115532).

MCEER-08-0025 "Building Inventory Compilation for Disaster Management: Application of Remote Sensing and Statistical Modeling," by P. Sarabandi, A.S. Kiremidjian, R.T. Eguchi and B. J. Adams, 11/20/08 (PB2009-110484).

MCEER-08-0026 "New Experimental Capabilities and Loading Protocols for Seismic Qualification and Fragility Assessment of Nonstructural Systems," by R. Retamales, G. Mosqueda, A. Filiatrault and A. Reinhorn, 11/24/08 (PB2009-110485).

MCEER-08-0027 "Effects of Heating and Load History on the Behavior of Lead-Rubber Bearings," by I.V. Kalpakidis and M.C. Constantinou, 12/1/08 (PB2009-115533).

MCEER-08-0028 "Experimental and Analytical Investigation of Blast Performance of Seismically Resistant Bridge Piers," by S.Fujikura and M. Bruneau, 12/8/08 (PB2009-115534).

MCEER-08-0029 "Evolutionary Methodology for Aseismic Decision Support," by Y. Hu and G. Dargush, 12/15/08.

MCEER-08-0030 "Development of a Steel Plate Shear Wall Bridge Pier System Conceived from a Multi-Hazard Perspective," by D. Keller and M. Bruneau, 12/19/08 (PB2010-102696).

MCEER-09-0001 "Modal Analysis of Arbitrarily Damped Three-Dimensional Linear Structures Subjected to Seismic Excitations," by Y.L. Chu, J. Song and G.C. Lee, 1/31/09 (PB2010-100922).

MCEER-09-0002 "Air-Blast Effects on Structural Shapes," by G. Ballantyne, A.S. Whittaker, A.J. Aref and G.F. Dargush, 2/2/09 (PB2010-102697).

MCEER-09-0003 "Water Supply Performance During Earthquakes and Extreme Events," by A.L. Bonneau and T.D. O'Rourke, 2/16/09 (PB2010-100923).

MCEER-09-0004 "Generalized Linear (Mixed) Models of Post-Earthquake Ignitions," by R.A. Davidson, 7/20/09 (PB2010-102698).

MCEER-09-0005 "Seismic Testing of a Full-Scale Two-Story Light-Frame Wood Building: NEESWood Benchmark Test," by I.P. Christovasilis, A. Filiatrault and A. Wanitkorkul, 7/22/09.

MCEER-09-0006 "IDARC2D Version 7.0: A Program for the Inelastic Damage Analysis of Structures," by A.M. Reinhorn, H. Roh, M. Sivaselvan, S.K. Kunnath, R.E. Valles, A. Madan, C. Li, R. Lobo and Y.J. Park, 7/28/09 (PB2010-103199).

MCEER-09-0007 "Enhancements to Hospital Resiliency: Improving Emergency Planning for and Response to Hurricanes," by D.B. Hess and L.A. Arendt, 7/30/09 (PB2010-100924).

MCEER-09-0008 "Assessment of Base-Isolated Nuclear Structures for Design and Beyond-Design Basis Earthquake Shaking," by Y.N. Huang, A.S. Whittaker, R.P. Kennedy and R.L. Mayes, 8/20/09 (PB2010-102699).

MCEER-09-0009 "Quantification of Disaster Resilience of Health Care Facilities," by G.P. Cimellaro, C. Fumo, A.M Reinhorn and M. Bruneau, 9/14/09.

MCEER-09-0010 "Performance-Based Assessment and Design of Squat Reinforced Concrete Shear Walls," by C.K. Gulec and A.S. Whittaker, 9/15/09 (PB2010-102700).

MCEER-09-0011 "Proceedings of the Fourth US-Taiwan Bridge Engineering Workshop," edited by W.P. Yen, J.J. Shen, T.M. Lee and R.B. Zheng, 10/27/09 (PB2010-500009).

MCEER-09-0012 "Proceedings of the Special International Workshop on Seismic Connection Details for Segmental Bridge Construction," edited by W. Phillip Yen and George C. Lee, 12/21/09.

MCEER-10-0001 "Direct Displacement Procedure for Performance-Based Seismic Design of Multistory Woodframe Structures," by W. Pang and D. Rosowsky, 4/26/10.

MCEER-10-0002 "Simplified Direct Displacement Design of Six-Story NEESWood Capstone Building and Pre-Test Seismic Performance Assessment," by W. Pang, D. Rosowsky, J. van de Lindt and S. Pei, 5/28/10.

MCEER-10-0003 "Integration of Seismic Protection Systems in Performance-Based Seismic Design of Woodframed Structures," by J.K. Shinde and M.D. Symans, 6/18/10.

MCEER-10-0004 "Modeling and Seismic Evaluation of Nonstructural Components: Testing Frame for Experimental Evaluation of Suspended Ceiling Systems," by A.M. Reinhorn, K.P. Ryu and G. Maddaloni, 6/30/10.

MCEER-10-0005 "Analytical Development and Experimental Validation of a Structural-Fuse Bridge Pier Concept," by S. El-Bahey and M. Bruneau, 10/1/10.

MCEER-10-0006 "A Framework for Defining and Measuring Resilience at the Community Scale: The PEOPLES Resilience Framework," by C.S. Renschler, A.E. Frazier, L.A. Arendt, G.P. Cimellaro, A.M. Reinhorn and M. Bruneau, 10/8/10.

MCEER-10-0007 "Impact of Horizontal Boundary Elements Design on Seismic Behavior of Steel Plate Shear Walls," by R. Purba and M. Bruneau, 11/14/10.

MCEER-10-0008 "Seismic Testing of a Full-Scale Mid-Rise Building: The NEESWood Capstone Test," by S. Pei, J.W. van de Lindt, S.E. Pryor, H. Shimizu, H. Isoda and D.R. Rammer, 12/1/10.

MCEER-10-0009 "Modeling the Effects of Detonations of High Explosives to Inform Blast-Resistant Design," by P. Sherkar, A.S. Whittaker and A.J. Aref, 12/1/10.

MCEER-10-0010 "L'Aquila Earthquake of April 6, 2009 in Italy: Rebuilding a Resilient City to Multiple Hazards," by G.P. Cimellaro, I.P. Christovasilis, A.M. Reinhorn, A. De Stefano and T. Kirova, 12/29/10.

MCEER-11-0001 "Numerical and Experimental Investigation of the Seismic Response of Light-Frame Wood Structures," by I.P. Christovasilis and A. Filiatrault, 8/8/11.

MCEER

EARTHQUAKE ENGINEERING TO EXTREME EVENTS

University at Buffalo, The State University of New York
Red Jacket Quadrangle ▪ Buffalo, New York 14261
Phone: (716) 645-3391 ▪ Fax: (716) 645-3399
E-mail: *mceer@buffalo.edu* ▪ WWW Site *http://mceer.buffalo.edu*

University at Buffalo *The State University of New York*

ISSN 1520-295X